PB2007-108150

SEISMIC PERFORMANCE OF RC BRIDGE FRAMES WITH ARCHITECTURAL-FLARED COLUMNS

Report No. CCEER 03-03

Hisham Nada
David Sanders
M. Saiid Saiidi

A Report for the
California Department of Transportation
Sacramento, California
under contract 59A0069

January 2003

Center for Earthquake Engineering Research
Department of Civil Engineering/258
University of Nevada
Reno, Nevada 89557

DISCLAIMER

❖ This document has been reproduced from the best copy furnished by the sponsoring agency.

ABSTRACT

Design of flared columns to resist earthquake loading is a complicated issue due to the changing cross section along the column length. It was believed that if the flares had low longitudinal and transverse reinforcement ratios, they would fail during earthquakes. Therefore, the column core would be the element remaining to resist the earthquake. Past earthquakes have shown that flared columns are susceptible to premature shear failures. In the 1994 Northridge Earthquake, shear failures were caused by plastic hinge formation at the base of the flare and a subsequent increase in the level of column shear demand above design levels. This study presents an experimental and analytical study that is examining new details for flared columns, base hinges and joints. The purpose is to maintain the aesthetic value of the flare without impacting the system performance. The primary feature is a gap at the top of the column and the amount of transverse flare reinforcement. Four bents were tested using the shake table to examine dynamic effects as well as column and beam interaction. The test specimens had different amounts of confining reinforcement in the flare. An analytical non-linear finite element analysis study was conducted using the DIANA program to explore different parameters effects. A strut-and-tie model was created based on the finite element analysis that is capable of predicting the yielding, maximum load carrying capacity of system and the stresses in different parts of the structure.

ACKNOWLEDGEMENT

The research described in this report was carried out under CALTRANS Grant No. 59A0069. Conclusions and recommendations of this report are those of the authors only, and should not be construed to be endorsed by CALTRANS.

Special appreciation is deserved for Dr. Saad El-Azazy, the Caltrans contract monitor for his insight, advice, assistance and team atmosphere that was part of this project. Many other Caltrans engineers also participated in this project and their assistance is also greatly appreciated. Thanks are also due to University of Nevada personnel such as Dr. Patrick Laplace, Paul Lucas, and Erik Reinhardt for their efforts in the structures laboratory. This report is based on the dissertation of Dr. Hisham Nada.

TABLE OF CONTENTS

LIST OF TABLES

LIST OF FIGURES

1. INTRODUCTION

1.1. GENERAL PRESPECTIVE

The California State Highway system has more than 12,000 bridges in its inventory and an additional 11,500 city and county bridges. The majority of these bridges were constructed prior to San Fernando Earthquake of 1971, which initiated a major change in bridge design philosophy. Caltrans has been heavily involved in research and bridge retrofit programs since 1971[3].

Past earthquakes have shown that flared columns have poor behavior due to the large increase of column flexural capacity at the top of the column. The increased capacity can cause the plastic hinge region to shift away from the column-beam interface into the column. This causes the column to behave like a much shorter column and therefore have increased shear demand. The shifting of the hinge and the larger shear demand was not included in many previous designs and has led to brittle shear column failures, which, may lead to significant damage and/or complete collapse of the bridge.

One of the examples that show the poor seismic behavior of flared columns was the damage occurred on State Route 118 at San Fernando Mission Blvd. and Gothic Ave. (Caltrans Bridge No. 53-2205), Fig. 1-1. Because the bridge was designed in 1972, after the San Fernando earthquake, the bridge contains improved seismic details. Most notably, the spiral hoops in the bridge columns were closely spaced. Nonetheless, the columns of the Mission-Gothic Undercrossing suffered severe damage in the Northridge earthquake, 1994, and one of the two parallel spans partially collapsed[8] Fig. 1-2.

The most important reason of the columns failure was their geometry. The columns were all relatively short, roughly 7200 mm (24 ft) by 1800 mm (6 ft) across, making an aspect ratio of only 4:1. However the columns also featured architectural flares at the tops, roughly 3600 mm (12 ft) tall. These flares were intended to be non-structural features of the columns. The columns initially suffered severe shear damage, followed by crushing of a number of columns in compression. Although unseating at abutments did occur, this was probably a secondary effect, as the seats lengths were generous by current standards. Failure was probably initiated by damage to the columns. In this case the failure of columns has important theoretical implications, as the columns of this bridge contained quantities of lateral reinforcement similar to those required by current seismic standards[8]. The flares did not fail during the earthquake. An experimental and analytical study of bridge columns with structural flares revealed that architectural flares with minimum longitudinal reinforcement behave essentially the same as structural flares under static[24] and dynamic[25] loads.

The lightly reinforced flares contributed to increasing the column flexural capacity[3]. To solve this problem, Caltrans has developed new details attempting to separate the flared portion of the column from the overall flexural stiffness and capacity of the column. This is achieved by separating the flare from the bent cap using a gap between the top of the flare and the beam bottom surface. Caltrans recommends that the minimum gap thickness shall be 2.0 inches in the prototype unless the calculations based on curvature analysis shows that a higher value[5] is required. The recommendations state that a higher amount of lateral flare reinforcement should be provided at the top. A detailed description of the recommendation and its implementations are included in Chapter 2.

Caltrans recommendations came as a result of single column slow-cyclic tests and not on system bent tests[3]. This research is the only study made to evaluate the dynamic performance of flared columns with gaps. Ten, forty-percent scale model columns were tested. Four test units were models of columns of the Mission and Gothic undercrossing of SR-118 in Los Angeles County. The second phase of testing consisted of a more lightly reinforced flares. For each phase, a prismatic reference column, as-built/as-designed column, and retrofit/improved flare designs were tested. In the final two test units, increased transverse reinforcement was incorporated into the flares to keep the damage down to acceptable levels even at large seismic drifts. The as-built and as-designed test units showed significant stiffness and strength contributions from the flares with plastic hinges forming away from the over-strengthened soffits. This resulted in increased shear and moment transfer into the cap beam and failures at decreased drifts and ductility. The seismic performance problems were solved with the retrofit and improved new flare design solutions, where the flares were decoupled from the cap beams[3]. Some of the specimens, the gap was not wide enough to prevent the gap from closing. The specimens that had wide gaps didn't have gap closure and hence, lower level of damage. Figs. 1-3 shows the load displacement curves of the one specimen that had gap closure, while Fig. 1-4 shows the load-displacement curve for another one that didn't have gap closure.

1.2 OBJECTIVES

The objectives of this research can be summarized as follows.

1. To experimentally verify the seismic behavior of the current Caltrans detail of

providing gap between the flare and the beam and how it affects the overall system performance.

2. To investigate the effect of the gap on short flared columns.
3. To investigate the need for the high transverse confinement steel associated with the Caltrans recommendations.
4. To conduct an analytical study using non-linear finite element analysis to investigate the following:
    a. The gap width effect on the overall frame performance,
    b. The base hinge dimension effect on the overall frame performance, and
    c. A method of correction to account for the P-Δ effect.
5. To develop a strut-and-tie model that enables improves understanding of the element behavior and capable of predicting the system capacity.

1.3 SCOPE OF WORK

The first three objectives were achieved by constructing four $1/5^{th}$-scale frame bents modeled from recently designed flared columns. The specimens were divided into two categories: tall columns and short columns. Two different flare confinement ratios were used in each category to investigate the need of the high confinement in the top portion of the flare. All specimens were tested by simulating the 1994 Sylmar Northridge Earthquake using the shake table. The tests were conducted in the large-scale structures laboratory at the University of Nevada, Reno.

The fourth objective was achieved by conducting a non-linear finite element analysis using the program DIANA. Comparisons were made between the finite element analysis

and the experimental results. The results were used to develop a strut-and-tie model.

1.4 DOCUMENT LAYOUT

This document contains 6 more chapters as follows.

- Chapter 2 “Seismic Evaluation of R/C Bents with Flare”:

  This chapter contains the survey made in order to obtain a prototype that was used in creating the models. The preliminary design and analysis is also included.

- Chapter 3 “Experimental Program”:

  This chapter includes the construction process and data as well as the loading program of the test.

- Chapter 4 “Testing and Results”:

  The processed data and measurements are included in this chapter with comparison between the specimens.

- Chapter 5 “Post-Test Analysis”:

  The results of the finite element analysis using DIANA program and the parametric study are included in this chapter.

- Chapter 6, “Strut-and-Tie Model”:

  In this chapter a strut-and-tie model is developed and verified using the experimental and finite element analysis results.

- Chapter 7 “Summary, Conclusions, and Recommendations”:

  This chapter summarizes the work performed in this research, condenses the findings and provides important recommendations for analysis and design.

2. SEISMIC EVALUATION OF R/C BENTS WITH FLARE

2.1. INTRODUCTION

In this chapter, the factors contributing in the choice of specimens and their configurations will be discussed. The survey that was conducted on existing bridges will be presented. This survey was used to create a prototype, which was scaled to form the models. In order to pre-analyze the specimens, a non-linear finite element analysis was performed for the models. The analysis was followed by a design using the current code recommendations and Caltrans Seismic Specifications[5]. Finally, a seismic analysis was performed to identify the test plan for each specimen.

2.2. CODE PROVISIONS

As was described in Chapter 1, flared columns tend to fail due to a shifting of the plastic hinges within the flare height accompanied by an increase in the shear level. A new detail was proposed by Caltrans to prevent the flares from contributing to the column stiffness and forces the plastic hinge to occur at the top of the column. The idea of the proposed detail is to simply isolate the flare from the beam by creating a gap between the flare and the bottom of the beam that is filled with a compressible material. Fig. 2-1a shows the new proposed detail, and Fig. 2-1b shows the reinforcement detail of the flare region. The new procedure of detailing the flare region is accompanied by recommendations that were obtained from previous pushover tests[3]. The previous tests were single columns without investigating the effect of the beam.

The following points summarize the design provisions[5]:

- For analysis and design of different bent elements, the specifications recommend the use of the column core only and to ignore the existence of the flare.
- Typically the thickness of the flare gap shall be 50 mm (2 inches). However, if significant relative rotation between the cap and the column is expected, then the required gap thickness to accommodate this rotation should be calculated and provided.
- The longitudinal flare reinforcement is nominal. The maximum spacing between longitudinal flare reinforcement shall not exceed 450 mm (18 inches) and the spacing shall not be less than 150 mm (6 inches).
- The transverse flare reinforcement ratio in the upper 1/3 of the flare height is ρ_h=0.45%±0.05 while that ratio for the lower 2/3 of the flare height is ρ_h=0.075%±0.025.

Where;

$\rho_h = 2 A_b / s D$ (2.1)

s = Tie spacing

D = Diameter of the non-flared part of the column

A_b = Area of ties

2.3. PROTOTYPE SELECTION

A prototype was created using the dimensions of existing bridges. This was used as the basis for the model. In order to create a prototype, a survey was made of existing bridges in California that have architecturally flared columns. After the data were

collected, average dimensions, reinforcement ratios, and confinement ratio for the columns were obtained.

Because the project is concerned with new design methods, only recent bridges with details shown in Fig. 2-1 were considered in the survey. This limited the number of the available bridges that have the same features (circular columns, pinned base and architectural parabolic flares) to two existing bridges; “Hov. Connector” in California and “RTE 9I/5N” in California. The dimensions, reinforcements of the survey result and the calculated prototype are summarized in Table 2-1.

2.4. MODEL SELECTION

The two main objectives that controlled the number and details of the specimens under study were:

1. To study the effect of column height in using the recommended detail. For this purpose, two limits were used in column heights. The first was obtained from the prototype where the columns are subjected to low shear value of 2.58 MPa (0.374) Ksi and the second was to use the flare height as the column height, which subject the columns to higher shear force level of 4.23 MPa (0.613 Ksi). In both cases the columns were flexure dominated.
2. To study the necessity of using high confinement ratio at the top third of the flare height by using the minimum confinement ratio along the entire flare height.

To obtain a model from the prototype, a scale factor is needed. Choosing a scale factor is a task that is controlled by many factors. One of which is that the model should

be as large as possible when compared to the actual structures for better modeling of the behavior. The second factor is the maximum capacity of the tools used in the experimental work; which is mainly the maximum capacity of the shake tables.

Due to the first factor, researchers tend to choose a high scaling factor, however, the second one places the upper limit on their choice. In other word, the desire to make the model close to the prototype defines the lower limit of the scaling factor and the equipments capacity defines the upper limit. Table 2-2 contains a summary of the shake table specifications.

The maximum payload weight that the shake table withstands is 444.8 KN (100 kips). This weight is the total weight that includes the specimen, the footing, the weight of the mass mounted over the specimen and any device used in the specimen. If all the above-mentioned factors were considered while keeping the total mass mounted over the specimen, a relatively small scale factor would be used. In order to increase the scaling factor, a coupled experimental test setup was used. This was achieved by attaching the specimen to an off-specimen mass that represents part of the total mass. The off-specimen mass is linked to the specimen by a rigid link that transfers the inertial force to the model, Fig. 2-2. A detailed description of the system setup is included in Chapter 3. In creating the model, all the dimensions of the prototype were multiplied by the scaling factor. The reinforcement ratios were kept the same for the prototype and model columns.

All the dimensions were scaled to form the model as described except for the beam span. If the beam span was calculated by the scaling the prototype, the result would have been a relatively short span that would be totally covered by the mounted mass. It was important to observe the joint behavior during the test and any crack propagation. To

achieve this objective, the beam span and the cantilever lengths were increased in the specimen when compared to the scaled the prototype. The beam dimension was chosen so that the relative stiffness between the beam and the column would remain the same as that obtained from the scaled prototype. Also, the load was distributed along the span and the cantilever in a manner that creates dead load moments almost the same as the one obtained from the scaled prototype.

Four specimens were constructed; LFCD1, LFCD2, SFCD1 and SFCD2. The first two specimens have the same layout with a column clear height of 1626 mm (64”). The only difference is that LFCD1 has the flare confinement detail as described in the Caltrans code, while LFCD2 has the lower confinement ratio extended along the entire flare height. The other two specimens, SFCD1 and SFCD2, have the same reinforcement detailing, as LFCD1 and LFCD2 respectively, with a short clear height of 991 mm (39”). Table 2-3 shows prototype dimensions and reinforcement versus those of the four specimens, also, it contains the reinforcements of the flare based on Caltrans specifications[5].

2.5. SPECIMENS DESIGN

As mentioned previously, the dimensions and the reinforcement of the columns were obtained directly from the prototype. Beam dimensions, reinforcement and detailing were determined by performing new design implementing the latest Caltrans seismic provisions[5]. The new design helped in ensuring the formation of the plastic hinge at the end of columns and not in the beam or in the joint. In order to design the beams, an analysis was needed. The second step was to use the obtained data to design the bent

using the current codes and specifications. The following sections describe in detail the analysis and design procedure.

2.5.1. Preliminary Analysis

Before the final specimen design, a preliminary analysis was needed in order to estimate the load-carrying capacity of the system. The value of the bent capacity was obtained through section analysis to evaluate section ultimate capacity. Two programs were used in estimating the ultimate section capacity; RCMC2, a program that was developed at the University of Nevada, Reno[17], and xSECTION program which was developed and used by Caltrans[26]. The reason behind using the two programs is to verify them with respect to each other.

The unconfined and confined concrete property was calculated using Mander's method[16]. For the base hinge section, the confinement characteristics are under question as the section is highly confined by the rigid footing surface and the column core section. There was no available data that could be referred to in order to calculate the confinement criteria for such a sections. An assumption was made that the base hinge section has the same confinement concrete characteristics as for the column core. Table 2-4 summarizes the assumed material property for steel and concrete.

The axial load for each column was evaluated so that it was equal to the following:

$$P = 0.1 A_g f_c' \quad (2.2)$$

Where;

A_g = the area of the column core

f_c' = Specified compression strength

Substituting in the above equation by the values of the model's core area and using the value of f_c' = 31.0 MPa (4500 psi) as the target cylinder strength, resulted in a 226.4 KN (50.9) kips axial load per column. The above value was chosen for it is the level of axial forces for which most of current bridges sustain from dead load. The value of the axial loads was used in calculating the distributed load along the beam span.

The resulting M-ϕ Diagram for the core cross section is shown in Fig. 2-3 for both programs. The two results correlate well, however, xSECTION results are not as smooth as the case for the RCMC2 program and showed higher yield force with lower ultimate curvature value. Fig. 2-4 shows the M-ϕ curve for the base hinge cross section. xSECTION program results were significantly high than those obtained from RCMC2 with sudden jumps in the diagram. Also the ultimate curvature obtained from the program are far from those obtained from RCMC2. It was observed that while the program interactive processor plots smooth curves, plotting the results using another program gives the sudden jumps in the data. The RCMC2 program was considered for the analysis of the sections for the remaining portion of this document.

In both cases the gap was assumed to remain open. At ultimate condition, the lateral load could be simply evaluated by equation 2.3.

$$V = 2\frac{(M_C + M_b)}{H_C} \qquad (2.3)$$

Where;

M_C = Column core ultimate moment capacity at the top.

M_b = Column base hinge ultimate moment capacity

H_C = Column clear height

The results were 150.3 KN (33.1 Kips) for the tall columns and 246.9 KN (55.3 Kips) for the short columns.

2.5.2. Gap Closure Analysis

To estimate the gap closure status, an analysis based on the curvature[3, 5] was performed to the prototype section and the model section as well. Using the effective yield curvature value and the ultimate curvature value, the yield rotation and plastic rotation at the top section of the flare could be calculated. The yield rotation, θ_y, could be calculated using the moment-area method by integrating the moment along the column height. For the plastic rotation, θ_p, equation 2.4 was used[18, 20].

$$\theta_p = L_p (\phi_u - \phi_y) \quad (2.4)$$

Where;

L_p = Plastic hinge length

ϕ_y = Effective yield curvature

ϕ_u = Ultimate yield curvature

The value of the plastic hinge length is calculated using equation 2.5 provided be Caltrans[5].

$$L_p = G + 0.3 f_{ye} d_{bl} \quad (2.4)$$

Where;

G = Gap width

f_{ye} = Expected yield stress for longitudinal reinforcement

d_{bl} = Bar diameter for longitudinal reinforcement

The total deformation of the flare edge could be calculated by multiplying the total rotation, which is the summation of θ_p and θ_y, by the distance from the neutral axis of the section at ultimate curvature to the edge of the flare. The gap would not close as long as the calculated deformation is less than the gap width.

Following the above procedure resulted in a neutral axis that is offset from the center of the column core by 17.7 % and 17.8 % of the column diameter for the prototype and the model respectively. The plastic hinge length was calculated to be 851 mm (33.5 in) for the prototype and 238 mm (9.375 in) for the model. The deformation at the edge of the flare was calculated to be 38 mm (1.5 in) for the prototype which is 77 % of the gap width. The deformation in the case of the model was calculated to be 9 mm (0.372 in), which is 99.2 % of the gap width.

Despite that the above method shows that in both cases the gap would not close, the huge difference between the level of deformation of the flare edge for the prototype and the model raise the question about the efficiency of the method. The main reason behind that difference is the equation provided by Caltrans for the plastic hinge calculations[5]. The equation is a function of the yield stress and the bar diameter. In fact this equation is the same equation used for the steel jacketed columns. Because the bar diameter could not be scaled exactly in the model for practical issues, the plastic hinge length was calculated to be 14.6 % of the column height versus 9.8 % for the prototype for the tall columns.

In order to verify the efficiency of the equation, the results reported in the previous study for flared columns with gaps[3] were used in order to estimate the plastic hinge length. Specimen RDS-4 in the report was picked to conduct the calculations. This

specimen was chosen because it had a gap width that was wide enough to prevent gap closure. The plastic hinge length obtained from the experimental results was 277 mm (10.9 in) while that calculated using equation 2.4 is 371 mm (14.6 in). This means that the equation over-estimates the plastic length by 34 %.

2.5.3. Detailed Design

The preliminary analysis served in evaluating the maximum load carrying capacity of the whole structure and to estimate the ultimate moments. Using the results of the analysis, a linear static structural analysis was performed on each frame using prismatic frame elements. The section properties of the columns were calculated by dividing the column height into segments and calculating the average section property of each part. The boundary conditions used were frictionless hinges at the base. A horizontal concentrated load was applied at the top of the bent with a value equal to the previously calculated load-carrying capacity of the system. The resulting actions obtained from the analysis along with the column capacity were used in performing the design of the cap beam, the base hinge and the beam-column connection reinforcements using the current Caltrans code. The following section outlines the procedure and code recommendations that were used for each element. Figs. 2.5 through 2.11 show the dimensions and details of each of the four specimens.

2.5.3.1. Beam Design

For the beam, Caltrans Seismic Specifications[5] state that the nominal moments of the bent cap beam at the column face shall be related to the column ultimate moments by equation (2.4).

$M_b = M_u\ (col)\ x\ 1.2$ (2.4)

Where;

M_b = Nominal beam moment

M_u (col) = Column ultimate capacity

Based on the above requirement, the cross section and reinforcement were chosen. The section then was designed for shear according to ACI provisions[2].

2.5.3.2. Joint Design

The design of the beam-column joint is based on Caltrans Seismic Design Criteria[5], which is based on calculating the principal stresses in the joint region using Equation (2.5) through (2.11).

$$p_t = \frac{(f_h + f_v)}{2} - \sqrt{\left(\frac{f_h - f_v}{2}\right)^2 + v_{jv}^2} \quad (2.5)$$

$$p_c = \frac{(f_h + f_v)}{2} + \sqrt{\left(\frac{f_h - f_v}{2}\right)^2 + v_{jv}^2} \quad (2.6)$$

$$v_{jv} = \frac{T_c}{A_{jv}} \quad (2.7)$$

$$A_{jv} = l_{ac} \times B_{cap} \quad (2.8)$$

$$f_v = \frac{P_c}{A_{jh}} \quad (2.9)$$

$$A_{jh} = (D_c + D_s) \times B_{cap} \quad (2.10)$$

$$f_h = \frac{P_b}{B_{cap} \times Ds} \quad (2.11)$$

Where;

p_c = principal compression stresses in the joint

p_t = principal compression stresses in the joint

A_{jh} = Effective horizontal joint area

A_{jv} = Effective vertical joint area

B_{cap} = Bent cap width

D_c = Cross-sectional dimension of column in the direction of bending

D_s = Bent cap depth

l_{ac} = Length of column reinforcement embedded into the bent cap.

P_c = Column axial force including the effect of overturning.

P_b = Effective beam axial force at the center of the joint including prestressing

T_c = The column tensile force associated with ultimate moment capacity for the column M_u *(col)*

If the principal tension stress, P_t is less than or equal $3.5 \times \sqrt{f_c^{'}}$ psi no additional joint reinforcement is required. If the principal stresses exceeded the above mentioned limit, additional vertical stirrups, horizontal stirrups and horizontal side reinforcement shall be provided according to the Caltrans Seismic Design Criteria[5]. The equations controlling the minimum volumetric stirrups ratios, stress limits and the additional reinforcements could be found in Caltrans Seismic Design Criteria[5]. The recommendations resulted in additional stirrup reinforcement horizontally and vertically.

2.5.3.3. Base Hinge Design

The base hinge design in reinforced concrete structures is one of the subjects that is needing research. It is hard to make a pure hinge that carries no moments using concrete hinges, however, they are usually treated as frictionless hinges in analysis. For there are no clear provisions regarding the dimensions of the base hinges or the base hinge gap thickness, its dimensions and spirals were scaled from the prototype. This resulted in a hinge that is 8" diameter and 0.5" gap thickness in the model. The reinforcement was designed using the shear friction design criteria in the ACI 318-99[5].

2.5.3.4. Footing Design

The role of the footing in the experimental work is to provide a rigid platform that would be tied to the shake table. The footing was dimensioned to be very stiff to assure that its stiffness will not contribute to the overall deflection during the test. The actions obtained from the linear static analysis were used to analyze the footing as a plate supported by the tie down rods. The footing was dimensioned and detailed using the ACI code provisions, Fig. 2-5.

2.6. ANALYSIS

The purpose of estimating the load-displacement curve is to have an estimate of the initial stiffness of the frame, yield point and the maximum load carrying capacity. These values are needed for the design process and to perform seismic analysis that estimates the most suitable earthquake record to fail the specimen. Another important objective of

this analysis is to make sure that the maximum load-carrying capacity of the specimen would not exceed the shake table actuator capacity.

The analysis of such systems is not straightforward process as the single member. The beam-column interaction, the existence of the flare, gap and the base hinge create problems that make the conventional analysis method not suitable in analyzing these types of structures. The existence of the gap and the base hinge create discontinuity regions along the column heights due to the abrupt change in the column geometry. Considering Saint Venant's principle[27] in determining the boundaries of the D-regions, it could be shown that almost two-thirds of the tall specimen columns and nearly the entire short specimen columns are considered D-region where Bernoulli's hypothesis does not apply, Fig. 2-12.

The complexity associated with the existence of the flare and its unclear role in confining the circular core of the column makes the confined concrete properties hard to estimate with a high level of confidence, especially since there are no previous experimental results for such cases.

A non-linear finite element program called ADINA[1] was used in performing pre-test analysis. To model the structure, two choices were available. The first was to model the whole structure using 3-D configuration. The second was to use 2-D plane stress elements in modeling the whole structure with element thickness equal to the structure out of plane dimension at any location.

2.6.1. 3-D Versus 2-D Analysis

3-D modeling of the structure in concern is very complicated due to the complexity of the structure configuration and time consuming as well. The question that arises is whether the 3-D structure can be analyzed as a 2-D structure with enough level of confidence that the solution is close to reality. In the case where the analysis is performed after experimental work, the answer could be achieved by simply matching the results. In the case under study, the situation is different for the analysis is needed as a step towards experimental work.

In cases where loading and structures layout fall in one plane, the third dimension configurations have no effect on the overall equilibrium and external compatibility. However, in case of failure analysis, the level of the ultimate stresses, bond, cracking and the degradation in shear strength due to cracking needs to be taken into account. To study the problem, the difference between the 3-D configuration and 2-D configuration need to be identified. Solving the 3-D configuration into 2-D configuration is merely the change of the stress state from a 3-D stress state to a 2-D stress state where the out of plane stress direction equals to zero, Fig. 2-13. This has an impact on the confined ultimate stress and strain of concrete.

To study the difference, a failure material model needs to be considered. Drucker-Prager material model[34], equation (2.12), is one of the efficient models that is used to model the concrete failure envelope.

$$f(I_1, J_2) = I_1\alpha + \sqrt{J_2} - k = 0 \qquad (2.12)$$

Where;

$$I_1 = \sigma_{11} + \sigma_{22} + \sigma_{33} \tag{2.13}$$

$$J_2 = \frac{1}{6}[(\sigma_1 - \sigma_2)^2 + (\sigma_2 - \sigma_3)^2 + (\sigma_3 - \sigma_1)^2] \tag{2.14}$$

Assuming a principal stress state and adjusting the envelope to match Mohr-Coloumb criteria compressive strength, f_c', in case of 3D and 2D plane stress state results in the following definitions of the variable[34, 8].

For 3D stress state:

$$\alpha = \frac{2Sin\varphi}{\sqrt{3}(3 - Sin\varphi)} \tag{2.15}$$

$$k = \frac{6cCos\varphi}{\sqrt{3}(3 - Sin\varphi)} \tag{2.16}$$

$$c = \frac{f_c^{'}(1 - Sin\varphi)}{2Cos\varphi} \tag{2.17}$$

Now let ϕ = 30º for normal weight concrete[8] and f_c' = 31.0 MPa (4.5 ksi). The confining pressure for a circular column, considering the column core of the model would be f_l = -1.74 MPa (-0.253 ksi). Fig. 2-14 shows the confining pressure and its stress state on any arbitrary element within the column core, assuming the column is under pure axial load. By converting the column into 2D configuration and lumping the effective confining cross sectional areas of the spirals into one line of stirrups, the confining pressure in the middle of the column would remain almost the same. At the extreme edge of the column, the pressure will be f_l = -4.23 MPa (-0.613 Ksi) due to the decrease of the concrete out-of-plane dimension and assuming the steel stress would be the same along the stirrup length, Fig. 2-15. The confining pressure in the 3D stress state is uniform along the spiral circumference that produces constant pressure at any section of the column. In the 2D configuration, the confining pressure is acting along the middle

thickness of the elements and hence produces variable stresses at each section depending on the element thickness.

Using equation (2.12) and substituting for $\sigma_1=\sigma_2=f_l$ and the appropriate coefficients to solve for the value of σ_3, which would be the ultimate confined concrete compressive strength, f_{cc}', results in a value of f_{cc}' = -36.29 MPa (-5.263 Ksi). Using the same procedure for the 2D stress state where $\sigma_1=0$ and $\sigma_2=f_l$ obtained from the 2D configuration, the result would be f_{cc}' = -33.6 MPa (-4.88 Ksi) in the middle of the column and –37.1 MPa (-5.38 Ksi) at the edge. In other words, the 2D stress state estimates the ultimate stress within a range of 92.7 % to 102.2 % of its 3D solution value. A similar analysis could be used for strains, or, the empirical equations could be used that results in a minor differences in strain values between 3D and 2D.

This concept of dealing with a 3D structure as a 2D one was previously used in analytical studies[31, 32] that proved highly effective in matching the experimental results. These studies were limited to rectangular or square cross sections. In order to verify the robustness of the method, a previously tested circular column[4] from NIST was analyzed using 2D and 3D finite element idealizations. Table 2-5 summarizes the basic properties of the column, which are similar to the core of model columns. The two results were compared to the experimental results.

Despite the efficiency of the program and its wide capabilities, it has some limited capabilities dealing with complicated reinforced concrete structures for research purposes. The analysis diverges at the beginning of the plastic stage. This occurs due to the fact that it uses very small stiffness (that could be specified as a fraction of the original stiffness) for crushed concrete elements and also the propagation of cracking. In

order to avoid the effect of the problem, multiple runs were made and at each run the crushed elements are defined (location and load step where crushing occurs) and a subsequent run is made by removing of these elements at the appropriate load step. The method is cumbersome, but it showed close agreement with the experimental results.

Fig. 2-16 and Fig. 2-17 show the finite element mesh of the NIST column and the material stress-strain curves respectively. Fig. 2-18 shows the achieved load-displacement curves. The results show good agreement except that the 3D analysis underestimated the ultimate displacement while the 2D analysis overestimated it. This does not imply that the procedure used, removal of crushed elements manually, is an excellent procedure due to the fact that the analysis considered the materials non-linearity only. Nevertheless, it resulted in a good estimate of the horizontal part of the load-displacement curve.

2.6.2. Model Idealization

The previously described procedure was used to model the specimens. In meshing the specimen two factors controlled the process. The specimen needs to be meshed using a considerably low number of joints to reduce the solution process as much as possible. Also, the spacing between the modeled stirrups needs to be chosen close enough to reality so that the confinement of concrete would be modeled accurately. The footing was modeled as two separate blocks with rigid linear elastic material model. Contact elements were provided at the location of probable gap closures, Fig. 2-19. The boundary conditions were assigned as rollers around the sides of the footings excluding the top face. The vertical load was kept a constant value during the analysis. The areas of

longitudinal reinforcement were lumped to represent the total steel area at each specific location, Fig. 2-20. The specimen weight was implicitly added to the elements, while, the external load was applied as concentrated loads distributed along the beam span. The horizontal load was applied as two equal concentrated loads at beam both ends. The horizontal loads were increased gradually with small steps. Figs. 2-21 and 2-22 show the full finite element mesh for LFCD1 and SFCD1, respectively.

The stress-strain curves for concrete and steel were the same as that shown in Fig. 2-17. Figs. 2-23 and 2-24 show the load-displacement curves for LFCD1 and SFCD1. The dashed lines shown in the curves are the bilinear idealization of the curves that is used in the subsequent seismic analysis. The first line of the bilinear curve is drawn by connecting the origin by the first point of yielding, while the second line is drawn by choosing a line that creates equal areas between the line and the actual curve. Detailed description of the process of idealization is included in Chapter 4. The analysis results and observations are summarized in Table 2-6.

2.6.3. Seismic Analysis

Seismic evaluation of the model is one of the most important steps towards the experimental work. Performing seismic analysis is important for the following reasons:

- To make sure that the capacity of the system would not exceed the shake table maximum capacity and to ensure that the specimen could be taken to ultimate.
- To choose the most suitable earthquake record to be used in the test. For failure of the system is not only dependent on the earthquake magnitude, but, its frequency as well.

- To plan the test procedure, i.e. the load increment, in order to capture the important points that could generate a continuous and smooth load-displacement curve.

In order to achieve these targets, a simple, yet efficient, program was used to perform seismic analysis to the specimens. The RC-Shake program that was developed at the University of Nevada, Reno, is based on performing responses history analysis to a single-degree-of-freedom system. The program is a non-linear program that implement a modified equation of motion to account for the effect of the test setup used. The Qhyst model[23] is used to model the hysteretic properties of concrete[22]. Load-displacement curve reflects the stiffness change versus the displacement of the system, which could be used to assume a SDOF system that has the same curve. The idealized load-displacement curves from the finite element analysis were used, shown as dashed lines in Figs. 2-23 and 2-24.

Several earthquake records were used to excite the system to choose the most suitable earthquake that would cause the specimens to fail. The time steps of the original records were scaled by the square root of the scale factor to account for the change in structure dynamic response due to the scaling of the prototype. The records of Kobe, El-Centro, Newhall and Sylmar were used, Figs. 2-25 through 2-28. Table 2-7 summarizes the information for these earthquakes.

Each earthquake was scaled to a maximum acceleration of 1.2g. Results showed that the Kobe earthquake and Sylmar Northridge earthquake were the most capable earthquakes to fail LFCD1, Figs. 2-29 through Fig. 2-32. Despite that Kobe gave higher displacements, it was preferred to use Sylmar record as it occurred in California. Results

for SFCD1 were in contrast to those obtained for LFCD1. Newhall and El-Centro showed better results than Kobe and Sylmar for the short specimens, however, it was preferred to use the same earthquake for both tall and short specimens, Fig. 2-33 through Fig. 2-36. Table 2-8 summarizes maximum displacement demand for both specimens.

Multiple runs were made using factored earthquake records to develop an experimental plan that ensures that important points would be captured during the runs. It was found that the most suitable record factors to be used were 0.15 times Sylmar, 0.25 times Sylmar and then increments of 0.25 times Sylmar would be used until specimen failure. Another run was made for the accumulated runs. Fig. 2-37 shows the accumulative results for LFCD1, while Fig. 2-38 shows the accumulative results for SFCD1.

3. EXPERIMENTAL PROGRAM

3.1. INTRODUCTION

This chapter describes the experimental work. The discussion starts with the construction phase and the material properties. The locations of the instruments and the specimens' setup phase are all discussed. The test program and loading steps for each specimen are summarized in this chapter.

3.2. CONSTRUCTION

The specimens were constructed by a local contractor at the large-scale earthquake laboratory on the University of Nevada, Reno campus. The footing was constructed first followed by the columns and then finally the bent cap beam in the last stage. Due to the complexity of the column flare shape and their size, foam forms were used. The foam forms were blocks of foam that were cut to the shape of the column. The blocks were then assembled and covered by wood forms.

Grade 60 steel was specified with yield strength less than 78 Ksi, according to the recommendations of ACI 318-99[2]. Three samples of each diameter were tested in advance to assure that they meet the requirement. Table 3-1 shows the average yield stress of each diameter used in the specimens. The diameter used in the footings is not included because the footing was designed with excessive amount of steel.

Target concrete strength was a minimum of 31.0 MPa (4500 psi) and a maximum of 37.9 MPa (5500 psi). The concrete was delivered from a local batch plant that was

responsible for the concrete mix to meet these limits. Table 3-2 shows the design criteria and mix design of the concrete. Normal curing was performed to the concrete after casting. To ensure that the concrete met the target strength limits, 12 standard cylinders were taken from the concrete for each part of the structure at the time of casting. The cylinders were left in the same weather and curing conditions of the specimens, so that, their strength would reflect the real concrete strength. Three cylinders were tested at 7 and 28 days after casting, and on the day of testing. Tables 3-3 through 3-6 show the concrete strength for each specimen at 28 days and on the day of testing. Figs. 3-1 through 3-8 show different construction stages and the columns, beam and joint detailing.

Caltrans specifications states that the hoops of the flares should be mechanically spliced[6]; which is difficult due to the small wire diameter used in reinforcement of the flare. The mechanical splices were substituted by fillet welding of hoop splices to assure that no relative slippage would occur during the test. To make sure that the type of fillet weld was effective, a welded bar was subjected to tensile stress until failure. The bar failed while the welded connection remained intact. Fig. 3-1 shows the welded hoops.

3.3. TEST SETUP

The first step in the test setup was to prepare the shake table and then mount the specimen. In order to make sure that the bottom surface of the footing is in full contact with shake table surface, the specimens were placed on spacers of constant thickness and then a non-shrink grout was used to fill the gap between the footing and the shake table. After the hardening of the grout, 15 high strength rods were screwed into the shake table hold down grids. The rods pass through hollow tubes that were installed in the footing

during construction. All the rods were tied at the top of the footings and then prestressed. The fixation system ensures that the footing will not move upward during the test and generates high normal force that increases the friction between the shake table and the footing that prevents it from sliding.

In order to model the inertial force resulting from the mass of concrete superstructure in real bridges, an external mass need to be added to the specimens. Four buckets filled with lead blocks were distributed along the span of the beam to represent the part of the mass that the specimen should carry if the whole bridge was to be modeled, Figs. 3-9 through 3-12.

Each bucket consisted of three small buckets attached together. The buckets were designed so that they surround the beam section, and a prestressing self-equilibrating force was applied to the system through high strength threaded rods to transfer higher normal force to the top and bottom surface of the beam. The normal force increases the resisting friction force of the system and hence guarantees the bucket would not slip as the beam moves.

If all the mass were modeled using the lead, the total weight of the specimen would exceed the shake table capacity as was previously discussed in chapter 2. An off-specimen mass was mounted over a mass rig and attached to one end of the beam through a rigid link. The mass rig is a structure supported over four frictionless bearings and can support the additional mass mounted over it. The structure cannot resist any lateral loads due to the internal frictionless hinges at its joints, Fig. 3-9.

The concrete blocks on the mass rig were rigidly attached to the mass rig through prestressed rods that integrate them together and prevent any relative movement between

them. The total inertial force generated from the mass rig and the attached concrete block represents 18.2 t (40 Kips-mass). The off-specimen mass is attached to one end of the beam using a rigid link between the concrete block and the beam. The link has two frictionless hinges at its ends to transfers normal force only. As the top of the beam moves due to the earthquake motion at the base, the mass rig moves with the same acceleration of the beam, and hence, the inertial force of the off-specimen mass transfers through the rigid link to the beam.

Because the off-specimen weight contribute to the system by inertial force only and its weight goes directly to the mass rig bearings, an additional load needed to be applied to the columns to substitute the weight of the off-specimen. Four hydraulic rams were used for this purpose, two of which were mounted over the top surface of the beam at the center of each column. The rams were connected to long high strength threaded rods that were fixed to the footings to balance the applied load. The load was transferred from the rams to the column through 2 rigid beams as shown in Fig. 3-10. In order to reduce additional confinement at the top of the beam column connection resulting from the pressure of the rams, the steel beams used to transfer the load were chosen as wide as possible. The advantage of this system is that it is self-equilibrated, which means that it exerts normal loads to the columns while it does not affect the weight that reach to the shake table. The use of the rams proved to have another advantage of providing out-of-plane restraint to the system and reduce the transverse displacement that may occur during the test.

The reason why the off-specimen mass was not used to model the total mass for the bent is that the link produce a concentrated tensile and compressive force at one end of

the beam. The tensile force is transferred through the beam and hence reduces the shear strength for the beam that might lead to shear failure in the beam during the test. Figs. 3-11 and 3-12 show the final setup of both tall and short specimens.

3.4. INSTRUMENTATION

The most important part of this instrumentation process was to identify the location of each instrument. To achieve that, it was required to set the objectives and the location where detailed information was needed and at the locations which through the behavior of the each element could be investigated. The pre-test analysis that was described in chapter 2 served as a tool to identify the locations that needed special attention. The objectives were set to be:

1. Monitor the global performance of the frame (displacement and acceleration),
2. Obtain sufficient data to plot the curvature along the column,
3. Monitor the efficiency of the joint detailing, and
4. Monitor yielding of rebars in locations where yielding of the steel is most likely to occur.

The following section categorizes the instruments that were used based on their function.

3.4.1. Dispalcement, Acceleration and Load Cells

Five global displacements needed to be measured:

1. Absolute in-plane beam displacement,

2. Absolute transverse displacement in order to monitor the out-of-plane stability of the bent during the test,
3. Mid-span vertical deflection to monitor beams' deflection during the test,
4. Base hinge horizontal slippage for each column to monitor shear transfer mechanism at the base, and
5. Absolute shake table displacement.

Five displacement transducers were installed to measure the above displacements for the four specimens under study, except for LFCD1 the mid-span deflection was not measured. The permanent deflection observed in LFCD1 beam was the reason why the mid-span displacement was measured in the remaining specimens. For these five locations, the transducer was attached to the point under consideration either by hooking it to a bar that was penetrating core of the specimen, or attached to the extreme of the specimen where spalling was not anticipated. The shake table displacement was measured using a built-in device. An external frame was used as a reference for both the in-plane and out-of-plane displacements while the footing was used as the reference for the base slippage and for the mid-span deflection.

Four accelerometers were installed.

1. Two accelerometers were installed to measure the in-plane acceleration; one was mounted on the top concrete surface of the beam and the other was mounted on the top surface of lead in the taller lead bucket. The purpose of using two in-plane accelerometers was to evaluate the performance of the buckets with respect to the beam acceleration.

2. One accelerometer was mounted on the top concrete surface of the beam to measure the out-of-plane acceleration.
3. The last accelerometer was built in the shake table to measure the achieved acceleration.

To measure the load variation in the hydraulic rams, two load cells, one at each column, were installed under two of the rams during the test. Another load cell was installed on the rigid link that was attached to the mass rig to measure the transferred load from the mass rig. Fig. 3-13 shows a schematic drawing for the location of the above mentioned devices. Instrumentation was the same for all the four specimens.

3.4.2. Curvature

Five sections in each column were chosen to measure curvature. Four of which were distributed along the flare height and the remaining one is at the column base. The instruments were concentrated in the flare region for the curvature variation would mostly occur at the top portion of the column. To measure curvature, two transducers were installed between two sections on the sides of extreme fibers of the column. Fig. 3-14 shows the locations of the installed transducers used to measure the curvatures for both tall and short specimens.

3.4.3. Strain

Tensile and compressive strains in steel reinforcement were measured using strain gauges. The locations of the strain gauges were distributed to measure probable yielding or in locations where performance was needed to be investigated. 110 strain gauges were

installed in the dowels of the base hinge, column longitudinal bars, flare reinforcement, beams stirrups and beam longitudinal reinforcement. As a matter of redundancy in critical locations, two strain gauges were assigned to measure the same reading at the same cross section. The assigned locations for the four specimens are shown in Fig. 3-15.

Strain gauge installation process was done by polishing the part of the rebar where the strain gauge was to be installed then attaching it using an adhesive material manufactured for this purpose. To protect of the strain gauge, rubber was placed over the strain gauge then both of them were wrapped tightly. The wires coming out of the specimen were encased in a small diameter tube to protect them during concrete casting and during the test. The above procedure proved, from previous tests, to be ideal in preserving the strain gauges from being damaged till late stages of the test. There were only a small number of the strain gauges that did not function. The strain gauges were measured before installing the lead and applying the loads from the hydraulic rams to measure the strains generated from the dead loads.

3.5. TUNING

After specimens' preparation, an important and critical stage was done prior to testing the specimens, which is shake table tuning. In shake table testing, structure inertial force has an impact in changing the records that were intended to excite specimen under consideration. Tuning is a process that defines the specimen's initial stiffness to the system in order to decrease the gap between the target and achieved accelerations. To tune the table, a specimen was excited with an earthquake record that has a relatively low maximum acceleration value. It is very important to choose that record so that none of the

reinforcement would approach yielding. From the analysis that was done using RC-Shake program, it was found that 0.15 times Sylmar earthquake was a safe tuning load for the four specimens. At this level, the highest strain in the specimens was 835 με, well below the yield strain of 2138 με

3.6. TESTING PROGRAM

The loading sequence was chosen so that it would capture the important points along the load-displacement curve like cracking, yield and ultimate. The specimens were excited with scaled versions of the Sylmar record (Northridge Earthquake, 1994), Fig. 2-25. The reason for selecting Sylmar was provided in Section 2.6.3. This earthquake has a peak acceleration of 0.61g. The following sections describe the loading sequence for each specimen.

3.6.1. LFCD1

The loading factors are shown in Table 3-7. The maximum achieved accelerations are included in the table for comparison. The table shows that the last two runs are a repeat of 1.75 times Sylmar. The reason of not increasing the record beyond 2.125 times Sylmar was that after 2.125 Sylmar the frequency of the specimen dropped from an initial value of 2.78 Hz. to 1.02 Hz. The total collapse of the system was avoided as it might lead to the damage to the shake table. It was decided not to increase the motion but to repeat lower motions to characterize the system. The 1.75 Sylmar record was chosen as a safe record for that purpose. To differentiate between each 1.75 times Sylmar run, the first 1.75 after the 2.125 is called 1.75-2 and the following one is called 1.75-3.

3.6.2. LFCD2

Since the LFCD2 dimensions are the same for that of LFCD1, the loading steps were chosen to be the same as for LFCD1. The only difference is that 0.25 times Sylmar was inserted between 0.15 and 0.5 times Sylmar to have smoother transition in loading. The last run of 1.75 times Sylmar was eliminated from LFCD2. The loading factors are shown in Table 3-8. The maximum values of the achieved accelerations are included in the table as well. The same tuning setup for LFCD1 was used.

3.6.3. SFCD1

During the tuning process of SFCD1, the shake table went out of control and moved vigorously with the ultimate acceleration that the shake table can produce and the table displacement reached its maximum values (± 12in) hitting the safety bumpers four times to the east and the west direction. A huge noise was heard from the shake table and the specimen was severely damaged. It was estimated that the maximum acceleration reached a value of 2.5 g while the maximum base displacement reached a value of 12 in. A brief discussion is included in Chapter 4 as part of this research.

3.6.4. SFCD2

The specimen was excited with time scaled versions of Sylmar record (Northridge Earthquake, 1994). The loading factors are shown in Table 3-9. The maximum values of the achieved accelerations are included in the table as well. The 0.15 times Sylmar record was used to tune the shake table. The table shows that the last runs equals of 3.25 times

Sylmar. The reason for not increasing the record beyond that was that the shake table approached its maximum driving force capacity.

4. TESTING AND RESULTS

4.1. INTRODUCTION

Four specimens were tested using the shake table by exciting each of them by a series of time-scaled Sylmar records until failure. This chapter contains the test procedure and results for each of the specimens. The measurements obtained from each channel are also included in Appendix A. Specimen characteristics through each test are calculated. The behavior of each specimen is explained in the light of the obtained data and observations. Evaluation and comparison of specimens are included.

4.2. LFCD1 TESTING AND RESULTS

4.2.1. Test Procedure and Observations

Each specimen was equipped with 110 strain gauges. During the tests, some strain gauges were damaged or their wires were cut. This usually happened due to concrete spalling or, sometimes, during the handling process. Figs. 4-1 and 4-2 show the devices and strain gauges that were undamaged until the end of the test and their identification numbering. A complete plot for measurement histories is included in Appendix A. The observations during the test and crack propagations are summarized in Table 4-1. The table describes the observed behavior for column, beam-column connection, and the base hinges.

No cracking was observed during the first run of 0.15 times Sylmar. Cracking developed slowly in both the beam-column connections and the columns until 1.25 times

Sylmar, Figs. 4-3 through 4-5, where crack propagation had a significant increase in number and length. At the same load step, shear cracks starts to appear at the top of the flare Fig. 4-6. After 1.25 times Sylmar, very little crack development occurred in the beam-column joint, Fig. 4-6, while most of the crack formation concentrated in the columns. At 2.0 times Sylmar, significant cracking occurred in the beam-column connection and extended to cover approximately the whole length of the columns, Fig. 4-7. Shear cracks appeared especially in the lower part of the column, Fig. 4-9b under 1.75-2.

The first concrete spalling occurred at the base hinge of the columns at 1.0 times Sylmar, Fig. 4-5. At 2.0 times Sylmar, concrete cover spalling started to occur at the edge of the flare due to the gap closure and permanent gap widening occurred at the other side of the flare, Fig. 4-7, and concrete spalling started to appear at the middle third of the flare height. At 2.125 times Sylmar, spalling of concrete at the base of the two columns occurred, Fig. 4-8. During the second run of 1.75-2, the concrete spalling increased significantly and buckling of flare longitudinal reinforcements started to occur, Figs. 4-9 through 4-11. After bucket removal extensive shear and flexural cracks were found in the beam, Fig. 4-10.

4.2.2. Load-Displacement Relationship and Dynamic Properties

Load-displacement relationship is one of the most important data needed to evaluate the structural behavior throughout the loading history. Element cracking, first yield, maximum load, maximum displacement and element ductility ratios, which is defined as the ratio of the ultimate displacement Δ_u divided by the effective yield displacement Δ_y,

are all important data that can be obtained from the load-displacement curve. For a well-detailed bent, the load-displacement curve would have the same trend as for a single column, Fig. 4-12[5].

The philosophy of such design is based on assuring that the plastic hinges form in the columns for bridges, and hence, the structure would sustain large post-yield displacement that enables the structure to absorb enough energy to pass the earthquake safely without total collapse. Such structures are expected to suffer from some damage. The purpose of the design recommendations is to limit damage to a repairable level. Displacement ductility is an index that measures the whole structure seismic performance of the structure. Caltrans Seismic Specifications[5] states that the displacement ductility ratio capacity should not be less than 6.

Figs. 4-13 through 4-23 show the measured load-displacement relationship plotted for each run individually while Table 4-2 summarizes the maximum and the minimum measured displacements and the corresponding forces. The permanent displacement after each run, chord stiffness and the dynamic properties of the system are also included in Table 4-2. The maximum and minimum displacements refers to the displacements in the west and east direction respectively. The permanent displacement refers to the horizontal plastic displacement measured at the top of bent at the end of each run. The maximum and minimum net displacement refers to the maximum or minimum displacement for each run after subtracting the net displacement from the previous run.

The chord stiffness, which is calculated using the inclination of a line connecting the points of maximum and minimum displacements for each run individually, is used to calculate the structure period and frequency using equations[6]. The values are also

summarized in Table 4-2.

$$T_n = 2\pi\sqrt{\frac{m}{k}} \tag{4.1}$$

$$f_n = \frac{1}{T_n} \tag{4.2}$$

Where;

T_n = Structure period

f_n = Structure natural frequency

m = Total mass on the structure

k = chord stiffness

The table shows that the initial structure period is 0.36 sec and its natural frequency is 2.78 Hz. At 1.25 times Sylmar, the stiffness dropped to almost 27% of its initial value with a rapid rate of stiffness degradation. Between 1.25 times Sylmar and the conclusion of the test, the rate of stiffness degradation was slower than that at the beginning of testing. This is because of the increase in stiffness that is caused by the gap closure.

It is important to mention that the base hinge slippage is included in these recorded displacement data. It was preferred not to subtract them for they play a role in energy absorption and because their movements are not equal in the east and the west column base hinges, Table 4-3. The observations of the load-displacement curves are as follows:

- At 0.15 times Sylmar, the system is almost linear elastic, Fig. 4-13.
- For both 0.5 and 0.75 times Sylmar, the load-displacements loops start to have very small widening in the loops with the first yield point at 0.50 times Sylmar, Figs. 4-14 and 4-15.

- At 1.0 times Sylmar, the system started to show wide loops, Fig. 4-16.
- At 1.25 times Sylmar, the load-displacement curve have significant change with wider loops and horizontal plateau at –209.1 KN (–47 Kips) between the displacements of approximately -46 mm (-1.8 in) to –64 mm (-2.5 in), Fig. 4-17.
- At 1.5 times Sylmar, the maximum force dropped to a value of –198.4 KN (–44.6 Kips) while the maximum displacement increased to –70 mm (-2.74 in), Fig. 4-18.
- At 1.75 and 2.0 times Sylmar the system started to generate wide loops and the maximum load started to increase reaching a value of approximately –266.9 KN (–60 Kips) at 2.0 times Sylmar, Figs. 4-19 and 4-20.
- At 2.125, very wide loops were generated with a slight force increase from the previous run. The system had horizontal plateau between displacement values of approximately –142 mm (-5.6 in) to –165 mm (–6.5 in), Fig. 4-21.
- At the final two runs 1.75-2 and 1.75-3 times Sylmar, the system showed higher force than that obtained in the first 1.75 times Sylmar, -279.6 KN (-62.86 Kips) versus -226.1 KN (-50.82 Kips), which is a 23 % force increase, Figs. 4-22 and 4-23, while the displacement increased to -185.2 mm (–7.29 in), which is 89.4 % higher than that measured at 1.75 times Sylmar.

Fig. 4-24 shows the accumulated load-displacement curve in solid lines, while the load-displacement envelope is shown with a dashed line. It is important to mention that the last two runs, 1.75-2 and 1.75-3 times Sylmar, were not included in the formation of the envelope as they were a lower load value than 2.125 times Sylmar. From the figure, it can be shown that the envelope is different than that was expected as a standard curve

trend. At -68.6 mm (–2.7 in) the envelope has a kink after which the system started to gain stiffness. Beyond this point, the curve started to climb showing higher force level reaching a maximum force value that is almost 35% higher than that at the beginning of first plastic deformations. Despite that, the chord stiffness degraded as the load factor increased, see Table 4-2. The system showed higher force level at 1.75-2 and 1.75-3 times Sylmar than that obtained at 1.75 times Sylmar.

As a summary of all observations, it is obvious that the system started to gain stiffness at 68.6 mm (2.7 in). Although no new elements were added to the system during the runs, the increase of the system stiffness was through gap closure. Visual evidence of gap closure is the amount of concrete spalling the top edge of the flare suffered during the late runs.

The results from the last two runs shows that the maximum displacement exceeds that obtained at 1.75 times Sylmar by 75% and the measured force exceeds by 23 % while the chord stiffness dropped by about 33 % in the last two runs. The chord stiffness is not that representative to structure stiffness for it does not describe the change occurring in the stiffness for such cases where gain of stiffness occurred in a later stage. A closer look at the load-displacement loops at the last cycle shows that the tangential stiffness of the system is about 1.09 KN/mm (6.25 Kip/in) up to a displacement of about 5 inches where the gap was closed and the tangential stiffness increased to almost 2.3 KN/mm (13 Kip/in) which is close to the tangential stiffness of the first 1.75 times Sylmar.

4.2.3. Base Hinge

Two displacement transducers were installed at the bottom of the columns to monitor

any sliding. Figs. 4-25 and 4-26 show the history of the measured displacements. Table 4-3 summarizes the maximum, minimum and permanent measured displacement at the base of east and west columns for each run. A maximum displacement of 27 mm (1.08 in) occurred in the west column while the east column had maximum displacement of 25 mm (0.997 in), which are approximately 15% and 11% of the maximum measured top displacement, respectively. The maximum recorded permanent sliding was 4 mm (0.14 in) in the west column and 2 mm (0.07 in) in the east column, which are 13.5% of that recorded at the bent top for the west column and 7% for the east column. This means that a significant percentage of the recorded maximum and permanent displacement at the top of the bent is due to base hinge displacement. Maximum and permanent slip recorded at both columns is not equal due to the framing action that causes the lateral load to be unequally distributed between the two columns.

The base hinge sliding has the advantage of absorbing the energy during the earthquake causing the overall stiffness to be lower than that calculated by assuming rigid hinge at the base. On the other hand, the base hinge displacement and the level of yield the dowels experienced raise the question about the efficiency and safety of the detail and design procedure. Certainly this kind of permanent sliding is very difficult to deal with after the earthquake for it would displace the whole bridge from its location with unequal movement at all the supporting frames.

4.2.4. Strain Data

4.2.4.1. Base Hinge Dowels

The maximum and minimum values of strains are summarized in Table 4-4. Where

strains passed yield, the strains are written in underlined bold font. The yield strain is calculated by dividing the yield stress included in Table 3-1 by Young's modulus for steel. The maximum recorded strain is 17956 micro strain while the minimum recorded strain is -15452. The base hinge dowels started to yield as early as 0.5 times Sylmar, Figs. 4-27 and 4-28.

4.2.4.2. Column Longitudinal Reinforcement

The maximum and minimum values of strains are summarized in Table 4-5. Where strains passed yield, the strains are written in underlined bold font. The maximum recorded strain is 38533 micro strain, which is the maximum value a strain gauge can measure, while the minimum recorded strain is -20224. Column longitudinal reinforcement started to yield as early as 0.5 times Sylmar at the gap location, Fig. 4-29. Yielding started to spread down in the column reinforcement as the runs continued. Yielding was recorded in column reinforcement within the beam-column connection region at 2.0 times Sylmar. The maximum records show that as the strain reach a value of 14246 micro strain at 1.25 times Sylmar, with a constant increase since the start of the runs, it started to show a lower value of 11895 micro strain at 1.5 times Sylmar. This behavior occurred as a result of the gap closure that added stiffness to the system, and hence, relaxed the strain level on the column longitudinal bars.

4.2.4.3. Column Spirals

The maximum and minimum values of strains are summarized in Table 4-6. Where strains passed yield, the strains are written in underlined bold font. The maximum

recorded strain is 2158 micro strain, while the minimum recorded strain is -738. Only one location yielded which was at the top of the beam-column connection of the east column, Fig. 4-30. Recorded strains in the spirals were generally low.

4.2.4.4. Flare Longitudinal Reinforcement

The maximum and minimum values of strains are summarized in Table 4-7. Where strains passed yield, the strains are written in underlined bold font. The maximum recorded strain is 17039 micro strain, while the minimum recorded strain is -24596. Column longitudinal flare reinforcement started to yield as early as 0.5 times Sylmar at the gap location, Fig. 4-31

4.2.4.5. Flare Hoops

The maximum and minimum values of strains are summarized in Table 4-8. Where strains passed yield, the strains are written in underlined bold font. The maximum recorded strain is 17035 micro strain, while the minimum recorded strain is -13004. Flare hoops started to yield as early as 0.5 times Sylmar in the top third of the flare height, Fig. 4-32. An explanation of this behavior is discussed in more detail in Chapter 6.

4.2.4.6. Beam Reinforcements

The maximum and minimum values of strains are summarized in Table 4-9. Where strains passed yield, the strains are written in underlined bold font. The maximum recorded strain is 17682 micro strain, while the minimum recorded strain is -629. The beam bottom reinforcement started to yield at 1.25 times Sylmar, Fig. 4-33. An

explanation of why it yielded is discussed in detail in Chapter 6. The measured strain level in the out-of-plane stirrups in the beam column connection showed very low values well below the yielding strain, which, raise the question about the efficiency of such a detail in the joint.

4.2.4.7. Summary for Strain Measurements

A summary of the yielded locations and when yielding started to occur are shown in Table 4-10. Fig. 4-34 shows a drawing for the location and the first yield occurrence where the number written beside the yield location represents the start of yield run. Plots for every gauge recording versus time are included in Appendix A. In summary the results for strains are as follows:

- Yielding occurred in all structures elements excluding the beam hoops and column spirals within the column height.
- The base hinge dowels, lower section of flare longitudinal reinforcement, flare hoops and column longitudinal reinforcement started yielding as early as 0.5 times Sylmar.
- Longitudinal column reinforcement started to yield in many locations at 1.0 times Sylmar.
- Starting from 1.75 times Sylmar, most of the yielding occurred in flare reinforcement, beam reinforcement and in the joint region.

4.2.5. Curvature

Curvature is calculated by converting measured lengths, d1 and d2, into strains at

both sides of the section in concern, Fig. 4-35. By knowing the horizontal distance, b, an approximate value for the curvature could be calculated using equation 4.3.

$$\phi = \frac{(d1 - d2)}{hb} \tag{4.3}$$

Figs. 4-36 through 4-45 show the measured curvature history. At the top sections it could be seen that between 1.25 and 1.5 times Sylmar, Figs. 4-40 and 4-45, the rate of peak curvature increase started to decrease because of gap closure that added stiffness to the columns. Figs. 4-46 through 4-49 show the maximum and minimum curvatures for the east and west side columns. It is important to note that the maximum and positive notations are arbitrary.

A closer look of the graphs shows that some sections at the top of the columns have curvature opposite in sign to the two sections above and below it, which in contrast of what is expected to be the deformed shape of the columns. This behavior occurred due to the shear deformations in the column in that region. The flares provide high shear stiffness and the effect of shear deformation cannot be neglected. The way the curvature is recorded does not differentiate between shear and flexural deformations. It is not possible to separate from each other. The final result is the summation of both flexural and shear deformation. A closer look with analytical proof is included in chapter 5.

Due to the flare existence, the instruments used at the top of the columns were at a large offset from the column core edge. This layout made the reference points in the beam to be relatively far from the beam-column connection vertical edges, which are the extreme fibers of the section under study. The deflection of the beam or cantilever is significant at these far points and has a significant contribution to the measured values. It

is important to mention that the reported curvatures include the flexural deformation of the beam.

4.2.6. Beam-Column Connections

One of the very important components of structures is the beam-column connection. The importance of this element is that it ensures framing action during loading history as long as its integrity is preserved. Beam-column connections are usually treated as point element in analysis, which is far from reality, for it has depth, width and breadth. Moreover, beam-column connections are responsible for transferring all types of loading, which causes stress concentration in a very limited volume[10].

The beam-column connection in this specimen suffered from extensive cracking through testing. Yielding occurred in a beams-column connection region in column spirals, column longitudinal reinforcement and beam bottom reinforcement as was previously shown. From the measured strains and the level of damage the joint suffered, it was important to calculate the level of stresses the concrete is subjected to.

Five transducers were attached to four fixed points in the joint region for this purpose. The recorded displacements at the nodes were used to calculate the stress in the beam-column connection region. In calculating the stresses the following assumptions were made:

1. The plane stress condition is applicable to the joint region.
2. The joint is treated as infinitesimal element.
3. Hooks law is assumed to be applicable because the objective is to know when the cracking started to occur and not to calculate the post-cracking stresses.

4. The deformations are small.

Doing so, the displacements were converted into strains according to equations 4.3 and 4.4. Fig. 4-163 shows the deformed joint with respect to the original beam-column connection configuration[12].

$$\varepsilon_x = \frac{\Delta_x}{b_x} \qquad \varepsilon_y = \frac{\Delta_y}{b_y} \qquad \varepsilon_{xy} = \frac{1}{2}\left(\frac{\Delta_x}{b_y} + \frac{\Delta_y}{b_x}\right) \tag{4.3}$$

$$\begin{Bmatrix} \sigma_x \\ \sigma_y \\ \sigma_{xy} \end{Bmatrix} = \frac{E}{1-\nu^2}\begin{bmatrix} 1 & \nu & 0 \\ \nu & 1 & 0 \\ 0 & 0 & (1-\nu)/2 \end{bmatrix}\begin{Bmatrix} \varepsilon_x \\ \varepsilon_y \\ \varepsilon_{xy} \end{Bmatrix} \tag{4.4}$$

Where;

Δ_x = Average horizontal deformation

Δ_y = Average vertical deformation

ε_x = Horizontal strain

ε_y = Vertical strain

ε_{xy} = Shear strain

b_x = Joint horizontal dimension

b_y = Joint vertical dimension

E = Concrete modulus of elasticity

ν = Concrete Poisson's ratio

The principal stresses were calculated using equations 4.5 and 4.6[12, 13].

$$\sigma_1 = \frac{\sigma_x + \sigma_y}{2} + \sqrt{\left(\frac{\sigma_x - \sigma_y}{2}\right)^2 + \sigma_{xy}^2} \tag{4.5}$$

$$\sigma_2 = \frac{\sigma_x + \sigma_y}{2} - \sqrt{\left(\frac{\sigma_x - \sigma_y}{2}\right)^2 + \sigma_{xy}^2} \qquad (4.6)$$

Figs. 4-50 through 4-53 show the stresses in the east and west joints. The maximum limits for tension and compression principal stresses that are recommended by Caltrans, $0.25 \times f_c^{'}$ psi for compression and $12 \times \sqrt{f_c^{'}}$ psi for tension, are shown in dashed lines. The figures show that the stresses started to exceed the tensile strength limit at 0.5 times Sylmar for the west joint. Also, they show significant change in stress values after 1.75 times Sylmar. The above results agree with the crack propagation observations listed in Table 4-1, where cracking started to appear in the joint at 0.5 times Sylmar and significant crack development took place at 2.0 times Sylmar.

At 0.5 times Sylmar, the maximum measured lateral force value is 139.2 KN (31.3 Kips), which is close to the value used in design. Cracking of the joint was minimal and the stresses exceeded the limits by small value. As the force increased, cracking started to increase significantly as well. It is important to note that plotted stresses after cracking are indicative and do not represent the real values for stress distribution, which is greatly affected by cracking and reinforcement detailing.

4.2.7. Strain Rate Effect

Due to the seismic loading, the yield force of the steel reinforcement increases due to the strain rate effect. Strain rate proved to have significant impact on steel yield stress and concrete strength[15, 19, 22]. In cases where random loading is applied, the strain rate is not a constant value that could be precisely evaluated. Instead, the rate is variable during each

run, and moreover, for each reinforcement location. However, it is evident that the strain rate effect has a significant contribution[19, 22].

To account for the change in yield stress and concrete property due to the strain rate, strain data for the longitudinal column reinforcement are considered at the gap top region. These strain gauges were chosen as the longitudinal reinforcement are the one that controls the yield point for the whole system. The strain rate is simply calculated by subtracting each strain record from the subsequent one and divided by the time interval[22].

Doing so resulted in strain rate with huge variations during the loading history. It was decided to use the strain rate calculated at the first yield in the longitudinal bars as the base value. The above concept resulted in a strain rate of 21810 με, this yield to an increase in the yield stress of 20.1 % and an increase in the concrete strength by 21.9 %.

4.3. LFCD2 TESTING AND RESULTS

4.3.1. Test Procedure and Observations

Figs. 4-54 and 4-55 show the active devices for the specimen and their ID numbering. A complete plot for channels recordings history is included in Appendix A. It is important to mention that instrumentation is the same for LFCD1 except that the observed deformation in the middle of LFCD1 beam was the reason of adding another displacement transducer in the middle of the beam span. The during-test observations and crack propagations are summarized in Table 4-11. The table describes the observed behavior for the columns, beam column-connection and the base hinges. Figs. 4-56 through 4-62 show cracking patterns through selected load steps that have significant change in the specimen's behavior.

No cracking was observed during the first two runs of 0.15 and 0.25 times Sylmar. Cracking developed slowly in both the beam-column connection and the columns until 1.25 times Sylmar where crack propagation had significant increase in number and length, Figs. 4-56 through 4-58. At 1.25 times Sylmar, shear cracks started to appear at the top of the flare. After 1.25 times Sylmar, little crack development occurred in the beam-column joint while most of the crack formation was concentrated in the columns. At 2.0 times Sylmar, a significant crack formation occurred in the beam-column connection and the beam and extended to cover approximately the whole length of the columns. Many shear cracks appeared especially in the lower part of the column, Fig. 4-59. At 1.75-2 times Sylmar, extensive shear cracks spread to cover the whole column's height, Fig. 4-62. After the bucket removal, extensive shear and flexural cracks were found in the beam, Fig. 4-61.

The first concrete spalling occurred at the base hinge of the columns at 1.0 times Sylmar. At 2.0 times Sylmar, concrete cover spalling started to occur at the edge of the flare due to the gap closure and to extend to cover the top two third of the flare height. The concrete spalling continued till the exposure of the flare hoops and longitudinal reinforcement at later stages of the runs, Fig. 4-60.

4.3.2. Load-Displacement Relationship

Figs 4-63 through 4-73 show load-displacement relationships plotted for each step individually while Table 4-12 summarize the maximum and the minimum displacements and the corresponding forces. The permanent displacement after each run, chord stiffness and dynamic properties of the system are also included in the table. The observations of

the load-displacement curve are as follows:

- At 0.15 and 0.25 times Sylmar, the system is linear elastic, Figs. 4-63 and 4-64.
- From 0.5 through 1.0 times Sylmar, the load-displacements loops start to show very small hysteretic behavior. The first yielding started at 0.75 times Sylmar, Figs. 4-65 through 4-67.
- At 1.25 times Sylmar, the load-displacement curve started to have significant change with wide loops and constant force of -205.1 KN (-46.1 Kips) between the displacements of approximately -30 mm (-1.2 in) to -41 mm (-1.6 in), Fig. 4-68.
- At 1.5 times Sylmar, the maximum recorded force dropped below that obtained in the previous run to -192.2 KN (-43.2 Kips) while the maximum displacement reached a value of -66 mm (-2.58 in), Fig. 4-69.
- At 1.75 times Sylmar, the system started to generate relatively wide loops and the maximum force started to increase reaching a value of -213.9 KN (-48.1 Kips) and a maximum displacement of -92 mm (-3.62 in), Fig. 4-70.
- At 2.0 times Sylmar the loops started to be wider and the maximum load increased to approximately -247.3 KN (-55.6 Kips), Fig. 4-71.
- At 2.125, very wide loops were generated with a slight force increase from the previous run of –268.7 KN (–60.4 Kips). It is also noted that the system had horizontal plateau between displacements values of approximately –140 mm (–5.5 in) to -175 mm (–6.9 in), Fig. 4-72.
- At the final run, 1.75-2, with a repeated factor of 1.75 times Sylmar, the system showed higher force than that obtained in the first 1.75 times Sylmar, -246.4 KN (-55.4 Kips) versus -213.9 KN (–48.1 Kips), which is almost 15.2% increase in

force, Fig. 4-73.

Fig. 4-74 shows the accumulative load-displacement curve in solid lines, while the load-displacement envelope is shown with a dashed line. At almost –66 mm (–2.6 in) the envelope has a kink which after, the system started to gain stiffness and force. The maximum force value is almost 33% higher than that at the first occurrence of plastic deformation. The discussion related to the load-displacement envelope and the gap closure for LFCD1 is applicable to LFCD2. It is important to mention that the lower flare confinement ratio used in the current specimen is the reason why LFCD2 had extensive concrete spalling in the flare. The maximum capacity of LFCD2 was 95 % of that measured for LFCD1.

The dynamic properties for this specimen were calculated in the same way as LFCD1, Table 4-12. Using the chord stiffness, the structure period and frequency were calculated. The table shows that the initial structure period is 0.4 sec and its natural frequency is 2.51 Hz. At 1.25 times Sylmar, the stiffness dropped to 34% of its initial value with a rapid rate of stiffness degradation. After 1.25 times Sylmar, the stiffness degradation had lower value than that at the beginning of the structure where the gap started to close.

4.3.3. Base Hinge

Two displacement transducers were installed at the bottom of the columns to monitor any sliding. Figs. 4-75 and 4-76 show the history of the measured displacements. Table 4-13 summarizes the maximum, minimum and permanent measured displacement at the base of east and west columns for each run. As shown from the strain measurements, base hinge dowels started to yield as early as 0.75 times Sylmar. A maximum

displacement of 9 mm (0.367 in) occurred during 1.75-2 times Sylmar, which is almost 5.1% of the maximum displacement recorded at the top of the bent. The frame experienced a maximum permanent sliding of 0.8 mm (0.033 in) in the west column and 0.4 mm (0.016 in) in the east column. The permanent displacement is 2.73% of that recorded at the bent's top for the west column and 1.32% for the east column.

From sliding history graphs and table, it is noted that the permanent sliding started to change direction at 2.0 times Sylmar. Referring to the strain history in the base hinge dowels, Figs. 4-77 and 4-78, show that the permanent strain in the dowels changed direction from tensile strain to compressive strain at 1.5 and 1.75 times Sylmar. One possible reason of such behavior is partial crushing of the base hinge core that transferred higher axial compressive load to the dowels directly.

4.3.4. Strain Measurements

4.3.4.1. Base Hinge Dowels

The maximum and minimum values of strain data are summarized in Table 4-14. Where strains passed yield, the strains are written in underlined bold font. The maximum recorded strain is 7745 micro strain while the minimum recorded strain is -14621. The base hinge dowels started to yield as early as 0.75 times Sylmar, Figs. 4-77 and 4-78.

4.3.4.2. Column Longitudinal Reinforcement

The maximum and minimum values of strains are summarized in Table 4-15. Where strains passed yield, the strains are written in underlined bold font. The maximum recorded strain is 23007 micro strain, while the minimum recorded strain is –9775.

Column longitudinal reinforcement started to yield as early as 0.75 times Sylmar at the gap location, Fig. 4-79. Yielding started to spread down in the column reinforcement as the runs continues. Yielding was recorded in column reinforcement within the beam-column connection region at 1.0 times Sylmar.

4.3.4.3. Column Spirals

The maximum and minimum values of strains are summarized in Table 4-16. Where strains passed yield, the strains are written in underlined bold font. The maximum recorded strain is 9095 micro strain, while the minimum recorded strain is -6676. A few locations yielded at the top of the beam-column connection of the east column and in the beam-column connection region, Fig. 4-80. Recorded strains in the spirals were in general low.

4.3.4.4. Flare Longitudinal Reinforcement

The maximum and minimum values of strains are summarized in Table 4-17. Where strains passed yield, the strains are written in underlined bold font. The maximum recorded strain is 11285 micro strain, while the minimum recorded strain is -23636. Flare longitudinal reinforcement started to yield as early as 1.0 times Sylmar near the top of the flare location, Fig. 4-81.

4.3.4.5. Flare Hoops

The maximum and minimum values of strains are summarized in Table 4-18. Where strains passed yield, the strains are written in underlined bold font. The maximum

recorded strain is 428 micro strain, while the minimum recorded strain is -3327. The flare hoops started to yield at 2 times Sylmar at one location in the flare hoops, which is in the top third of the flare height, Fig. 4-82. An explanation of this behavior is included in more detail in Chapter 6.

4.3.4.6. Beam Reinforcements

The maximum and minimum values of strain data are summarized in Table 4-19. Where strains passed yield, the strains are written in underlined bold font. The maximum recorded strain is 21517 micro strain, while the minimum recorded strain is -680.The beam bottom reinforcement started to yield at 1.25 times Sylmar, Fig. 4-83. An explanation of why it yielded is discussed in more detail in Chapter 6. The measured strain level in the out-of-plane stirrups provided in the beam-column connection showed very low values, well below the yielding strain. This raises the question about the necessity of such a detail in the joint.

4.3.4.7. Summary for Strain Data

A summary of the yielded locations and when yield started to occur are shown in Table 4-20. Figure 4-84 shows more representative drawing for the location and the first occurrence of the yield strain. The numbers written adjacent to the yielded locations indicate the run factor where yield started to occur. Plots for every gauge recording versus time are included in Appendix A.

In summary the results for strains are as follows:

- Yielding occurred in all parts of the bent.

- Base hinge dowels and column reinforcement at the gap started to yield at the early stage of 0.75 times Sylmar.
- Most of the column reinforcement in the gap yielded at 1.0 times Sylmar accompanied by yielding of spirals in the joint region, base dowels and the extending of the yielding in the column reinforcements at a sections below the gap. Some yielding occurred in longitudinal flare reinforcement in the top third of the flare height.
- At 1.25 times Sylmar, yielding occurred in column longitudinal reinforcement extending to cover sections within flare height. Another spiral location yielded in the joint region and the beams' bottom reinforcement.
- At 1.5 and 1.75 times Sylmar, few new locations at column longitudinal reinforcement started to yield. Yield occurred mainly in the column reinforcement and in one location in the column spirals.
- At 2.0 times Sylmar, many locations started to yield in the column reinforcement to cover the whole height of the flare. Yielding occurred in the flare reinforcement at the top third and bottom third of the flare height.
- Few locations started to yield in the last two runs, 2.125 and 1.75-2 times Sylmar, in the column reinforcement and the beam bottom reinforcement.

4.3.5. Curvature

Figs. 4-85 through 4-94 show the measured curvature history. Figs. 4-95 through 4-98 show the maximum and minimum curvatures for the columns. The discussion made for the curvature measurements in LFCD1 is applicable for LFCD2. The main point is

that the calculated curvatures include the deformation caused by shear strains and that they cannot be separated from the vertical deformations.

4.3.6. Beam-Column Connections

The same procedure in calculating the stresses for LFCD1 was used for LFCD2. Figs. 4-99 through 4-102 show the stresses in east and west joints. The limits for tension and compression principal stresses recommended by Caltrans are shown in dashed lines. The figures show that the stresses started to exceed the tensile strength limit at 0.5 times Sylmar for the west joint. Also, they show significant change in stress values after 1.75 times Sylmar. The above results agree with the crack propagation observations listed in Table 4-11.

At 0.5 times Sylmar, the maximum measured horizontal force value is 23.2 Kips. Cracking of the joint was minor and the stresses exceeded the limits by very small value at this stage. As the force increased, cracking started to increase significantly as well.

4.3.7. Strain Rate Effect

The same concept used in LFCD1 is used in calculating the strain rate effect for LFCD2. This resulted in a strain rate of 19200 με, this yielded to an increase in the yield stress of 19.8 % and an increase in the concrete strength by 21.6 %.

4.4. SFCD1 TESTING AND RESULTS

As described in Chapter 3, this specimen was destroyed before starting the test, Fig. 4-103. Unfortunately the system did not record any data; however, the plastic residuals

were obtained after the shake table came to rest. The following are post failure observations:

- Severe cover spalling occurred at the top edge of the flare exposing the flare hoops, Fig. 4-104.
- Permanent gap widening in one side accompanied by permanent gap closure in the other side, Fig. 4-105b
- Severe concrete spalling at the base hinge, Fig. 4-105a.
- Extensive shear cracks extended along the columns height to the base hinge, Fig. 4-106.
- Extensive joint cracking, Fig. 4-106.

Table 4-21 shows the permanent readings for the bent displacement and base hinges sliding. These data were collected from the screen of the computer after the damage of the specimen, which showed the residual records only. The data in the table shows a severe permanent displacement of 19 mm (0.76 in). The east column had permanent sliding of almost 50% of the measured permanent displacement at the top of the frame.

Although the testing program was not completed as was planned, one of the objectives is achieved that the specimen sustained a severe random vibration that has an estimated maximum acceleration equal to 4 times the maximum acceleration of Sylmar earthquake.

4.5. SFCD2 TESTING AND RESULTS

4.5.1. Test Procedure and Observations

Figs. 4-107 and 4-108 show the devices for the specimen and their ID numbering.

The during-test observations and crack propagations are summarized in Table 4-22. The table describes the observed behavior for column, beam column-connection and the base hinges. Figs. 4-109 through 4-116 shows the crack patterns through selected load steps that have significant change in the specimen's behavior. The behavior can be summarized as follows:

No cracking was observed during the first runs up to 0.25 times Sylmar. Cracking developed slowly in both the beam-column connections and the columns until 1.0 times Sylmar, Fig. 4-110, where shear and flexural cracks propagation had significant increase in number and length. At 1.25 and 1.5 times Sylmar, minor crack development occurred in the beam-column connection while most of cracks propagation occurred in columns, Fig. 4-111. Between 1.75 to 2.5 times Sylmar, Figs. 4-112 through 4-114, little crack development occurred in all the specimen elements. At 2.75 times Sylmar, a significant crack was formed in columns. Significant increase in shear cracks and in joint cracks occurred at 3.0 and 3.25 times Sylmar, Figs. 4-115 and 4-116. After bucket removal, significant shear and flexural cracks were found in the beam.

The first observed concrete spalling occurred at the top edge of the flare started at 2.5 times Sylmar, Fig. 4-114. At 3.0 and 3.25 times Sylmar, extensive concrete spalling started to occur at the edge of the flare due to the gap closure, Fig. 4-115. No concrete spalling was observed at the base hinges.

4.5.2. Load-Displacement Relationship

The measured load-displacement relationship showed small loops at the end of each loop and sudden jumps in the records. To eliminate these records, the data were smoothed

and filtered from 10 Hz and above. Figs. 4-117 through 4-130 show the filtered load-displacement relationships plotted for each step individually while Table 4-23 summarizes the maximum and minimum filtered displacements and the corresponding forces. The permanent displacement after each run, chord stiffness of the system and dynamic properties are also included in the table. The observations of the load-displacement curve are as follows:

- Up to 0.25 times Sylmar, the system is almost linear elastic, Figs. 4-117 and 4-118.
- For both 0.5 and 0.75 times Sylmar, the load-displacements loops start to show small non-linearity in the loops. The first yielding occurred at 0.50 times Sylmar, Figs. 4-119 and 4-120.
- At 1.0 times Sylmar, the system started to have wider loops, Fig. 4-121.
- At 1.25 times Sylmar, the load-displacement curve started to have significant change with wide loops and constant force of almost -324.7 KN (–73 Kips) between the displacements of approximately -30 mm (-1.2 in) to -36 mm (–1.4 in). The minimum recorded force level is –341.2 KN (-76.7 Kips) with a minimum displacement of –42 mm (–1.67 in), Fig. 4-122.
- At 1.5 times Sylmar, the minimum load dropped to –316.3 KN (–71.1 Kips) with a displacement of 42 mm (–1.67 in), which is the same value of the previous run displacement, Fig. 4-123.
- From 1.75 to 2.5 times Sylmar the system started to generate wider loops from the previous run with an increase in the absolute maximum force, Figs. 4-124 through 4-127.

- At 2.75 times Sylmar, a significant increase occurred in the absolute maximum displacement and absolute maximum force with respect to the previous runs, Fig. 4-128.
- At 3.0 and 3.25 times Sylmar, the absolute maximum displacement started to increase at a higher rate while, the rate of force increase stared to drop, Fig. 4-129 and 4-130.

Fig. 4-131a shows the filtered accumulative load-displacement curve in solid lines, while the load-displacement envelope is shown with a dashed line. To show the effect of filtration on the data, the unfiltered results are plotted in Fig. 4-131b. The filtration smoothed the curve. It is important to mention that as the process generates smooth loops that shows the trend of the curve and easier to study, it also decrease the peaks of the original records.

At –43 mm (–1.7 in) the envelope has a kink, after which the system started to gain stiffness. The curve started to have a higher force level reaching a maximum force value that is almost 27% higher than that recorded at the beginning of the first plastic phase. Referring to test observations summarized in Table 4-22, it could be seen that between 1.75 and 2.25 times Sylmar, a significant change in crack development was noted; very little crack development occurred in all specimen's elements. Starting from 2.75 times Sylmar, cracking started to increase significantly as well as concrete spalling.

In summary, it is clear that the system started to gain stiffness at almost 43 mm (1.7 inches). Since no new elements were added to the system during the runs, the increase of the system stiffness was through a gap closure. Evidence of gap closure is the concrete spalling at the top edge of the flare during the late runs.

The chord stiffness is calculated using the inclination of a line connecting maximum displacement to minimum displacement for each run individually. Table 4-23 shows that the initial structure's period is 0.19 sec and its natural frequency is 5.29 Hz. At 1.0 times Sylmar, the stiffness dropped to 25% of its initial value with a rapid rate of stiffness degradation. After 1.00 times Sylmar, the stiffness degradation has lowered because the gap started to close.

4.5.3. Base Hinge

Two displacement transducers were installed at the bottom of the columns to monitor any sliding. Figs. 4-132 and 4-133 show the history of the measured displacements. Table 4-24 summarizes the maximum, minimum and permanent measured displacement at the base of east and west columns for each run. A maximum displacement of 9 mm (0.365 in) occurred during the runs, which is 9.5 % of the maximum top displacement. The frame experienced a maximum permanent sliding of 0.6 mm (0.024 in) in the west column and 0.5 mm (0.02 in) in the east column. The permanent displacement is 5.3 % of that recorded at the bent's top for the west column and 4.4 % for the east column.

4.5.4. Strain Measurements

4.5.4.1. Base Hinge Dowels

The maximum and minimum values of strain data are summarized in Table 4-25. Where strains passed yield, the strains are written in underlined bold font. The maximum recorded strain is 17506 micro strain while the minimum recorded strain is -9448.The base hinge dowels started to yield as early as 0.5 times Sylmar, Figs. 4-134 and 4-135.

4.5.4.2. Column Longitudinal Reinforcement

The maximum and minimum values of strain data for column bars are summarized in Table 4-26. Where strains passed yield, the strains are written in underlined bold font. The maximum recorded strain is 19267 micro strain, while the minimum recorded strain is -11364. The column longitudinal reinforcement started to yield as early as 0.5 times Sylmar at the gap location, Fig. 4-136. Yielding started to spread down in the column reinforcement as the runs continued. Yielding was recorded in column reinforcement within the beam-column connection region at 1.0 times Sylmar.

4.5.4.3. Column Spirals

The maximum and minimum values of strain gauges are summarized in Table 4-27. Where strains passed yield, the strains are written in underlined bold font. The maximum recorded strain is 3286 micro strain, while the minimum recorded strain is -2179. Only one location yielded near the top of the flare, Fig. 4-137. Recorded strains in the spirals were very low.

4.5.4.4. Flare Longitudinal Reinforcement

The maximum and minimum values of strain gauges are summarized in Table 4-28. Where strains passed yield, the strains are written in underlined bold font. The maximum recorded strain is 3715 micro strain, which is the maximum record a strain gauge can measure, while the minimum recorded strain is -1583. As shown from tables and strain measurements, flare longitudinal reinforcements started to yield as early as 1.0 times

Sylmar at the gap location, Fig. 4-138.

4.5.4.5. Flare Hoop Reinforcement

The maximum and minimum values of strain gauges are summarized in Table 4-29. Where strains passed yield, the strains are written in underlined bold font. The maximum recorded strain is 13796 micro strain, while the minimum recorded strain is -2288. The flare hoops started to yield at 1 times Sylmar at one location, Fig. 4-139.

4.5.4.6. Beam Reinforcement

The maximum and minimum values of strain gauges are summarized in Table 4-30. Where strains passed yield, the strains are written in underlined bold font. The maximum recorded strain is 21872 micro strain, while the minimum recorded strain is -696. Beam bottom reinforcement started to yield at 1.25 times Sylmar, Fig. 4-140. The measured strain level in the out-of-plane stirrups provided in the beam column connection was very low, well below the yielding.

Table 4-31 summarizes the yielded locations and when they started to yield. Figure 4-141 show more representative drawing for the location and the first occurrence of the yield strain where the numbers written beside the yielded locations indicate the run when yielding started. Plots for every gauge recording versus time are included in Appendix A.

4.5.4.7. Summary of Maximum Strain Data

In summary the results for strains are as follows:

- Yielding occurred in all elements.

- Base hinge dowels and column reinforcement started to yield as early as 0.5 Sylmar.
- Column reinforcement at the gap started to yield at 0.5 times Sylmar.
- At 1.0 times Sylmar, many locations started to yield in beam top and bottom reinforcement.
- Column spirals within the joint region started to yield at late stage of 3.0 times Sylmar

4.5.5. Curvature

Figs. 4-142 through 4-151 show the measured curvature history. Figs. 4-152 through 4-155 show the maximum and minimum curvatures for the east and west side column. The discussion made for the curvature measurements in LFCD1 is applicable for SFCD2 as well. The main point is that the calculated curvatures include the deformation caused by shear strains and that they cannot be separated from the vertical deformations.

4.5.6. Beam-Column Connections

The same procedure in calculating the stresses was used for SFCD2 as was used in the other specimens. Figs. 4-156 and 4-157 show the stresses in east joints. The west joint was excluded from the results because the obtained measurements were many times higher than the other values in the beam-column connection region. This reflects an error in the measurements that happen during the test process. The limits for tension and compression principal stresses that are recommended by Caltrans are shown in dashed lines. The figures show that the stresses started to exceed the tensile strength limit at 1.0

times Sylmar for the east joint. Also, they show significant change in stress values after 1.75 times Sylmar. The stress limit was exceeded before the gap closed

At 0.75 times Sylmar, the maximum measured force value is 58.2 Kips, which is close to the design force value from the preliminary finite element analysis. Cracking of the joint was minor and the stresses exceeded the limits by very small value at this stage. As the force increased, cracking started to increase significantly as well.

4.5.7. Strain Rate Effect

The same concept used in LFCD1 is used in calculating the strain rate effect for LFCD2. This resulted in a strain rate of 20800 με, this yielded to an increase in the yield stress of 19.9 % and an increase in the concrete strength by 21.8 %.

4.6. OVERALL EVALUATION

One of the objectives of the current research is to evaluate the proposed detailing efficiency with respect to Caltrans Seismic Specifications. This evaluation includes the study of the achieved ductility and efficiency of structural elements performance (base hinge, beam-column connection, flare detailing and beam design).

4.6.1. Displacement Ductility

In order to calculate the ductility index, a yield displacement is needed. An equivalent bilinear load-displacement curve is obtained using the measured one. An effective yield point is calculated by connecting the origin of the load-displacement curve to the first yield point occurring in the longitudinal column reinforcement, which is calculated from

the measured strains. The second line of the curve is chosen so that it divides the plastic deformation part into equal areas above and below the new line. The end point is at the location of ultimate displacement and force, Fig. 4-158. Figs. 4-159, 4-160 and 4-161 show the measured envelope in solid line and the idealized curve in dashed lines for LFCD1, LFCD2 and SFCD2 respectively. The values of loads and displacements are summarized in Table 4-32 along with the calculated ductility of each specimen. The yield displacement of LFCD2 has a higher value than that of LFCD1, which resulted in a lower ductility ratio of the specimen. Since the load didn't drop, the maximum displacement is the maximum recorded displacement.

The ductility ratio for the three specimens exceeded a ductility ratio of 6, which was set as the minimum ductility demanded by Caltrans Seismic Specifications. The ductility ratio at gap closure is below the minimum ductility demand. It is important to note that the calculated ductility ratio included the rigid body displacement due to base slippage. In order to show the difference in ductility level due to this behavior, an average value of the base slippage is calculated and subtracted from the specimens' maximum displacement, which resulted in a lower level of ductility.

4.6.2. Gap Closure

Despite that preliminary finite element analysis and hand calculations showed that the gap does not close using the current detailing, the three specimens had gap closure. The two tall specimens (LFCD1 and LFCD2) had gap closure almost at the same displacement at a ductility level lower than that set as the minimum limit of ductility demand, Table 4-32. Closure of the gap increased the flexural capacity at the top of

columns, which altered the strain increase in the column reinforcement.

One of the impacts of the gap closure was that the load-carrying capacity of the whole system increased to a level that was not taken into account during the design phase. This increased the level of the applied shear force to the columns and the base hinge. The higher shear force caused shear cracks to appear in the tall columns while most of the cracks in the short columns were shear cracks. It also changed the systems structural configuration. This subjected the beam to a higher moment and shear force that caused shear cracks in the beam.

An advantage of gap closure is that it restrained the system displacement and increased the load-carrying capacity of the system in the late stage of loading history after the dissipation of considerable amount of energy. This behavior prevented the collapse of the system and allowed it to withstand higher force level.

4.6.3. Base Hinge

The behavior of the base hinge was not satisfactory for the following reasons:

- Base dowels yield at a very early stage for the three specimens.
- Base hinge had considerable amount of sliding that affected system ductility.
- They had permanent displacement that is hard to repair after the earthquake event.

4.6.4. Beam-Column Connection

Significant cracking occurred in the beam-column connections in the early stages of the testing despite that it was proportioned and detailed according to the current

specifications. The measured principal stresses exceeded the maximum limit set by the current specifications. The out-of-plane stirrups proved that they have little contribution to the confinement or enhancing the joint behavior. The effect of these stirrups in confining the joint needs to be evaluated especially with the existence of the out-of-plane girders and slab decks.

The problem of severe damage occurring in connections is that it is one of the most important elements of the structure as it keeps the integrity of the framing actions of the elements. The other problem is that the joint is very difficult to repair for its location and detailing. One of the issues that might have an effect in the joint behavior is the bridge slab and crossing beams, which were not modeled in the specimens under study.

4.6.5. LFCD1 Versus LFCD2

The two specimens performed well with respect to the achieved ductility ratios that exceeded the minimum requirement. The load-displacement relationship is similar for LFCD1 and LFCD2, Fig. 4-162. The load-displacement curves for both the specimens are almost identical prior to gap closure, which after, LFCD2 had lower maximum load capacity. The reason behind that difference is that the lower confinement ratio allowed higher level of concrete spalling that reduced the capability of the flare to transfer load. The crack pattern and crack propagation are almost same. The only difference was in the amount of spalled concrete in the flare region.

4.6.6. SFCD1 Versus SFCD2

Despite the fact there are no available records for SFCD1, the two specimens were

comparable to each other from the following points:

1. Crack patterns had the same trend for both specimens: extensive beam-column connection cracking, extensive shear cracking in the columns and extensive shear and flexural cracking in the beams.
2. SFCD2 withstood an earthquake record of 3.5 times Sylmar and the test stopped not because the specimen failed, but, because the shake table achieved its maximum permissible capacity. SFCD1 was destroyed at a record that was estimated to be 4.0 times Sylmar.
3. Concrete spalling in the flare had the same trend for both the specimens of concrete cover spalling at the top of the flare where gap closed, however, SFCD1 had small amount of spalling that were not existing in the case of SFCD2.

5. POST-TEST ANALYSIS

5.1. INTRODUCTION

The experimental results presented in Chapter 4 showed that the actual response of the test models was different than the results of the pre-test analysis. The pre-test finite element analysis and the hand calculations showed lower force level and lower displacements than those obtained from the testing. It is important to conduct more reliable analysis for the following reasons:

- To investigate behaviors that were revealed through data processing that needed verification and explanation, and
- To investigate parameters not examined in the tests such as the effect of flare gap size, and base hinge dimension.

DIANA[9], a non-linear finite element program that was designed to model behavior of reinforced concrete structures[32], was used in this stage of study. Many studies were conducted using DIANA and good correlations were seen with the experimental results[32]. Three groups of analytical models were created.

5.1.1. "Group I" – Test Specimens

The objective of creating the first group was to perform analysis for the tested specimens. This enables a more complete understanding of how the specimens behaved. It will also permit the study of the P-Δ effect in the analysis. It is also important to correlate the validity of the model before investigating the parameters.

Four specimens that have the same configurations and reinforcement detailing as those in LFCD1, LFCD2, SFCD1 and SFCD2, Table 5-1, were modeled. In addition four more models LFCD3, SFCD3, LFSS1 and SFSS1 were studied.

The same column detailing of LFCD2 and SFCD2 was used in LFCD3 and SFCD3 but the P-Δ effect was excluded in the analysis to investigate its effect on the system and whether it could be ignored in practical analysis of the system, Table 5-1.

The beam span length in the experimented specimens was lengthened due to practical purposes as was described in Chapter 3. The question was whether this changed the behavior of the system. To answer this question two specimens were analyzed, LFSS1 and SFSS1, which have the same configuration as the experimental ones except that they have a shorter beam span that is equal to the span obtained from scaling one of the bridges as a guideline for the prototype, Table 5-1.

5.1.2. "Group II" – Flare Gap

A basic question for the project is the impact of the flare gap. Does it change the yield capacity and ductility of the system? Does the existence of the gap make the specimens closer to prismatic columns with constant column diameter? What is the minimum gap width to be used so that the gap would not close?

This group contains 10 specimens: five tall columns and five short columns. As SFCD1 was destroyed during the tuning process, the low flare confinement ratio was used as the basic detailing for creating the other specimens, which are LFCD2 and SFCD2. LFWG0 and SFWG0 are two specimens that have no gap. The longitudinal flare reinforcement does not extend into the beam depth, Table 5-1. LFWG1 through LFWG3

and SFWG1 through SFWG3 are specimens with gap sizes of 12.7 mm (0.5 in), 19 mm (0.75 in) and 25.4 mm (1.0 in), Table 5-1. Specimens LWNF1 and SWNF2 are two specimens that have prismatic columns with no flares, Table 5-1.

5.1.3. "Group III" – Base Hinge Size

Another factor is the effect of the size of the base hinge on the bent behavior. This group focuses on studying the effect of the base hinge size on the overall behavior of the specimens. This group consists of six models with the same reinforcement configuration and different base hinge sizes. LFBH1 and SFBH1 are two specimens that have base hinge gap of zero. LFBH2, LFBH3, SFBH2 and SFBH3 are specimens with same gap size as the specimens but different base hinge diameters of 101 mm (4 in) and 304 mm (12 in) respectively, Table 5-1.

5.2. FINITE ELEMENT MODELING

5.2.1. Idealization

The same two-dimensional meshes that were used in the pre-test analysis using ADINA were used with the DIANA program. Contact elements were replaced with spring elements that have zero stiffness till the gaps close at the top of the flare and at the base hinges, Fig. 5-1. Interface elements were added between the base dowels and the surrounding footing concrete to model yield penetration or base dowels slippage.

The concrete was modeled as plane stress elements with thickness equal to the structure out-of-plane dimension at the location of each element. The reinforcement was modeled as truss elements with perfect bond between the reinforcement and the

surrounding concrete elements except at the base dowels as was mentioned previously.

5.2.2. Material Models

DIANA enables the use of accurate stress-strain curves for materials by using multi-linear idealization with flexibility on the number of segments to be used. To model the biaxial failure stress state, the material stress-strain curve is combined with a specified failure envelope and suitable cracking model.

For concrete, a uniaxial stress-strain relationship was used based on the Kupfer's model[1,18]. In the construction phase, the cylinder moisture was preserved as they were encased and covered till testing. The specimens did not have the same curing conditions as they were exposed to air and the formwork was removed as soon as the concrete was hardened. To take into account the pre-test cracking due to handling of the specimens and the difference of curing conditions among the specimen and the test cylinders, the uniaxial stress-strain relationship was multiplied by a factor of 0.85[17]. An average value for the strain rate effect based on the calculations reported in Chapter 4 is then taken by multiplying the reduced curve by 1.2. The final magnification factor for the uniaxial stress-strain curve is 1.02, Fig. 5-2. In order to model the biaxial stress state in tension and compression, Drucker-Prager failure criteria[9,34], Fig. 5-3, is combined with cracking mode in order to model the concrete behavior where one of the principal stresses is tension in the biaxial stress-state[9,34]. This concept is usually done because the model cannot model the brittle behavior of concrete[9,34]. A friction angle of 30º is used for Drucker-Prager model as recommended for concrete in the DIANA manuals[9].

Cracking is specified as a combination of tension cut-off, tension softening, and shear

retention . The tension cut-off is the failure envelope of the concrete for the tension-tension or tension-compression stress state. Mode 2 tension cut-off was used which indicates linear stress cut-off where a crack arises if the major principal tensile stress exceeds the minimum of f_t and $f_t\ (1+\sigma_{lateral} / f_c)$, with $\sigma_{lateral}$ being the lateral principal stress[9], Fig. 5-3. The tension softening relates the stress to the concrete post cracking stress strain. A linear relationship was chosen in order to model the tension softening, Fig. 5-3. The shear retention reflects the capability of the elements to transfer shear stress after cracking through aggregate interlock mechanism. A value of 0.2 was used in previous studies for plain and reinforced concrete and was merely chosen based on experience[32]. It was found that this value was satisfactory in estimating the maximum load-carrying capacity. In the current study, reinforcement was modeled as truss elements; no dowel action was taken into account after cracking. Therefore, a higher value of 0.6 was used for shear retention to account for this behavior, and proved to provide better correlation with experimental results. This value is close to what is recommended by the ACI code of practice, which reduces the concrete shear strength to 0.5 of its value before cracking[2]. In general, the change of the value did not cause significant change in the overall behavior of the specimens, however, it ensured the stability of the solution until the failure of the system.

In reinforced concrete the interaction between the reinforcement and the concrete is highly complex. The interaction is controlled by secondary transverse and longitudinal cracks in the vicinity of the reinforcement. This behavior can be modeled with a bond-slip mechanism where the relative slip of the reinforcement and the concrete is described in a phenomenological sense. The mechanical behavior of the slip zone is then described

by the interface element with a zero thickness. In DIANA, the relationship between the normal traction and the normal relative displacement is assumed to be linear elastic, whereas the relationship between the shear traction and the slip is assumed as a nonlinear function. DIANA offers two pre-defined curves for the relationships between shear traction and slip: a Cubic function according to Dörr, Fig. 5-4a, and a power law relation proposed by Noakowski[9], Fig. 5-4b. The cubic function was used to model the bond slippage between the dowels and the footings to account for yield penetration. Ignoring the yield penetration in the joint would result in structure with higher stiffness, and hence, upper bound solution.

Since the differences between yield stress values for the different bar sizes were not large, Table 3-1, and for the sake of simplifying the process of modeling, one stress-strain curve was used for all bar sizes, which is standard grade 60 stress-strain curve[34]. The strain rate effect was taken into account by increasing the yield value by 20%, Fig. 5-5. The Von-Mises failure criterion was used to model the biaxial stress state for the steel.

The gap spring elements have stiffness-displacement relationship as shown in Fig. 5-6. The forces generated in the elements are zero until the gap closes then a constant stiffness is generated. The choice of the stiffness value is difficult because high values might lead to instability of the solution especially if the stiffness is added after the occurrence of yielding and the stiffness of the structure is degraded. Moreover, the high stiffness would cause most of the load to flow through the springs that would deviate the load path from the real behavior. The experimental results were used as a tool in the choice of the spring stiffness value. It was found that the high stiffness is needed at the flare while relatively small stiffness is needed at the base hinge to approach the

experimental results. It is important to note that the spring elements do not completely prevent the relative displacements between the faces of the gap because they do not have infinite stiffness.

5.2.3. Loading and Boundary Conditions

The same loading configuration and boundary conditions that were used in the pre-test analysis were used in this analysis (Chapter 2). The lateral load was modeled as single concentrated load acting on one end of the beam. It is important to mention that one run was made using distributed lateral loads that represent the load distribution generated from the test setup. It was found that the difference in the load-displacement curve was negligible between the two cases of single lateral load and the distributed ones. It was decided to use the single load configuration for the rest of the runs. The lateral load was incrementally increased until the failure of the system.

The test specimens were subjected to dynamic loading with the direction of the load changing as the shake table moves in each direction. Since the analysis is a pushover static analysis, two separate runs were made for the same structure. The first run with the lateral load applied in the west direction and increasing it until failure. The second run was made using the same load increments in the opposite direction. The results obtained from the two runs were plotted on the same graph for LFCD1, LFCD2, SFCD1 and SFCD2. As the lateral load is applied as concentrated load at one end, the load direction has an impact on the beam-column connections stiffness and the crack formation in the beam for in the west direction it generates compressive force while in the east direction it generates tensile force.

5.2.4. Solver Technique

In an ordinary iteration process the predictions for the displacement increments can become very large when force increments are used. This is the case especially if the load-displacement curve is almost horizontal. If a fixed load increment is prescribed, this results in very large predictions for the displacements. The problem can be overcome with the use of an arc-length method. Using the arc-length method, the snap-through behavior can be analyzed, just as it could in displacement control. However, it is possible to define a system of loads in different locations with different values that could not be substituted by prescribed displacements. Moreover, the arc-length method is also capable of passing snap-back behavior where displacement control fails, Fig. 5-7.

The arc-length method constrains the norm of the incremental displacements to a prescribed value. This is done by simultaneously adapting the size of the increment. Note that the size is adapted within the iteration process and is not fixed at the moment the increment starts. A detailed description can be found in references 9 and 14. The arc-length method with snap back was found to be the most suitable for the current problems due to the fact that the load-displacement curve stiffens after yielding. It was used throughout all the analysis.

5.3. GROUP "I" ANALYTICAL RESULTS

The results of this group are of great importance with respect to the other groups for it contains the analysis of the tested specimens, hence, they draw a datum of comparison for the other specimens and ensure the reliability of the finite element analysis results for further parametric study. Due to that reason, the results of these runs are discussed in

more details and more results are presented. In the other groups, the specimens are discussed in less detail for the main focus was to compare the overall behavior with experimental specimens. Specimen LFCD2 and SFCD2 were chosen from this group as the base for comparing other specimens responses as there are no measured data available for SFCD1.

5.3.1. LFCD1 & LFCD2

Load-Displacement Relationship

The load-displacement curve is an important measure of the structure behavior, its ductility, and its strength. It is used to judge the effectiveness and soundness of the analysis by comparing the one obtained from the analysis with that obtained from the test results. The deformed shape of the structure at the last load step is shown in Fig. 5-8 for LFCD2. It can be seen that the gap springs were closed and provided contact between the flare and the beam and between the base hinge and the footing.

The load-displacement curves obtained from the analysis for LFCD1 and LFCD2 are shown in Figs. 5-9 and 5-10 respectively. The solid lines in the plots represent the analytical results while the measured load-displacement curve is the dashed lines. An analytical effective yield value was calculated based on the displacement where longitudinal column reinforcement started to yield following the same method described in Chapter 4, Fig. 4-158.

Tables 5-2 and 5-3 show the obtained results of maximum displacements and forces in comparison to the measured data, which show very good agreement in both specimens in forces, displacements and ductility ratios. The results were calculated as a percentage

of the measured response to show the efficiency of the analysis in estimating the structure response. The finite element analysis did undergo much higher displacements and forces than the experiment. It is important to note that the specimens were not taken to complete failure. The estimated measured gap closure displacement is close to the one obtained from the analytical results in both cases. One of the advantages of using the spring elements is that through their loading history a precise calculation for the gap closure is possible.

The analytical load-displacement curves showed a slight increase in initial structure stiffness because the cross section of the analytical specimen has a higher moment of inertia than that of the real one due to the 2D idealization of the cross section. Also, the biaxial stress state for the plane stress elements has higher strength at the edges of column as mentioned in Chapter 2. Another factor that contributed to this difference is ignoring bond-slip in the beam-column connection for the column.

Plasticity Status

DIANA enables the graphical presentation of plasticity status for concrete and steel elements at the integration points of the elements. The program gives a symbol of a triangle at these locations. The relative size of the triangle is a measure of the plastic strain. A plot of these elements enables comparing with the crushed or spalled locations in the experiments. Moreover, it enables an investigation of the failure mode.

A plot of the concrete elements that reached or passed the plasticity limit is shown in Fig. 5-11. The figure shows the results of the load in the west direction. The figure shows that the highest strains are located on the elements at the top of the column, base hinge

section, and middle third region of the flare height of the west column and at the top edge of the flare. The concrete spalling locations from the experiments, Fig. 5-12, shows that concrete cover spalling location is the same as the one from the analysis. While the west column suffered from concrete spalling at the top and the middle third region of the flare region, only the top portion of the flare suffered from spalling in the east column.

Fig. 5-13 shows the steel elements that entered the plasticity limit. The figure shows that the yield is distributed along the column reinforcement in the top gap region, the flare longitudinal reinforcement, and the beam bottom reinforcement at the face of the beam-column connection. The analysis showed high yield value at the base dowels penetrating inside the foundation. Referring to the yielded locations recorded experimentally in Chapter 4, a good correlation between the two results could be found. DIANA is capable of estimating the failure mode and failure location to a high level of accuracy.

Cracking Pattern

The cracking pattern obtained from the analysis for LFCD2 is shown in Figs. 5-14 and 5-15 for the lateral load in the east and the west directions respectively. The figures show extensive cracking in the columns, the beam-column connection and the beam at generally the same locations marked during test runs, Fig. 5-16. The number of cracks and its distribution is higher in the analytical models due to the fact that the specimen was pushed to failure in both directions while in the test, it achieved the maximum displacement in one direction only. Also, in the experiment, the two-direction loading causes some cracks to be closed during each run that were not captured using static

pushover analysis. DIANA draws cracking for each element at the location of its integration points that has reached to cracking even if the crack width is invisible. This can give wrong impression about the number of the cracks in comparison to the test.

System Capacity and Gap Closure

Figs. 5-17 and 5-18 show the results M-ϕ curve of section analysis performed for the column core based on the real material properties data obtained from the test specimens and including the strain rate effect. The calculations show a maximum moment capacity for the core of 125.4 KN-m (1110 in-kips) and 19.8 KN-m (175.3 in-kips) for the base hinge. Using the above values in calculating the system maximum capacity leads to ultimate force of 178.6 KN (40.16 Kips), which is 13.3 % lower than the measured load at yield for LFCD1 and 12.3 % lower than that of LFCD2. While, the simple plastic mechanism solution is supposed to be an upper bound solution, it showed lower force value.

The reason behind this difference is that section analysis is based on Bernoulli's assumption that plane sections before deformations remain plane after deformation[13]. This assumption is considered true where no abrupt changes in the cross section or loading occurs and in cases where shear deformations are negligible (Bernoulli regions or B-regions). The gap at the top of the flare and the bottom of the columns presents discontinuity (D-region) because of the sudden change in the cross section.

In order to show that the above mentioned assumption is invalid in case of a flare with a gap, the vertical deformations obtained from the finite element analysis are drawn for the west column before gap closure, Fig. 5-19a. The figure shows that the top section

and the top flare sections are not plane after deformation. For comparison, another section is shown at the middle of the column section far from the D-regions, which is plane after deformation. As the gap closure did not cause the flare projection to fully contact with the beam, the section is expected to deviate more from the planar shape after gap closure. Fig. 5-19b shows the same column after gap closure where the top sections are not plane while the section in the mid-height remains plane. It is now evident that section analysis is not applicable in this case for the estimation of the yield force or the maximum carrying capacity of the system, as it would lead to unsafe element design. Another method is needed for such cases, which is developed in Chapter 6. It is important to mention that the figure vertical deformation of the top section shows that the portion of the section under compression is subjected to higher strains than the other sections which concentrate higher stresses at the edges and, hence, increasing the moment arm to increase the section capacity.

Fig. 5-19 also shows that the gap closure calculations based on section analysis would deviate from reality. It is clear that the displacement at the edge of the gap would be higher than that calculated based on curvature, which explains why the preliminary calculations were unable to predict the gap closure.

Curvature

In Chapter 4, it was shown that the measured curvature along the column height has an unexpected change in sign or decrease in the curvature value mainly in sections 3 and 4 which are located within the flare height. This occurred because the method used in measuring the curvature does not differentiate between the displacements occurring due

to shear deformation and those due to flexural deformation. The finite element analysis helped in investigating this behavior. Fig. 5-20a shows section 3 and its location where instrumentations were mounted for LFCD1. The corresponding displacement values for each point were obtained from the finite element analysis. The final deformed shape of the segment under study is shown in Fig. 5-20 (b) with respect to the undeformed configuration of section 3 boundaries. Finite element analysis made it possible to separate the horizontal displacements from the vertical ones, Figs. 5-20 (c) and (d) respectively. The rods carrying the transducers are assumed to maintain the same angle between the column surface and the rods before and after deformation.

Locating the displacement transducers on the deformed structure shows that the horizontal deformations caused the transducer on the right hand side to shorten and the one on the other side to elongate. In contrast to that, the vertical deformations caused the right hand side transducer to elongate and the opposite side to shorten. It should be noted that this effect is due to the trapezoidal shape of the element and it would not occur in prismatic members.

To evaluate the effect of shear strain on the calculated curvature, the calculated curvature was obtained from each deformation and compared with the final curvature. The vertical deformations contributed to the final calculated curvature by a value of (0.000865) while the horizontal deformation adds (-0.0015397) to produce a final value of (–0.000675). This implies that the calculated curvature from shear strains is dominating in the method of curvature calculations where shear deformation is significant. Note that the calculated curvature from the finite element analysis is close to the maximum calculated value obtained from the experimental results, (-0.000725),

which gives another indication on the effectiveness of the finite element analysis. The instrumentation used to measure curvature should be able to separate between the vertical and horizontal displacements. This could be achieved by measuring the absolute displacements relative to a fixed reference.

Stress Trajectories

Principal stresses plots are a powerful tool of investigating how the load transfers through different parts of the structure. It also gives a visual idea where stress concentration occurs and finally they are used to develop strut-and-tie models. DIANA enables graphic output of the principal stresses. The principal stresses for LFCD2 are plotted at load level of 172.1 KN (38.7 Kips) before gap closure, Fig. 5-21, and at load level of 237.1 KN (53.3 Kips), Fig. 5-22, after the gap closure to compare the stress flow between the two cases. The loading is to the west in both figures. A closer look shows that before gap closure, the flare top edge have low stress level which is not the case after gap closure where stresses flow through the flare edge.

The same behavior can be observed at the base hinge region. Before gap closure, the stresses had low value at the base hinge edge. After the gap closure at the base, high stresses started to develop at the base hinge edge. A detailed analysis of the stress flow is included in Chapter 6.

5.3.2. LFCD3

This specimen is the same as LFCD1 except that the analysis was carried out without geometrical non-linearity, which accounts for the P-Δ effect. Fig. 5-23 shows the load-

displacement curve of LFCD3 and the one carried out for LFCD2. It shows that the difference between the two curves is very small until the beginning of yielding where significant difference occurs and they increase as the displacement increases. After the gap closes and the system gained additional stiffness, the difference between the two curves seems to be unchanged until a second yielding of the system occurred and the difference increases as the displacement increases. In other words, the P-Δ effect is not significant until yielding takes place. This kind of a behavior mainly occurred due to the change in modes of resisting the lateral load before and after yielding.

In the design phase, the P-Δ effect is not often included and the structure is solved only for the material non-linearity. This leads to an over-estimated maximum-load carrying capacity, and hence, stiffer structure. To approach the actual load-displacement curve, a correction of the load-displacement curve due to the P-Δ effect is needed. For single columns fixed at the base, a correction is made based on converting the increase in moment due to the drift of the vertical load at the top of the column into an equivalent horizontal load as shown in equation 5.1[19].

$$\Delta F = (P \times \Delta) / H \qquad (5.1)$$

Where;

H = Height of the point of lateral load application

ΔF = Lateral load increase due to the P-Δ effect

Δ = Displacement at the top of the column.

P = Total vertical weight

This approach is used for the current structure, which is shown in Fig. 5-23. It over-

estimated the yield load value slightly. It almost intersects the curve of LFCD2 but continues to a higher displacement. In fact, the gap closure and the increase in stiffness made the difference between the curves better than it would be in structures without gap closure.

In frames and multi-story structures as well, the lateral load is resisted through shear deformation, flexural deformation, or combined action, Fig. 5-24. The flexural deformation mode causes the load to be resisted through axial compression and tension forces in the columns. The shear deformation mode occurs in structures where columns have relatively small flexural stiffness with respect to the slab diaphragms or rigid beams. The same concept is applicable for one-story frames as well. The flexural mode causes part of the lateral load to be resisted by axial tension and compression in the columns as long as the structure's elements keep their strength and integrity. As the hinges formed at the top of the columns, the frame loses a great deal of its framing action, and hence, the only available mode is the shear mode that is capable to resist lateral load and no significant change in the axial load occurs. This change of behavior affects the correction for the P-Δ effect.

To understand this behavior more clearly, let us idealize the system by a rigid bar attached to translational spring k_t at the top and another rotational spring k_r at the base, Fig. 5-25. The translational spring represents the shear stiffness of the structure while the rotational spring represents the flexural stiffness. Now let the system be subjected to a lateral load F and another vertical load P. It is clear that the load generated in the translational spring would be equal to the lateral applied load plus an increment ΔF that represent the P-Δ effect. The load generated in the spring could be calculated by

considering equilibrium of the system, Equation 5.2.

$$K_t \times \Delta = F + \Delta F = F + (P \times \Delta) / H - M / H \quad (5.2)$$

Where;

F = Lateral applied load

M = Moment generated in the rotational spring due to the flexural mode

K_t = Translational spring that represent structure's shear stiffness

As the system loses its flexural strength by the formation of plastic hinges, the last term becomes negligible and the equation reduces to Equation 5.3.

$$F + \Delta F = K_t \times \Delta = F + (P \times \Delta) / H \quad (5.3)$$

A comparison between the values of ΔF in the two equations shows that the first case has lower value of ΔF than that in the second case due to flexural mode existence. Knowing that the flexural mode is the predominant mode in regular reasonably proportioned frames would imply that as the plastic hinges form in a system, the P-Δ effect has greater impact.

Another issue is that these columns are in double curvature. The correction of a single column in single curvature is not applicable. To understand the difference, let us assume the case of prismatic columns with moment capacity at the base equals to 15 % of the top of the column moment. This is almost the ratio between the capacities of the core ultimate moment and the base hinge obtained from the sections analysis. The column deformed shape and the moment diagram along the column height is as shown in Fig. 5-26. It is clear that at ultimate conditions, the ratio between the heights H_1 and H_2 is equal to the ratio between M_b and M_t. Assuming that the ratio would remain the same through the loading history, the point of zero moment would remain at the same elevation from

the base, H_1.

Now, let us separate the structure at the point of zero moment and study each part individually, Fig. 5-27. The deflection values at the top and the bottom parts of the column could be calculated using equations 5.4 and 5.5 respectively.

$$\Delta_1 = \frac{F \times H_1^{\,3}}{3 \times E \times I} \tag{5.4}$$

$$\Delta_2 = \frac{F \times H_2^{\,3}}{3 \times E \times I} \tag{5.5}$$

From which the ratio between the Δ_1 and Δ_2 could be evaluated. Each part of the column could be considered as a separate column that needs correction where equation 5.1 is applicable. Doing so would lead to ΔF_1 for the lower part and ΔF_2 for the upper part that is equals to $[(P \times \Delta_1) / H_1]$ and $[(P \times \Delta_2) / H_2]$ respectively. This means that the applied load needs to be reduced by the summation of ΔF_1 and ΔF_2 as shown in equation 5.6.

$$\Delta F = \Delta F_1 + \Delta F_2 \tag{5.6}$$

Substituting the values of ΔP_1 and ΔP_2 and carrying out this equation leads to equation 5.7.

$$\Delta F = \frac{\Delta_1 \times H_2 + \Delta_2 \times H_1}{H_1 \times H_2} \times P \tag{5.7}$$

The ratio between H_1, H_2 and H is known and so is the ratio between Δ_1, Δ_2 and Δ. Solving the equation in terms of H, P and Δ for the assumed ratio between the base hinge moment and the top moment leads to equation 5.8.

$$\Delta F = \frac{1.2 \times \Delta \times P}{H} \qquad (5.8)$$

The 1.2 factor in the above equations reflects a magnification factor need to be taken into account in case of double curvature problem with a base moment capacity of 15 % of that at the top of the column.

For concrete flared columns, situation is not that simple in terms of calculating the deflections as the cross-section increases and the section modulus is changing due to cracking throughout the loading history. To simplify the process, the values are calculated at the effective yield force where the correction is considered significant. The ratios between the top deflection in the top portion of the column at the total height and that for the bottom portion is obtained from the finite element analysis before gap closure and found to be 0.87 to 0.13. Using these two values, the magnification factor can be calculated to be 1.85.

The results of the analysis are shown in Table 5-4. The results were compared in reference with LFCD2. An important result from the analysis is that the P-Δ effect did not affect the first gap closure displacement greatly. However, it over-estimated the ductility ratio of the structure by 32.9 % of its measured value. The maximum force is 20 % more than that of LFCD2.

In order to make the corrections to the load-displacement curve, the following steps are implemented.

1. The first yield point, defined as the first yield occurring in the column longitudinal bars, is identified.
2. No correction was made before this point assuming that flexural behavior is

predominant.

3. After this point a correction to the force was calculated based on equation 5.8 up to the first point of gap closure.
4. Between the first gap closure and the last point of gap closure, at the east base hinge, no correction was made assuming full framing action. However, the curve was shifted by an amount equals to the last correction value obtained before gap closure.
5. After the last gap closure, the system was assumed to have half of its framing action because complete plastic hinges here not formed, the beam-column connection didn't lose all of its strength, therefore, only half of the moment corrections was applied

Fig. 5-28 shows the results of the method described above, it shows good agreement between load-displacement curve of LFCD2 and that of the corrected LFCD3. It is also important that the corrected LFCD3 has almost the same tangential stiffness of the LFCD2 curve.

To verify the double curvature correction method for P-Δ effect, the LWNF1 specimen, which is the case where the columns are prismatic and no flare exists, was solved including the P-Δ effect and was solved without including the P-Δ effect. The results are presented in the section describing the results of LWNF1.

5.3.3. LFSS1

As was previously mentioned, this specimen has a shorter beam span than that of the span used in the experiments. The load-displacement curve obtained from the analysis is

plotted in Fig. 5-29 along with LFCD2 analytical results for comparison. The figure shows that the two specimens have almost no difference in behavior, gap closure displacements and ductility ratios. This proves that shortening the span did not deviate the experimental results from the original prototype.

5.3.4. SFCD1 & SFCD2

Load-Displacement Relationship

Because there is only limited data available for SFCD1, as it has been destroyed before testing, there is not much to be said about the experimental results of the specimen versus the analytical results. However, the specimen was analyzed to be compared with the results of SFCD2, for this reason, the results of SFCD2 are presented in advance to those of SFCD1

The deformed shape of SFCD2 at the last load step is shown in Fig. 5-30. The figure shows gap closure of the flare and the base hinge gaps. The analytical load-displacement curve for SFCD2 is shown in Fig. 5-31 as a solid line while the measured load-displacement curve is shown as a dashed line. The analytical load-displacement curve for SFCD1 is shown in Fig. 5-32 as a solid line while the one obtained from the analysis of SFCD2 as a shown in dashed line. The curve was constructed in the same manner discussed previously by superimposing two separate runs. The load-displacement curve for SFCD1 shows good correlation between the measured and the analytical curves. An analytical effective yield value was calculated based on analytical results and was used to calculate structure's ductility. A look at the results obtained between SFCD1 and SFCD2 show that the two specimens are almost identical. SFCD1 has higher strength due to the

high flare confinement that altered spalling in the flare region and enables for high force transfer.

Table 5-5 shows the obtained results of maximum displacements and forces in comparison to the measured data for SFCD2. The table shows very good agreement in both specimens. The results were calculated as a percentage of the measured response to show the efficiency of the analysis in estimating the structure response. It is important to mention that the analytical maximum displacement and force are much different because the finite element analysis went through higher displacements than what was applied in the experiment because the shake table reached its maximum permissible driving force. The estimated measured gap closure displacement is almost the same as the one obtained from the analytical results. In general, the difference between the analytical and measured responses of SFCD2 is higher than those obtained in LFCD2. This mainly occurred due to the filtration and smoothing process, which reduced the peaks of the load-displacement curve.

The results for SFCD1 are summarized in Table 5-6 in comparison to those of SFCD2. The difference between the two specimens is very small. This means that the destroyed specimen would not have different behavior than that obtained in SFCD2.

Plasticity Status

A plot of the concrete elements that reached or passed the plasticity limit is shown in Fig. 5-33. The figure shows that the highest strains are located on the elements at the top of the column and base hinge section. Recalling the concrete spalling locations from the experiments shows that concrete cover spalling locations are the same as those obtained

from the analysis.

Fig. 5-34 shows the steel elements that entered the plasticity limit. The figure shows that the yield is distributed along the column reinforcement in the gap region, the flare longitudinal reinforcement, and the beam's bottom reinforcement at the face of the beam-column connection. The analysis shows a high yield value at the base dowels. Referring to the yielded locations recorded experimentally in Chapter 4, a good correlation between the two results could be found. The similarity between the location of the spalled concrete in the tested specimens and the analytical ones prove that DIANA is capable of estimating the failure mode and failure location to a high level of accuracy.

Cracking Pattern

The cracking pattern obtained from the analysis for SFCD2 is shown in Fig. 5-35 and 5-36 for the lateral load in the west and the east directions respectively. The figures show extensive cracking in the columns, the beam-column connection and the beam at almost the same locations marked during test runs, Fig. 5-37. The number of cracks and their distribution is higher in the analytical models due to the fact that the specimen was pushed to failure in both directions while in the test, it achieved the maximum displacement in one direction only. Also, in the experiment, the two-direction loading causes some cracks to be closed during each run that were not captured using pushover static analysis. DIANA draws cracking for each element at the location of its integration points that has reached to cracking even if the crack width is invisible, which, gives a wrong impression about the number of the cracks.

System Capacity and Gap Closure

As was shown for LFCD1 and LFCD2, the section analysis under-estimated the maximum load carrying capacity and yield force of the system; it was the same case for the short specimens. Using the values obtained from sections analysis, the system yield force was calculated to be 291.8 KN (65.61 Kips), which is 10 % lower than the measured load at yield for SFCD1. Fig. 5-38 shows the vertical deformation of the west column. The figure shows that the top section and the top flare sections are not plane after deformation. Another section is shown at the bottom of the flare, which is not plane after deformation as well. Both the top and bottom of the column are D-regions. As a result, the gap closure calculations based on section analysis would deviate from the experimental results. Referring to Fig. 5-38, it is clear that the displacement at the edge of the gap would be higher than that calculated based on curvature that assumes plane sections remains plane after deformation.

Curvature

As was done for the tall columns, the segment of section 4 for the west column was separated to study the effect of vertical and horizontal deformation on the measured curvature. Locating the displacement transducers on the deformed structure, Fig. 5-39, shows that the horizontal deformations caused the transducer on the right hand side to shorten and the one on the other side to elongate. In contrast to that, the vertical deformations caused the right hand side transducer to elongate and the opposite side to shorten.

To evaluate the effect of shear strain on the calculated curvature, the calculated

curvature was obtained from each deformation and compared with the final curvature. The horizontal deformations contributed to the final calculated curvature by a value of (0.00183) while the vertical deformation adds (-0.001786) to produce a final value of (–0.000044). This implies that the calculated curvature from shear strains is dominating in the method of curvature calculations where shear deformation is significant. Note that the calculated deformation from the finite element analysis is close to the maximum calculated value obtained from the experimental results.

Stress Trajectories

The principal stresses for SFCD2 are plotted at a load level of 181.2 KN (40.73 Kips) before gap closure, Fig. 5-40, and at a load level of 470.2 KN (105.7 Kips), Fig. 5-41, after the gap closure to compare the stress flow between the two cases. A closer look shows that before gap closure, the flare top edge have a low stress level which is not the case after the gap closure. A detailed analysis of the stress flow is included in Chapter 6.

5.3.5. SFCD3

This specimen is the same as SFCD2 except that the analysis was carried out without geometrical non-linearity, which account for the P-Δ effect. Fig. 5-42 shows the result of the analysis of SFCD3 and the one carried out for SFCD2 in dashed lines. The graph shows the corrected SFCD3 curve using the same procedure described in LFCD3. The procedure proved to have good results comparing with SFCD2 results.

The results of the analysis are summarized in Table 5-7. The results of SFCD2 are included in the table for comparison. The analysis without P-Δ effect overestimated the

maximum load by 21.6 % of that obtained in SFCD2 and the ductility ratio by 38.3 %. The gap closure displacement is close to that obtained for SFCD2, however, it deviated at the last base hinge gap closure.

5.3.6. SFSS1

As was previously mentioned, this specimen has a shorter beam span than that of the span used in the experiments. The load-displacement curve obtained from the analysis is plotted in Fig. 5-43 along with SFCD2 analytical results for comparison. The figure shows that the two specimens have almost no difference in behavior, gap closure displacements and ductility ratios. This proves that shortening the span did not deviate the experimental results from the original prototype.

5.4. GROUP "II" ANALYTICAL RESULTS

As the purpose of group II analysis is to study the effect of the gap width on the overall behavior and frame capacities, the specimens were analyzed and plotted on the same graphs for comparison.

5.4.1. LFWG0

This specimen is the same as LFCD2 except that the gap width at the top equals zero. Fig. 5-44 shows the load-displacement curve for LFWG0 with the load-displacement curve for LFCD2 as a dashed line, while Table 5-8 summarizes the results obtained from the analysis for this group of specimens. The obtained values of maximum force and forces at yield are also calculated as a percentage of those obtained from the analysis of

LFCD2. The specimen showed a significant increase in the yield forces, 44 % of that for LFCD2. The maximum force was not affected greatly due to the gap closure in LFCD2. The ductility index for bent without flare gap is 4.88, which is below the minimum limit set by Caltrans. An important result could be obtained from the table is decrease in the ductility ratio of the system which means that the gap existence enhanced the system seismic performance.

5.4.2. LFWG1 through LFWG3

These specimens were created with variable gap widths of 12.7 mm (0.5 in), 19 mm (0.75 in) and 25.4 mm (1.0 in) respectively. Fig. 5-44 shows the load-displacement curve for LFWG0 through LFWG3 plotted with the load-displacement curve for LFCD2, which had a gap width of 9.5 mm (0.375 in), while Table 5-8 summarizes the results obtained from the analysis of these specimens. The obtained values of maximum forces and forces at yield plateau are also calculated as a percentage of those obtained from the analysis of LFCD2.

The results show that the gap has a small impact on the yield force value. As the gap widens, the yield force drops to a lowest value of 97.6% of that of LFCD2. The value of the maximum force also dropped as the gap was widened, however, the difference between LFCD2 and the other specimens is not significant.

The gap width proved to have significant impact on the ductility ratio of the system. The 12.7 mm (0.5 in) gap had lower ductility index due to the increase in the effective yield force and the decrease of the maximum displacement. The 19 mm (0.75 in) gap width had almost the same ductility ratio as for LFCD2. The 25.4 mm (1.0 in) gap width

had the highest ductility index of 9.86. The table shows that as the gap widens, the gap closes at a higher lateral displacement. The gap width has great impact on the gap closure. As the gap width increases, the gap closure is altered to a higher displacement. It is important to mention that the relation between the gap width and the displacement at which the gap closes is almost linear.

5.4.3. LWNF1

The purpose of creating this model is to compare the flare existence with prismatic columns with constant cross section. Fig. 5-44 shows the load-displacement curve with respect to LFCD2 while Table 5-8 summarizes the results. As seen from the load-displacement relationship, the flare gap closure has great effect in allowing the structure to undergo higher displacement by adding stiffness to the system at a stage where it is close to collapse. The flare has negligible impact on increasing the yield force of the system, however, it increased the maximum force greatly. The ductility ratio obtained from LWNF1 is lower than that obtained from the flares with gaps. This occurs because the existence of the flare enhanced the section properties for LFCD2 by providing additional confinement to the column core which is not the case for this model. Also, the gap closure caused the load-displacement to gain stiffness that reduced the stresses on the column core and altered the model failure. The gap closure of the base hinges did not contribute much in adding stiffness to the system.

One of the objectives of creating this model is to apply the double curvature correction to a prismatic column where it is easy to handle the problem and to show the difference between the two methods clearly. Fig. 5-45 shows the load-displacement curve

of the analysis including P-Δ effect in dashed line and the one that is not including the P-Δ effect in solid line. The magnification factor was calculated using the same method previously described in discussing LFCD3 and was found to be 1.9. The solution was corrected using the single curvature and double curvature correction.

The graph shows that the single curvature correction was not successful in approaching the curve of LWNF1 including P-Δ effect, the double curvature correction traced the curve including the P-Δ effect very accurately. This shows the validity and efficiency of the method in correcting frames.

5.4.4. SFWG0

Fig. 5-46 shows the load-displacement curve for SFWG0 with the load-displacement curve for SFCD2 while Table 5-9 summarizes the results obtained from the analysis for these specimens. The obtained values of maximum force and forces at yield are also calculated as a percentage of those obtained from the analysis of SFCD2. The specimen showed very high initial stiffness that caused the maximum force of 120 Kips to be achieved at a low displacement value of 17 mm (0.67 in).

The solution stopped at this point due to the premature failure of the base hinge that exceeded the shear capacity of it, Fig. 5-47. No ductility ratio is calculated for this specimen as it failed prematurely. This proves that gap existence is important in short columns not only to increase its ductility index as in the case of tall columns, but also to prevent the failure of the system due to high shear force at the base hinges.

5.4.5. SFWG1 through SFWG3

These specimens were created with variable gap widths of 12.7 mm (0.5 in), 19 mm (0.75 in) and 25.4 mm (1.0 in) respectively. Fig. 5-46 shows the load-displacement curve for SFWG0 through SFWG3 plotted with the load-displacement curve for SFCD2, which had a gap width of 9.5 mm (0.375 in), in dashed line while Table 5-9 summarizes the results obtained from the analysis for these specimens. The obtained values of maximum forces and forces at yield are also calculated as a percentage of those obtained from the analysis of SFCD2.

The results show the same trend of that obtained in the tall specimen. An insignificant decrease in the yield force is achieved by gap widening, while, significant increase in the system ductility is achieved. The maximum force of the system almost remained the same for the three specimens. As in the case of the tall specimens, the gap closure was altered by increasing the gap width with a linear relation between the gap width and gap closure displacement.

5.4.6. SWNF1

The purpose of creating this specimen is to compare the flare existence with prismatic columns with constant cross section. Fig. 5-46 shows the load-displacement curve with respect to LFCD2 while Table 5-9 summarizes the results. As seen from the load-displacement relationship, that the flare gap closure has great effect in allowing the structure to undergo higher displacement by adding stiffness to the system at a stage where it is close to collapse. The flare has negligible impact on increasing the yield force of the system, however, it increased the maximum force greatly. The ductility ratio

obtained from SWNF1 is much lower than that obtained from the flares with gaps. The system has very poor performance with respect to SFCD2 as the ductility index dropped to 64 % of that achieved for SFCD2.

5.5. GROUP "III" ANALYTICAL RESULTS

The varying parameter in this group is the base hinge diameter. The original models had base hinge diameter of 8 inches. This group contained three different base hinge diameters of zero, 101 mm (4 in) and 304 mm (12 in). Zero base hinge diameter means that there is a perfect idealized hinge at the base. The base hinge for LFBH2 and SFBH2 has the same base hinge reinforcement and gap width as the specimens but the base hinge diameter is 101 mm (4 in). The 304 mm (12 in) diameter hinge has no gap.

Fig. 5-48 shows the load-displacement curves for LFBH1 through LFBH3 plotted with the load-displacement curve for LFCD2 while Fig. 5-49 shows the load-displacement curves for SFBH1 through SFBH3 plotted with the load-displacement curve for SFCD2. Table 5-10 summarizes the results obtained from the analysis for LFBH1 through LFBH3. Table 5-11 summarizes the results obtained from the analysis for SFBH1 through SFBH3. The obtained values of maximum forces and forces at yield are also calculated as a percentage of those obtained from the analysis of LFCD2 and SFCD2 for comparison.

5.5.1. LFBH1 and SFBH1

These specimens represent the case where the base hinge dimension equals to zero with perfect hinge. The purpose of making such an analysis is to evaluate the effect of the

base hinge stiffness on the overall behavior. Caltrans specifications do not have specific recommendations concerning the base hinge design and whether its capacity should be taken into account or not. As shown from the graphs, considering the base hinge dimensions greatly affected the yield force and maximum force more than the flare gap width did. An average drop of 15 % in the value of the yield force could be observed from the tables, which is almost the ratio between the hinge core capacity and the column core capacity. This implies that the assumption made during section analysis in Chapter 2 that the base hinge concrete has the same confinement level of the column core may be valid in estimating the base hinge capacity. The displacement at gap closure almost matched what is obtained from LFCD2 and SFCD2.

As a conclusion, the perfect hinge solution is a valid solution that needs to be shifted by the ratio between the capacity of the column core and the base hinge as long as the shear capacity and axial loads do not exceed the base hinge capacity. A system supported on pure hinges is capable to estimate the flare gap closure to considerable level of accuracy.

5.5.2. LFBH2 and SFBH2

These two specimens represent tall and short specimen with reduced base hinge dimension of 4 inches rather than 8 inches as was used in the specimens. The results showed poor performance due to premature failure of the base hinges at a very early stage of the loading history, Fig. 5-48. Fig. 5-50 shows the factored deformed shape of LFBH2 to a factor of 15 at load level of 136.1 KN (30.6 Kips). It is clear from the figure that concrete at the base hinge of the west column failed. Figs. 5-51 and 5-52 show that

plasticity status for the reinforcement and concrete, respectively. The figures show that the highest strains occurred at the base hinge region.

The results from the analysis showed that the concrete elements at the base had compressive stress value of 55.5 MPa (8.05 Ksi) prior to failure and the base hinge dowels yielded in compression at lateral load level of 70.7 KN (15.9 Kips) and maximum compressive stresses were 546.4 MPa (79.25 Ksi). The results of SFBH2 showed the same behavior of premature failure in concrete elements at the base and compression yielding of the dowels.

5.5.3. LFBH3 and SFBH3

These two specimens represent tall and short models with base hinge dimension equal to the column core without any additional reinforcement. The increase in the base hinge cross section resulted in a large increase in the yield force and the maximum load for the frame. The yield load value increased 30.4 % for the tall columns and 31.3 % for the short columns. The ductility enhanced significantly for both tall and short columns. The analysis shows that where higher strength is needed without impacting the ductility or the configuration of the structure, the base hinge dimensions can be increased.

5.6. SUMMARY

This chapter described the finite element analysis that was successfully matched the experimental results of the models. An analysis based on material non-linearity could be used in design after correcting the results considering double curvature. The analysis proved that new method of measuring the curvature need to be developed to separate the

vertical deformations from the horizontal deformations.

The flare gap width has significant impact on the displacement ductility and minor impact on the structure capacity. The flare gap existence prevented the short columns from failing prematurely due to base hinge shear failure. It also enhanced the system ductility compared to the prismatic columns systems.

The base hinge dimension has significant impact on the system maximum capacity. Small base hinge performed very badly due to premature failure of the concrete at the base, while base hinge diameter equal to the column core increased the load-carrying capacity significantly, which affected system ductility and, consequently, stresses generated in other members. The base hinge cannot be assumed as a perfect hinge in practical design while ignoring its capacity as it proved to have significant contribution. More research needs to focus on the base hinge behavior under seismic loading.

6. STRUT-AND-TIE MODEL

6.1. INTRODUCTION

The non-linear finite element analysis has provided very good results in estimating structure capacity and ductility, however, it is not a simple process. Also, it requires a sophisticated finite element program, such as DIANA, to deal with the complexity of reinforced concrete problems. Moreover, it is very time consuming to get reasonable results. All what is mentioned is in contrast to what any engineer is looking for in the design process. An efficient design procedure is needed to design these systems.

Strut-and-tie model is one of the efficient methods that is widely used in analyzing and designing different elements of the structure. The method has been implemented in many of the current design codes[2]. The strut-and-tie model is based on studying the crack pattern and stress path. The compression fields are idealized as struts while the tensile fields are lumped at the location of the reinforcement. A detailed description of the theory and its implementations can be found in many references[7,10,18,27,28].

The first step towards creating a strut-and-tie model is to identify the D-regions and the B-regions in the structure. Saint Venant's principal is used to identify the location of the D-region[27]. Applying this principle gives the D-region layout shown in Fig. 6-1 for the tall and short columns. As shown, most of the tall column is considered a D-region while almost the whole short column is a D-region. For B-regions, where Bernoulli hypothesis apply, the truss model that was first presented by Mörsch[18] can be used. For the D-regions, there is not such a standard model to be used. The model in these regions

should be built taking into consideration the geometry of the structure, cracking pattern and the reinforcement details. In the specimens there are three regions that are considered D-regions. The first region is at the base hinge where a sudden change in the column cross section, loading and reinforcement detail occurs. The second one is located at the beam-column connection where abrupt change in structure's geometry occurs. The third one is at the flare region where the gap exists.

6.2. BASE HINGE D-REGION

As was proved by the finite element analysis, the base hinge behavior is different than the behavior of a pure hinge. Instead, it has significant flexural strength that increases the stiffness of the structure and its load carrying capacity. Fig. 6-2 shows the base hinge and the D-region with the acting loads defined as follows.

T_R = Tensile force generated at the column right hand side

C_C = Compressive force generated at the left hand side of the column

V = Lateral load acting on the column

T_b = Base hinge dowels tensile force

C_b = Compression force generated at the base hinge.

This case is different than that of the frictionless hinge in that it has moment acting at the base end. The tensile force in the column longitudinal reinforcement has to be delivered to the base dowels. As the reinforcement of the column is not directly connected to the base dowels, direct force transfer is not possible.

Recalling the principal stress vectors and the cracking pattern in the area under study, Fig. 6-3, the principal stress vectors show a compression fields acting at the compression

side of the column and diagonal fields at the upper part of the figure that transfer the lateral load. As the compression force approach the hinge, the inclination of the diagonal field increases. As the principal compression stresses get into the hinge area, the inclined compression fields deviates to meet with footing surface. Another field appears in the lower part of the column with upward inclination that bends sharply to meet the other compression fields, Fig. 6-3c.

At ultimate conditions, the moment at the base is controlled by the capacity of the base hinge section. The ultimate moment, the number of the yielded bars and the location of the neutral axis are information needed to construct the strut-and-tie model. An analysis for the base hinge section using RCMC program[17], that was developed in the University of Nevada, Reno, was used for this purpose.

Now it is clear that tensile forces are generated in the right hand side of the column reinforcement near the base hinge section, T_R, Fig. 6-2. This tensile force should be transferred to the dowel reinforcements, T_b. Since there is no direct connection between the column longitudinal reinforcement and the concrete tensile strength is negligible, an upward inclined strut is developed from the column reinforcement to the dowels while the compression force developed in the column from the moment, C_c, is delivered directly through an inclined strut to the location of the force at the base, C_b. The lateral load V is transferred to the location of the compression force at the base through standard inclined strut to the location of the compression force, C_b,

The strut-and-tie model for the base hinge could be constructed as shown in Fig. 6-4. The dashed lines indicate struts while the solid lines indicate the ties of the model. The ties should be positioned so that they follow the direction and location of the

reinforcement detailing. Node 3 in the model was chosen to be in the middle of the development length of the dowels. Node 2 was chosen in the same way except that the development length was scaled by the ratio between the stress generated in the column steel in tension and the yield stress. The inclination of the strut generated from the compression force C_b to node 1 is the inclination of resultant of the two forces C_b and V. Knowing the elevation of node 2 and the inclination of the resultant, the location of node 1 could be obtained. In choosing the location of the struts and nodes, the model was evaluated with respect to the principal stresses and cracking pattern obtained. Struts and ties were set to have almost the same inclination of the principle stresses trajectories as the finite element analysis and avoiding that struts cross the major cracks trend[33].

The model is not limited to the case and dimensions in hand. It could be used for flared columns with gaps having different dimensions using the method described. The model was evaluated and the internal forces were calculated for every member in section 6.6 of this chapter.

6.3. BEAM COLUMN CONNECTION D-REGION

Much research has been done in order to investigate the performance of the beam-column connection[7,10,18,27,29]. It was found that the reinforcement details are critical. For the current specimens, the joint was designed and detailed according to Caltrans seismic provisions which states that the length of the column reinforcement penetrating the beam depth is to be calculated according to the provided equation, otherwise, the reinforcement would be terminated just below the beam top reinforcement. Some research has been done to study and create strut-and-tie model for joints detailed according to Caltrans

specifications[29,30], Fig. 6-5. The proposed model proved to be efficient in estimating joint behavior, but was complicated to be used by the designer. The model also suggested that part of the column longitudinal reinforcement to be developed to the beam top reinforcement was based on the assumption that the compression field would clamp the reinforcement in a very small distance. This assumption needs to be examined, as it does not deal with situation where the column reinforcement is far from the beam top reinforcement in case of relatively deep beams. It is evident that compression fields enhance the bond criteria[18] but it is uncertain that it could decrease the development length to less than quarter of its length.

Due to the asymmetry of the load, each beam-column connection has a different behavior as the internal stresses vary between them. The main difference is that for the east beam-column connection, a tensile force is developed at the bottom of the beam while for the other one, tensile force is developed at the top of the beam. This is, of course, reversed under cyclic loading. This difference has significant effect on the load path inside the joint. The analysis of the east beam-column connection is presented first. The behavior for the west joint is a modification to that model. The model configuration changes during the test due to the gap closure. Two strut-and-tie models are constructed for the case before and after the gap closure.

6.3.1. Before Gap Closure

East Beam Column Connection D-region:

Recalling the principal stress vectors and the cracking pattern in the area under study, Fig. 6-6, the principal stress vectors show a compression fields acting from the top of the

beam towards the compression resultant of the column with a slight deviation as a result of intersecting the column and spiral reinforcements. Also another compression field is initiated from the lower left hand side of the beam-column connection acting upward to meet the downward diagonal field.

Looking at the forces acting on the joint under seismic loading, Fig. 6-6d, the compression force acting on the left hand side, C_L, and the shear force, V_L, meets the compression force in the column, C_C, through a diagonal strut acting along the center of the joint. These forces generate a vertical tensile force in the upward direction that connects to the column reinforcement, T_c. If the reinforcement of the column were extended inside the beam axis, this shape of force transfer would be possible. Due to the detailing in use which allows the column longitudinal bars to be terminated below the beam top reinforcement depending on the development length calculations, the resultant of both the compression and the tensile force could not be fully developed to the top of the beam. Instead, the compression struts must meet at a node where tensile forces could be developed; which is located half way along the development length of the column longitudinal reinforcement and bending back to meet the compression resultant of the column. Observing what occurred with the principal stress vectors and cracking pattern while taking into account the location and the direction of the reinforcement, a strut-and-tie model of the joint could be constructed as shown in Fig. 6-7. Node 20 is located at half the development length of the column reinforcement extending in the beam depth, while node 21 is located at the face of the beam-column connection. The tie between 21 and 23 must be developed in the beam shear reinforcement.

West Beam-Column Connection D-region:

For the west beam-column connection, the principal stress vectors are as shown in Fig. 6-8. The figure shows that the joint has the same compression fields as the east joint. This implies that the same configuration of struts could be used. The only difference is that there are no tensile stresses at the bottom of the beam. Instead, the tensile forces are acting on the top reinforcement only. Fig. 6-9 shows the forces acting on the joint. The difference between the tensile forces at the top of the column should be transferred to the reinforcement of the column on the left hand side. For there is no direct connection between the column reinforcement and the beam's top reinforcement, this difference in tensile force would be transferred through vertical stirrups that are at the edge of the joint region. This behavior creates the inclined compression field from the top left hand side corner to the bottom right hand side corner. As a result, the strut-and-tie model would be as shown in Fig. 6-10. The model's evaluation and the internal forces are all included in section 6.6 of this chapter.

6.3.2. After Gap Closure

After gap closure, the section moment of inertia is increased and hence the system carrying capacity. Due to the existence of the gap, the flare did not fully engaged with the beam, Fig. 6-11. As a result, part of the compression field is transferred through the flare while the main part is transferred through the column core by the original mechanism before gap closure, Fig. 6-12. This requires that a strut be added to account for the load transferred to the flare region, Fig. 6-13.

The location of node 22' is not directly known since part of the flare is in contact with

the beam. The finite element analysis was used in order to verify the distance that was in contact with the beam. Almost, half of the flare width was found in contact with the beam at ultimate conditions. Based on this, the resultant point could be calculated. Detailed calculations for the locations of the nodes and the forces in the members are included in section 6.6 of this chapter.

6.4. FLARE D-REGION

6.4.1. Before Gap Closure

Recalling the principal stress vectors and the cracking pattern in the area under study, Fig. 6-14, the principal stress vectors show compression fields acting from the top of the column and moving longitudinally along with the axis of the column. Also another compression field is initiated from the top of the column and as soon as it passes the gap region, it deviates to hit the boundary of the flare and then return to meet the original vertical compression field.

It is clear that the flare existence causes the compression force at the top of the column to be split into two components, one in the direction of the column axis and the other one through the flare section. The stress field is spreading into the flare region. This spreading generates transverse tensile forces that cause the shown vertical cracks. The strut-and-tie model for this region is simple to be constructed as it is just a modification to the standard truss model used in the B-regions. The same concept is used for short columns. The same strut-and-tie model is used by adjusting the model to match the structure's height. Fig. 6-15 shows the strut-and-tie model for the flare D-region.

It is important to mention that the flare longitudinal reinforcement was ignored in

the model as they have small area compared to the column main reinforcement. Another reason for ignoring the effect of flare longitudinal reinforcement is to simplify the model as much as possible.

6.4.2. After Gap Closure

The gap closure caused part of the compression force to be transferred through the flare region as was previously mentioned in section 6.3.2. This implies that the original strut-and-tie model could be used by adding strut from the location of the gap closure transferring the load to the column core, Fig. 6-16. Detailed calculations for the locations of the nodes and the forces in the members are included in section 6.6 of this chapter.

6.5. COMPLETE STRUT-AND-TIE MODEL

As the D-regions of the structure were analyzed and the strut-and-tie models for them were constructed, a model of the whole structure could be constructed by simply assembling the models for different parts of the structure. A strut-and-tie model in the form of the standard truss model is used to describe the stress flow in the B-regions that are located between the D-regions. Fig. 6-17 shows the structure's final strut-and-tie model before gap closure while Fig. 6-18 shows the final model after gap closure.

6.6. ANALYSIS AND EVALUATION

One of the objectives of creating the model is to evaluate the maximum load-carrying capacity of the system. It was initially assumed that yielding of the columns longitudinal reinforcement was the controlling condition. Two methods could be used to solve for the

maximum load the system can sustain. The first method is to locate where yielding occurs and solve the system as a function of the applied load. Following this method is lengthy, cumbersome and requires the handling of the whole system under the lateral unknown load. The other method is to assume a value for the lateral load and check if it would cause yielding of the column longitudinal reinforcement. Despite the fact that this method requires several runs, it was adopted for it is easier to be used and the final result, usually, is obtained using few runs.

As a result of the above discussion, only part of the column model needs to be solved to calculate the yield force that causes the longitudinal column reinforcement to yield. The lateral load reduces the vertical load applied to one of the columns while it increases the load on the other column due to framing action. This means that the lateral load to cause the column reinforcement to yield would not be equal for the east and west columns and two separate analysis is needed to calculate the total force. The process requires assuming a lateral force value to calculate the change in the axial load for each column.

A first estimate of the lateral load value could be made by ignoring the change in the axial load and then solving the columns. The two columns will be identical because they have the same axial load. Using the value of the lateral load, the change in axial load for each column could be obtained. Each column is assumed to be acted upon by a fraction of the lateral load while the other one would be acted upon by the remaining part of the force. These values need to be adjusted until yielding occurs in the two columns and the assumed axial loads are correct.

As the experimental and finite element analysis showed that the base hinge dowels

yielded prematurely, the maximum tensile force at the base could be calculated as the force generated in the yielded dowels bars. Section analysis of the base was performed for each column to evaluate the number of yielded bars at ultimate curvature for each of them. From section equilibrium, the summation of the tensile force at the base and the compression force should be equal to the applied axial force per column, thus the compression force could be obtained. To account for the strain rate effect, as was shown in Chapter 4, the yield force was increased by 20% in calculating the forces in the yielded members.

6.6.1. Before Gap Closure

From the experimental results, the flare hoops yielded at ultimate conditions. Thus the force in tie 17-18, Fig. 6-19, could be calculated by simply multiplying half the hoops area enclosed in the distance between nodes 15 and 19 by the yield stress of the hoops. This would yielded a tensile force of 26.9 KN (6.05 Kips) taking into account the strain rate effect. This limited the compression force transferred through struts 19-18 and 11-18 to a specific value that would balance the tensile force. It is important to note that higher flare hoops would attract higher compression force to flow through these struts, which have an impact on node strength. This explains why concrete spalling occurred at the bottom third of LFCD1 while none occurred in at the same location of LFCD2.

When the previous assumptions are made, the system is statically determinate and the internal forces in each member could be obtained by applying force equilibrium to the joints. While creating the model, it was intended to simplify the model as much as possible by making it statically determinate for the indeterminate systems internal forces

are sensitive to the area of each member. The areas of the ties are easy to calculate while the areas of the struts for the case in hand are of a great complexity.

The initial estimate of the lateral force was 212.6 KN (47.8 Kips) by ignoring the effect of the lateral load on the axial load change and assuming each column to have axial load of 224.6 KN (50.5 Kips). This value of lateral load produced a change in axial load of 145 KN (32.6 Kips) for each column. The west column had an axial load of 360.3 KN (81 Kips) while the east column had an axial load of 89.4 KN (20.1 Kips). The yield force generated in the base hinge dowels was calculated by multiplying the area of the yielded bars in each hinge by the yield stress. This resulted in a tensile force at the base hinge of 264.8 KN (59.52 Kips) for east column and 198.6 KN (44.64 Kips) for west column.

In order to solve the system, the number of column bars under tension need to be evaluated. Section analysis for the columns core was made and the results were that 8 # 4 bars yielded for the west column while 8.71 # 4 bars yielded in the east column. Different values of the applied horizontal force at the base were used to solve the model. At each run the force in tie 16-20 was compared with the yield force until the force, 576 KN (129.5 Kips) for east column and 529.3 KN (119 kips) for west column, was determined. The horizontal force to cause yielding was calculated to be 88.7 KN (19.95 Kips) for the east column and 109 KN (24.5 Kips) for the west column, Fig. 6-19. This implies that the maximum horizontal load for the bent equals 197.7 KN (44.45 Kips). The final axial forces were 89.9 KN (20.2 Kips) for the east column and 359.4 KN (80.8 Kips) for the west column. The measured horizontal force at the yield plateau was 205.95 KN (46.3 Kips) for LFCD1 and 203.6 KN (45.77 Kips) for LFCD2. The model estimated the yield

force to be 96 % of that obtained in LFCD1 and 97.1 % of that of LFCD2.

The short columns were solved using the same concept, which lead to the system of internal forces shown in Fig. 6-20. The analysis showed that the maximum force that would cause yielding in the east column is 145.9 KN (32.8 Kips) and 187.7 KN (42.2 Kips) for the west column. This yielded a total horizontal load of 333.6 KN (75 Kips). The final axial load in the east column was 374.1 KN (84.1 Kips) and 75.2 KN (16.9 Kips) for the west column. The experimental results showed a lateral load level of 338 KN (76 Kips) at the yield plateau, which means, that the system is capable of estimating the failure load to 98.7 % of its value for SFCD2.

6.6.2. After Gap Closure

The only difference in the case of gap closure is the added strut 18-22', as was previously discussed. The finite element analysis showed almost half the dimension of the flare projection was in contact at the maximum load condition. An assumption was made that the vertical component of the strut is limited by the capacity of the area in contact. The vertical stress distribution at the flare region was obtained from the finite element analysis. An idealized stress linear distribution in this area was assumed with a peak of f_c' at the flare edge and zero at the mid-distance, Fig. 6-21. The force could be calculated using equation 6.1.

$$V_{strut} = A \times f_c' \times 1.2 \times 0.85 / 2 \qquad (6.1)$$

Where;

V_{strut} = Vertical component at node 22'

A = Area in contact

f_c' = concrete strength

The 1.2 factor is used to account for the strain rate effect in concrete, while the 0.85 factor to account for the difference in cylinder strength and specimen strength as was described in Chapters 2 and 5. This lead to a vertical component of 336.9 KN (75.74 Kips) at node 22'. By calculating the vertical component of the strut, the force in the strut could be evaluated and the system would be statically determinate. It is important to mention that the strut is assumed to act on the middle of the area in contact.

As was previously seen, the number of yielded bars is important information that is needed to evaluate the maximum load. Section analysis assumes plane sections remain plane after deformation. The partial engagement of the flare makes this assumption questionable. It is assumed in this analysis that the number of yielded bars before gap closure is the same as the one after the gap closure, which is not far from reality as shown by the finite element analysis.

The finite element analysis presented in Chapter 5 showed that the base hinge gap closure had little contribution in stiffening the system. As a result, the base hinge gap is assumed not to be closed and that the ultimate moment that it can carry would remain almost the same. It is important to mention that the objective of making this analysis is to evaluate the system capacity. A strut-and-tie model for the base hinge gap closure would be essential to check the stresses at the base hinge region.

The same procedure that was used before gap closure is used to calculate the maximum load for the frame after gap closure. The same assumption of the flare hoops yielding is utilized here. It was seen from experimental measurements that tensile strains did not decrease after gap closure but increased as the load increased. Fig. 6-22 shows the

final internal forces of the east and west column. The maximum force that causes yield of the system for the east column is 121.4 KN (27.3 Kips). For the west column a maximum force of 152.6 KN (34.3 Kips) was obtained. This means that the maximum load that frame can carry after gap closure is 274 KN (61.6 Kips). The measured maximum load for LFCD1 and LFCD2 were 284.6 KN (63.98 Kips) and 268.6 KN (60.38 Kips) respectively. This implies that the model is capable of predicting the load to 96.3 % of the actual load for LFCD1 and 102 % for LFCD2.

It is important to mention that at the bottom of the east column, the two sides of the column are subjected to tensile force. To understand what is the reason behind this behavior, consider the cracking pattern in the lower part of the column, Fig. 6-3c. From the figure, it is clear that the cracks tend to have diagonal inclination. To calculate the force on the left hand side of the column we separate the lower part with section A-A, Fig. 6-23a, which is aligned with the cracking direction at this region[27,33]. The forces acting on the section would be as shown in the Fig. 6-23b, where;

C_1 = Internal Compression force acting on the column right hand side.

C_2 = Internal Compression force acting on the column left hand side.

T_b = Tensile force of the dowels

C_b = Compression force at the base hinge section

V = Applied horizontal force

$V_{c1,2}$= shear force carried by the aggregate interlock in the compression zone and the dowel action of the longitudinal reinforcement.

V_s = Shear force carried by the spirals

To simplify the problem, the forces in the figure have been drawn to scale relative to

each other and the distance between the forces is assumed as shown in the figure. Another assumption is made, that the resultant of the shear forces carried by concrete and dowel action, $V_{c1,2}$, and the shear force carried by spirals, V_s, is acting at the middle of the height, d/2 from the top surface of the section. This assumption is not far from reality as the forces $V_{c1,2}$ are small compared to that carried by the spirals. To calculate the value of the compression force C_2, the moment is taken at the point of application of the compression force C_1. Note that the column axial force is included in the compression forces. Then the moment equation would be as shown in equation 6.2.

$$T_b\ (d/2) + V\ (2d) + C_2\ (d) - Vs\ (d/2) - C_b\ (d) = 0 \qquad (6.2)$$

From force equilibrium, V_s is equal to the applied lateral force, V. Carrying out equation 6.2, the value of the compression force, C_2, can be calculated using equation 6.3.

$$C_2 = C_b - T_b / 2 - 1.5\ V \qquad (6.3)$$

Knowing that the value of $(C_b - T_b)$ equals to the applied axial force on the column, P, the equation reduces to 6.4.

$$C_2 = [\ P + T_b / 2\ ] - 1.5\ V \qquad (6.4)$$

This means that as long as the term between the brackets is greater than 1.5 the applied lateral load, the force on the left hand side of the column is compression, otherwise, the force changes sign into a tensile force.

This is a common behavior where diagonal cracks occur. If the cracks were only flexural cracks, no increase in tensile force would occur. Plastic hinges are exposed to this behavior where extensive shear cracks exist with flexural cracks[18]. It is important to mention that this behavior conforms to the results obtained from the finite element analysis.

Looking to the model, member 1-4, Fig. 6-19, is in tension while it is inclined and all the reinforcement is orthogonal to the column axis. As the inclination of the strut is small and the force generated in the reinforcement is small as well, it was decided not to change the model configurations for the sake of the simplicity. For design, the force generated in the tie could be assumed to be equal to the force in the reinforcement.

It is important to note also that the compression force passing in the flare due to the gap closure, attracted higher forces to flow through strut 11-18 and 18-19, Fig. 6-22. This behavior causes the flare to sustain high compression force that was not included in the design of the flare.

The short columns were solved using the same concept, which lead to the system of internal forces shown in Fig. 6-24. The analysis showed that the maximum force that would cause yielding in the east column was 197.9 KN (44.5 Kips) and 258.9 KN (58.2 Kips) for the west column. This produced a total load of 456.8 KN (102.7 Kips). The experimental results showed lateral load level of 433.3 KN (97.4 Kips), which means. The estimated load is 105 % of the maximum measured load. The potential reason behind the overestimation is that the test was stopped before the maximum load was reached.

6.6.3. Beam-Column Connection

As the lateral loads are calculated, the internal forces of the system could be calculated and used to solve for the internal forces of the remaining parts of the system by applying the loads obtained from the columns to the beam. The primary interest is in the beam-column connection because the rest of the beam could be designed using the conventional design methods. Fig. 6-25 shows the numbering used for both models while

Fig. 6-26 shows the calculated internal forces for the beam-column connection in the east and west direction. The solution was carried out only for the tall columns before gap closure, as the short columns analysis would be the same analysis procedure and so would be for the case after gap closure. For the analysis after gap closure, the model shown in Fig. 6-13 would be used.

The forces in the east beam-column connection shows that the beam's bottom force in the joint region passed yield force which is conforming to what was obtained from experimental results which showed that the strain in beam's reinforcement passed yield and entered the strain hardening phase.

The analysis so far has been done for an existing specimen to verify the maximum loads and stresses obtained. In design, no reinforcement is allowed to pass yield. If the forces in the beam reinforcement were found to pass yielding, the amount of the reinforcement could be increased or different detail is to be used.

Caltrans seismic specifications were developed based on ensuring plastic hinge formation in the columns by increasing the column moment by 20 % and designing the beam accordingly, a concept that was used in the design of the specimen. The results in hand prove that while the columns yielded, the beams yielded as well in the beam-column connection region, and, at the face of the joint the tensile force is below yield force by more than 20 %. In well-detailed joints, the tensile force generated in the beam-column connection region is expected to be lower than the values obtained at the face of the column and gets lower as it penetrate inside the joint. It is important to mention that evidences from experimental results showed that yielding in beam reinforcement occurred inside the joint at stages earlier than those outside the joint. The results obtained

from the finite element analysis also proved the same behavior.

The reason behind this is the column reinforcement detail used inside the beam-column connection region. In cases where the column reinforcement are extended in the beam, the strut-and-tie model for the joint would change the inclination of struts 20-21 and 20-22 to produce lower horizontal component, and, hence lower tensile force in the reinforcement, Fig. 6-27. The current detail caused the beam depth to be implicitly reduced in the beam column connection region.

Another important observation is the high tensile forces that are generated vertically at the face of the joint, members 21-23 in Fig. 6-26, that has to be resisted by the existing stirrups at the face of the joint boundary. It is also important to mention, that this high tensile force in the west beam-column connection model did not generate cracking in the cantilever for high amount of stirrups were used along the full length of the cantilever.

To show how the detailing affects the forces generated in the beam bottom reinforcement, assume the same structure under study detailed as in Fig. 6-27. If the proposed detail is used, the force in the bottom reinforcement would drop to 269.6 KN (60.6 Kips) for the east column, which is 63.4 % of that obtained in case that Caltrans joint detail is used. Moreover, the high tensile force developed in the ties is eliminated in this case.

6.6.4. Stress Check

After the loads acting on each member is obtained, the stresses and the node need to be checked against what is recommended by the code[2]. Checking the stresses of the ties is straightforward since the area of the ties is known. For struts, the situation is different as

the area of the struts should be defined first. The most efficient method is a graphical solution by calculating the area of each strut and node based on the maximum stress capacity of the strut and the node. For the areas, a strut width could be calculated as the structure out-of-plane dimension is known. The struts and nodes could now be drawn using the calculated widths. If the nodes and struts intersect the structure boundary, this means that the stresses in concrete are unsafe and the cross sections at this specific location need to be increased to accommodate the struts and the nodes.

To show an example of how the procedure works, node 11 for the west column after gap closure of the tall specimens is considered for stress check. The out-of-plane dimension in the case of a circular column is changing according to the location of the struts which makes the situation hard to be calculated. As an assumption, the section depth at the location of the node would be considered for all the struts, which is 189 mm (7.45 in). This value was calculated graphically as the structure out-of-plane dimension at the location of the node under study.

Fig. 6-28 shows the selected node with respect to the column boundaries. The node has four struts and one tie. The code provisions were built for three member nodes[2]. The three member node are ideal if the stresses on the boundary of the nodes are equal compression stresses, then the stress state of the joint is what is known as a hydrostatic stress where the stress in any direction equals to the stress on the boundaries. A node at which more than three members meet can be converted into three member node by substituting each two intersecting struts by a resultant strut through a three-strut node[28]. This process is applied in all directions towards the original node until a three-strut meets at the location of the original node.

The above method is applied to the selected node to check the nodes safety. Fig. 6-28 shows the struts widths drawn inside the column. A look to the figure shows that the node is intersecting with the column boundary which means that the node needs to be smaller in size to be safe. To check the possibility of the node reduction, the node stresses need to be checked first.

The final configuration shows that the node has two struts and one tie. According to ACI 318R-02[2] the stress limit in such nodes should not exceed the value of equation 6.5.

$$f_{cu} = 0.85\,\beta_n f_c' \qquad (6.5)$$

Where;

f_{cu} = is the effective compressive strength of the concrete in a strut or a nodal zone

β_n = reduction factor equal to 0.8 for the case of a node between 2 struts and one tie

f_c' = specified compressive strength of concrete

As all the members were dimensioned using stress value equals to ($0.85 \times 1.2 \times f_c'$) and all the accessory nodes are hydrostatic nodes, the node in concern would have the same stress value. This implies that stress wise, the node needs to be enlarged. The conclusion is that the node could not be enlarged nor reduced to be contained in the structure boundary. This implies that the structure boundary needs to be changed or else, crushing of concrete would occur as was observed during the test.

The process is to be done for each node and strut in the structure. Despite that it seems to be a lengthy method, it is very efficient in estimating the location where crushing would occur. It is important to mention that much research has been done to develop computer programs to handle the process of stress check.

6.7. SUMMARY

The model generated in this chapter proved to be capable in estimating the yield force and the maximum load after gap closure to a good accuracy level. It also explained some behaviors that were observed in the experimental work. The model highlighted two regions that need more efficient details as they proved that the load path in them is complicated and yield undesirable stress values. These are the base hinge and the beam-column connection regions

6.7.1. Base Hinge Region

The base hinge dimensions have significant moment resistant that subjects the system to tensile forces at the base of the column. The base hinge reinforcement detail forces the tensile stresses generated in the column rebar to be transferred through inclined struts to transfer the load to the vertical dowels. Such a detail creates nodes under two tensile stresses that weakens the node strength dramatically and cause the concrete spalling to be increased in this area.

The other problem is that the current detail creates transverse tensile forces near the base of the column. These tensile forces need to be resisted by spirals that are not adequately anchored near the bottom of the column. A solution to this problem is to use welded hoops at the bottom of the column and to design the spirals in this region based on the force obtained from the model.

Using another base hinge detail can enhance the performance of the base hinge greatly by using the detail shown in Fig. 6-29a. This detail has the advantage of delivering the tensile forces in the column rebar directly to the base hinge dowels without

the need for the struts. The strut-and-tie model for such a detail can be as shown in Fig. 6-30b, which has the advantage of not having a transverse tensile force near the base hinge.

6.7.2. Flare Region

The force flowing in the flare region is mainly controlled by the amount of flares lateral reinforcement. The recommendation of the increasing the lateral reinforcement in the top third of the flare was base on the desire to eliminate the vertical cracks at the column core face[3]. Previous research used and recommended linear elastic finite element analysis for the calculations of the lateral reinforcement level[3]. The linear elastic analysis gives higher tensile stiffness to the concrete and hence over-estimates the amount of stresses transferring through the flares.

The vertical cracks mainly occur due to the fanning of the stresses in this region. Controlling the vertical cracks implies the elimination of the stresses passing through the flare region. To do so, the amount of the lateral reinforcement needs to be minimized.

6.7.3. Beam-Column Connection

The beam-column connection strut-and-tie model showed that the beam-column connection performance is unsatisfactory. The beam bottom reinforcement yielded and the stirrups were subjected to high tensile forces that were taken into account in the design phase. The solution to this problem is to enhance the beam-column connection detailing by developing the tensile forces to the top of the beam. This could be achieved either by bending part of the column longitudinal reinforcement inside the beam, Fig. 6-30a, or to use headed bars for the column reinforcement, Fig. 6-30b.

7. SUMMARY, CONCLUSIONS, AND RECOMMENDATIONS

7.1. SUMMARY AND CONCLUSIONS

The work that has been done in this research can be summarized as follows:

- A survey was made for the existing flared column bents that were designed recently to generate a prototype. The prototype was scaled in order to create 1/5 scale model.
- Four different 1/5 scale specimens (LFCD, LFCD2, SFCD1 and SFCD2) that represent architecturally flared-columns were designed according to Caltrans seismic specifications. The four specimens had a gap that separated the flare from the beam by 0.375 in, which represents 2.0 inch gap in the prototype, which is set as the minimum gap thickness by the specifications.
- Two of the specimens (LFCD1 and LFCD2) had taller columns while two others (SFCD1 and SFCD2) were shorter to study shear demand. Each two geometrically identical specimens had different lateral flare reinforcement. One of them was detailed according to the current specifications with high flared confinement steel at the top third of the flare height while the other one had a constant low flare confinement.
- The specimens were characterized using 2D non-linear finite element analysis performed using the ADINA program. They were seismically analyzed using the RC-SHAKE program and various earthquake records. The Northridge Sylmar Earthquake, 1994, provided the greatest specimen response.

- The four specimens were seismically tested using the shake table in the Large-Scale Structures Laboratory of the University of Nevada, Reno. Three specimens were successfully incrementally tested until failure of the system. One specimen, SFCD1, was destroyed during the tuning process.
- The data obtained were processed to characterize the specimens' behavior. All the specimens showed satisfactory seismic behavior in terms of the ductility ratio that exceeded the minimum ductility limit set by the specifications. However, the gap closed at a ductility ratio lower than the minimum recommended ductility ratio causing the system load carrying capacity to be increased and transferring higher load to the columns and the beam that led to extensive shear cracks in both of them.
- The beam-column connection detail showed unsatisfactory behavior by premature extensive joint cracking and yielding of the beam bottom reinforcement even before gap closure.
- The base hinge detailing showed unsatisfactory behavior by the premature yielding of the dowels that took place even before the column longitudinal reinforcement yielding. The base hinge also experienced significant permanent sliding that led to higher overall specimen displacement.
- A non-linear 2D finite element analysis was carried out using a more powerful program called DIANA that was mainly created to simulate reinforced concrete behavior. The analysis was made for the test specimens and the results showed good correlation with the experimental results.
- The finite element analysis was extended to make a parametric study to

investigate the effect of the gap width, span length, geometrical non-linearity and the base hinge dimension. The results of the analysis can be summarized as follows:

- The base hinge dimension has significant contribution to the load-carrying capacity of the system that showed the importance of considering section capacity at the base hinge in the analysis and design phase.
- The maximum force that the frame sustained after gap closure is almost equal to the maximum force for a frame without a gap.
- A gap size of 1.0 inch in the model ensures the non-closure of the gap till a very late stage of the loading history where the gap closure does not contribute much to the system capacity.
- The analysis also showed that the existence of the gap is important for short columns as without the gap, the system failed prematurely due to brittle shear failure.
- The analysis showed that the P-Δ effect has minor contribution in the pre-yielding stage of the load-displacement curve but a significant effect after yielding.

- A strut-and-tie model was constructed with the guidance of the experimental results and the finite element analysis obtained using DIANA program. The model proved to be capable of estimating the maximum-load carrying capacity of the system to a satisfactory level of accuracy.
- The strut-and-tie model explains behaviors that were under question in the beam-column connection, the flare area and the base hinge.

7.2. RECOMMENDATIONS

7.2.1. Recommendations for Flare and Gap Detail

- The minimum size of the gap needs to be increased to 5 inches in the full scale frame.
- In calculating whether the gap would close or not, the deflection of the beam needs to be taken into consideration. Because of non-linear behavior in the gap region, a factor of safety of at least 3 needs to be applied to the gap width calculated based on curvature analysis with ignoring the beam deflection to prevent the gap closure.
- Another option for the gap design is to allow the gap to close. This enables a higher ductility level to be achieved over a column without gap closure. However the elements of the system should be designed to resist higher force value caused by the gap closure.
- Another option for the gap design is to be allowed to close which showed higher ductility level rather than a column without gap closure. However the elements of the system should be designed to resist higher force value caused by the gap closure.
- Low flare confinement ratio of 0.075 % should be used in practice as it allowed for higher level of concrete spalling, and hence, transferring less load to the columns and the beam.
- The strut-and-tie model needs to be implemented in the design and detailing of the flare. The safety of the nodes and struts needs to checked against code requirements.

7.2.2. Recommendations for Beam and Beam-Column Connection Design

- The beam design needs to account for the increase in tensile force in the bottom reinforcement due to the use of the current beam-column connection detail.

- The stirrups at the face of the beam-column connection need to be designed using the strut-and-tie model.
- The beam-column connection detail need more sophisticated analysis to ensure the integrity of the joint up to the end of the loading history.
- A more reliable detail needs to be used and seismically investigated for the beam-column connection that ensures direct force transfer from the beam reinforcement to the column reinforcement by extending the column bars inside the beam or using headed bars for the column reinforcement.
- The strut-and-tie model can be used in the design and detailing of the beam-column connection.

7.2.3. Recommendations for Base Hinge Design:

- The base hinge dimensions needs to be chosen carefully so that it would not significantly increase the load-carrying capacity of the system without endangering the safety of the system.
- The gap size needs to be dimensioned so that it ensures that no gap closure would occur during the loading history.
- The dowels need to be designed so that they remain below the yielding limit through the loading history using the strut-and-tie model analysis.
- The base hinge sliding needs to be controlled using higher amounts of dowel reinforcement.
- The strut-and-tie model needs to be implemented in the design and detailing of the base hinge.

REFERENCES

1. ADINA Reference Manuals, ADINA R&D, Inc, Watertown, MA, 1999.

2. American Concrete Institute Committee 318, “Building Code Requirements for Structural Concrete (ACI 318-99),” American Concrete Institute, Farmington Hills, Michigan, 1999.

3. Sanchez, Anthony V., Frieder Seible, and M.J. Nigel Priestley, “Seismic Performance of Flared Bridge Columns,” Report No. SSRP-97/06, The University of California, San Diego, 1997.

4. Kunnath, Sashi K., Ashraf El-Bahy, Andrew Taylor, and William Stone, “Cumulative Seismic Damage of Reinforced Concrete Bridge Piers,” Report NCEER-97-0006, University of Central Florida, Orlando, 1997.

5. California Department of Transportation, “Seismic Design Criteria Version 1.1,” Engineering Service Center, Earthquake Engineering Branch, California, July 1999.

6. Chopra, A., ”Dynamics of Structures,” Prentice Hall, USA 1995.

7. Cook, William D. and Mitchel Denis, “Studies of Disturbed Regions near Discontinuities in Reinforced Concrete Members,” ACI Journal, V 85, No. 2 Mar.-Apr. 1988, pp 206-216.

8. Diana, Todd, Nicholas Carino, Riley M. Chung, H.S. Lew, Andrew W. Taylor, William D. Walton, James D. Cooper, and Roland Nimis, “1994 Northridge Earthquake Performance of Structures, Lifelines, and Fire Protection Systems,” NIST Special Publication 862, May 1994.

9. DIANA User’s Manuals, TNO Building and Construction Research, Inc, Netherlands, 1999.

10. El-Metwally, Salah El-Din, "On The Behavior And Design of Reinforced Concrete Beam-Column Connection,” Journal of Helwan University, V 1, January, 1992 pp.104-121.

11. Fu, H.C., M. Seckin, M.A. Erki, “Review of Effect of Loading Rate on Reinforced Concrete,” ASCE Structural Journal, Vol. 117, pp. 3660-3679, October - December 1991.

12. Fung, Y. C., “A First Course in Continuum Mechanics,” 2nd Edition, Prentice-Hall Inc., Englewood cliff, NJ, 1977

13. Gere, James, "Mechanics of Materials," Thomson Learning, USA, 2001.

14. Bathe, Klaus-Jürgen, "Finite Element Procedures," Prentice Hall, USA, 1996.

15. Kulkarni, Sha, "Response of R/C Beams at High Strain Rates," ACI Structural Journal, Vol. 95, No. 5, pp 705-715, November - December 1998.

16. Mander, J., M.J.N. Priestley, and R. Park, "Theoretical Stress-Strain Model for Confined Concrete Columns," ASCE Journal of Structural Engineering, Vol.114, No.8, August 1988, pp 1804-1826.

17. Wehbe, Nadim, M. Saiid Saiidi, "User's Manual for RCMC v 1.2," Report No. CCEER-97-4, University of Nevada, Reno.

18. Park, R. and T. Paulay, "Reinforced Concrete Structures," John Wiley *8* Sons, USA, 1975.

19. Laplace, Patrick, David Sanders, M. Saiid Saiidi, "Experimental Study and Analysis of Retrofitted Flexure and Shear Dominated Circular Reinforced Concrete Bridge Columns Subjected to Shake Table Excitation," Report No. CCEER-01-6, University of Nevada, Reno, 2001.

20. Paulay, T. and M.J.N. Priestley, "Seismic Design of Reinforced Concrete and Masonry Buildings," John Wiley & Sons, USA, 1992.

21. Paulay, T., "Equilibrium Criteria for Reinforced Concrete Beam-Column Joints," ACI Journal V. 86, No 6, Nov.-Dec. 1989, pp 635-643.

22. Pulido-Collantes, Claudia, M. Saiid Saiidi, David Sanders, Ahmed Itani, "Seismic Performance and Retrofitting of Reinforced Concrete Bridge Bents," Report No. CCEER-02-01, University of Nevada, Reno, 2002.

23. Saiidi, M, "Hysteresis Model for Reinforced Concrete," Journal of Bridge Engineering, ASCE, Vol. 108, No. ST5, pp. 1077-1087, May 1982.

24. Saiidi, M., N. Wehbe, D. Sanders, and C. Caywood, "Shear Retrofit of Flared RC Bridge Columns Subjected to Earthquakes," Journal of Bridge Engineering, ASCE, Vol. 6, No. 2, March/April 2001, pp. 189-197.

25. Saiidi, M., D. Sanders, F. Gordaninejad, F. Martinovic, and B. McElhaney, "Seismic Retrofit of Non Prismatic Bridge Columns with Fibrous Composites," Proceedings, 12th World Conference on Earthquake Engineering, Auckland, New Zealand, Topic 6, Paper No. 0143, February 2000.

26. Sehed-Mayan M., “User’s Manual for xSECTION,” Version 2.40, California Department of Transportation, USA March 1999.

27. Schlaich Jörg and Schaefer Kurt, “The Design of Structural Concrete.” IABSE Workshop report, 1993.

28. Schlaich, Michael and Anagnostou George, “Stress Fields for Nodes of Strut-and-Tie Models,” Journal of Structural Engineering V.116, No.1, January 1990, pp 13-23.

29. Scott, R.H., "The effects of Detailing on RC beam/column connection behavior," The Structural Engineer, V.70 No.18, September 1992, pp 318-324.

30. Sritharan, Sri, M.J.N. Priestley, Frieder Seible, “Seismic Design and Performance of Concrete Multi-Column Bents for Bridges,” Report No. SSRP-97/03, University of California, San Diego, 1997.

31. Sritharan, Sri, M.J.N. Priestley, Frieder Seible, “Nonlinear Finite Element Analyses of Concrete Bridge Joint Systems Subjected to Seismic Actions,” Finite Elements in Analysis and Design, 36 (2000), pp 215-233.

32. Van Mier, J.G.M. "Examples of Non-Linear Analysis of Reinforced Concrete Structures With DIANA," Heron, V.32, No.3, August 1987, pp 5-57.

33. Vecchio, Frank J. and Michael Collins, “The Modified Compression-Field Theory For Reinforced Concrete Elements Subjected to Shear,” ACI Journal, V.83, No.2, Mar.-Apr. 1986 pp 219-231.

34. Chen, W.F., “Plasticity in Reinforced Concrete,” McGraw-Hill, USA, 1982.

Table 2-1 Summary of existing bridges dimensions and prototype.

Bridge	RTE 9I/5N	HOV Connector	Prototype
Col. Dia.	1676 mm (66”)	1676 mm (66”)	1676 mm (66”)
Col. Reinf.	32 # 14	36 # 14	34 # 14
Column’s Steel Ratio	2.31 %	2.6 %	2.45 %
Spirals	#6 @ 100 mm (4”)	#6 @ 95 mm (3.75”)	#6 @ 99 mm (3.88”)
Spirals Steel Ratio	0.0045	0.0048	0.0046
Flare Width	3353 mm (132”)	3353 mm (132”)	3353 mm (132”)
Base Hinge Diameter	1143 mm (45”)	1143 mm (45”)	1143 mm (45”)
Hinge Thickness	13 mm (0.5”)	13 mm (0.5”)	13 mm (0.5”)
Hinge Dowels	12 # 10	12 # 10	12 # 10
Dowels Spiral	# 4 @ 305 mm (12”)	# 4 @ 305 mm (12”)	# 4 @ 305 mm (12”)
Beam Depth	2134 mm (84”)	2210 mm (87”)	2172 mm (85.5”)
Beam Width	2286 mm (90”)	2286 mm (90”)	2286 mm (90”)
Beam Span	10439 mm (411”)	6096 mm (240”)	8268 mm (325.5”)
Cantilever Length (in)	2819 mm (111”)	1651 mm (65”)	2235 mm (88”)

Table 2-2 Shake Table Specifications

Table Size	4267 mm x 4420 mm (14’ x 14.5’)
Maximum Payload	444.8 KN (100 Kips)
Maximum Pitch Moment	1355.8. m-KN (1000 ft-Kips)
Maximum Yaw Moment	542.3 m-KN 400 ft-Kips
Maximum Roll Moment	542.3 m-KN (400 ft-Kips)
Maximum Actuator Force	733.9 KN (165 Kips)
Vertical Live Load	± 667.2 KN (150 Kips)
Maximum Dynamic Displacement	± 305 mm (12 in)
Maximum Static Displacement	± 356 mm (14 in)
Maximum Velocity	± 1016 in/sec (40 in/sec)
Maximum Acceleration at Full Payload	1g
Operating Frequency	1-30 Hz

Table 2-3 Specimens' dimensions and reinforcement versus those of Prototype

Description	Prototype	Model	Factor
Column Diameter	1676 mm (66")	305 mm (12")	0.181
Flare Width	3353 mm (132")	635 mm (25")	0.189
Column Reinforcement	30 # 14	14 # 4	N/A
Column Reinforcement Ratio	2.39	2.4	1
Column Spirals	# 6 @ 100 mm (4")	0.192 @ 32 mm (1.25")	N/A
Spiral Volume Ratio ($2A_b/SD$)	0.0037	0.0039	1
Column Height	8128 mm (320")	1626/991 mm (64/39")	0.2
	Flare Detail for LFCD1 & SFCD1	**Flare Detail for LFCD2 & SFCD2**	
Transverse reinforcement at top 1/3 of flare height	0.192" Dia. @ 28 mm (1.1")	0.148" Dia. @ 97 mm (3.8")	
Transverse Ratio	0.439 %	0.075 %	
Transverse reinforcement at remaining 2/3 of flare height	0.148" Dia. @ 97 mm (3.8")	0.148" Dia. @ 97 mm (3.8")	
Transverse Ratio	0.075 %	0.075 %	
Vertical Flare Reinforcement	6 Wires - 0.148" Dia.	6 - Wires 0.148" Dia.	

Table 2-4 Summary of Material's Properties

	Maximum Strength	Strain at Maximum Strength	Ultimate Strain
Unconfined Concrete Properties	31 MPa (4500 psi)	0.002	0.0035
Confined Concrete Properties	41.2 MPa (5980 psi)	0.0053	0.0155

	Young's Modulus	Yield Stress	Strain at strain Hardening	Ultimate Strength	Ultimate Strain
Steel Properties	1.99948×10^5 MPa (29000 psi)	413.7 MPa (60000 psi)	0.008	551.6 MPa (80000 psi)	0.1

Table 2-5 Summary of NIST Column Properties

Bridge	Prototype
Col. Dia.	305 mm (12”)
Col. Reinf.	21 # 3
Column’s Steel Ratio	2 %
Spirals	0.159” Dia @ 127 mm (5”)
Spirals Steel Ratio	0.0044
Axial Load	202.4 KN (45.5 Kips)

Table 2-6 Summary of FEM results using ADINA

	LFCD1	SFCD1
Maximum Horiz. Displacement	57.9 mm (2.28”)	25.4 mm (1”)
Maximum Load	160.1 KN (36 Kips)	255.8 KN (57.5 Kips)
Gap Closure	No gap closure occurred at any location	No gap closure occurred at any location
Effective Yield Displacement	7.6 mm (0.3)	2.3 mm (0.09”)
Effective Yield Force	142.3 KN (32 Kips)	195.7 KN (44 Kips)

Table 2-7 Summary of Maximum and Minimum Earthquakes Accelerations

Earthquake	Max. Acceleration (g)	Min. Acceleration (g)
Sylmar	0.606	-0.298
Kobe	0.599	-0.448
Newhall	0.599	-0.548
El-Centro	0.317	-0.251

Table 2-8 Maximum Displacement Demand

Earthquake	LFCD1	SFCD1
Kobe	59.7 mm (2.35”)	19.3 mm (0.76”)
Sylmar	51.6 mm (2.03”)	13.2 mm (0.52”)
Newhall	36.1 mm (1.42”)	13.7 mm (0.54”)
El-Centro	42.4 mm (1.67”)	23.6 mm (0.93”)

Table 3-1 Yield Stress for Different bar Diameters

Reinforcement Diameter	Yield Stress
#5	482.6 MPa (70 Ksi)
#4	427.5 MPa (62 Ksi)
0.195 Dia.	417.8 MPa (60.6 Ksi)
0.147 Dia.	491.6 MPa (71.3 Ksi)

Table 3-2 Concrete Mix Design

Design Criteria	
28 Day Compression Strength	31 MPa (4500 psi)
Design Slump	100 mm (4")
Design Air Content (%)	6
Theoretical Unit Weight	2221.9 Kg/m^3 (138.7 lb/ft^3)
Water Cement Ration by Weight	0.41
One Cubic Yard	
Cement-Nevada Type II	341 Kg (752 lb)
Water	138.3 Kg (305 lb)
No. 8 Stone – Palute Pit	508 Kg (1120 lb)
Sand – Palute Pit	711.7 Kg (1569 lb)

Table 3-3 Concrete Strength for LFCD1

LFCD1	Casting Date	28 Days KN (Kips)			Ave. Load KN (Kips)	Stress MPa (psi)	Testing Date	Testing Day KN (Kips)			Ave. Load KN (Kips)	Stress MPa (psi)
Footing	3/16/2001	650.9	623.9	653.0	642.6	35	8/28/2001	695.8	719.3	716.3	710.5	39
		146.3	140.3	146.8	144.5	5107		156.4	161.7	161.0	159.7	5647
Columns	4/16/2001	676.0	694.8	681.5	684.1	37	8/28/2001	768.3	700.3	793.2	753.9	41
		152.0	156.2	153.2	153.8	5437		172.7	157.4	178.3	169.5	5992
Girder	5/9/2001	697.6	702.5	706.5	702.2	38	8/28/2001	806.6	792.9	862.6	820.7	45
		156.8	157.9	158.8	157.9	5581		181.3	178.3	193.9	184.5	6523

Table 3-4 Concrete Strength for LFCD2

LFCD1	Casting Date	28 Days KN (Kips)			Ave. Load KN (Kips)	Stress MPa (psi)	Testing Date	Testing Day KN (Kips)			Ave. Load KN (Kips)	Stress MPa (psi)
Footing	1/26/2001	604.2	629.9	576.5	603.5	33	10/17/2001	874.6	863.5	858.9	865.7	47
		135.8	141.6	129.6	135.7	4797		196.6	194.1	193.1	194.6	6880
Columns	2/19/2001	478.2	493.8	501.8	491.3	27	10/17/2001	791.7	801.2	797.4	796.8	44
		107.5	111.0	112.8	110.4	3905		178.0	180.1	179.3	179.1	6333
Girder	3/2/2001	628.5	603.3	613.4	615.1	34	10/17/2001	683.2	640.5	659.0	660.9	36
		141.3	135.6	137.9	138.3	4888		153.6	144.0	148.2	148.6	5253

Table 3-5 Concrete Strength for SFCD1

LFCD1	Casting Date	28 Days KN (Kips)			Ave. Load KN (Kips)	Stress MPa (psi)	Testing Date	Testing Day KN (Kips)			Ave. Load KN (Kips)	Stress MPa (psi)
Footing	2/2/2001	623.3	613.9	643.0	626.7	34	11/8/2001	671.7	683.2	648.8	667.9	37
		140.1	138.0	144.6	140.9	4981		151.0	153.6	145.9	150.2	5308
Columns	3/16/2001	650.9	623.9	653.0	642.6	35	11/8/2001	671.1	558.7	736.6	655.5	36
		146.3	140.3	146.8	144.5	5107		150.9	125.6	165.6	147.4	5210
Girder	3/23/2001	668.6	701.8	671.7	680.7	37	11/8/2001	815.4	799.1	776.7	797.1	44
		150.3	157.8	151.0	153.0	5410		183.3	179.6	174.6	179.2	6335

Table 3-6 Concrete Strength for SFCD2

LFCD1	Casting Date	28 Days KN (Kips)			Ave. Load KN (Kips)	Stress MPa (psi)	Testing Date	Testing Day KN (Kips)			Ave. Load KN (Kips)	Stress MPa (psi)
Footing	3/29/2001	698.8	705.5	702.2	702.1	38	11/20/2001	778.4	750.4	769.5	766.1	42
		157.1	158.6	157.9	157.8	5580		175.0	168.7	173.0	172.2	6089
Columns	4/26/2001	699.7	729.1	714.1	714.3	39	11/20/2001	828.0	795.3	848.6	824.0	45
		157.3	163.9	160.5	160.6	5677		186.2	178.8	190.8	185.2	6549
Girder	5/23/2001	643.3	637.5	641.5	640.8	35	11/20/2001	784.2	800.7	784.7	789.9	43
		144.6	143.3	144.2	144.1	5093		176.3	180.0	176.4	177.6	6278

Table 3-7 Maximum Target and Achieved Accelerations for LFCD1

Times Sylmar	0.15	0.5	0.75	1	1.25	1.5	1.75	2	2.215	1.75	1.75
Max. Record Acceleration (g)	0.091	0.30	0.46	0.61	0.76	0.91	1.06	1.21	1.34	1.06	1.06
Achieved Acceleration (g)	0.086	0.32	0.53	0.73	0.95	1.19	1.40	1.60	1.72	1.37	1.39
% of Max. Record	95	107	115	120	125	131	132	132	128	129	131

Table 3-8 Maximum Target and Achieved Accelerations for LFCD2

Times Sylmar	0.15	0.25	0.5	0.75	1	1.25	1.5	1.75	2	2.215	1.75
Max. Record Acceleration (g)	0.09	0.15	0.30	0.46	0.61	0.76	0.91	1.06	1.21	1.34	1.06
Achieved Acceleration (g)	0.08	0.14	0.31	0.51	0.72	0.92	1.15	1.34	1.52	1.64	1.36
% of Max. Record	89	93	103	111	118	121	126	126	126	122	128

Table 3-9 Maximum Target and Achieved Accelerations for SFCD2

Times Sylmar	0.15	0.25	0.50	0.75	1.00	1.25	1.50	1.75	2.00	2.25	2.50	2.75	3.00	3.25
Max. Record Acceleration (g)	0.09	0.15	0.30	0.45	0.61	0.76	0.91	1.06	1.21	1.36	1.52	1.67	1.82	1.97
Achieved Acceleration (g)	0.15	0.22	0.47	0.43	0.55	0.73	0.88	1.05	1.22	1.40	1.60	1.77	1.93	2.08
% of Max. Record	167	147	157	96	90	96	97	99	101	103	105	106	106	106

Table 4-1 Observations recorded for LFCD1

Times Sylmar	Columns	Beam-Column Connection	Base Hinge
0.15	No Damage	No Damage	No Damage
0.5	Start of flexural cracking at the top of the flare.	Start of vertical crack development	No Damage
0.75	Minor flexural crack propagation in the flare region towards the lower portion of the flare.	Little crack development	No Damage
1.0	Previous Cracks extending inside the flare depth forming shear cracks with small amount of new crack development.	Very Little crack development	Minor Concrete Spalling
1.25	Significant increase of vertical and shear cracks at the top of the flare formed at the middle of the flare depth	Significant increase in diagonal cracks with higher rates of development	Increase in Concert Spalling
1.5	New flexural and shear cracks extending inside the flare region with higher rate of development extending to the lower portion of the flare	Minor crack development	Minor increase in Concert Spalling
1.75	Previous cracks are connected to cover almost the whole depth of the flare.	Very minor crack development	Concrete spalling stopped
2.0	Shear cracks distribution extending in lower portion of the flare height. Permanent deformations in the gap. Concrete spalling at the edge of the flare.	Significant crack development	Concrete spalling stopped
2.125	Flare cracks increased and widened. Increase of concrete spalling at the top of the flare. Concrete spalling in the middle third of the column and at the top of the flare.	Extensive crack development.	Extensive Concrete spalling
1.75-2	Extensive shear cracking extends along the column height. Extensive spalling at the top of the flare and in the middle third of the column and at the top of the flare extending inside the flare core. Buckling of flare reinforcements.	Minor crack development	Minor increase in Concert Spalling
1.75-3	No development observed from the previous step.	No development observed	No development observed
After bucket removal	Wide shear cracks in the beam and extensive flexural cracks in the middle of the span. Permanent beam deflection.		

Table 4-2 Measured Cap Beam Displacement for LFCD1

Runs	0.15	0.5	0.75	1	1.25	1.5	1.75	2	2.125	1.75-2	1.75-3
Max. Disp.	5.6	14.2	16.0	23.4	43.2	56.4	66.3	86.1	92.7	87.6	96.8
mm (in)	0.22	0.56	0.63	0.92	1.7	2.22	2.61	3.39	3.65	3.45	3.81
Max. Force	83.8	131.1	136.4	161.4	185.7	201.6	200.1	206.6	212.7	189.0	198.2
KN (Kips)	18.83	29.47	30.66	36.28	41.75	45.33	44.98	46.45	47.81	42.48	44.56
Min. Disp.	-6.4	-18.3	-19.8	-33.3	-62.5	-69.6	-97.8	-135.9	-173.7	-173.0	-185.2
mm (in)	-0.25	-0.72	-0.78	-1.31	-2.46	-2.74	-3.85	-5.35	-6.84	-6.81	-7.29
Min. Force	-82.6	-139.2	-132.4	-173.2	-209.5	-198.5	-226.0	-267.0	-284.6	-271.1	-279.6
KN (Kips)	-18.57	-31.3	-29.77	-38.94	-47.09	-44.62	-50.82	-60.02	-63.98	-60.94	-62.86
Permanent Disp.	0.0	-0.5	-0.5	-1.0	-2.5	-3.6	-4.3	-14.0	-23.1	-24.4	-26.7
mm (in)	0	-0.02	-0.02	-0.04	-0.1	-0.14	-0.17	-0.55	-0.91	-0.96	-1.05
Max. Net Disp.	5.6	14.2	16.5	23.9	44.2	58.9	69.9	90.4	106.7	110.7	121.2
mm (in)	0.22	0.56	0.65	0.94	1.74	2.32	2.75	3.56	4.2	4.36	4.77
Min. Net Disp.	-6.4	-18.3	-19.3	-32.8	-61.5	-67.1	-94.2	-131.6	-159.8	-149.9	-160.8
mm (in)	-0.25	-0.72	-0.76	-1.29	-2.42	-2.64	-3.71	-5.18	-6.29	-5.9	-6.33
Dynamic Properties											
Chord Stiffness	79.57	47.48	42.86	33.73	21.36	18.14	14.83	12.18	10.66	10.08	9.68
KN/mm (Kips/in)	13.9	8.3	7.5	5.9	3.7	3.2	2.6	2.1	1.9	1.8	1.7
% of Initial Stiffness	100%	60%	54%	42%	27%	23%	19%	15%	13%	13%	12%
T_n (Sec.)	0.36	0.47	0.49	0.55	0.70	0.75	0.83	0.92	0.98	1.01	1.03
f_n (Hz)	2.78	2.14	2.04	1.81	1.44	1.33	1.20	1.09	1.02	0.99	0.97
% of Initial Frequency	100%	77%	73%	65%	52%	48%	43%	39%	37%	36%	35%

Table 4-3 Measured Base Hinge Displacement for LFCD1

Times Sylmar		0.15	0.5	0.75	1	1.25	1.5	1.75	2	2.125	1.75-2	1.75-3
East Column	Max. Disp. mm (in)	0.6 (0.023)	1.7 (0.068)	1.8 (0.072)	3.2 (0.126)	6.1 (0.242)	6.8 (0.266)	9.6 (0.376)	14.2 (0.558)	19.1 (0.751)	18.9 (0.745)	20.5 (0.809)
	Min. Disp. mm (in)	-0.5 (-0.02)	-1.5 (-0.06)	-1.8 (-0.07)	-2.5 (-0.1)	-4.6 (-0.18)	-6.1 (-0.24)	-7.4 (-0.29)	-9.1 (-0.36)	-9.7 (-0.38)	-8.9 (-0.35)	-9.9 (-0.39)
	Permanent Disp. mm (in)	0 (0)	0 (0)	0 (0)	0 (0)	0.03 (0.001)	0.03 (0.001)	0.03 (0.001)	0.8 (0.032)	1.5 (0.06)	1.6 (0.063)	1.9 (0.073)
West Column	Max. Disp. mm (in)	0.7 (0.028)	2.3 (0.09)	2.6 (0.104)	4.4 (0.173)	8.2 (0.324)	8.9 (0.35)	13 (0.511)	19 (0.748)	25 (0.985)	25.3 (0.997)	27.4 (1.079)
	Min. Disp. mm (in)	-0.5 (-0.02)	-1.8 (-0.07)	-2. (-0.08)	-2.8 (-0.11)	-5.6 (-0.22)	-7.1 (-0.28)	-8.4 (-0.33)	-10.7 (-0.42)	-11.2 (-0.44)	-10.2 (-0.4)	-11.2 (-0.44)
	Permanent Disp. mm (in)	0 (0)	(0.03) 0.001	0 (0)	0.08 (0.003)	0.31 (0.012)	0.31 (0.012)	0.48 (0.019)	1.83 (0.072)	3.2 (0.127)	3.6 (0.141)	3.6 (0.143)

Table 4-4 LFCD1, Maximum and Minimum Measured Strains for Base Hinge Dowels

Gauge No.		Times Sylmar										
		0.15	0.5	0.75	1	1.25	1.5	1.75	2	2.125	1.75-2	1.75-3
40	Max.	1372	5642	8497	14886	14687	5657	5173	5024	5226	5317	5928
	Min.	-849	-920	-430	624	2596	3017	2872	2813	2798	2901	3077
41	Max.	203	2033	2087	5207	7674	1844	1700	5163	4917	4299	6679
	Min.	-695	-732	-731	-733	38	-195	-1702	-4597	-12346	-14167	-15452
92	Max.	388	1760	48	635	1011	491	2622	9472	13136	14185	17956
	Min.	-811	-942	-4507	-4402	-2789	-2624	-1780	198	362	-943	333
93	Max.	885	5862	6326	11260	1750	962	1403	2778	4264	4305	4617
	Min.	-596	-626	687	-1202	-3130	-531	-392	-939	-2556	-3483	-4762
Max.		1372	5862	8497	14886	14687	5657	5173	9472	13136	14185	17956
Min.		-849	-942	-4507	-4402	-3130	-2624	-1780	-4597	-12346	-14167	-15452
									Max.=	17956	Min.=	-15452

Table 4-5 LFCD1, Maximum and Minimum Measured Strains for Columns Longitudinal Reinforcement

Gauge No.		Times Sylmar										
		0.15	0.5	0.75	1	1.25	1.5	1.75	2	2.125	1.75-2	1.75-3
43	Max.	1020	1800	1778	2409	2966	2970	3509	11605	15578	14873	16788
	Min.	123	-25	-40	-153	-280	-343	-357	-367	1244	1766	1725
52	Max.	1037	1918	1939	2650	3175	3280	3715	10085	11717	7554	6337
	Min.	148	26	-8	-156	-291	-371	-462	-476	-611	-655	-825
55	Max.	367	969	994	1374	1969	2377	4351	3821	10178	5069	6157
	Min.	-404	-489	-546	-601	-701	-967	-972	-1093	-1639	-1321	-1587
56	Max.	-111	409	435	1354	1838	11646	8541	10422	12069	14197	15307
	Min.	-1116	-1322	-1436	-1249	-1447	-1187	4730	3942	-37	4188	1805
62	Max.	348	1853	1931	2758	8604	10623	17812	24112	29075	28694	27467
	Min.	-304	-551	-588	-799	-827	-517	71	859	1972	880	2950
65	Max.	97	932	1140	1769	2532	2807	10818	14658	16872	16170	18173
	Min.	-384	-528	-519	-604	-1241	-1515	-1488	-809	-325	148	292
66	Max.	288	1271	1513	2228	2995	6717	8852	14585	16589	16118	17880
	Min.	-599	-1049	-1009	-1335	-1690	-3455	-4510	-4226	-4224	-4249	-4232
67	Max.	484	1689	1760	2519	3894	9403	12652	11792	9193	9573	6535
	Min.	-37	-115	-67	-314	-880	-842	507	1701	2713	801	1941
71	Max.	963	2776	2885	12864	14246	1324	1125	2805	4283	38533	5878
	Min.	-483	-790	-856	-823	-4194	-4936	-5469	-20224	-3824	-3243	-2583
72	Max.	424	1354	1440	2732	10084	11664	16753	22282	22524	13417	6255
	Min.	-167	-215	-191	-237	-182	2445	3493	4360	1172	-522	3873
74	Max.	521	1345	1493	2059	9208	11376	14661	14423	4945	4723	4594
	Min.	-252	-325	-303	-250	-231	2984	3325	3050	2114	1939	1423
75	Max.	19	633	797	1098	1317	1406	1584	1765	1854	1860	1879
	Min.	-102	-153	-201	-284	-430	-521	-615	-726	-844	-904	-968
76	Max.	317	1613	1796	2268	9062	11895	14860	18790	7653	7872	7622
	Min.	-232	-502	-522	-783	-1068	-544	-326	121	-950	-1591	-2228

Table 4-5 LFCD1, Maximum and Minimum Measured Strains for Columns Longitudinal Reinforcement (Cont'd)

Gauge No.		Times Sylmar										
		0.15	**0.5**	**0.75**	**1**	**1.25**	**1.5**	**1.75**	**2**	**2.125**	**1.75-2**	**1.75-3**
77	Max.	264	937	1003	1308	1734	1951	2116	**2313**	**2467**	**2600**	**2726**
	Min.	-140	-204	-215	-249	-550	-839	-1038	-1198	-1285	-1222	-1135
81	Max.	-11	568	667	924	1105	1125	1083	1027	1021	986	1004
	Min.	-239	-249	-173	-124	-125	-257	-418	-549	-598	-544	-503
98	Max.	-472	294	629	1054	1725	2004	**2167**	**2552**	**2742**	**2673**	**2952**
	Min.	-1032	-868	-709	-441	-378	-447	-707	-594	-685	-24	71
99	Max.	-444	432	845	1328	2101	**2359**	**2593**	**2971**	**3080**	**2902**	**3173**
	Min.	-1120	-904	-873	-771	-1218	-958	-1512	-1496	**-2184**	-1429	-1294
100	Max.	-433	677	773	1578	1887	**2229**	**2373**	**3584**	**11320**	**10460**	**11222**
	Min.	-1253	-1089	-1076	-712	-513	-633	-439	-525	-582	1041	1342
105	Max.	-4	1449	1545	**2429**	**2611**	**2624**	**4441**	**4311**	1503	1549	1319
	Min.	-1395	-1310	-1364	-1267	-1140	-1513	-1979	-2101	-1432	-1096	-1008
108	Max.	-284	679	1042	1564	**2418**	**2713**	**2951**	**3433**	**3857**	**3981**	**4692**
	Min.	-1054	-881	-617	-458	-316	-775	-1016	-1060	-1103	-499	-214
109	Max.	187	1324	1727	**2313**	**3108**	**3428**	**3627**	**6431**	**8412**	**7433**	**8345**
	Min.	-919	-793	-660	-664	-1070	-913	-1399	-1297	**-2991**	-1517	-1372
110	Max.	-524	694	768	1614	1938	**2299**	**2468**	**11109**	**14161**	**12987**	**13703**
	Min.	-1595	-1443	-1409	-1024	-877	-1054	-909	-926	1018	1538	1668
115	Max.	304	1865	2012	**2698**	**8227**	**8872**	**14296**	**19332**	**17470**	**12428**	**8271**
	Min.	-802	-1401	-1508	-1825	**-5369**	**-4804**	**-5436**	**-5396**	**-5497**	**-3279**	-1189
118	Max.	75	1225	1403	2047	**2864**	**7028**	**9866**	**13597**	**14762**	**14558**	**16392**
	Min.	-514	-567	-552	-567	-1059	-1196	-495	-123	376	**2263**	**3052**
119	Max.	169	1667	1877	**2371**	**3161**	**8189**	**10515**	**11130**	**5779**	**5348**	**4846**
	Min.	-577	-986	-999	-1396	-1862	**-3317**	**-4016**	**-3375**	**-2960**	**-3698**	**-3576**
124	Max.	-148	-148	-132	-123	-116	-185	-322	-569	-676	-823	-874
	Min.	-161	-169	-163	-173	-209	-418	-793	-1019	-1203	-1169	-1194
125	Max.	-218	1442	1588	1696	1371	1250	1054	966	-43	-38	-12
	Min.	-388	-432	-347	-424	-572	-415	-736	**-2247**	**-2168**	-1144	-1204
130	Max.	-172	328	478	786	1115	1224	1362	1621	1800	1908	2061
	Min.	-292	-333	-333	-388	-461	-576	-650	-726	-765	-749	-693
132	Max.	-338	155	256	433	711	816	1011	1481	1995	2072	1931
	Min.	-412	-411	-318	-349	-423	-488	-498	-628	-810	-966	-1301
133	Max.	-67	868	1034	1733	**5230**	**7379**	**9134**	**9504**	**9207**	**5523**	**4090**
	Min.	-348	-348	-334	-350	-289	97	425	1923	1619	1954	1300
134	Max.	-216	-27	74	143	341	424	531	718	943	1046	1178
	Min.	-244	-247	-170	-168	-170	-147	-182	-334	-515	-629	-700
147	Max.	12	771	834	1505	2135	2104	**2541**	**6256**	**11755**	**10669**	**11059**
	Min.	-967	-1243	-1279	-1469	-1728	-1852	-1903	**-2856**	**-3089**	-1239	-1121
150	Max.	-92	417	512	832	1249	1452	1630	1990	**2230**	**2343**	**2634**
	Min.	-691	-834	-810	-886	-941	-929	-971	-1027	-1138	-1187	-1218
Max.		1037	**2776**	**2885**	**12864**	**14246**	**11895**	**17812**	**24112**	**29075**	**38533**	**27467**
Min.		-1595	-1443	-1508	-1825	**-5369**	**-4936**	**-5469**	**-20224**	**-5497**	**-4249**	**-4232**
									Max.=	**38533**	Min.=	**-20224**

Table 4-6 LFCD1, Maximum and Minimum Measured Strains for Columns Spirals

Gauge No.		Times Sylmar										
		0.15	**0.5**	**0.75**	**1**	**1.25**	**1.5**	**1.75**	**2**	**2.125**	**1.75-2**	**1.75-3**
48	Max.	1	8	16	30	53	56	84	124	181	178	180
	Min.	-15	-19	-15	-9	-4	1	17	34	61	67	44
54	Max.	4	38	51	83	115	126	142	143	154	202	276
	Min.	-14	-16	4	18	28	52	54	8	-73	-80	-92
58	Max.	-50	11	32	59	72	64	45	21	8	-41	91
	Min.	-74	-74	-55	-43	-44	-20	-37	-128	-215	-218	-230
64	Max.	74	234	221	265	287	282	442	527	554	562	565
	Min.	57	56	77	85	44	-18	-97	-190	-264	-245	-241
68	Max.	32	74	92	222	238	29	87	199	288	387	421
	Min.	3	1	13	39	-39	-93	-72	-22	0	2	21
78	Max.	246	327	345	380	371	374	395	652	709	848	852
	Min.	176	193	277	260	241	236	249	309	353	407	425
82	Max.	120	134	128	128	151	435	724	795	2050	**2158**	**2103**
	Min.	101	83	71	-43	-208	-226	-245	-227	-66	334	508
97	Max.	-491	-21	39	341	449	517	586	681	707	838	914
	Min.	-715	-659	-655	-115	-73	-48	-140	-112	-158	548	357
101	Max.	-489	-34	58	348	561	620	627	640	641	721	782
	Min.	-706	-649	-654	-90	-26	-35	-177	-167	-246	505	331
107	Max.	-511	-42	40	342	518	614	641	662	667	753	828
	Min.	-738	-679	-687	-125	-66	1	-132	-80	-176	481	288
117	Max.	494	506	519	538	555	560	564	576	579	632	656
	Min.	484	479	493	484	524	516	528	526	552	513	606
129	Max.	-190	-129	-132	-133	-103	-57	-40	17	58	169	208
	Min.	-206	-208	-229	-293	-408	-471	-477	-508	-573	-538	-532
131	Max.	2	50	63	81	209	270	423	771	726	834	921
	Min.	-24	-16	4	-1	23	72	76	111	192	309	304
135	Max.	169	196	218	291	564	537	485	471	432	282	243
	Min.	138	133	133	128	224	194	194	120	-12	-231	-467
Max.		494	506	519	538	564	620	724	795	2050	**2158**	2103
Min.		-738	-679	-687	-293	-408	-471	-477	-508	-573	-538	-532
									Max.=	**2158**	Min.=	-738

Table 4-7 LFCD1, Maximum and Minimum Measured Strains for Flare Longitudinal Reinforcement

Gauge No.		Times Sylmar										
		0.15	**0.5**	**0.75**	**1**	**1.25**	**1.5**	**1.75**	**2**	**2.125**	**1.75-2**	**1.75-3**
49	Max.	159	783	634	662	1213	1204	718	449	**-4227**	**-9688**	**-9619**
	Min.	-1592	**-2535**	**-2613**	**-3882**	**-5689**	**-5810**	**-8243**	**-14782**	**-14868**	**-11850**	**-11640**
51	Max.	1259	2093	2044	**2619**	**3008**	**2875**	**2933**	**2641**	**2539**	2397	**2677**
	Min.	107	-69	-45	-106	-187	-105	125	108	162	724	628
57	Max.	607	904	974	1200	1575	1651	1482	1353	930	-66	-29
	Min.	-406	-715	-670	-854	-1080	-861	-1021	-1827	**-2446**	-1663	-1597
59	Max.	77	507	509	684	902	937	659	647	-315	-536	-408
	Min.	-1117	-1499	-1417	-1640	-1893	-1815	**-2723**	**-3956**	**-3247**	-1010	-929
69	Max.	861	907	990	1734	1946	2126	2374	**2775**	**2891**	**2534**	**2651**
	Min.	673	574	667	653	257	335	-214	-456	-562	-73	-211
94	Max.	317	777	333	973	1976	484	-1101	-1820	-2194	**-2989**	**-2915**
	Min.	-1552	**-2926**	**-3285**	**-4460**	**-6356**	**-7343**	**-7720**	**-7847**	**-7737**	**-24596**	**-16845**
102	Max.	-131	925	1239	1689	2412	2340	1611	1343	1238	596	771
	Min.	-1432	-1369	-1412	-1503	-1981	-1656	-2174	-1889	**-2865**	-1719	-1505
104	Max.	-285	778	763	1437	1495	1456	1595	2412	2414	1937	1988
	Min.	-1674	-1590	-1593	-1422	-1173	-1041	-549	-446	-442	-243	-85
114	Max.	-306	1264	1122	1032	1082	1097	1365	2053	**2693**	2427	2450
	Min.	-494	-606	-147	164	24	59	77	60	138	473	566
122	Max.	365	1913	2068	**3907**	**13874**	**16201**	**17039**	**5783**	**5408**	**5273**	**4943**
	Min.	-363	-483	-434	-456	-313	2117	**3580**	**3840**	**3423**	**2995**	**3124**
Max.		1259	2093	2068	**3907**	**13874**	**16201**	**17039**	**5783**	**5408**	**5273**	**4943**
Min.		-1674	**-2926**	**-3285**	**-4460**	**-6356**	**-7343**	**-8243**	**-14782**	**-14868**	**-24596**	**-16845**
									Max.=	**17039**	Min.=	**-24596**

Table 4-8 LFCD1, Maximum and Minimum Measured Strains for Flare hoops

Gauge No.		Times Sylmar										
		0.15	**0.5**	**0.75**	**1**	**1.25**	**1.5**	**1.75**	**2**	**2.125**	**1.75-2**	**1.75-3**
53	Max.	50	121	81	125	210	282	329	450	869	981	1153
	Min.	-21	-16	-12	-1	25	85	122	103	190	315	314
103	Max.	-567	-93	5	327	519	591	648	718	823	930	1027
	Min.	-783	-722	-719	-152	-76	-23	-98	-82	-141	596	426
106	Max.	-512	-49	18	308	399	436	442	433	422	696	778
	Min.	-748	-680	-686	-141	-167	-146	-408	-315	-580	-8	-223
113	Max.	-244	-227	-250	-245	-242	-246	-260	-285	-349	-435	-477
	Min.	-295	-301	-293	-323	-424	-529	-614	-737	-832	-794	-811
116	Max.	-169	-163	-210	-211	-231	-343	-420	-439	-433	-305	-318
	Min.	-200	-240	-254	-300	-525	-608	-774	-895	-944	-918	-919
123	Max.	583	**2252**	**2312**	**3077**	**17035**	**7975**	**4278**	**3348**	**3022**	**3086**	**8765**
	Min.	-526	-827	-908	-1426	-1294	-1597	**-2642**	**-3497**	**-6187**	**-9166**	**-13004**
149	Max.	-147	-55	-48	11	55	49	63	73	101	177	272
	Min.	-178	-175	-160	-177	-121	-108	-87	-78	-66	-51	-16
152	Max.	-190	-164	-159	-143	-144	-180	-122	-62	1	91	108
	Min.	-242	-258	-196	-209	-242	-292	-289	-328	-441	-373	-356
Max.		583	**2252**	**2312**	**3077**	**17035**	**7975**	**4278**	**3348**	**3022**	**3086**	**8765**
Min.		-783	-827	-908	-1426	-1294	-1597	**-2642**	**-3497**	**-6187**	**-9166**	**-13004**
									Max.=	**17035**	Min.=	**-13004**

Table 4-9 LFCD1, Maximum and Minimum Measured Strains for Beam

Gauge No.		Times Sylmar										
		0.15	**0.5**	**0.75**	**1**	**1.25**	**1.5**	**1.75**	**2**	**2.125**	**1.75-2**	**1.75-3**
80	Max.	365	595	848	1440	1624	1662	1998	**2347**	**2552**	**2466**	**2499**
	Min.	262	198	200	196	296	508	604	681	703	684	681
83	Max.	-3	122	145	210	376	452	543	692	791	824	876
	Min.	-87	-92	-73	-86	-103	-49	25	137	266	332	386
85	Max.	83	855	990	1452	2011	**2209**	**2271**	**2394**	**2460**	**2320**	**2477**
	Min.	-288	-408	-346	-405	-384	-222	-181	-167	-157	-117	-69
86	Max.	-101	89	195	455	889	1119	1265	1535	1846	1664	1780
	Min.	-153	-163	-146	-109	-80	76	125	196	188	178	220
87	Max.	452	836	894	1208	1508	1560	1793	2060	2237	2214	2254
	Min.	133	31	73	72	67	83	115	141	168	236	200
91	Max.	14	438	574	912	1616	1888	1971	2087	**2211**	2037	**2192**
	Min.	-57	-54	60	79	104	119	103	62	52	81	104
136	Max.	-233	14	93	122	-63	-50	3	313	765	882	1072
	Min.	-351	-312	-298	-321	-342	-269	-240	-152	71	231	225
137	Max.	465	1001	1127	1413	1732	1892	1993	2215	2308	2308	2378
	Min.	-263	-471	-455	-549	-629	-580	-611	-581	-574	-478	-477
138	Max.	-87	903	1031	1516	2033	2036	**2485**	**9582**	**13175**	**12681**	**13291**
	Min.	-365	-349	-274	-298	-239	-49	-23	49	**4714**	**7256**	**8098**
140	Max.	195	729	841	1112	1464	1635	1726	1946	2075	2188	2344
	Min.	-177	-322	-313	-392	-440	-364	-380	-375	-296	-152	-126
141	Max.	6	1138	1232	1823	**2391**	**2468**	**7149**	**12355**	**16894**	**16661**	**17682**
	Min.	-352	-328	-161	-138	-71	16	48	**3684**	**7024**	**10398**	**11649**
144	Max.	-160	387	493	1117	1749	1782	**2171**	**2395**	**2578**	**2645**	**2737**
	Min.	-256	-244	-90	-68	-16	30	51	-180	-289	-326	-168
145	Max.	164	657	726	1043	1365	1390	1595	1922	2087	2117	2164
	Min.	-299	-456	-438	-470	-409	-332	-250	-178	-168	-69	-80
148	Max.	110	186	114	162	180	183	207	356	445	465	577
	Min.	-32	-14	-15	-30	-28	-18	-14	-9	1	-25	-58
153	Max.	83	1019	1173	1690	**2504**	**2849**	**3581**	**8334**	**10120**	**9274**	**9769**
	Min.	-471	-507	-360	-294	-219	-171	-111	410	**4111**	**5828**	**6087**
Max.		465	1138	1232	1823	**2504**	**2849**	**7149**	**12355**	**16894**	**16661**	**17682**
Min.		-471	-507	-455	-549	-629	-580	-611	-581	-574	-478	-477
									Max.=	**17682**	Min.=	-629

Table 4-10 LFCD1, First Yield Occurrence

Gauge No.		Times Sylmar	Remarks
40	Max.	0.50	Base Dowels
49	Min.	0.50	Flare Reinf.
71	Max.	0.50	Column Reinf. At Gap
93	Max.	0.50	Base Dowels
94	Min.	0.50	Flare Reinf.
123	Max.	0.50	Flare Hoops
41	Max.	1.00	Base Dowels
43	Max.	1.00	Column Reinf.
51	Max.	1.00	Flare Reinf.
52	Max.	1.00	Column Reinf.
62	Max.	1.00	Column Reinf.
66	Max.	1.00	Column Reinf.
67	Max.	1.00	Column Reinf.
72	Max.	1.00	Column Reinf. At Gap
76	Max.	1.00	Column Reinf. At Gap
105	Max.	1.00	Column Reinf.
109	Max.	1.00	Column Reinf.
115	Max.	1.00	Column Reinf.
119	Max.	1.00	Column Reinf.
122	Max.	1.00	Flare Reinf.
40	Min.	1.25	Base Dowels
65	Max.	1.25	Column Reinf.
71	Min.	1.25	Column Reinf. At Gap
74	Max.	1.25	Column Reinf. At Gap
93	Min.	1.25	Base Dowels
108	Max.	1.25	Column Reinf.
115	Min.	1.25	Column Reinf.
118	Max.	1.25	Column Reinf.
133	Max.	1.25	Column Reinf. At Gap
141	Max.	1.25	Beam's Bot. Reinf.
153	Max.	1.25	Beam's Bot. Reinf.
55	Max.	1.50	Column Reinf.
66	Min.	1.50	Column Reinf.
72	Min.	1.50	Column Reinf. At Gap
74	Min.	1.50	Column Reinf. At Gap

Gauge No.		Times Sylmar	Remarks
85	Max.	1.50	Beam's Bot. Reinf.
99	Max.	1.50	Column Reinf.
100	Max.	1.50	Column Reinf.
110	Max.	1.50	Column Reinf.
119	Min.	1.50	Column Reinf.
92	Max.	1.75	Base Dowels
98	Max.	1.75	Column Reinf.
122	Min.	1.75	Flare Reinf.
123	Min.	1.75	Flare Hoops
138	Max.	1.75	Beam's Bot. Reinf.
144	Max.	1.75	Beam's Bot. Reinf.
147	Max.	1.75	Column Reinf.
41	Min.	2.00	Base Dowels
69	Max.	2.00	Flare Reinf.
77	Max.	2.00	Column Reinf. at joint
80	Max.	2.00	Beam's Side Reinf.
125	Min.	2.00	Column Reinf. At Gap
141	Min.	2.00	Beam's Bot. Reinf.
147	Min.	2.00	Column Reinf.
49	Max.	2.125	Flare Reinf.
57	Min.	2.125	Flare Reinf.
67	Min.	2.125	Column Reinf.
91	Max.	2.125	Beam's Bot. Reinf.
99	Min.	2.125	Column Reinf.
102	Min.	2.125	Flare Reinf.
109	Min.	2.125	Column Reinf.
114	Max.	2.125	Flare Reinf.
138	Min.	2.125	Beam's Bot. Reinf.
150	Max.	2.125	Column Reinf.
153	Min.	2.125	Beam's Bot. Reinf.
82	Max.	1.75-2	Spiral in the Joint
94	Max.	1.75-2	Flare Reinf.
118	Min.	1.75-2	Column Reinf.
62	Min.	1.75-3	Column Reinf.
76	Min.	1.75-3	Column Reinf. At Gap

Table 4-11 Observations recorded for LFCD2

Times Sylmar	Columns	Beam-Column Connection	Base Hinge
0.15	No Damage	No Damage	No Damage
0.25	No Damage	No Damage	No Damage
0.5	Start of flexural cracking at the middle height of the flare.	Start of vertical crack development	No Damage
0.75	Flexural and shear crack development extending down to include the lower portion of the flare height	Significant vertical crack development	No Damage
1.0	Previous cracks extending inside the flare depth forming shear cracks with little new crack development.	Significant crack development	Minor Concrete Spalling
1.25	Significant increase in shear and flexural cracks in the flare region formed at the top portion of the flare extending to the middle of the flare depth. Concrete cover spalling at the top of the flare.	Significant increase in diagonal cracks with higher rates of development	Increase in Concert Spalling
1.5	New flexural and shear cracks extending to the lower portion of the column	Minor crack development	Minor increase in Concert Spalling
1.75	Flexural and shear cracks increased in the flare and extending to cover whole height of the flare with some cracks below it.	Very minor crack development	Concrete spalling stopped
2.0	Flexural and shear cracks increased to cover whole height of the column. Concrete spalling at the top edge of the flare.	Extensive crack development.	Increase in concrete spalling
2.125	Flare cracks increased and widened. Shear cracks along the column height. Extensive concrete spalling occurred at top third of the flare region causing flare hoops to be exposed.	Significant crack development	Extensive Concrete spalling
1.75-2	Extensive shear cracking extends along the column height. Extensive spalling at the top of the flare extending to cover the middle third of flare. Buckling of flare reinforcement.	Minor crack development	Minor increase in Concert Spalling
After bucket removal	Wide shear cracks in the beam and extensive flexural cracks in the middle of the span. Permanent beam deflection.		

Table 4-12 Measured Cap Beam Displacement for LFCD2

Runs	0.15	0.25	0.5	0.75	1	1.25	1.5	1.75	2	2.125	1.75-2
Max. Disp. mm (in)	5.8 (0.23)	8.1 (0.32)	11.9 (0.47)	15.5 (0.61)	22.1 (0.87)	39.9 (1.57)	51.3 (2.02)	61.2 (2.41)	83.6 (3.29)	92.7 (3.65)	89.2 (3.51)
Max. Force KN (Kips)	69.7 (15.67)	87.9 (19.76)	103.1 (23.18)	116.6 (26.22)	147.7 (33.21)	181.4 (40.77)	198.3 (44.58)	189.8 (42.67)	196.7 (44.23)	209.5 (47.09)	183.8 (41.32)
Min. Disp. mm (in)	-6.9 (-0.27)	-9.7 (-0.38)	-11.7 (-0.46)	-17 (-0.67)	-31.5 (-1.24)	-58.4 (-2.3)	-65.5 (-2.58)	-91.9 (-3.62)	-132.8 (-5.23)	-177 (-6.97)	-183.4 (-7.22)
Min. Force KN (Kips)	-75.4 (-16.95)	-94.2 (-21.18)	-100.9 (-22.69)	-121.7 (-27.37)	-168.4 (-37.86)	-205.2 (-46.12)	-192.1 (-43.19)	-213.7 (-48.05)	-247.2 (-55.57)	-268.6 (-60.38)	-246.4 (-55.4)
Permanent Disp. mm (in)	0.5 (0.02)	0.8 (0.03)	0.8 (0.03)	0.3 (0.01)	-1.0 (-0.04)	-2.8 (-0.11)	-4.6 (-0.18)	-6.4 (-0.25)	-16 (-0.63)	-26.7 (-1.05)	-30.7 (-1.21)
Max. Net Disp. mm (in)	5.8 (0.23)	7.6 (0.3)	11.2 (0.44)	14.7 (0.58)	21.8 (0.86)	40.9 (1.61)	54.1 (2.13)	65.8 (2.59)	89.9 (3.54)	108.7 (4.28)	115.8 (4.56)
Min. Net Disp. mm (in)	-6.9 (-0.27)	-10.2 (-0.4)	-12.4 (-0.49)	-17.8 (-0.7)	-31.8 (-1.25)	-57.4 (-2.26)	-62.7 (-2.47)	-87.4 (-3.44)	-126.5 (-4.98)	-161 (-6.34)	-156.7 (-6.17)
Dynamic Properties											
Chord Stiffness KN/mm (Kips/in)	65.24 11.4	58.49 10.2	49.32 8.6	41.87 7.3	33.68 5.9	22.45 3.9	19.08 3.3	15.04 2.6	11.71 2.1	10.12 1.8	9.01 1.6
% of Initial Stiffness	100%	90%	76%	64%	52%	34%	29%	23%	18%	16%	14%
T_n (Sec.)	0.40	0.42	0.46	0.50	0.55	0.68	0.74	0.83	0.94	1.01	1.07
f_n (Hz)	2.51	2.38	2.19	2.01	1.81	1.47	1.36	1.21	1.06	0.99	0.93
% of Initial Frequency	100%	95%	87%	80%	72%	59%	54%	48%	42%	39%	37%

Table 4-13 Measured Base Hinge Displacement for LFCD2

Times Sylmar		0.15	0.25	0.5	0.75	1	1.25	1.5	1.75	2	2.125	1.75-2
East Column	Max. Disp. mm (in)	0.28 (0.011)	0.41 (0.016)	0.56 (0.022)	0.71 (0.028)	1.14 (0.045)	2.18 (0.086)	3.0 (0.118)	3.8 (0.148)	5.2 (0.206)	6.0 (0.236)	6.2 (0.245)
	Min. Disp. mm (in)	-0.33 (-0.013)	-0.43 (-0.017)	-0.51 (-0.020)	-0.81 (-0.032)	-1.7 (-0.068)	-3.2 (-0.126)	-3.5 (-0.137)	-4.7 (-0.184)	-6.6 (-0.258)	-9.0 (-0.355)	-9.3 (-0.367)
	Permanent Disp. mm (in)	0.03 (0.001)	0.05 (0.002)	0.08 (0.003)	0.08 (0.003)	0.05 (0.002)	0.08 (0.003)	0.08 (0.003)	0.08 (0.003)	-0.1 (-0.004)	-0.25 (-0.010)	-0.41 (-0.016)
West Column	Max. Disp. mm (in)	0.0 (0.0)	0.13 (0.005)	1.3 (0.051)	2.8 (0.110)	3.2 (0.127)	3.6 (0.143)	3.8 (0.149)	4.2 (0.166)	4.2 (0.166)	5.8 (0.228)	6.4 (0.250)
	Min. Disp. mm (in)	0.0 (0.0)	0.0 (0.0)	0.13 (0.005)	1.3 (0.049)	1.8 (0.070)	0.94 (0.037)	0.28 (0.011)	-0.56 (-0.022)	-5.7 (-0.225)	-6.2 (-0.246)	-6.5 (-0.254)
	Permanent Disp. mm (in)	0.0 (0.0)	0.13 (0.005)	1.3 (0.050)	2.8 (0.109)	2.7 (0.105)	2.7 (0.105)	2.5 (0.099)	2.9 (0.114)	-0.97 (-0.038)	-0.86 (-0.034)	-0.84 (-0.033)

Table 4-14 LFCD2, Maximum and Minimum Measured Strains for Base Hinge Dowels

Gauge No.		Times Sylmar										
		0.15	0.25	0.5	0.75	1	1.25	1.5	1.75	2	2.125	1.75-2
89	Max.	330	958	1460	1947	**6386**	**5058**	**2397**	1402	846	-557	-1027
	Min.	-1097	-1103	-1142	-1194	-1317	-763	-1774	**-3367**	**-6273**	**-7204**	**-4513**
144	Max.	376	1119	1560	**2536**	**7745**	1712	463	105	-88	-303	-589
	Min.	-1114	-1140	-1170	-1205	-1197	-1577	-1725	**-2289**	**-8020**	**-12233**	**-14621**
Max.		376	1119	1560	**2536**	**7745**	**5058**	**2397**	1402	846	-303	-589
Min.		-1114	-1140	-1170	-1205	-1317	-1577	-1774	**-3367**	**-8020**	**-12233**	**-14621**
									Max.=	**7745**	Min.=	**-14621**

Table 4-15 LFCD2, Maximum and Minimum Measured Strains for Columns Longitudinal Reinforcement

Gauge No.		Times Sylmar										
		0.15	0.25	0.5	0.75	1	1.25	1.5	1.75	2	2.125	1.75-2
43	Max.	83	274	400	709	1494	**2217**	**2258**	**2900**	**8816**	**11118**	**10962**
	Min.	-1004	-1130	-1246	-1340	-1610	-1933	-2051	-2132	**-2165**	**-2210**	-1323
45	Max.	-137	-35	75	165	459	821	1025	1113	1383	1613	1616
	Min.	-642	-682	-702	-758	-850	-898	-849	-860	-937	-1061	-1066
46	Max.	159	311	455	580	1043	1519	1752	1864	**2310**	**2650**	**3000**
	Min.	-773	-883	-962	-1094	-1410	-1701	-1690	-1838	**-2150**	**-2967**	**-3152**
51	Max.	224	483	683	1043	1803	**2382**	**2400**	**2842**	**8145**	**11584**	**8764**
	Min.	-984	-1102	-1209	-1335	-1561	-1829	-1971	**-2138**	**-2798**	**-3276**	**-3058**
54	Max.	185	359	515	650	1082	1734	1979	**2191**	**2586**	**2796**	**2843**
	Min.	-253	-269	-276	-318	-362	-409	-530	-694	-964	-1069	-1077
55	Max.	348	615	829	1032	1574	2093	**2305**	**2387**	**2758**	**3119**	**3678**
	Min.	-532	-615	-670	-765	-1009	-1319	-1357	-1526	-1832	**-2548**	**-3164**
56	Max.	-75	62	173	457	915	1449	1347	1457	1769	**5438**	**3245**
	Min.	-690	-746	-804	-839	-1044	-1233	-1305	-1412	-1693	-1944	-2035
59	Max.	104	338	579	1128	**2159**	**5783**	**9089**	**10717**	**5156**	**3550**	**2391**
	Min.	-824	-943	-1110	-1275	-1605	**-2718**	**-2783**	**-2214**	-1145	-968	-852
62	Max.	-34	125	467	783	1535	**2590**	**2900**	**5360**	**11563**	**13226**	**13344**
	Min.	-443	-455	-461	-496	-520	-790	-1075	-1461	-1528	-1419	-1046
64	Max.	-178	16	184	664	1678	**2555**	**6795**	**12340**	**17711**	**5152**	**4011**
	Min.	-874	-930	-988	-1042	-1195	-1852	**-2396**	-2132	-2080	-775	-436
68	Max.	660	1233	1594	**2301**	**10819**	**4938**	1522	1328	1550	2094	**2259**
	Min.	-884	-1007	-1156	-1420	-1521	**-4001**	**-4380**	**-4804**	**-5094**	-1534	-423
69	Max.	299	747	1021	1475	**3280**	**6886**	709	610	814	940	900
	Min.	-754	-799	-888	-886	-831	-943	-466	-952	-1495	-1888	-2120
71	Max.	129	426	701	1106	1868	**9927**	**12937**	**4892**	**4199**	**3837**	**3616**
	Min.	-413	-396	-408	-400	-351	-186	**3625**	**2172**	2047	1779	1609
72	Max.	139	356	578	1147	**2637**	**4038**	**5186**	**10431**	**8157**	**2396**	**2210**
	Min.	-347	-381	-437	-461	-540	-684	-562	-187	1056	648	942
74	Max.	92	253	430	798	1342	1731	1906	1978	**2632**	**4101**	**4022**
	Min.	-382	-467	-535	-650	-829	-1101	-1176	-1355	-1506	-1624	-1437

Table 4-15 LFCD2, Maximum and Minimum Measured Strains for Columns Longitudinal Reinforcement (Contd.)

Gauge No.		Times Sylmar										
		0.15	**0.25**	**0.5**	**0.75**	**1**	**1.25**	**1.5**	**1.75**	**2**	**2.125**	**1.75-2**
76	Max.	-40	132	275	676	1393	1450	1541	1671	**2182**	**2372**	**2773**
	Min.	-211	-196	-238	-276	-235	-343	-409	-569	-808	-905	-991
78	Max.	-32	63	303	686	1011	1162	1121	1181	1425	1739	1879
	Min.	-218	-246	-243	-266	-400	-540	-525	-597	-663	-716	-754
91	Max.	198	378	468	678	1088	1360	1220	1402	**3193**	**5768**	**2969**
	Min.	-709	-826	-927	-1073	-1350	-1592	-1642	-1658	-1749	-1860	-1814
94	Max.	-65	75	227	453	925	1484	1719	1843	2110	**2268**	**2247**
	Min.	-773	-859	-913	-991	-1162	-1248	-1223	-1360	-1689	-2088	-2135
95	Max.	-88	101	285	491	962	1586	1897	2072	**2485**	**3369**	1638
	Min.	-1243	-1400	-1495	-1693	**-2146**	**-2766**	**-2875**	**-4359**	**-8282**	**-9775**	**-9464**
96	Max.	-60	88	197	408	954	1424	1478	1866	**2589**	**10012**	**10607**
	Min.	-492	-530	-570	-614	-622	-654	-693	-806	-944	-1047	751
101	Max.	-86	29	120	280	589	750	825	1045	**4204**	**2505**	1873
	Min.	-397	-422	-439	-455	-496	-592	-658	-729	-1568	**-2698**	**-2567**
104	Max.	-126	31	225	481	970	1670	1916	2064	**2348**	**2621**	**3101**
	Min.	-783	-849	-902	-961	-1127	-1324	-1547	-1759	-2041	**-2795**	**-4399**
105	Max.	-71	102	319	601	1114	1751	2035	**2262**	**2672**	**3218**	**3747**
	Min.	-863	-966	-1031	-1172	-1519	-1911	-1958	**-2170**	**-2657**	**-8206**	**-8195**
106	Max.	-44	-40	-68	-88	-76	-54	-114	-160	**2227**	**3670**	**2842**
	Min.	-310	-346	-365	-394	-419	-527	-674	-856	-819	-683	-601
111	Max.	212	515	952	1799	**2818**	**9604**	**10432**	**8086**	**3302**	**3273**	**2899**
	Min.	-456	-528	-622	-743	-1113	-1437	-1090	-1133	-1322	-885	-505
113	Max.	-5	187	436	807	1522	**2199**	**2570**	**5949**	**4300**	**3661**	**2935**
	Min.	-766	-857	-920	-1011	-1204	-1679	-2041	**-2291**	**-2332**	**-2371**	-1916
114	Max.	9	166	378	751	1491	**2481**	**5151**	**7520**	**12393**	**10843**	**5462**
	Min.	-826	-969	-1084	-1304	-1864	**-2890**	**-5499**	**-7669**	**-8557**	**-7498**	**-3064**
115	Max.	266	605	988	1575	**2733**	**12478**	**13297**	**19536**	**17899**	**3866**	**3210**
	Min.	-391	-448	-521	-606	-711	-595	2036	**2593**	1387	1507	1781
119	Max.	511	865	1128	1697	**3238**	**12862**	**7201**	**6501**	**6513**	**6591**	**5652**
	Min.	-559	-654	-759	-866	-1130	-1009	-339	-1951	**-3125**	**-4058**	**-5848**
121	Max.	-71	-60	-80	-85	-98	-22	73	170	275	349	235
	Min.	-101	-106	-122	-153	-210	-313	-340	-371	-417	-461	-518
122	Max.	-136	78	289	675	1514	**2250**	**2540**	**2744**	**3904**	**9174**	**9177**
	Min.	-670	-699	-730	-760	-876	-900	-1022	-1207	-1396	-1238	-88
123	Max.	-36	-25	-24	-18	24	257	318	310	381	501	384
	Min.	-75	-76	-74	-74	-129	-204	-227	-241	-238	-225	-231
125	Max.	118	445	774	1179	1908	**9124**	**12304**	**11524**	**11616**	**5548**	**4581**
	Min.	-600	-598	-585	-599	-635	-697	**2344**	**2753**	**2443**	1137	1052
130	Max.	-43	41	198	449	1141	1306	1586	1810	2109	**2262**	**2330**
	Min.	-370	-474	-476	-436	-419	-376	-419	-523	-666	-731	-710
145	Max.	-195	-57	41	302	962	1605	1666	2019	**2751**	**9691**	**9435**
	Min.	-994	-1076	-1147	-1203	-1316	-1515	-1545	-1522	-1722	-1846	-973
146	Max.	222	593	975	1473	**2334**	**8433**	1566	275	108	219	83
	Min.	-843	-953	-1063	-1257	-1627	-2119	**-3285**	**-4413**	**-4899**	**-5818**	**-6951**

Table 4-15 LFCD2, Maximum and Minimum Measured Strains for Columns Longitudinal Reinforcement (Cont'd)

Gauge No.		Times Sylmar										
		0.15	0.25	0.5	0.75	1	1.25	1.5	1.75	2	2.125	1.75-2
149	Max.	-28	222	783	1213	**2155**	**2876**	**4032**	**9320**	**11070**	**9305**	**7546**
	Min.	-707	-790	-838	-992	-1366	-1996	**-2459**	**-4053**	**-5219**	**-3726**	**-3076**
150	Max.	57	327	553	975	**2655**	**10032**	**11693**	**16948**	**23007**	**7443**	**5626**
	Min.	-560	-562	-530	-532	-501	-308	**2541**	**3887**	**5112**	**3731**	**3575**
Max.		660	1233	1594	**2301**	**10819**	**12862**	**13297**	**19536**	**23007**	**13226**	**13344**
Min.		-1243	-1400	-1495	-1693	**-2146**	**-4001**	**-5499**	**-7669**	**-8557**	**-9775**	**-9464**
									Max.=	**23007**	Min.=	**-9775**

Table 4-16 LFCD2, Maximum and Minimum Measured Strains for Columns Spirals

Gauge No.		Times Sylmar										
		0.15	0.25	0.5	0.75	1	1.25	1.5	1.75	2	2.125	1.75-2
48	Max.	24	32	46	54	69	75	91	101	103	100	83
	Min.	-4	0	7	9	16	27	45	53	56	11	-20
53	Max.	-18	-10	-4	-2	13	30	41	24	-2	-39	-74
	Min.	-45	-39	-39	-39	-34	-20	-16	-39	-99	-141	-166
57	Max.	-59	-52	-50	-51	-39	-13	7	-4	-40	-84	-79
	Min.	-73	-69	-66	-66	-63	-56	-27	-59	-135	-203	-224
61	Max.	-64	-22	50	124	117	-5	-211	-455	-801	-1195	-1846
	Min.	-153	-150	-144	-125	-148	-486	-1062	**-2484**	**-3388**	**-5148**	**-6586**
65	Max.	-87	-60	-64	-53	-49	-43	-96	-142	-167	-184	-202
	Min.	-117	-94	-86	-108	-120	-201	-288	-448	-486	-517	-505
75	Max.	-31	-29	-6	-36	-157	93	158	354	466	-70	-293
	Min.	-65	-46	-42	-173	-386	-447	-499	-470	-916	**-3071**	**-4354**
77	Max.	18	23	46	26	26	108	158	134	131	-56	-91
	Min.	-168	-190	-190	-212	-232	-267	-330	-361	-472	-510	-603
79	Max.	-65	-40	-38	21	79	622	747	862	984	958	929
	Min.	-98	-73	-71	-76	-103	-120	-91	-156	-303	-649	-762
93	Max.	-65	-60	-55	-47	-23	8	49	51	22	-5	-202
	Min.	-79	-75	-77	-78	-76	-61	-47	-57	-80	-446	**-3495**
97	Max.	-50	-37	-19	-4	32	73	73	66	55	79	79
	Min.	-99	-93	-86	-86	-78	-55	-31	-25	-56	-135	-164
103	Max.	-55	-46	-44	-44	-49	-74	-132	-270	-254	-296	-296
	Min.	-99	-103	-104	-107	-130	-175	-411	-559	-759	-1433	-1526
107	Max.	-71	-72	-63	-45	1	44	45	13	-20	-39	-3
	Min.	-88	-87	-87	-84	-78	-63	-35	-96	-173	-284	-303
112	Max.	27	42	56	122	116	32	12	-29	186	342	408
	Min.	-8	-3	10	29	-2	-167	-241	-274	-270	-268	-203
116	Max.	14	19	28	52	141	379	197	186	327	456	459
	Min.	-30	-41	-54	-57	-49	5	2	-21	-27	-15	-4
124	Max.	214	409	567	968	1726	**2119**	**2275**	**2469**	**2612**	**6659**	**8229**
	Min.	-264	-297	-341	-381	-605	-851	-975	-1231	-1560	-1744	-1565

Table 4-16 LFCD2, Maximum and Minimum Measured Strains for Columns Spirals (Contd.)

Gauge No.		Times Sylmar										
		0.15	0.25	0.5	0.75	1	1.25	1.5	1.75	2	2.125	1.75-2
126	Max.	335	775	1205	1721	**2879**	**9095**	1071	44	110	519	623
	Min.	-1126	-1271	-1372	-1559	**-2141**	**-2946**	**-4313**	**-3323**	**-3735**	**-4507**	**-6676**
129	Max.	-49	-45	-47	-43	-60	-88	-144	-199	-227	-240	-242
	Min.	-70	-78	-87	-112	-257	-358	-405	-445	-463	-479	-483
131	Max.	-52	-51	-60	-77	-103	-171	-286	-329	-344	-467	-928
	Min.	-72	-75	-110	-179	-304	-508	-575	-667	-873	-1322	-1400
151	Max.	-209	-212	-199	-221	-178	-88	-69	-116	12	199	78
	Min.	-269	-285	-314	-338	-360	-380	-386	-423	-471	-555	-771
Max.		335	775	1205	1721	**2879**	**9095**	**2275**	**2469**	**2612**	**6659**	**8229**
Min.		-1126	-1271	-1372	-1559	**-2141**	**-2946**	**-4313**	**-3323**	**-3735**	**-5148**	**-6676**
									Max.=	**9095**	Min.=	**-6676**

Table 4-17 LFCD2, Maximum and Minimum Measured Strains for Flare Longitudinal Reinforcement

Gauge No.		Times Sylmar										
		0.15	0.25	0.5	0.75	1	1.25	1.5	1.75	2	2.125	1.75-2
49	Max.	177	407	493	792	1571	1437	636	567	992	1918	1804
	Min.	-1334	-1505	-1671	-1819	-2359	-2403	-2344	-2290	-2354	-2451	-1959
50	Max.	835	1234	1396	1526	1409	283	-1410	-2337	**-3349**	**-5998**	**-10158**
	Min.	-376	-478	-605	-844	-2319	**-5732**	**-6011**	**-7395**	**-11259**	**-15464**	**-14960**
58	Max.	214	440	487	650	932	1089	549	475	979	654	-29
	Min.	-1214	-1413	-1590	-1805	-2207	**-3197**	**-3797**	**-3781**	**-3967**	**-4112**	**-3046**
98	Max.	186	308	179	60	128	202	50	365	1468	**11285**	131
	Min.	-753	-937	-1104	-1307	-1703	-2284	**-2504**	**-2469**	**-2987**	**-8055**	**-7977**
100	Max.	8	126	25	-287	-730	-1482	-1693	-1758	**-3170**	-1260	**-16732**
	Min.	-1203	-1363	-1462	-1760	**-7103**	**-10776**	**-11284**	**-11389**	**-13313**	**-23636**	**-20832**
110	Max.	-48	-50	-59	-55	108	530	814	1004	1214	1207	1187
	Min.	-284	-347	-361	-432	-560	-707	-594	-961	-955	133	495
117	Max.	-246	-243	-142	762	1866	1867	1845	2024	**3469**	**5204**	**2811**
	Min.	-432	-476	-531	-504	-350	-186	-15	208	**-17724**	**-17945**	**-9119**
148	Max.	-210	-28	136	305	304	-136	-1755	-1931	-1975	-2131	**-4736**
	Min.	-1463	-1651	-1773	-2024	**-2845**	**-4898**	**-4078**	**-4303**	**-8064**	**-14380**	**-11496**
152	Max.	59	184	310	361	964	1837	1341	1342	1552	1940	**2612**
	Min.	-1263	-1418	-1541	-1741	-1991	-2115	-1832	-1388	**-2709**	**-6503**	**-7508**
Max.		835	1234	1396	1526	1866	1867	1845	2024	**3469**	**11285**	**2811**
Min.		-1463	-1651	-1773	-2024	**-7103**	**-10776**	**-11284**	**-11389**	**-17724**	**-23636**	**-20832**
									Max.=	**11285**	Min.=	**-23636**

Table 4-18 LFCD2, Maximum and Minimum Measured Strains for Flare hoops

Gauge No.		Times Sylmar										
		0.15	**0.25**	**0.5**	**0.75**	**1**	**1.25**	**1.5**	**1.75**	**2**	**2.125**	**1.75-2**
44	Max.	14	26	39	41	48	50	57	49	32	-1	-69
	Min.	-37	-35	-31	-20	-14	-21	-30	-43	-62	-136	-181
52	Max.	-5	15	35	28	62	95	55	32	40	96	156
	Min.	-26	-20	-15	-22	-23	-20	-33	-86	-110	-131	-153
67	Max.	-81	-56	-76	-90	-178	-195	-295	-751	-1368	-1451	-1547
	Min.	-111	-94	-134	-229	-325	-420	-1035	-2099	**-2812**	**-3327**	**-3313**
92	Max.	-131	-128	-120	-101	-81	-75	-100	-120	-137	-225	-407
	Min.	-153	-151	-152	-143	-145	-183	-287	-390	-495	-617	-610
99	Max.	-60	-46	-38	-26	-12	-19	3	4	23	120	90
	Min.	-78	-69	-71	-76	-72	-65	-60	-61	-52	-31	10
102	Max.	-42	-5	29	50	91	71	56	25	24	190	428
	Min.	-152	-152	-155	-146	-148	-145	-108	-105	-96	-165	-190
109	Max.	-93	-93	-97	-111	-142	-166	-168	-201	-238	-309	-372
	Min.	-127	-131	-145	-167	-208	-229	-229	-337	-592	-927	-1048
118	Max.	-311	-317	-319	-328	-326	-312	-291	-274	-145	-218	-222
	Min.	-335	-339	-344	-358	-363	-366	-358	-360	-342	-349	-354
Max.		14	26	39	50	91	95	57	49	40	190	428
Min.		-335	-339	-344	-358	-363	-420	-1035	-2099	**-2812**	**-3327**	**-3313**
									Max.=	428	Min.=	**-3327**

Table 4-19 LFCD2, Maximum and Minimum Measured Strains for Beam

Gauge No.		Times Sylmar										
		0.15	**0.25**	**0.5**	**0.75**	**1**	**1.25**	**1.5**	**1.75**	**2**	**2.125**	**1.75-2**
80	Max.	-83	-67	-59	-17	276	420	554	777	1113	1322	1386
	Min.	-114	-106	-101	-93	-51	0	147	222	262	283	342
81	Max.	321	486	619	800	1073	1377	1465	1483	1598	1685	1612
	Min.	-215	-274	-296	-353	-421	-519	-475	-497	-607	-612	-560
82	Max.	183	419	608	1000	1870	**2650**	**2802**	**3967**	**15687**	**21517**	**19519**
	Min.	-382	-397	-424	-391	-292	-181	-33	27	454	**7775**	**10113**
83	Max.	-84	-17	57	231	763	1123	1180	1482	**2155**	**4396**	**4551**
	Min.	-197	-185	-186	-157	-68	4	159	215	257	374	1966
85	Max.	246	575	816	1228	2047	**2709**	**2743**	**9796**	**13793**	**8872**	**2845**
	Min.	-354	-348	-321	-257	-173	-101	-28	4	**5754**	**2355**	1981
86	Max.	-110	-88	-52	174	504	959	1101	1247	1769	**2534**	**2606**
	Min.	-161	-156	-163	-171	-117	-55	135	191	251	286	317
87	Max.	213	282	365	529	672	872	910	817	804	769	656
	Min.	-82	-132	-149	-184	-247	-342	-297	-370	-571	-680	-638
133	Max.	592	739	857	1049	1374	1612	1575	1713	1912	2067	2076
	Min.	31	-15	-60	-104	-186	-193	-183	-175	-209	-220	-167
134	Max.	-32	-37	-38	-32	-28	-81	-83	-88	-79	-74	-69
	Min.	-52	-58	-61	-64	-97	-156	-174	-190	-217	-228	-224
135	Max.	-87	-61	-29	47	440	1051	1231	1357	1574	1664	1639
	Min.	-185	-188	-191	-183	-149	-21	142	195	212	256	264
136	Max.	417	529	632	841	1234	1543	1557	1755	2020	2216	2242
	Min.	19	-30	-82	-118	-175	-196	-176	-140	-123	-116	-23
137	Max.	271	625	905	1206	1905	**2812**	**3193**	**3937**	**9358**	**12448**	**11842**
	Min.	-536	-542	-531	-543	-498	-285	-145	-70	387	**4417**	**6951**
138	Max.	-145	-129	-98	18	494	826	855	1009	1238	1409	1377
	Min.	-172	-170	-163	-154	-128	-57	17	47	72	90	106
139	Max.	272	340	405	557	794	1040	1080	1277	1543	1697	1711
	Min.	101	75	46	14	-24	-27	-37	1	29	32	114
140	Max.	-159	-1	146	340	739	1310	1557	1630	1723	1837	1683
	Min.	-338	-325	-317	-308	-298	-286	-275	-312	-298	-281	-256
141	Max.	-29	-27	-36	-27	7	205	332	511	685	869	818
	Min.	-104	-111	-115	-100	-85	-85	-65	-49	-25	60	127
153	Max.	-470	-429	-395	-340	-258	-210	-143	-70	62	195	243
	Min.	-604	-618	-623	-620	-595	-550	-463	-438	-434	-390	-356
Max.		592	739	905	1228	2047	**2812**	**3193**	**9796**	**15687**	**21517**	**19519**
Min.		-604	-618	-623	-620	-595	-550	-475	-497	-607	-680	-638
									Max.=	**21517**	Min.=	-680

Table 4-10 LFCD1, First Yield Occurrence

Gauge No.		Times Sylmar	Remarks
68	Max.	0.75	Column Reinf. at Gap
144	Max.	0.75	Base Dowels
59	Max.	1.00	Flare Reinf.
69	Max.	1.00	Column Reinf. at Gap
72	Max.	1.00	Column Reinf. at Joint
89	Max.	1.00	Base Dowels
95	Min.	1.00	Column Reinf.
100	Min.	1.00	Flare Reinf.
111	Max.	1.00	Column Reinf.
115	Max.	1.00	Column Reinf.
119	Max.	1.00	Column Reinf. at Gap
126	Max.	1.00	Spirals in the Joint
126	Min.	1.00	Spirals in the Joint
146	Max.	1.00	Column Reinf. at Gap
148	Min.	1.00	Flare Reinf.
149	Max.	1.00	Column Reinf.
150	Max.	1.00	Column Reinf. At Gap
43	Max.	1.25	Column Reinf.
50	Min.	1.25	Flare Reinf.
51	Max.	1.25	Column Reinf.
58	Min.	1.25	Flare Reinf.
59	Min.	1.25	Column Reinf.
62	Max.	1.25	Column Reinf.
64	Max.	1.25	Column Reinf.
68	Min.	1.25	Column Reinf. at Gap
71	Max.	1.25	Column Reinf. at Gap
82	Max.	1.25	Beam Bot. Reinf.
85	Max.	1.25	Beam Bot. Reinf.
113	Max.	1.25	Column Reinf.
114	Max.	1.25	Column Reinf.
114	Min.	1.25	Column Reinf.
122	Max.	1.25	Column Reinf. at Gap
124	Max.	1.25	Spirals in the Joint
125	Max.	1.25	Column Reinf. at Joint
137	Max.	1.25	Beam Bot. Reinf.
55	Max.	1.50	Column Reinf.
64	Min.	1.50	Column Reinf.
71	Min.	1.50	Column Reinf. At Gap
98	Min.	1.50	Flare Reinf.
125	Min.	1.50	Column Reinf. at Gap
146	Min.	1.50	Column Reinf. at Gap
149	Min.	1.50	Column Reinf.
150	Min.	1.50	Column Reinf. at Gap

Gauge No.		Times Sylmar	Remarks
51	Min.	1.75	Column Reinf.
54	Max.	1.75	Column Reinf.
61	Min.	1.75	Column Spirals
89	Min.	1.75	Base Dowels
105	Max.	1.75	Column Reinf.
105	Min.	1.75	Column Reinf.
113	Min.	1.75	Column Reinf.
115	Min.	1.75	Column Reinf.
144	Min.	1.75	Base Dowels
43	Min.	2.00	Column Reinf.
46	Max.	2.00	Column Reinf.
46	Min.	2.00	Column Reinf.
50	Max.	2.00	Flare Reinf.
67	Min.	2.00	Flare Hoops
74	Max.	2.00	Column Reinf. at Joint
76	Max.	2.00	Column Reinf. at Joint
83	Max.	2.00	Beam Hoops
85	Min.	2.00	Beam Bot. Reinf.
91	Max.	2.00	Column Reinf.
95	Max.	2.00	Column Reinf.
96	Max.	2.00	Column Reinf.
100	Max.	2.00	Flare Reinf.
101	Max.	2.00	Column Reinf.
104	Max.	2.00	Column Reinf.
106	Max.	2.00	Column Reinf.
108	Max.	2.00	Flare Reinf.
117	Max.	2.00	Flare Reinf.
117	Min.	2.00	Flare Reinf.
119	Min.	2.00	Column Reinf. At Gap
145	Max.	2.00	Column Reinf.
152	Min.	2.00	Flare Reinf.
55	Min.	2.125	Column Reinf.
56	Max.	2.125	Column Reinf.
75	Min.	2.125	Column Spirals in Joint
82	Min.	2.125	Beam Bot. Reinf.
86	Max.	2.125	Beam Hoops
94	Max.	2.125	Column Reinf.
98	Max.	2.125	Flare Reinf.
101	Min.	2.125	Column Reinf.
104	Min.	2.125	Column Reinf.
130	Max.	2.125	Column Reinf. at Joint
137	Min.	2.125	Beam Bot. Reinf.
93	Min.	1.75-2	Column Spirals
148	Max.	1.75-2	Flare Reinf.
152	Max.	1.75-2	Flare Reinf.

Table 4-21 Measured Residual Records for SFCD1

Description	Cap Beam Disp. (in)	East Column Base Hinge Sliding (in)	West Column Base Hinge Sliding (in)	Base Dowels Strain	Column Long. Reinf. Strain	Beam Bottom Reinf. Strain
Permanent Reading	-0.7654	-0.373	-0.105	1224	3309	6561

Table 4-22 Observations recorded for SFCD2

Times Sylmar	Columns	Beam-Column Connection	Base Hinge
0.15	No Damage	No Damage	No Damage
0.25	No Damage	No Damage	No Damage
0.5	No Damage	Start of vertical crack development	No Damage
0.75	Flexural and shear cracks development at the top third of the flare height.	Start of diagonal crack development	No Damage
1.0	Previous cracks extending inside the flare depth forming shear cracks with new flexural crack development at the bottom third of flare height. New shear crack development at the top third.	Significant crack development	No Damage
1.25	New shear crack development within the top two third of the height	Little crack development	No Damage
1.5	New shear crack development within the top two third of the height	Minor crack development	No Damage
1.75	Little shear crack development within the top two thirds of the height	Minor crack development	No Damage
2.0	Very minor crack development	Very minor crack development	No Damage
2.25	Little new cracks were observed	Very minor crack development	No Damage
2.5	Very minor shear crack development. Start of concrete spalling at the top edge of the flare.	Minor crack development	No Damage
2.75	Significant shear crack development along the column height. Increase of spalling concrete	Minor crack development	No Damage
3.0	Significant flexural crack development at the top third of the height and Minor shear crack. Significant concrete spalling at flare's top edge.	Significant increase in crack development	No Damage
3.25	Little flexural crack development. Minor increase of shear cracks. Significant increase in concrete spalling	Significant increase in crack development	No Damage
After bucket removal	Wide shear cracks in the beam		

Table 4-23 Measured Cap Beam Displacement for SFCD2

Runs	0.15	0.25	0.50	0.75	1.00	1.25	1.50	1.75	2.00	2.25	2.50	2.75	3.00	3.25
Max. Disp. mm (in)	1.3 (0.05)	2.5 (0.1)	6.6 (0.26)	10.2 (0.4)	18.5 (0.73)	25.4 (1.0)	25.7 (1.01)	26.7 (1.05)	27.7 (1.09)	28.4 (1.12)	33.3 (1.31)	39.6 (1.56)	46.2 (1.82)	51.1 (2.01)
Max. Force KN (Kips)	71.4 (16.05)	112.5 (25.29)	171.9 (38.64)	221.6 (49.81)	282.0 (63.39)	298.1 (67.03)	287.4 (64.62)	285.7 (64.22)	279.4 (62.82)	270.2 (60.74)	293.6 (66)	324.7 (73)	345.9 (77.76)	347.3 (78.08)
Min. Disp. mm (in)	-1.5 (-0.06)	-2.8 (-0.11)	-8.6 (-0.34)	-16.5 (-0.65)	-28.2 (-1.11)	-42.4 (-1.67)	-42.4 (-1.67)	-46.5 (-1.83)	-50.5 (-1.99)	-56.6 (-2.23)	-64.5 (-2.54)	-74.2 (-2.92)	-85.6 (-3.37)	-97.8 (-3.85)
Min. Force KN (Kips)	-70.3 (-15.8)	-115.2 (-25.9)	-209.9 (-47.2)	-258.9 (-58.2)	-315.4 (-70.9)	-341.2 (-76.7)	-316.3 (-71.1)	-330.9 (-74.4)	-344.3 (-77.4)	-357.6 (-80.4)	-372.3 (-83.7)	-391.9 (-88.1)	-417.7 (-93.9)	-433.2 (-97.4)
Permanent Disp. mm (in)	0.0 (0)	0.3 (0.01)	0.0 (0)	-0.5 (-0.02)	-1.0 (-0.04)	-2.0 (-0.08)	-2.5 (-0.1)	-2.8 (-0.11)	-3.8 (-0.15)	-5.3 (-0.21)	-6.4 (-0.25)	-7.4 (-0.29)	-8.9 (-0.35)	-11.4 (-0.45)
Max. Net Disp. mm (in)	1.3 0.05	2.5 0.1	6.4 0.25	10.2 0.4	19.1 0.75	26.4 1.04	27.7 1.09	29.2 1.15	30.5 1.2	32.3 1.27	38.6 1.52	46.0 1.81	53.6 2.11	59.9 2.36
Min. Net Disp. mm (in)	-1.5 -0.06	-2.8 -0.11	-8.9 -0.35	-16.5 -0.65	-27.7 -1.09	-41.4 -1.63	-40.4 -1.59	-43.9 -1.73	-47.8 -1.88	-52.8 -2.08	-59.2 -2.33	-67.8 -2.67	-78.2 -3.08	-88.9 -3.5
Dynamic Properties														
Chord Stiffness KN/mm (Kips/in)	289.6 (50.7)	243.8 (42.7)	143.1 (25.1)	102.9 (18.0)	72.98 (12.8)	53.83 (9.4)	50.64 (8.9)	48.13 (8.4)	45.53 (8.0)	42.13 (7.4)	38.88 (6.8)	35.96 (6.3)	33.08 (5.8)	29.95 (5.2)
% of Initial Stiffness	100%	84%	49%	36%	25%	19%	17%	17%	16%	15%	13%	12%	11%	10%
T_n (Sec.)	0.19	0.21	0.27	0.32	0.38	0.44	0.45	0.46	0.48	0.50	0.52	0.54	0.56	0.59
f_n (Hz)	5.29	4.86	3.72	3.16	2.66	2.28	2.21	2.16	2.10	2.02	1.94	1.87	1.79	1.70
% of Initial Frequency	100%	92%	70%	60%	50%	43%	42%	41%	40%	38%	37%	35%	34%	32%

Table 4-24 Measured Base Hinge Displacement for SFCD2

Times	Sylmar	0.15	0.25	0.5	0.75	1	1.25	1.5	1.75	2	2.25	2.5	2.75	3	3.25
East Col.	Max. Disp. (in)	0.1 (0.005)	0.2 (0.008)	0.6 (0.023)	1.0 (0.038)	1.7 (0.068)	2.4 (0.096)	2.5 (0.098)	2.6 (0.103)	2.7 (0.106)	2.7 (0.107)	3.2 (0.125)	4.0 (0.157)	4.9 (0.191)	5.5 (0.217)
	Min. Disp. (in)	-0.1 (-0.002)	-0.2 (-0.006)	-0.6 (-0.023)	-1.2 (-0.046)	-2.2 (-0.085)	-3.3 (-0.131)	-3.3 (-0.128)	-3.5 (-0.139)	-3.8 (-0.151)	-4.3 (-0.168)	-4.9 (-0.193)	-5.7 (-0.225)	-6.7 (-0.264)	-7.7 (-0.305)
	Perm. Disp. (in)	0.1 (0.002)	0.1 (0.002)	0.1 (0.003)	0.1 (0.002)	0.1 (0.004)	0.1 (0.004)	0.1 (0.004)	0.2 (0.006)	0.1 0.004	0.1 0.004	0.1 0.005	0.2 0.009	0.4 0.014	0.5 0.02
West Col.	Max. Disp. (in)	0.1 (0.002)	0.2 (0.007)	0.8 (0.033)	1.5 (0.06)	2.5 (0.098)	4.0 (0.157)	4.0 (0.156)	4.3 (0.171)	4.7 (0.186)	5.3 (0.207)	6.1 (0.24)	7.1 (0.28)	8.2 (0.323)	9.3 (0.365)
	Min. Disp. (in)	-0.1 (-0.004)	-0.2 (-0.007)	-0.6 (-0.022)	-0.9 (-0.037)	-1.7 (-0.066)	-2.8 (-0.109)	-2.9 (-0.113)	-3.0 (-0.12)	-3.2 (-0.125)	-3.3 (-0.129)	-3.7 (-0.147)	-4.7 (-0.184)	-5.8 (-0.23)	-7.2 (-0.285)
	Perm. Disp. (in)	0.0 (0)	0.0 (0)	0.0 (0.001)	0.1 (0.002)	0.1 (0.003)	0.1 (0.004)	0.1 (0.004)	0.1 (0.004)	0.1 (0.005)	0.2 (0.008)	0.2 (0.009)	0.1 (0.005)	-0.1 (-0.005)	-0.6 (-0.024)

Table 4-25 SFCD2, Maximum and Minimum Measured Strains for Base Hinge Dowels

Gauge		Times Sylmar													
		0.15	0.25	0.5	0.75	1	1.25	1.5	1.75	2	2.25	2.5	2.75	3	3.25
43	Max.	240	449	555	1621	**3013**	**6112**	**6573**	**6571**	**6719**	**6699**	**7687**	**11718**	**14828**	**15216**
	Min.	-70	-99	**-3006**	-1612	244	572	715	611	643	633	192	917	1036	1405
44	Max.	-264	-86	1387	**4994**	**14970**	**17506**	**4039**	**3878**	**3756**	**3595**	**3694**	**3925**	**4283**	**4063**
	Min.	-395	-427	-471	-486	202	**2287**	1771	1638	1496	1546	1614	-369	**-4007**	**-9448**
103	Max.	55	365	1967	**4767**	**10964**	**7747**	**3745**	**2724**	**2272**	2024	**3310**	**3521**	**4196**	**7252**
	Min.	-320	-342	-409	-410	206	1193	976	754	-353	-1568	-1730	**-3430**	**-7606**	**-7966**
104	Max.	-190	-64	722	1794	**2718**	**8081**	**8397**	**9145**	**9646**	**11075**	**12892**	**14512**	**12350**	**11290**
	Min.	-287	-308	-349	-390	-844	-1074	766	1075	1435	1842	**2171**	**2571**	**2650**	**3198**
Max.		240	449	1967	**4994**	**14970**	**17506**	**8397**	**9145**	**9646**	**11075**	**12892**	**14512**	**14828**	**15216**
Min.		-395	-427	**-3006**	-1612	-844	-1074	715	611	-353	-1568	-1730	**-3430**	**-7606**	**-9448**
												Max.=	**17506**	Min.=	**-9448**

Table 4-26 SFCD2, Maximum and Minimum Measured Strains for Columns Longitudinal Reinforcement

Gauge		Times Sylmar													
		0.15	0.25	0.5	0.75	1	1.25	1.5	1.75	2	2.25	2.5	2.75	3	3.25
46	Max.	90	128	217	274	615	1026	1061	1291	1508	1753	1965	**2168**	**2319**	**2457**
	Min.	15	-36	-90	-157	-224	-189	-157	-156	-152	-140	-159	-182	-197	-217
50	Max.	-98	-55	-5	65	703	897	957	992	1019	1008	1037	1176	1258	1309
	Min.	-174	-202	-301	-343	-373	-446	-417	-448	-475	-508	-549	-569	-589	-594
51	Max.	-102	7	115	242	1258	1538	1607	1654	1669	1654	1716	1980	**2165**	**2217**
	Min.	-277	-350	-570	-631	-682	-733	-636	-652	-668	-701	-733	-760	-786	-796
52	Max.	16	40	133	163	497	831	879	1063	1240	1419	1590	1741	1846	1973
	Min.	-19	-41	-67	-98	-88	-45	-41	-54	-53	-43	-39	-44	-49	-58
57	Max.	54	102	904	1437	**2235**	**2547**	**2565**	**2723**	**2838**	**2977**	**3102**	**3229**	**3440**	**3913**
	Min.	-56	-90	-139	-232	-331	-413	-420	-440	-448	-446	-496	-553	-566	-493
60	Max.	-20	31	122	859	1799	2025	2051	2081	2104	2106	**2193**	**2418**	**2593**	**2694**
	Min.	-163	-210	-376	-420	-432	-541	-626	-677	-702	-722	-728	-722	-764	-793
61	Max.	-20	66	182	1029	2070	**2414**	**2492**	**2539**	**2560**	**2544**	**2642**	**2889**	**3030**	**3119**
	Min.	-244	-327	-594	-672	-806	-898	-820	-863	-894	-951	-1001	-1013	-1017	-988
62	Max.	-16	14	647	1174	1925	**2175**	2128	**2264**	**2384**	**2521**	**2654**	**2779**	**2904**	**3054**
	Min.	-71	-87	-99	-82	-23	-122	-128	-139	-144	-156	-183	-223	-259	-301
68	Max.	83	156	1025	**2439**	**3251**	**11476**	**11488**	**11772**	**11183**	**11013**	**10641**	**9732**	**8689**	**6468**
	Min.	-92	-142	-190	-412	-669	-723	1125	1531	1892	**2203**	1500	513	-1121	**-3351**
72	Max.	7	86	657	1562	**2847**	**3793**	**4667**	**6333**	**7545**	**7963**	**9412**	**12792**	**16932**	**18500**
	Min.	-228	-282	-415	-534	-584	-821	-896	-894	-704	-402	-136	164	529	1258
74	Max.	25	94	473	1236	**2256**	**2952**	**4063**	**5989**	**7060**	**7528**	**8927**	**12027**	**17457**	**14161**
	Min.	-184	-255	-483	-902	-1297	-1481	-1686	**-2232**	**-2513**	**-2562**	**-2593**	**-2473**	**-2196**	-1946
75	Max.	15	79	954	**2297**	**3134**	**10951**	**11023**	**12190**	**13481**	**15208**	**14246**	**8475**	**8454**	**7504**
	Min.	-103	-119	-125	-83	-300	-302	2132	**2531**	**2828**	**3187**	**3636**	**3016**	**2654**	**2911**
79	Max.	60	255	1324	**3139**	**13418**	**19267**	**7738**	**7296**	**6564**	**5666**	**4302**	**3761**	**3044**	**2378**
	Min.	-141	-170	-178	-148	180	**3607**	**2179**	1316	848	157	-1298	**-3937**	**-8448**	**-11364**
80	Max.	90	609	1976	**2822**	**6252**	**2535**	**2287**	**2274**	**2252**	**2202**	**2291**	**2483**	**2659**	**2748**
	Min.	-496	-625	-1061	-1831	**-2476**	-735	-448	-38	81	-22	63	142	-389	-773
81	Max.	51	295	1127	1756	**3407**	**9956**	**5847**	**4935**	**4852**	**4692**	**4612**	**4764**	**5090**	**5471**
	Min.	-232	-265	-260	-252	-168	3	**3577**	**2675**	1985	1805	1960	1862	1910	1164
82	Max.	78	109	630	1279	1522	1707	1759	1836	1895	1969	2053	**2150**	**2242**	**2328**
	Min.	-27	-63	-95	-133	-310	-489	-561	-635	-694	-755	-849	-957	-1058	-1176
85	Max.	67	286	1125	1741	**2344**	**2673**	**2710**	**2755**	**2772**	**2764**	**2923**	**3267**	**4085**	**5439**
	Min.	-41	-38	-63	-214	-340	-464	-567	-651	-760	-886	-989	-1062	-1150	-1191
87	Max.	32	47	215	321	463	691	698	725	743	763	783	807	845	866
	Min.	19	24	22	23	17	32	45	16	34	39	49	47	43	58

Table 4-26 SFCD2, Maximum and Minimum Measured Strains for Columns Longitudinal Reinforcement (Contd.)

Gauge		Times Sylmar													
		0.15	**0.25**	**0.5**	**0.75**	**1**	**1.25**	**1.5**	**1.75**	**2**	**2.25**	**2.5**	**2.75**	**3**	**3.25**
89	Max.	-151	-128	104	72	570	612	628	642	660	662	683	748	799	849
	Min.	-176	-179	-147	-169	-151	-33	-24	-39	-40	-70	-111	-124	-169	-202
106	Max.	-122	-9	226	845	1521	1916	1823	1999	2135	**2289**	**2467**	**2639**	**2885**	**2996**
	Min.	-319	-362	-469	-526	-614	-610	-517	-506	-497	-472	-480	-510	-570	-663
109	Max.	-30	-29	-17	25	123	252	276	301	335	373	420	510	710	889
	Min.	-56	-70	-101	-113	-114	-100	-87	-92	-87	-95	-95	-94	-103	-123
110	Max.	2	25	74	120	349	532	537	556	582	617	693	854	1159	1330
	Min.	-79	-126	-227	-308	-321	-363	-334	-351	-363	-382	-411	-436	-488	-510
111	Max.	-66	11	230	788	1338	1673	1514	1620	1730	1849	2006	**2153**	**2386**	**2536**
	Min.	-208	-239	-303	-323	-377	-386	-327	-314	-307	-305	-318	-330	-365	-428
118	Max.	-32	-3	171	663	1550	1974	1976	1991	1989	1960	2023	**2185**	**2239**	**2369**
	Min.	-114	-151	-213	-164	-118	-114	-136	-147	-835	-712	-334	-346	-461	-562
119	Max.	67	107	440	824	785	1058	1053	986	980	937	932	1016	909	939
	Min.	-62	-114	-236	-300	-468	-675	-779	-868	-1310	-1136	-1173	-1212	-1446	-1570
121	Max.	47	44	184	257	296	229	-114	-259	-399	-595	-603	-778	-868	-1236
	Min.	35	29	29	62	-73	-730	-1772	**-3009**	**-4307**	**-4666**	**-5419**	**-6488**	**-7306**	**-7925**
124	Max.	40	43	71	68	133	119	-36	-67	-116	-182	-206	-219	-229	-268
	Min.	29	28	25	23	7	-111	-183	-220	-1004	-1006	-444	-383	-497	-530
128	Max.	158	241	1175	1916	**2847**	**3603**	**5899**	**7929**	**8452**	**8987**	**10670**	**13396**	**16398**	**17893**
	Min.	-27	-93	-258	-398	-732	-879	-837	-195	341	460	522	510	266	601
129	Max.	5	112	1309	**2192**	**2650**	**9004**	**9345**	**10555**	**11812**	**13582**	**16043**	**15870**	**15082**	**14659**
	Min.	-205	-261	-325	-386	-895	-924	-222	11	-194	161	789	1282	**2190**	**2368**
131	Max.	19	92	976	1801	**2754**	**3373**	**3763**	**5769**	**6902**	**7377**	**8786**	**11216**	**13721**	**15223**
	Min.	-101	-138	-160	-97	-252	-407	-349	-215	608	884	1347	1466	1668	**2280**
134	Max.	21	27	385	667	848	899	747	619	578	529	533	589	533	667
	Min.	9	11	9	-3	17	29	65	78	-533	-454	-130	-92	-220	-152
136	Max.	36	63	508	893	1227	1484	1507	1576	1616	1691	1865	**2164**	**2402**	**2812**
	Min.	-32	-56	-113	-144	-174	-204	-218	-221	-854	-742	-409	-415	-623	-694
137	Max.	-3	15	353	741	1176	1341	1337	1394	1426	1517	1637	1930	2107	**2490**
	Min.	-90	-133	-156	-196	-252	-293	-261	-269	-920	-783	-315	-286	-477	-657
140	Max.	64	264	1578	**2397**	**2851**	**3315**	**3353**	**3544**	**3743**	**4516**	**6436**	**5597**	2079	2037
	Min.	-14	-39	-64	-63	-219	-381	-412	-447	-1157	-865	-351	-238	52	138
148	Max.	158	639	**2373**	**4010**	**11379**	1714	752	801	841	965	1292	926	1050	1482
	Min.	-265	-364	-692	-990	-1879	**-4596**	**-3759**	**-4041**	**-4749**	**-5305**	**-5929**	**-8207**	**-8295**	**-8070**
151	Max.	92	323	1570	**2745**	**10911**	**14080**	**13291**	**13958**	**5326**	**4118**	**4055**	**4131**	**4531**	**5054**
	Min.	-125	-157	-183	-111	51	**3659**	**3619**	**3814**	1638	1886	1995	**2387**	**2522**	**2848**
Max.		158	639	**2373**	**4010**	**13418**	**19267**	**13291**	**13958**	**13481**	**15208**	**16043**	**15870**	**17457**	**18500**
Min.		-496	-625	-1061	-1831	**-2476**	**-4596**	**-3759**	**-4041**	**-4749**	**-5305**	**-5929**	**-8207**	**-8448**	**-11364**
												Max.=	**19267**	Min.=	**-11364**

Table 4-27 SFCD2, Maximum and Minimum Measured Strains for Columns Spirals

Gauge		Times Sylmar													
		0.15	**0.25**	**0.5**	**0.75**	**1**	**1.25**	**1.5**	**1.75**	**2**	**2.25**	**2.5**	**2.75**	**3**	**3.25**
49	Max.	68	71	67	64	67	141	156	157	140	134	132	135	129	119
	Min.	55	57	51	48	45	51	69	57	56	53	43	33	12	-2
53	Max.	100	103	109	117	211	207	201	190	174	167	156	145	126	98
	Min.	86	86	81	83	80	74	82	74	70	65	25	-21	-68	-92
59	Max.	57	56	91	117	127	110	173	233	278	325	366	420	466	511
	Min.	45	43	41	42	-57	-88	-99	-112	-131	-146	-146	-160	-180	-185
64	Max.	196	199	207	188	274	220	190	182	184	210	205	232	270	322
	Min.	162	179	161	142	122	9	8	-38	-55	-62	-73	-72	-67	-61
71	Max.	69	77	150	372	482	519	440	439	447	406	450	623	711	687
	Min.	36	58	55	87	140	71	31	-11	-40	-105	-105	-148	-249	-322
76	Max.	69	81	104	109	430	519	424	417	442	483	549	601	671	748
	Min.	36	63	56	62	83	113	92	62	83	83	87	88	99	101
83	Max.	60	73	93	103	202	264	281	297	300	302	320	381	408	420
	Min.	35	37	28	-6	-48	-50	-32	-36	-38	-39	-51	-66	-84	-95
86	Max.	54	61	118	109	172	336	377	397	417	443	450	489	525	580
	Min.	42	44	23	-40	-77	-83	-114	-132	-149	-174	-200	-219	-254	-300
91	Max.	106	123	399	559	825	1368	1288	1384	1470	1620	1824	2001	**2233**	**2367**
	Min.	82	79	27	1	7	51	46	36	35	48	78	177	268	362
108	Max.	43	47	47	69	194	222	188	205	232	269	318	369	412	438
	Min.	30	34	33	29	38	62	73	92	86	80	74	71	60	56
112	Max.	40	39	39	37	36	41	43	46	31	-10	-10	2	-11	60
	Min.	29	26	23	22	21	21	24	13	-742	-790	-110	-141	-209	-245
117	Max.	783	782	800	867	921	916	904	914	894	843	829	848	839	878
	Min.	767	764	775	782	804	793	819	836	76	21	684	681	613	529
122	Max.	297	297	311	275	217	82	-72	-105	-122	-305	-287	-264	-325	-275
	Min.	281	277	244	69	-80	-740	-759	-813	-1590	-1231	-1055	-1010	-1267	-1383
126	Max.	-26	10	831	1493	1994	**2202**	**2115**	**2222**	**2292**	**2348**	**2411**	**2576**	**2636**	**3286**
	Min.	-141	-174	-211	-220	-314	-400	-412	-430	-1125	-1029	-639	-668	-887	-949
135	Max.	96	98	101	158	277	303	201	161	123	94	40	21	-101	87
	Min.	82	79	79	69	104	73	42	-71	-939	-719	-890	-1603	**-2179**	-1286
152	Max.	149	153	185	103	111	149	185	218	245	337	453	622	734	773
	Min.	117	108	3	-28	-104	-137	-136	-150	-165	-173	-185	-204	-246	-301
153	Max.	83	85	97	85	206	307	407	471	449	478	641	1418	**2260**	**3104**
	Min.	71	71	43	-208	-245	-263	-254	-260	-270	-303	-590	-587	-1199	-1646
Max.		783	782	831	1493	1994	**2202**	2115	**2222**	**2292**	**2348**	**2411**	**2576**	**2636**	**3286**
Min.		-141	-174	-211	-220	-314	-740	-759	-813	-1590	-1231	-1055	-1603	**-2179**	-1646
												Max.=	**3286**	Min.=	**-2179**

Table 4-28 SFCD2, Maximum and Minimum Measured Strains for Flare Longitudinal Reinf.

Gauge		Times Sylmar													
		0.15	**0.25**	**0.5**	**0.75**	**1**	**1.25**	**1.5**	**1.75**	**2**	**2.25**	**2.5**	**2.75**	**3**	**3.25**
45	Max.	145	207	323	342	646	1255	1333	1700	2038	2346	**2551**	**2709**	**2821**	**2885**
	Min.	6	-73	-159	-279	-432	-239	-78	-71	-62	-53	-90	-106	-125	-180
54	Max.	983	1151	1290	1431	**2500**	**2700**	**2603**	**2698**	**2699**	**2599**	**2595**	**2797**	**2895**	**2893**
	Min.	728	630	320	233	108	-3	-1	-5	-5	-104	-207	-209	-309	-209
56	Max.	89	155	1421	1636	2095	2184	2120	2219	2256	2287	2305	2315	2305	2240
	Min.	-86	-160	-201	-453	-572	-577	-460	-435	-410	-374	-415	-433	-371	-209
65	Max.	59	203	406	1214	1483	1189	999	955	910	899	886	896	922	880
	Min.	-357	-485	-907	-1021	-1337	-1583	-1429	-1494	-1523	-1482	-1436	-1416	-1460	-1383
67	Max.	-94	-87	-101	1501	1844	1752	1474	1215	1081	1157	1282	1292	1219	1212
	Min.	-192	-241	-299	-302	-290	-206	123	271	433	574	616	642	634	598
77	Max.	60	91	77	33	435	928	1084	1160	1196	1232	1221	1234	1562	1600
	Min.	-29	-130	-501	-345	-355	-521	-420	-687	-634	-741	-865	-725	-143	-1
105	Max.	-239	-9	400	1304	1949	2366	2122	2273	2366	**2493**	**2668**	**2898**	**3324**	**3715**
	Min.	-650	-746	-934	-1052	-1212	-1217	-1143	-1145	-1146	-1138	-1095	-1023	-911	-763
113	Max.	41	104	231	263	551	691	625	631	641	638	708	989	1404	1590
	Min.	-160	-271	-442	-596	-633	-710	-684	-719	-1013	-860	-891	-878	-1059	-1064
115	Max.	39	84	1009	1333	1578	1701	1563	1631	1663	1673	1681	1789	2000	**2574**
	Min.	-100	-150	-238	-452	-590	-554	-469	-430	-880	-685	-416	-465	-565	-492
Max.		983	1151	1421	1636	**2500**	**2700**	**2603**	**2698**	**2699**	**2599**	**2668**	**2898**	**3324**	**3715**
Min.		-650	-746	-934	-1052	-1337	-1583	-1429	-1494	-1523	-1482	-1436	-1416	-1460	-1383
												Max.=	**3715**	Min.=	-1583

Table 4-29 SFCD2, Maximum and Minimum Measured Strains for Flare hoops

Gauge		Times Sylmar													
		0.15	**0.25**	**0.5**	**0.75**	**1**	**1.25**	**1.5**	**1.75**	**2**	**2.25**	**2.5**	**2.75**	**3**	**3.25**
48	Max.	119	120	121	120	120	185	195	221	240	256	268	269	277	284
	Min.	106	108	106	103	102	107	117	115	114	117	119	120	114	104
55	Max.	48	62	57	46	67	41	26	15	11	4	-2	-14	-24	-49
	Min.	8	-2	-40	-52	-73	-111	-104	-118	-145	-175	-207	-244	-280	-319
58	Max.	-184	-181	-117	-182	-166	-10	43	98	116	148	171	196	233	278
	Min.	-208	-205	-225	-247	-276	-256	-211	-189	-205	-194	-196	-205	-202	-187
66	Max.	63	78	103	182	329	216	187	201	230	216	201	287	261	238
	Min.	21	12	-3	-14	-33	-127	-158	-184	-194	-228	-228	-248	-280	-293
69	Max.	61	60	48	59	65	-106	-343	-445	-564	-647	-618	-612	-571	-592
	Min.	47	27	15	17	-140	-711	-837	-937	-1022	-1130	-1222	-1413	-1612	-1824
78	Max.	87	88	62	99	139	6	-349	-404	-457	-506	-591	-757	-630	448
	Min.	51	51	14	21	-37	-468	-631	-695	-754	-848	-1097	-1420	-2008	-2288
107	Max.	121	156	215	200	301	239	196	219	369	423	296	303	-21	-2
	Min.	81	92	78	60	40	-40	-53	-68	-109	-107	-168	-216	-282	-255
114	Max.	30	40	45	58	67	74	71	77	57	20	-8	16	-29	45
	Min.	15	17	15	14	13	13	13	6	-751	-806	-126	-123	-217	-247
116	Max.	31	34	38	35	9	4	-6	-12	-33	-97	-102	-132	-151	-225
	Min.	10	8	-10	-78	-360	-455	-443	-440	-930	-874	-521	-493	-626	-595
123	Max.	91	180	1192	2300	**2980**	**9991**	**10089**	**10849**	**11916**	**13796**	**13134**	**4357**	**2658**	2078
	Min.	-156	-253	-549	-780	-1121	-1194	-917	-838	-1178	-787	-743	-1522	-2208	-999
125	Max.	32	33	37	43	53	85	118	148	128	89	81	93	67	76
	Min.	21	19	16	19	23	26	45	71	-694	-742	-50	-78	-146	-220
130	Max.	57	62	79	91	105	152	-38	-97	-151	-184	-246	-130	-100	137
	Min.	37	36	18	-5	-17	-69	-153	-214	-1002	-1048	-426	-466	-611	-648
Max.		121	180	1192	2300	**2980**	**9991**	**10089**	**10849**	**11916**	**13796**	**13134**	**4357**	**2658**	2078
Min.		-208	-253	-549	-780	-1121	-1194	-917	-937	-1178	-1130	-1222	-1522	-2208	-2288
												Max.=	**13796**	Min.=	-2288

Table 4-30 SFCD2, Maximum and Minimum Measured Strains for Beam

Gauge		Times Sylmar													
		0.15	0.25	0.5	0.75	1	1.25	1.5	1.75	2	2.25	2.5	2.75	3	3.25
92	Max.	6	20	102	722	1054	1257	1265	1403	1590	1786	1964	2116	**2239**	**2385**
	Min.	-11	-8	3	47	134	214	301	341	378	405	419	433	432	434
93	Max.	215	261	493	917	1226	1702	1583	1658	1705	1803	1931	2055	2231	2318
	Min.	157	139	156	191	219	246	332	344	358	386	405	422	415	432
95	Max.	34	87	434	607	1019	1269	1297	1338	1371	1351	1467	1636	1739	1753
	Min.	-20	-30	-29	-23	111	210	276	294	309	311	315	318	316	336
96	Max.	246	407	889	1392	1668	1895	1706	1743	1762	1844	1959	2055	2226	2346
	Min.	141	118	138	159	123	138	171	177	181	198	198	206	202	227
97	Max.	76	291	1107	1761	**2511**	**2881**	**2910**	**2984**	**2992**	**2956**	**3364**	**5913**	**8453**	**8891**
	Min.	-85	-124	-164	-53	130	191	241	267	296	325	382	638	**2680**	**4900**
98	Max.	36	79	383	580	915	1085	1106	1140	1173	1198	1284	1431	1531	1582
	Min.	-2	-10	33	102	144	254	340	372	391	410	437	446	455	477
99	Max.	260	586	1149	1704	2078	2342	2079	2131	2168	2269	2395	**2480**	**2634**	**2737**
	Min.	103	80	91	85	86	121	160	163	161	174	174	177	173	189
100	Max.	84	462	1116	1704	**2251**	**2499**	**2506**	**2535**	**2511**	**2485**	**2686**	**2839**	**2909**	**2881**
	Min.	-76	-130	-234	-213	-150	-57	62	86	120	156	212	209	184	156
101	Max.	117	136	175	170	165	263	236	243	222	235	254	301	269	277
	Min.	87	91	61	16	10	-3	2	9	23	40	37	52	22	51
102	Max.	66	148	179	168	168	168	154	154	156	165	168	172	177	186
	Min.	47	47	75	57	42	25	24	19	17	19	20	18	24	31
133	Max.	24	30	181	346	913	1234	1266	1357	1427	1505	1585	1863	2022	**2404**
	Min.	-15	-33	-39	88	209	375	538	594	-108	136	612	739	716	737
138	Max.	57	277	1056	1694	**2273**	**2801**	**2681**	**2802**	**2858**	**2985**	**3334**	**10298**	**11401**	**14433**
	Min.	-174	-244	-338	-305	-251	-194	-90	-60	-665	-569	-482	-341	**3123**	**3582**
139	Max.	22	173	1307	**2163**	**2870**	**6137**	**6878**	**8998**	**9905**	**10875**	**12813**	**15627**	**18340**	**21872**
	Min.	-109	-156	-185	-35	55	116	2075	**2816**	**4398**	**4365**	**5295**	**6284**	**7889**	**9881**
141	Max.	166	162	162	117	123	200	203	229	233	232	258	388	363	582
	Min.	129	101	90	38	15	15	18	54	-655	-696	-25	-5	-79	-126
144	Max.	46	77	465	1213	1886	**2161**	2043	2116	2117	**2172**	**2243**	**2353**	**2505**	**2772**
	Min.	23	22	36	142	214	188	170	137	104	52	0	-27	-52	26
145	Max.	150	191	235	232	226	215	228	221	223	226	219	220	230	229
	Min.	111	124	128	137	123	123	162	168	173	159	142	127	109	97
146	Max.	230	265	735	1030	1372	1453	1508	1582	1565	1578	1560	1616	1675	1784
	Min.	170	154	106	156	156	173	234	233	227	207	178	150	151	144
149	Max.	370	612	1255	1743	**2439**	**2585**	**2521**	**2525**	**2486**	**2473**	**2453**	**2603**	**2723**	**2909**
	Min.	217	192	144	169	188	235	301	277	263	242	259	315	418	520
150	Max.	311	523	933	1142	1395	1470	1392	1386	1350	1348	1303	1344	1383	1379
	Min.	138	103	101	96	138	180	185	179	181	179	137	177	177	172
Max.		370	612	1307	**2163**	**2870**	**6137**	**6878**	**8998**	**9905**	**10875**	**12813**	**15627**	**18340**	**21872**
Min.		-174	-244	-338	-305	-251	-194	-90	-60	-665	-696	-482	-341	-79	-126
												Max.=	**21872**	Min.=	-696

Table 4-31 SFCD1, First Yield Occurrence

Gauge No.		Times Sylmar	Remarks
43	Min.	0.50	Base Dowel
148	Max.	0.50	Column Reinf. At Gap
44	Max.	0.75	Base Dowel
75	Max.	0.75	Column Reinf.
79	Max.	0.75	Column Reinf. At Gap
80	Max.	0.75	Column Reinf. At Gap
103	Max.	0.75	Base Dowel
129	Max.	0.75	Column Reinf.
139	Max.	0.75	Beam Bot. Reinf.
140	Max.	0.75	Column Reinf. At Joint
151	Max.	0.75	Column Reinf. At Gap
43	Max.	1.00	Base Dowel
54	Max.	1.00	Flare Hoops
57	Max.	1.00	Column Reinf.
72	Max.	1.00	Column Reinf.
74	Max.	1.00	Column Reinf.
80	Min.	1.00	Column Reinf. At Gap
81	Max.	1.00	Column Reinf. At Gap
85	Max.	1.00	Column Reinf. At Joint
97	Max.	1.00	Beam Bot. Reinf.
100	Max.	1.00	Beam Bot. Reinf.
104	Max.	1.00	Base Dowel
123	Max.	1.00	Flare Hoops
128	Max.	1.00	Column Reinf.
131	Max.	1.00	Column Reinf.
138	Max.	1.00	Beam Bot. Reinf.
149	Max.	1.00	Beam Top Reinf.
44	Min.	1.25	Base Dowel
61	Max.	1.25	Column Reinf.
62	Max.	1.25	Column Reinf.
79	Min.	1.25	Column Reinf. At Gap
126	Max.	1.25	Column Spirals

Gauge No.		Times Sylmar	Remarks
144	Max.	1.25	Beam Bot. Reinf.
148	Min.	1.25	Column Reinf. At Gap
151	Min.	1.25	Column Reinf. At Gap
81	Min.	1.50	Column Reinf. At Gap
74	Min.	1.75	Column Reinf.
75	Min.	1.75	Column Reinf.
121	Min.	1.75	Column Reinf.
139	Min.	1.75	Beam Bot. Reinf.
105	Max.	2.25	Flare Reinf.
106	Max.	2.25	Column Reinf.
45	Max.	2.50	Flare Reinf.
60	Max.	2.50	Column Reinf.
104	Min.	2.50	Base Dowel
46	Max.	2.75	Column Spirals
82	Max.	2.75	Column Reinf. At Joint
99	Max.	2.75	Beam Top Reinf.
103	Min.	2.75	Base Dowel
111	Max.	2.75	Column Reinf.
118	Max.	2.75	Column Reinf.
136	Max.	2.75	Column Reinf. At Gap
51	Max.	3.00	Column Reinf.
91	Max.	3.00	Column Spirals At Joint
92	Max.	3.00	Beam Stirrups
97	Min.	3.00	Beam Bot. Reinf.
129	Min.	3.00	Column Reinf.
135	Min.	3.00	Column Spirals At Joint
138	Min.	3.00	Beam Bot. Reinf.
153	Max.	3.00	Column Spirals At Joint
115	Max.	3.25	Flare Reinf.
131	Min.	3.25	Column Reinf.
133	Max.	3.25	Beam Stirrups
137	Max.	3.25	Column Reinf. At Joint

Table 4-32 Ductility Ratios

Runs	LFCD1	LFCD2	SFCD2
Effective Yield Disp. mm (in)	23.4 (0.92)	23.9 (0.94)	10.2 (0.40)
Effective Yield Force KN (Kips)	181.5 (40.8)	184.2 (41.4)	279.3 (62.8)
Min. Disp. mm (in)	165.1 (6.5)	165.1 (6.5)	94 (3.7)
Max. Measured Force KN (Kips)	284.6 (63.98)	268.6 (60.38)	433.2 (97.38)
Ductility Ratio	7.07	6.9	9.1
Disp. at Gap Closure mm (in)	67.3 (2.65)	64.8 (2.55)	42 (1.65)
Ductility Ratio at Gap Closure	2.88	2.71	4.0
Ductility Ratio without Base Hinge Disp.	6.12	6.67	8.5

Table 5-1 Analytical Models Parameters

Specimen	Gap width mm (in)	Base Hinge Diameter mm (in)	Col. Height mm (in)	Beam Span mm (in)	Notes
LFCD1	9.53 (0.375)	203.2 (8)	1626 (64)	2718 (107)	Experimented
LFCD2	9.53 (0.375)	203.2 (8)	1626 (64)	2718 (107)	Experimented
LFCD3	9.53 (0.375)	203.2 (8)	1626 (64)	2718 (107)	No P-Δ effect
LFSS1	9.53 (0.375)	203.2 (8)	1626 (64)	1905 (75)	Short Span
SFCD1	9.53 (0.375)	203.2 (8)	991 (39)	2718 (107)	Experimented
SFCD2	9.53 (0.375)	203.2 (8)	991 (39)	2718 (107)	Experimented
SFCD3	9.53 (0.375)	203.2 (8)	991 (39)	2718 (107)	No P-Δ effect
SFSS1	9.53 (0.375)	203.2 (8)	991 (39)	1905 (75)	Short Span
LFWG0	0 (0)	203.2 (8)	1626 (64)	2718 (107)	No Gap
LFWG1	12.7 (0.5)	203.2 (8)	1626 (64)	2718 (107)	
LFWG2	19.1 (0.75)	203.2 (8)	1626 (64)	2718 (107)	
LFWG3	25.4 (1.00)	203.2 (8)	1626 (64)	2718 (107)	
LWNF1	N/A	203.2 (8)	1626 (64)	2718 (107)	No Flare
SFWG0	0 (0)	203.2 (8)	991 (39)	2718 (107)	No Gap
SFWG1	12.7 (0.5)	203.2 (8)	991 (39)	2718 (107)	
SFWG2	19.1 (0.75)	203.2 (8)	991 (39)	2718 (107)	
SFWG3	25.4 (1.00)	203.2 (8)	991 (39)	2718 (107)	
SWNF1	N/A	203.2 (8)	991 (39)	2718 (107)	No Flare
LFBH1	9.53 (0.375)	0 (0)	1626 (64)	2718 (107)	Frictionless Hinge
LFBH2	9.53 (0.375)	101.6 (4)	1626 (64)	2718 (107)	
LFBH3	9.53 (0.375)	304.8 (12)	1626 (64)	2718 (107)	
SFBH1	9.53 (0.375)	0 (0)	991 (39)	2718 (107)	Frictionless Hinge
SFBH2	9.53 (0.375)	101.6 (4)	991 (39)	2718 (107)	
SFBH3	9.53 (0.375)	304.8 (12)	991 (39)	2718 (107)	

Table 5-2 Analytical and Experimental results for LFCD1

	LFCD1	Measured	% of Measured
Yield force [KN (Kips)]	228.2 (51.3)	210.3 (47.27)	108%
Max. Force [KN (Kips)]	314.4 (70.68)	284.2 (63.9)	N/A
Max. Disp. [mm (in)]	182.9 (7.2)	165.1 (6.5)	N/A
Effective Disp. mm (in)	20.8 (0.82)	23.4 (0.92)	89%
Ductility	8.78	7.07	124%
Disp. at West Flare Gap Closure [mm (in)]	74.9 (2.95)	67.3 (2.65)	111%
Disp. at East Flare Gap Closure [mm (in)]	76.2 (3.0)	N/A	N/A
Disp. at West Base Hinge Gap Closure mm (in)	109.2 (4.3)	N/A	N/A
Disp. at East Base Hinge Gap Closure mm (in)	144.8 (5.7)	N/A	N/A

Table 5-3 Analytical and Experimental results for LFCD2

	LFCD2	Measured	% of Measured
Yield force [KN (Kips)]	220.2 (49.5)	203.3 (45.7)	108.3%
Max. Force [KN (Kips)]	298.0 (67)	268.6 (60.38)	N/A
Max. Disp. [mm (in)]	185.2 (7.29)	165.2 (6.5)	N/A
Effective Disp. mm (in)	24.4 (0.96)	23.9 (0.94)	102%
Ductility	7.59	6.9	110%
Disp. at West Flare Gap Closure [mm (in)]	74.7 (2.94)	64.8 (2.55)	115.3%
Disp. at East Flare Gap Closure [mm (in)]	74.7 (2.94)	N/A	N/A
Disp. at West Base Hinge Gap Closure mm (in)	110.5 (4.35)	N/A	N/A
Disp. at East Base Hinge Gap Closure mm (in)	144.8 (5.7)	N/A	N/A

Table 5-4 Analytical Comparison between LFCD3 and LFCD2

	LFCD3	LFCD2	% of LFCD2
Yield force [KN (Kips)]	246.5 (55.42)	220.2 (49.5)	112.0%
Max. Force [KN (Kips)]	362.5 (81.50)	298 (67)	121.6%
Max. Disp. [mm (in)]	267.7 (10.54)	185.2 (7.29)	144.6%
Effective Disp. mm (in)	26.7 (1.05)	24.4 (0.96)	109.4%
Ductility	10.04	7.59	132.2%
Disp. at West Flare Gap Closure [mm (in)]	71.9 (2.83)	74.7 (2.94)	96.3%
Disp. at East Flare Gap Closure [mm (in)]	86.4 (3.40)	74.7 (2.94)	115.7%
Disp. at West Base Hinge Gap Closure mm (in)	118.4 (4.66)	110.5 (4.35)	107.1%
Disp. at East Base Hinge Gap Closure mm (in)	167.6 (6.60)	144.8 (5.7)	115.8%

Table 5-5 Analytical and Experimental results for SFCD2

	SFCD2	Measured	% of Measured
Yield force [KN (Kips)]	367.9 (82.7)	325.6 (73.2)	113.0%
Max. Force [KN (Kips)]	504.9 (113.5)	445.7 (100.2)	N/A
Max. Disp. [mm (in)]	108 (4.25)	94 (3.7)	N/A
Effective Disp. mm (in)	11.7 (0.46)	10.2 (0.4)	115.0%
Ductility	9.24	9.25	99.9%
Disp. at West Flare Gap Closure [mm (in)]	41.4 (1.63)	41.9 (1.65)	98.8%
Disp. at East Flare Gap Closure [mm (in)]	41.9 (1.65)	N/A	N/A
Disp. at West Base Hinge Gap Closure mm (in)	79.5 (3.13)	N/A	N/A
Disp. at East Base Hinge Gap Closure (in)	89.9 (3.54)	N/A	N/A

Table 5-6 Analytical Comparison between SFCD1 and SFCD2

	SFCD1	SFCD2	% of SFCD2
Yield force [KN (Kips)]	376.3 (84.6)	367.9 (82.7)	102.3%
Max. Force [KN (Kips)]	508.4 (114.3)	504.9 (113.5)	100.7%
Max. Disp. [mm (in)]	(104.1) 4.1	108 (4.25)	96.5%
Effective Disp. mm (in)	11.9 (0.47)	11.7 (0.46)	0.42%
Ductility	8.72	9.24	101.7%
Disp. at West Flare Gap Closure [mm (in)]	41.7 (1.64)	41.4 (1.63)	100.61%
Disp. at East Flare Gap Closure [mm (in)]	41.7 1.64	41.9 (1.65)	99.39%
Disp. at West Base Hinge Gap Closure mm (in)	80.5 (3.17)	79.5 (3.13)	101.28%
Disp. at East Base Hinge Gap Closure mm (in)	88.9 (3.5)	89.9 (3.54)	98.87%

Table 5-7 Analytical Comparison between SFCD3 and SFCD2

	SFCD3	SFCD2	% of SFCD2
Yield force [KN (Kips)]	402.2 (90.44)	367.9 (82.7)	109.4%
Max. Force [KN (Kips)]	(613.9) 138	504.9 (113.5)	121.6%
Max. Disp. [mm (in)]	175.3 (6.9)	108 (4.25)	162.35%
Effective Disp. mm (in)	13.7 (0.54)	(11.6) 0.46	117.39%
Ductility	12.78	9.24	138.30%
Disp. at West Flare Gap Closure [mm (in)]	40.6 (1.60)	41.4 (1.63)	98.16%
Disp. at East Flare Gap Closure [mm (in)]	48.5 (1.91)	41.9 (1.65)	115.76%
Disp. at West Base Hinge Gap Closure mm (in)	86.4 (3.40)	79.5 (3.13)	108.63%
Disp. at East Base Hinge Gap Closure (in)	108.2 (4.26)	89.9 (3.54)	120.34%

Table 5-8 Analytical results for LFWG0 through LWNF1

Specimen	LFCD2	LFWG0	% of LFCD2	LFWG1	% of LFCD2	LFWG2	% of LFCD2	LFWG3	% of LFCD2	LWNF1	% of LFCD2
Yield force KN (Kips)	220.2 (49.5)	317.6 (71.4)	144.2%	221.5 (49.8)	100.6%	215.7 (48.5)	98.%	214.8 (48.3)	97.6%	210.7 (47.36)	95.7%
Max. Force KN (Kips)	298.0 (67)	317.6 (71.4)	106.6%	288.7 (64.9)	96.9%	272.5 (61.27)	91.4%	259.3 (58.3)	87.%	210.7 (47.36)	70.7%
Max. Disp. mm (in)	185.2 (7.29)	148.6 (5.85)	80.2%	177.5 (6.99)	95.9%	198.1 (7.8)	107.%	202.9 (7.99)	109.6%	158.8 (6.25)	85.7%
Effective Disp. mm (in)	24.4 (0.96)	30.5 (1.2)	125.%	29.5 (1.16)	120.8%	26.4 (1.04)	108.3%	20.6 (0.81)	84.4%	24.9 (0.98)	102.1%
Ductility	7.59	4.88	64.2%	6.03	79.4%	7.5	98.8%	9.86	129.9%	6.38	84.%
Disp. at West Flare Gap Closure [mm (in)]	74.7 (2.94)	N/A	N/A	94.0 (3.7)	125.9%	133.1 (5.24)	178.2%	174.2 (6.86)	233.3%	N/A	N/A
Disp. at East Flare Gap Closure [mm (in)]	74.7 (2.94)	N/A	N/A	95.5 (3.76)	127.9%	138.9 (5.47)	186.1%	182.1 (7.17)	243.9%	N/A	N/A
Disp. at West Base Hinge Gap Closure [mm (in)]	110.5 (4.35)	85.1 (3.35)	77.%	116.3 (4.58)	105.3%	139.2 (5.48)	126.%	167.6 (6.6)	151.7%	111.8 (4.4)	101.1%
Disp. at East Base Hinge Gap Closure [mm (in)]	144.8 (5.7)	120.9 (4.76)	83.5%	144.8 (5.7)	100%	144.8 (5.7)	100.%	144.3 (5.68)	99.6%	135.9 (5.35)	93.9%

Table 5-9 Analytical results for SFWG0 through SWNF1

Specimen	SFCD2	SFWG0	% of SFCD2	SFWG1	% of SFCD2	SFWG2	% of SFCD2	SFWG3	% of SFCD2	SWNF1	% of SFCD2
Yield force KN (Kips)	367.8 82.7	459.0 103.2	124.8%	366.1 82.3	99.5%	365.5 82.18	99.4%	362.5 81.5	98.5%	358.8 80.67	97.5%
Max. Force KN (Kips)	504.8 113.5	533.8 120	105.7%	513.3 115.4	101.7%	499.5 112.3	98.9%	476.6 107.14	94.4%	358.8 80.67	71.1%
Max. Disp. mm (in)	108.0 4.25	17.0 0.67	15.8%	138.9 5.47	128.7%	155.7 6.13	144.2%	169.2 6.66	156.7%	71.1 2.8	65.9%
Effective Disp. mm (in)	11.7 0.46	N/A	N/A	10.9 0.43	93.5%	10.4 0.41	89.1%	10.2 0.4	87.%	11.7 0.46	100.%
Ductility	9.24	N/A	N/A	12.72	137.7%	14.9	161.8%	16.65	180.2%	6.09	65.9%
Disp. at West Flare Gap Closure [mm (in)]	41.4 1.63	N/A	N/A	53.3 2.1	N/A	77.7 3.06	N/A	102.4 4.03	N/A	N/A	N/A
Disp. at East Flare Gap Closure [mm (in)]	41.9 1.65	N/A	N/A	55.4 2.18	N/A	78.0 3.07	N/A	108.0 4.25	N/A	N/A	N/A
Disp. at West Base Hinge Gap Closure [mm (in)]	79.5 3.13	N/A	N/A	81.3 3.2	102.2%	82.0 3.23	103.2%	111.8 4.4	140.6%	80.3 3.16	101%
Disp. at East Base Hinge Gap Closure [mm (in)]	89.9 3.54	N/A	N/A	92.2 3.63	102.5%	92.5 3.64	102.8%	108.0 4.25	120.1%	90.4 3.56	100.6%

Table 5-10 Analytical results for LFBH1 through LFBH3

Specimen	LFCD2	LFBH1	% of LFCD2	LFBH2	% of LFCD2	LFBH3	% of LFCD2
Yield force KN (Kips)	220.2 (49.5)	189.0 (42.5)	85.9%	136.1 (30.6)	61.8%	269.3 (60.53)	122.3%
Max. Force KN (Kips)	298 (67)	234.9 (52.8)	78.8%	136.1 (30.6)	45.7%	(388.8) 87.4	130.4%
Max. Disp. mm (in)	(185.2) 7.29	110 (4.33)	59.4%	27.7 (1.09)	15.0%	211.6 (8.33)	114.3%
Effective Disp. mm (in)	24.4 (0.96)	44.5 (1.75)	182.3%	24.6 (0.97)	101.0%	24.8 (0.975)	101.6.3 %
Ductility	7.59	2.47	32.6%	1.12	14.8%	8.54	112.6%
Disp. at West Flare Gap Closure [mm (in)]	74.7 (2.94)	75.7 (2.98)	101.4%	No	N/A	68.3 (2.69)	91.5%
Disp. at East Flare Gap Closure [mm (in)]	74.7 (2.94)	77.2 (3.04)	103.4%	No	N/A	70.6 (2.78)	94.6%
Disp. at West Base Hinge Gap Closure [mm (in)]	110.5 (4.35)	N/A	N/A	28 (1.1)	25.3%	N/A	N/A
Disp. at East Base Hinge Gap Closure [mm (in)]	144.8 (5.7)	N/A	N/A	No	N/A	N/A	N/A

Table 5-11 Analytical results for LFBH1 through LFBH3

Specimen	SFCD2	SFBH1	% of SFCD2	SFBH2	% of SFCD2	SFBH3	% of SFCD2
Yield force KN (Kips)	367.9 (82.7)	309.2 (69.5)	84.0%	No	N/A	482.9 (108.57)	131.3%
Max. Force KN (Kips)	504.9 (113.5)	475.5 (106.89)	94.2%	202.6 (45.55)	40.1%	702.8 (158)	139.2%
Max. Disp. mm (in)	108 (4.25)	95.3 (3.75)	88.2%	10.9 (0.43)	10.1%	154.7 (6.09)	143.3%
Effective Disp. mm (in)	11.7 (0.46)	11.7 (0.46)	100.0%	N/A	N/A	12.2 (0.48)	104.3%
Ductility	9.24	8.15	88.2%	N/A	N/A	12.69	137.3%
Disp. at West Flare Gap Closure [mm (in)]	41.4 (1.63)	37.6 (1.48)	N/A	No	N/A	39.9 (1.57)	N/A
Disp. at East Flare Gap Closure [mm (in)]	41.9 (1.65)	46.2 (1.82)	N/A	No	N/A	46.7 (1.84)	N/A
Disp. at West Base Hinge Gap Closure [mm (in)]	79.5 (3.13)	N/A	N/A	9.9 (0.39)	12.5%	N/A	N/A
Disp. at East Base Hinge Gap Closure [mm (in)]	89.9 (3.54)	N/A	N/A	No	N/A	N/A	N/A

Fig. 1-1 Damage to Columns of the SR 118 Mission-Gothic Undercrossing (1994 Northridge Earthquake)

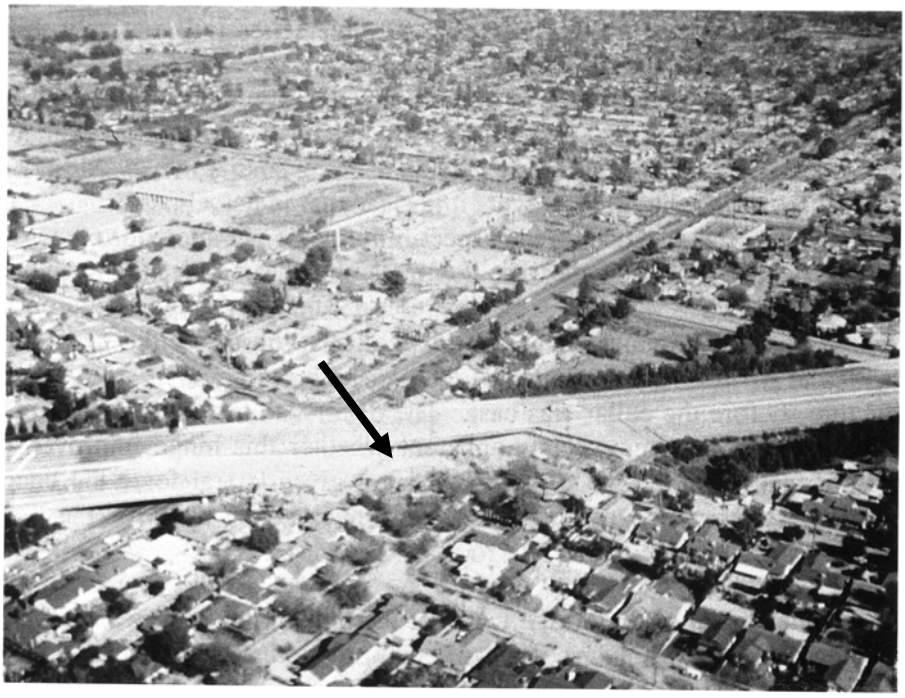

Fig. 1-2 Aerial View of the SR 118 Mission-Gothic Undercrossing Showing Collapsed Eastbound Bridge (1994 Northridge Earthquake)

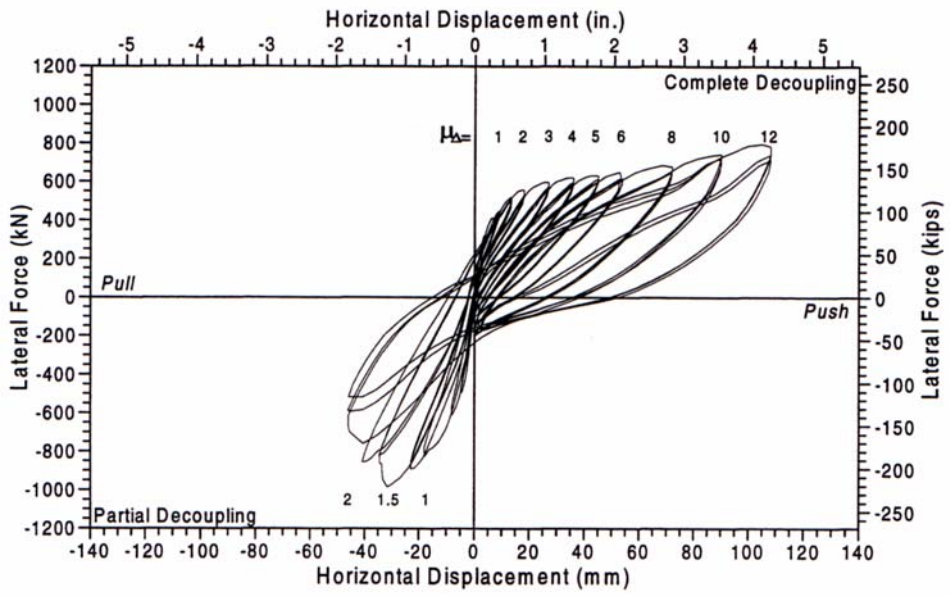

Fig. 1-3 Load-displacement Hysteresis for Test Unit MG-4, 1" Gap Width[3]

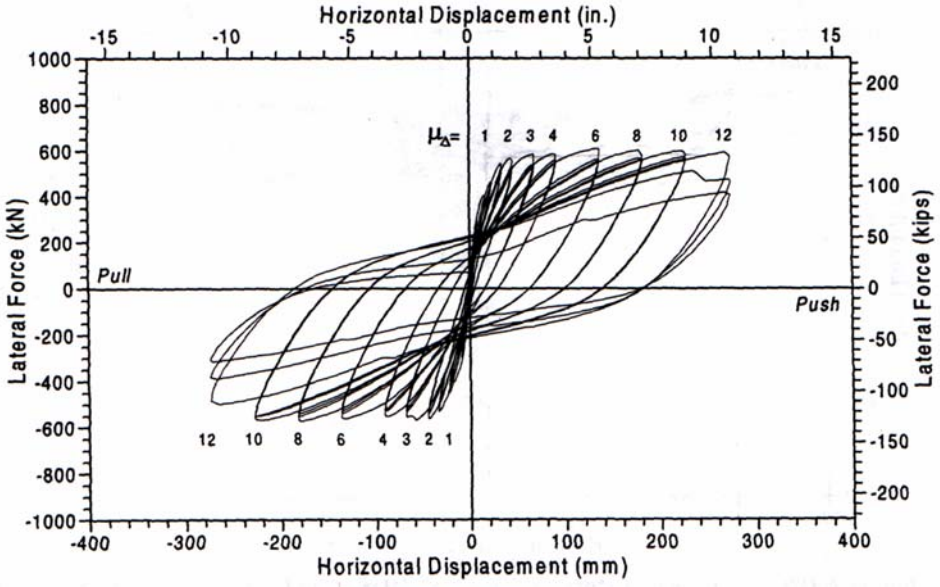

Fig. 1-4 Load-Displacement Hysteresis for Test Unit RDS-4, 2" Gap Width[3]

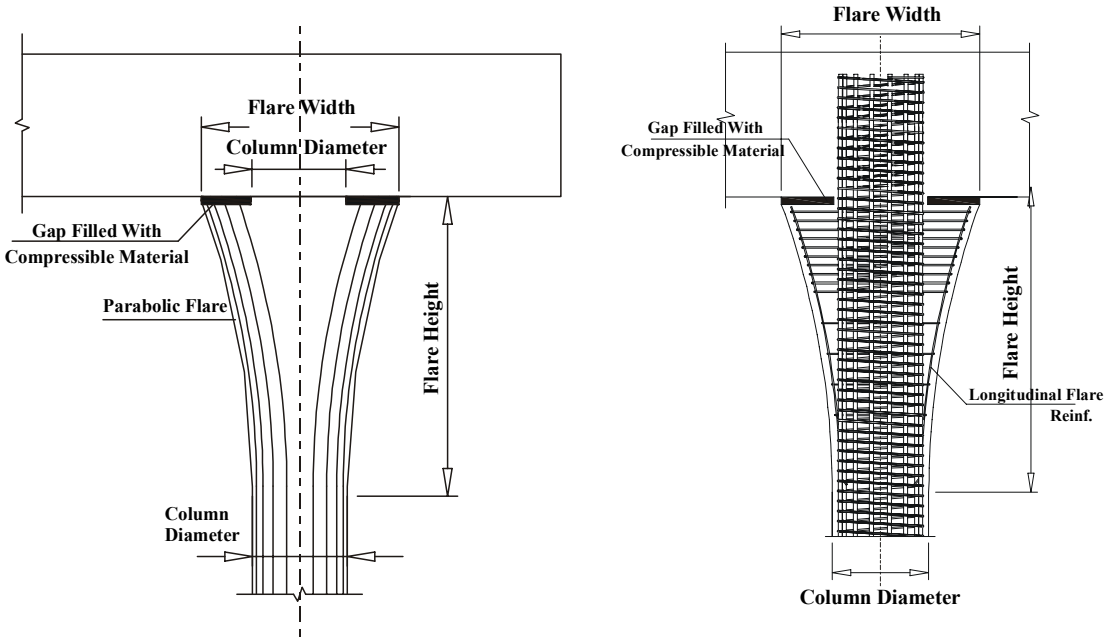

Fig. 2-1 Caltrans Gap Specifications (a) Proposed Detail Layout (b) Reinforcement Detail

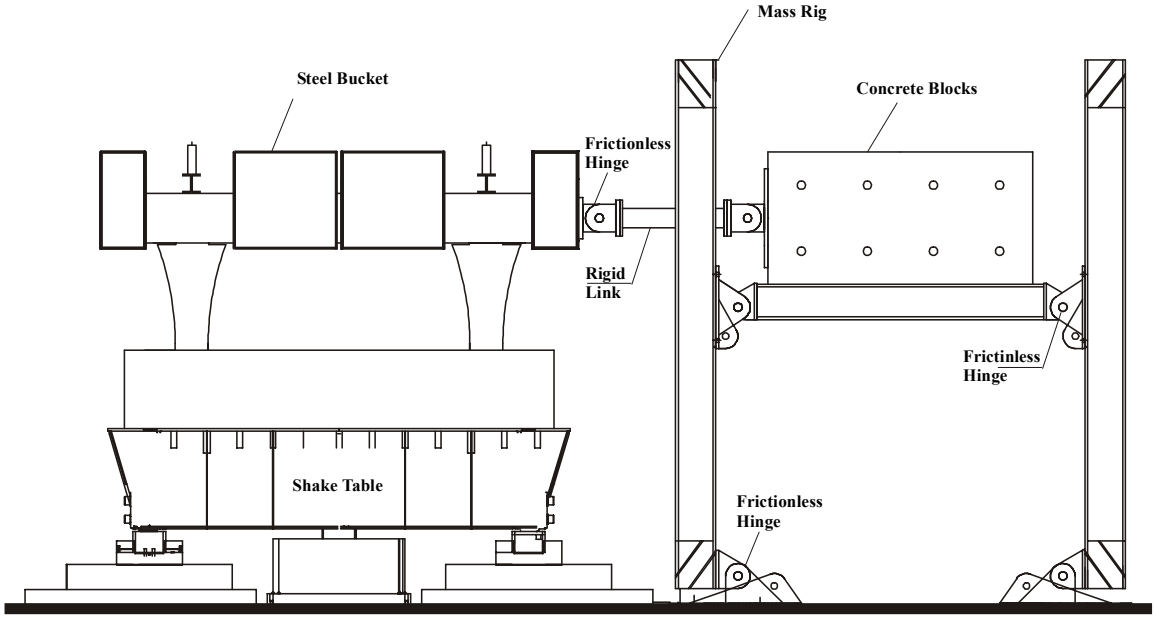

Fig. 2-2 Specimen Setup

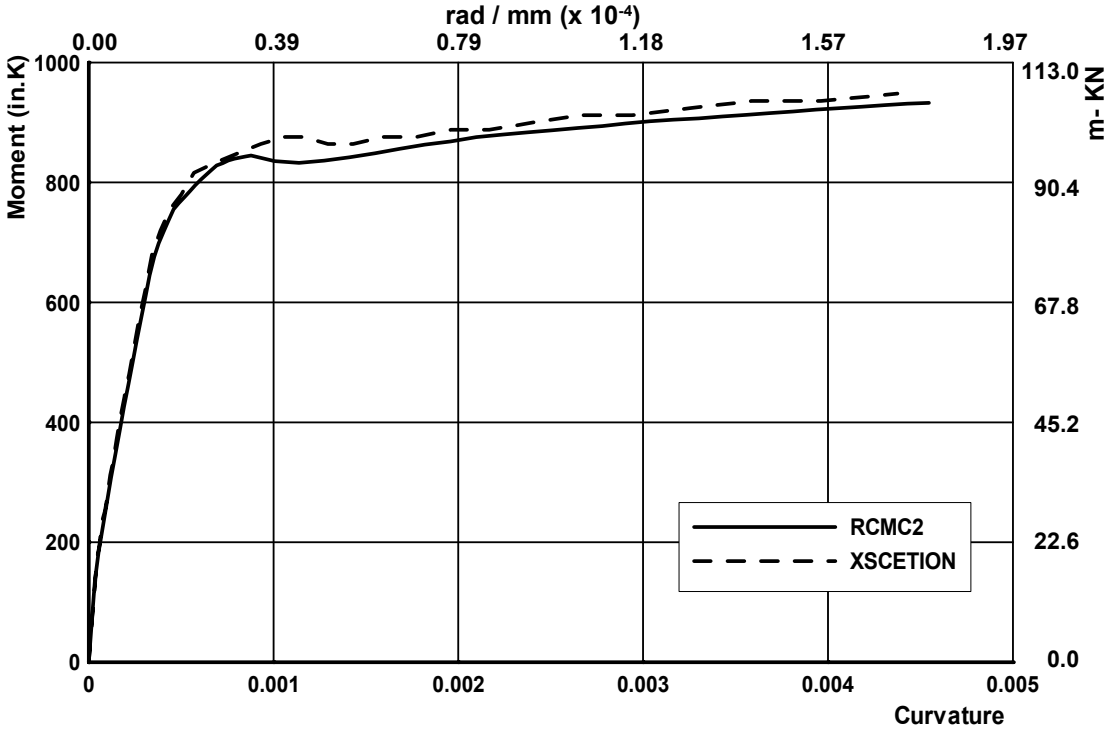

Fig. 2-3 Moment-Curvature Curve for Core Section

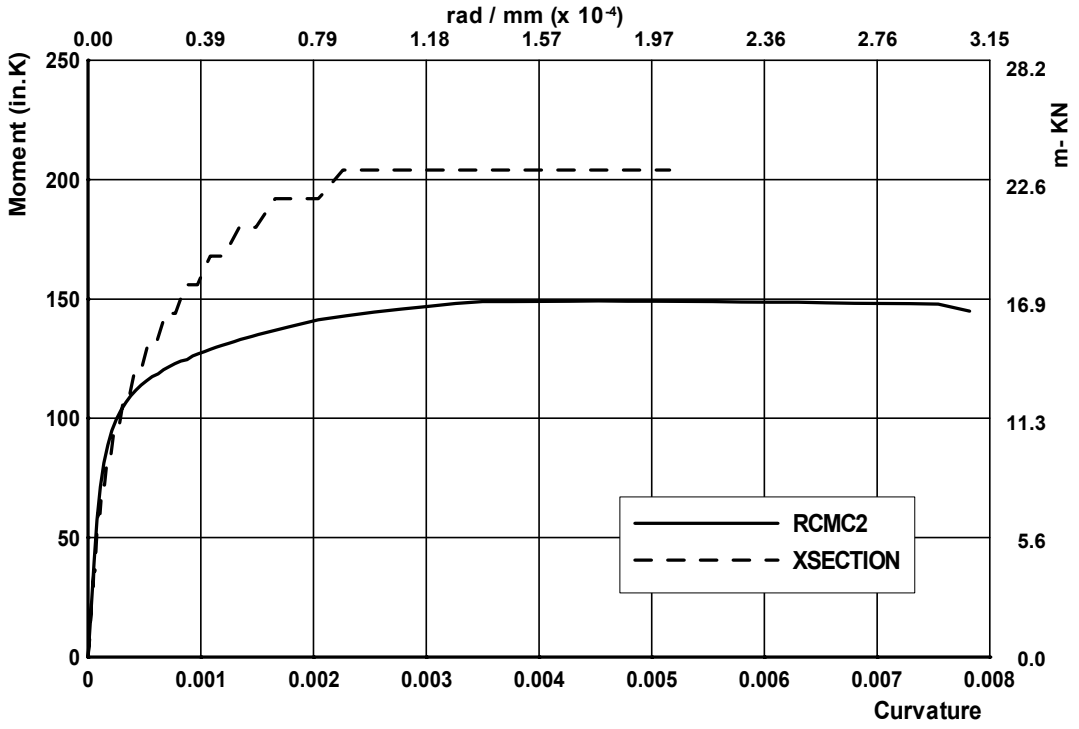

Fig. 2-4 Moment-Curvature Curve for Base Hinge Section

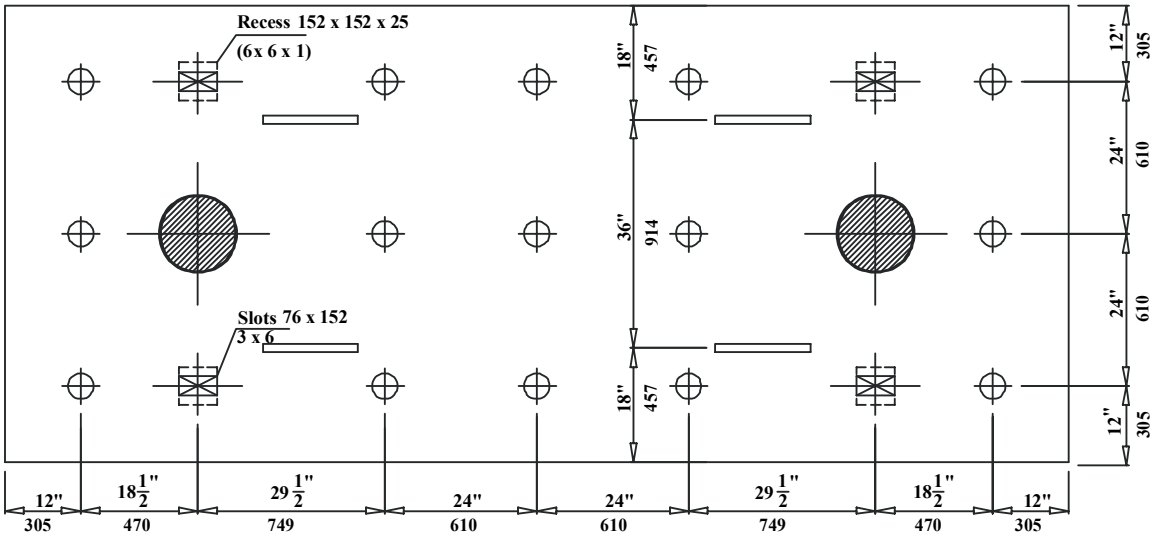

Fig. 2-5 Footing Layout.

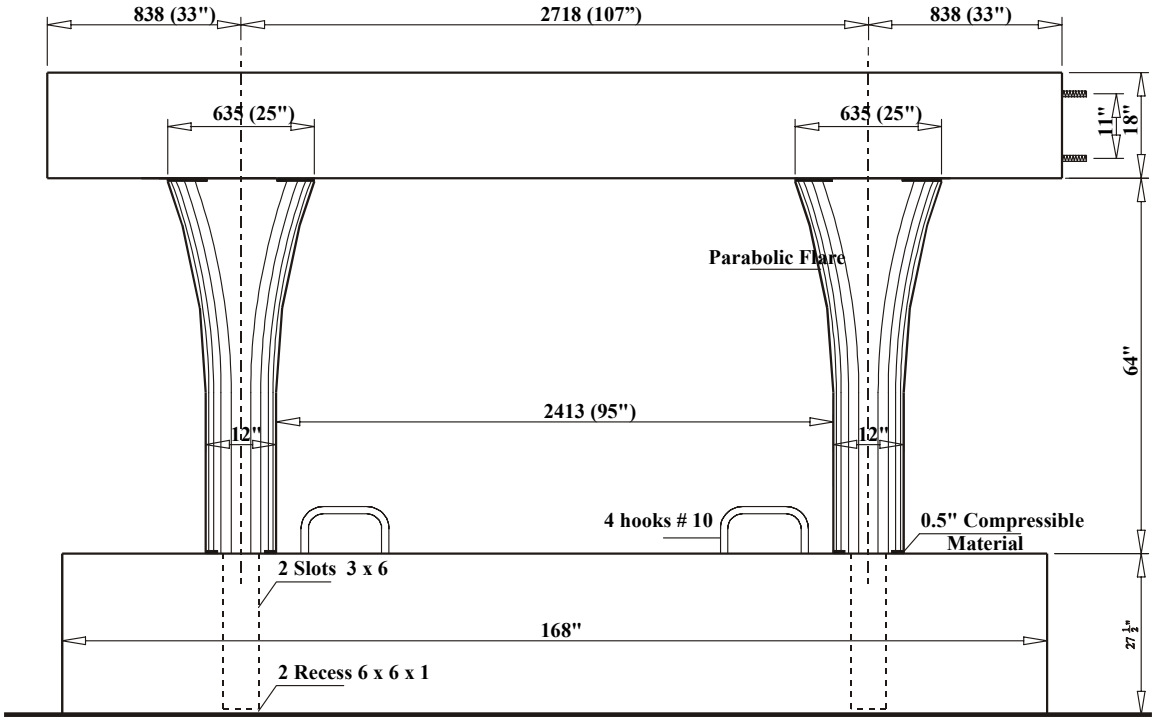

Fig. 2-6 Concrete Layout for LFCD1 and LFCD2.

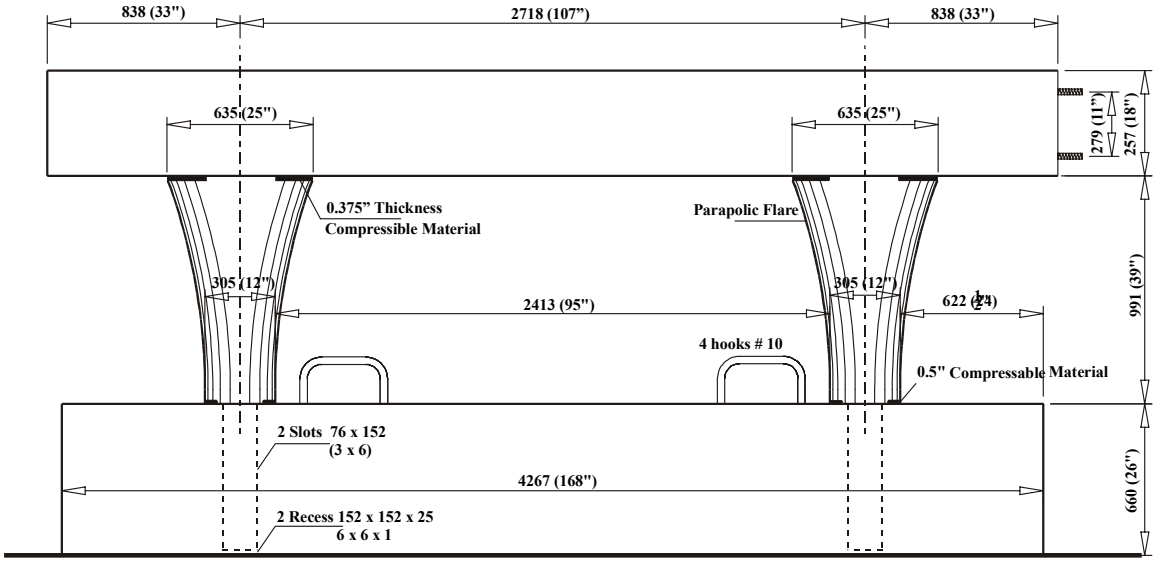

Fig. 2-7 Concrete Layout for SFCD1 and SFCD2.

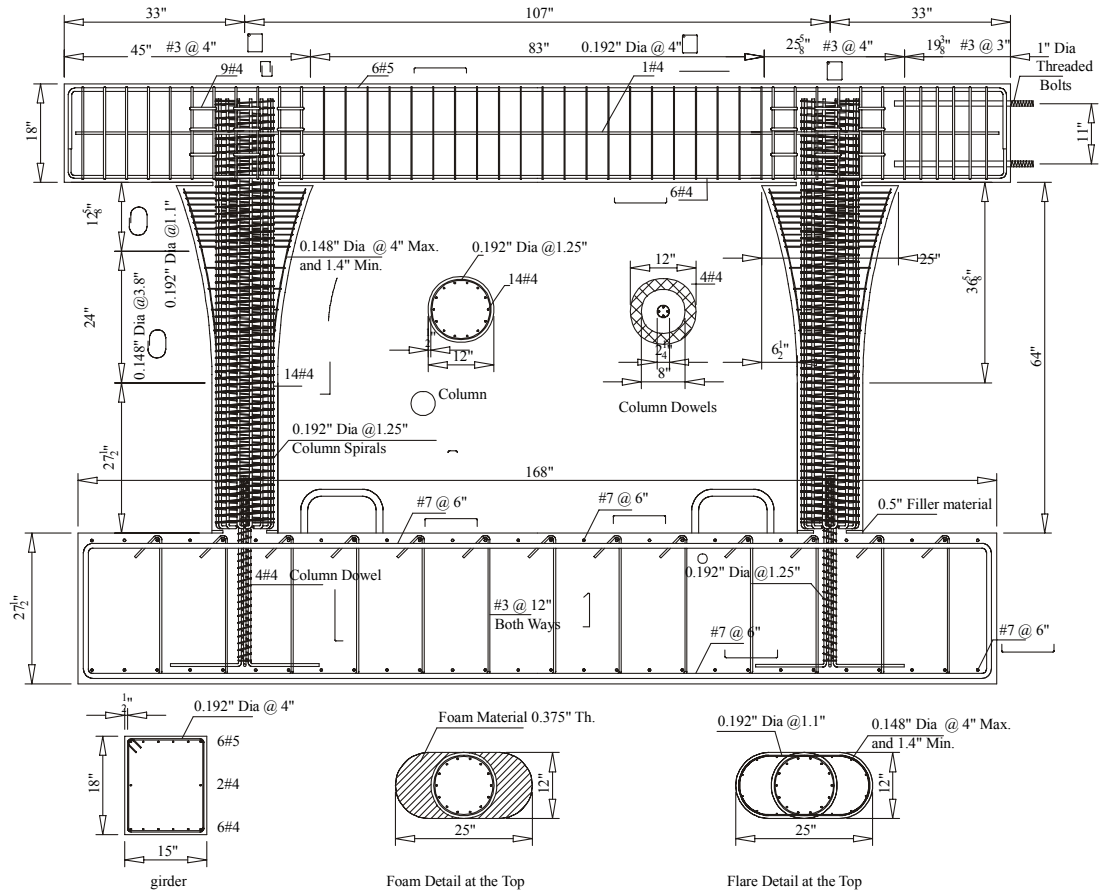

(a)

Fig. 2-8 Reinforcement Detail LFCD1 (a) Dimensions in Inches (b) SI System

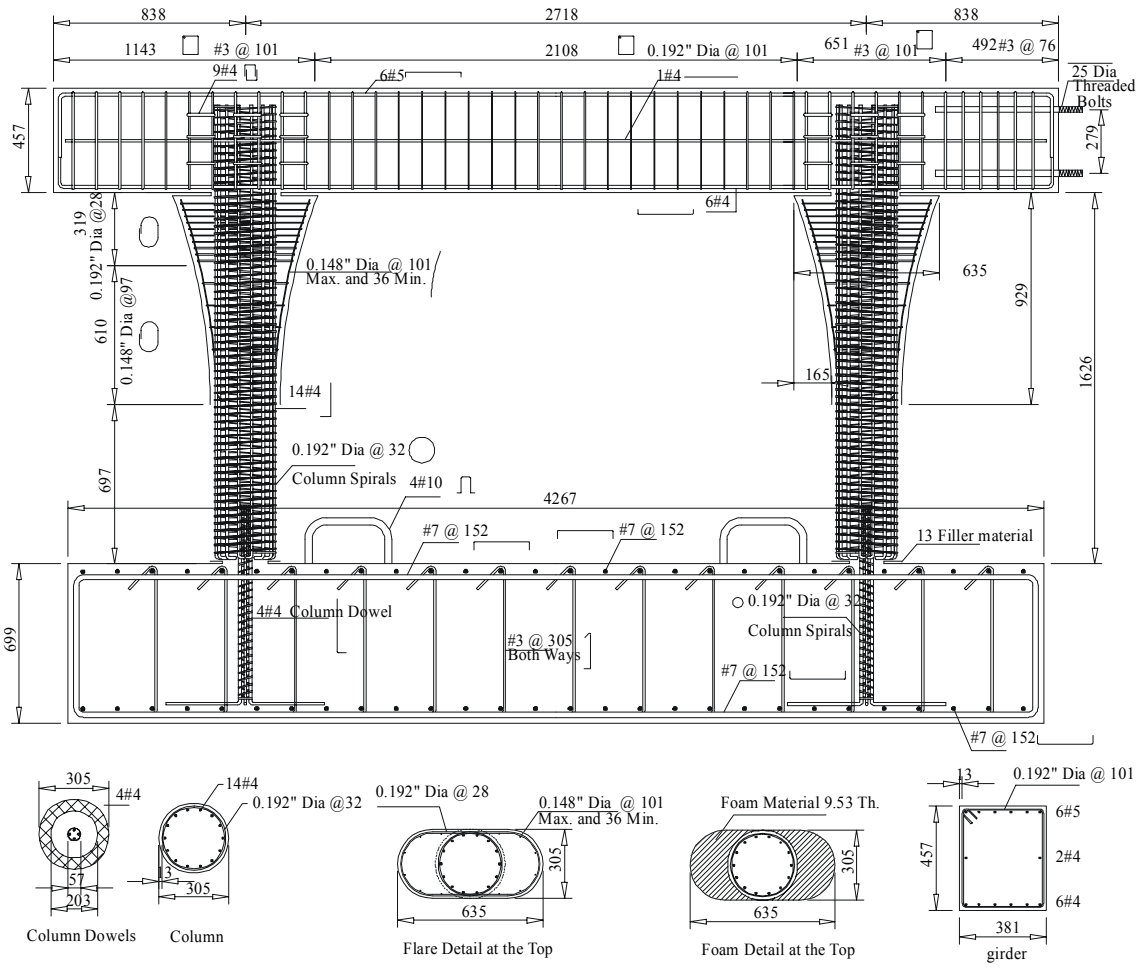

(b)

Fig. 2-8 Reinforcement Detail LFCD1 (a) Dimensions in Inches (b) SI System

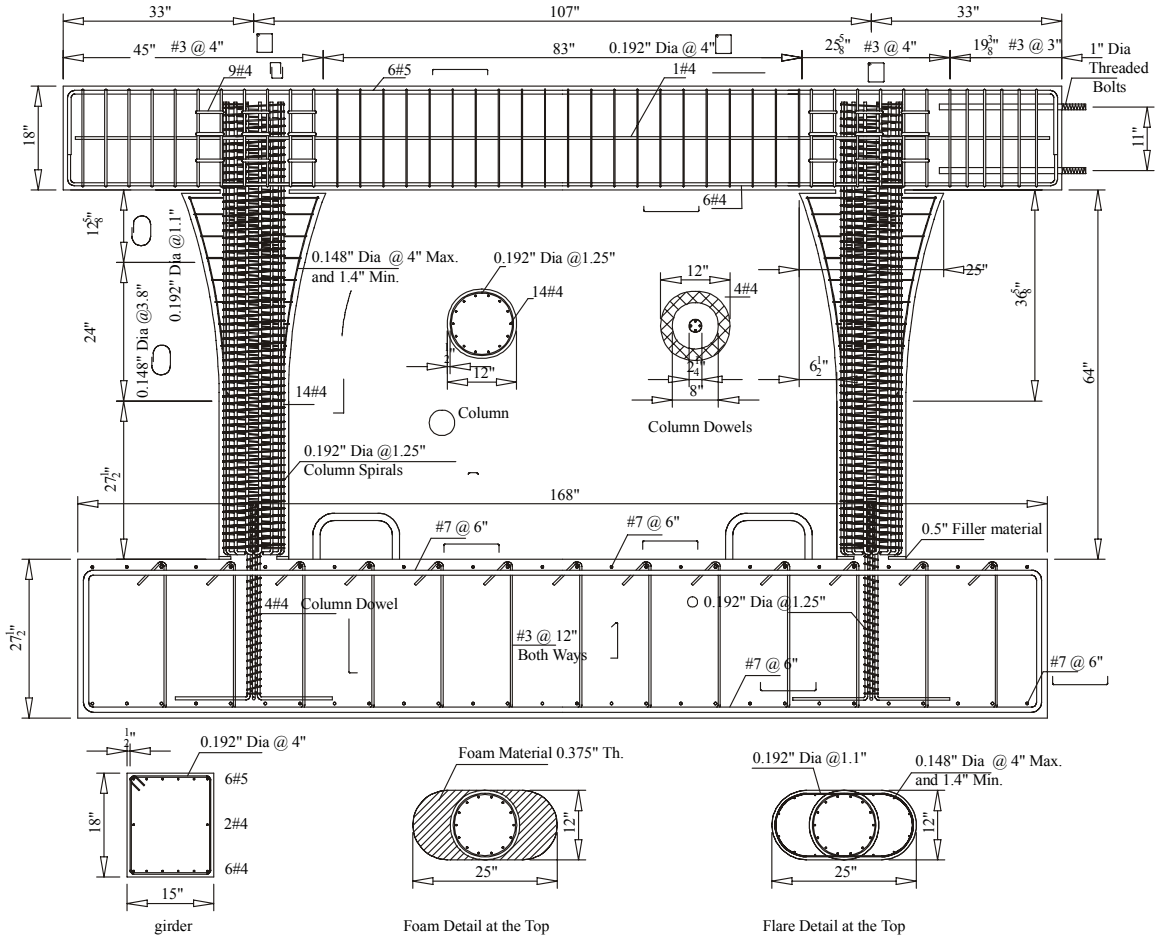

(a)

Fig. 2-9 Reinforcement Detail LFCD2 (a) Dimensions in Inches (b) SI System

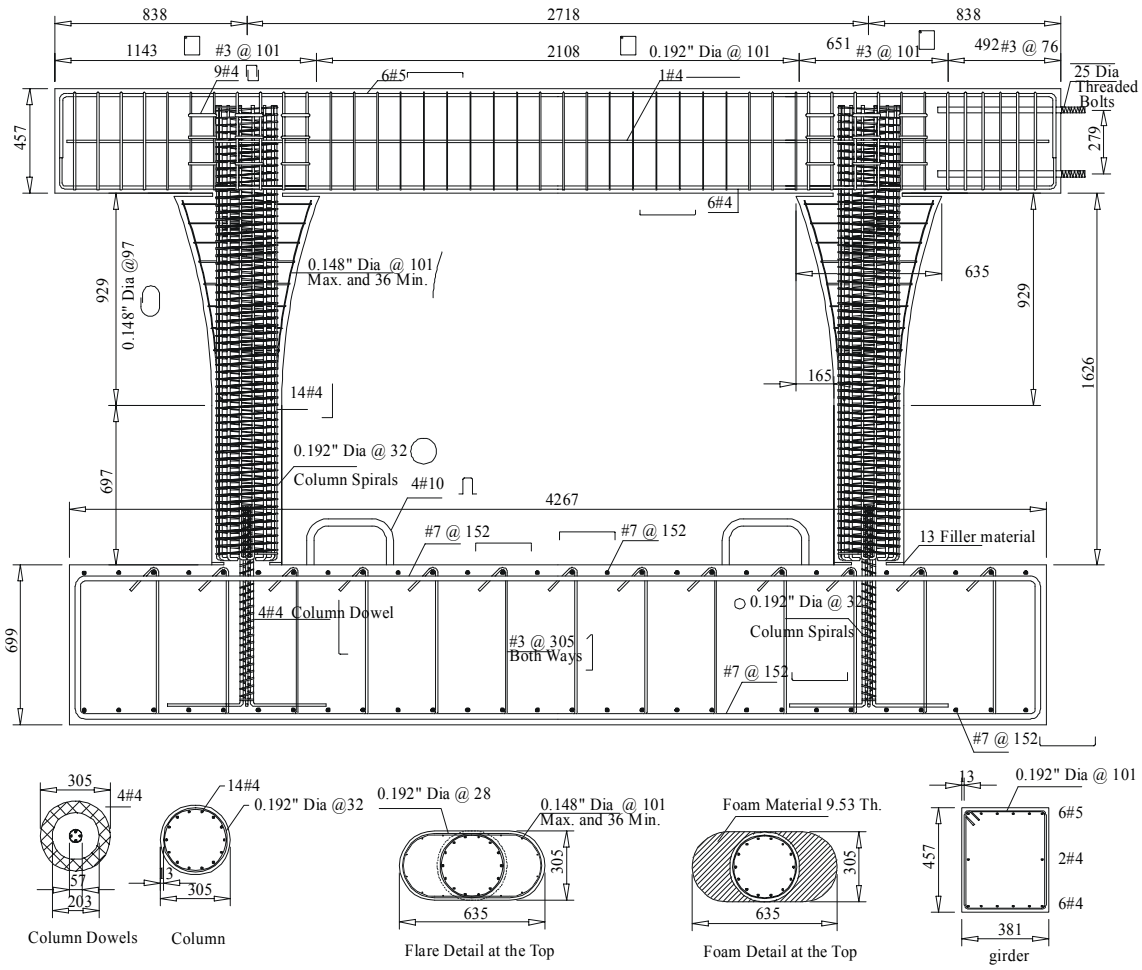

(b)

Fig. 2-9 Reinforcement Detail LFCD2 (a) Dimensions in Inches (b) SI System

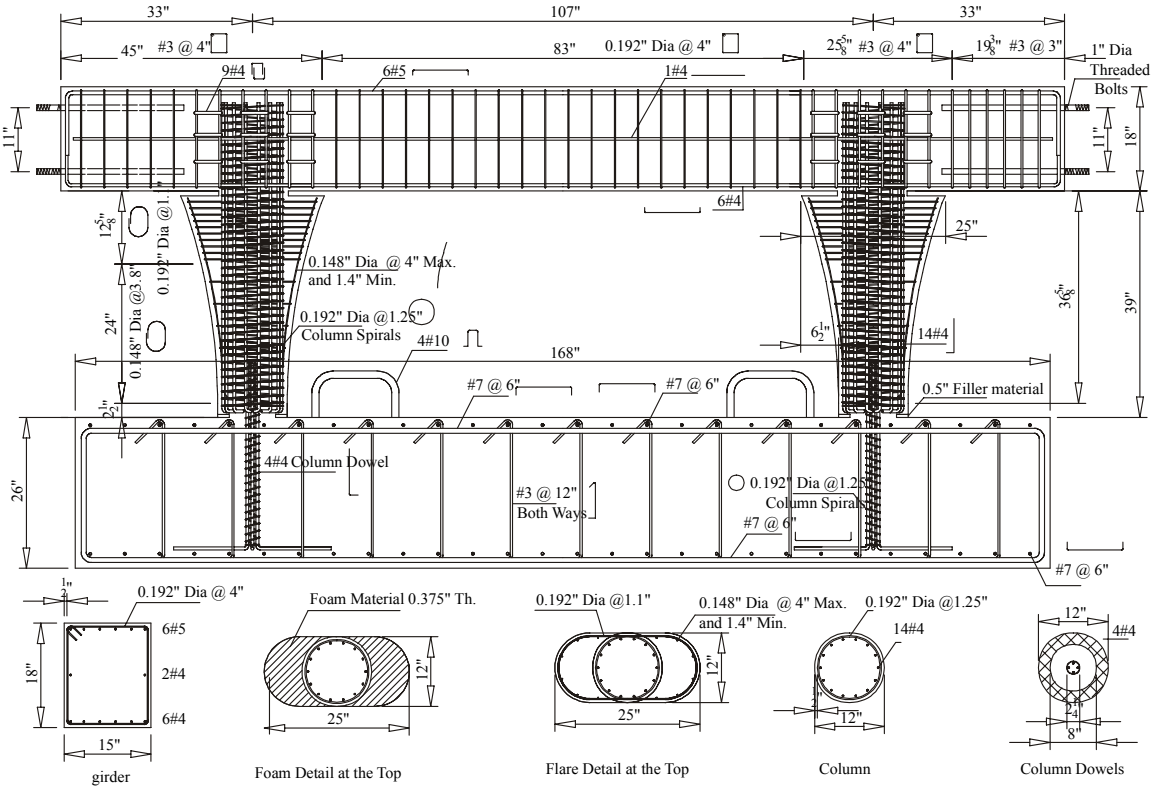

(a)

Fig. 2-10 Reinforcement Detail SFCD1 (a) Dimensions in Inches (b) SI System

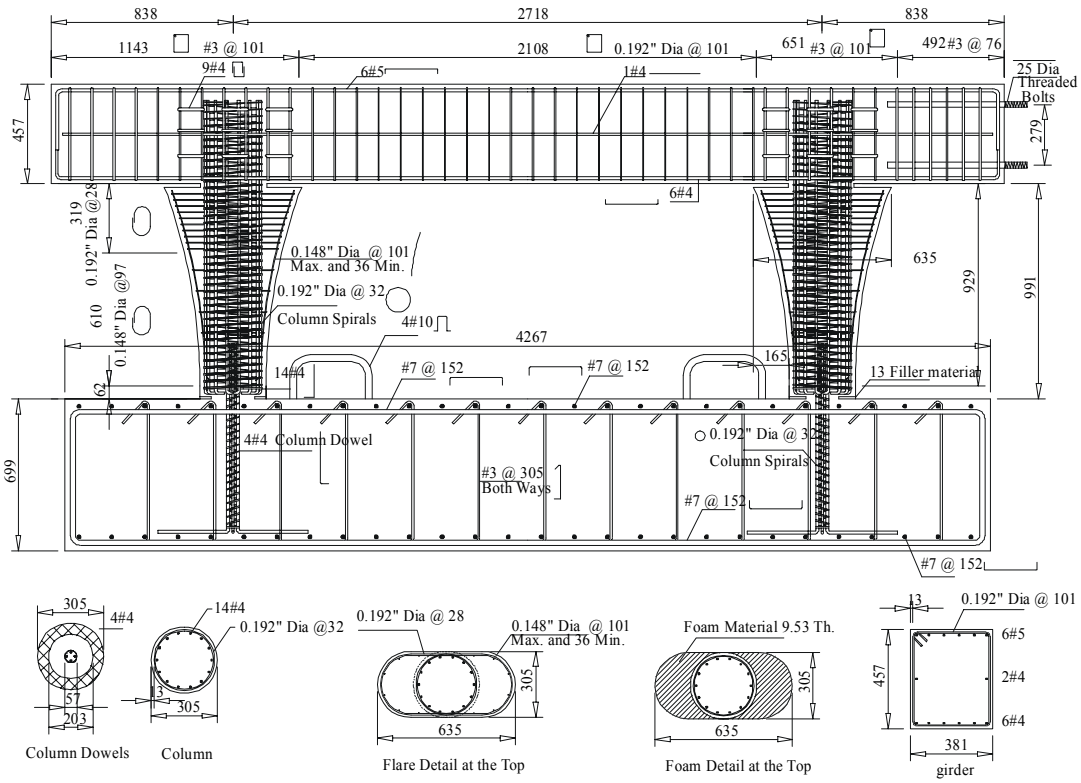

(b)

Fig. 2-10 Reinforcement Detail SFCD1 (a) Dimensions in Inches (b) SI System

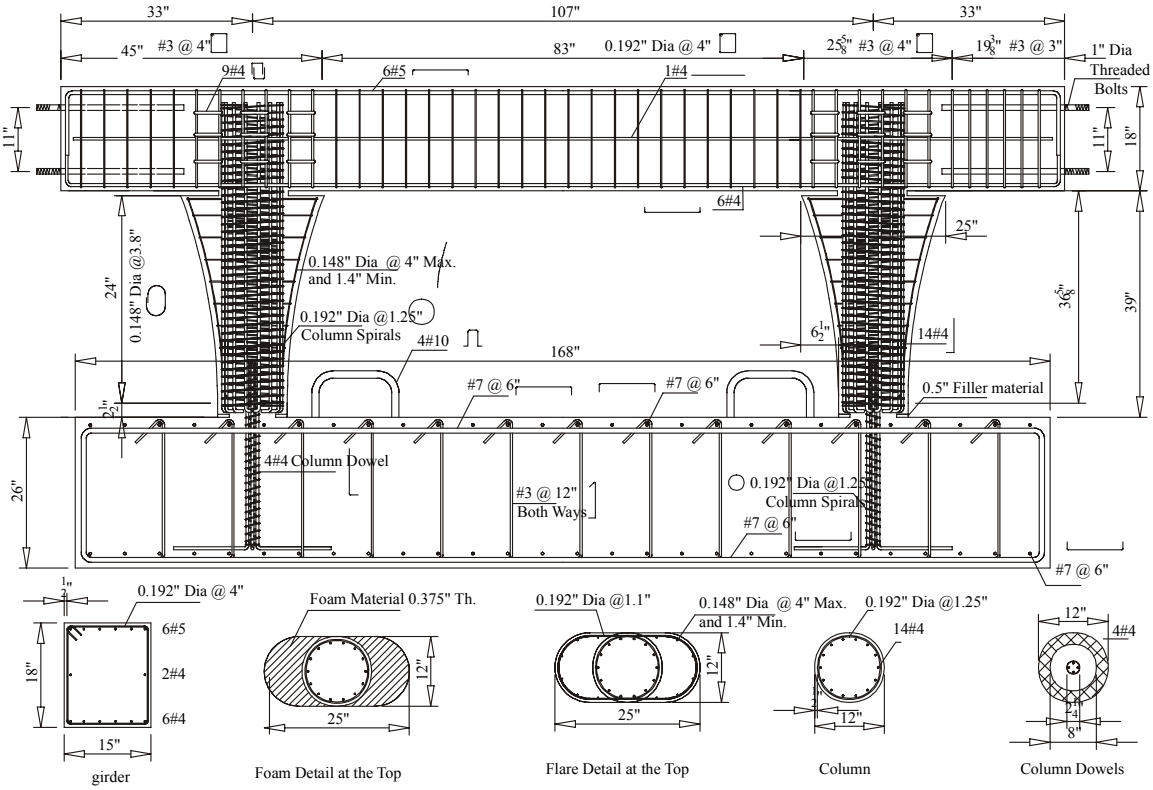

(a)

Fig. 2-10 Reinforcement Detail SFCD1 (a) Dimensions in Inches (b) SI System

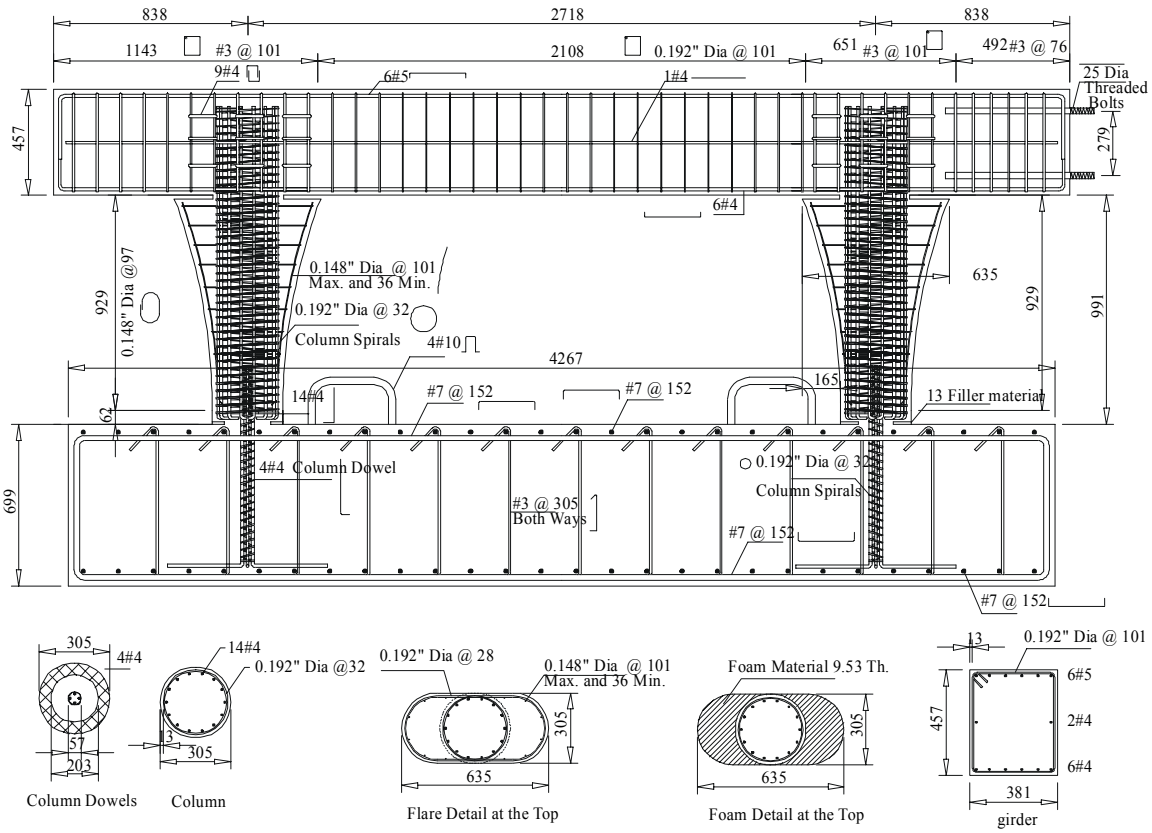

(b)

Fig. 2-10 Reinforcement Detail SFCD1 (a) Dimensions in Inches (b) SI System

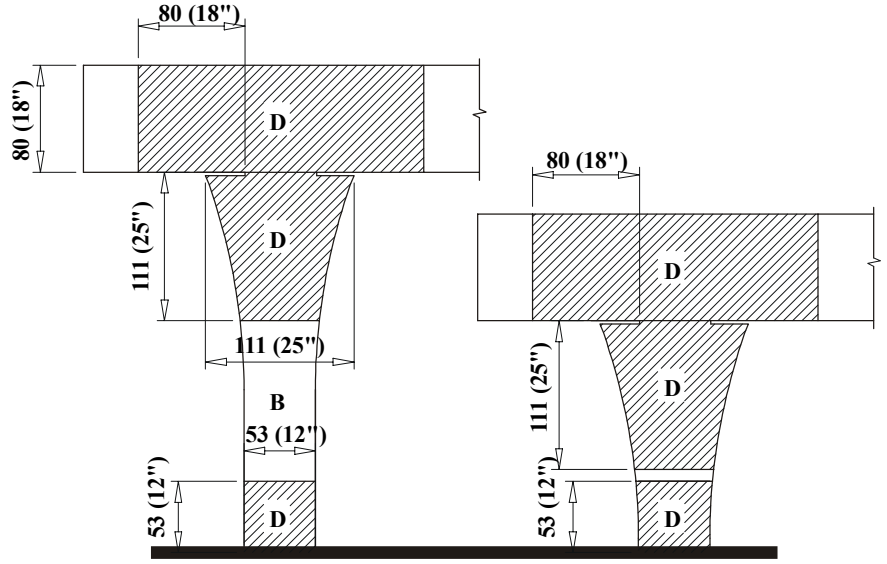

Fig. 2-12 D-Regions and B-Regions for flared columns with a gap (based on Saint Venant's principle)

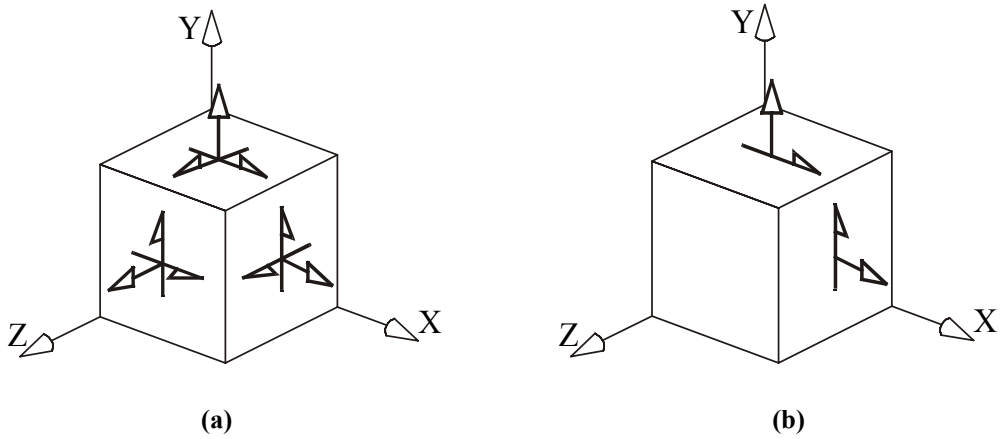

Fig. 2-13 Stress State (a) 3-D Stress State (b) Plane Stress Element Stress State

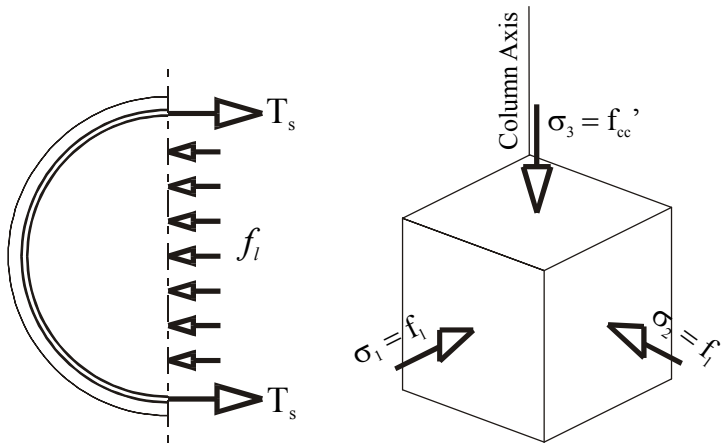

Fig. 2-14 Confined Circular Column 3D Configuration

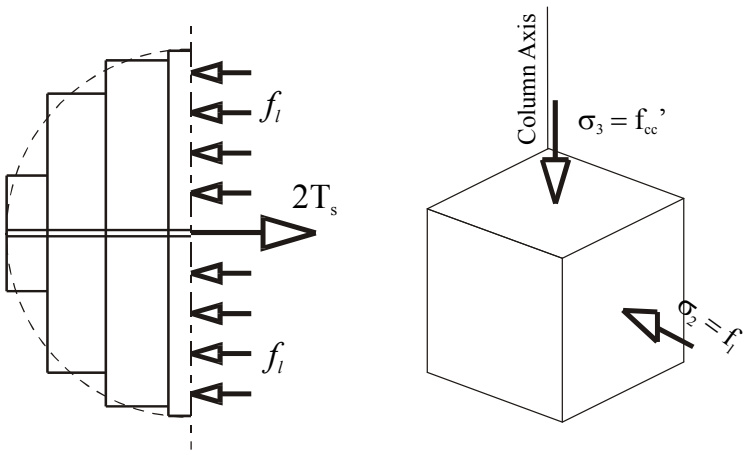

Fig. 2-15 Confined Circular Column 2D Plane Stress Configuration

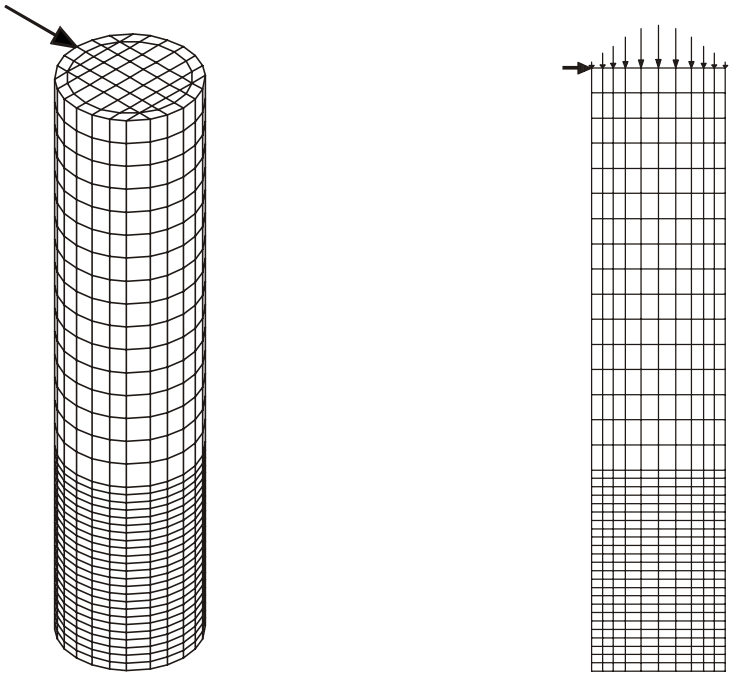

(a) (b)

Fig. 2-16 Finite Element Idealization for NIST column (a) 3D configuration (b) 2D configuration

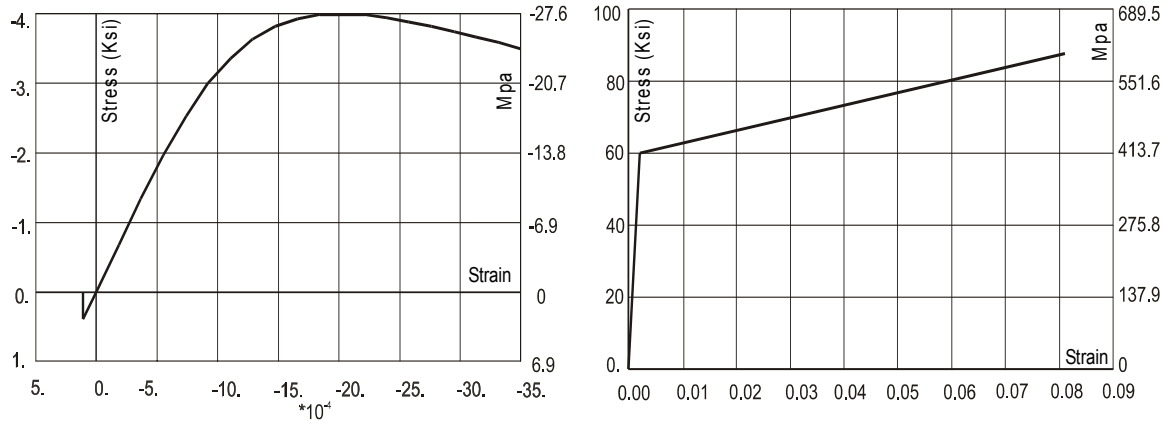

(a) **(b)**

Fig. 2-17 Materials' Stress-Strain (a) Concrete (b) Steel

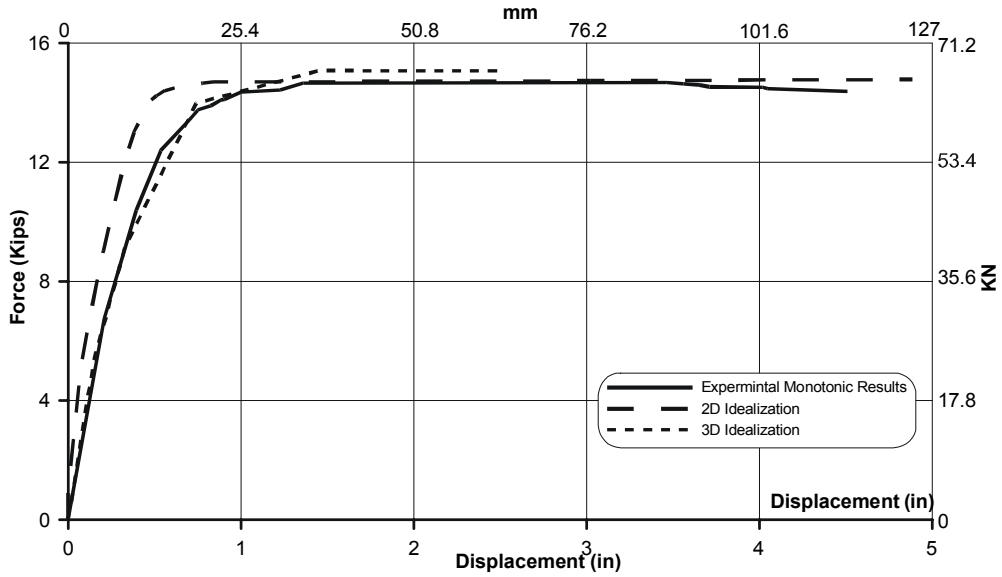

Fig. 2-18 Load-Displacement Curve for NIST Column

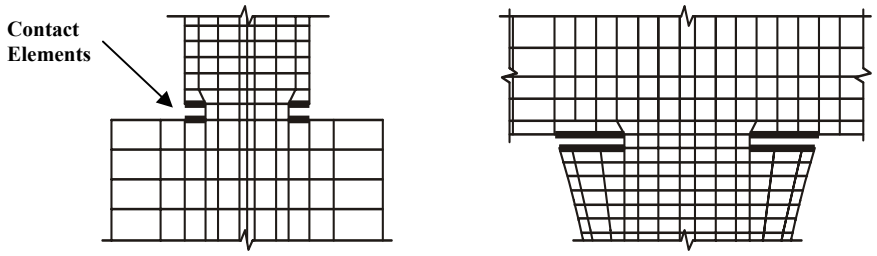

(a) (b)

Fig. 2-19 Contact Elements Location (a) at the base hinge (b) at the flare gap

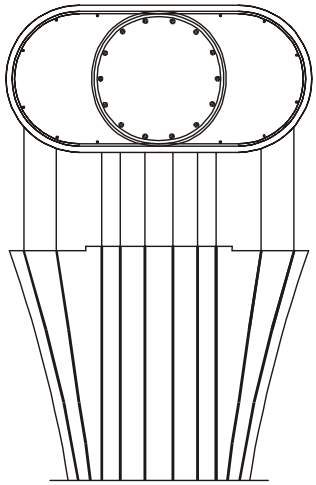

Fig. 2-20 Lumped Reinforcements into 2-D Model

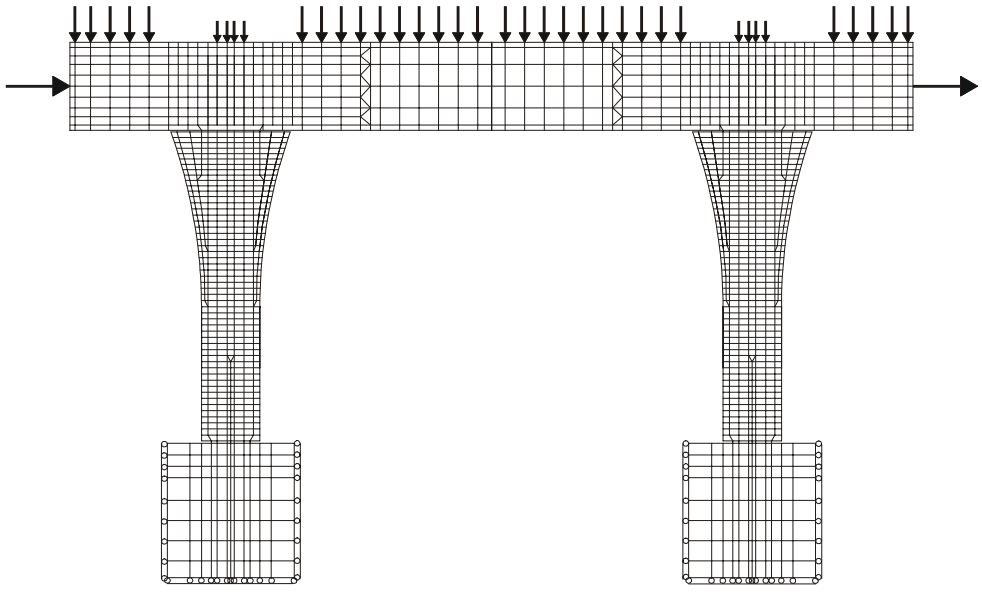

Fig. 2-21 Finite Element Idealization for LFCD1

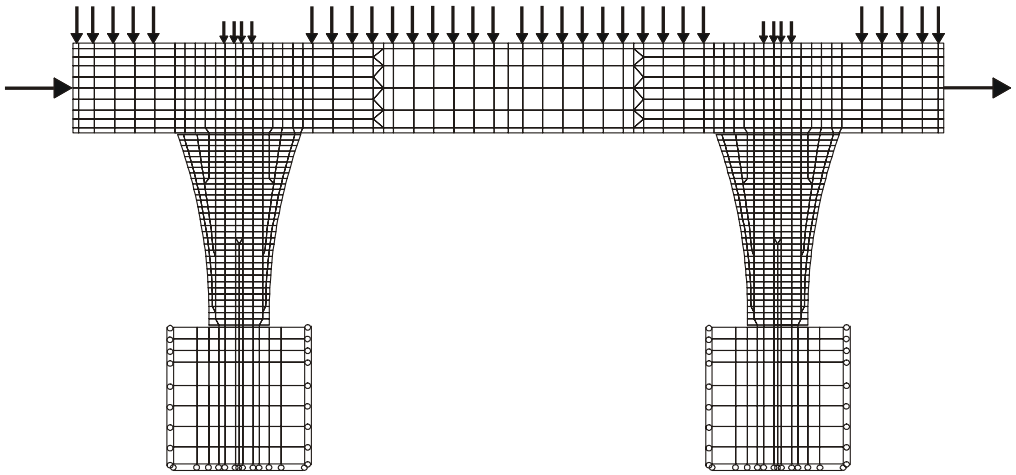

Fig. 2-22 Finite Element Idealization for SFCD1

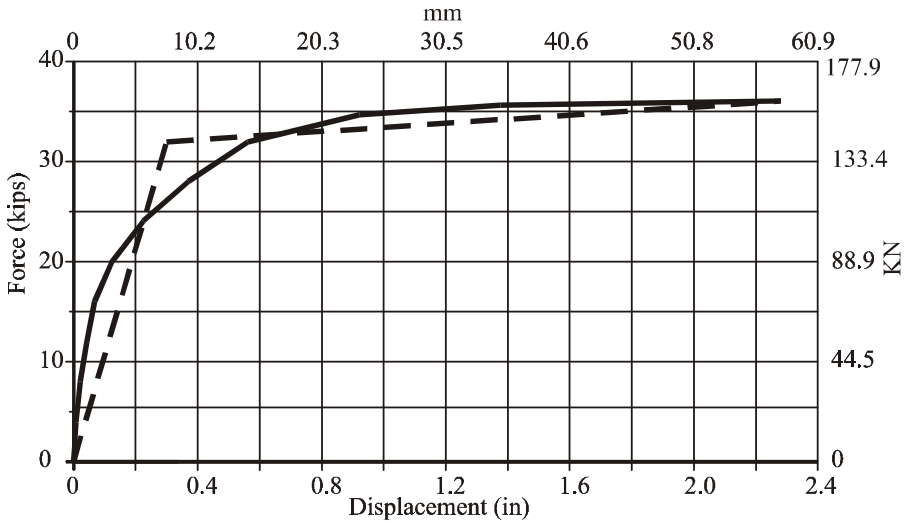

Fig. 2-23 Load Displacement Curve LFCD1

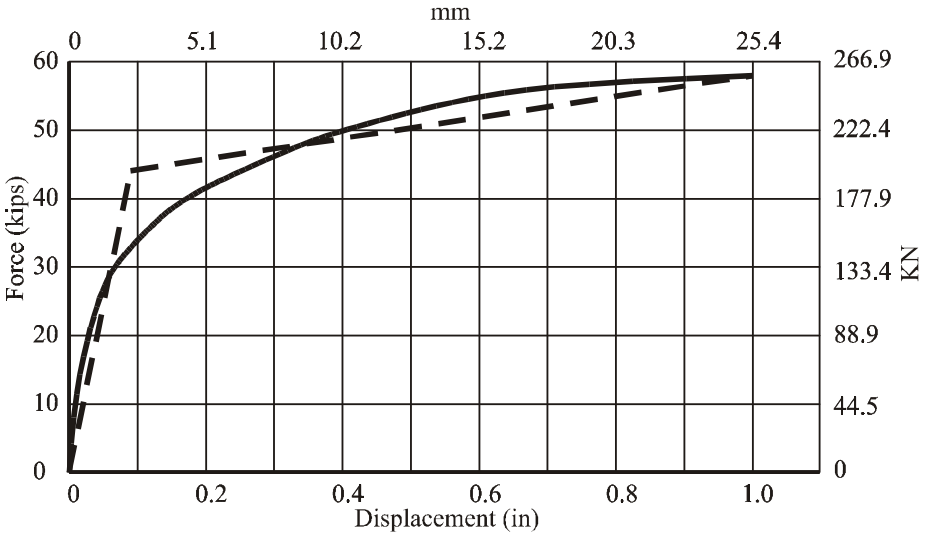

Fig. 2-24 Load Displacement Curve SFCD1

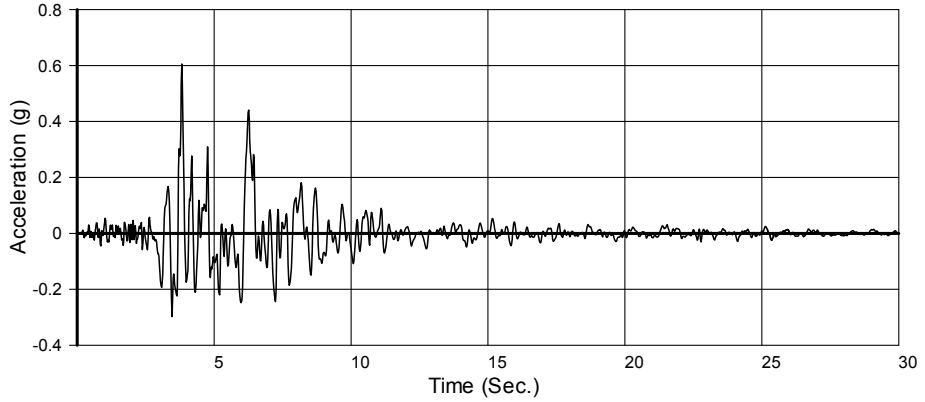

Fig. 2-25 Acceleration Record for Sylmar Earthquake

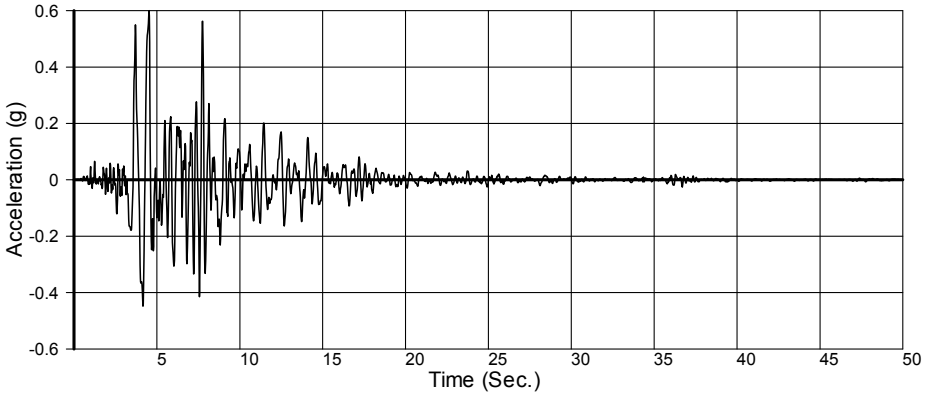

Fig. 2-26 Acceleration Record for Kobe Earthquake

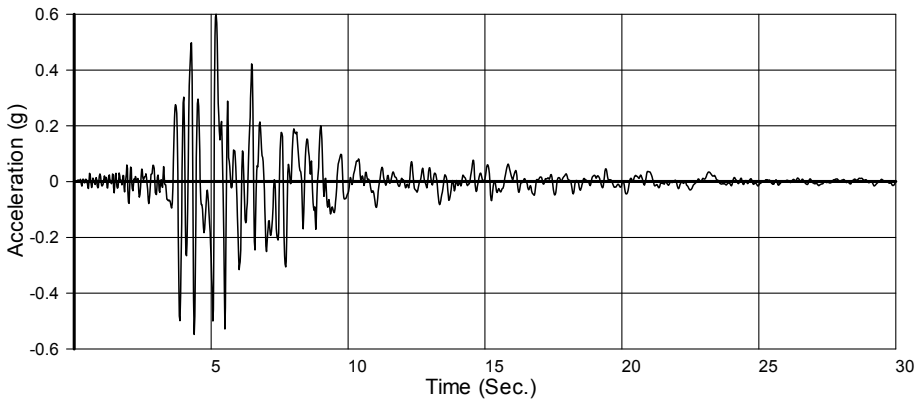

Fig. 2-27 Acceleration Record for Newhall Earthquake

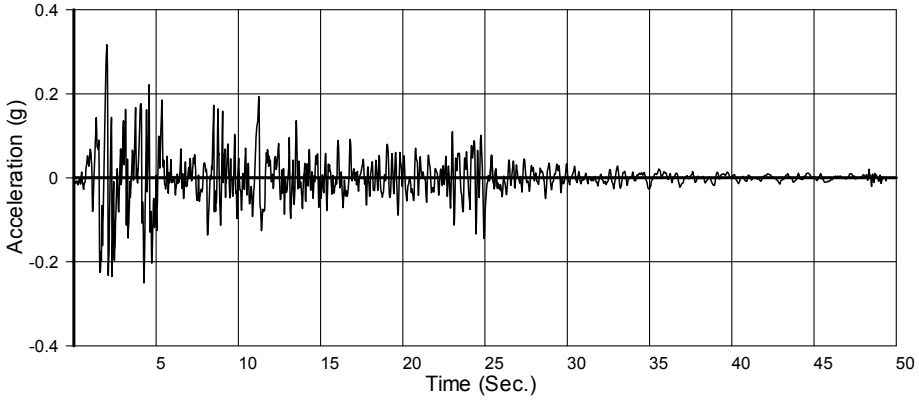

Fig. 2-28 Acceleration Record for El -Centro Earthquake

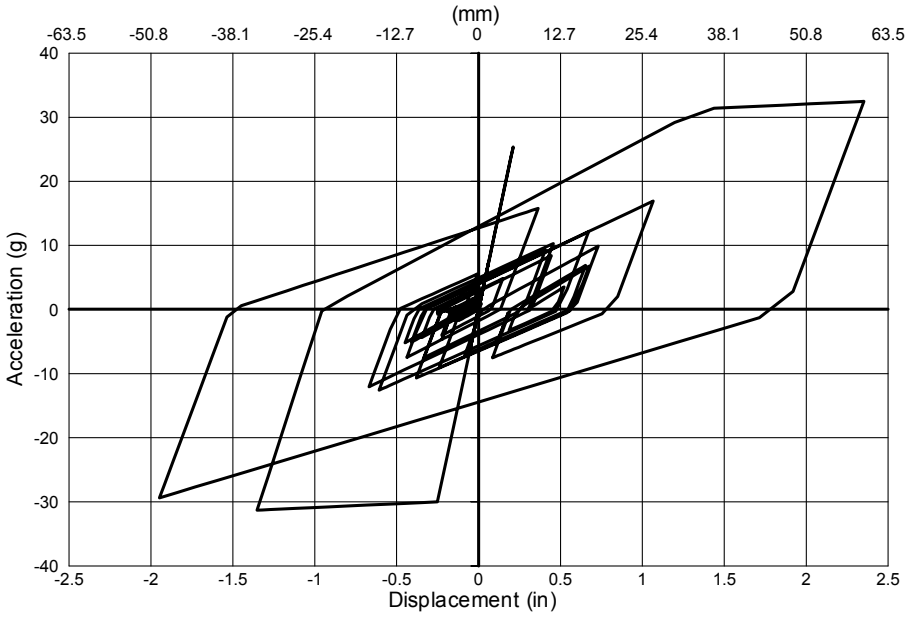

Fig. 2-29 Estimated Load-Displacement Relationship for LFCD1 Excited with 2.0 Times Kobe

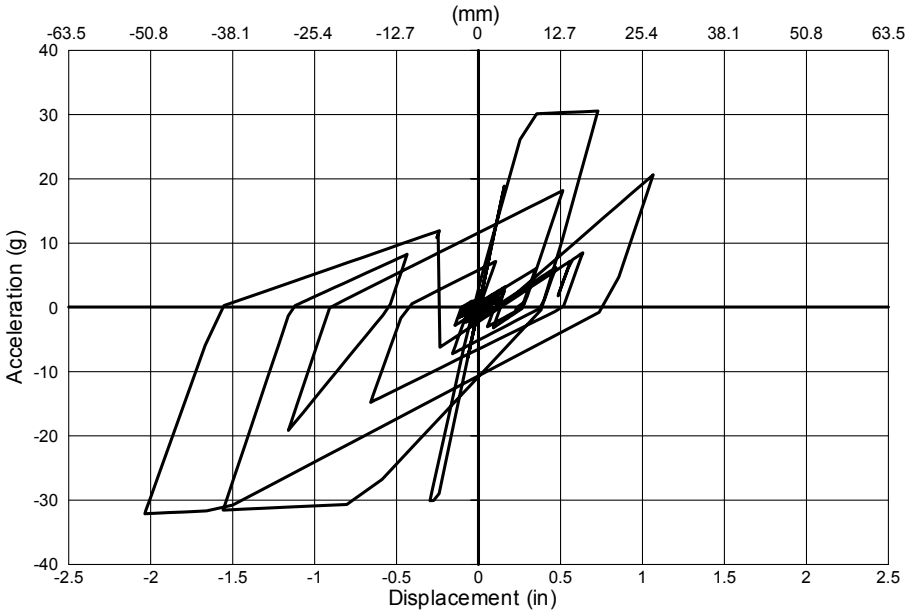

Fig. 2-30 Estimated Load-Displacement Relationship for LFCD1 Excited with 1.98 Times Sylmar

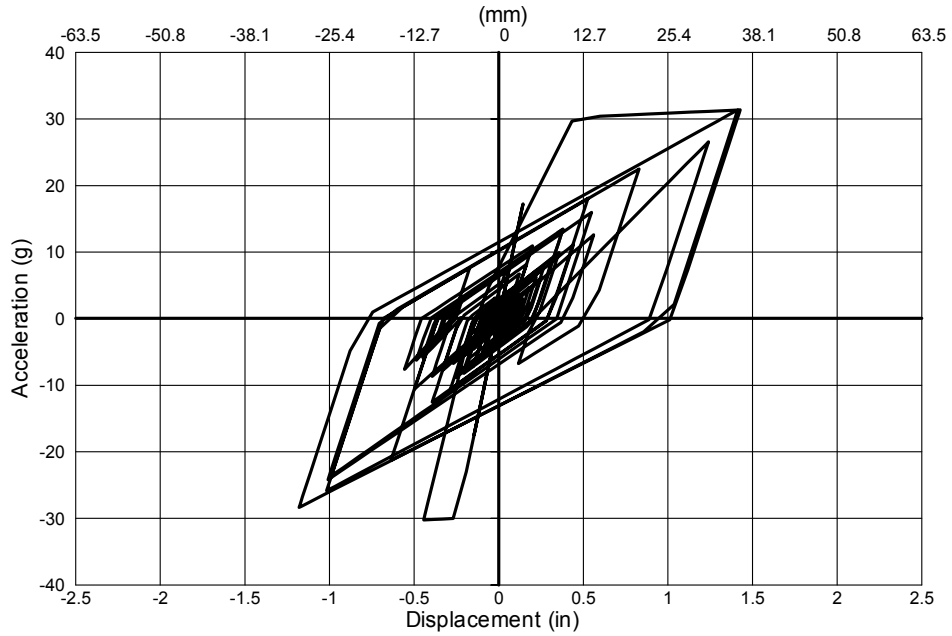

Fig. 2-31 Estimated Load-Displacement Relationship for LFCD1 Excited with 3.79 Times El-Centro

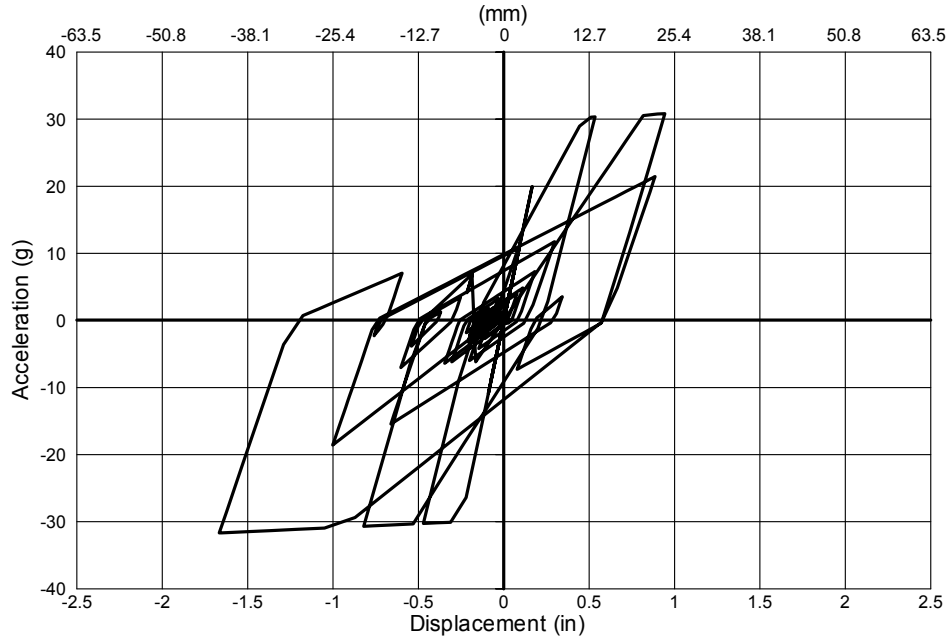

Fig. 2-32 Estimated Load-Displacement Relationship for LFCD1 Excited with 2.0 Newhall

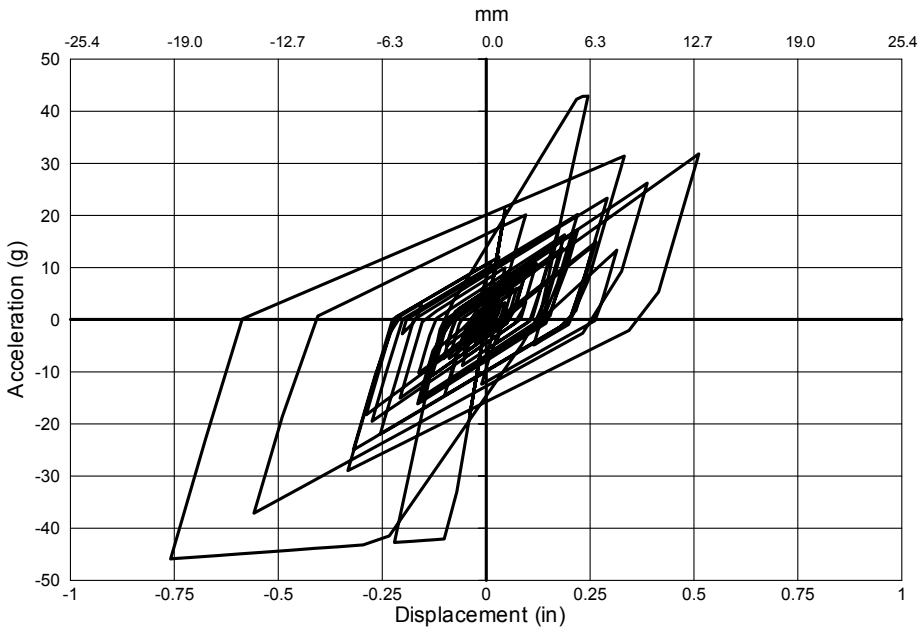

Fig. 2-33 Estimated Load-Displacement Relationship for SFCD1 Excited with 2.0 Times Kobe

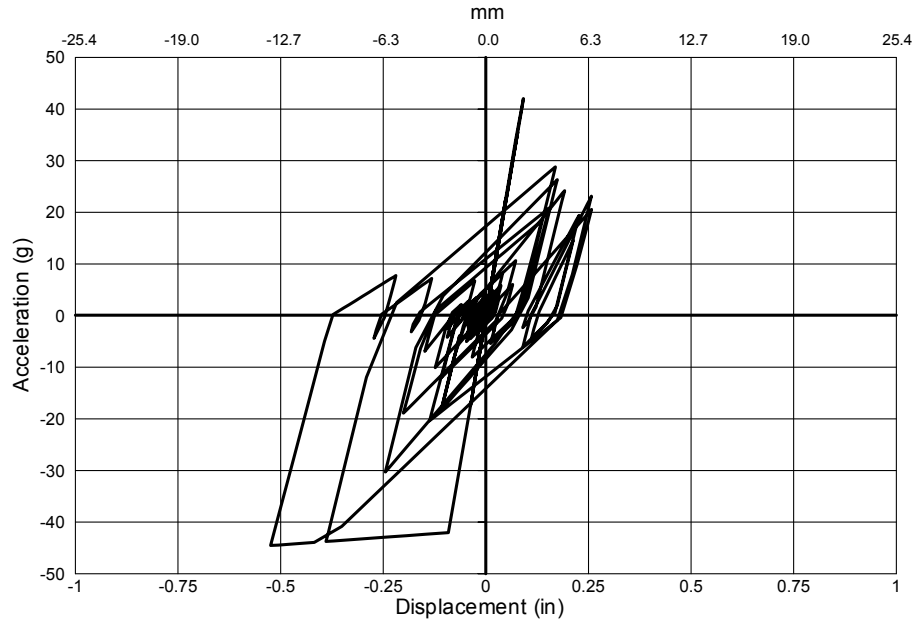

Fig. 2-34 Estimated Load-Displacement Relationship for SFCD1 Excited with 1.98 Times Sylmar

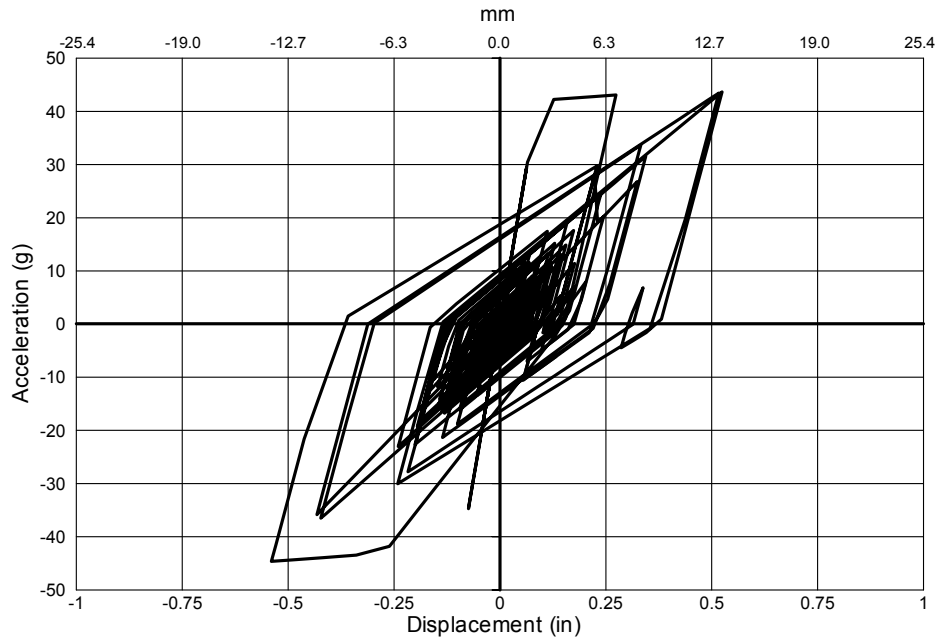

Fig. 2-35 Estimated Load-Displacement Relationship for SFCD1 Excited with 3.79 Times El-Centro

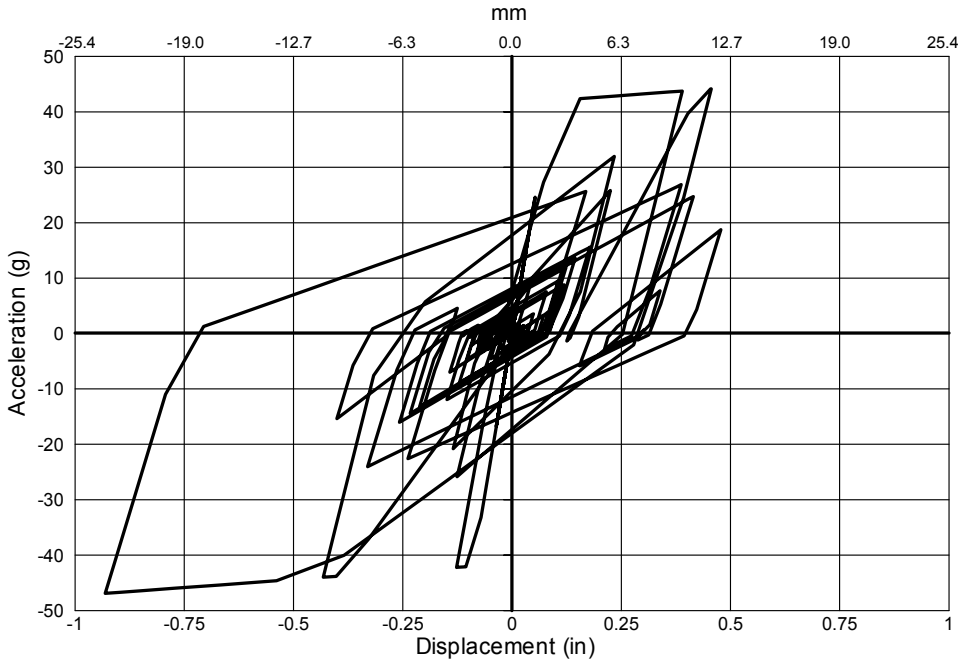

Fig. 2-36 Estimated Load-Displacement Relationship for LFCD1 Excited with 2.0 Newhall

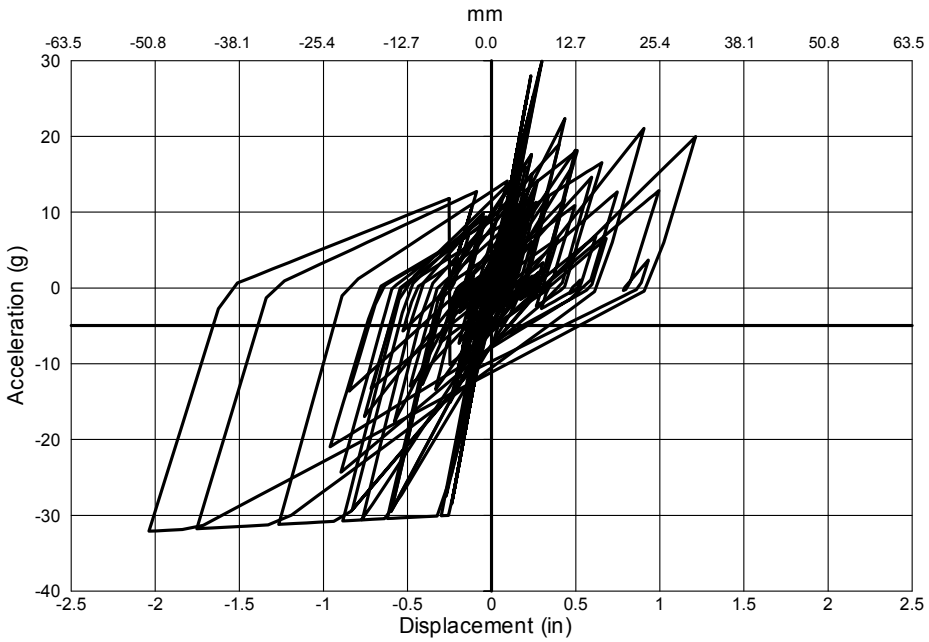

Fig. 2-37 Accumulative Load-Displacement Relationship for LFCD1 Excited with (0.15 0.25 0.50 …. 2.0 Times Sylmar)

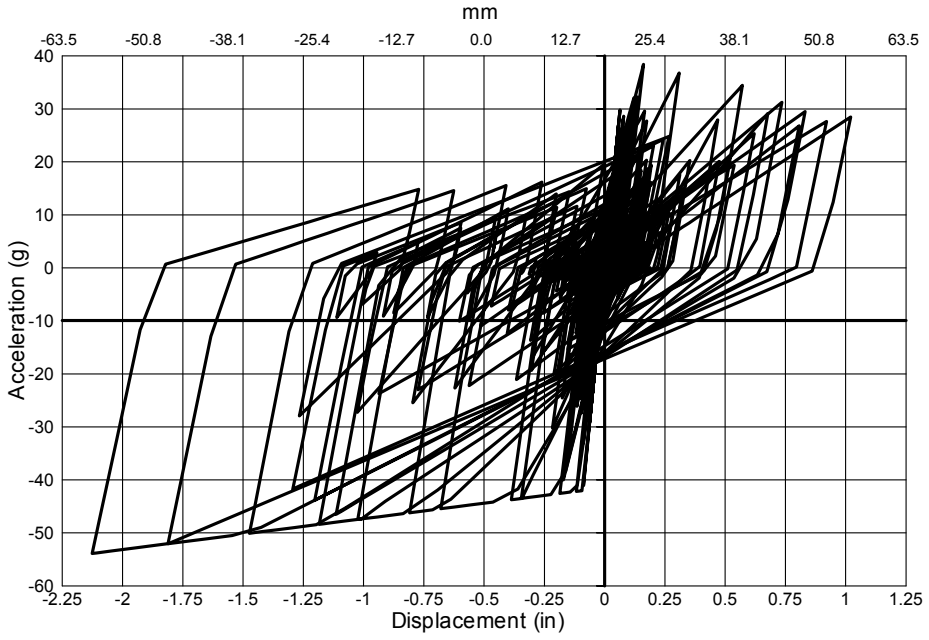

Fig. 2-38 Accumulative Load-Displacement Relationship for SFCD1 Excited with (0.15 0.25 0.50 …. 3.0 Times Sylmar)

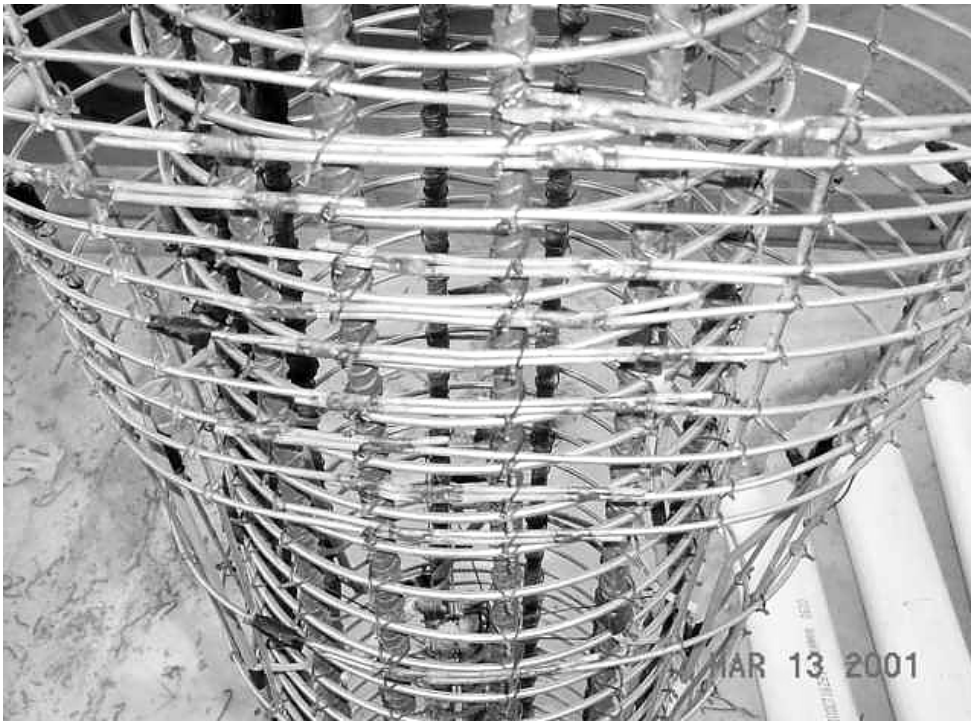

Fig. 3-1 Welded Flare Hoops

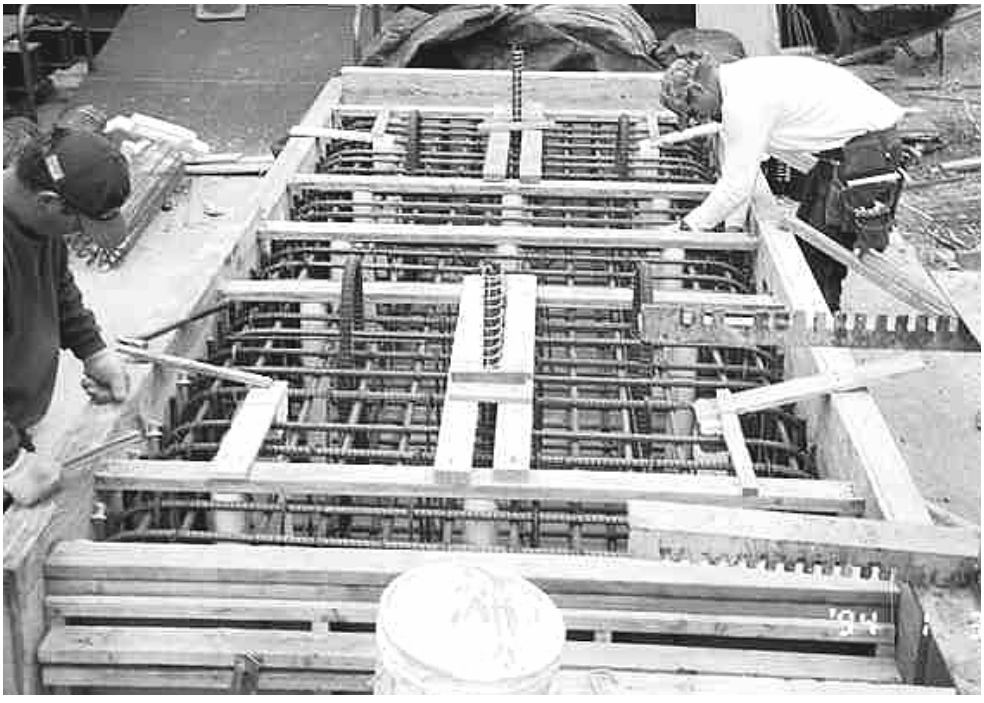

Fig. 3-2 Footing Construction

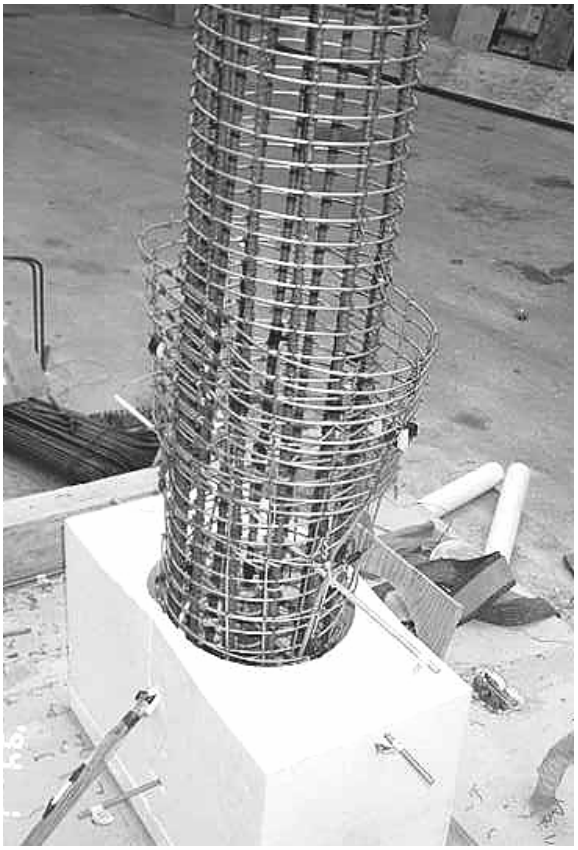

Fig. 3-3 Column and Flare Reinforcement Encased in Foam Forms

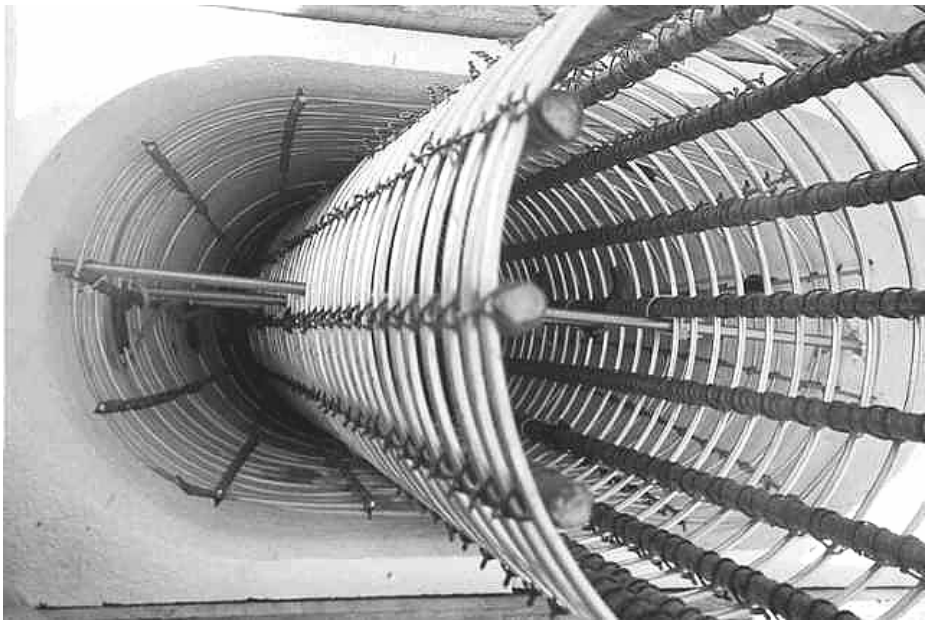

Fig. 3-4 Top View for Column and Flare Reinforcement

Fig. 3-5 Typical Beam Reinforcements

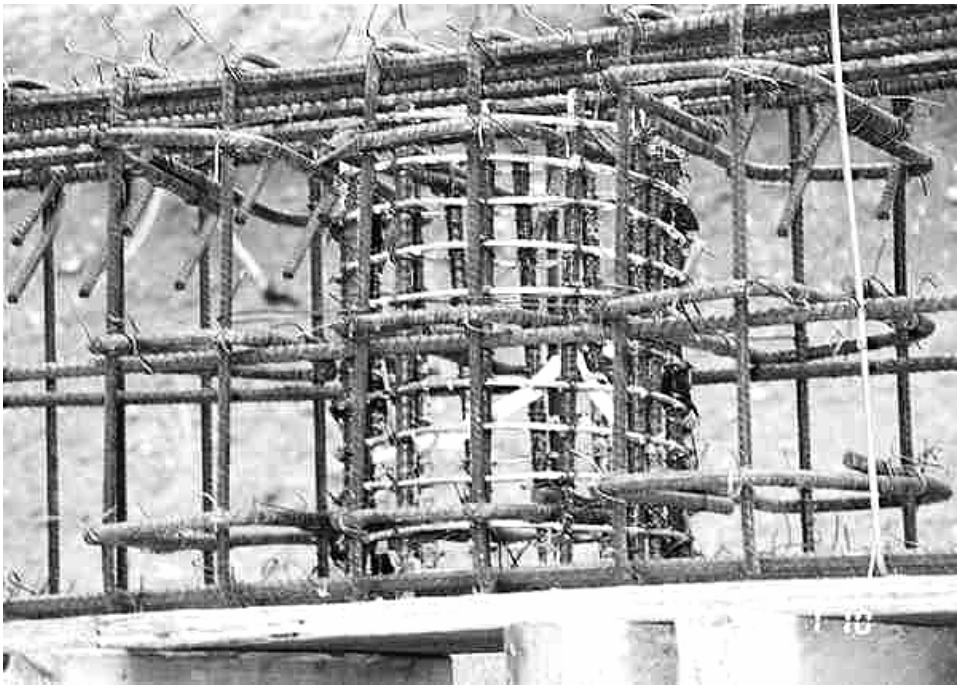

Fig. 3-6 Typical Joint Reinforcement

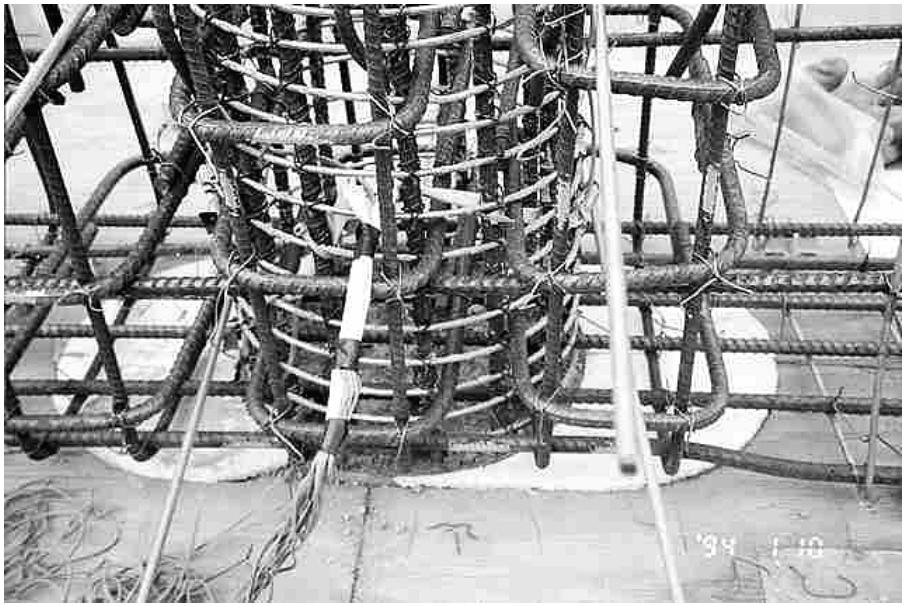

Fig. 3-7 Typical Gap Compressible Material

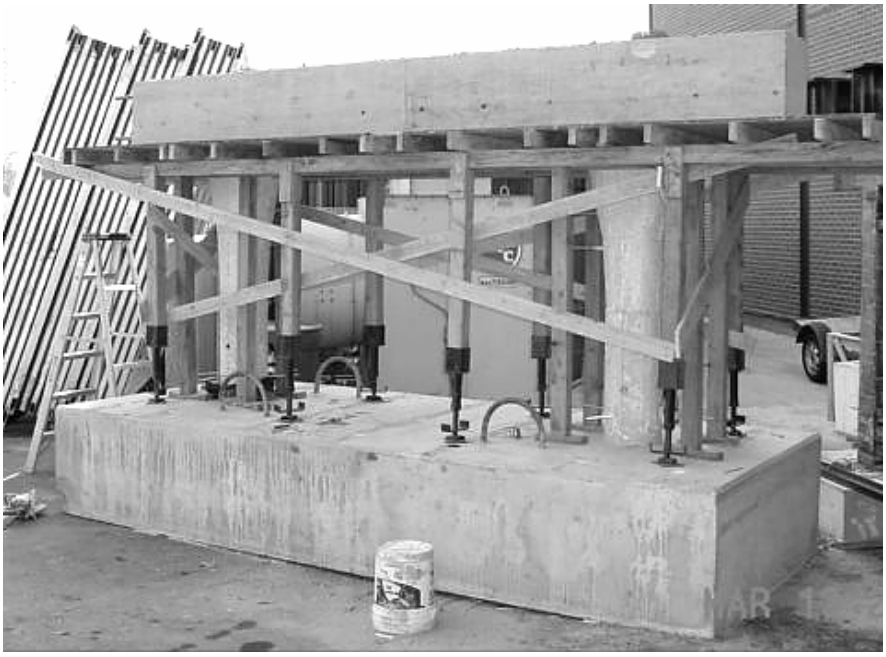

Fig. 3-8 LFCD1 after Construction

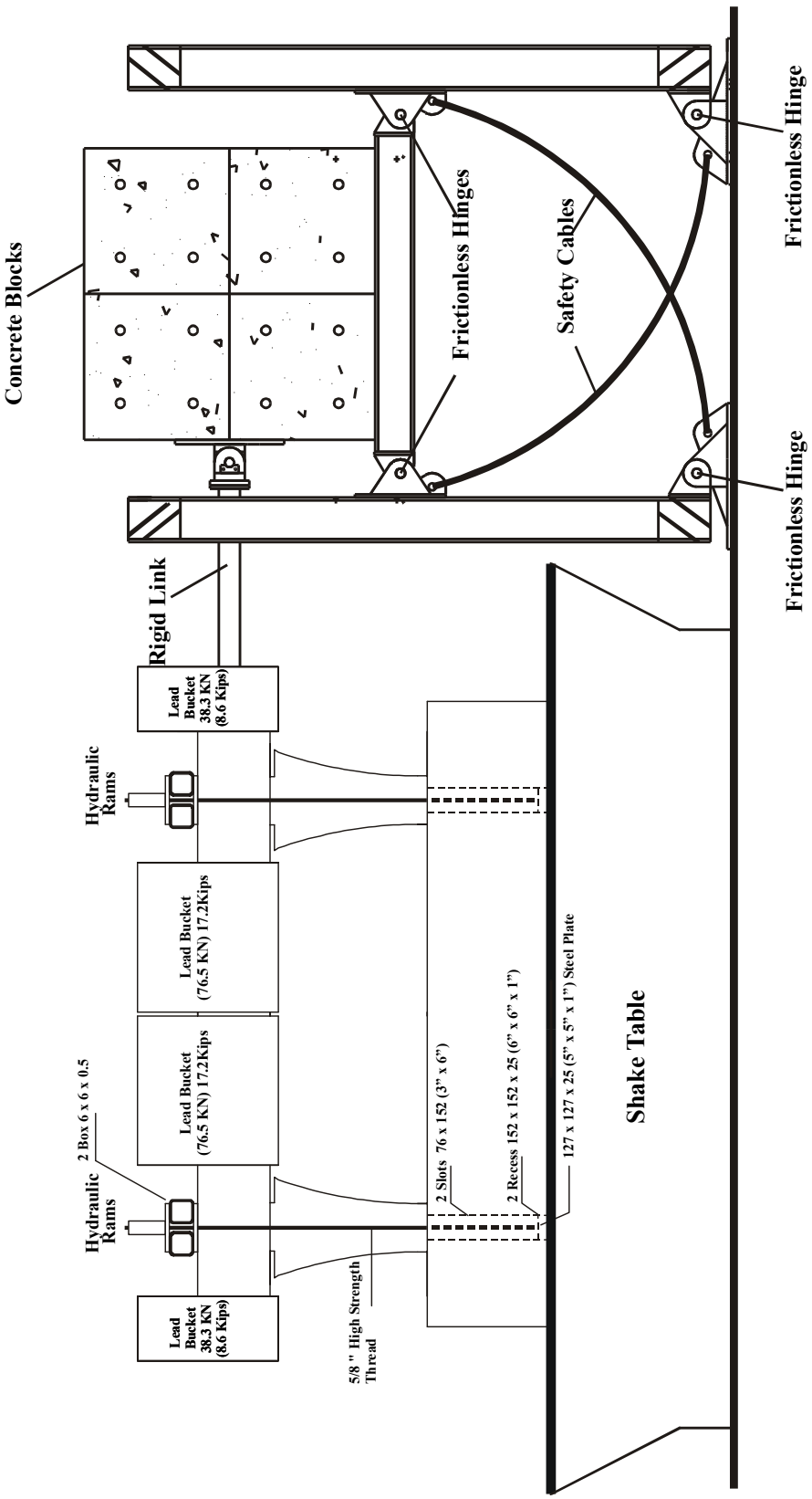

Fig. 3-9 Layout of the Mass Rig

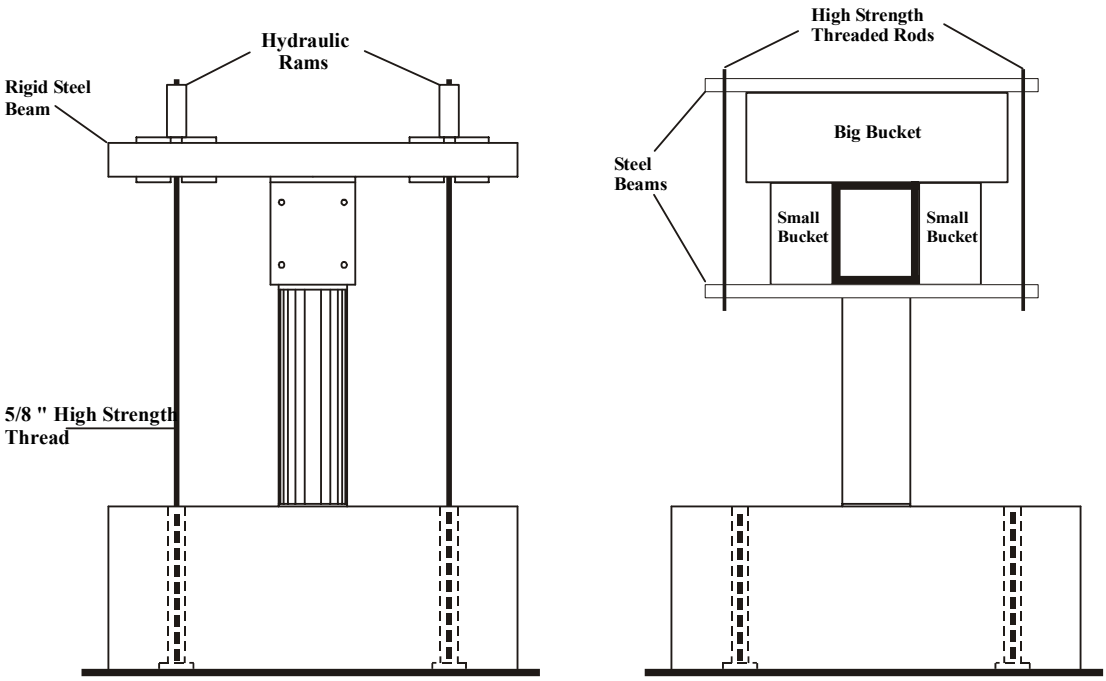

Fig. 3-10 (a) Hydraulic Rams Setup (b) Lead Bucket Setup

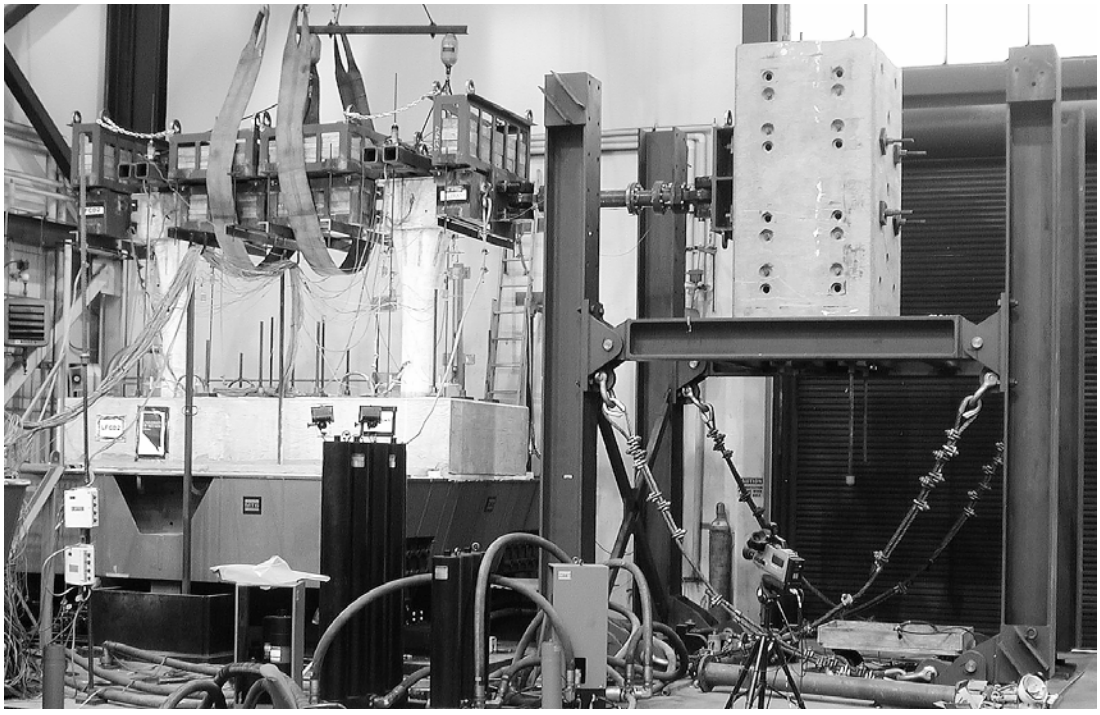

Fig. 3-11 Typical Test Setup for LFCD1 & LFCD2

Fig. 3-12 Typical Test Setup for SFCD1 & SFCD2

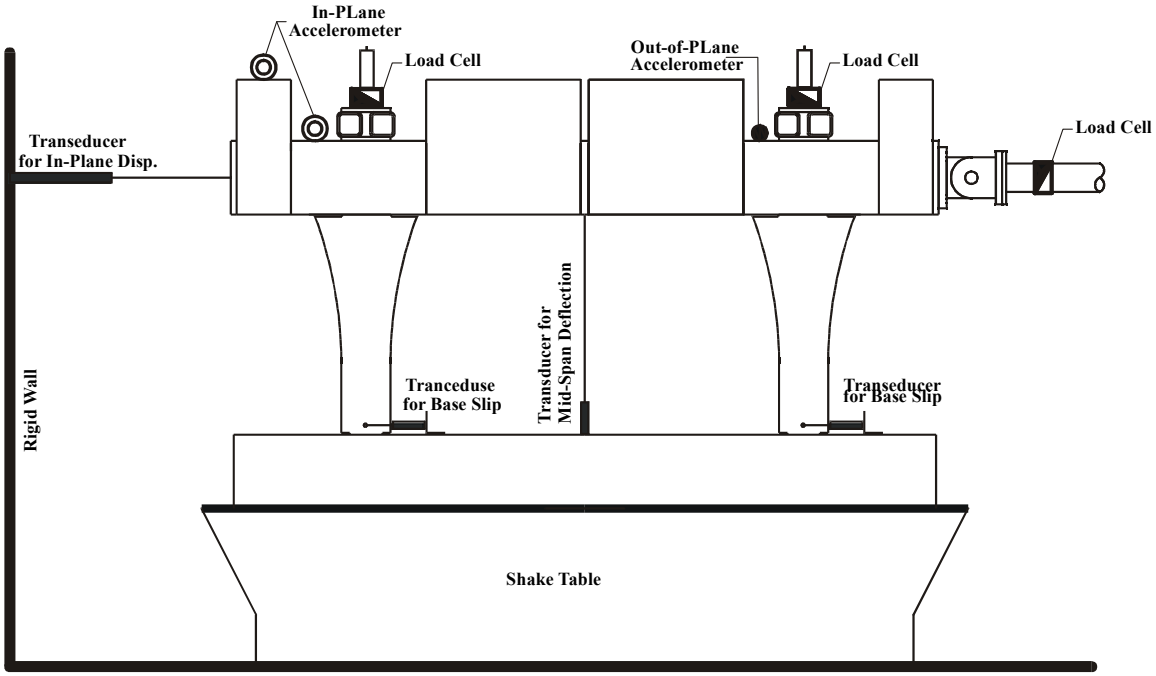

Fig. 3-13 Typical Layout of Displacement Transducers Load Cells and Accelerometer

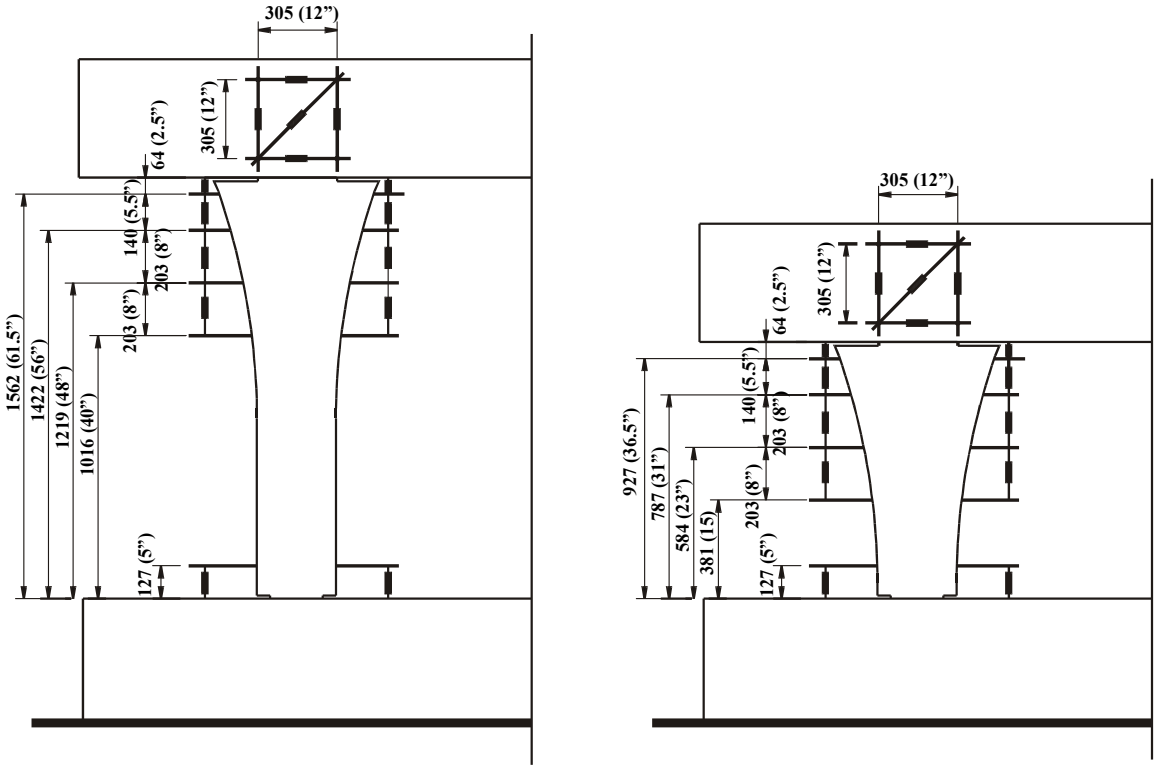

Fig. 3-14 Location of Installed Transducers to Measure Curvature

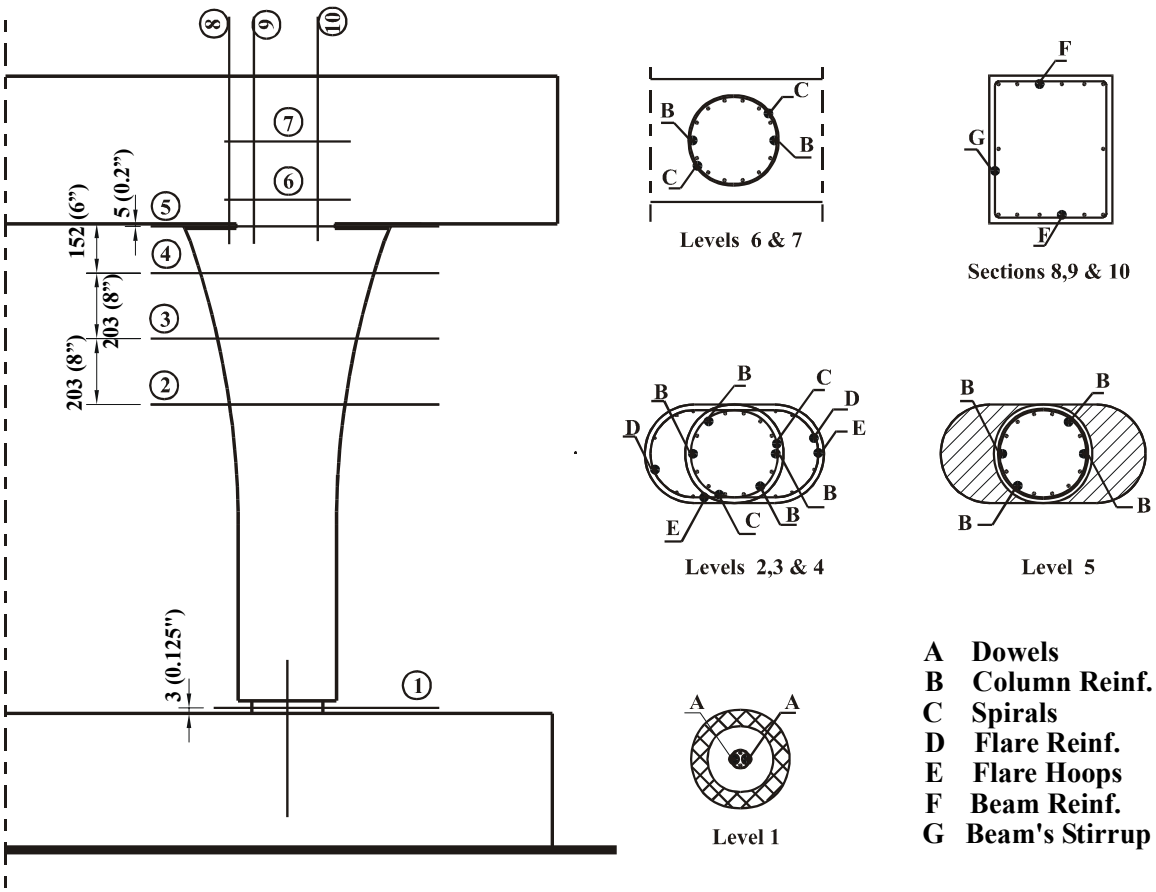

Fig. 3-15 Typical Strain Gauge Layout

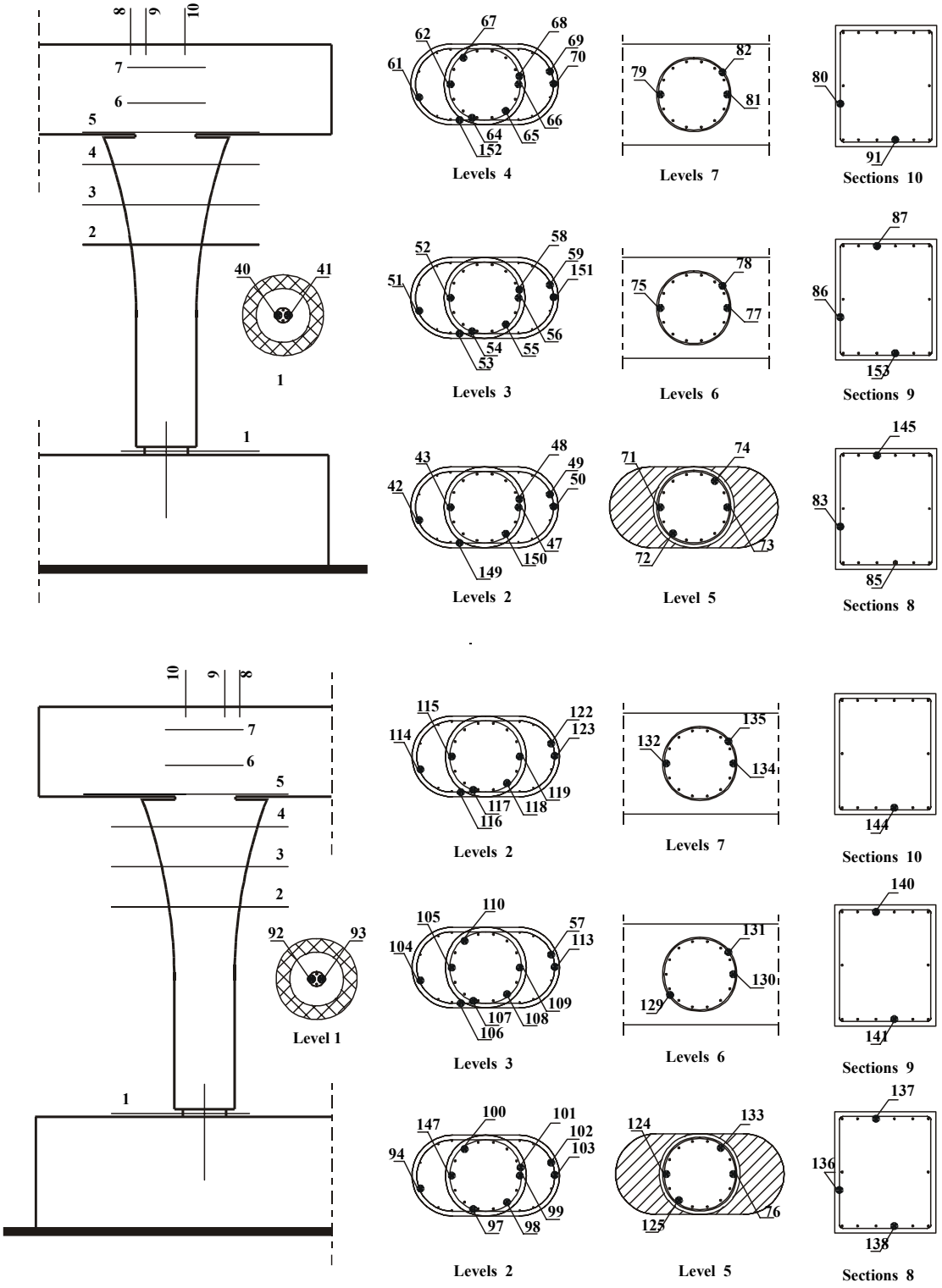

Fig. 4-1 LFCD1, Strain Gauge Identification Numbering

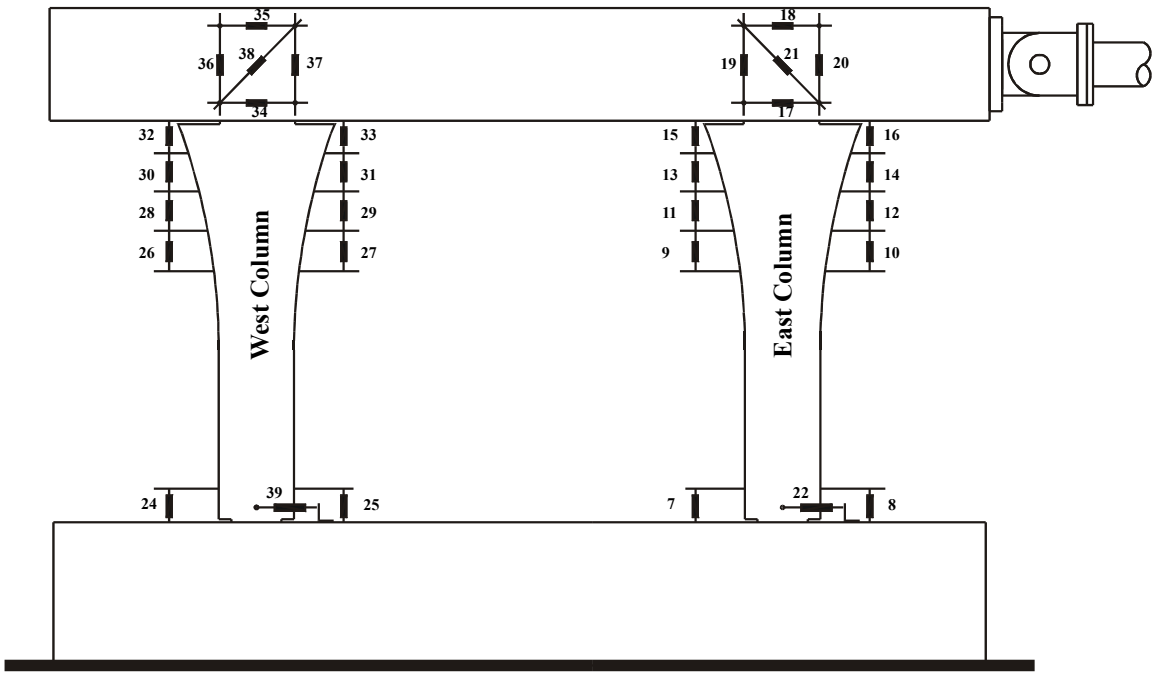

(b)

Fig. 4-2 LFCD1, Displacement Transducers Numbering

(a)

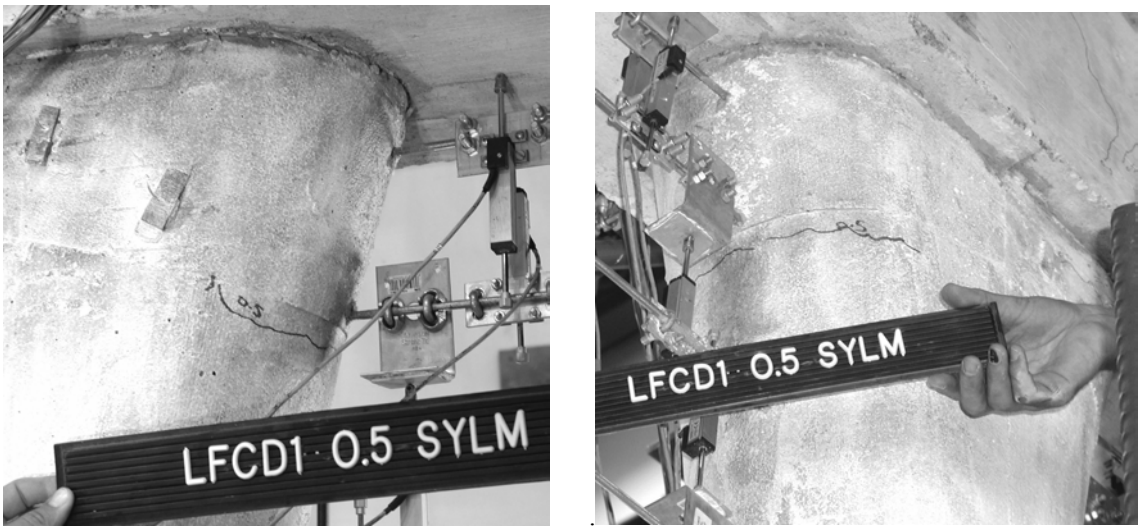

(b)

Fig. 4-3 LFCD1 at 0.5 times Sylmar (a) Joint Cracks (b) Flare Cracks

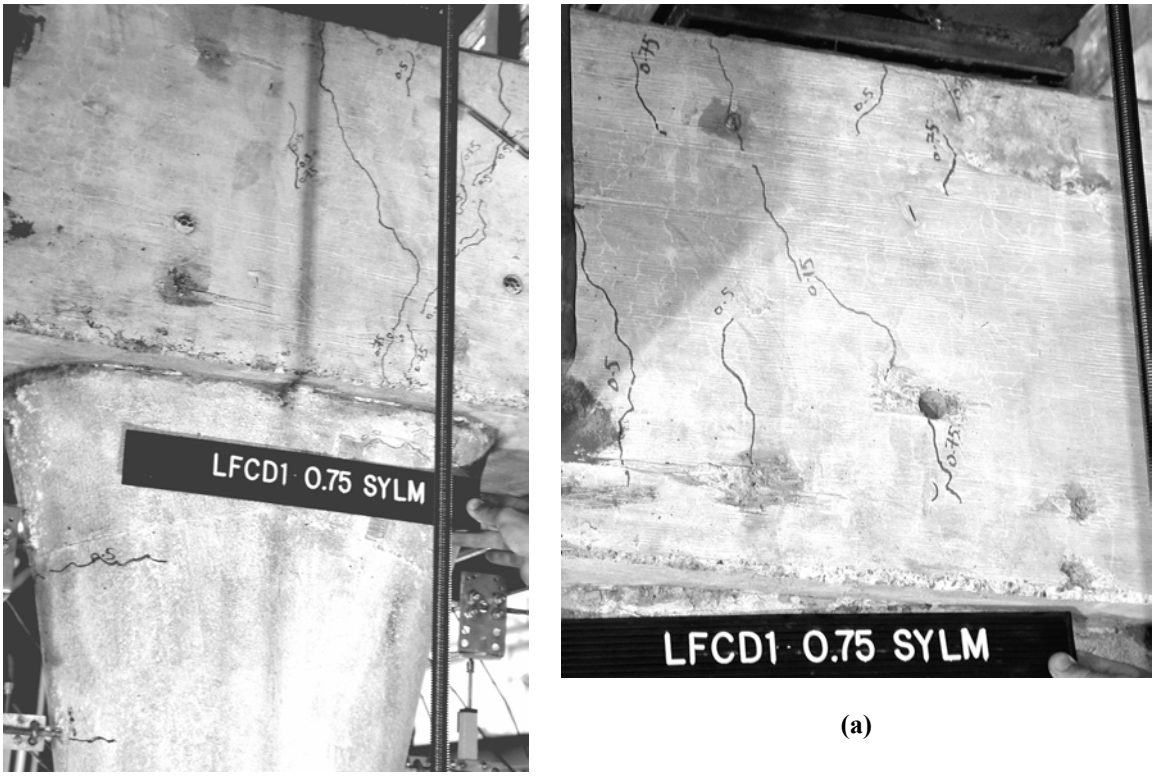

(a)

(a)

Fig. 4-4 LFCD1 at 0.75 times Sylmar (a) Joint and Flare Crack (b) Flare Crack

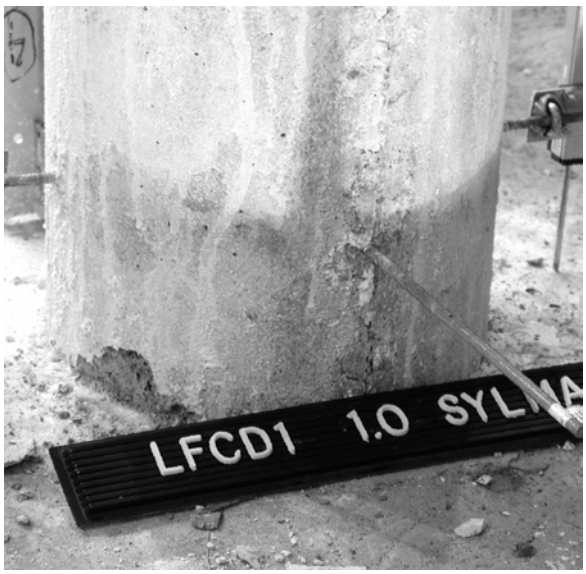

Fig. 4-5 LFCD1 at 1.00 times Sylmar , Concrete Spalling at the Base Hinge

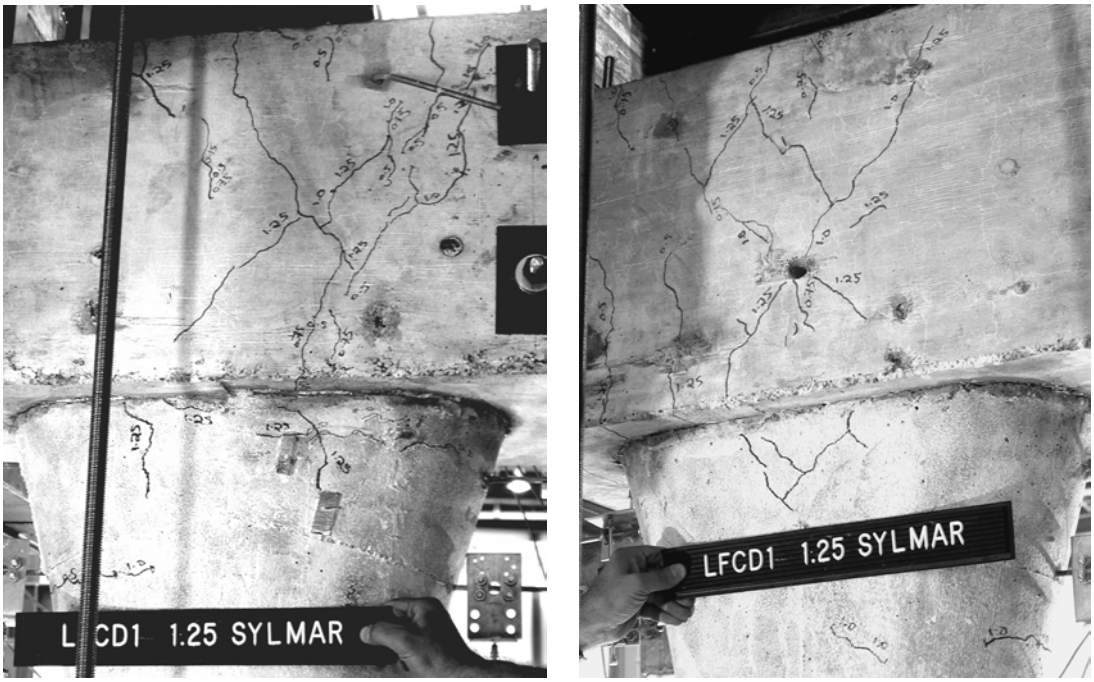

(a)

(b)

Fig. 4-6 LFCD1 at 1.25 times Sylmar (a) Joint and Flare Crack (c) Base Hinge Spalling

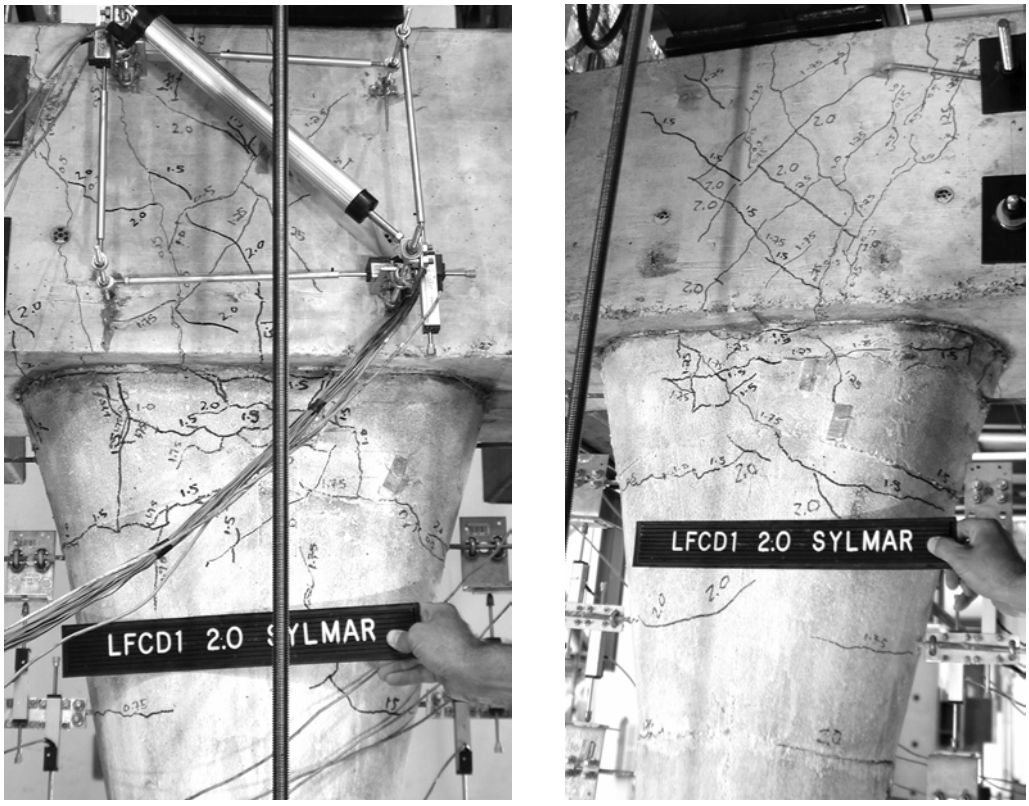

(a)

(b) **(c)**

Fig. 4-7 LFCD1 at 2.0 times Sylmar (a) Joint and Flare Crack (b) Concrete Spalling Flare edge (c) Permanent Gap Closure

(a)

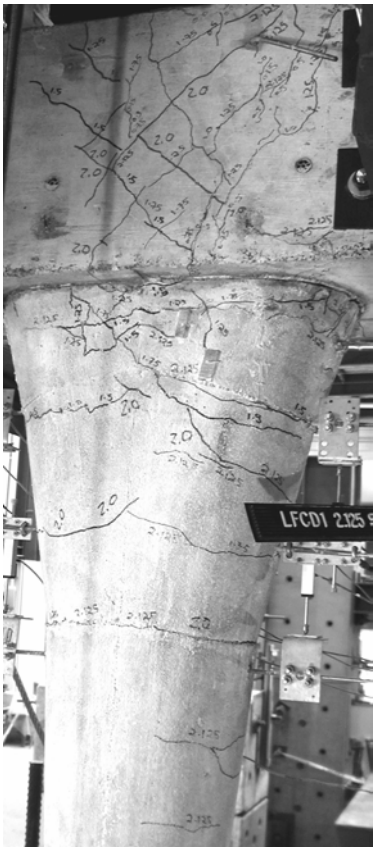

(b)

(c)

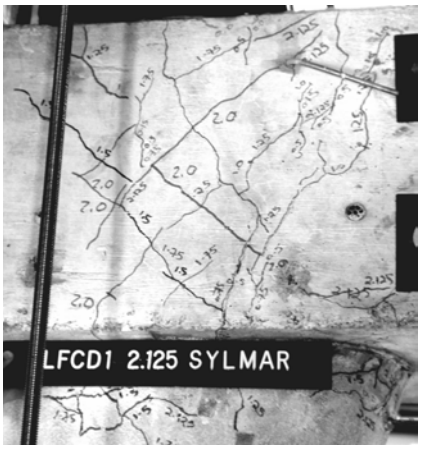

(d)

Fig. 4-8 LFCD1 at 2.125 times Sylmar (a) Concrete Spalling (b) Column Cracking (c) Base Hinge Concrete Spalling (d) Joint Cracking

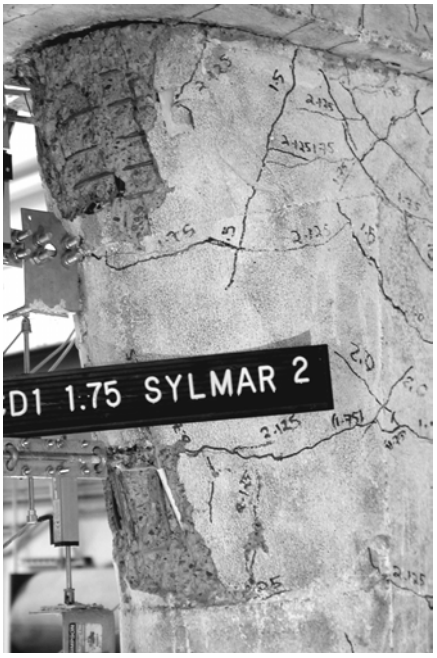

(a)

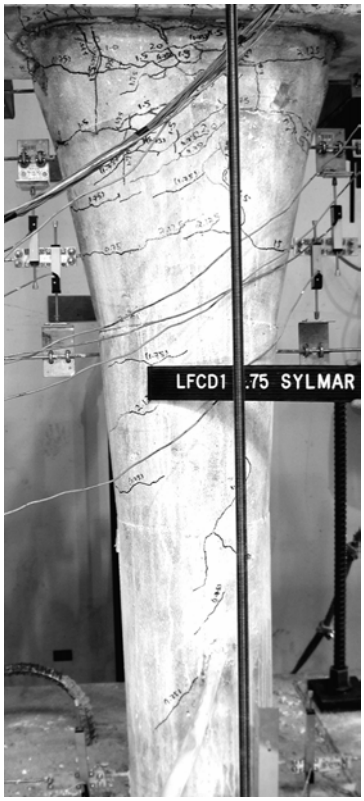

(b)

(c)

(d)

Fig. 4-9 LFCD1 at 1.75-2 times Sylmar (a) Concrete Spalling (b) Column cracking (c) Joint Cracking (d) Concrete Spalling

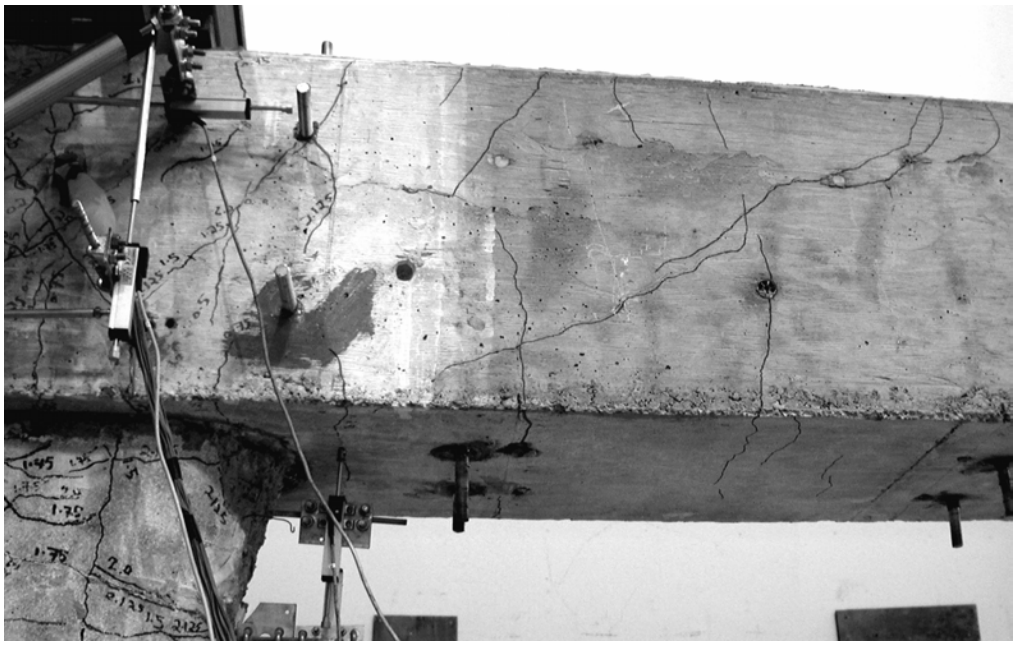

(a)

(b)

Fig. 4-10 LFCD1 after Bucket Removal, Shear cracks in the beam

(a) (b)

Fig. 4-11 LFCD1 after Bucket Removal (a) Concrete Spalling (b) Column and joint Cracks

Fig. 4-12 Typical Load-Displacement Curve for PBD Bents

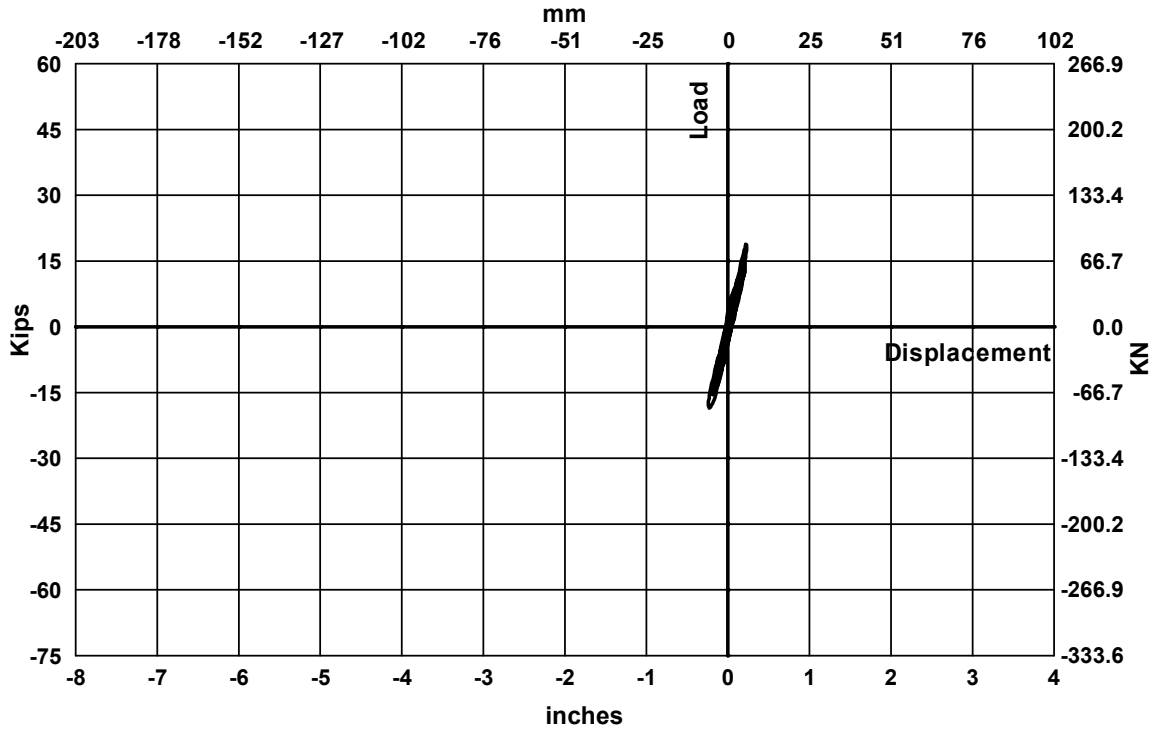

Fig. 4-13 Measured Load-Displacement Curve for LFCD1 at 0.15 times Sylmar

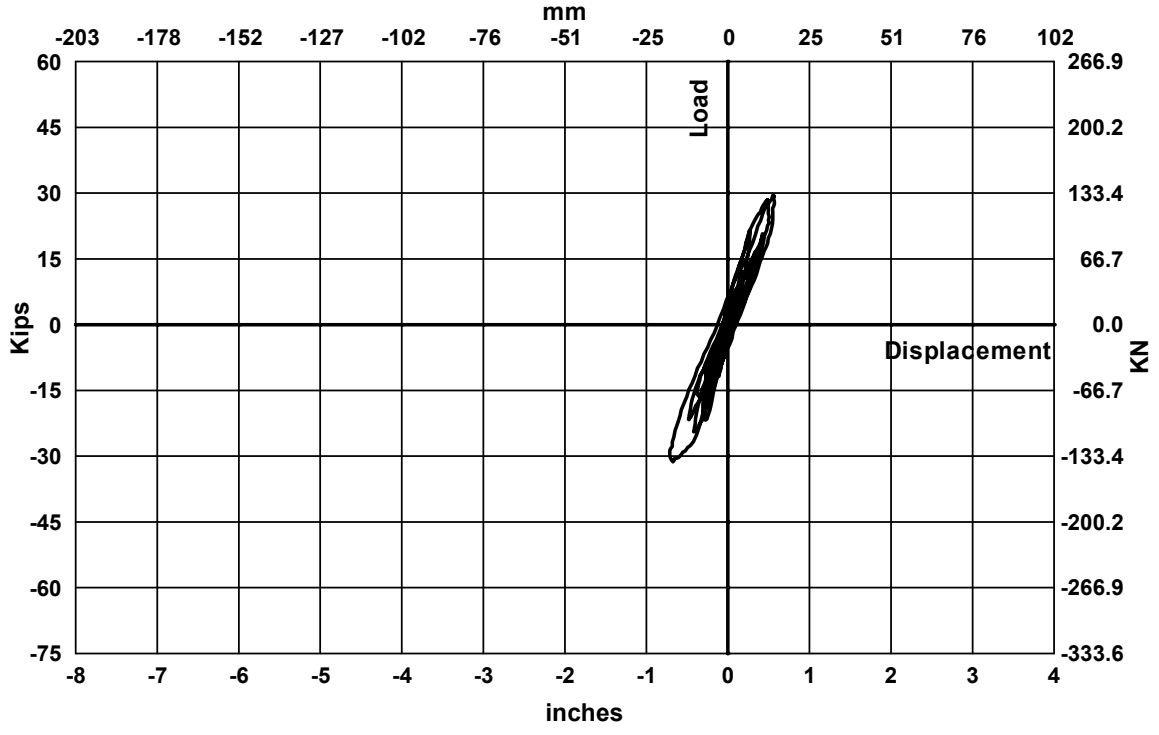

Fig. 4-14 Measured Load-Displacement Curve for LFCD1 at 0.5 times Sylmar

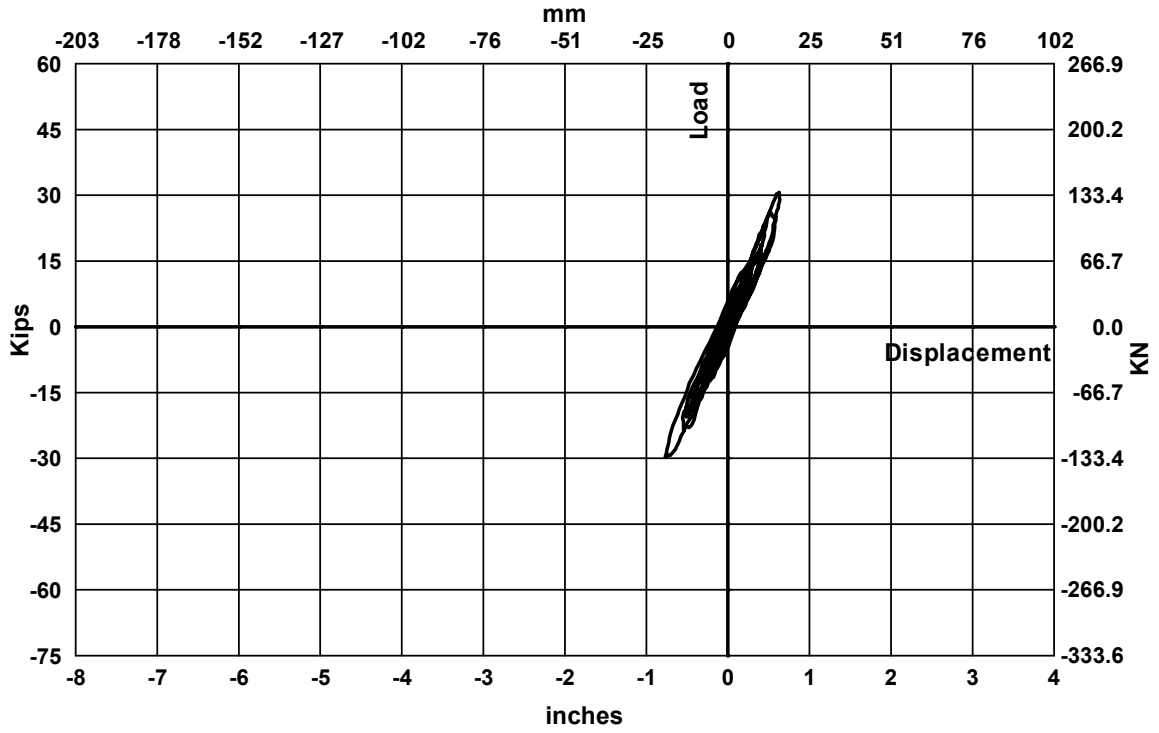

Fig. 4-15 Measured Load-Displacement Curve for LFCD1 at 0.75 times Sylmar

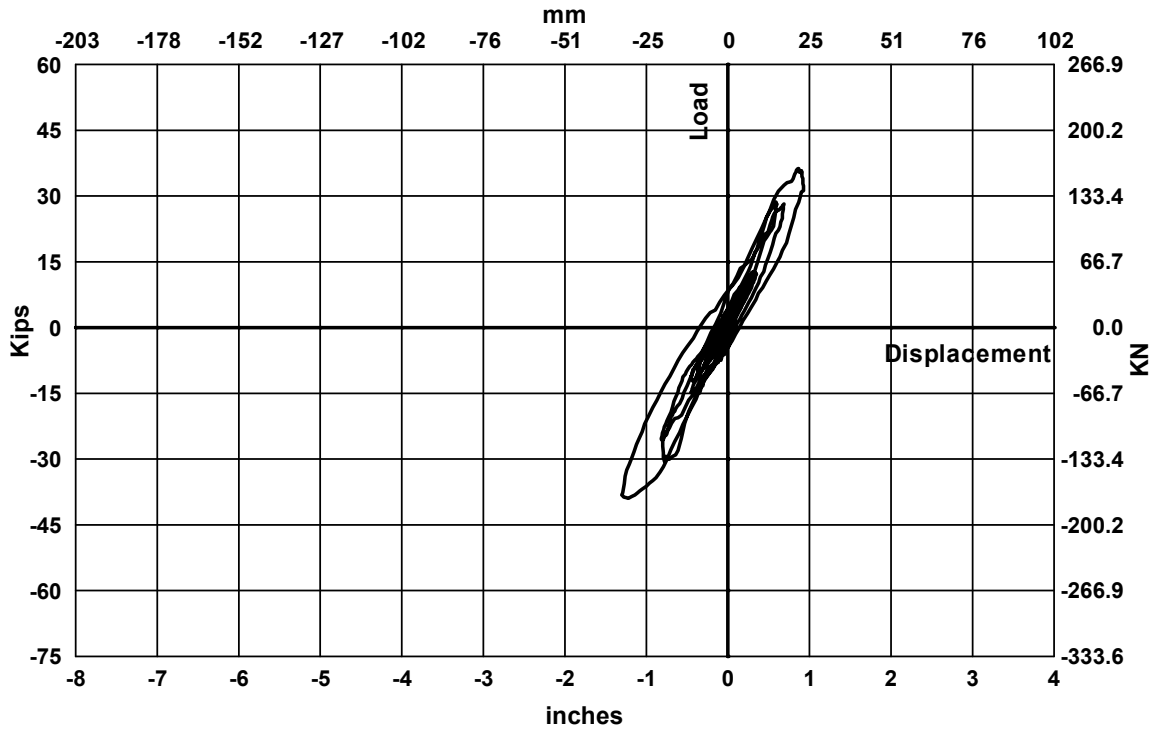

Fig. 4-16 Measured Load-Displacement Curve for LFCD1 at 1.0 times Sylmar

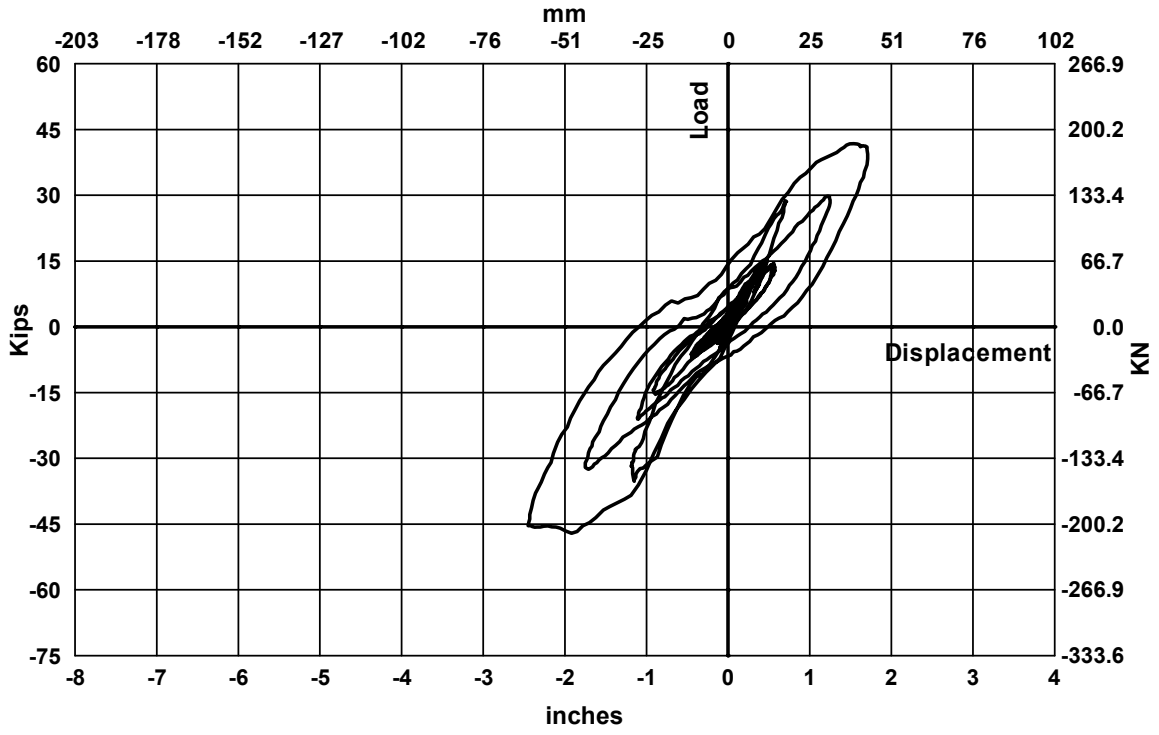

Fig. 4-17 Measured Load-Displacement Curve for LFCD1 at 1.25 times Sylmar

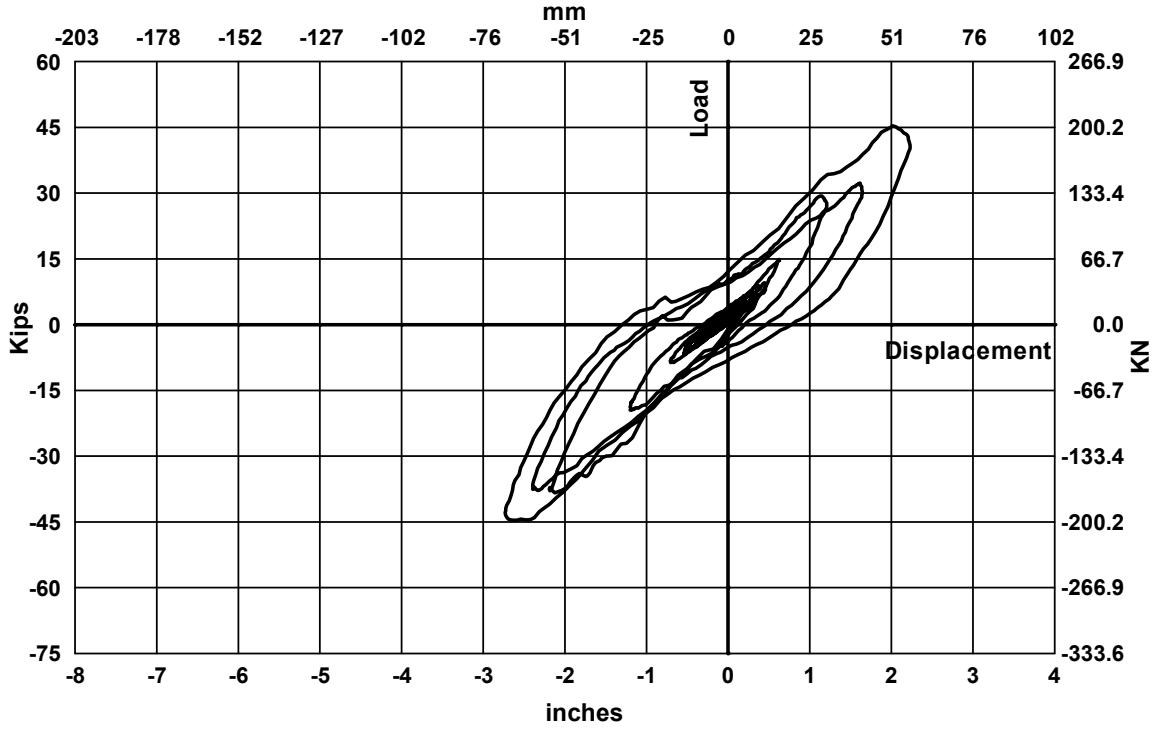

Fig. 4-18 Measured Load-Displacement Curve for LFCD1 at 1.5 times Sylmar

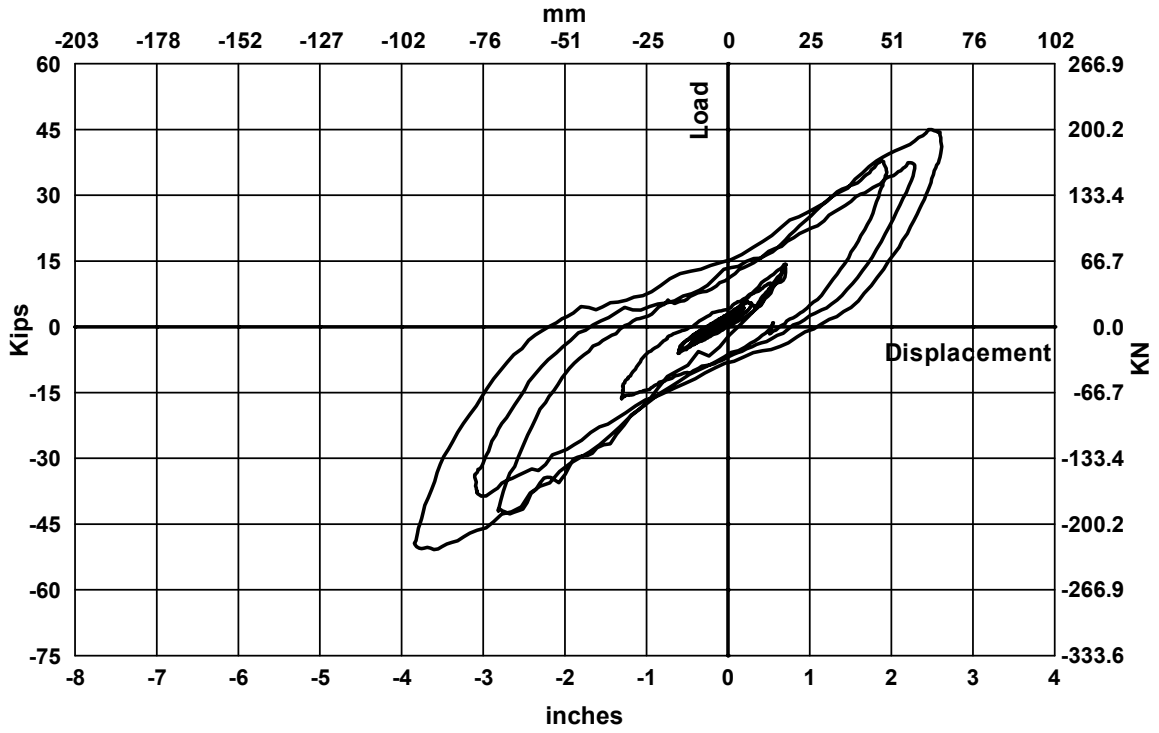

Fig. 4-19 Measured Load-Displacement Curve for LFCD1 at 1.75 times Sylmar

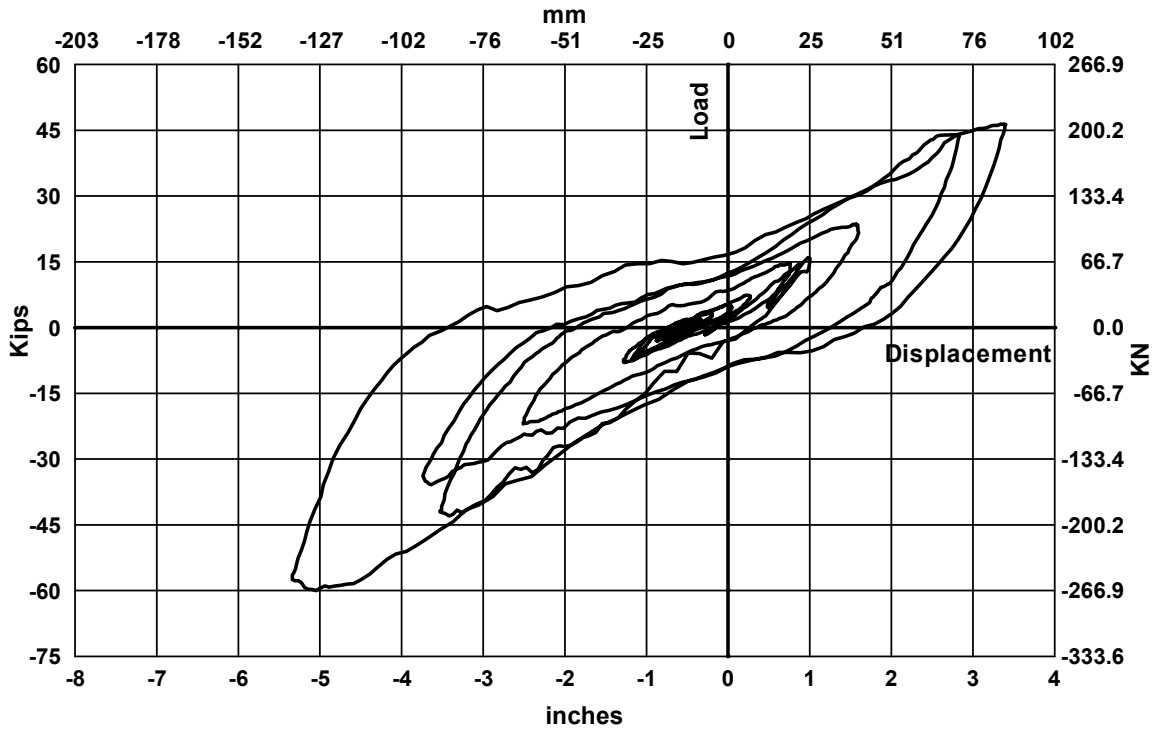

Fig. 4-20 Measured Load-Displacement Curve for LFCD1 at 2.0 times Sylmar

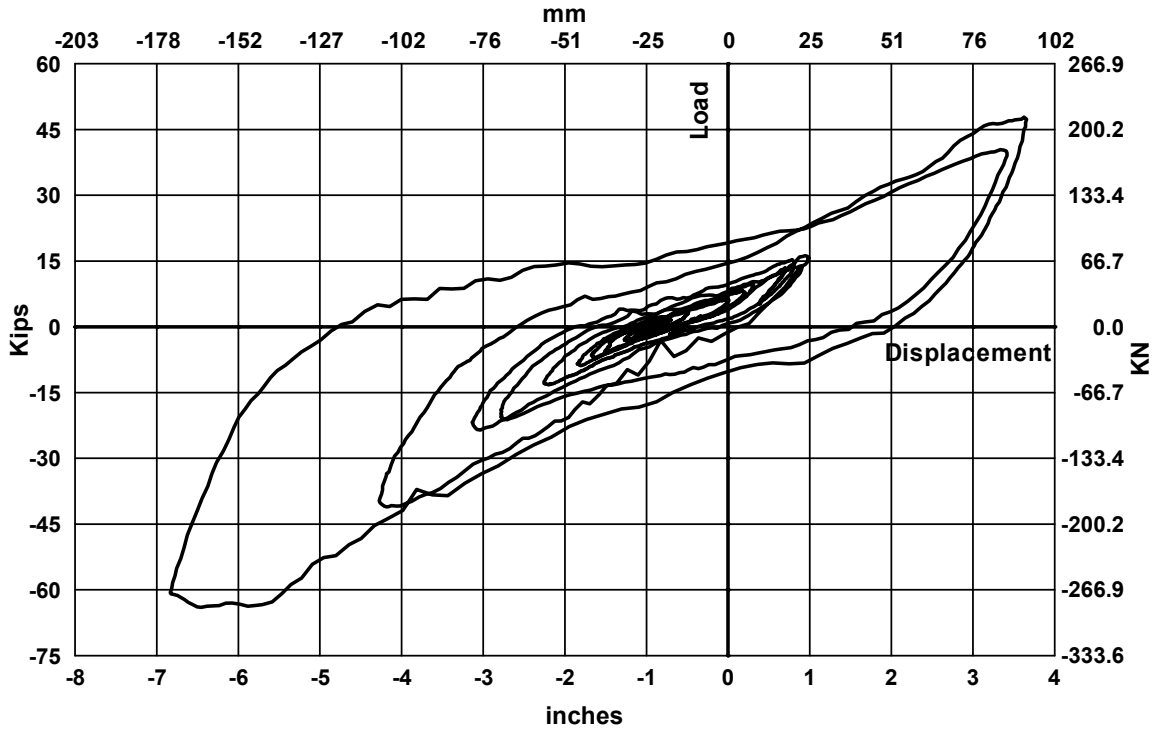

Fig. 4-21 Measured Load-Displacement Curve for LFCD1 at 2.125 times Sylmar

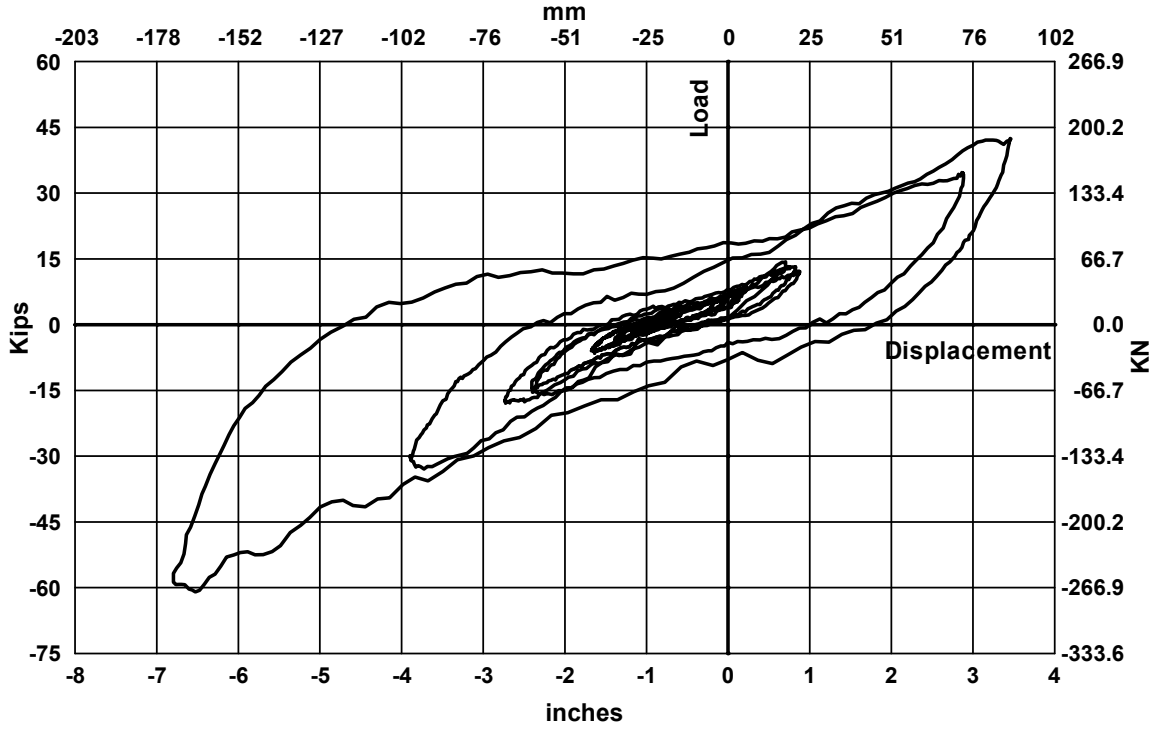

Fig. 4-22 Measured Load-Displacement Curve for LFCD1 at 1.75-2 times Sylmar

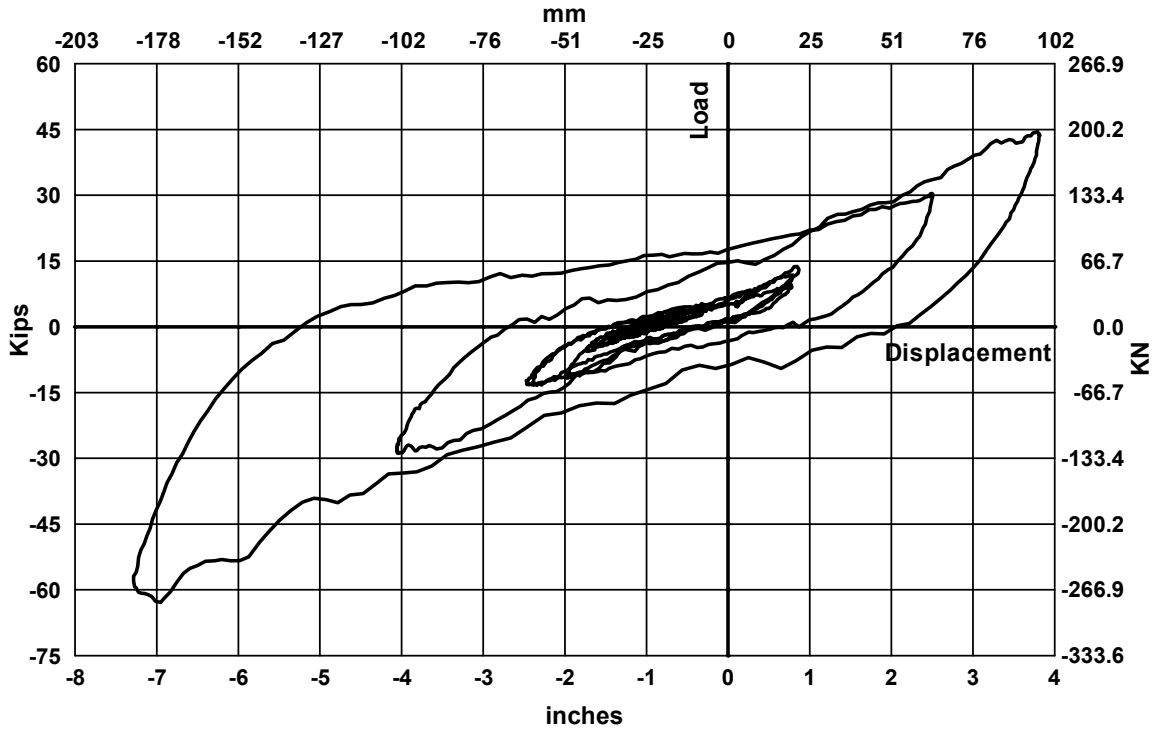

Fig. 4-23 Measured Load-Displacement Curve for LFCD1 at 1.75-3 times Sylmar

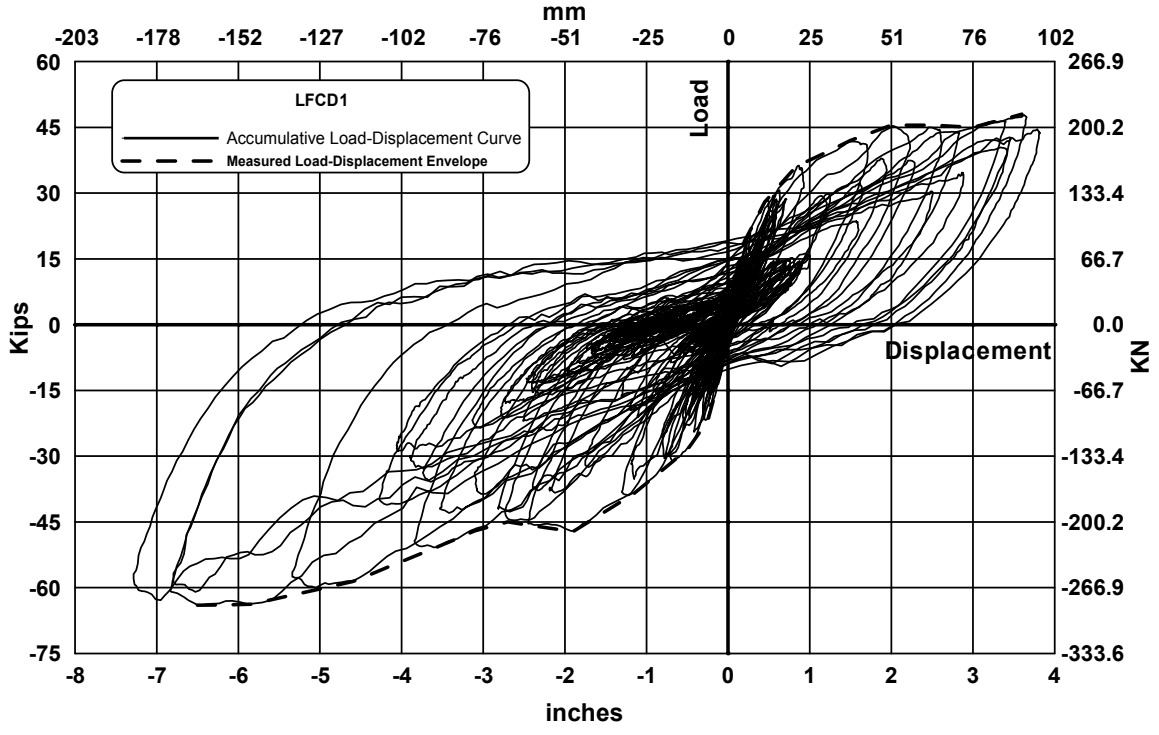

Fig. 4-24 Accumulative Measured Load-Displacement Curve for LFCD1

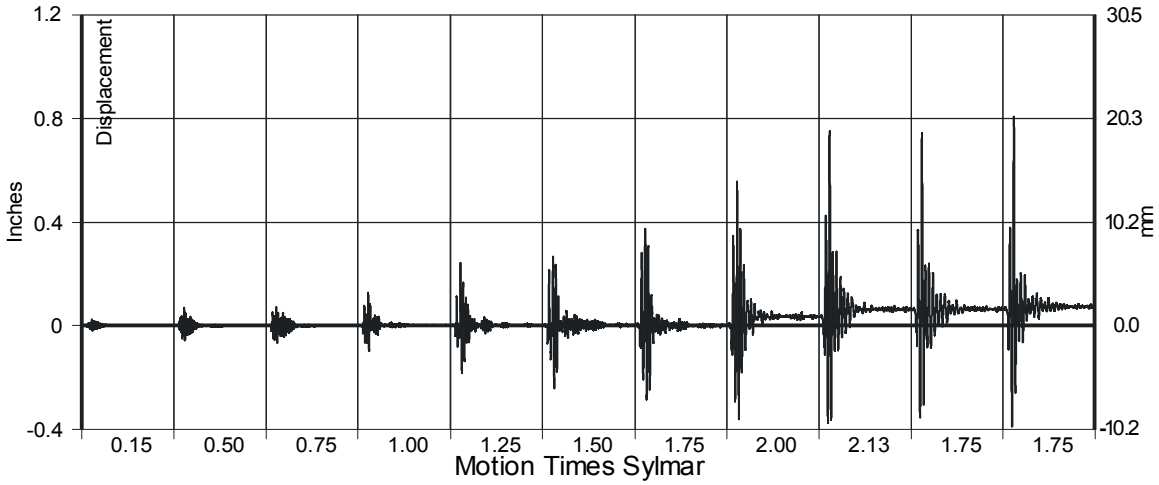

Fig. 4-25 Measured Base Hinge Displacement for East Column

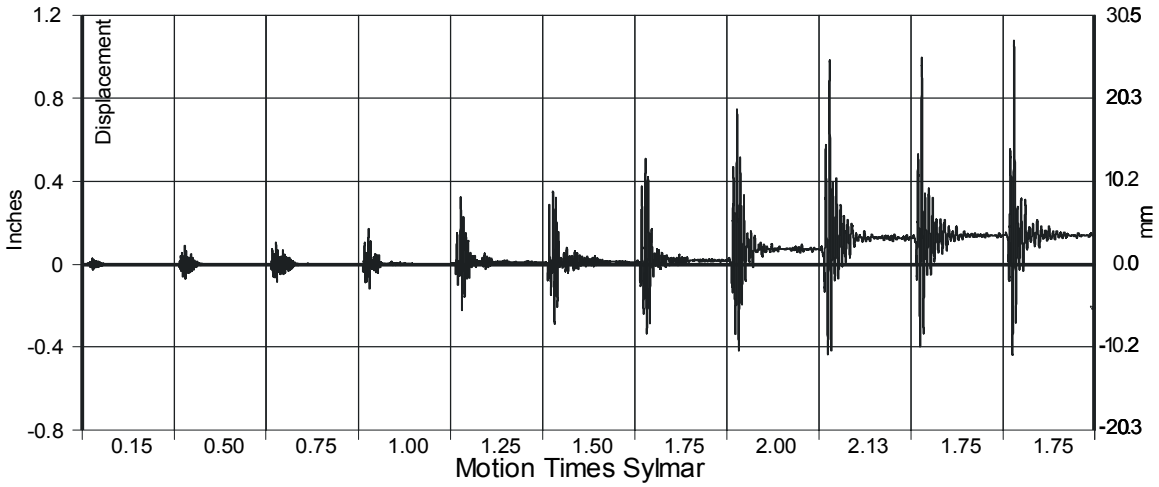

Fig. 4-26 Measured Base Hinge Displacement for West Column

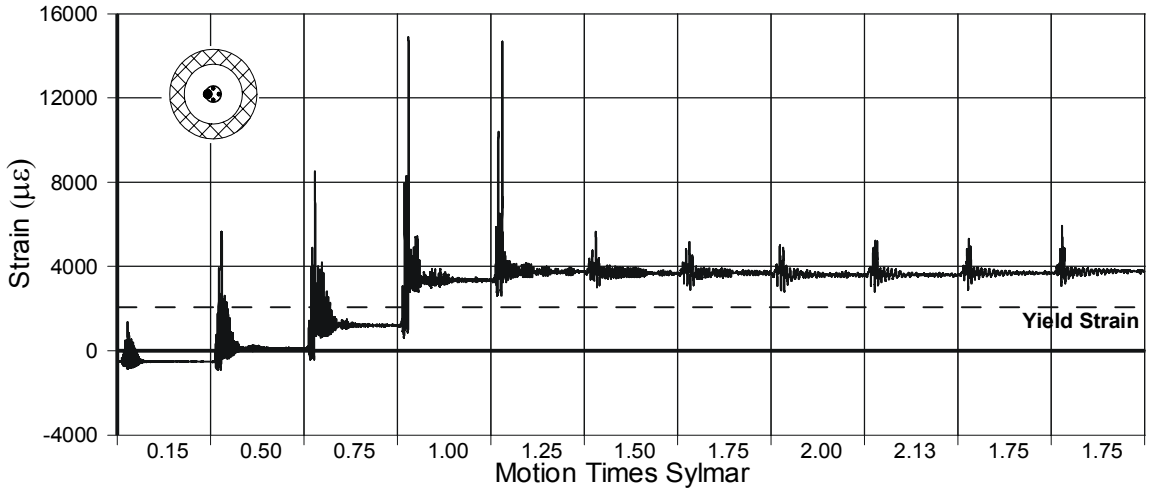

Fig. 4-27 Measured Strain at East Column Dowels

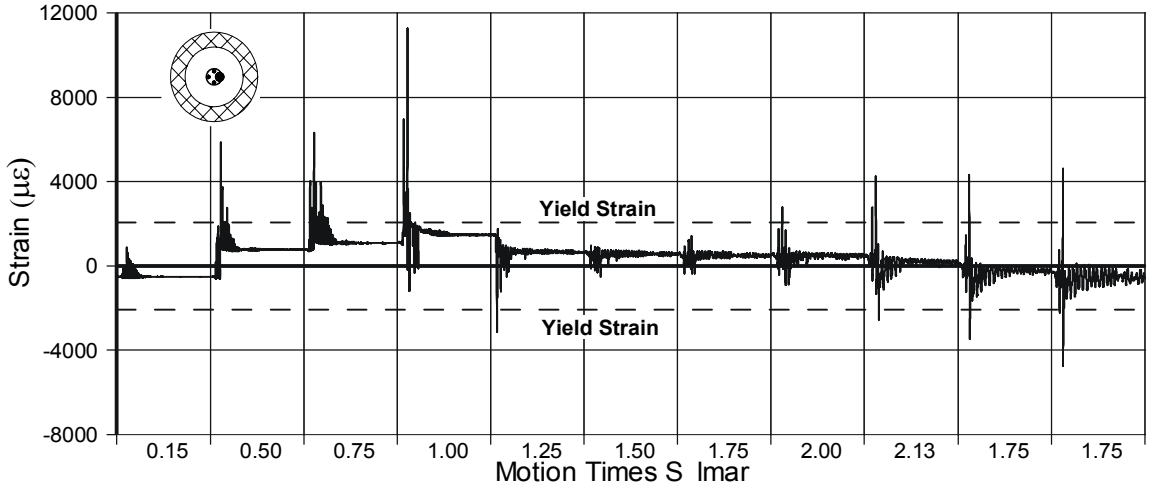

Fig. 4-28 Measured Strain at West Column Dowels

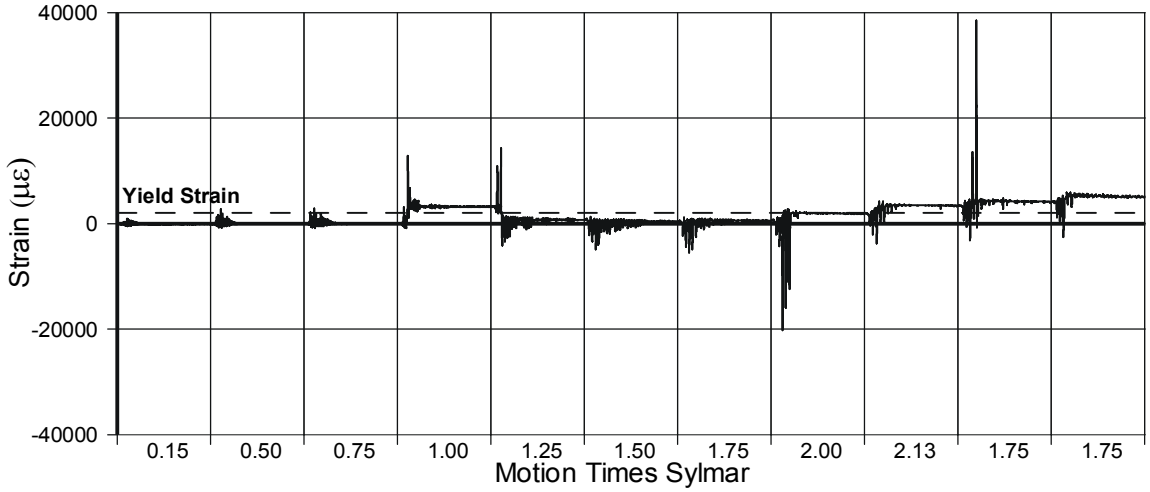

Fig. 4-29 Measured Strain for Longitudinal Column Reinforcement, Gauge 71

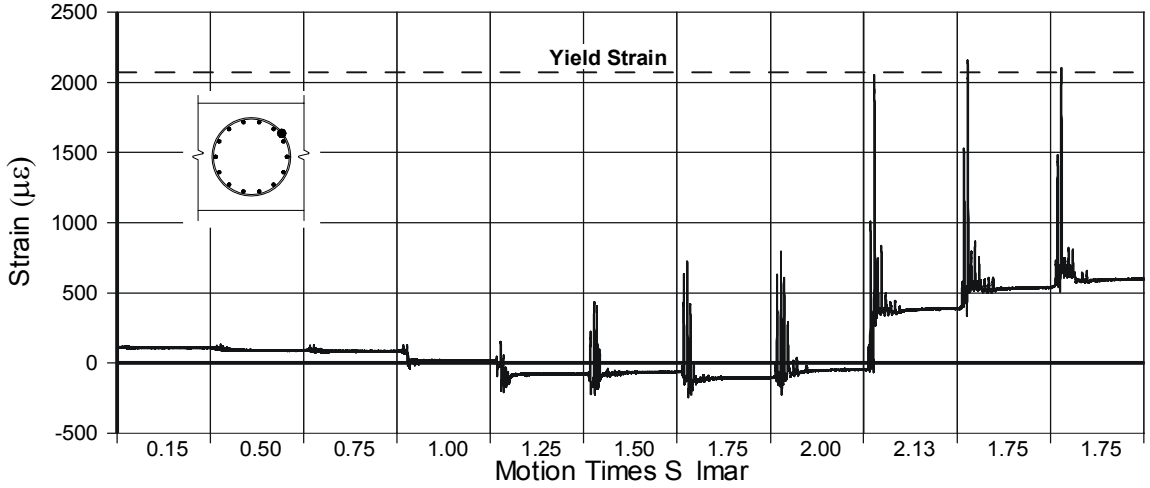

Fig 4-30 Measured Strain for Column Spirals, Gauge 82

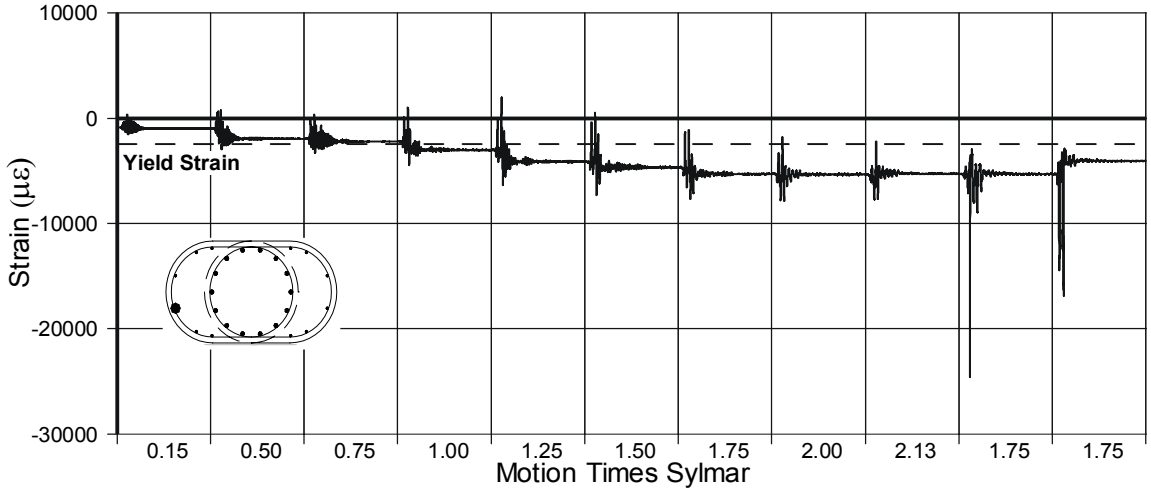

Fig. 4-31 Measured Strain for Flare Longitudinal Reinforcement, Gauge 94

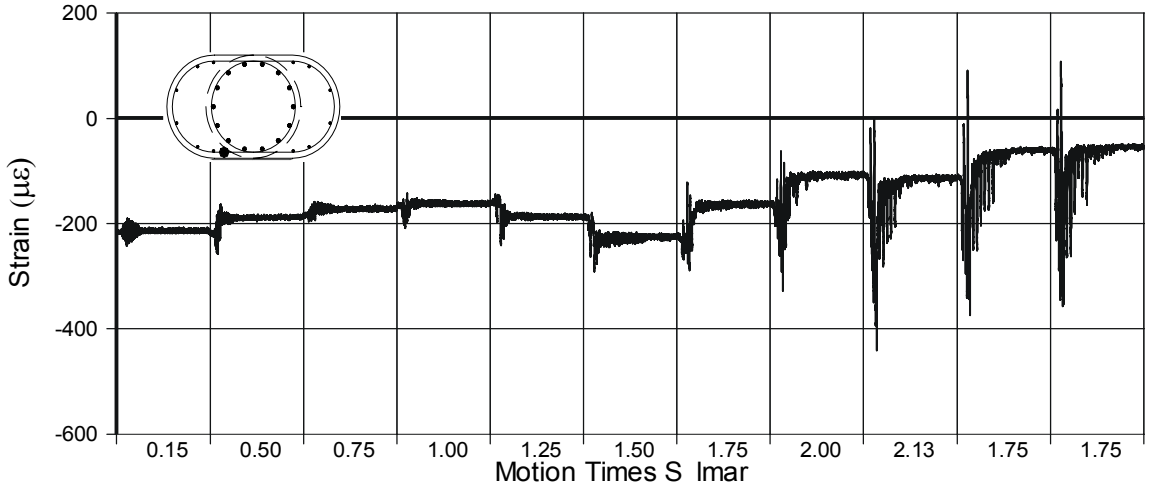

Fig. 4-32 Measured Strain for Flare Hoops, Gauge 123

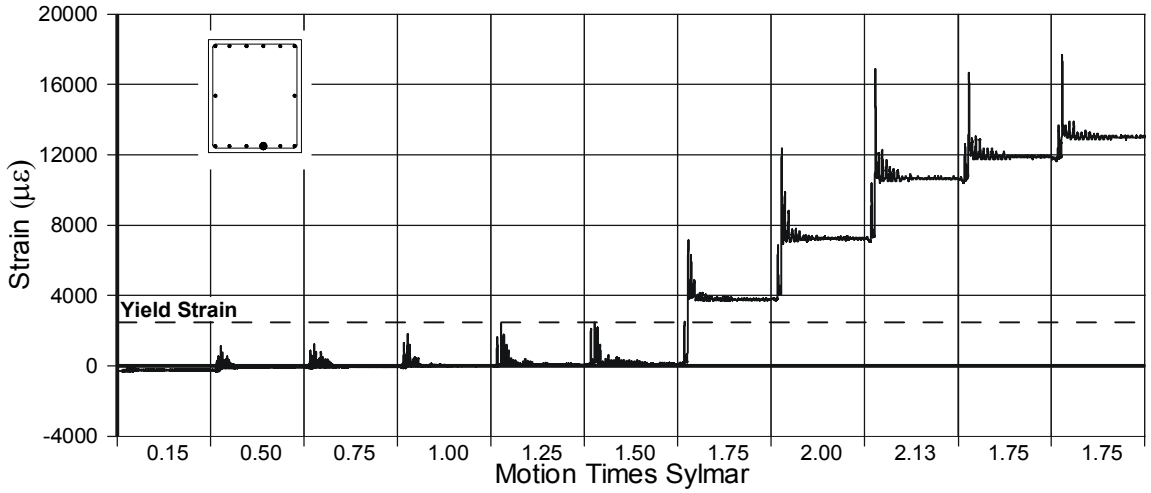

Fig. 4-33 Measured Strain for Beam's Bottom reinforcement, Gauge 141

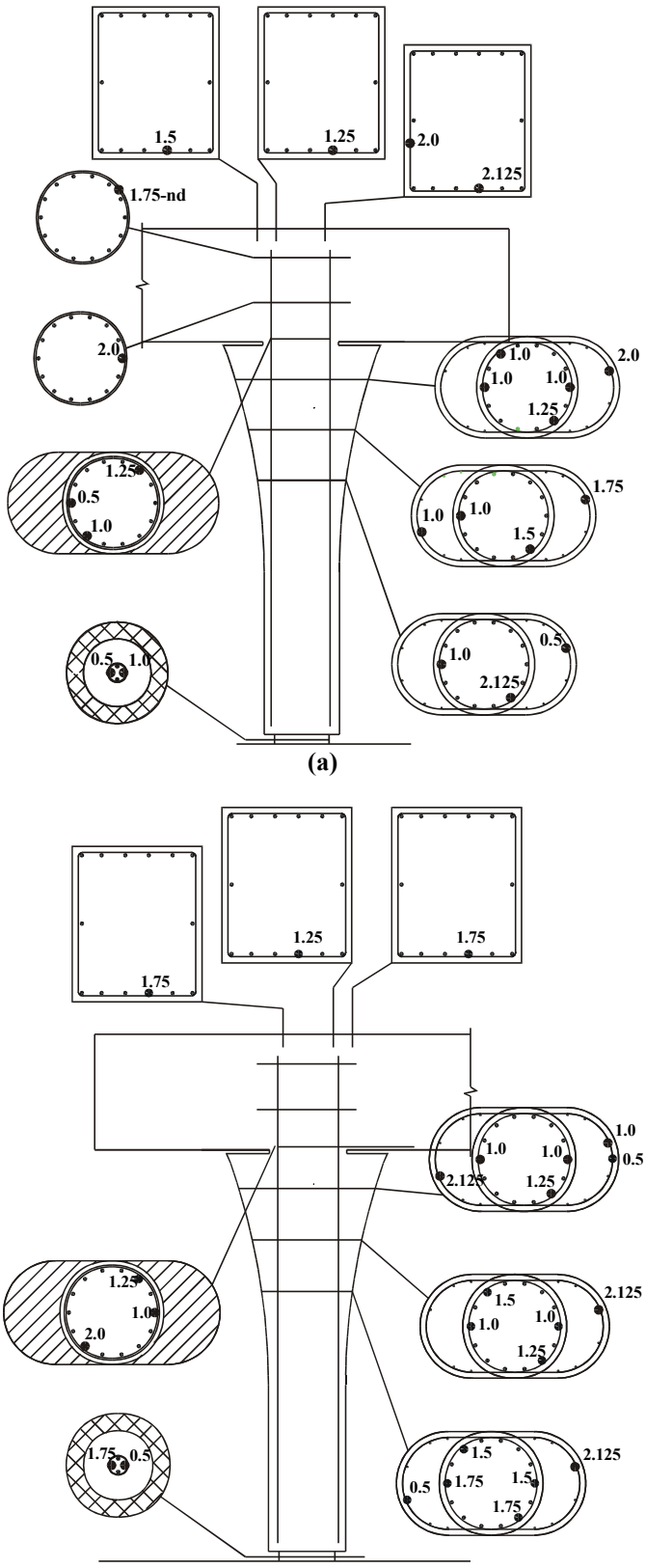

Fig. 4-34 Yield Distribution in LFCD1 (a) East Column (b) West Column

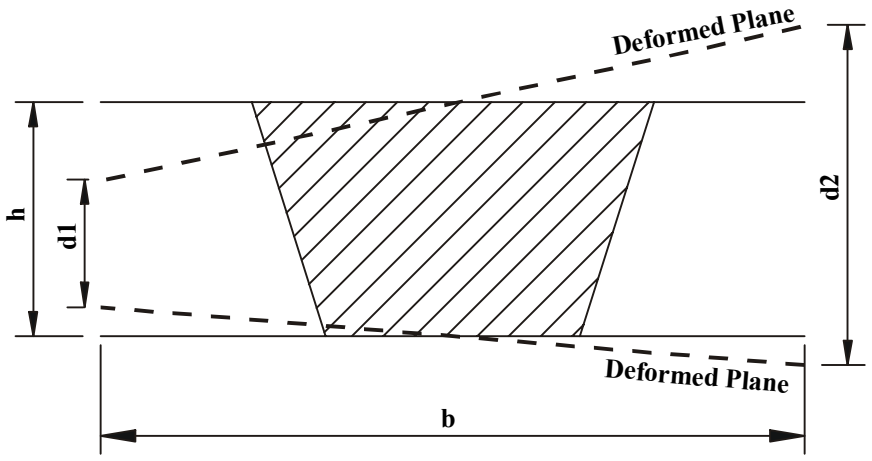

Fig. 4-35 Curvature Calculation

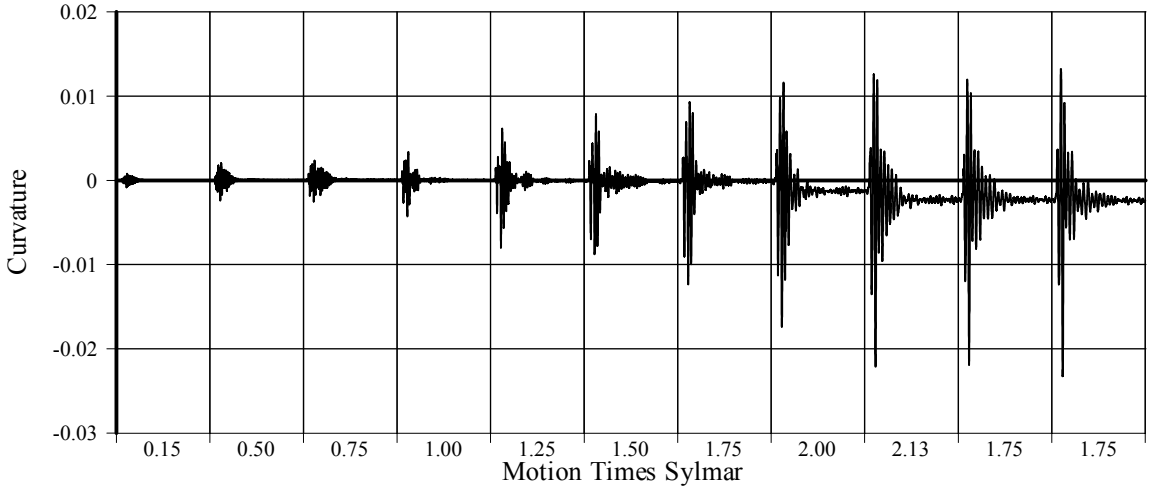

Fig. 4-36 Measured Curvature at Section 1 of East Column for LFCD1

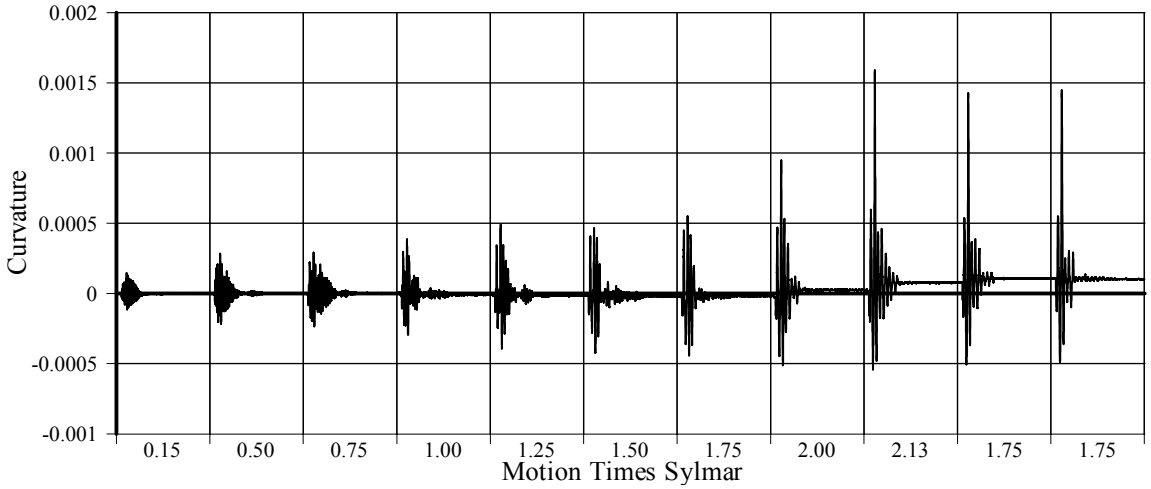

Fig. 4-37 Measured Curvature at Section 2 of East Column for LFCD1

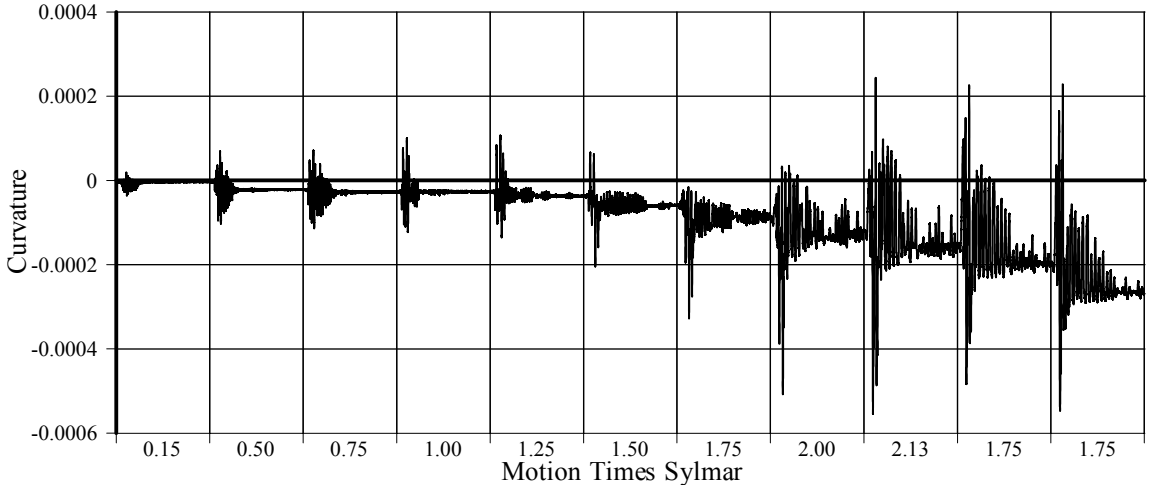

Fig. 4-38 Measured Curvature at Section 3 of East Column for LFCD1

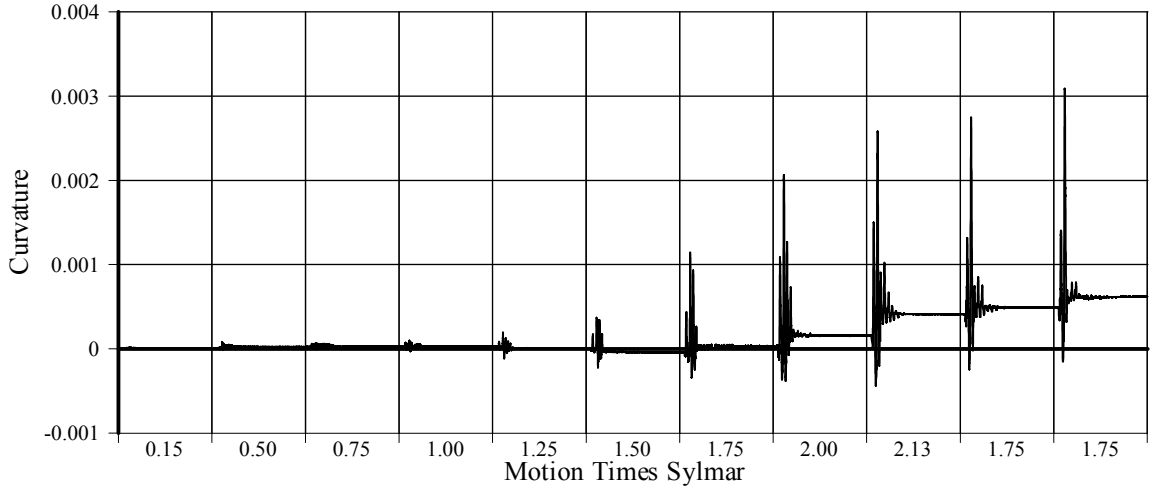

Fig. 4-39 Measured Curvature at Section 4 of East Column for LFCD1

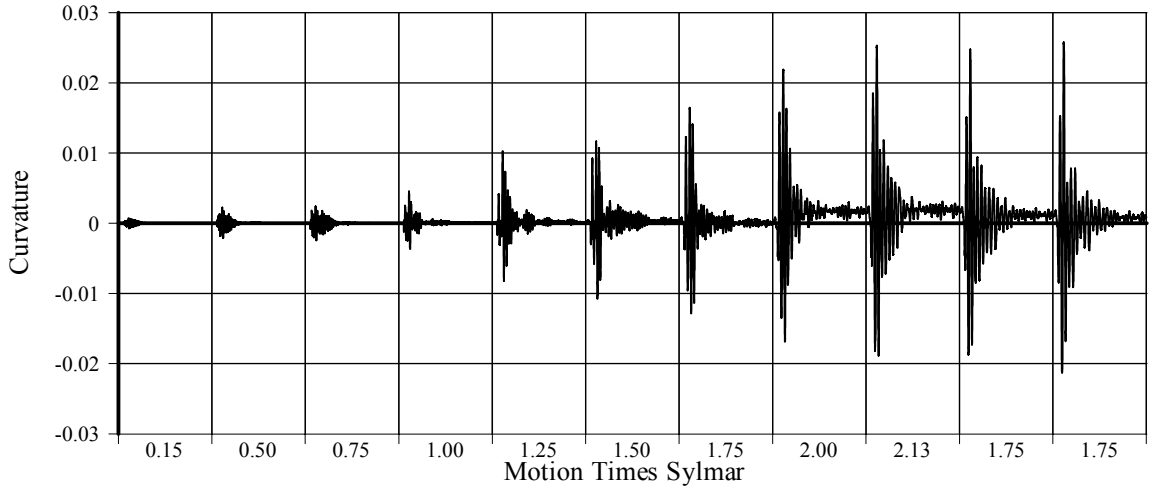

Fig. 4-40 Measured Curvature at Section 5 of East Column for LFCD1

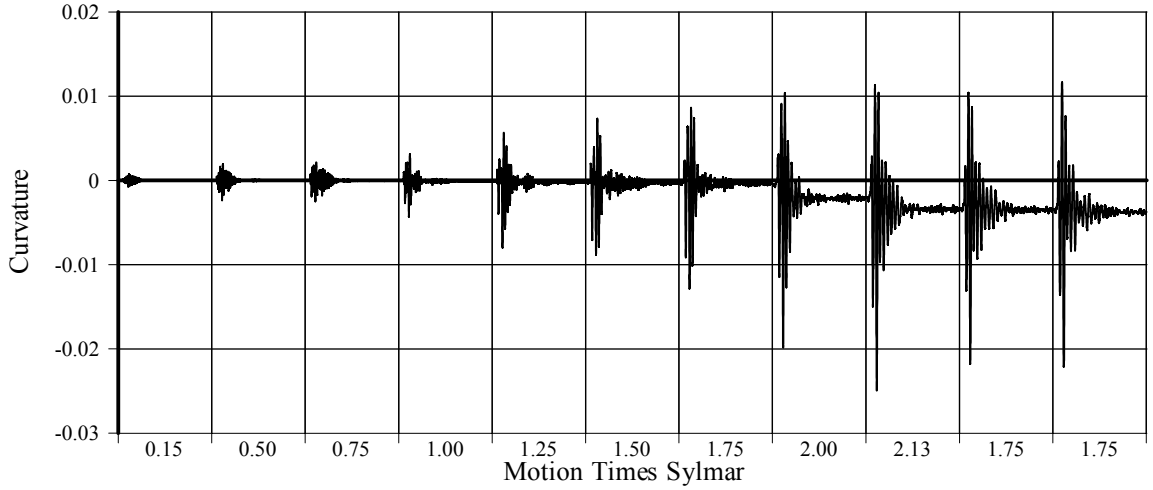

Fig. 4-41 Measured Curvature at Section 1 of West Column for LFCD1

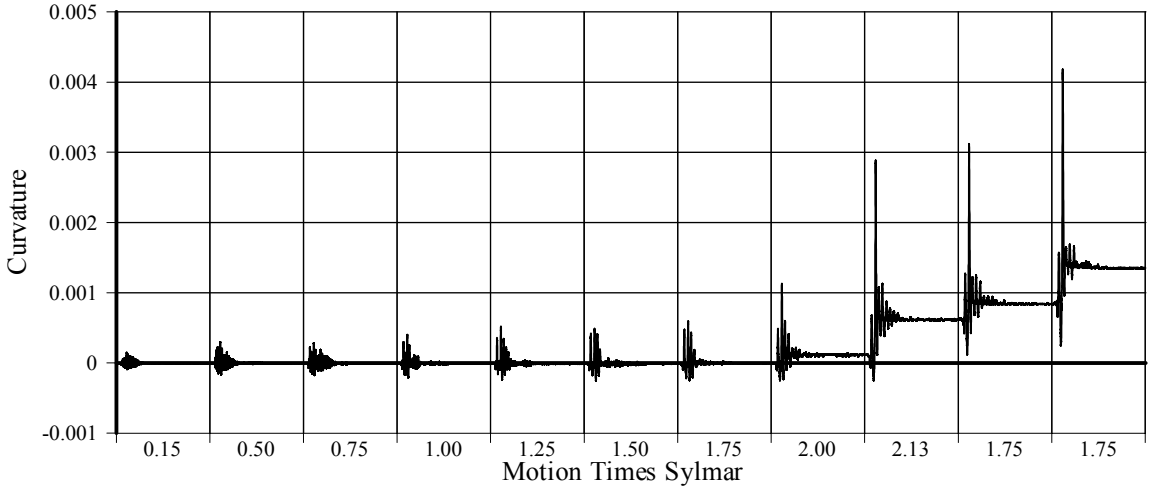

Fig. 4-42 Measured Curvature at Section 2 of West Column for LFCD1

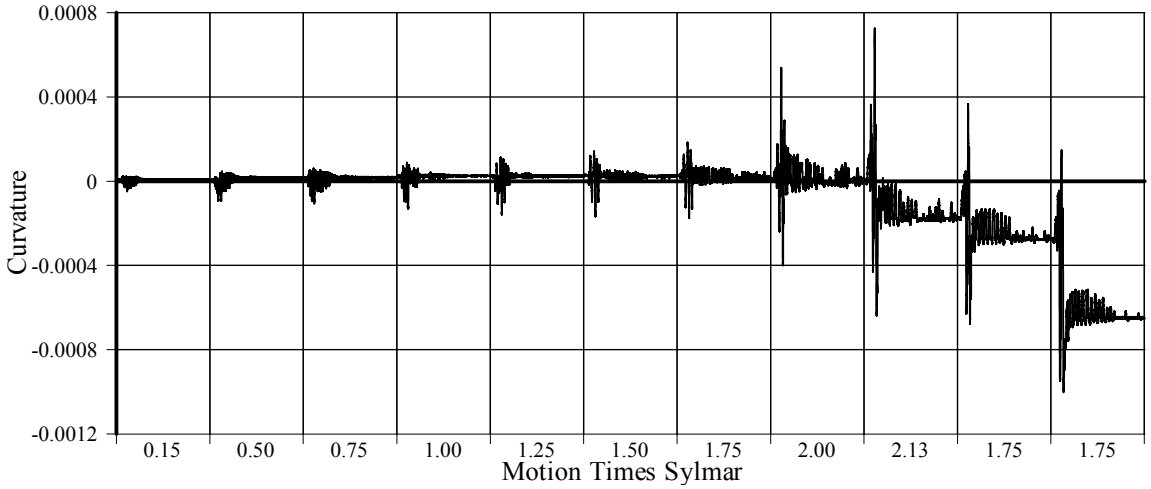

Fig. 4-43 Measured Curvature at Section 3 of West Column for LFCD1

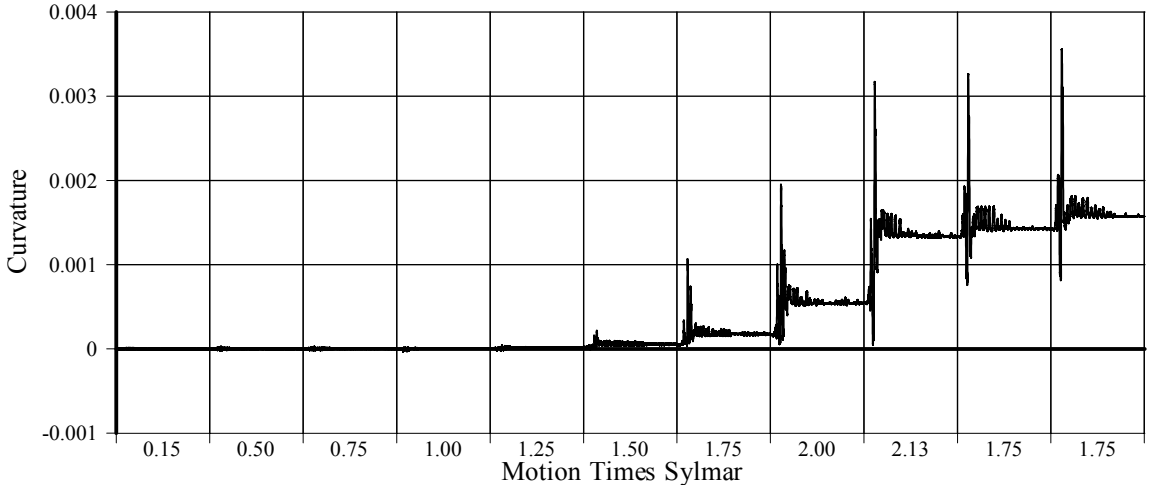

Fig. 4-44 Measured Curvature at Section 4 of West Column for LFCD1

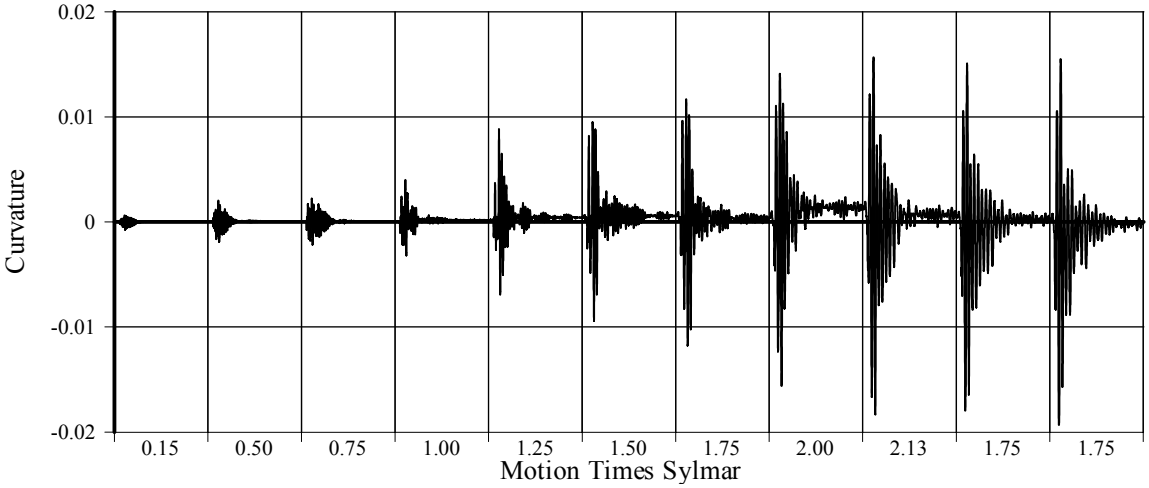

Fig. 4-45 Measured Curvature at Section 5 of West Column for LFCD1

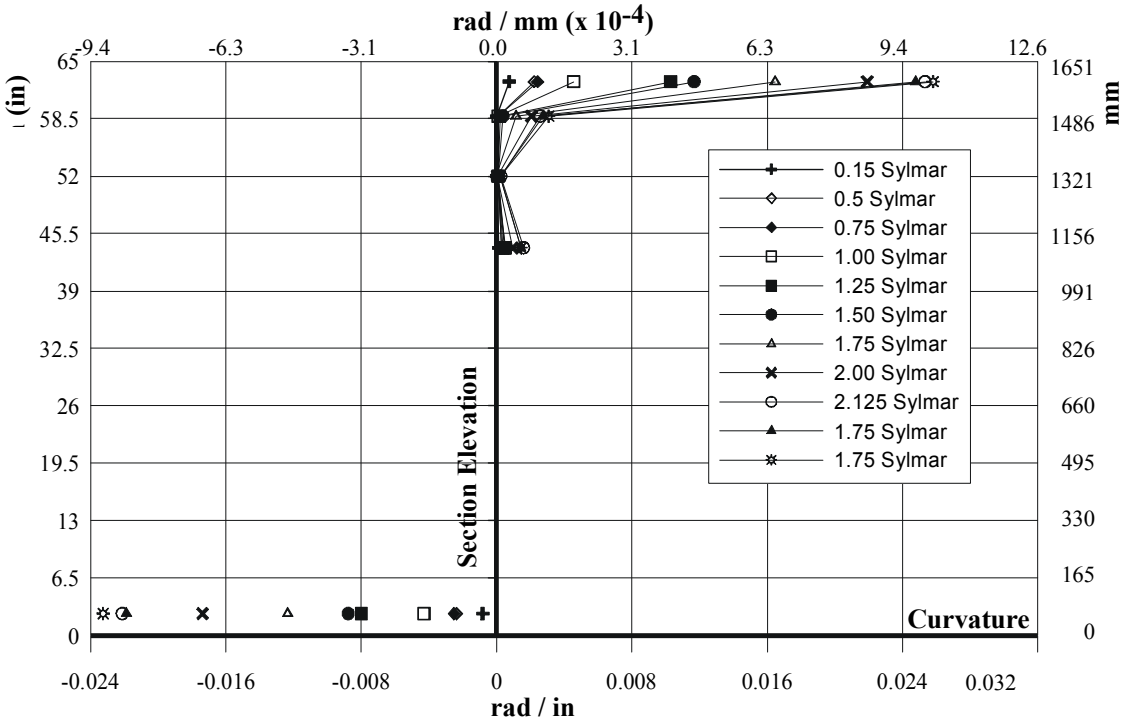

Fig. 4-46 Measured Maximum Curvature for East Column of LFCD1

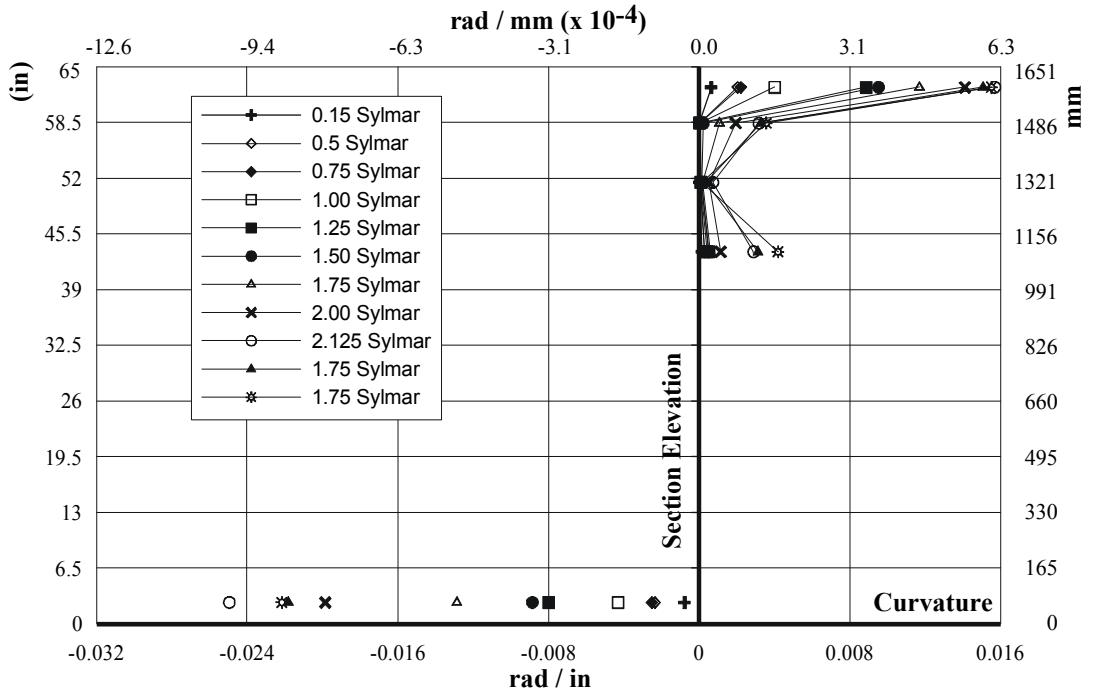

Fig. 4-47 Measured Maximum Curvature for West Column of LFCD1

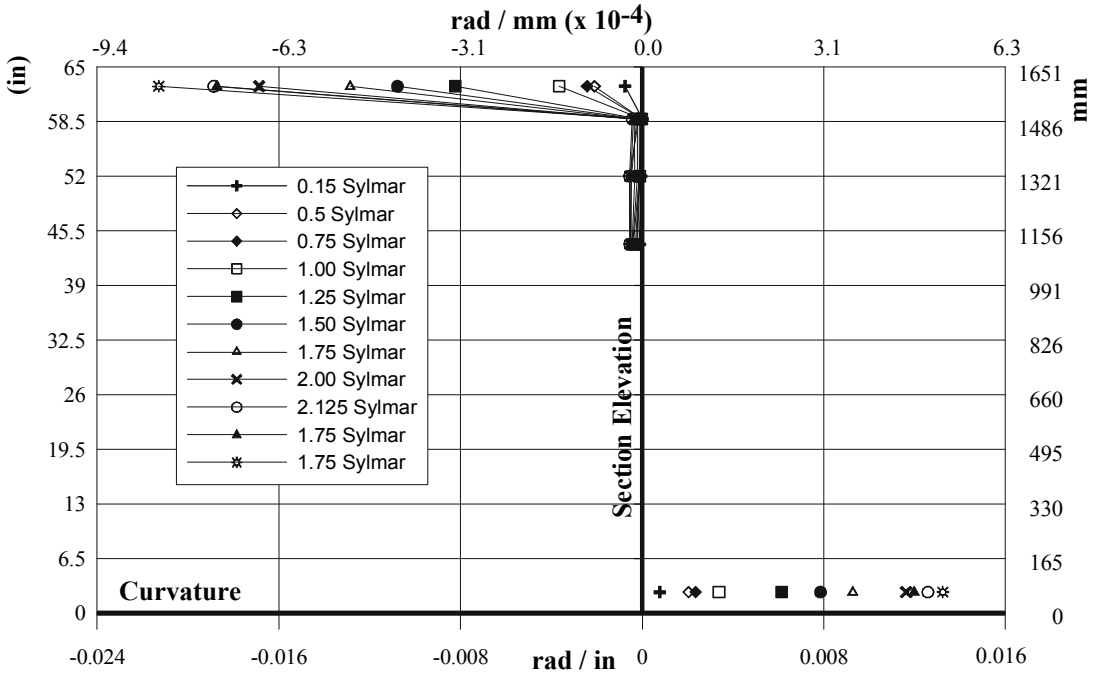

Fig. 4-48 Measured Minimum Curvature for East Column of LFCD1

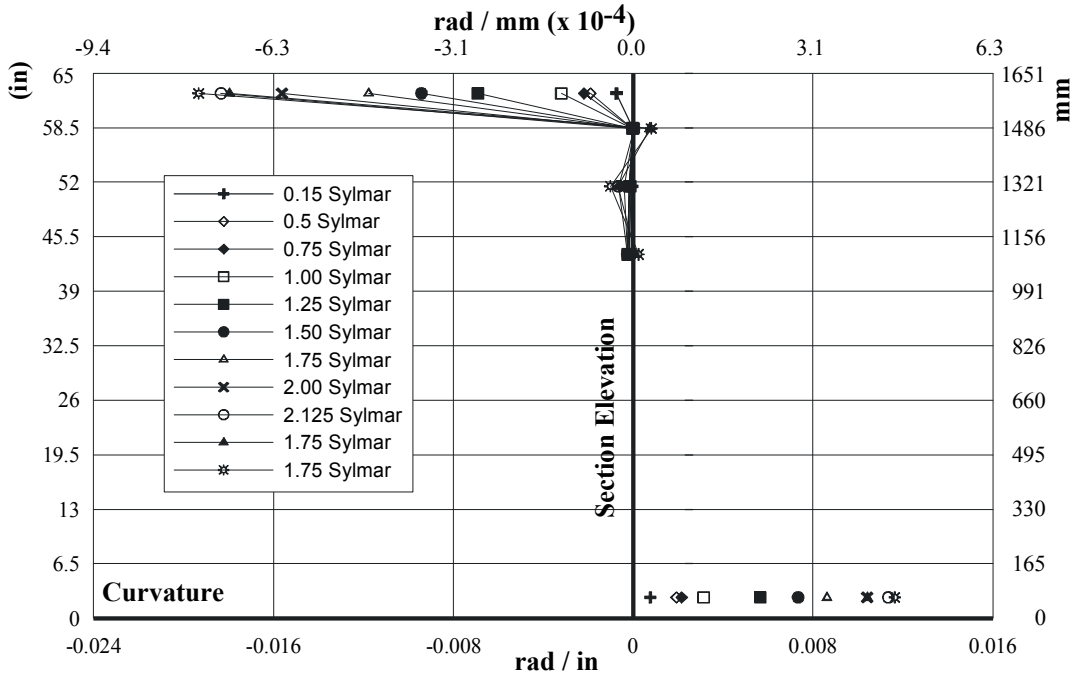

Fig. 4-49 Measured Minimum Curvature for West Column of LFCD1

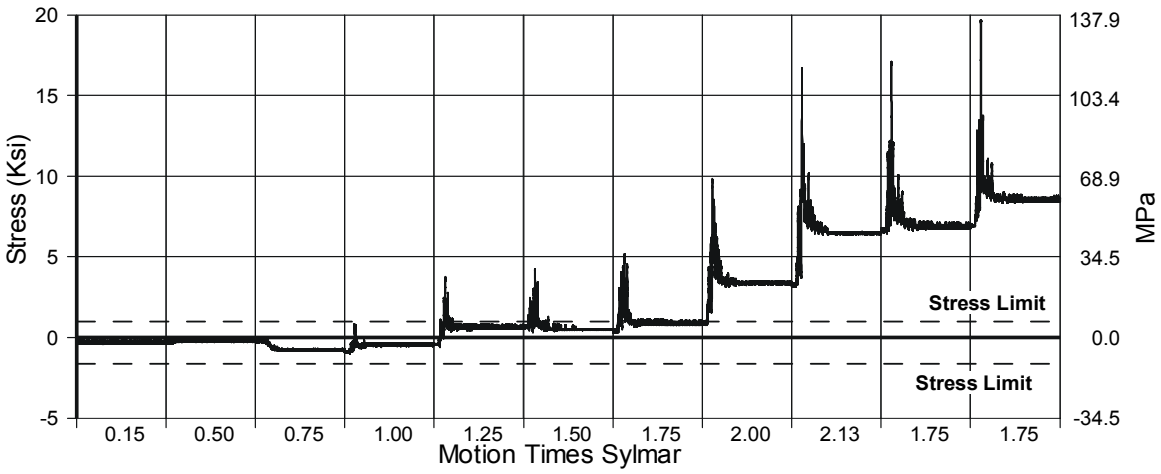

Fig. 4-50 Principal Stress (σ_1) in East Beam-Column Connection for LFCD1

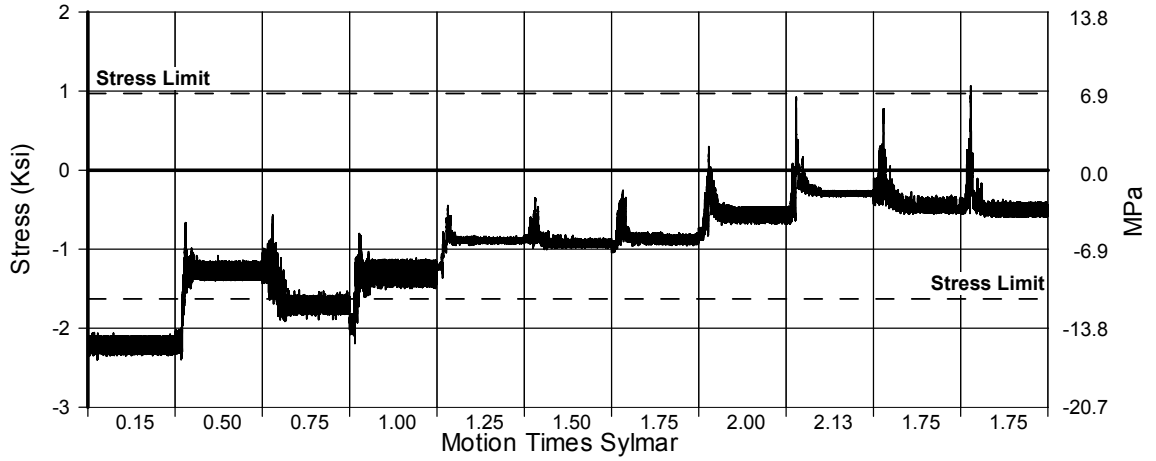

Fig. 4-51 Principal Stress (σ_2) in East Beam-Column Connection for LFCD1

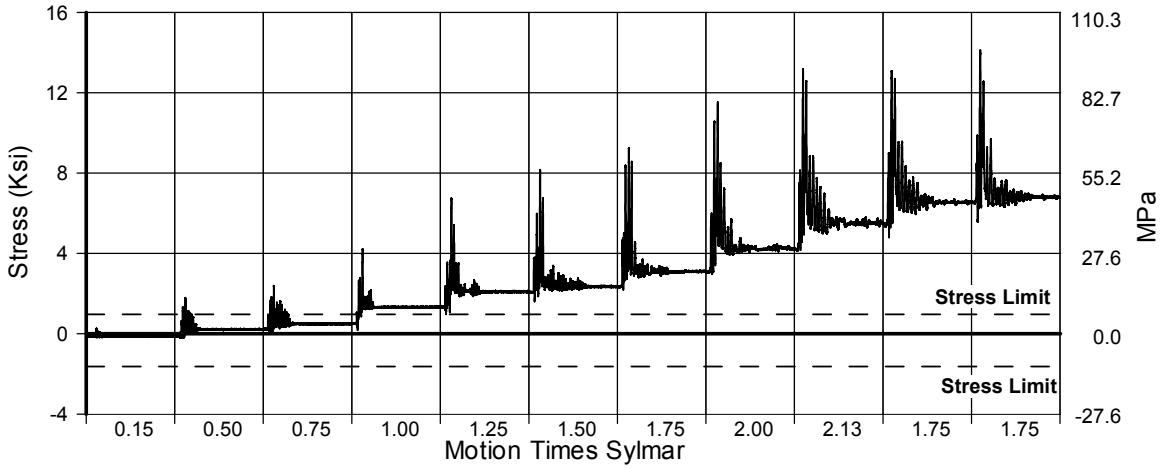

Fig. 4-52 Principal Stress (σ_1) in West Beam-Column Connection for LFCD1

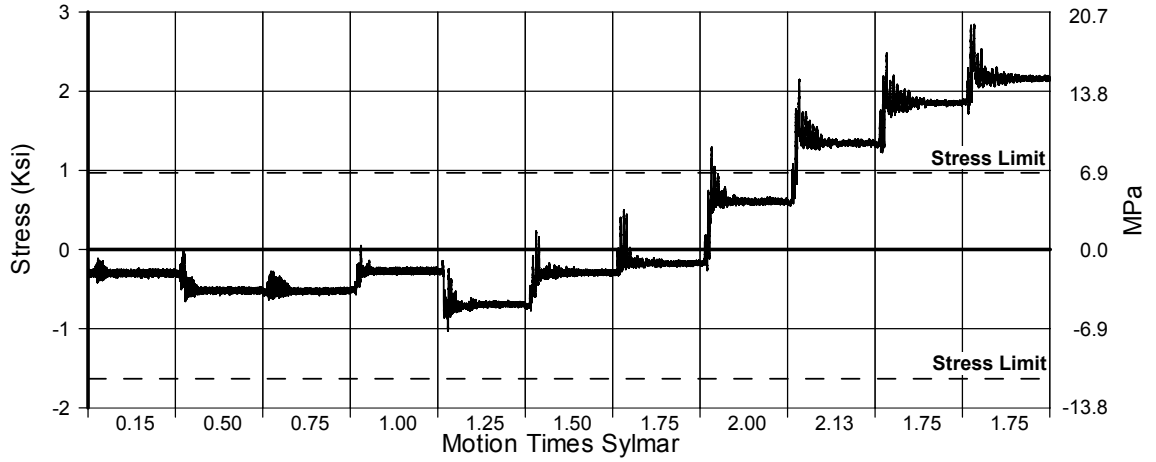

Fig. 4-53 Principal Stress (σ_2) in West Beam-Column Connection for LFCD1

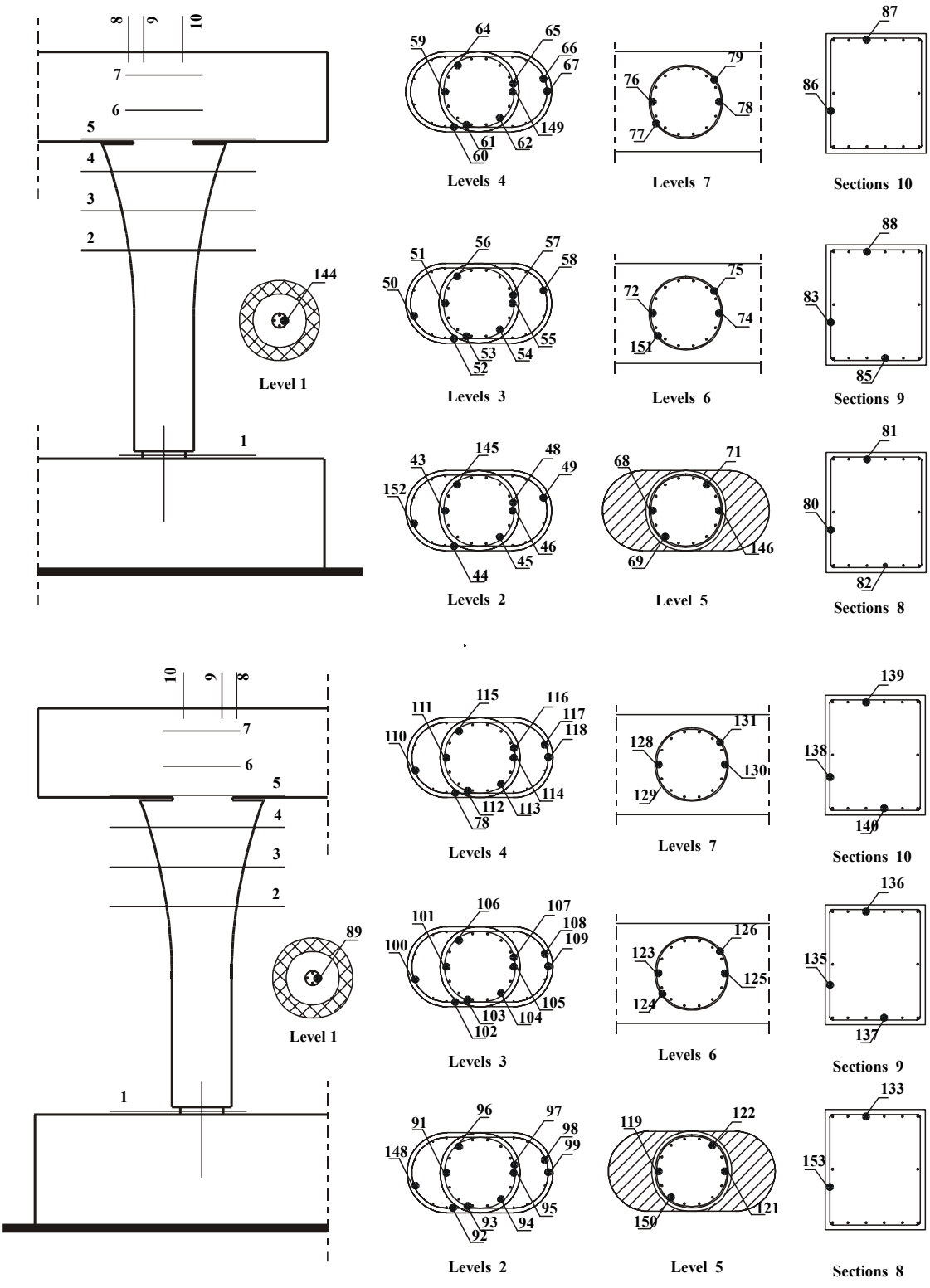

Fig. 4-54 LFCD2, Strain Gauge Identification Numbering

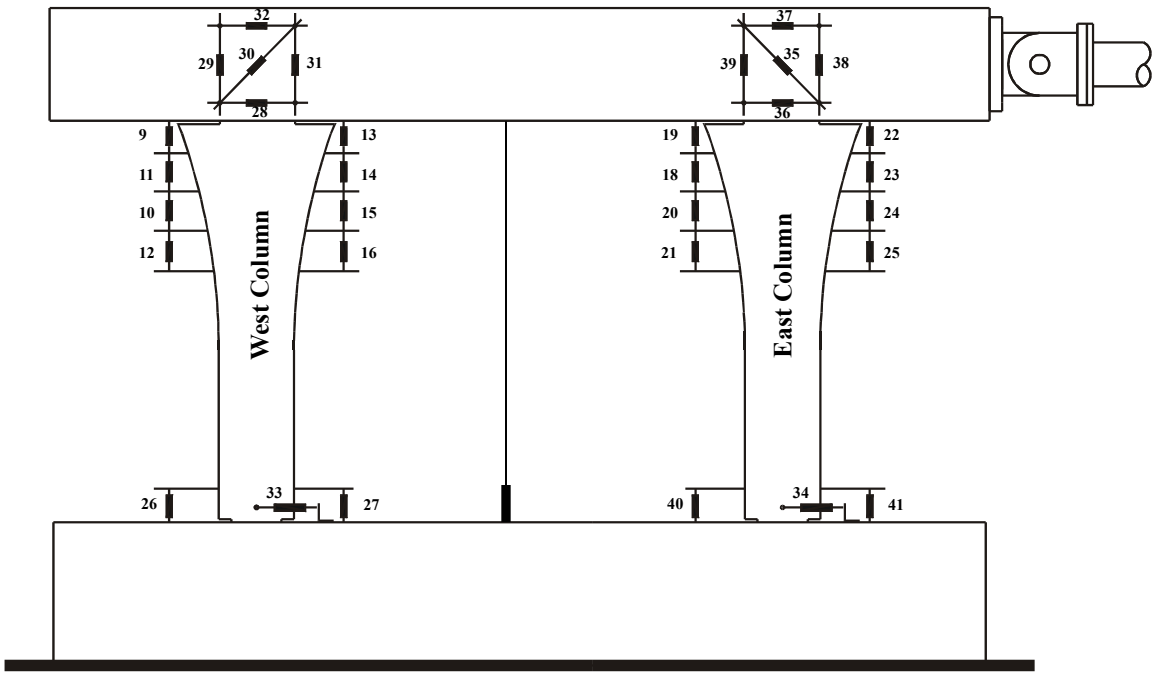

Fig. 4-55 LFCD2, Displacement Transducers Numbering

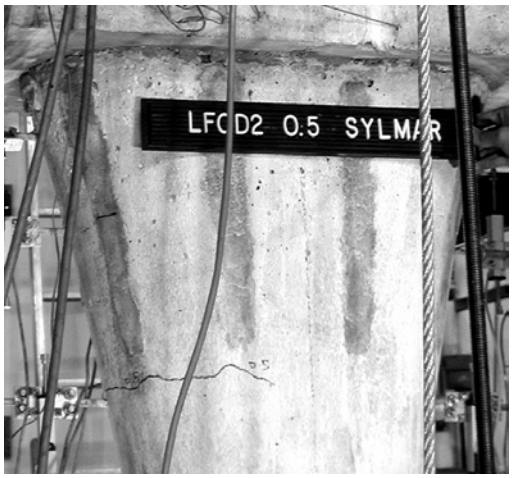

(a)

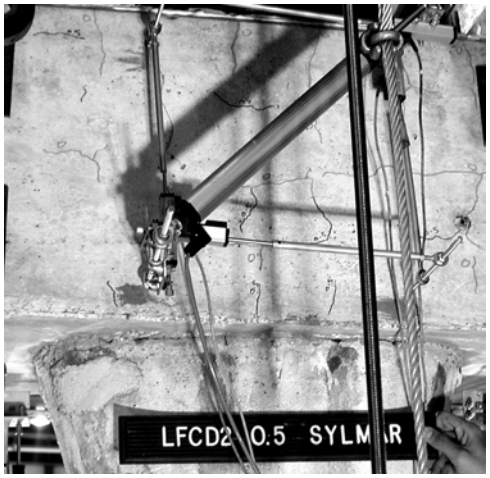

(b)

(c)

Fig. 4-56 LFCD2 at 0.5 Times Sylmar (a) Flare Crack (b) Joint Crack (c) Flare Crack

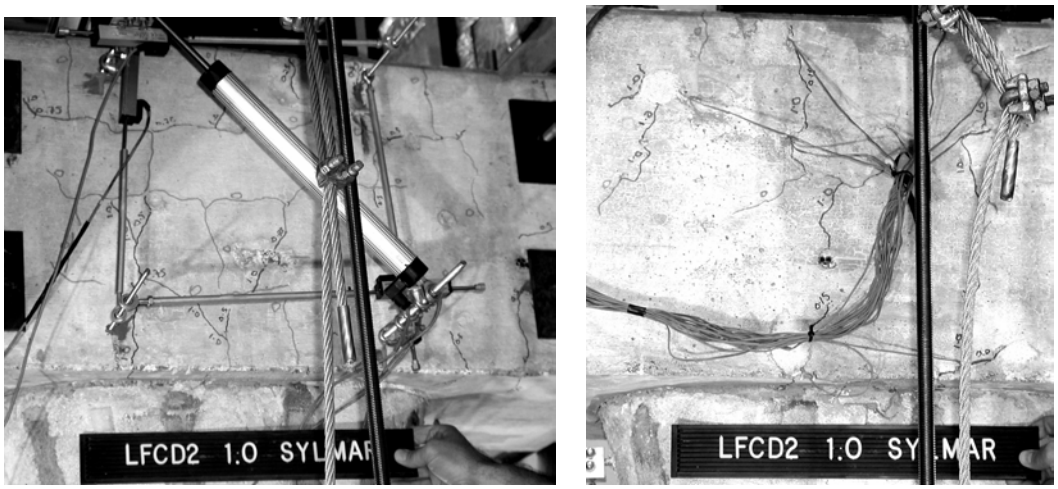

(a)

(b)

Fig. 4-57 LFCD2 at 1.0 Times Sylmar (a) Joint Crack (b) Column Crack

(a) (b)

(c) (d)

Fig. 4-58 LFCD2 at 1.25 Times Sylmar (a) Concrete Spalling (b) Base Hinge Spalling (c) Joint Crack (d) Column Crack

(a)

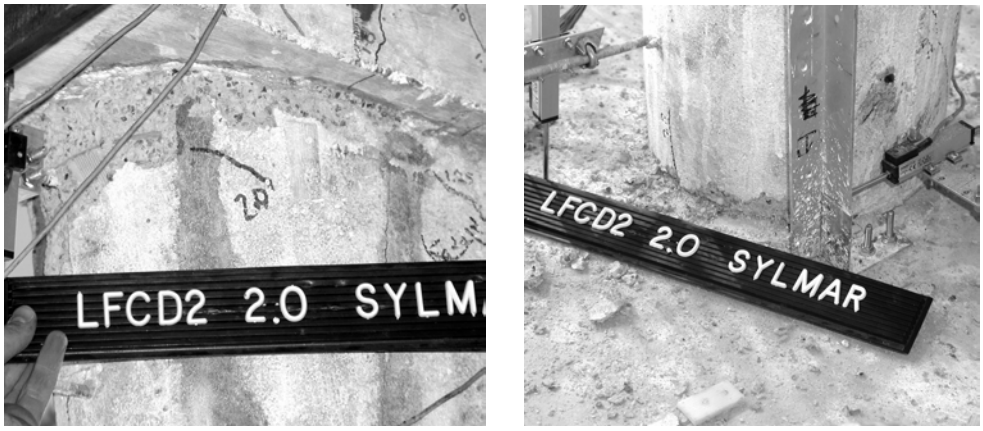

(b)

Fig. 4-59 LFCD2 at 2.0 Times Sylmar (a) Joint Crack (b) Column Crack

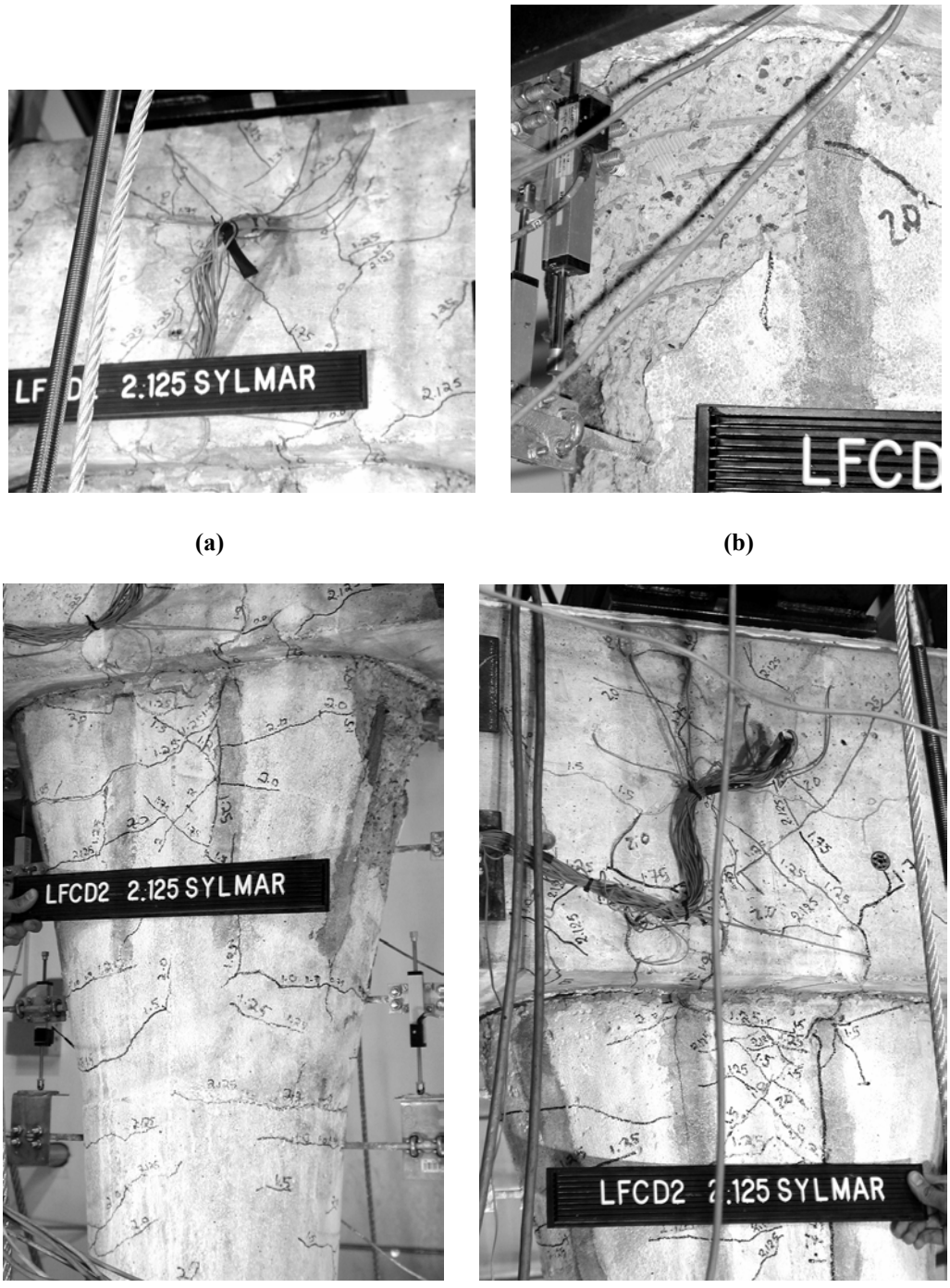

(a) **(b)**

(c) **(d)**

Fig. 4-60 LFCD2 at 2.125 Times Sylmar (a) Joint Crack (b) Concrete Spalling (c) Column Crack (d) Joint and flare Crack

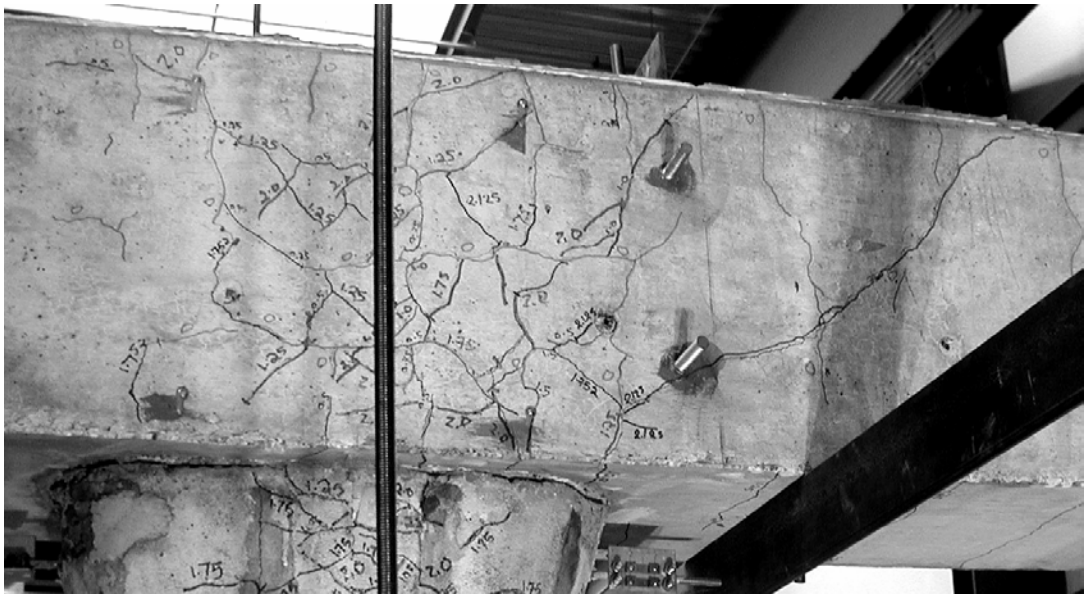

(a)

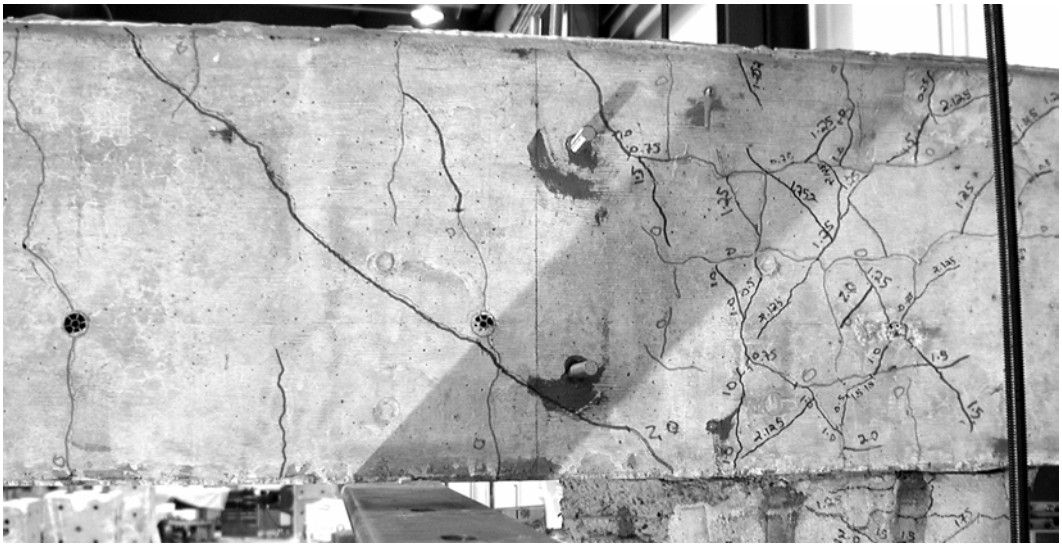

(b)

Fig. 4-61 LFCD2 after Bucket Removal (a) & (b) Shear cracks in the beam

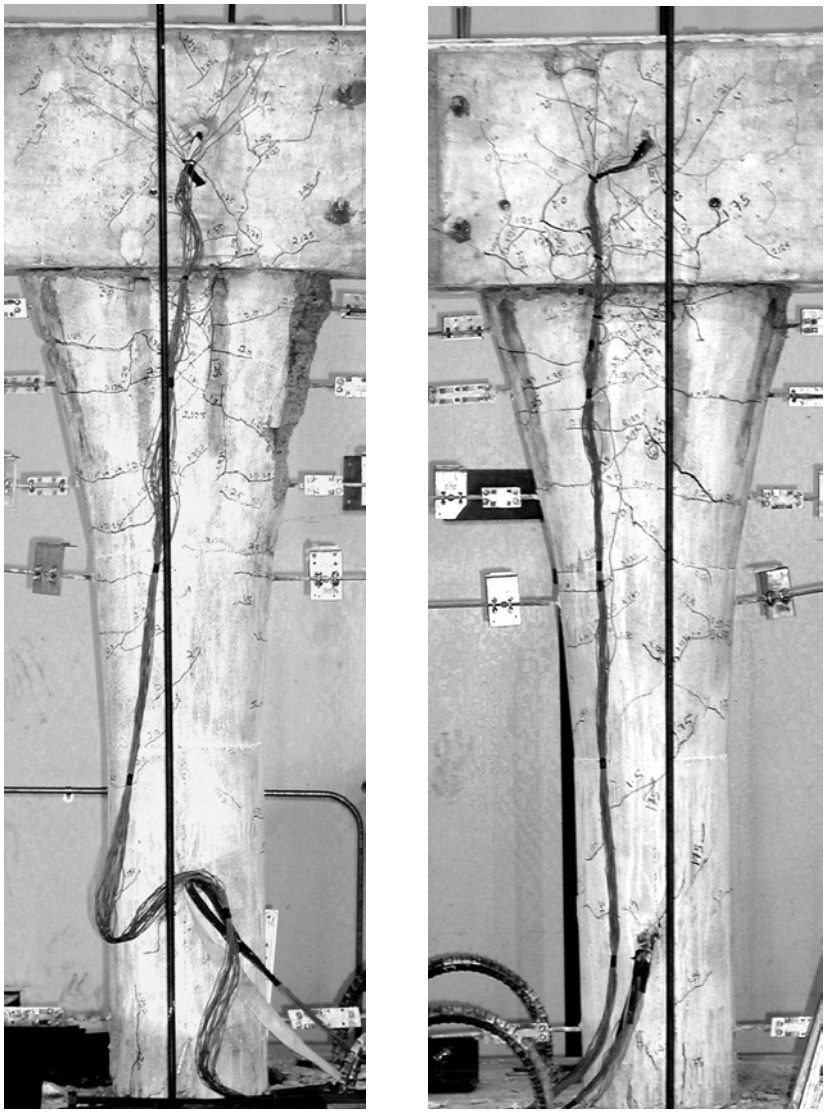

Fig. 4-62 LFCD2 after Bucket Removal Column Cracks

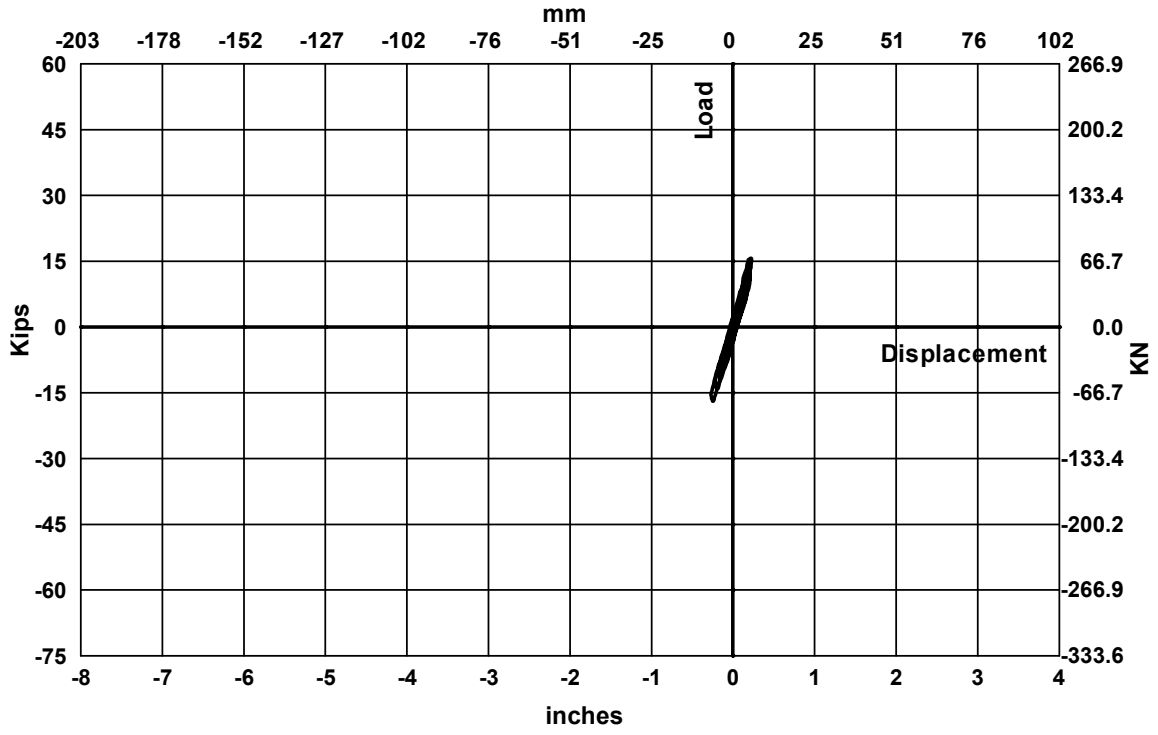

Fig. 4-63 Measured Load-Displacement Curve for LFCD2 at 0.15 Times Sylmar

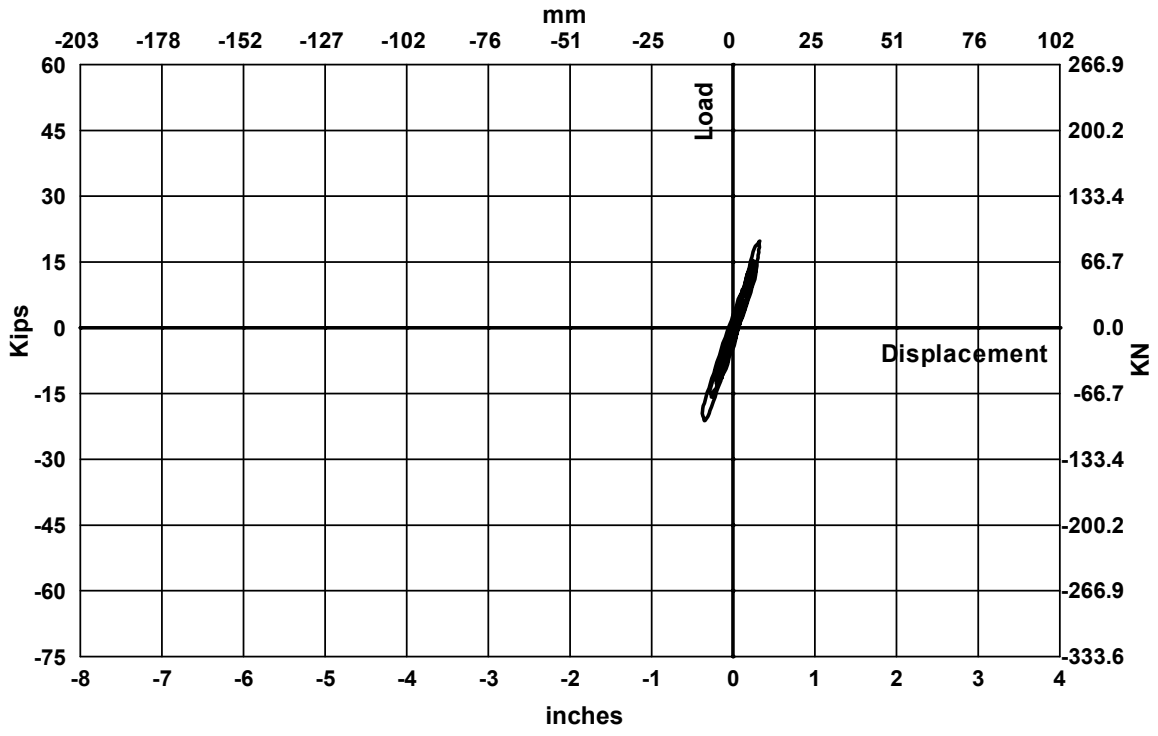

Fig. 4-64 Measured Load-Displacement Curve for LFCD2 at 0.25 Times Sylmar

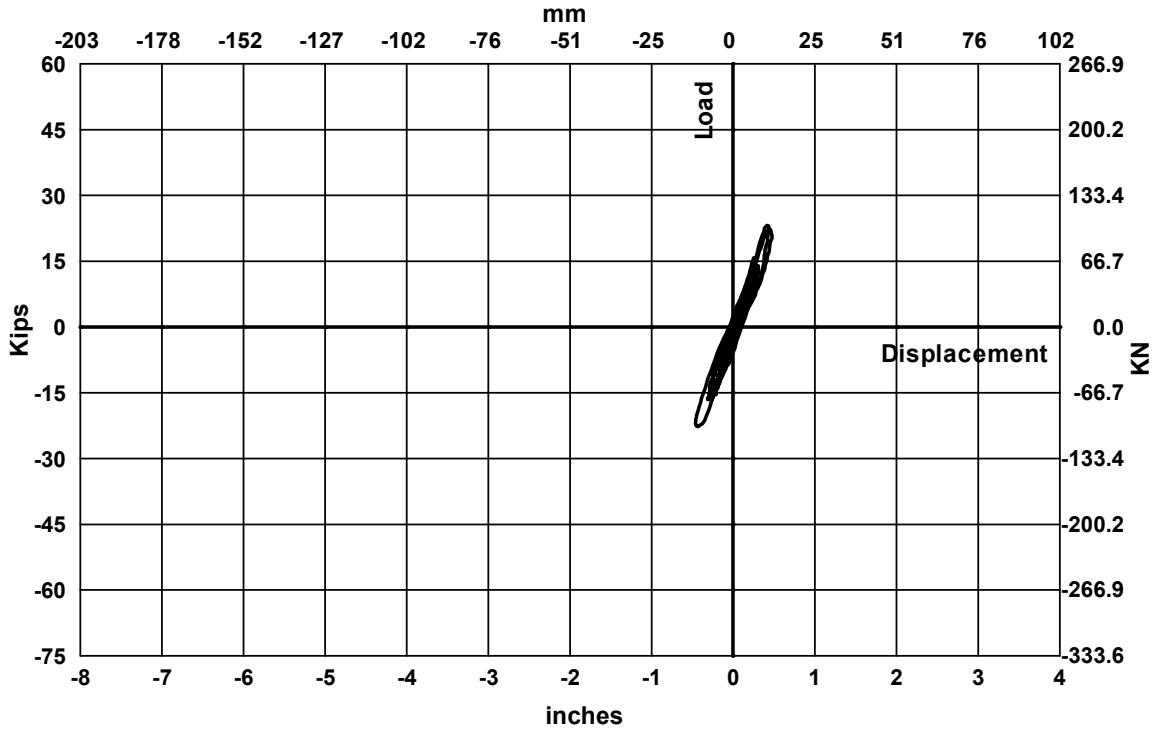

Fig. 4-65 Measured Load-Displacement Curve for LFCD2 at 0.5 Times Sylmar

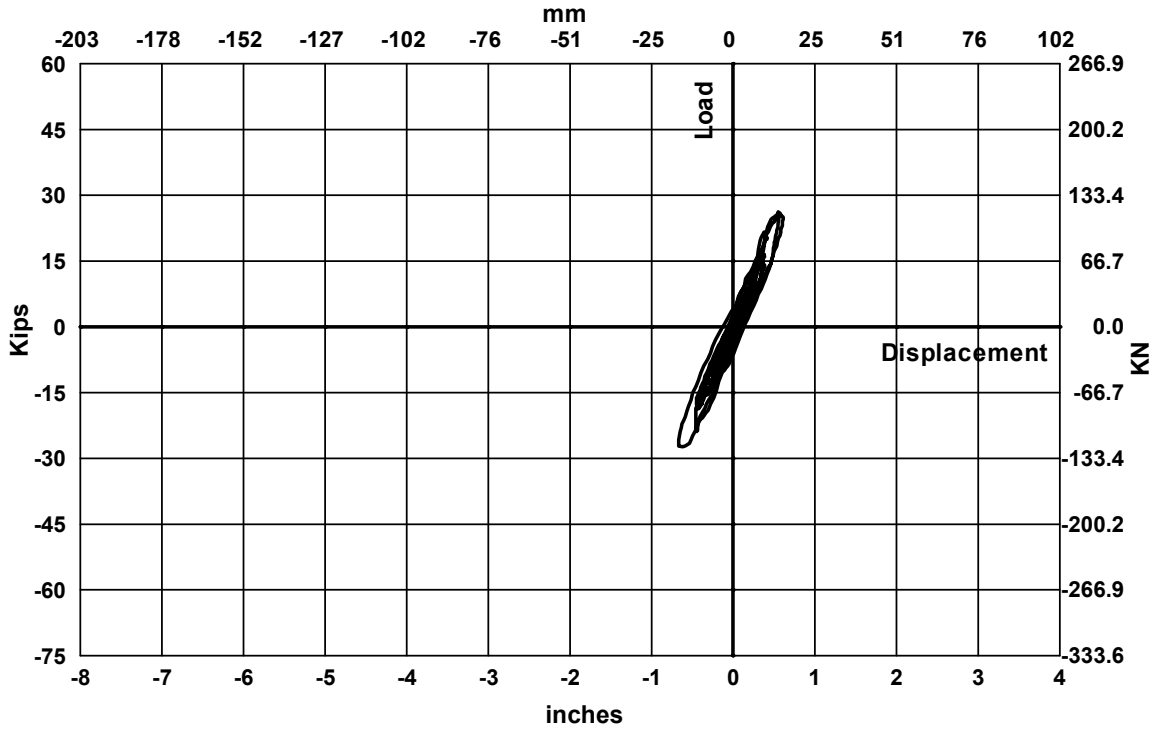

Fig. 4-66 Measured Load-Displacement Curve for LFCD2 at 0.75 Times Sylmar

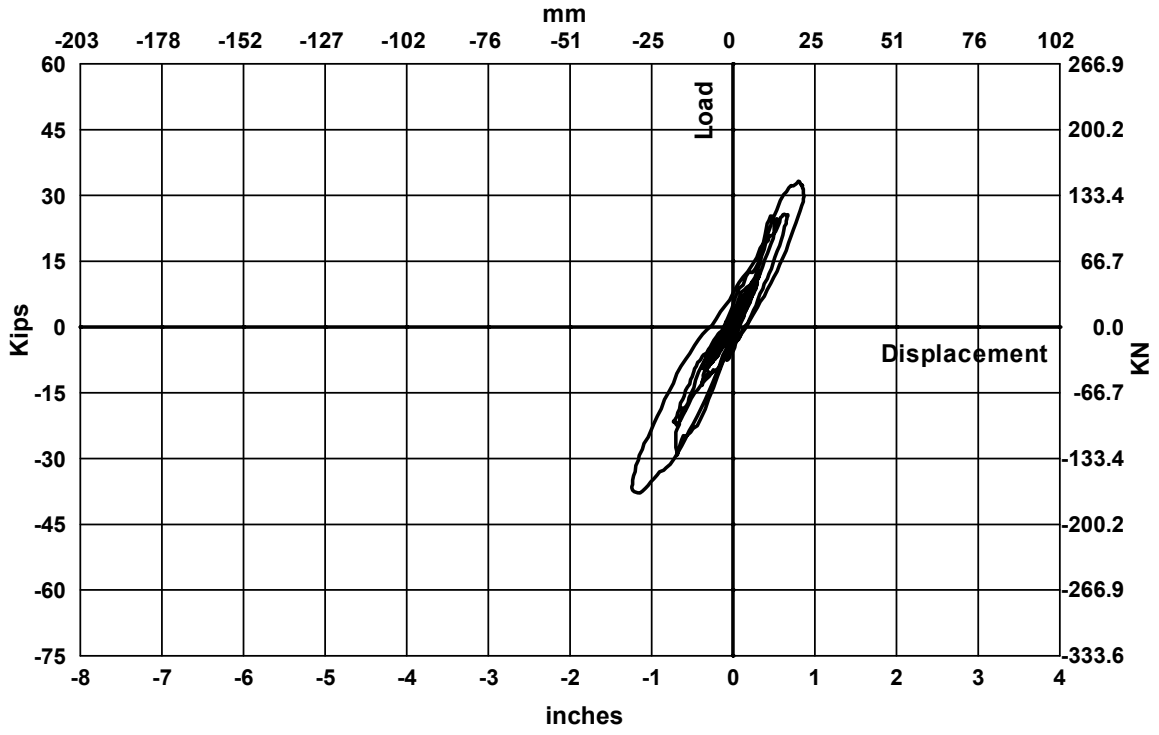

Fig. 4-67 Measured Load-Displacement Curve for LFCD2 at 1.0 Times Sylmar

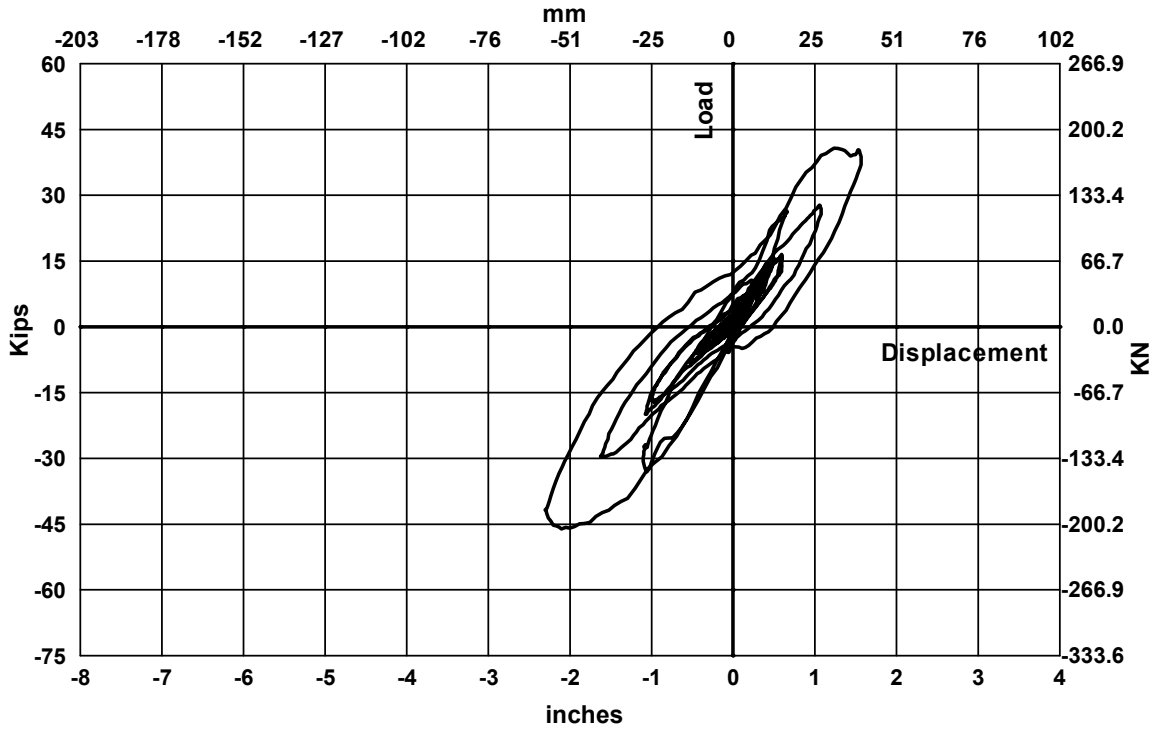

Fig. 4-68 Measured Load-Displacement Curve for LFCD2 at 1.25 Times Sylmar

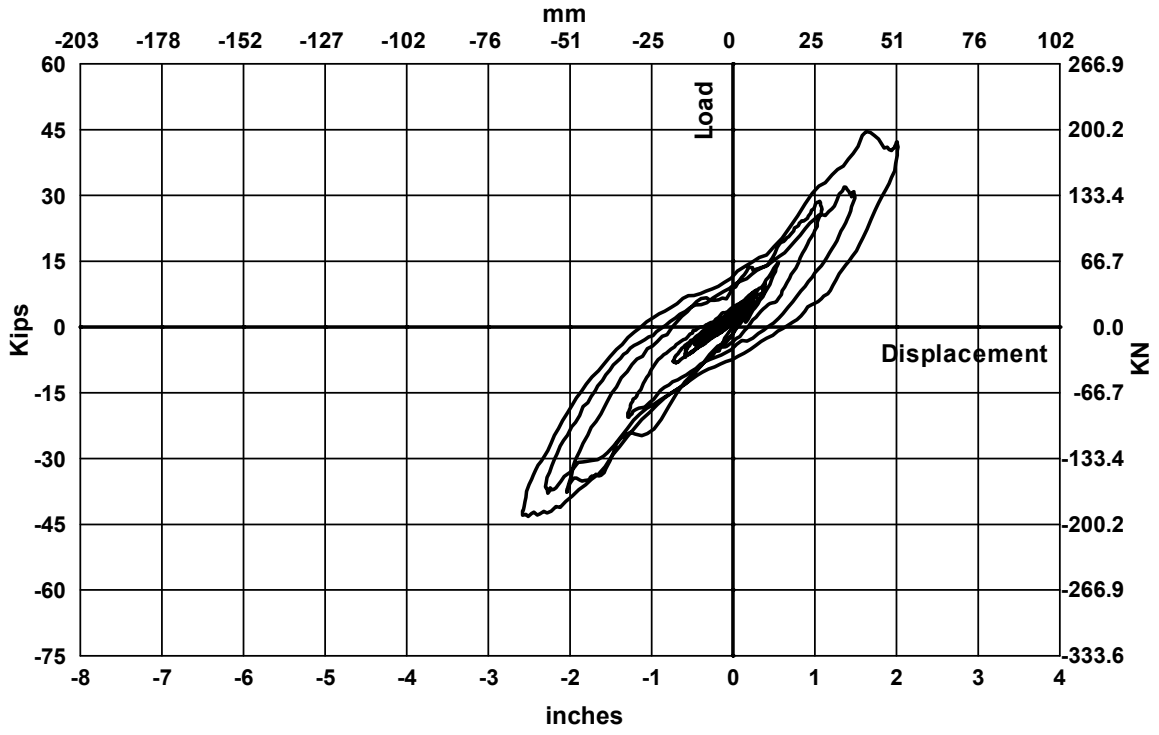

Fig. 4-69 Measured Load-Displacement Curve for LFCD2 at 1.5 Times Sylmar

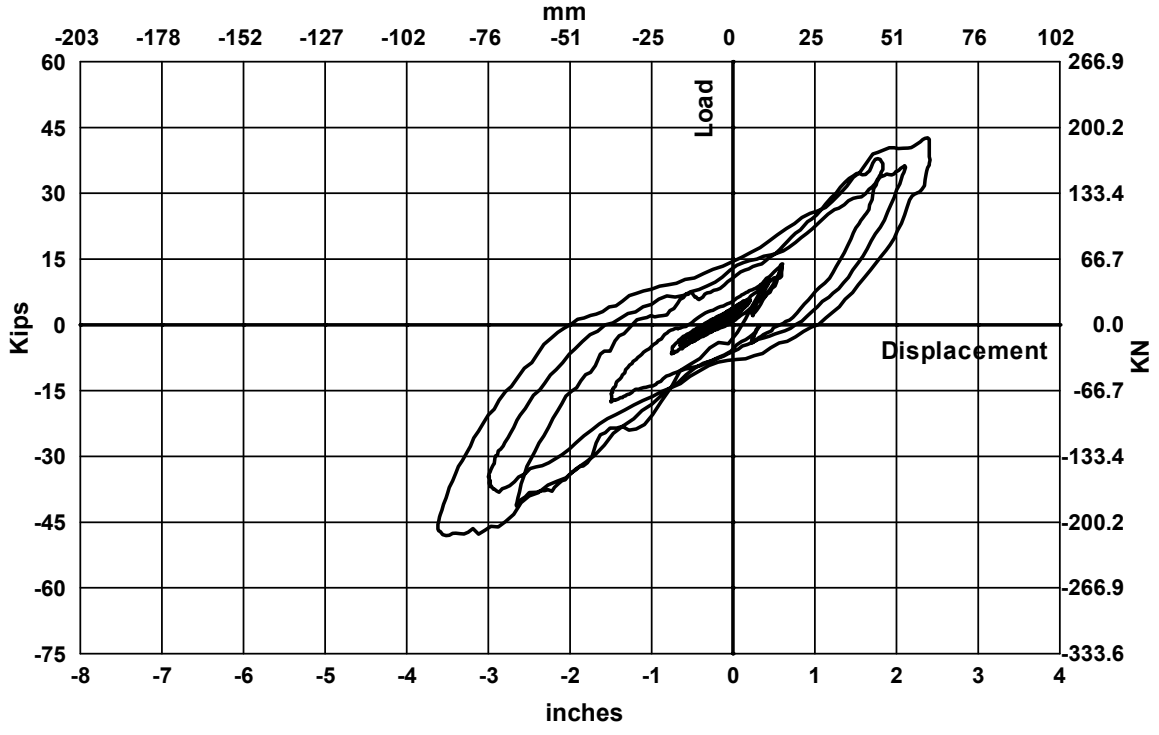

Fig. 4-70 Measured Load-Displacement Curve for LFCD2 at 1.75 Times Sylmar

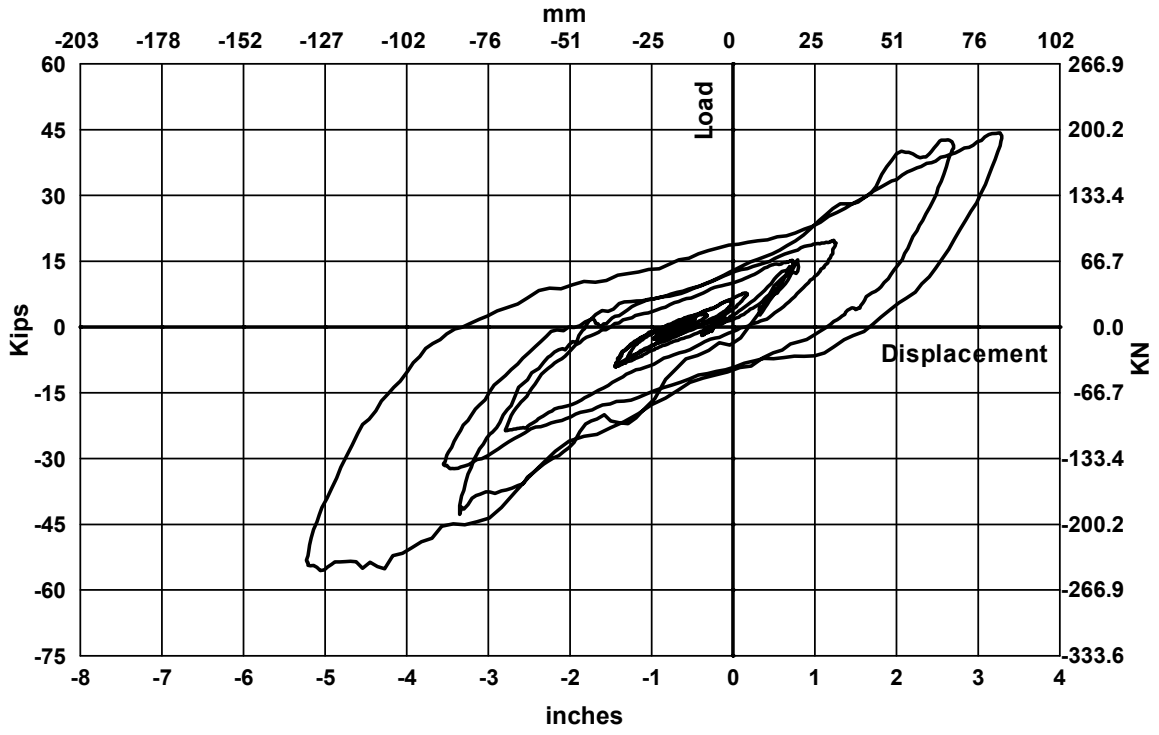

Fig. 4-71 Measured Load-Displacement Curve for LFCD2 at 2.0 Times Sylmar

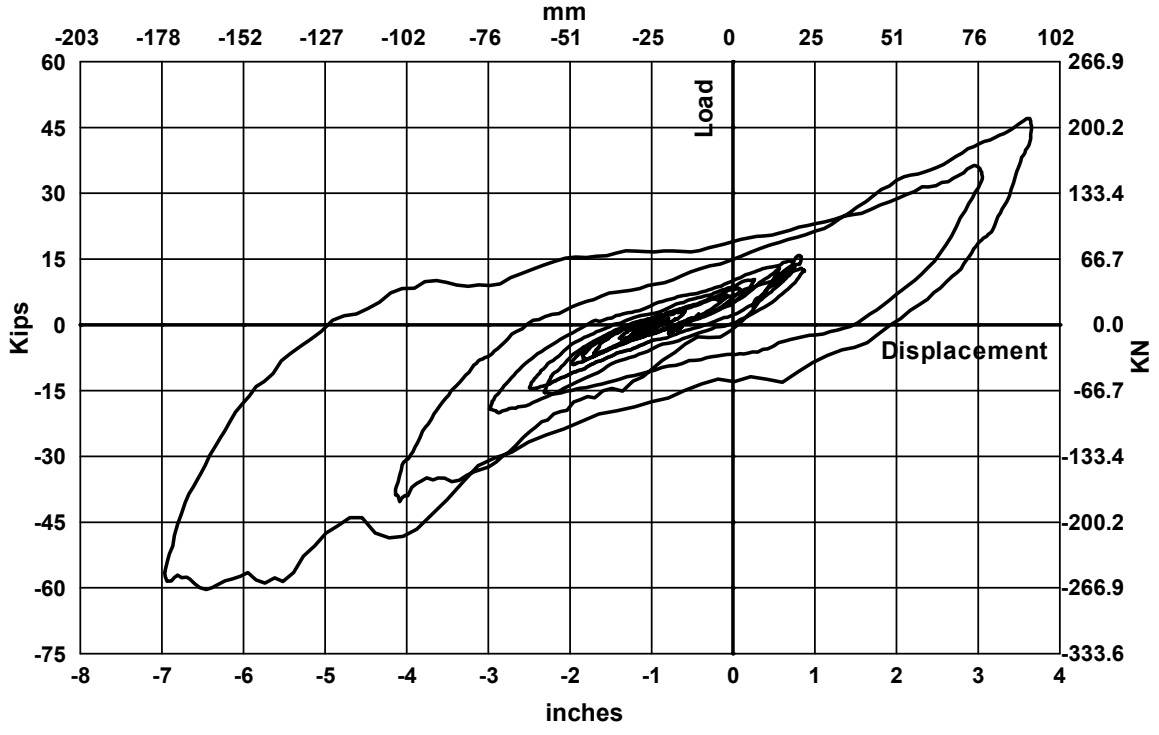

Fig. 4-72 Measured Load-Displacement Curve for LFCD2 at 2.125 Times Sylmar

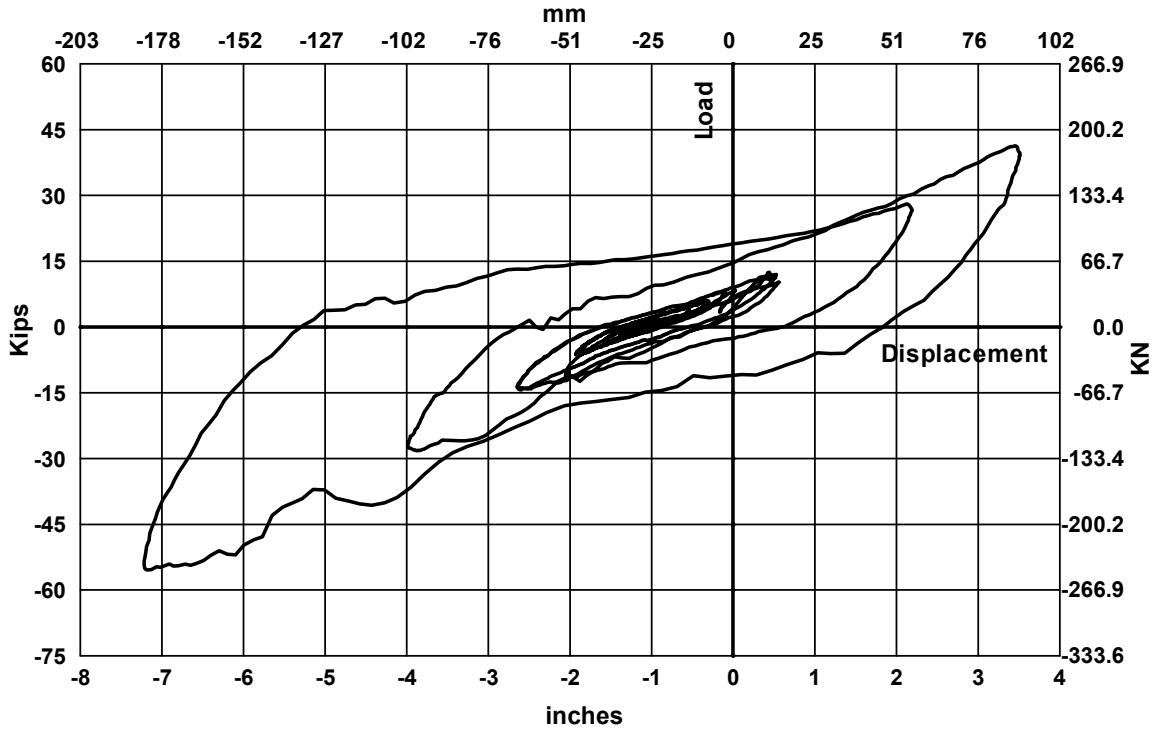

Fig. 4-73 Measured Load-Displacement Curve for LFCD2 at 1.75-2 Times Sylmar

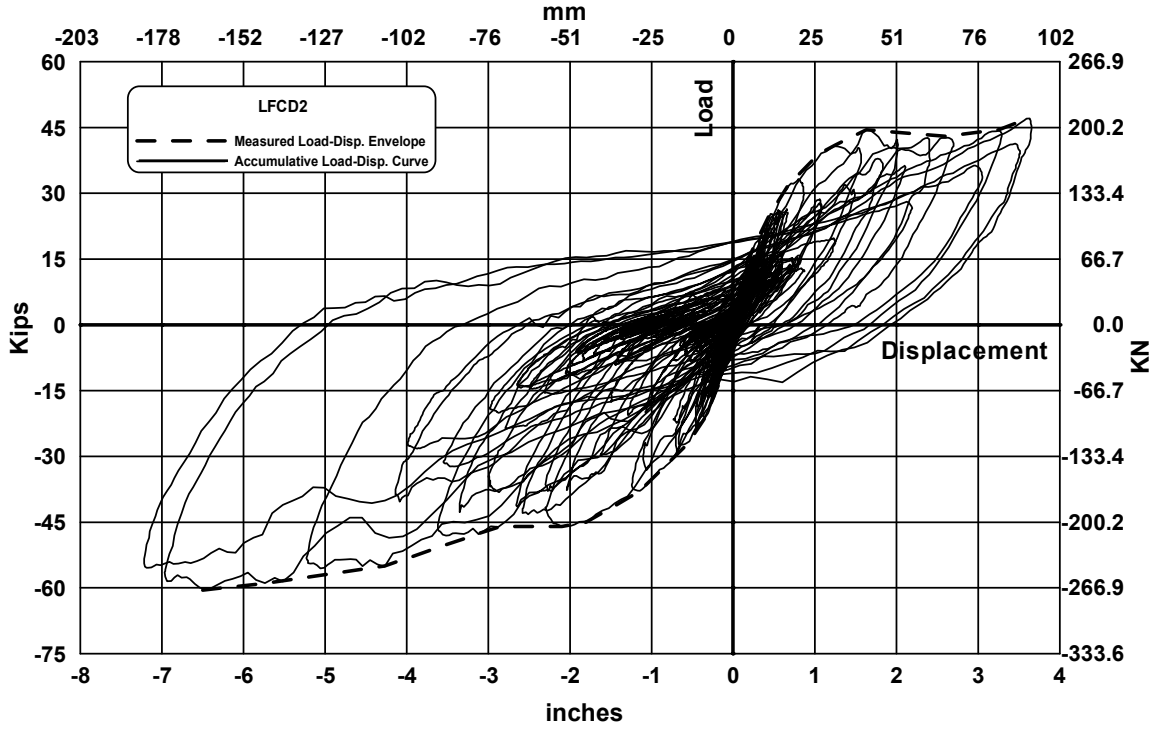

Fig. 4-74 Accumulative Measured Load-Displacement Curve for LFCD2

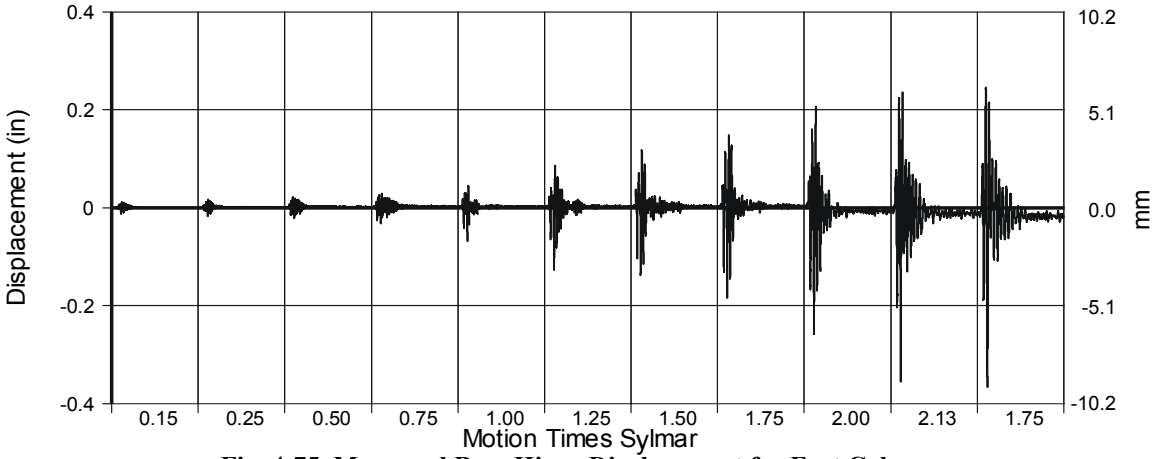

Fig. 4-75 Measured Base Hinge Displacement for East Column

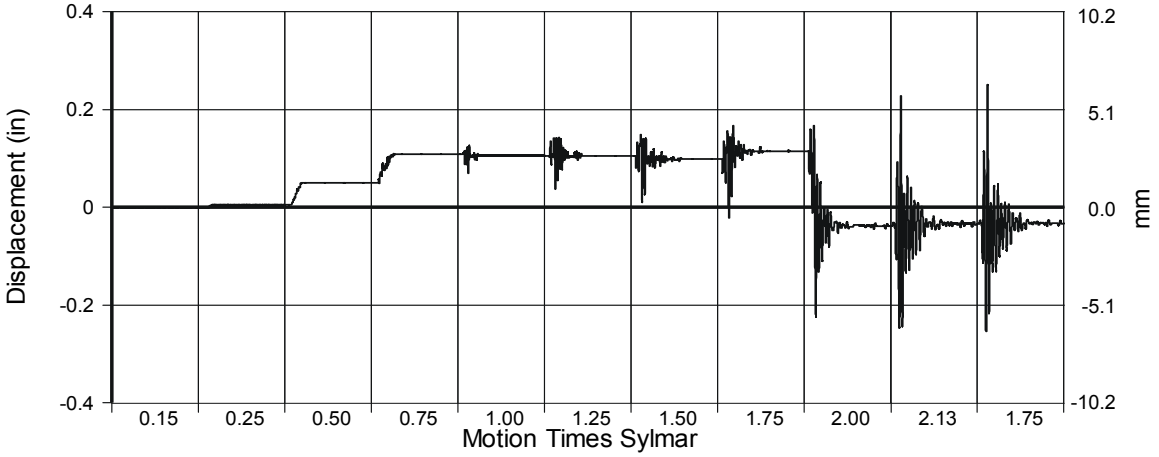

Fig. 4-76 Measured Base Hinge Displacement for West Column

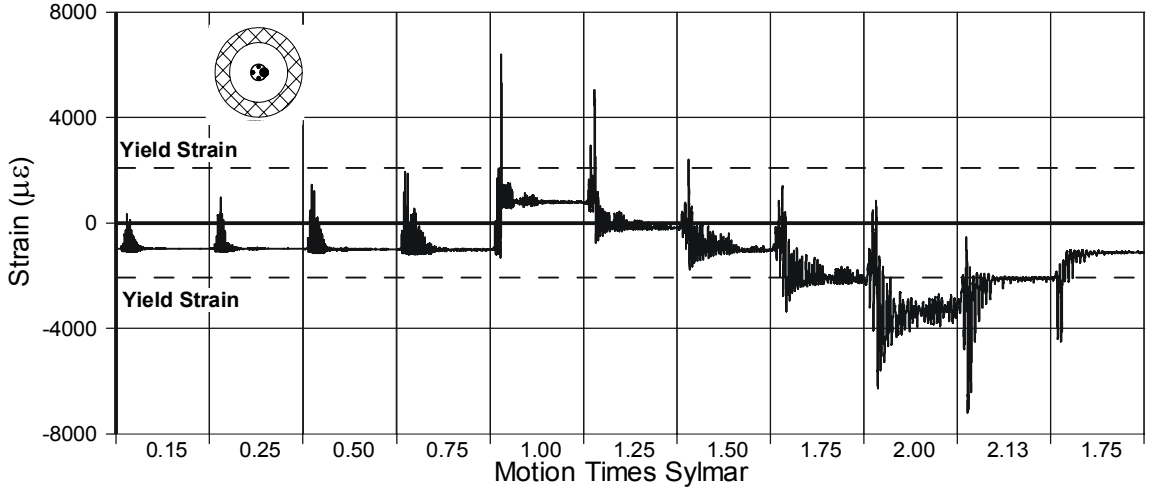

Fig. 4-77 Measured Strain at East Column Dowels

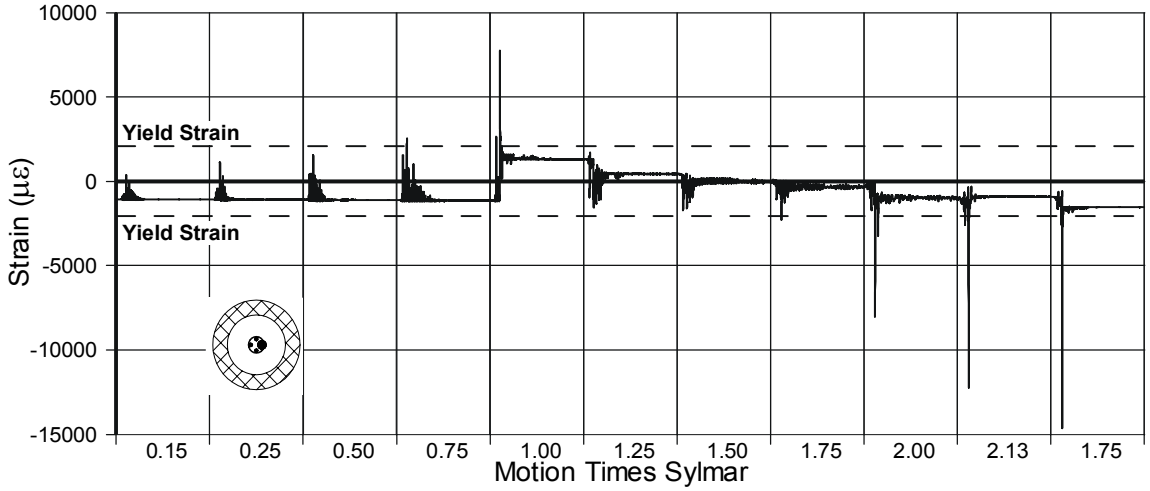

Fig. 4-78 Measured Strain at West Column Dowels

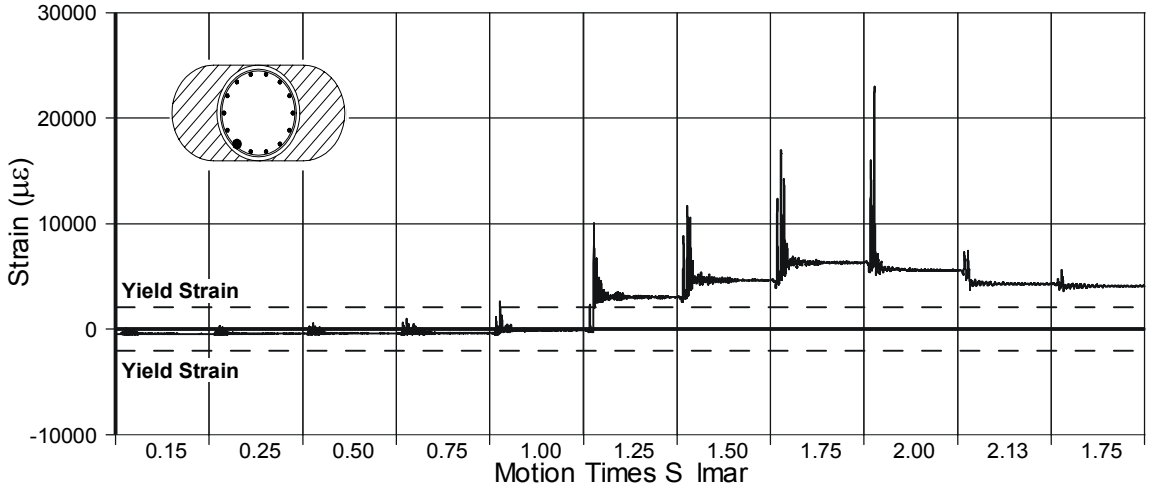

Fig. 4-79 Measured Strain for Longitudinal Column Reinforcement Gauge 150

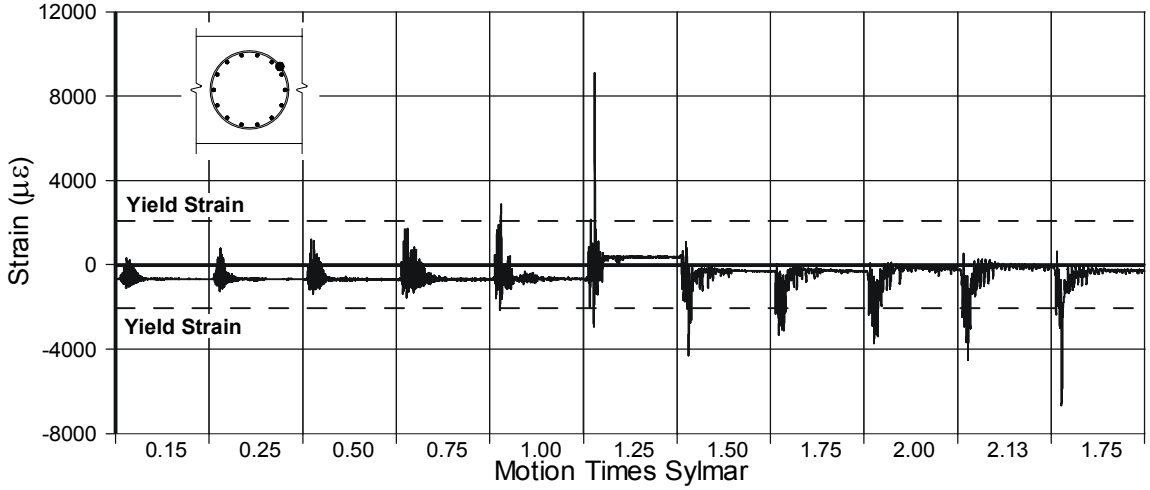

Fig. 4-80 Measured Strain for Column Spirals Gauge 126

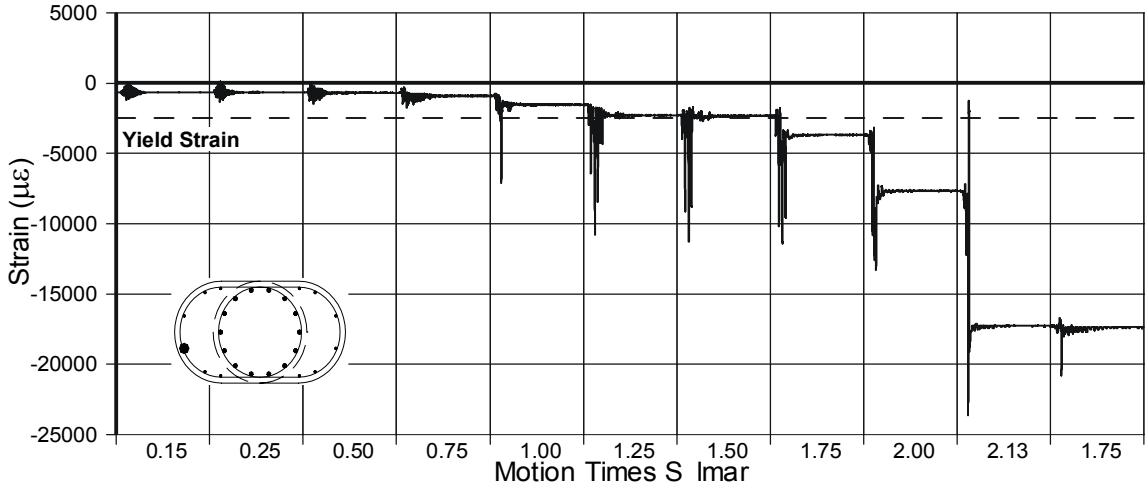

Fig. 4-81 Measured Strain for Flare Longitudinal Reinforcement Gauge 100

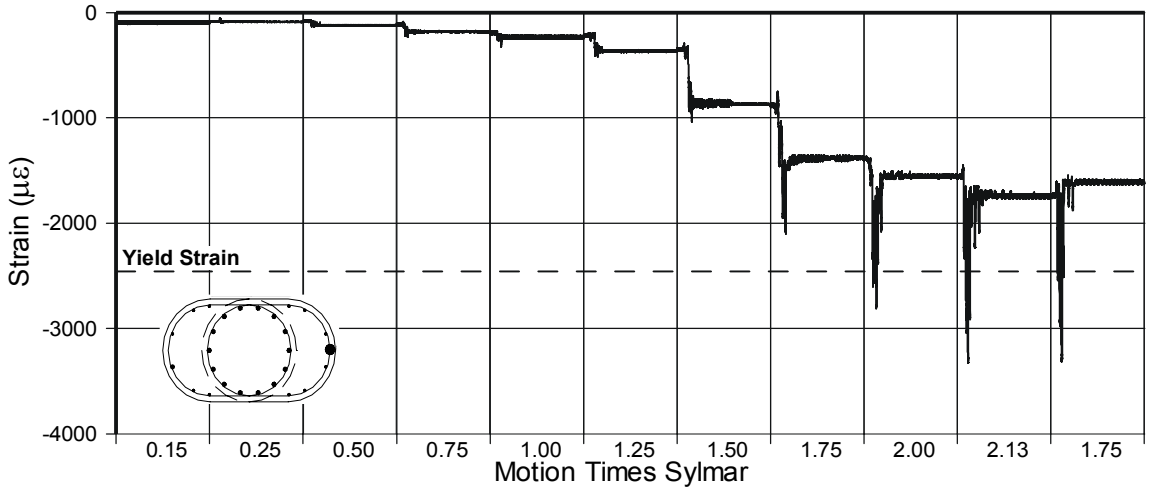

Fig. 4-82 Measured Strain for Flare Hoops Gauge 67

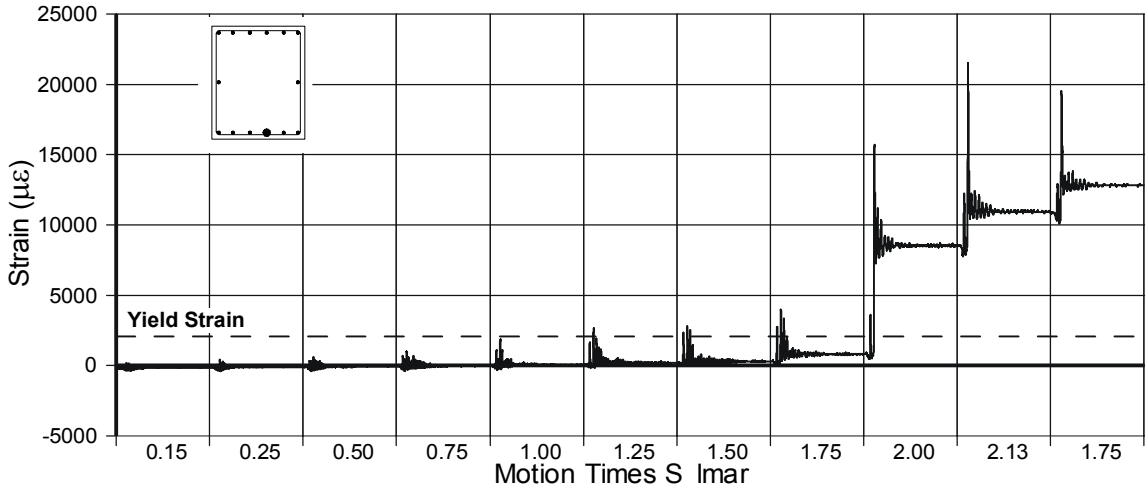

Fig. 4-83 Measured Strain for Beam's Bottom Reinforcement Gauge 82

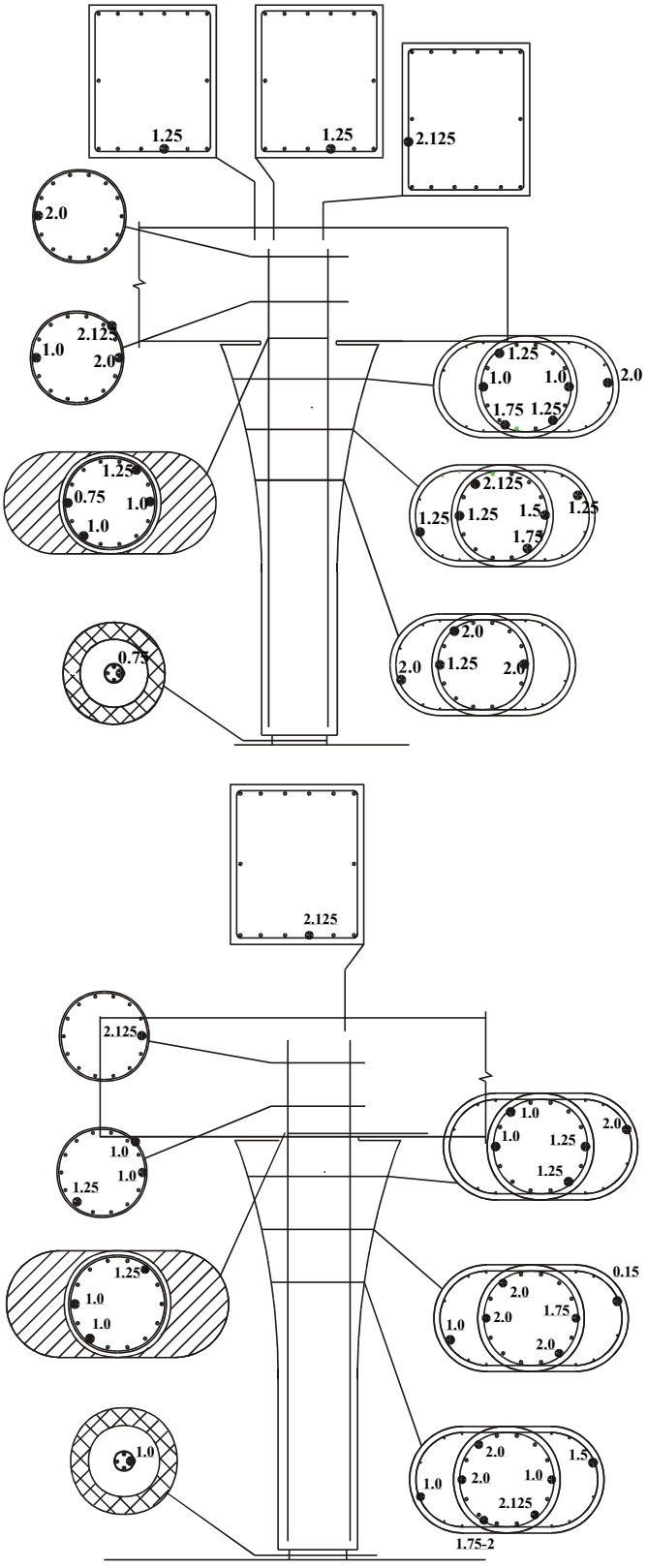

Fig. 4-84 Yield Distribution in LFCD2

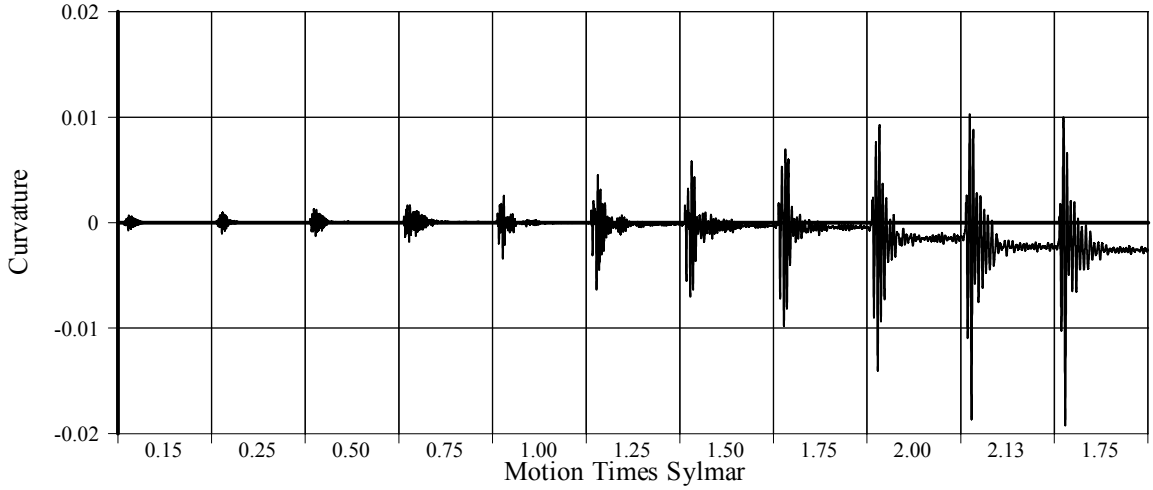

Fig. 4-85 Measured Curvature at Section 1 of East Column for LFCD2

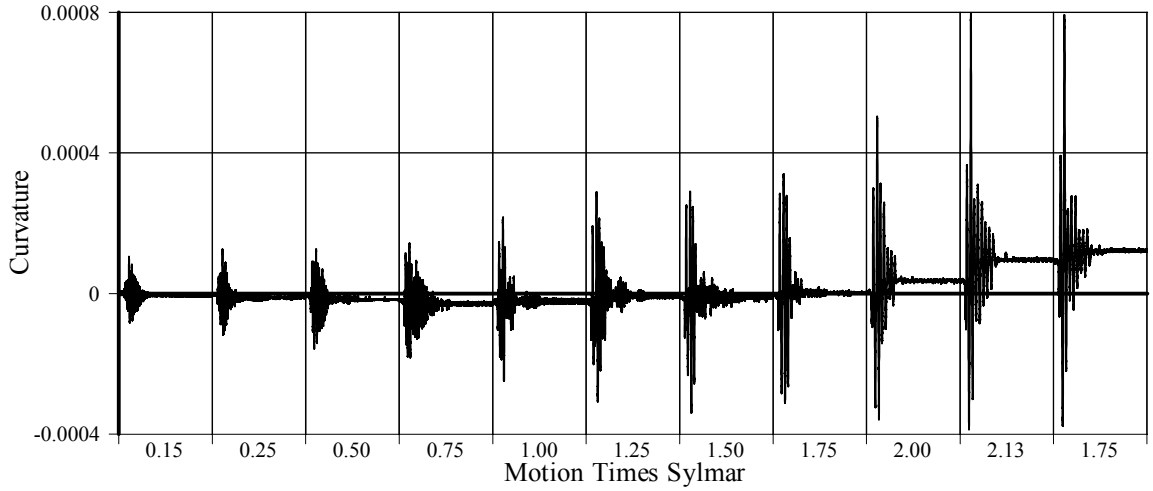

Fig. 4-86 Measured Curvature at Section 2 of East Column for LFCD2

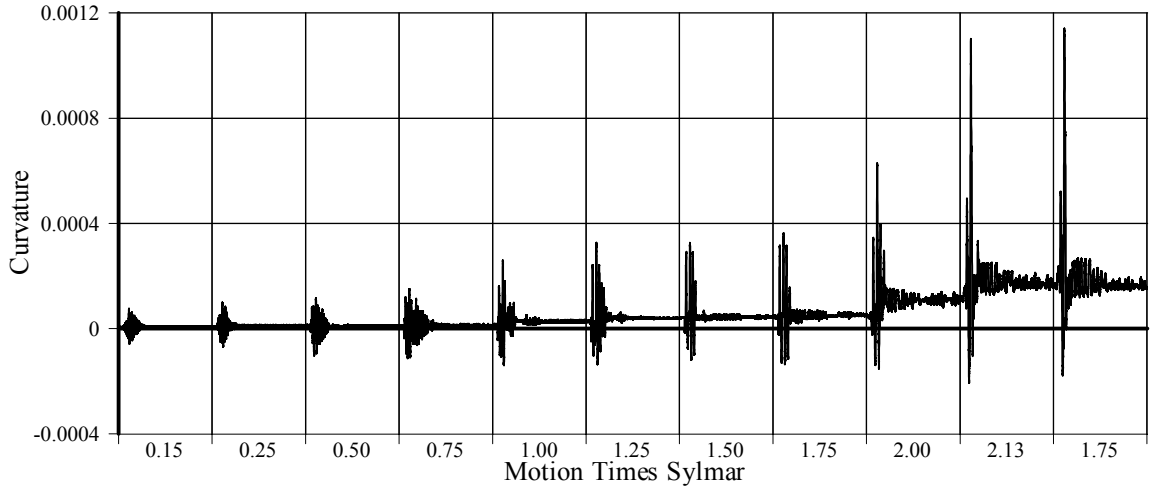

Fig. 4-87 Measured Curvature at Section 3 of East Column for LFCD2

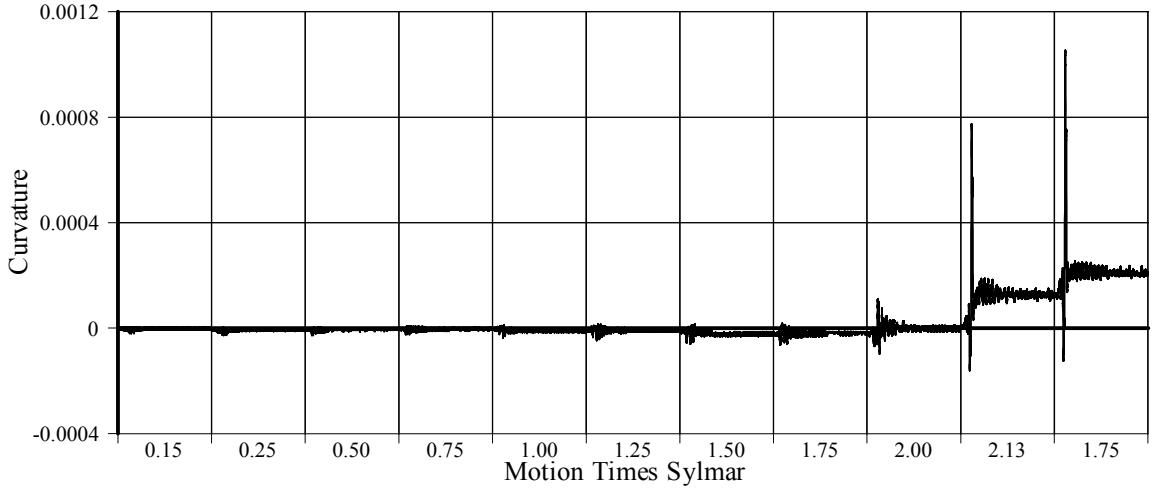

Fig. 4-88 Measured Curvature at Section 4 of East Column for LFCD2

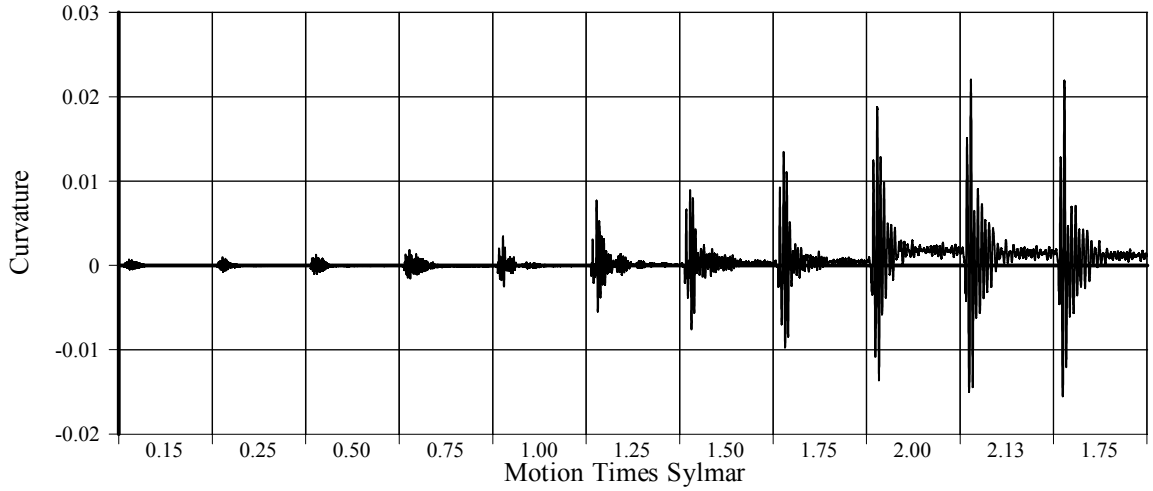

Fig. 4-89 Measured Curvature at Section 5 of East Column for LFCD2

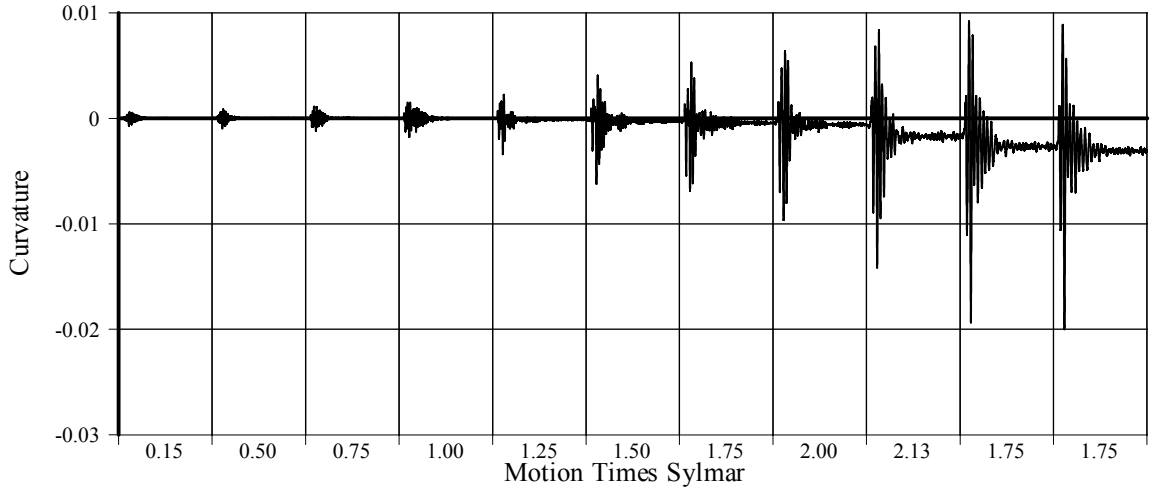

Fig. 4-90 Measured Curvature at Section 1 of West Column for LFCD2

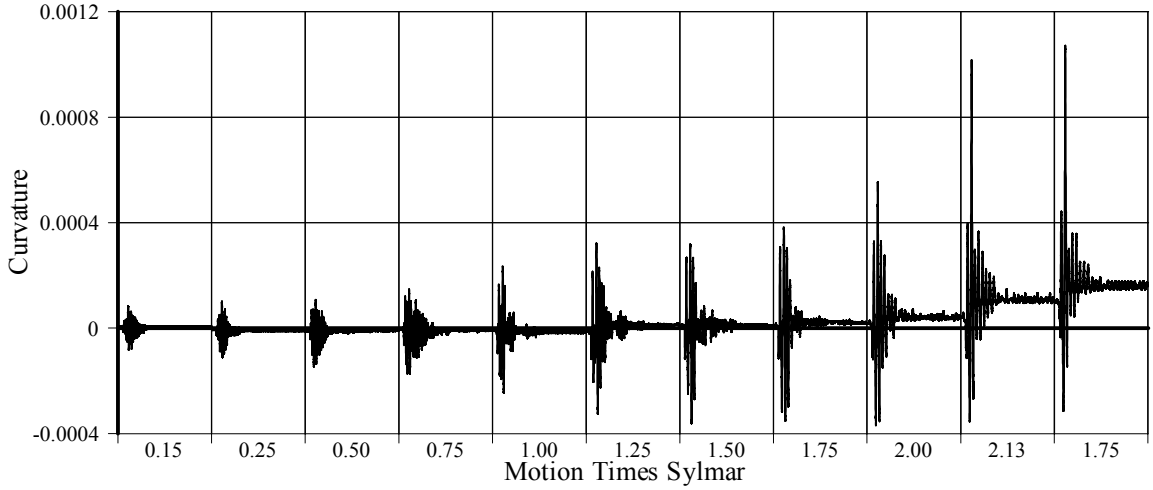

Fig. 4-91 Measured Curvature at Section 2 of West Column for LFCD2

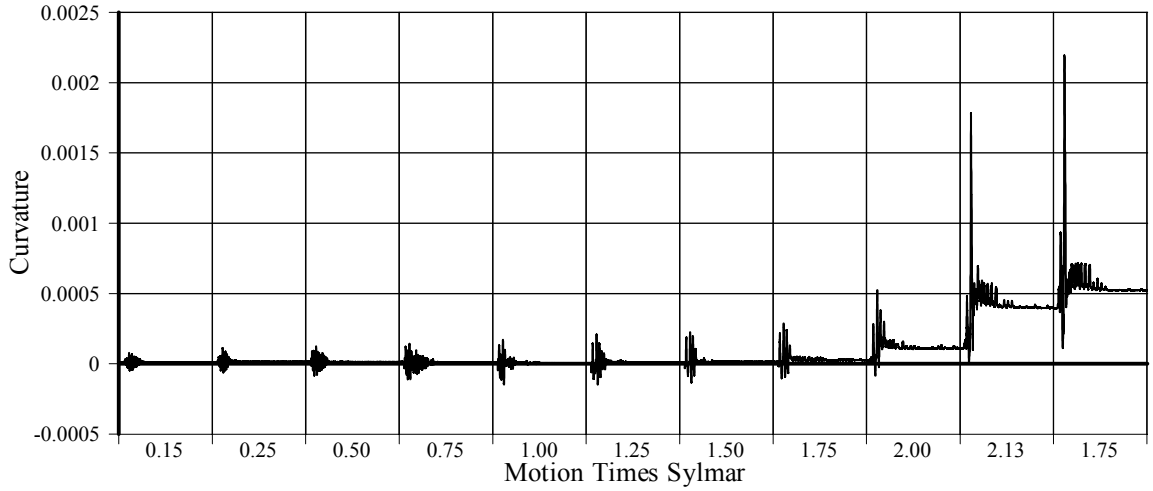

Fig. 4-92 Measured Curvature at Section 3 of West Column for LFCD2

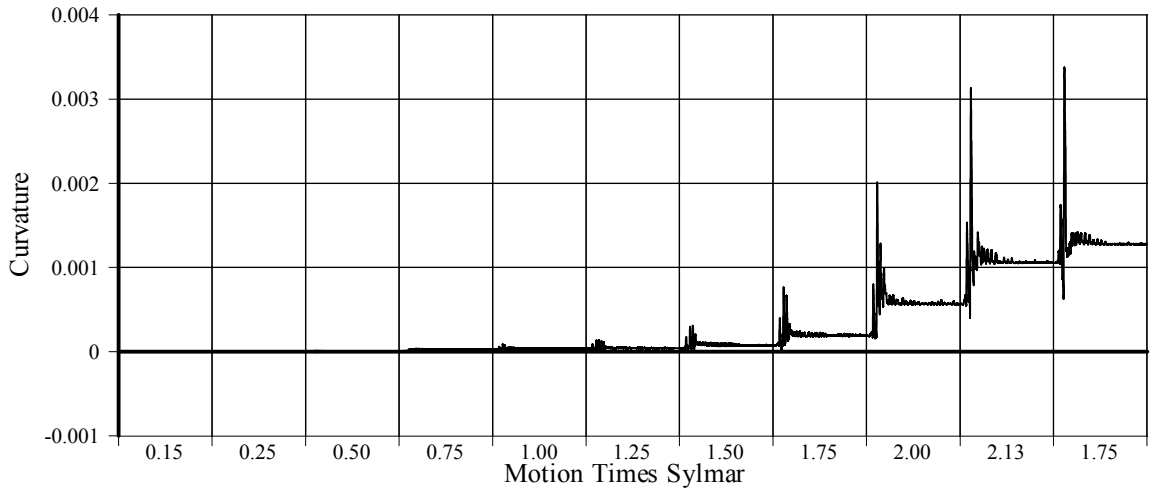

Fig. 4-93 Measured Curvature at Section 4 of West Column for LFCD2

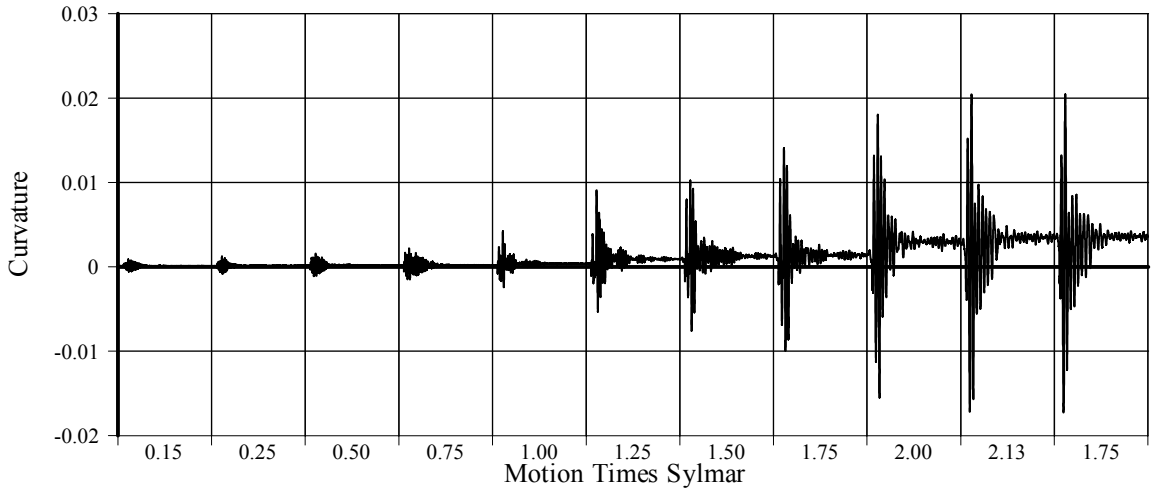

Fig. 4-94 Measured Curvature at Section 5 of West Column for LFCD2

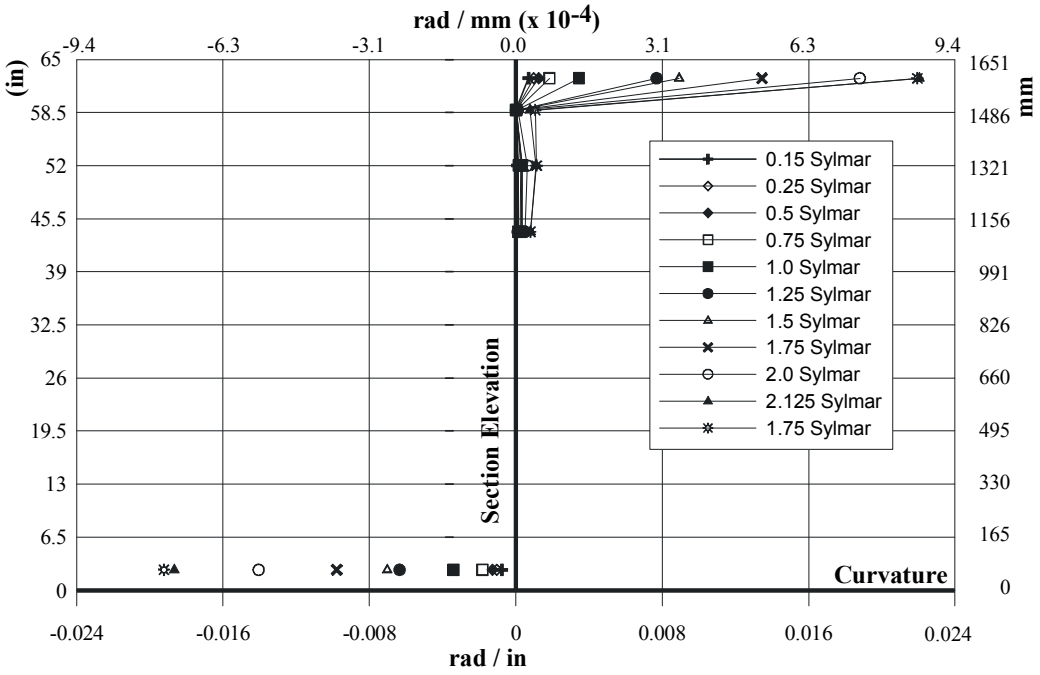

Fig. 4-95 Measured Maximum Curvature for East Column of LFCD2

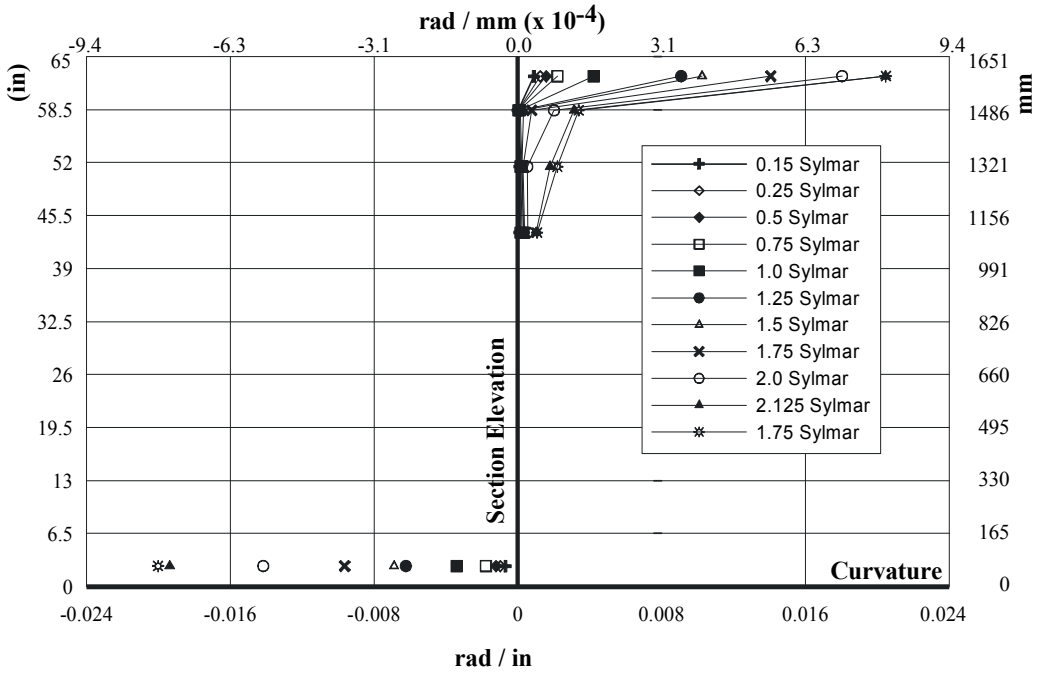

Fig. 4-96 Measured Maximum Curvature for West Column of LFCD2

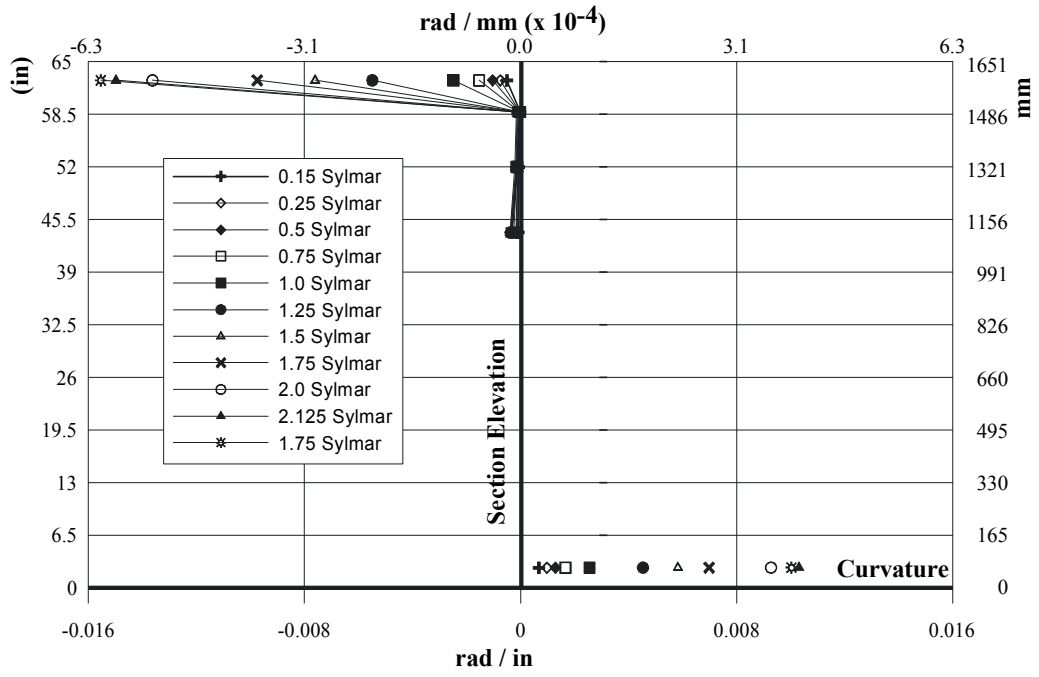

Fig. 4-97 Measured Minimum Curvature for East Column of LFCD2

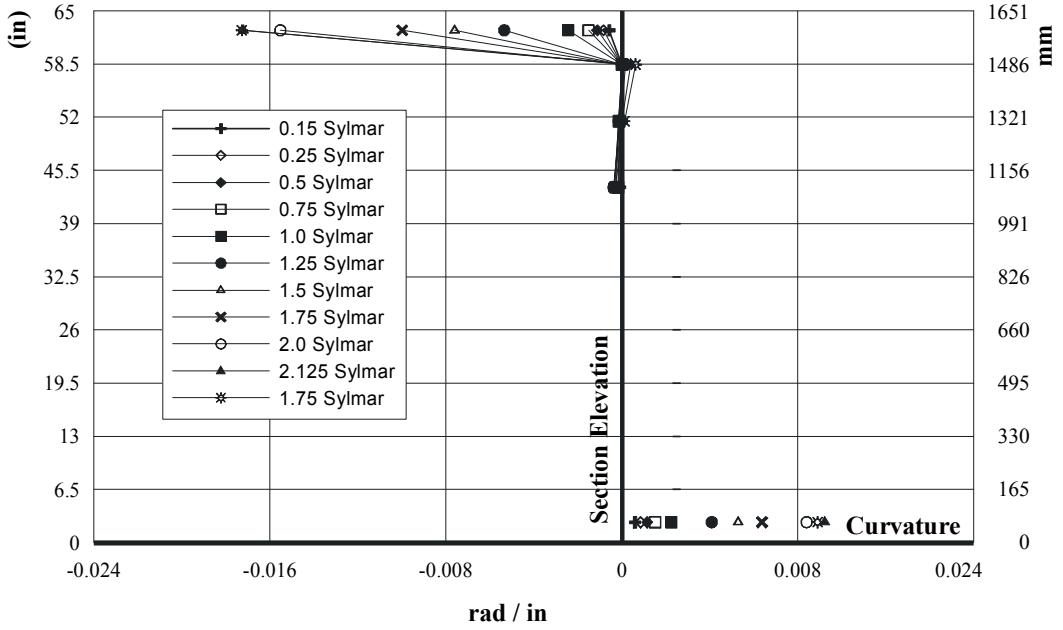

Fig. 4-98 Measured Minimum Curvature for East Column of LFCD2

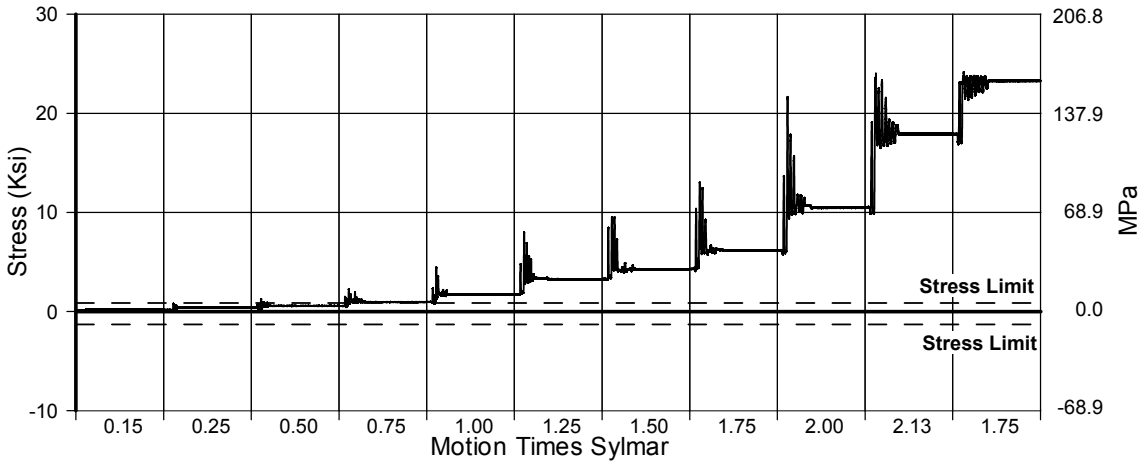

Fig. 4-99 Principal Stress (σ1) in East Beam-Column Connection for LFCD2

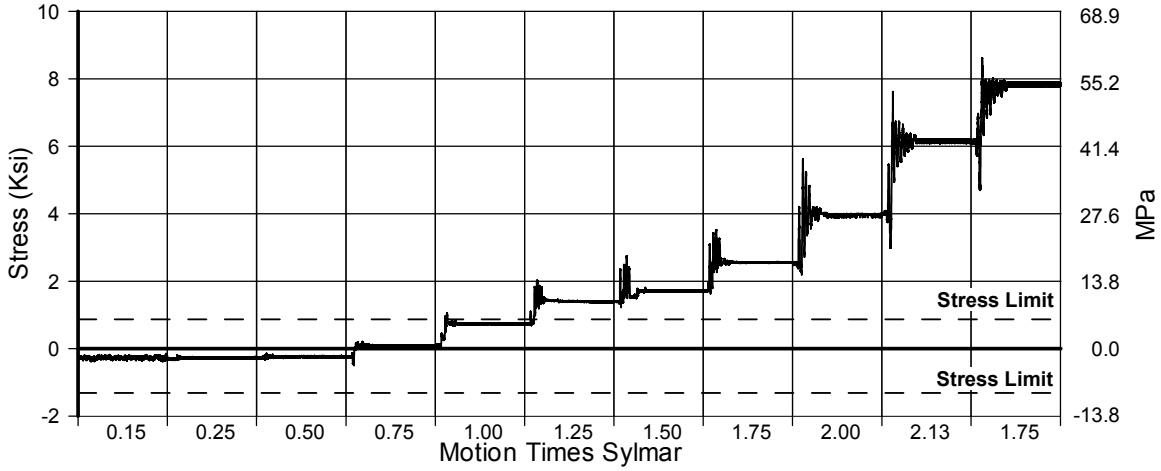

Fig. 4-100 Principal Stress (σ2) in East Beam-Column Connection for LFCD2

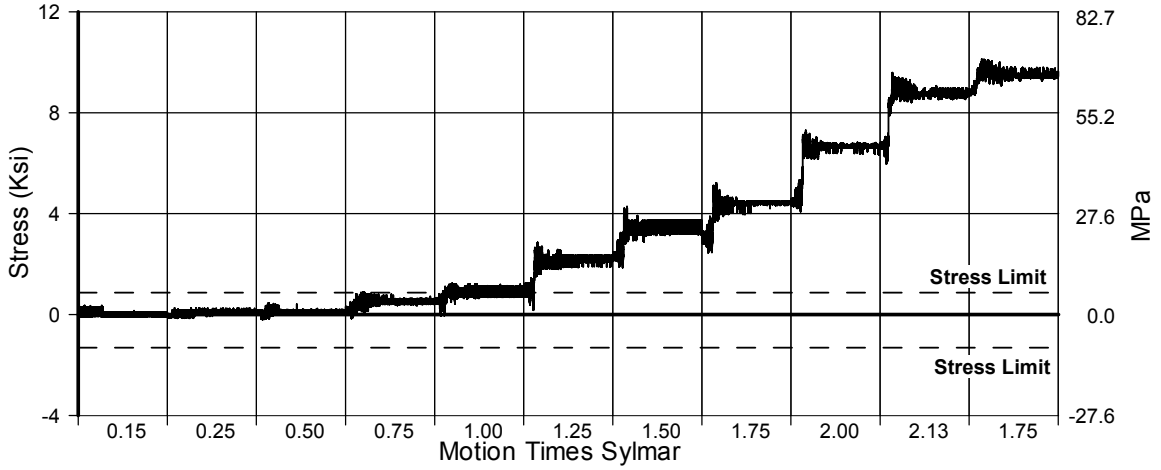

Fig. 4-101 Principal Stress (σ1) in West Beam-Column Connection for LFCD2

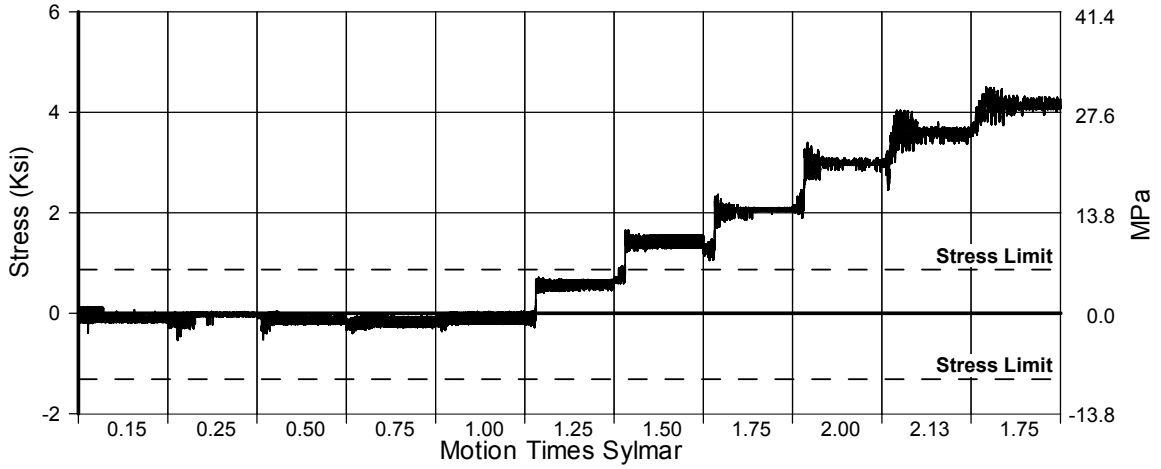

Fig. 4-102 Principal Stress (σ2) in West Beam-Column Connection for LFCD2

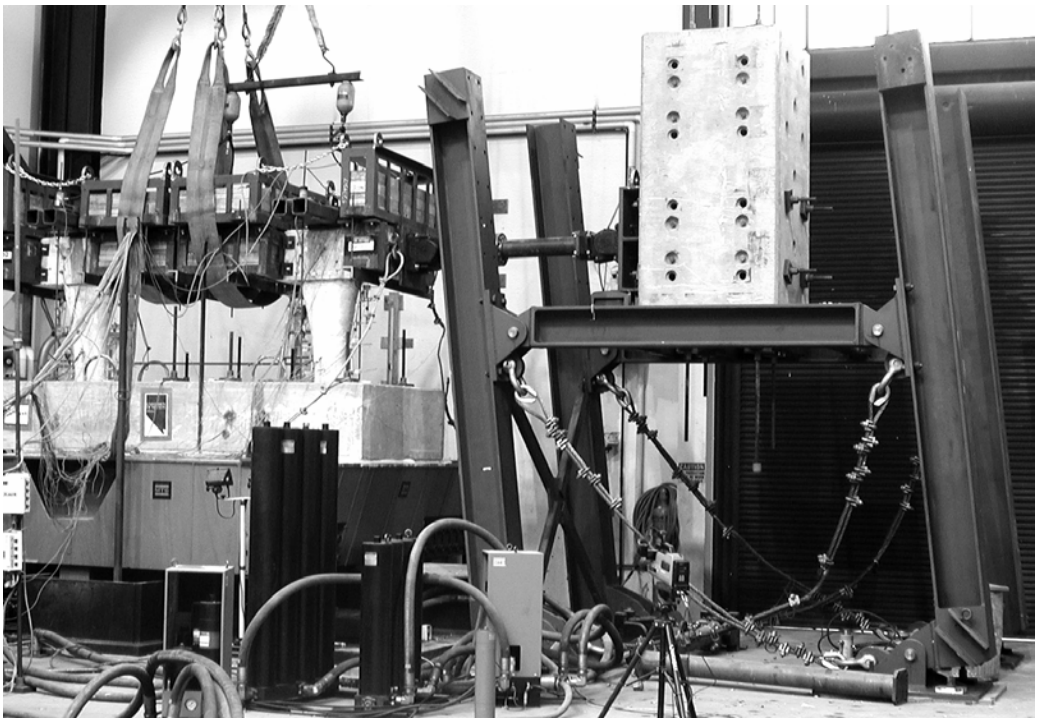

Fig. 4-103 SFCD1, Global View of the Specimen and The Mass Rig

Fig. 4-104 SFCD1, Concrete Spalling at Top of the Flare

(a) (b)

Fig. 4-105 SFCD1, Concrete Spalling at Top of the Flare

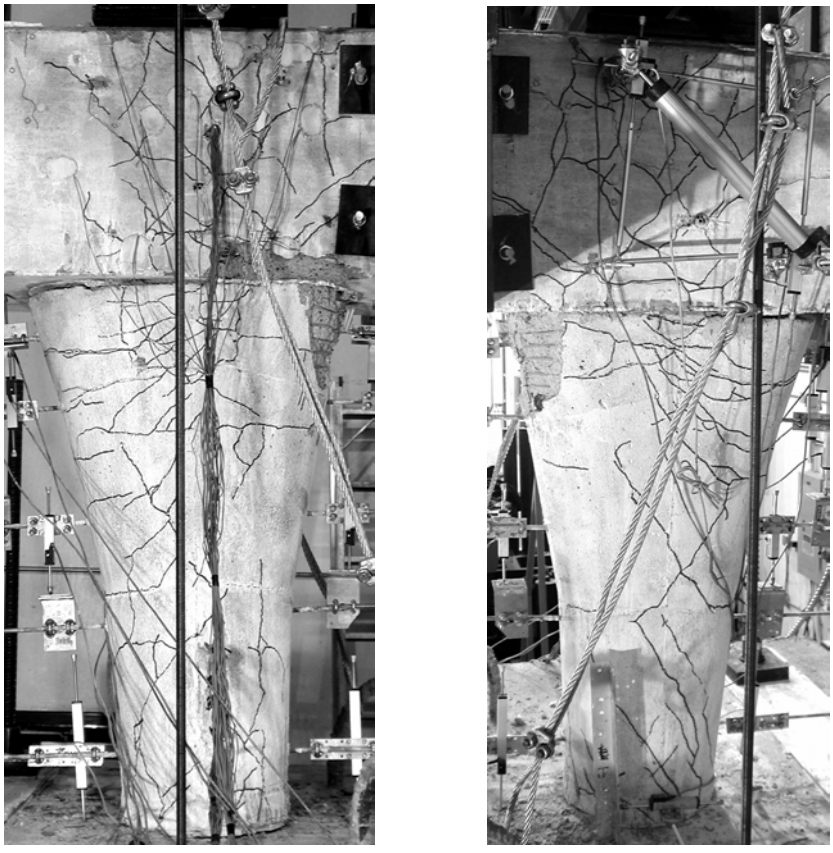

(c) (d)

Fig. 4-106 SFCD1, Concrete Spalling at Top of the Flare

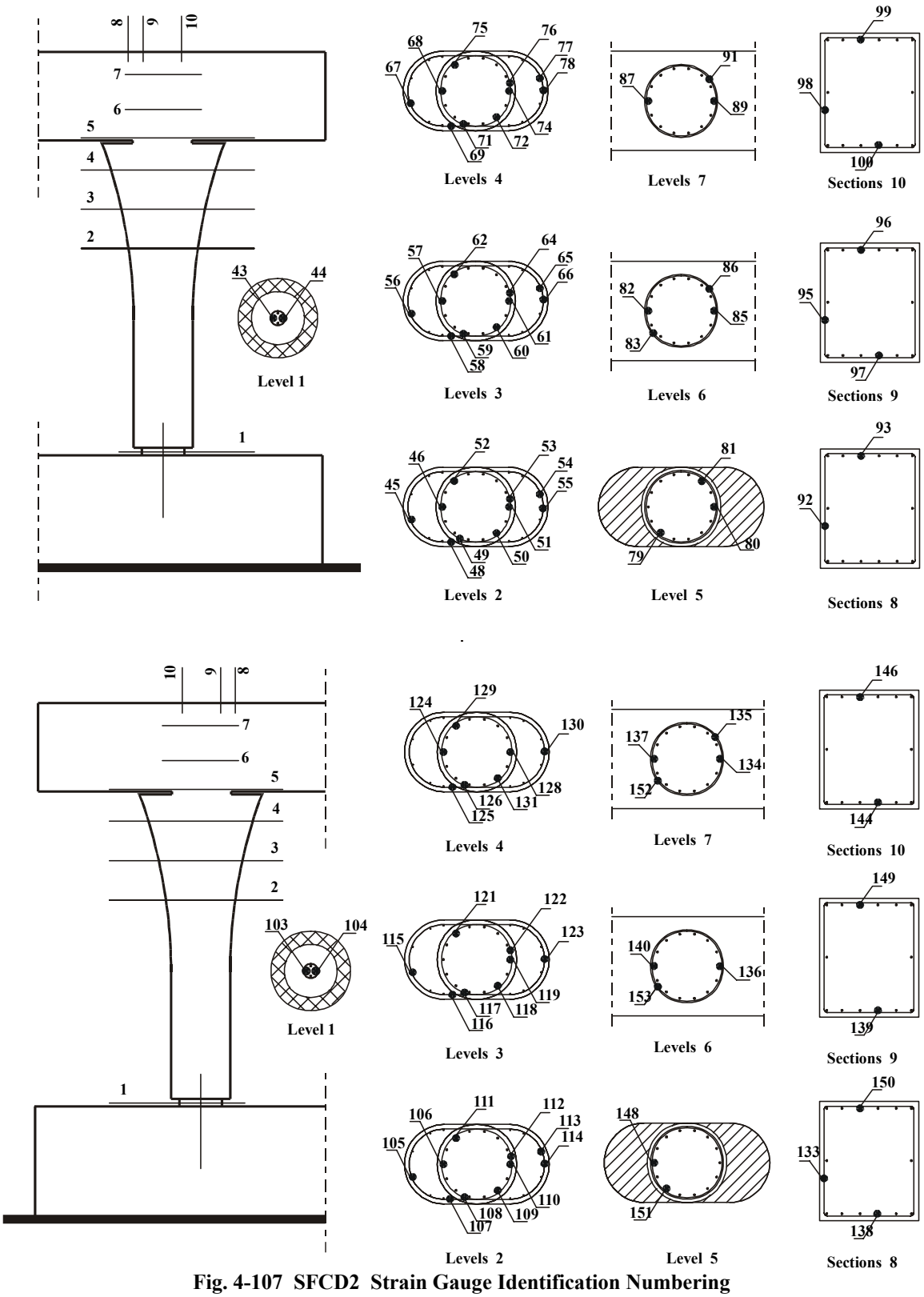

Fig. 4-107 SFCD2 Strain Gauge Identification Numbering

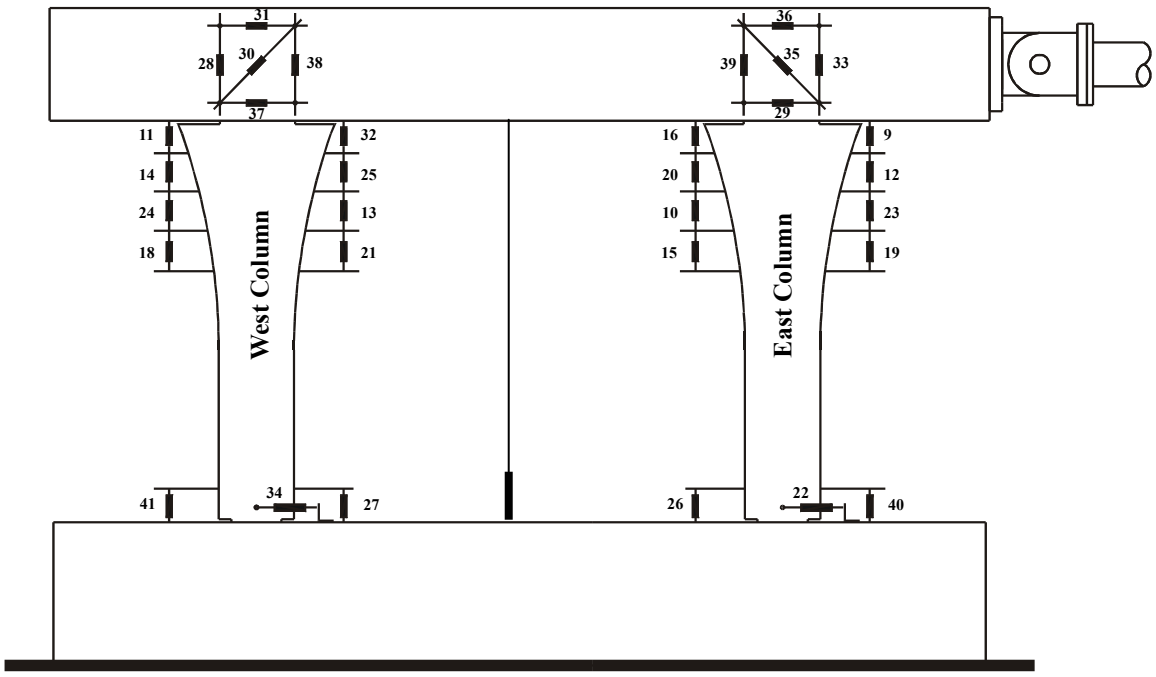

Fig. 4-108 SFCD2 Displacement Transducers Numbering

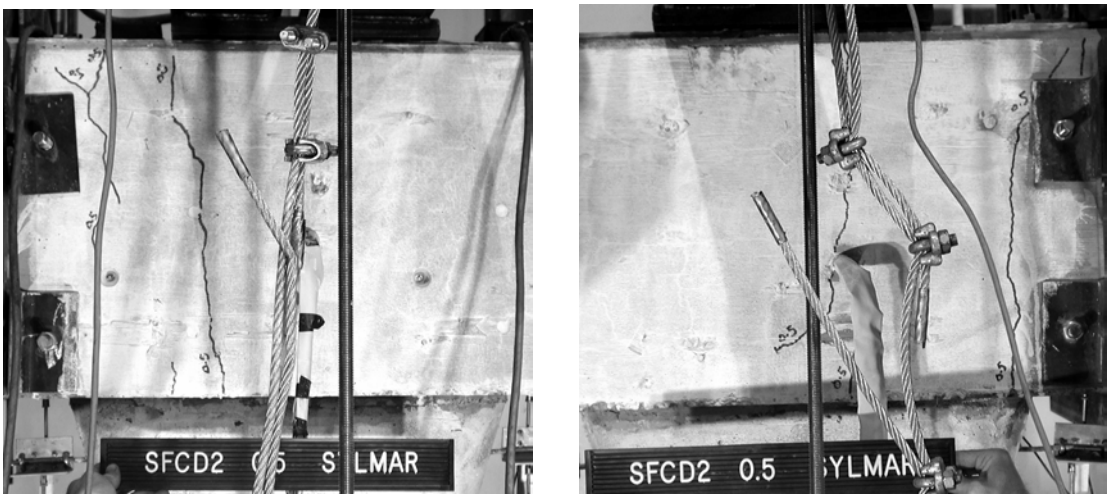

Fig. 4-109 SFCD2 at 0.5 Times Sylmar Joint Crack

Fig. 4-110 SFCD2 at 1.0 Times Sylmar (a) Column & Joint (b) Joint Crack

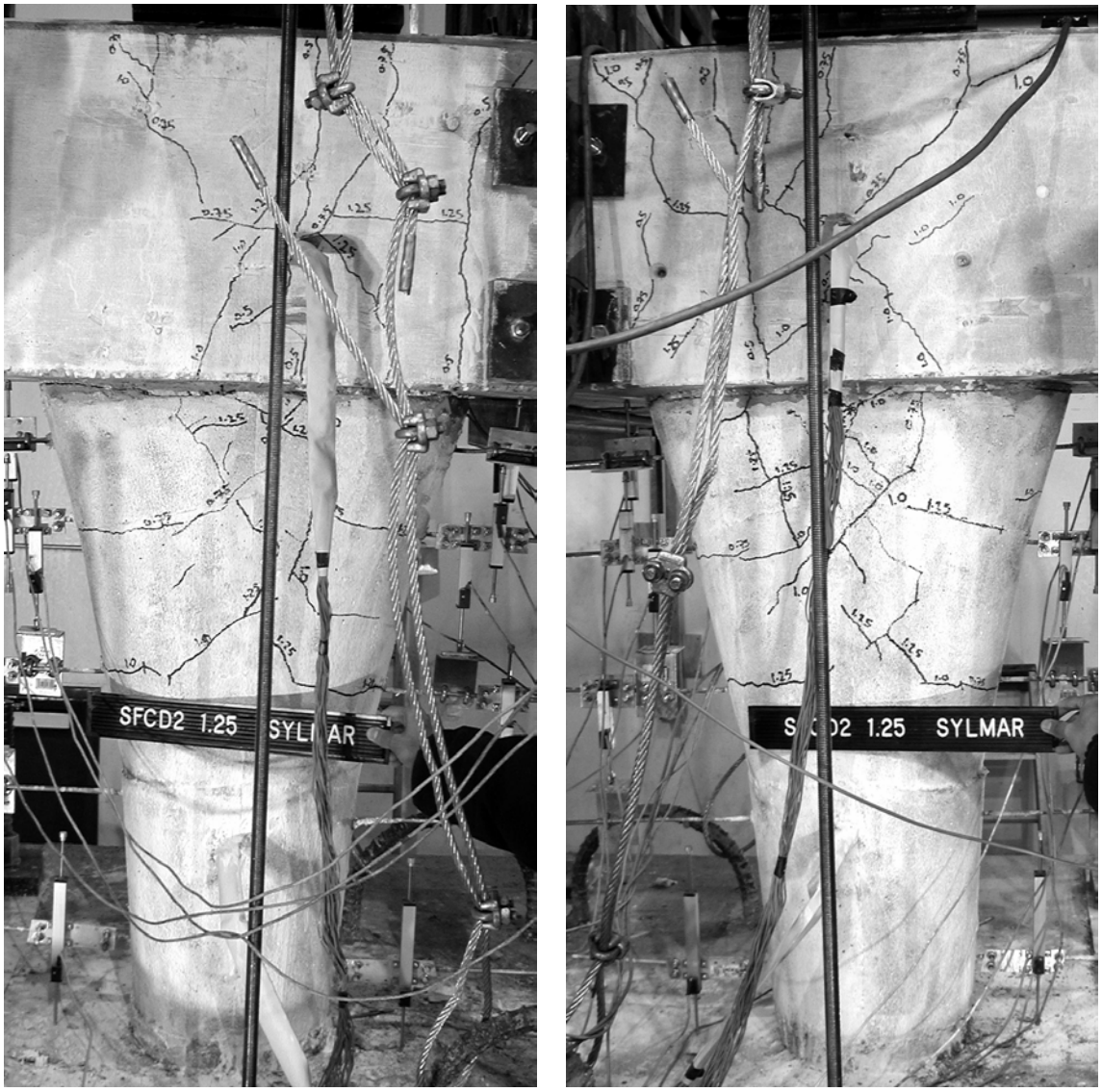

Fig. 4-111 SFCD2 at 1.25 Times Sylmar

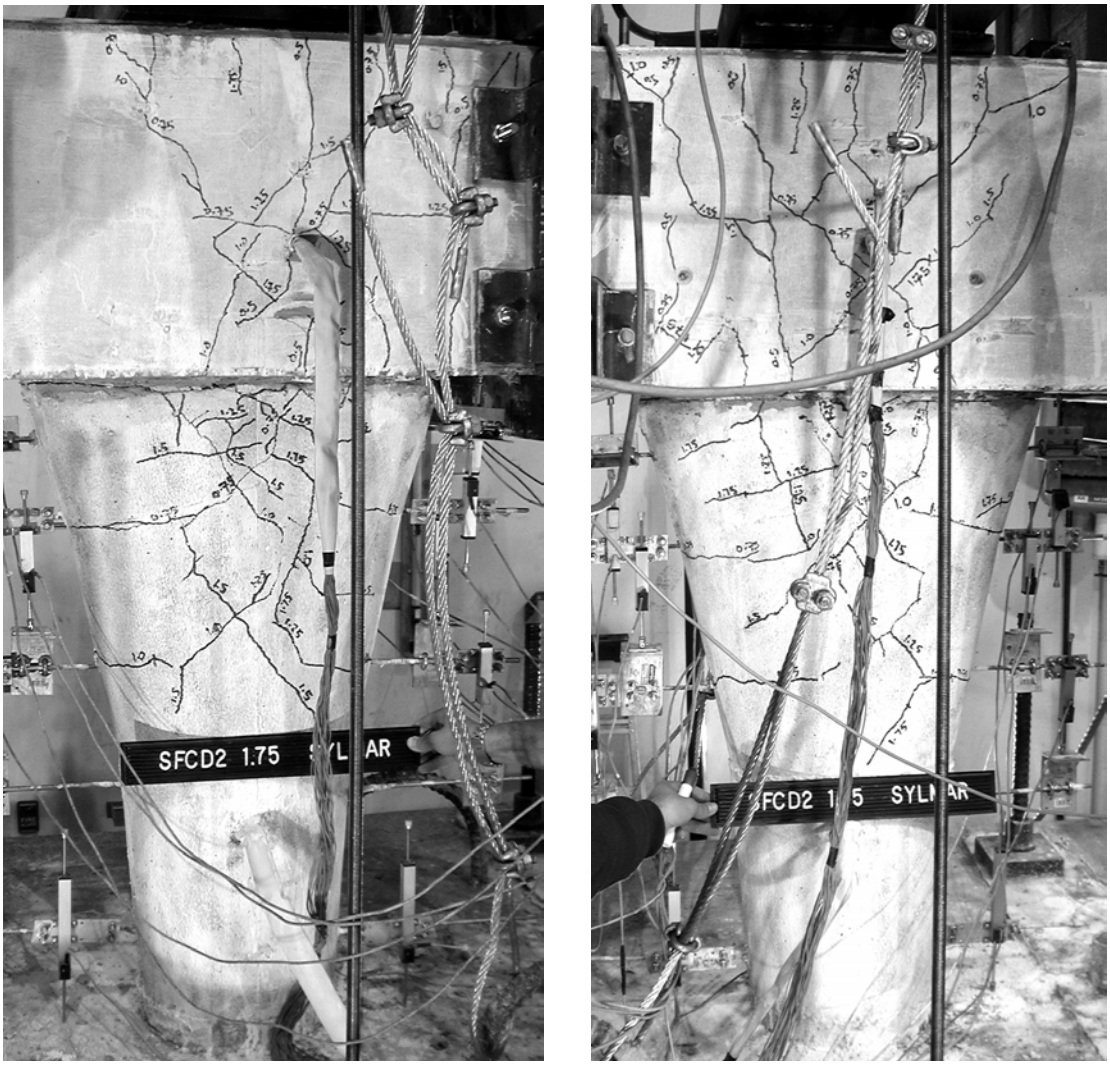

Fig. 4-112 SFCD2 at 1.75 Times Sylmar (a) Column & Joint (b) Joint Crack

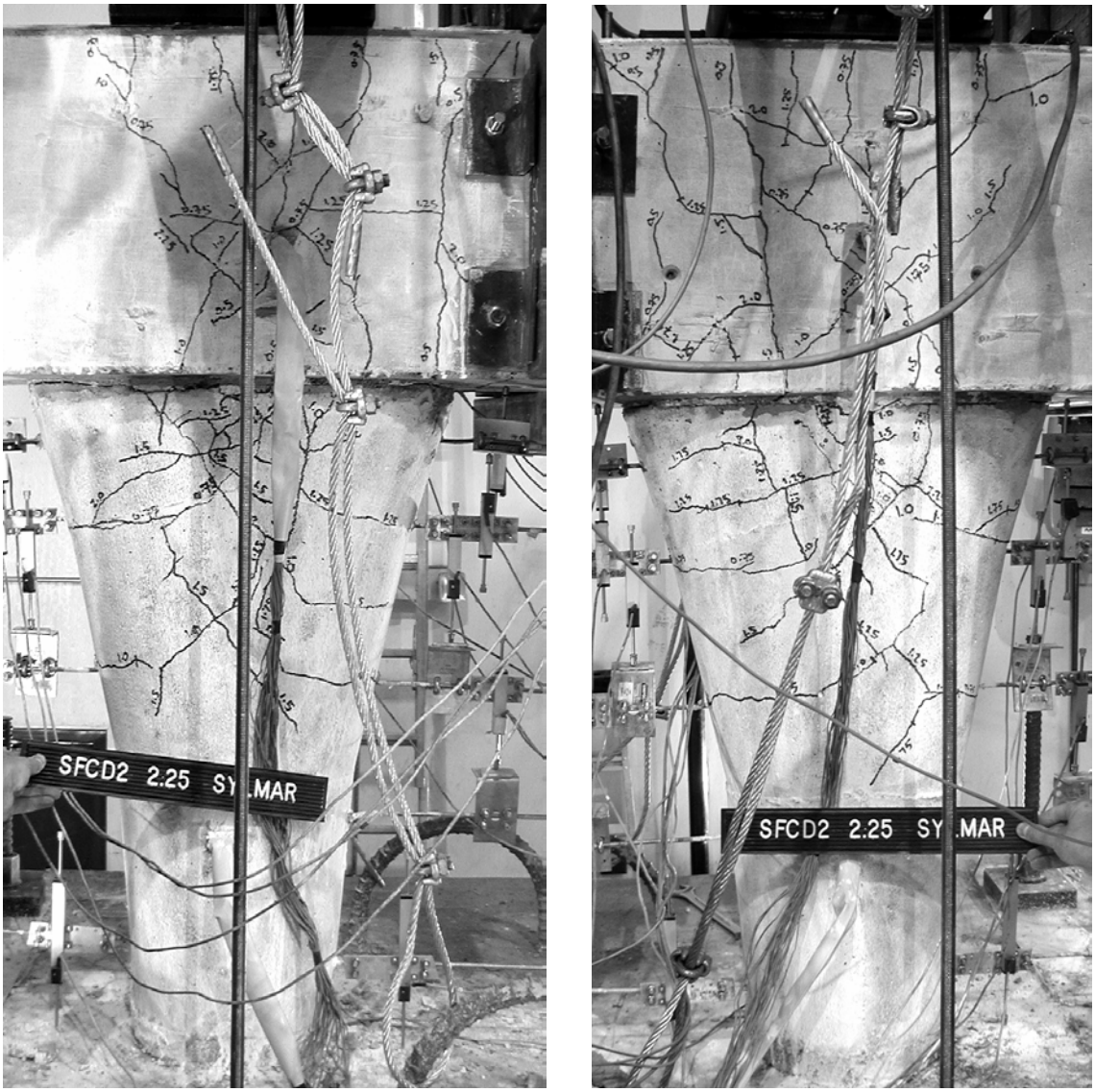

Fig. 4-113 SFCD2 at 2.25 Times Sylmar (a) Column & Joint (b) Joint Crack

(a)

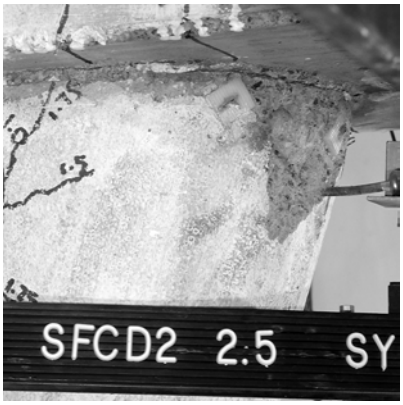

(b)

Fig. 4-114 SFCD2 at 2.5 Times Sylmar (a) Column & Joint (b) Concrete Spalling

(a)

(b)

Fig. 4-115 SFCD2 at 2.5 Times Sylmar (a) Column & Joint (b) Concrete Spalling

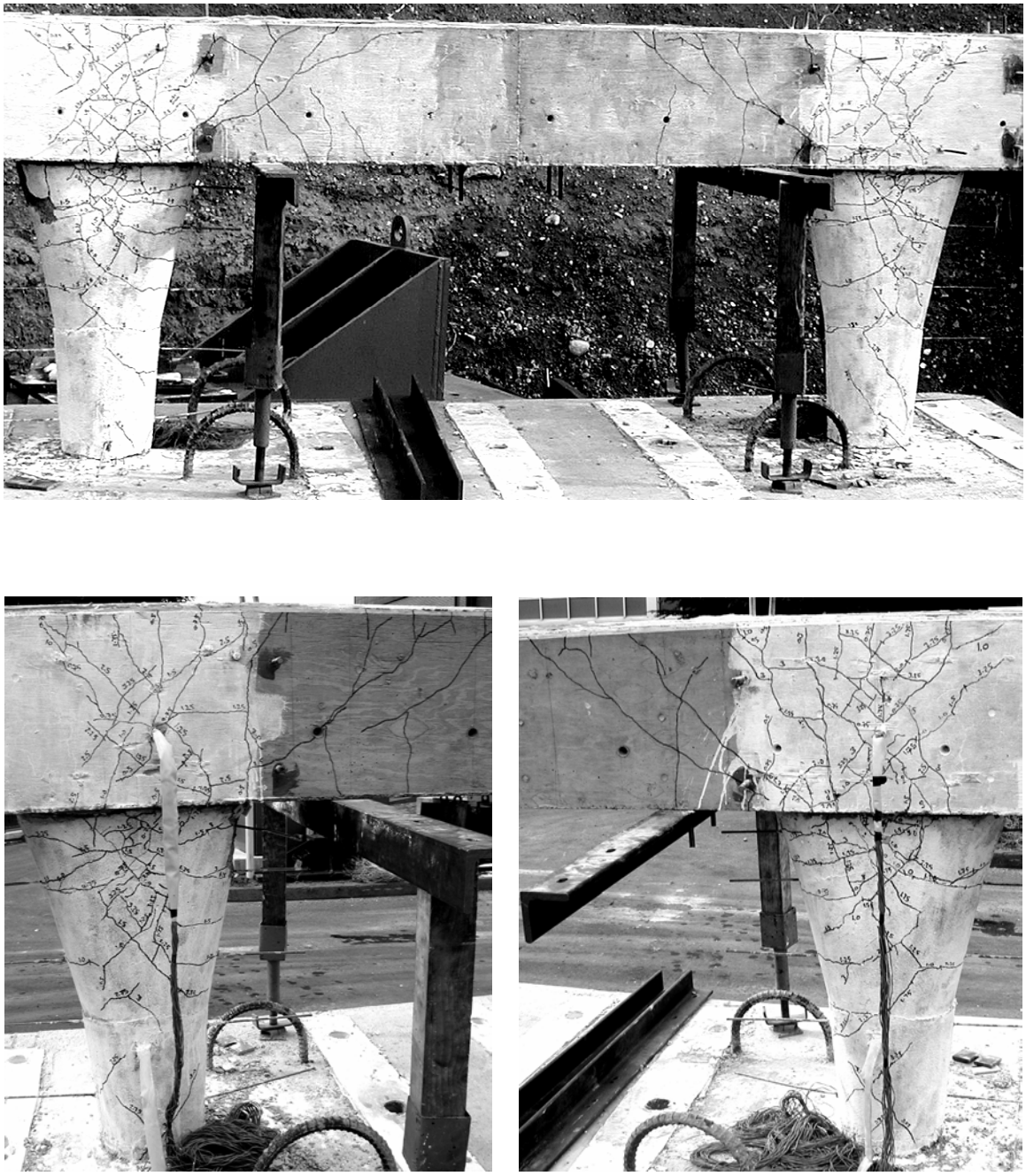

Fig. 4-116 After Bucket Removal Cracking Pattern

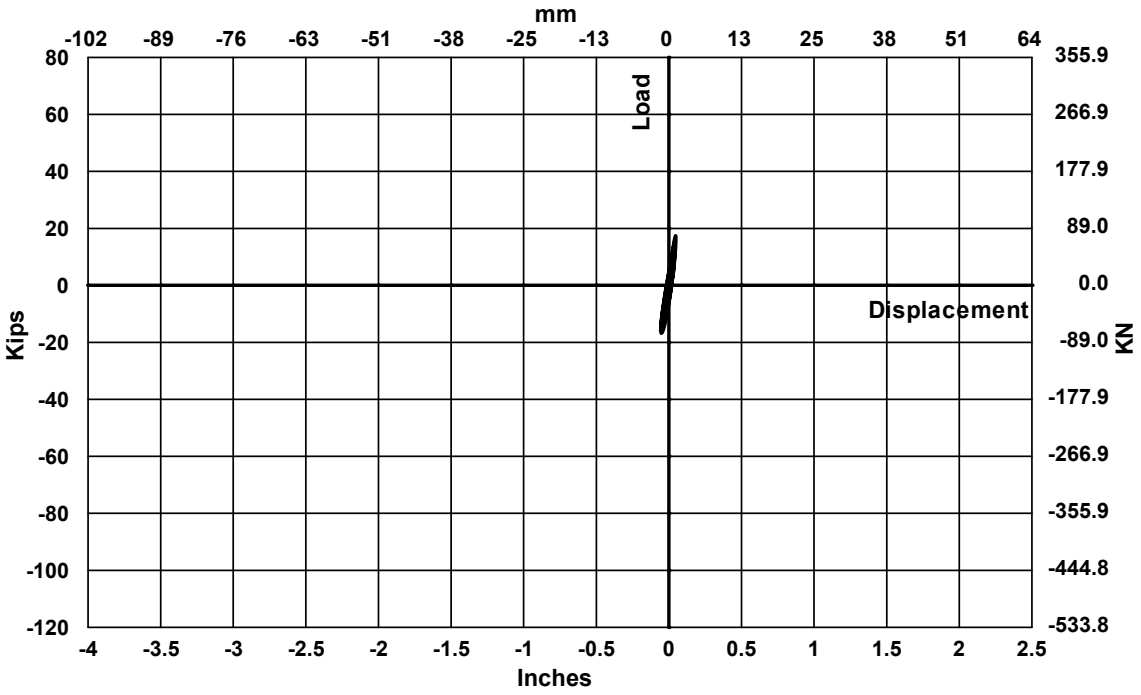

Fig. 4-117 Measured Load-Displacement Curve for SFCD2 at 0.15 Times Sylmar

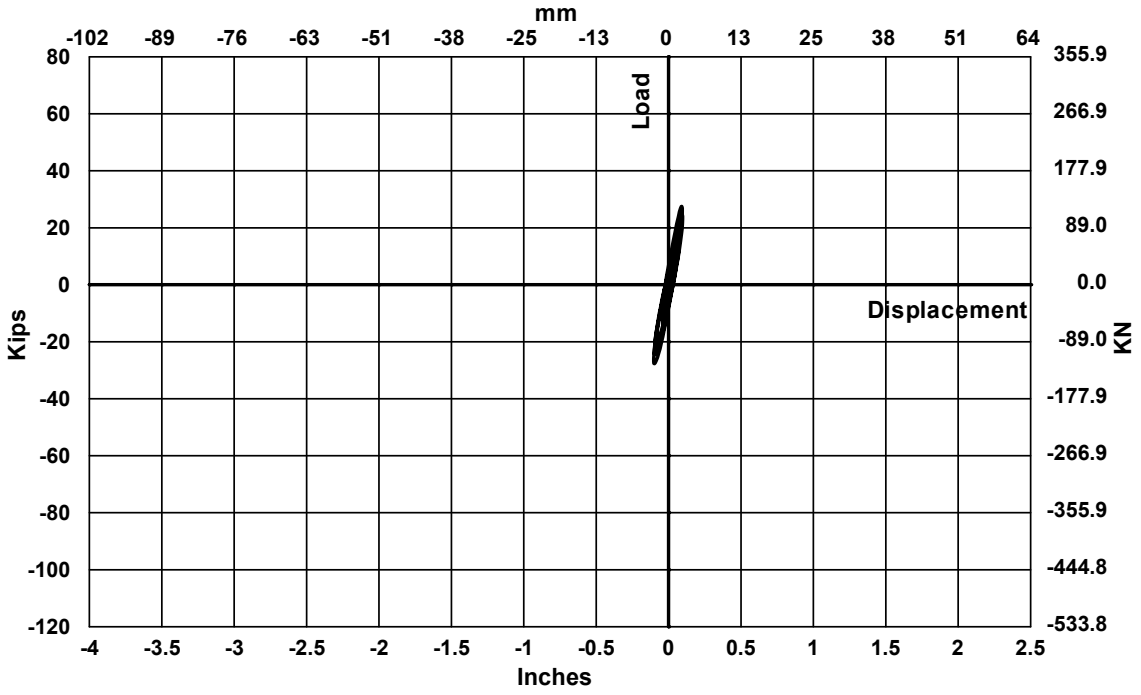

Fig. 4-118 Measured Load-Displacement Curve for SFCD2 at 0.25 Times Sylmar

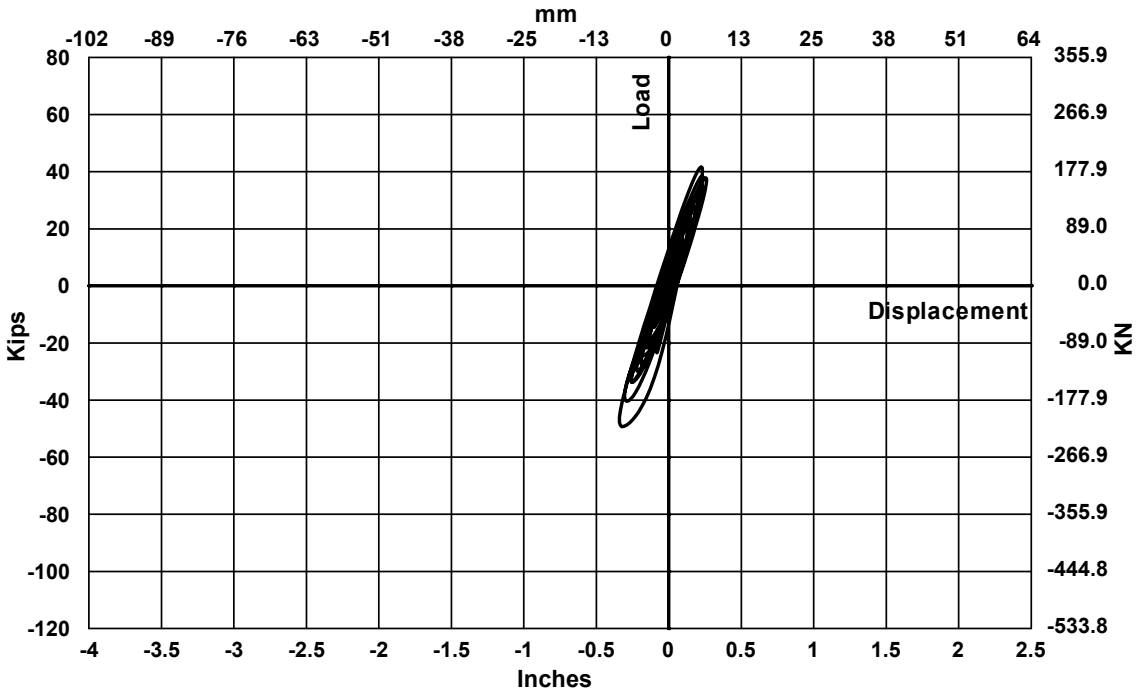

Fig. 4-119 Measured Load-Displacement Curve for SFCD2 at 0.50 Times Sylmar

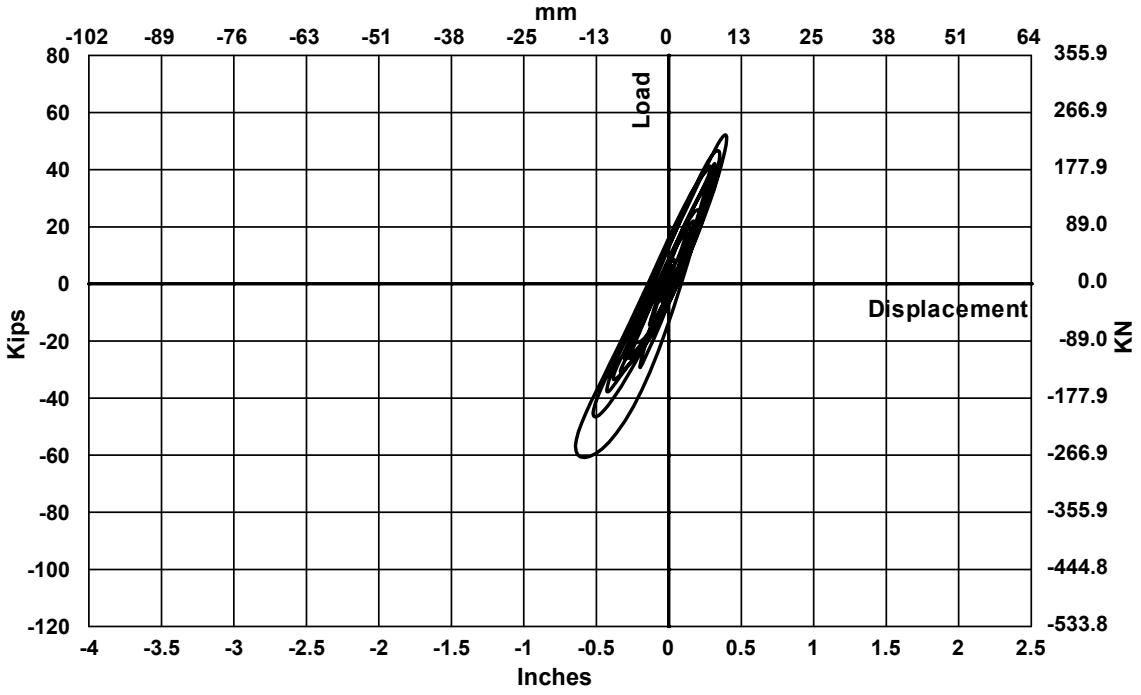

Fig. 4-120 Measured Load-Displacement Curve for SFCD2 at 0.75 Times Sylmar

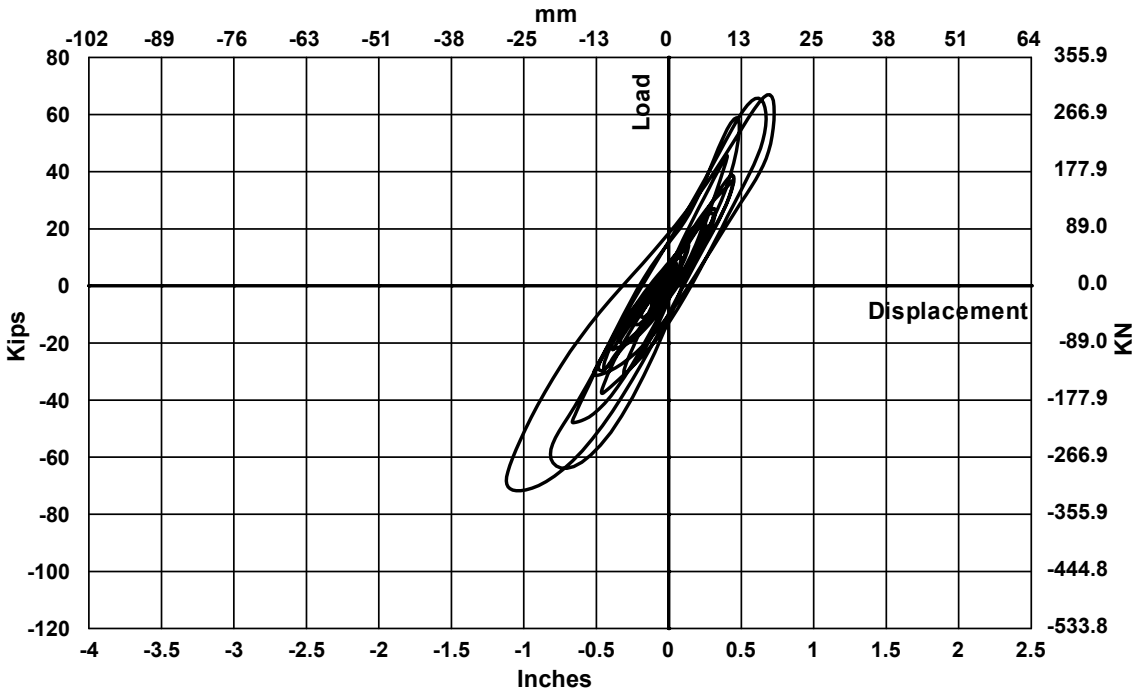

Fig. 4-121 Measured Load-Displacement Curve for SFCD2 at 1.00 Times Sylmar

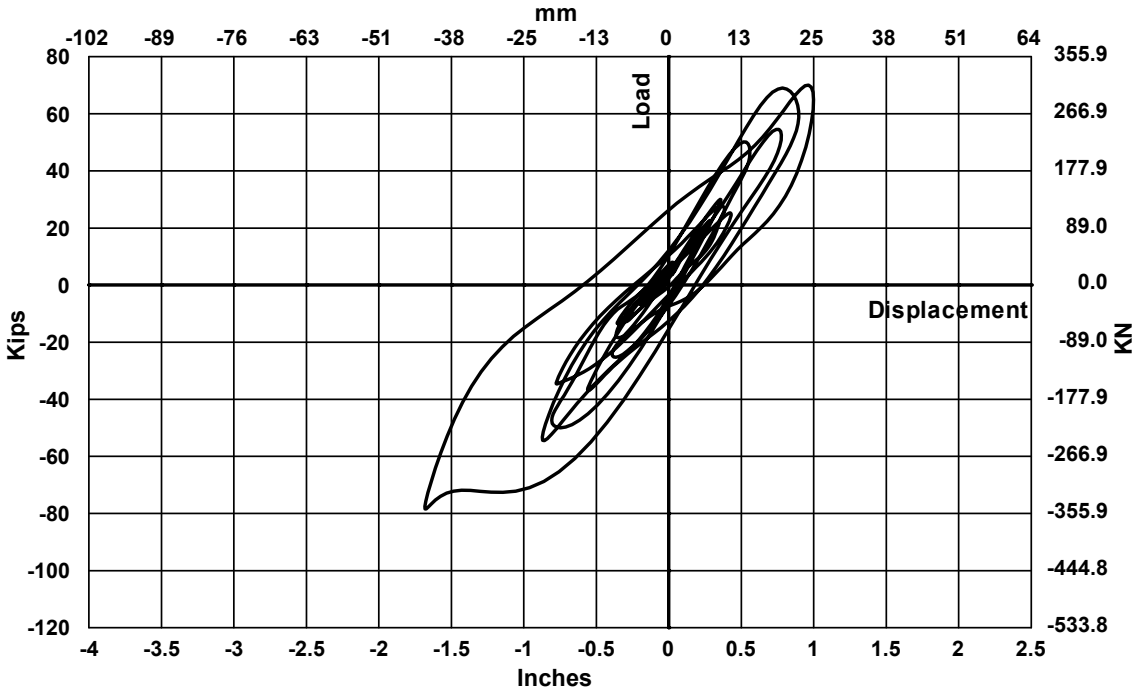

Fig. 4-122 Measured Load-Displacement Curve for SFCD2 at 1.25 Times Sylmar

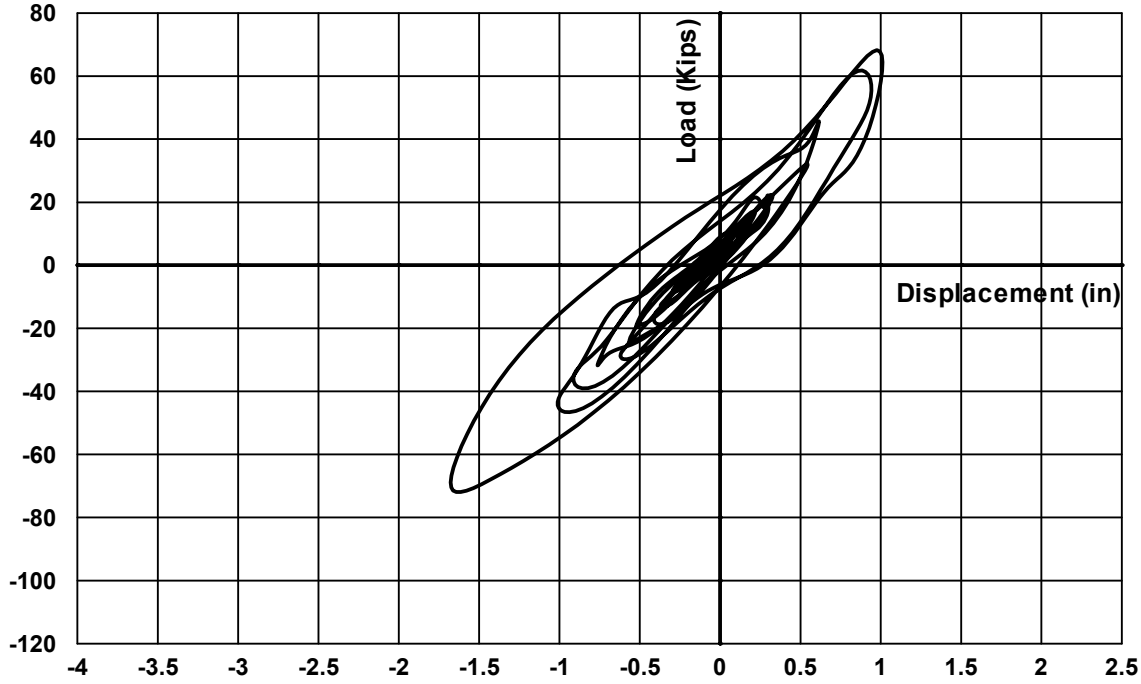

Fig. 4-123 Measured Load-Displacement Curve for SFCD2 at 1.50 Times Sylmar

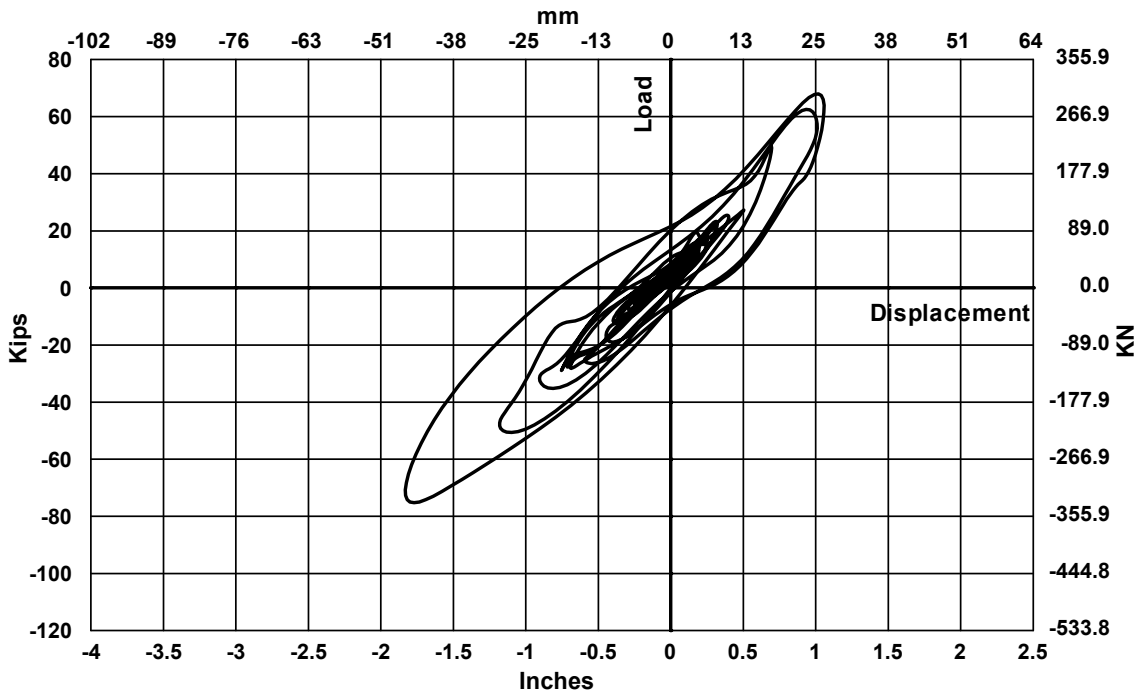

Fig. 4-124 Measured Load-Displacement Curve for SFCD2 at 1.75 Times Sylmar

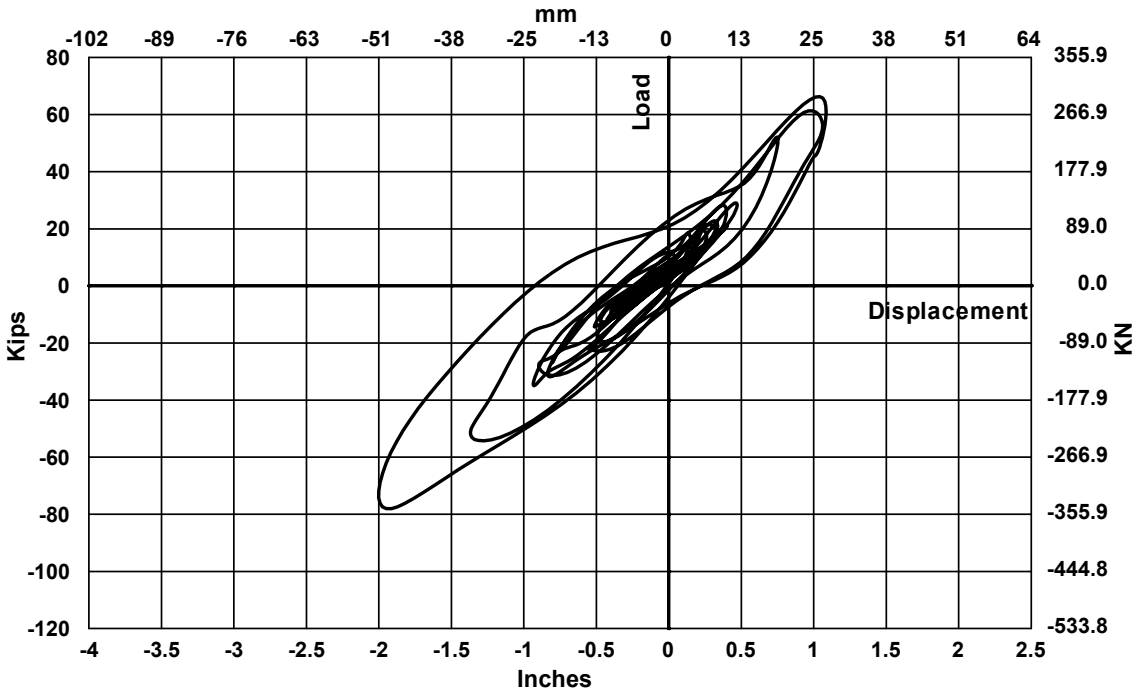

Fig. 4-125 Measured Load-Displacement Curve for SFCD2 at 2.00 Times Sylmar

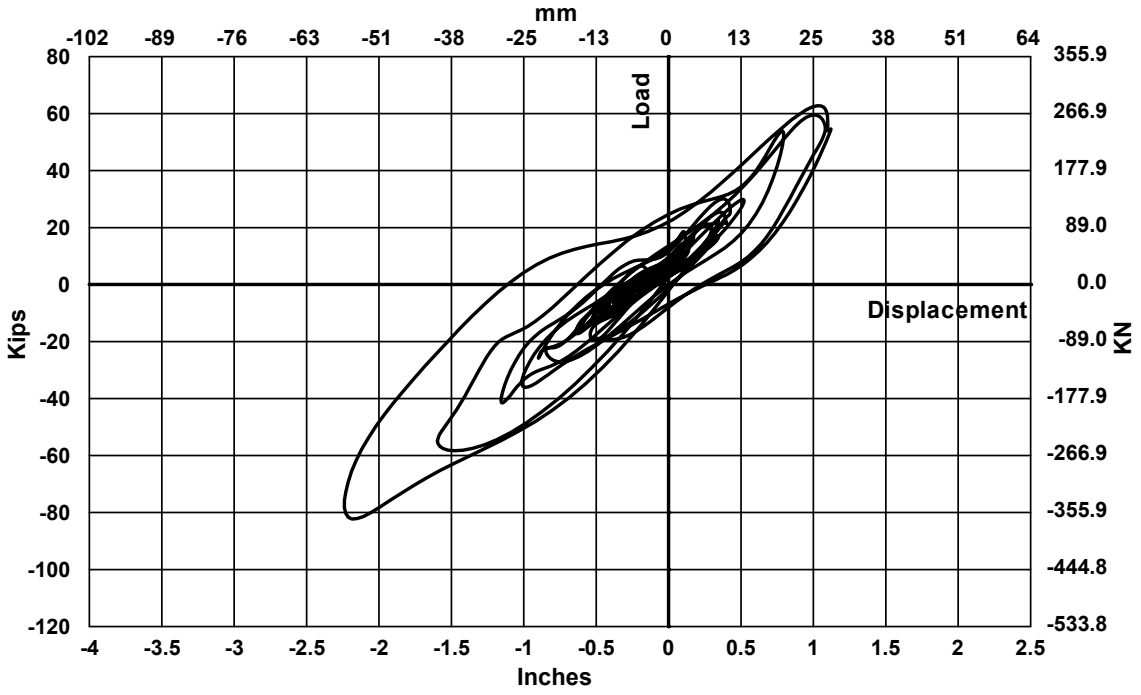

Fig. 4-126 Measured Load-Displacement Curve for SFCD2 at 2.25 Times Sylmar

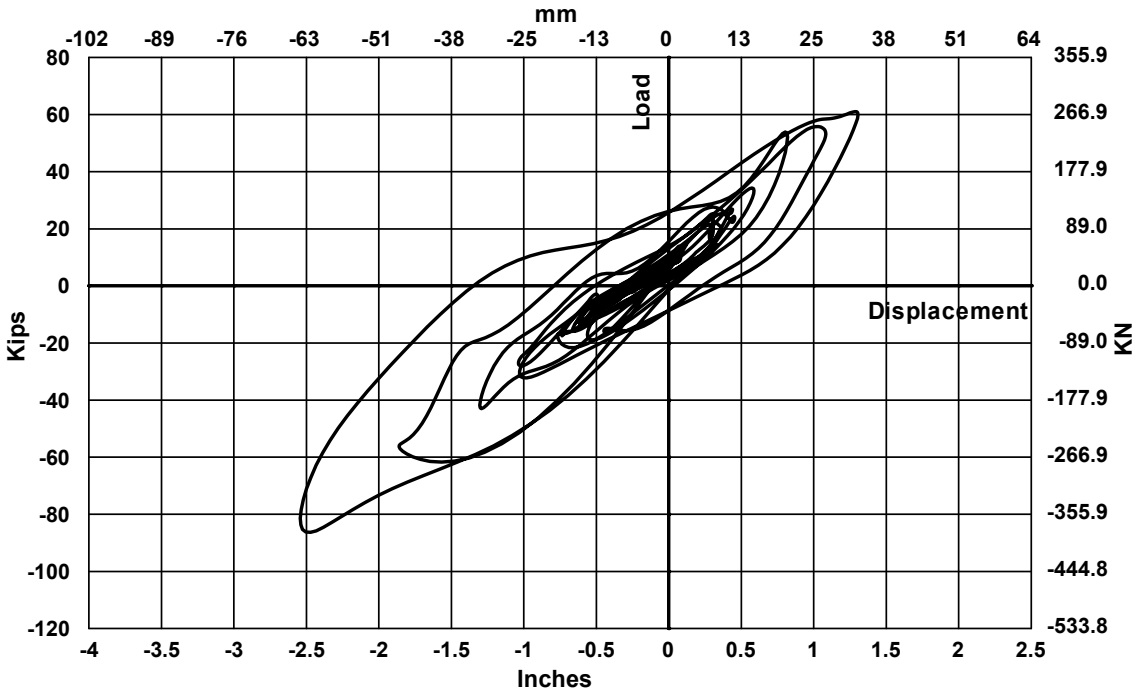

Fig. 4-127 Measured Load-Displacement Curve for SFCD2 at 2.50 Times Sylmar

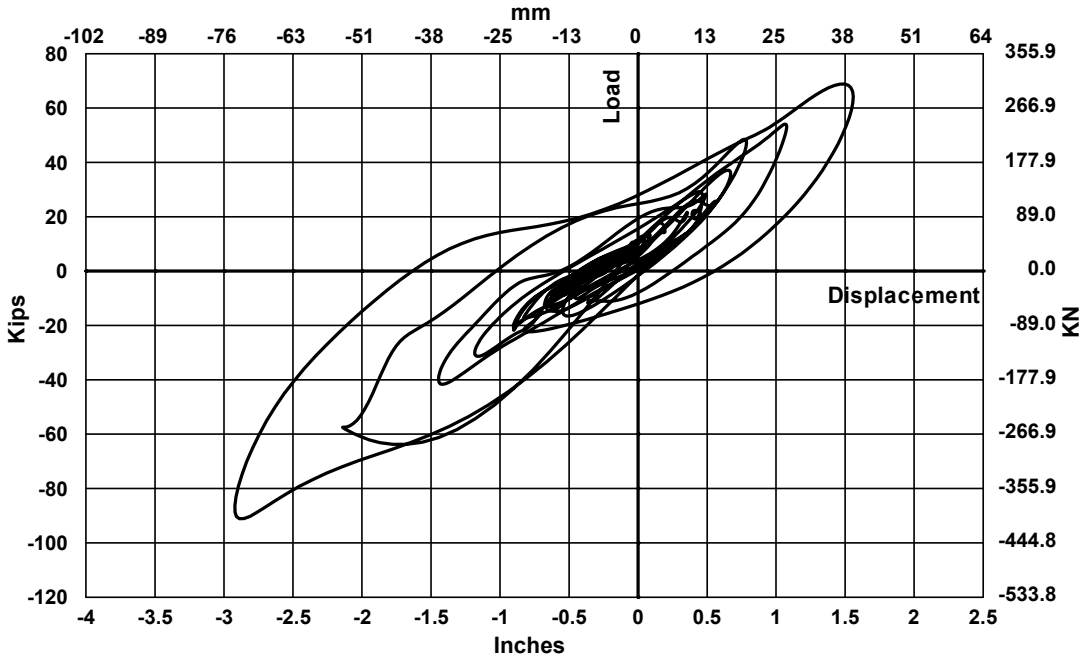

Fig. 4-128 Measured Load-Displacement Curve for SFCD2 at 2.75 Times Sylmar

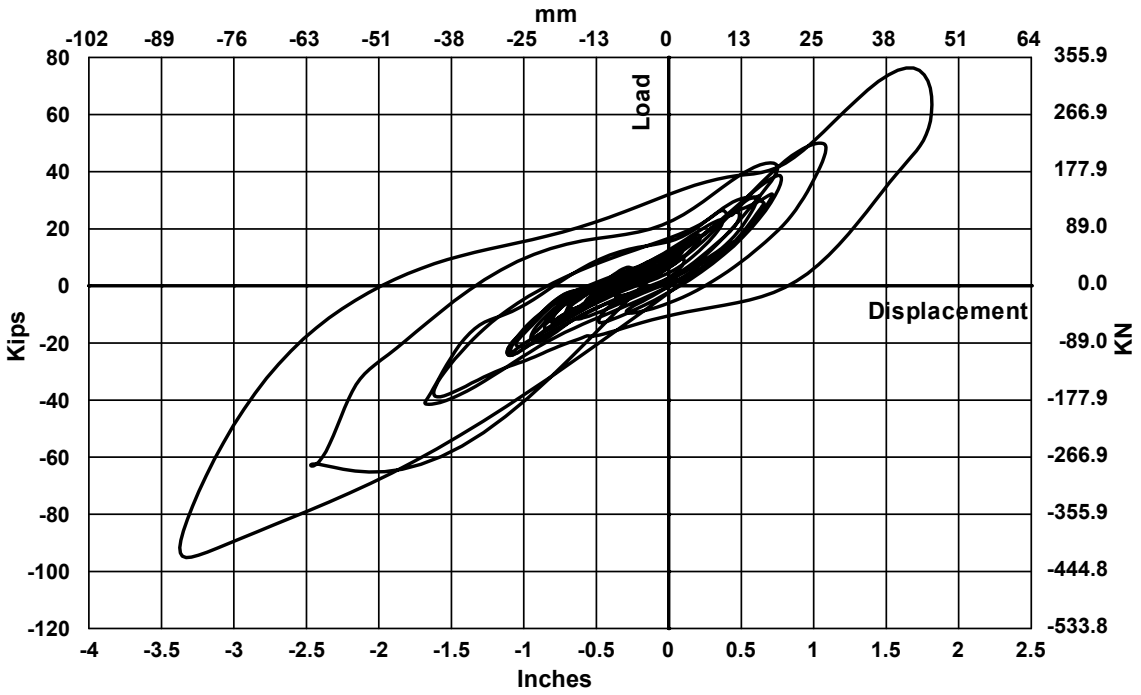

Fig. 4-129 Measured Load-Displacement Curve for SFCD2 at 3.00 Times Sylmar

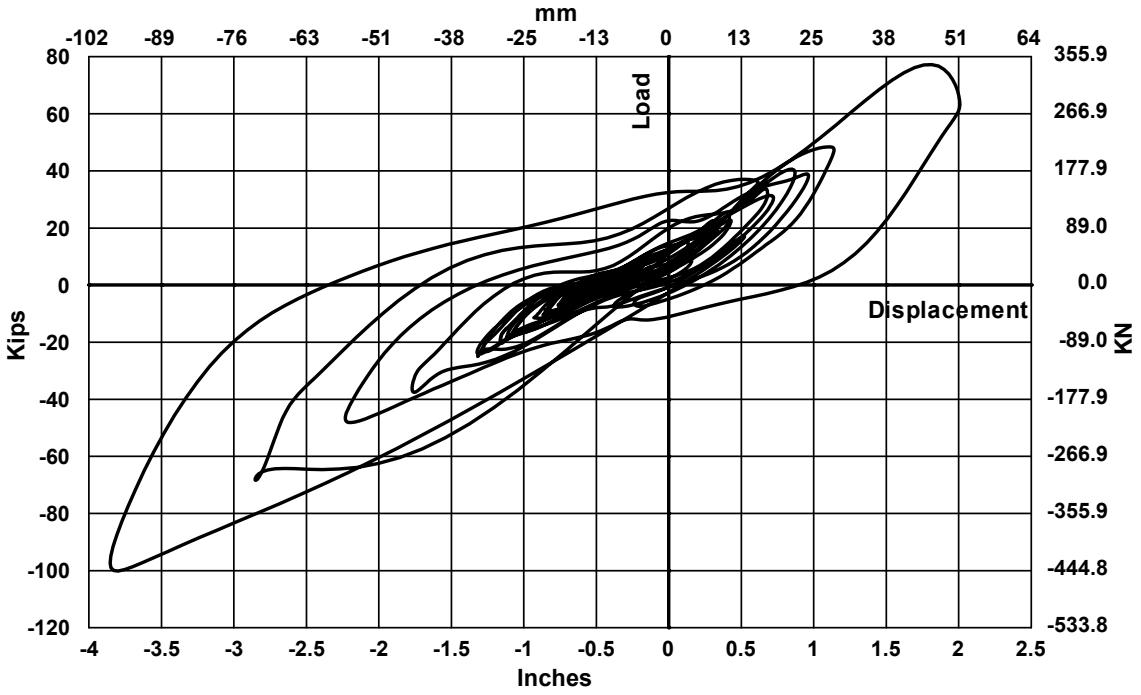

Fig. 4-130 Measured Load-Displacement Curve for SFCD2 at 3.25 Times Sylmar

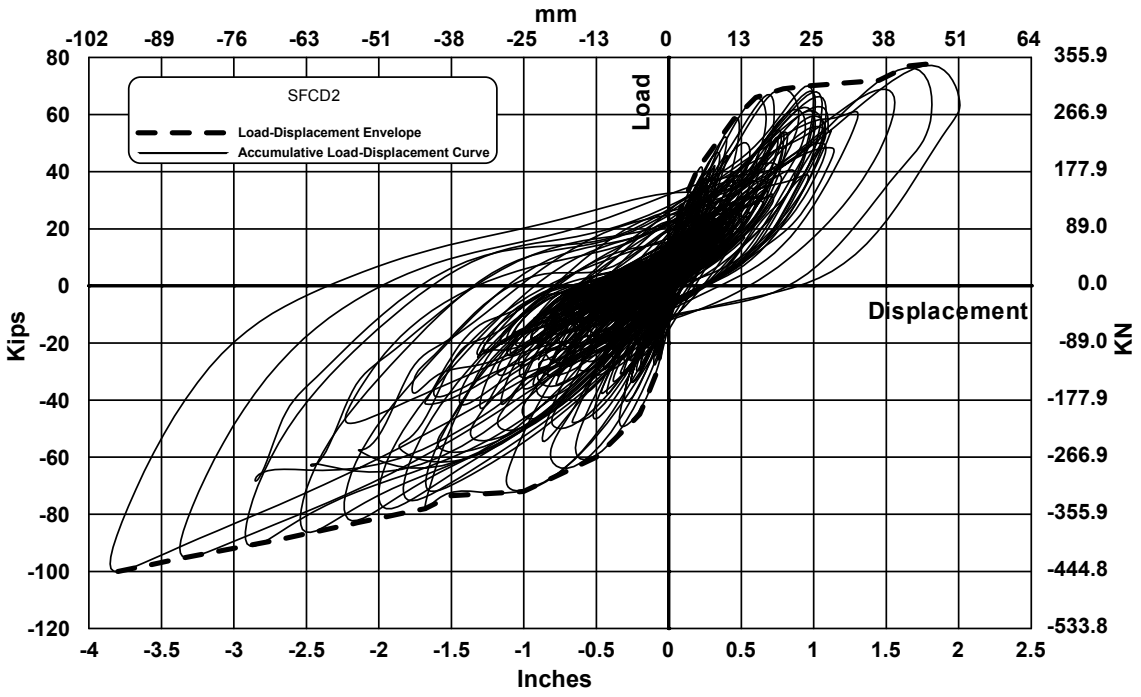

(a)

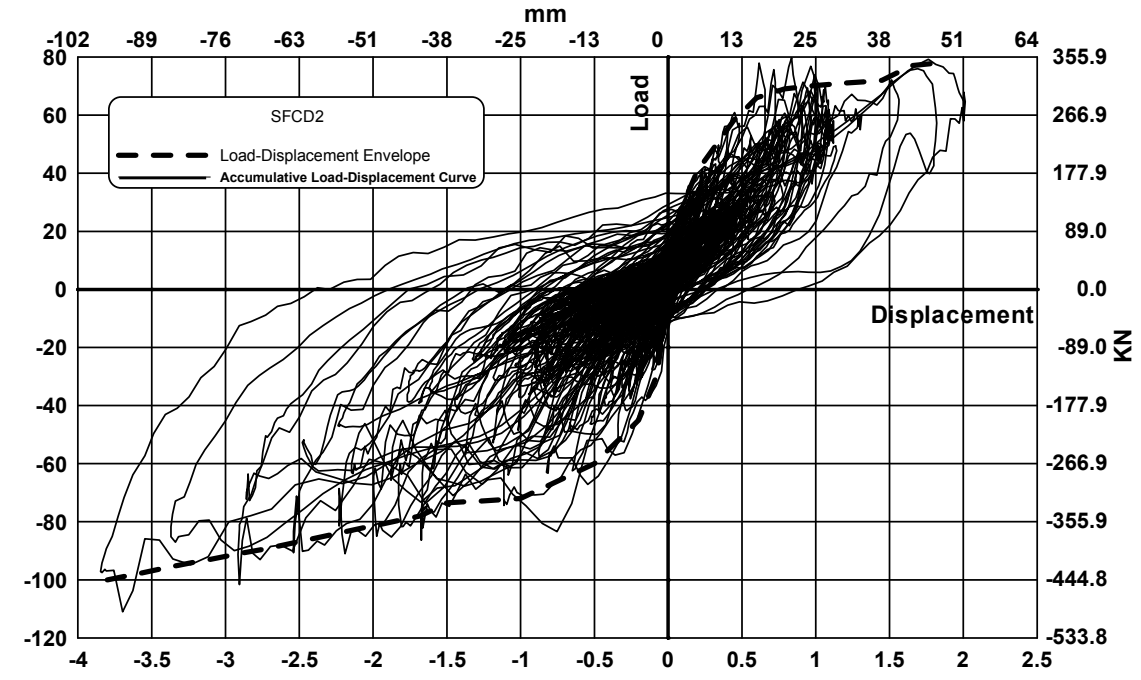

(b)

Fig. 4-131 Accumulative Measured Load-Displacement Curve for SFCD2 (a) Filtered results

(b) Unfiltered results

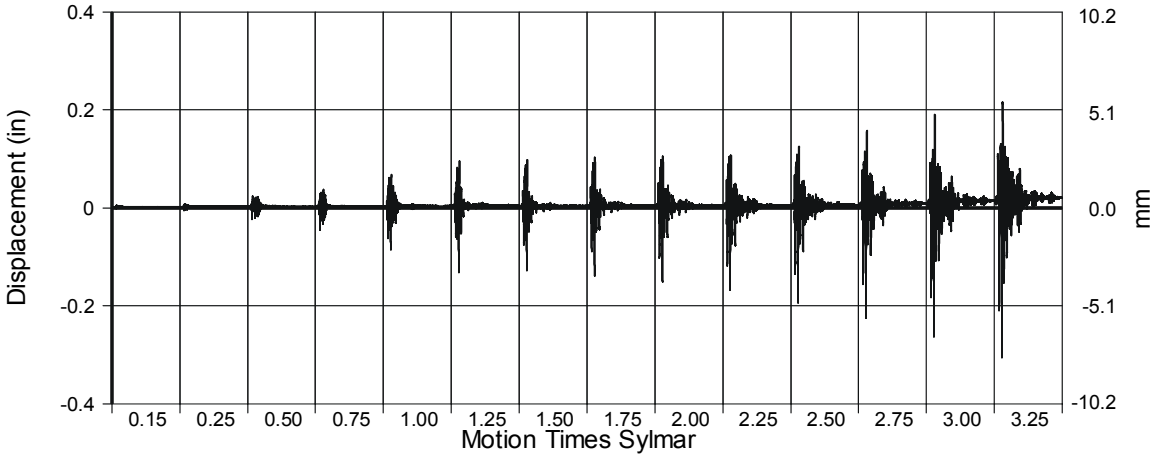

Fig. 4-132 Measured Base Hinge Displacement for East Column

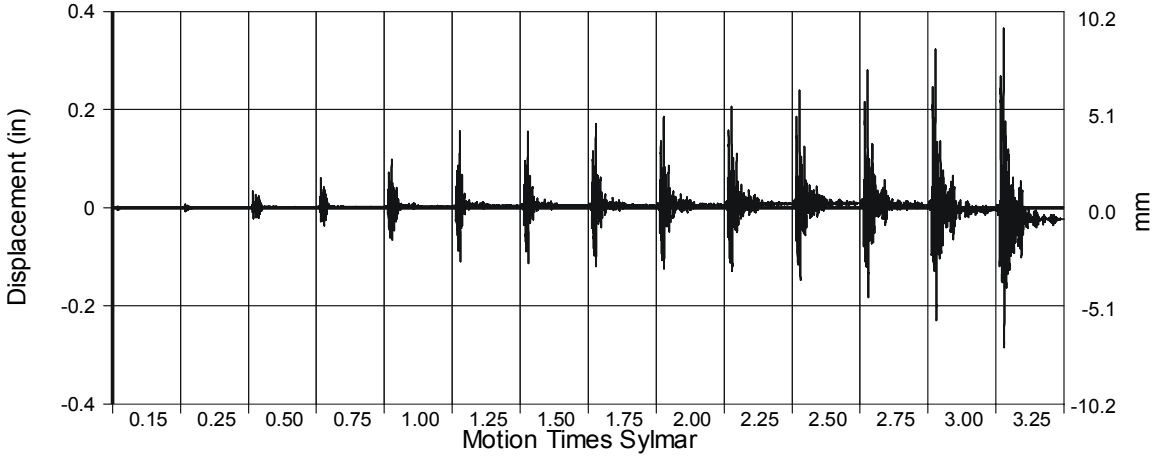

Fig. 4-133 Measured Base Hinge Displacement for West Column

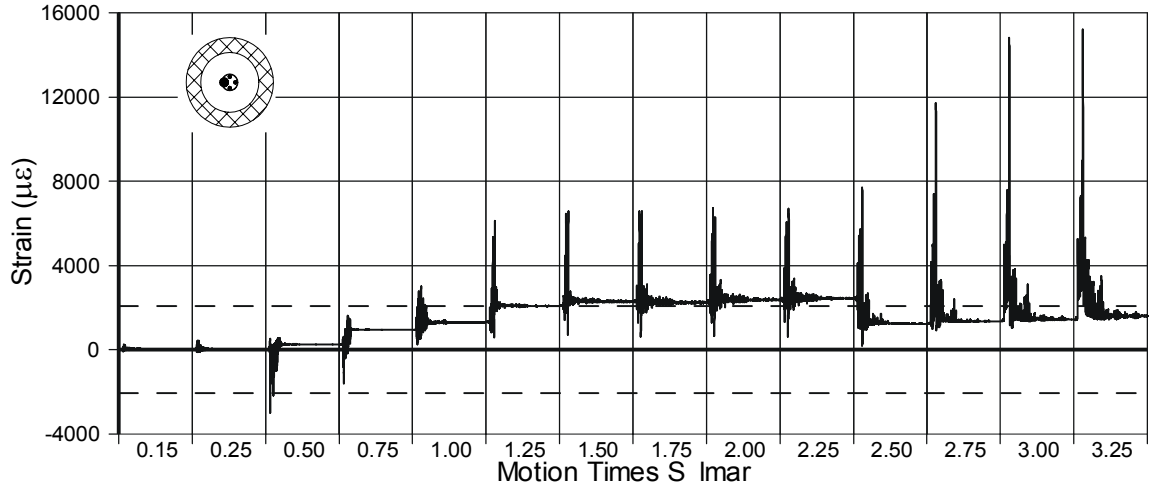

Fig. 4-134 Measured Strain at East Column Dowels

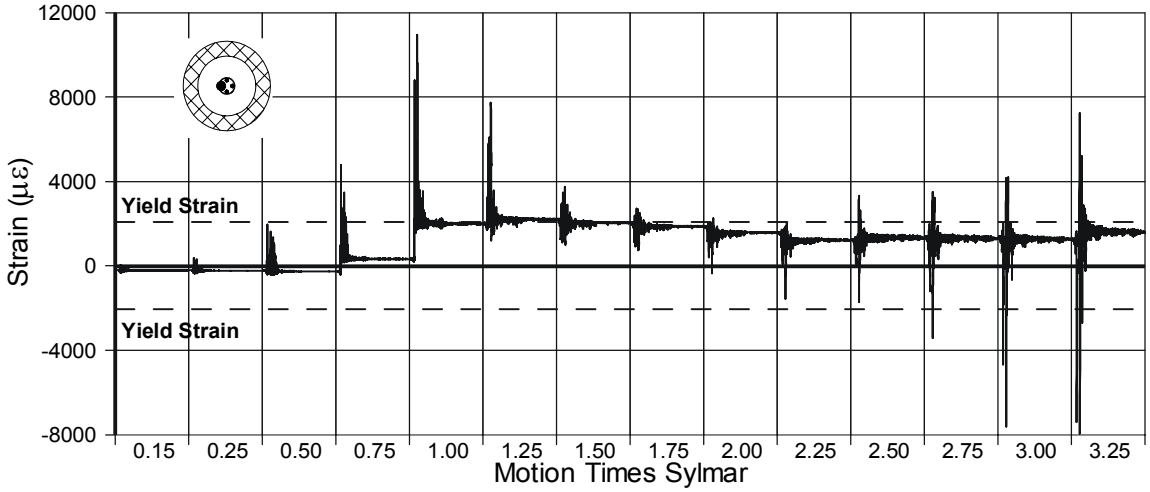

Fig. 4-135 Measured Strain at West Column Dowels

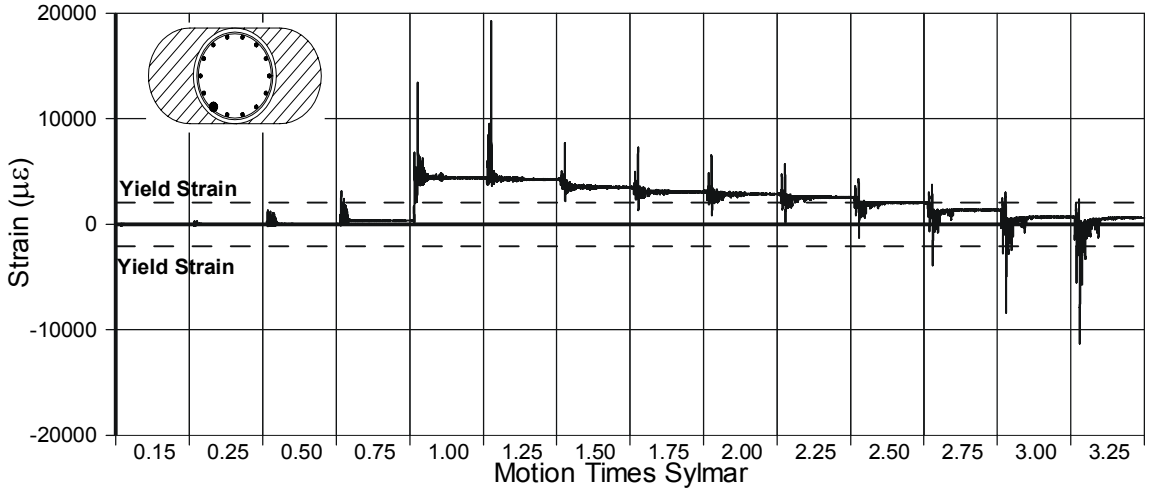

Fig. 4-136 Measured Strain for Longitudinal Column Reinforcement Gauge 79

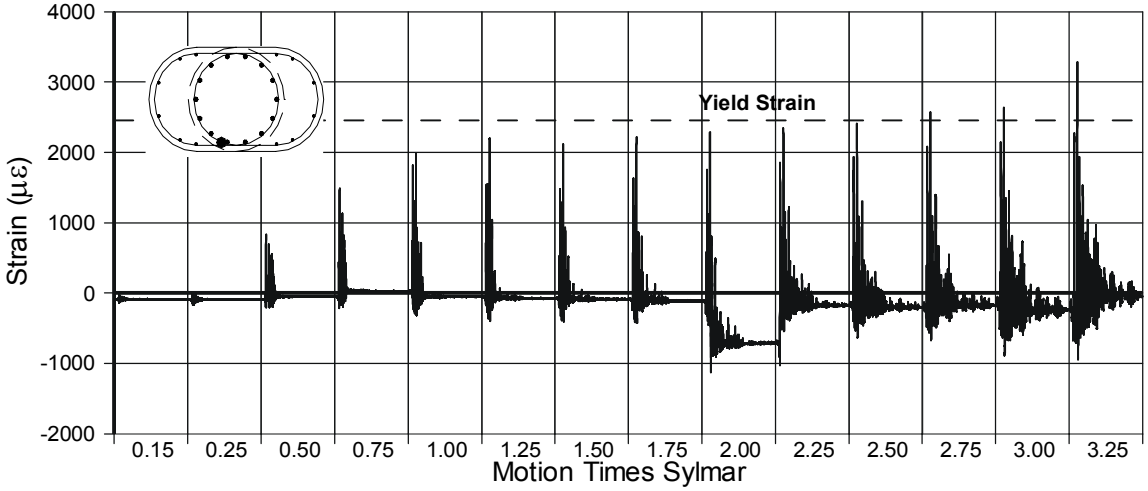

Fig. 4-137 Measured Strain for Column Spirals Gauge 126

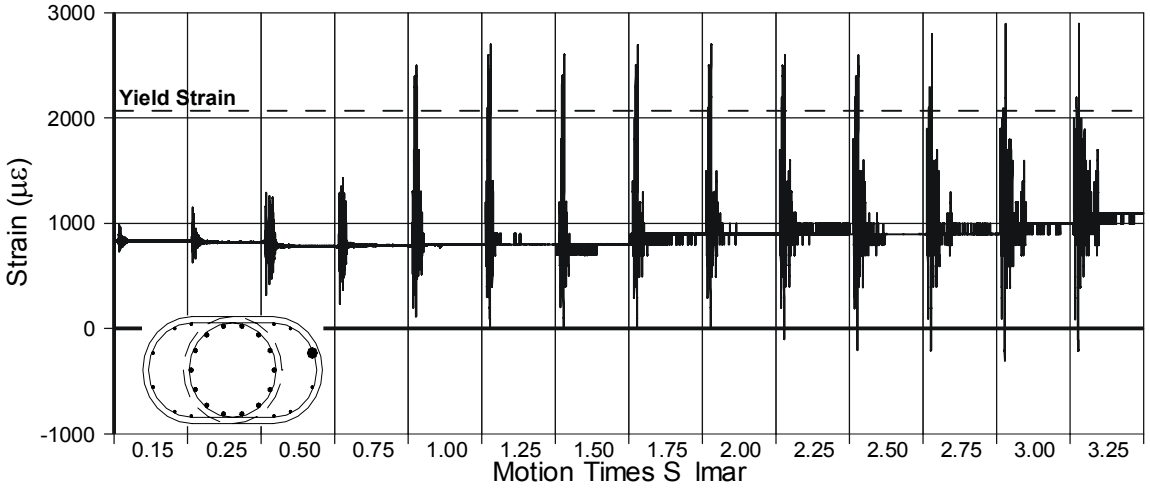

Fig. 4-138 Measured Strain for Flare Longitudinal Reinforcement Gauge 54

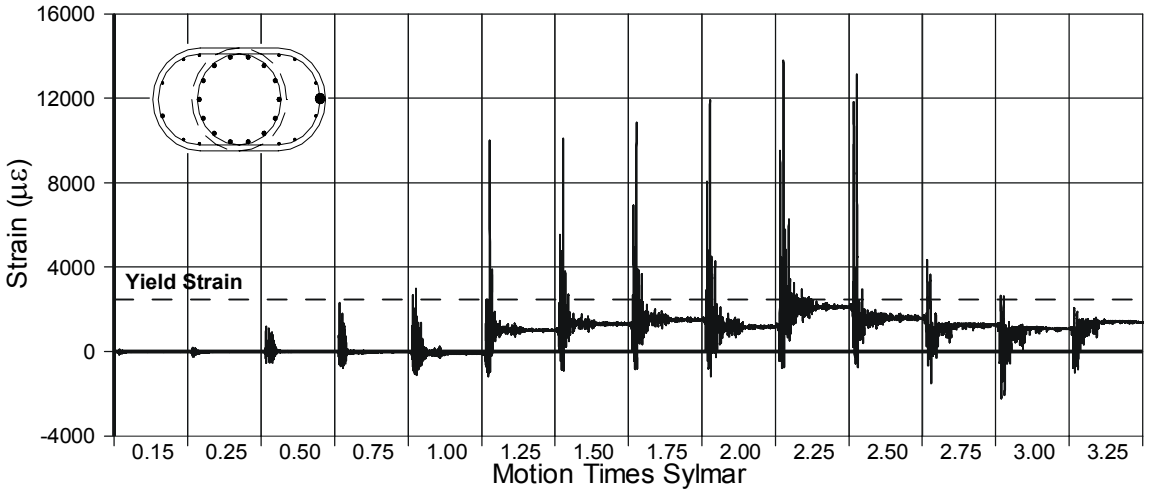

Fig. 4-139 Measured Strain for Flare Hoops Gauge 123

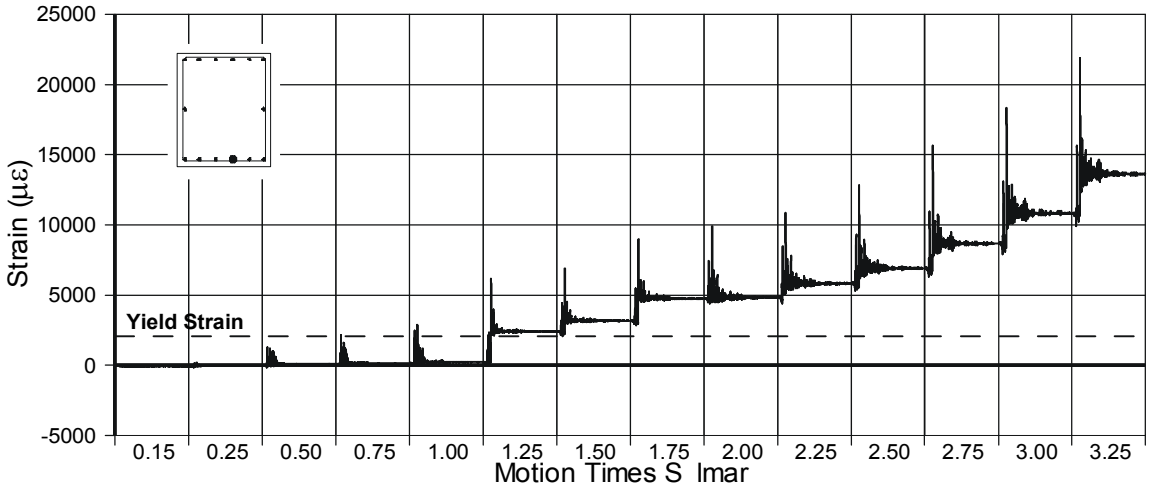

Fig. 4-140 Measured Strain for Beam's Bottom Reinforcement Gauge 139

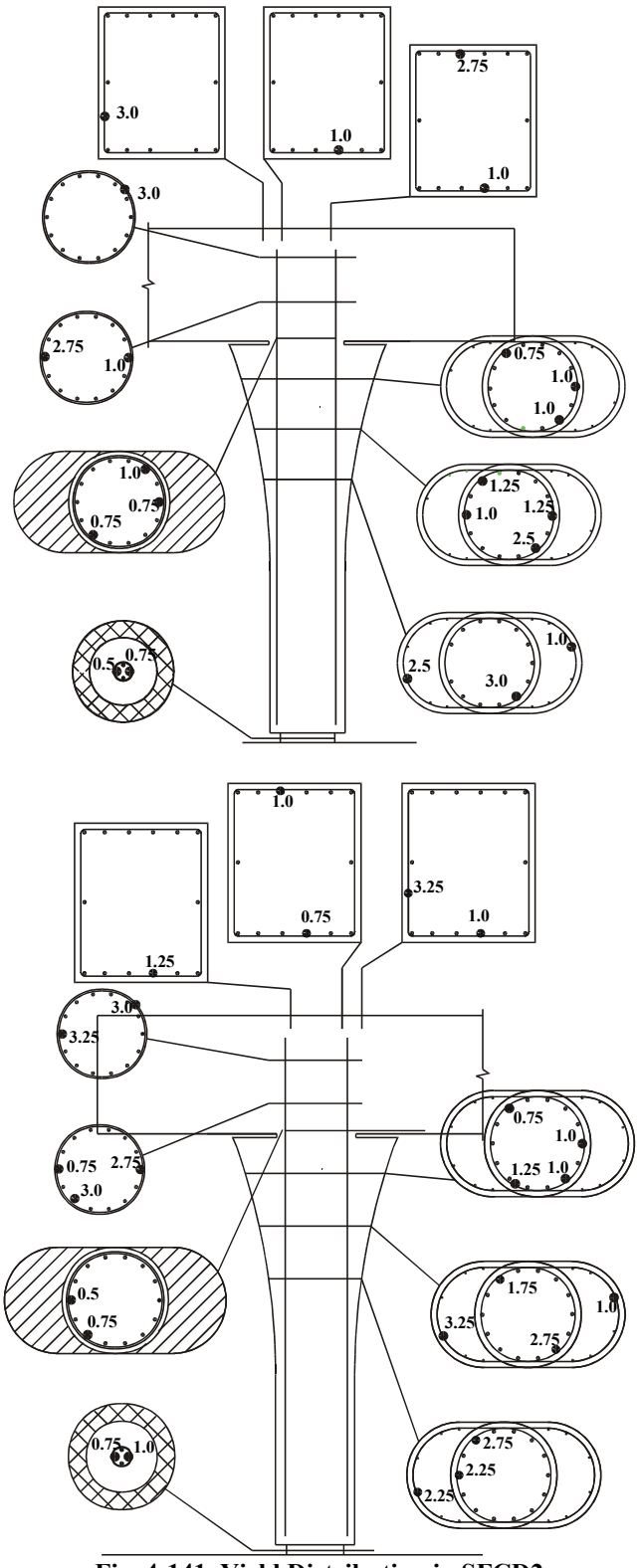

Fig. 4-141 Yield Distribution in SFCD2

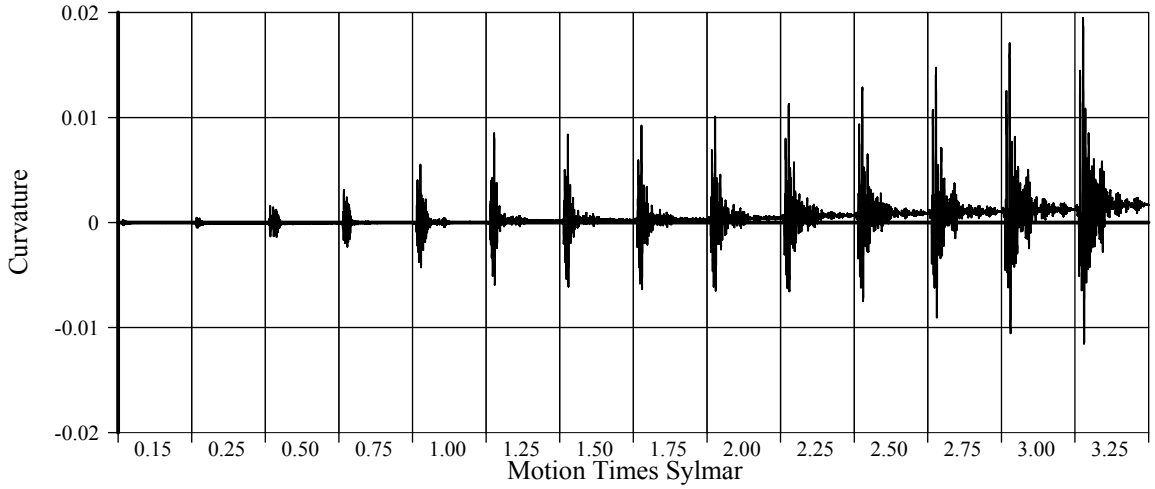

Fig. 4-142 Measured Curvature at Section 1 of East Column for SFCD2

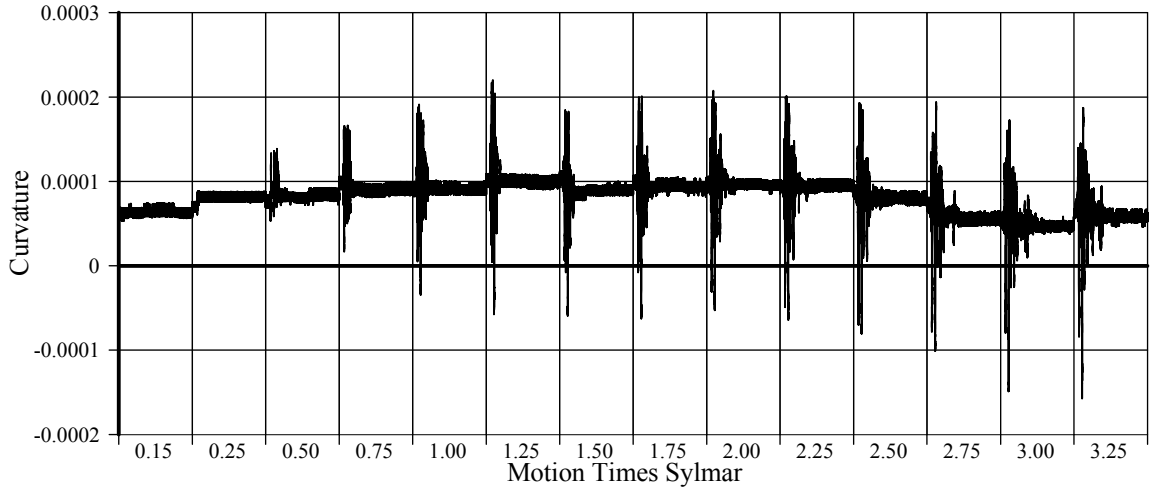

Fig. 4-143 Measured Curvature at Section 2 of East Column for SFCD2

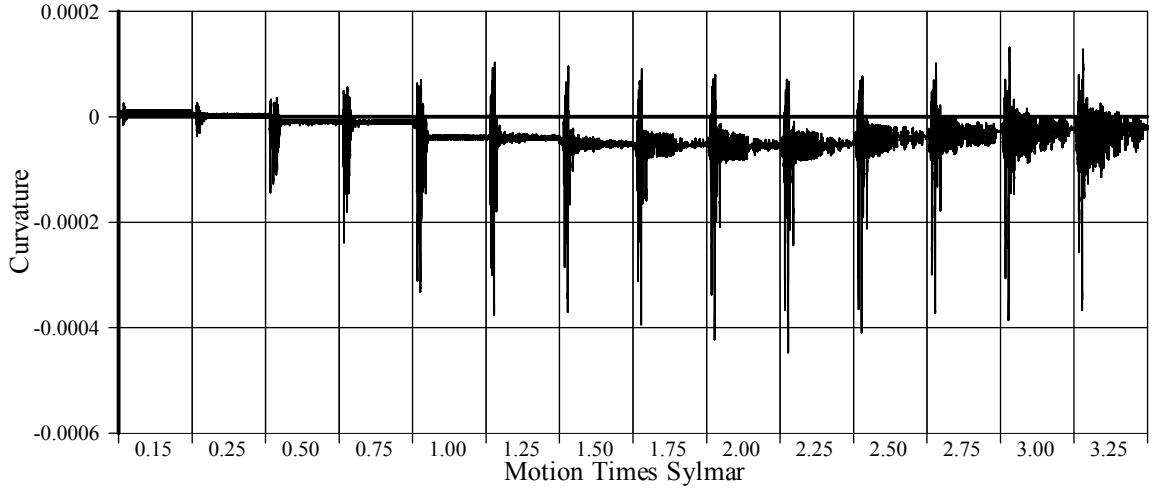

Fig. 4-144 Measured Curvature at Section 3 of East Column for SFCD2

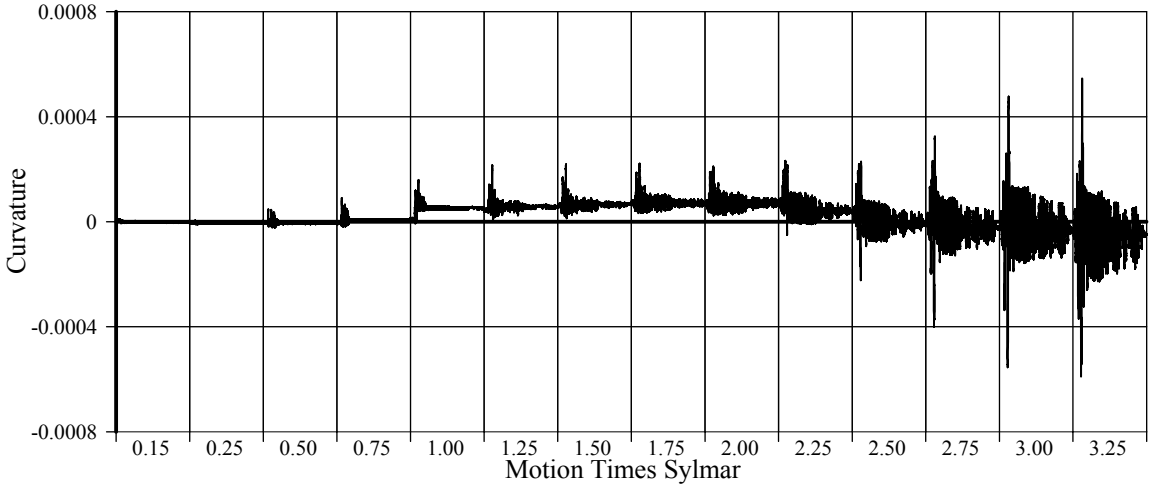

Fig. 4-145 Measured Curvature at Section 4 of East Column for SFCD2

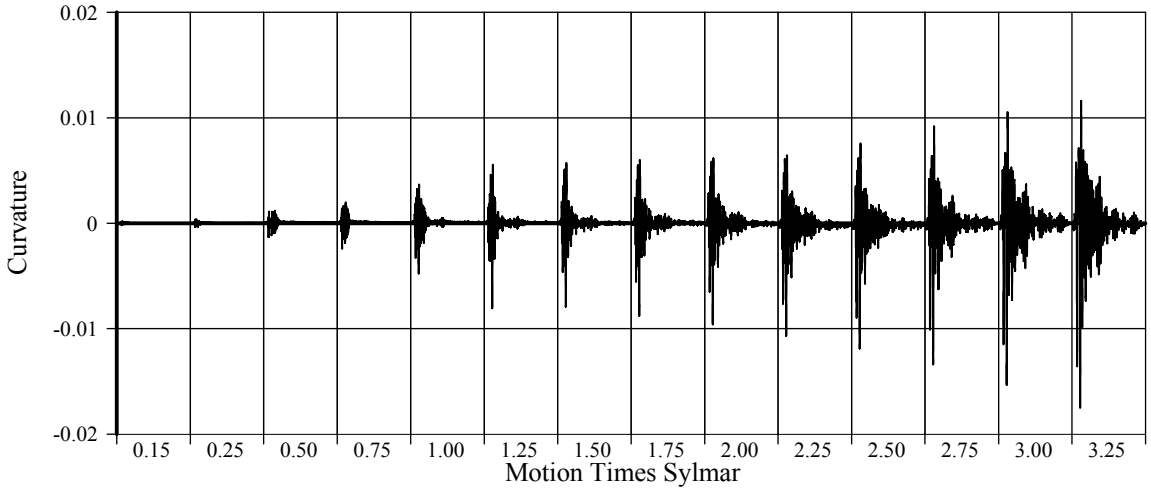

Fig. 4-146 Measured Curvature at Section 5 of East Column for SFCD2

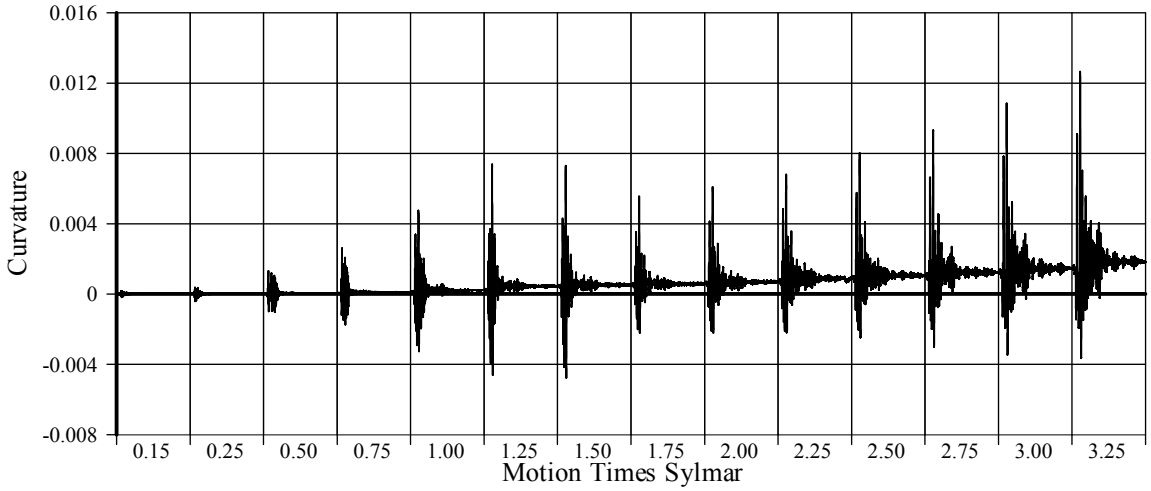

Fig. 4-147 Measured Curvature at Section 1 of West Column for SFCD2

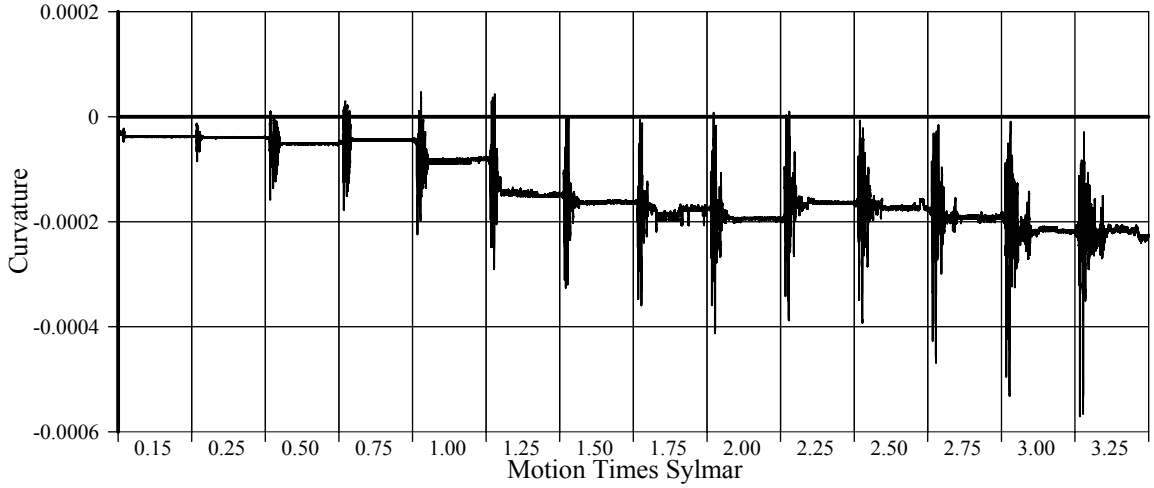

Fig. 4-148 Measured Curvature at Section 2 of West Column for SFCD2

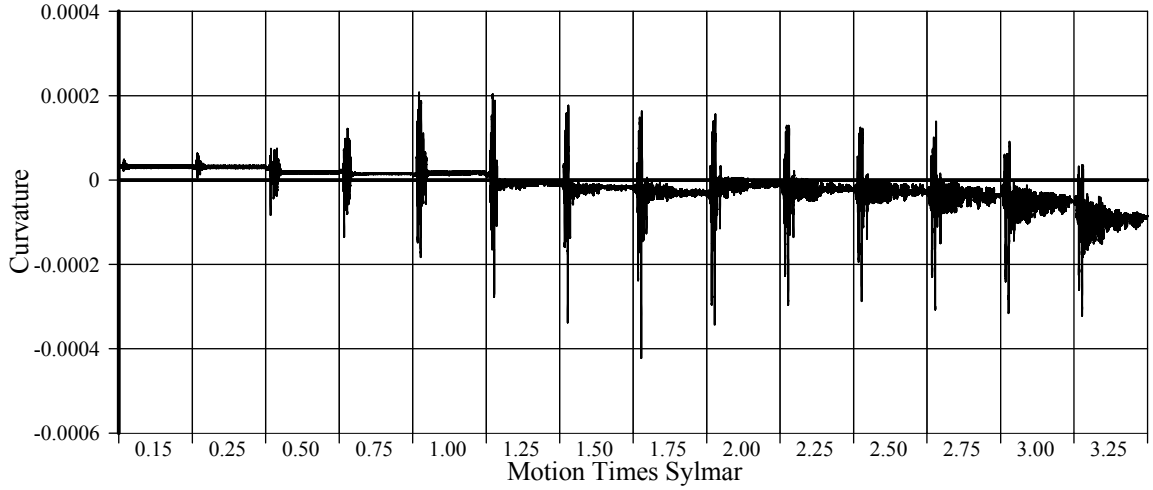

Fig. 4-149 Measured Curvature at Section 3 of West Column for SFCD2

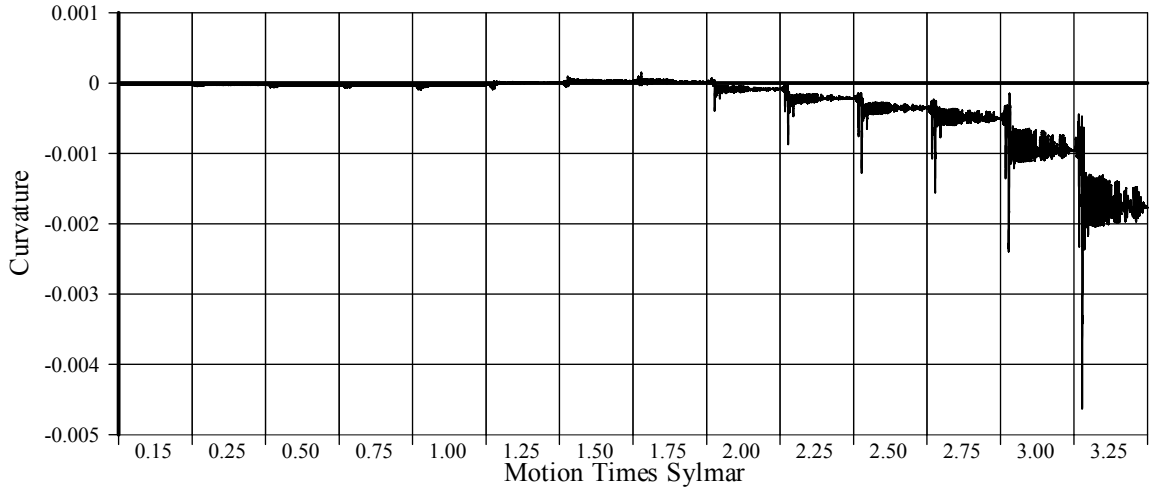

Fig. 4-150 Measured Curvature at Section 4 of West Column for SFCD2

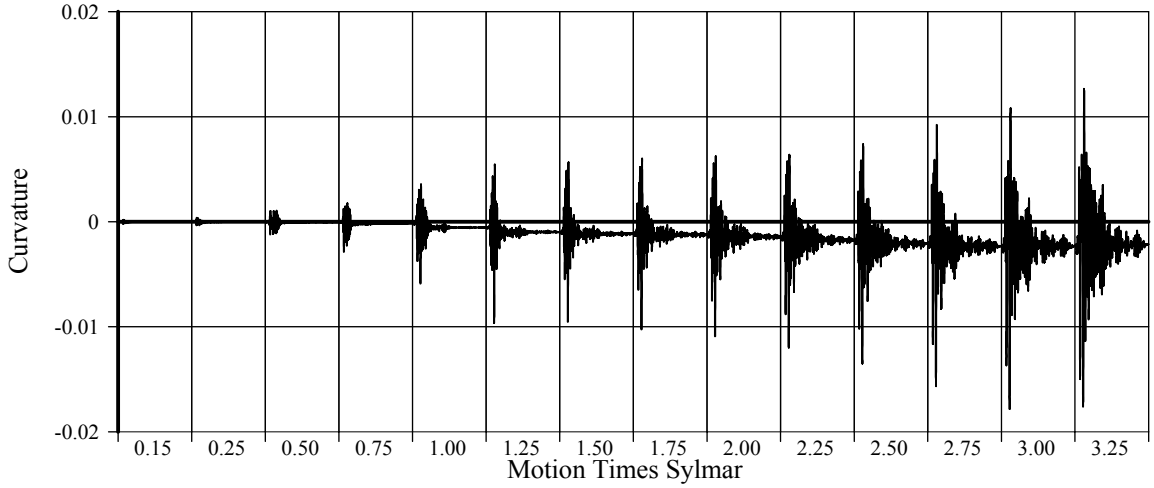

Fig. 4-151 Measured Curvature at Section 5 of West Column for SFCD2

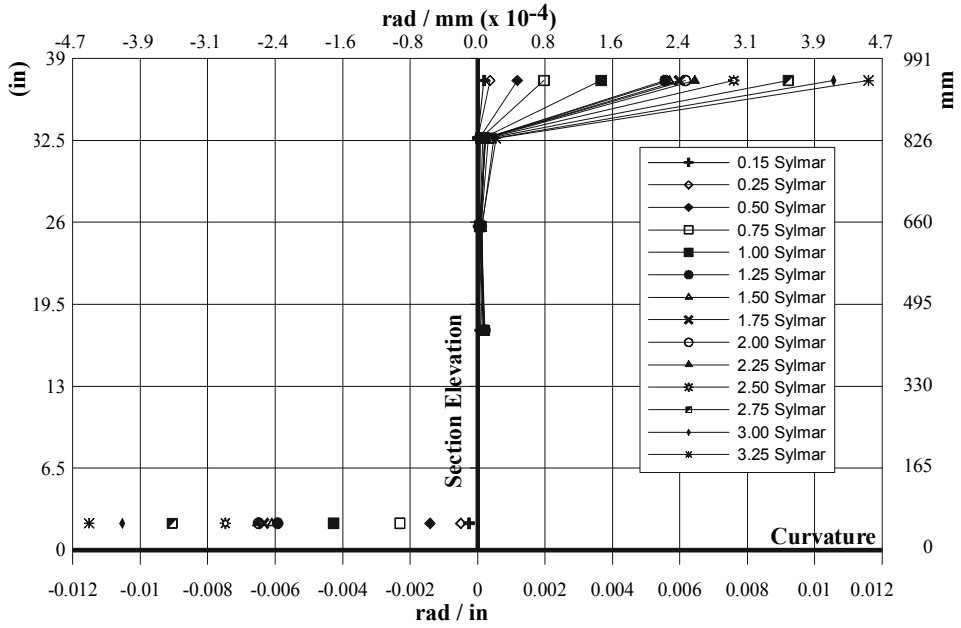

Fig. 4-152 Measured Maximum Curvature for East Column of SFCD2

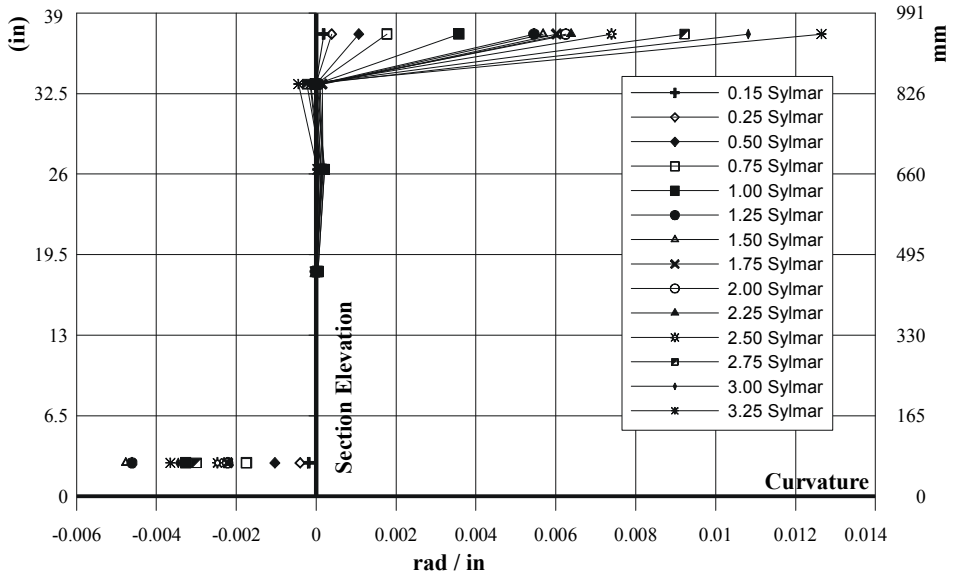

Fig. 4-153 Measured Minimum Curvature for East Column of SFCD2

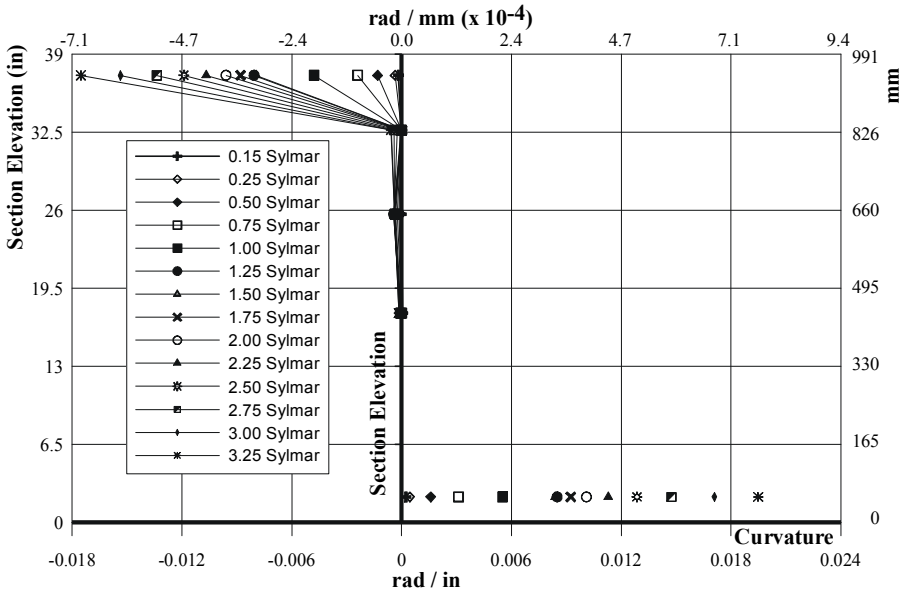

Fig. 4-154 Measured Maximum Curvature for West Column of SFCD2

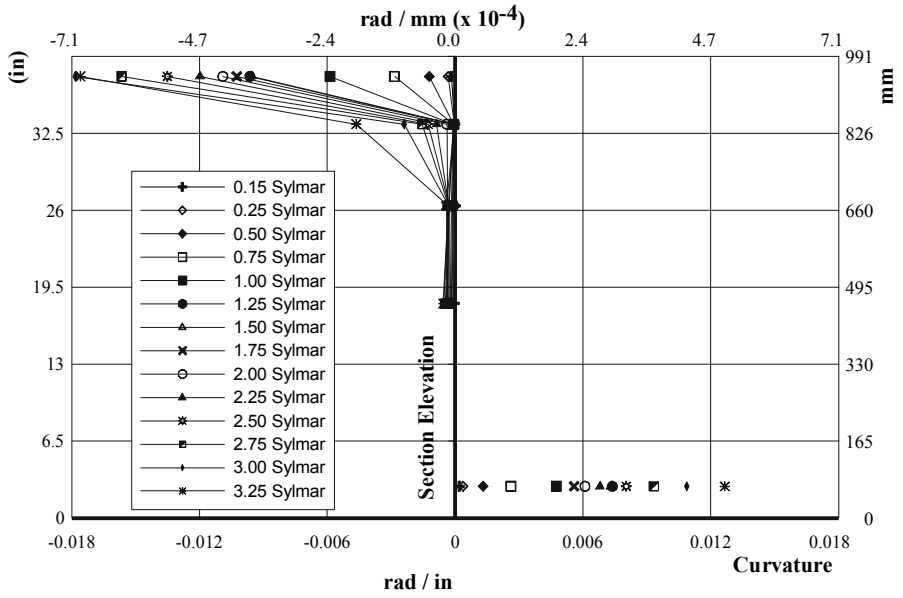

Fig. 4-155 Measured Minimum Curvature for West Column of SFCD2

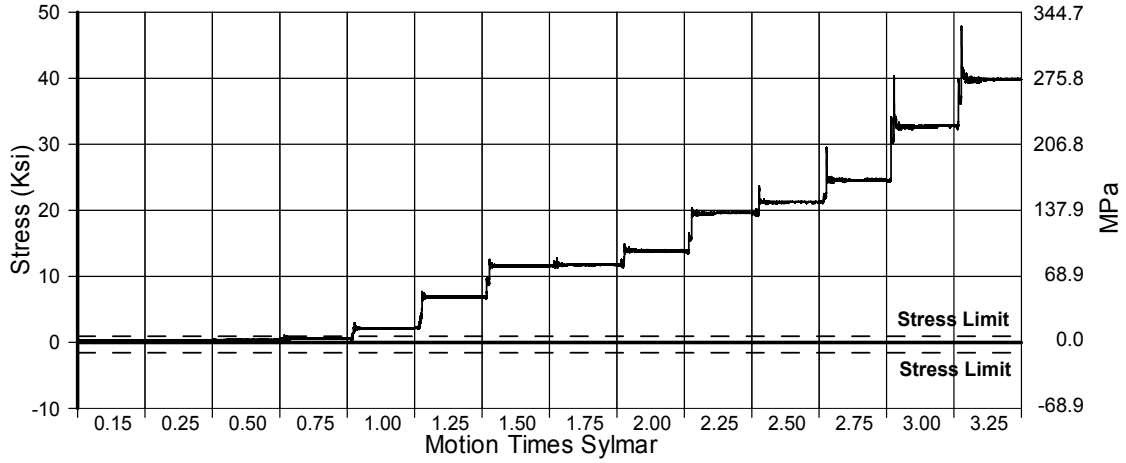

Fig. 4-156 Principal Stress (σ1) in East Beam-Column Connection for SFCD2

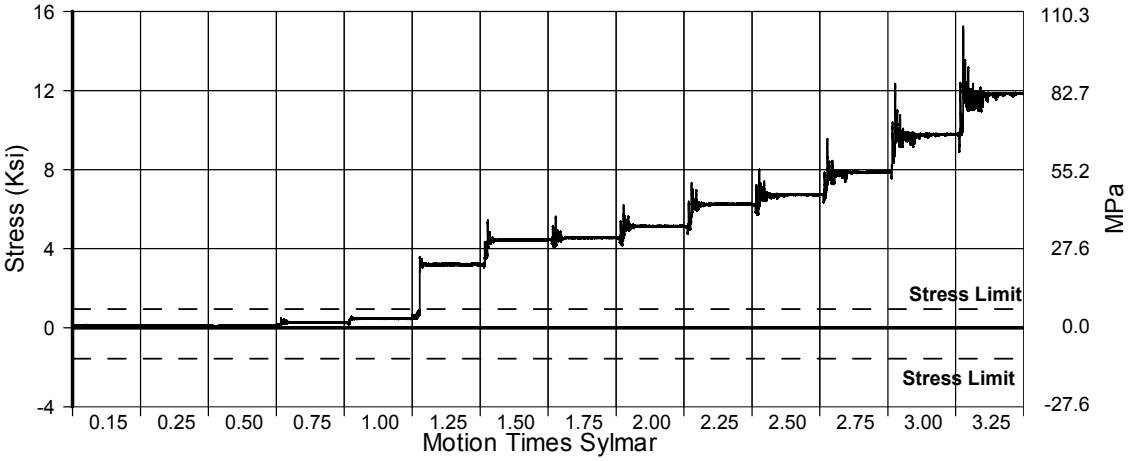

Fig. 4-157 Principal Stress (σ2) in East Beam-Column Connection for SFCD2

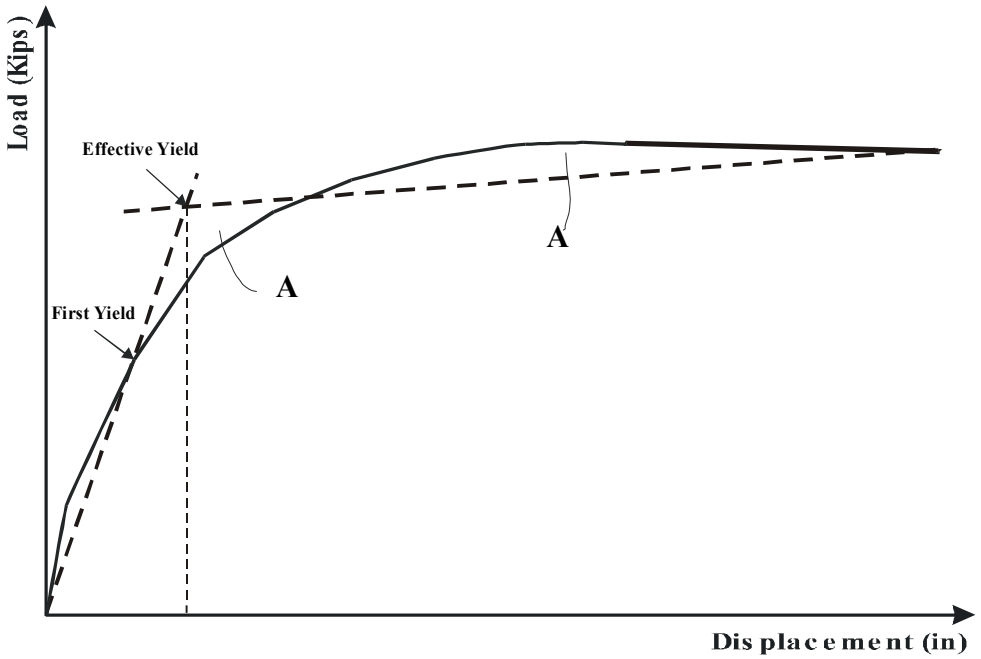

Fig. 4-158 Method of Calculating Idealized Load Displacement Curve

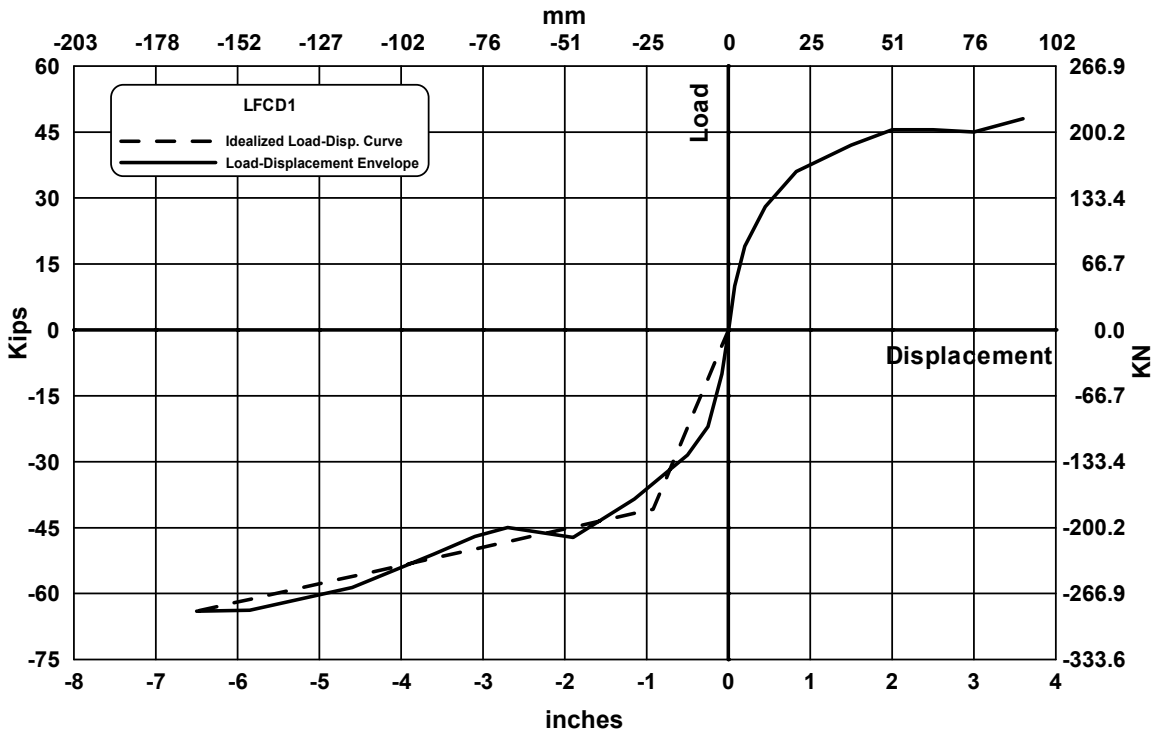

Fig. 4-159 Idealized Load-Displacement Curve for LFCD1

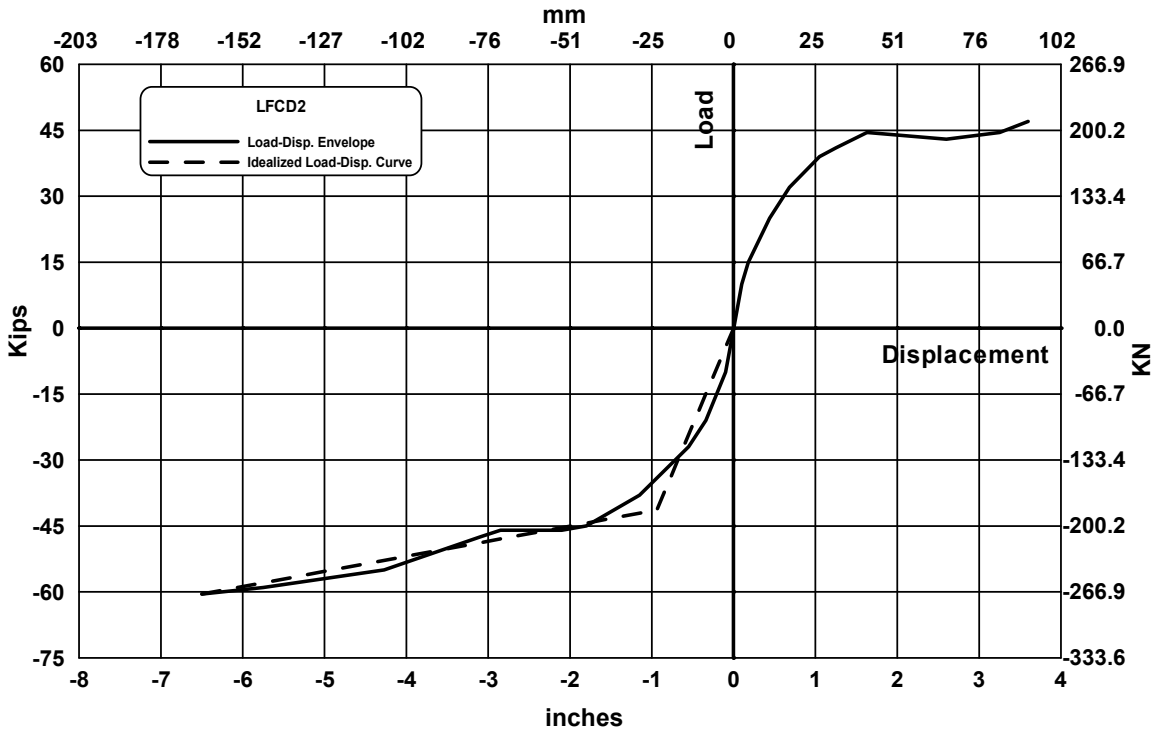

Fig. 4-160 Idealized Load-Displacement Curve for LFCD2

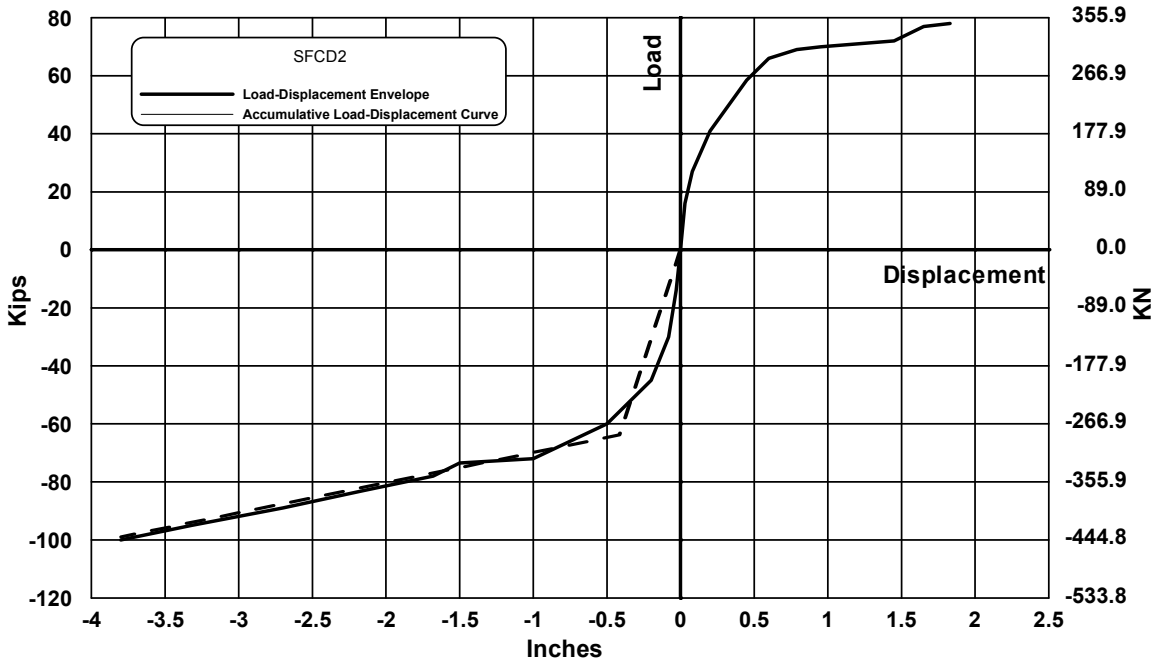

Fig. 4-161 Idealized Load-Displacement Curve for SFCD2

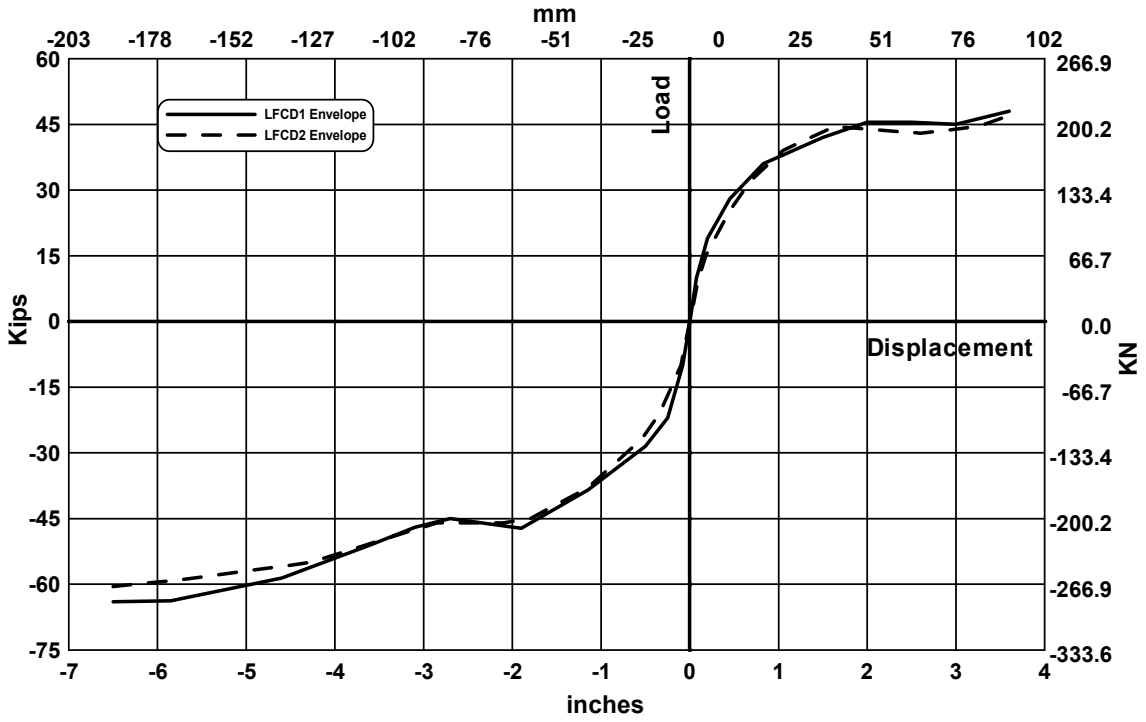

Fig. 4-162 Comparison between LFCD1 and LFCD2 Envelopes

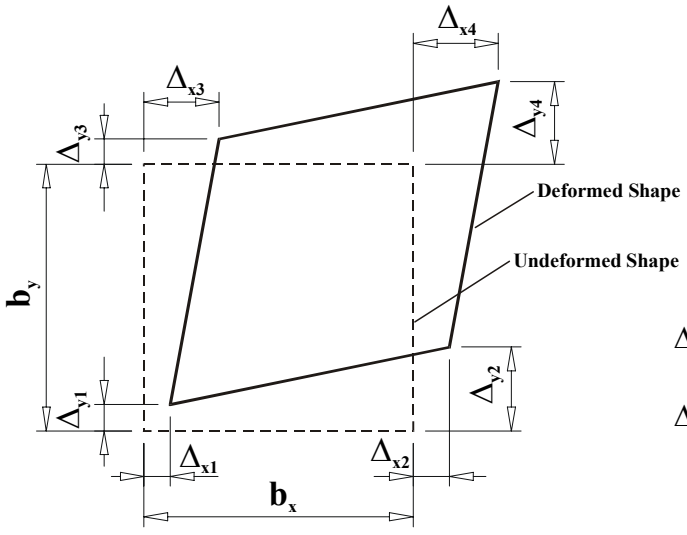

$$\Delta_x = [(\Delta_{x2}-\Delta_{x1})+(\Delta_{x4}-\Delta_{x3})] / 2$$

$$\Delta_y = [(\Delta_{y3}-\Delta_{y1})+(\Delta_{y4}-\Delta_{y2})] / 2$$

Fig. 4-163 Beam-Column Connection Deformation

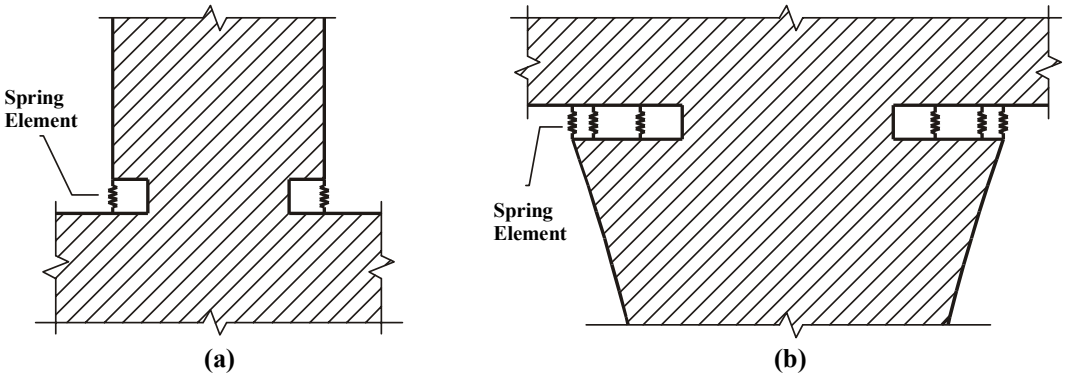

Fig. 5-1 Spring Elements (a) At Base Hinge gap (a) At Flare gap

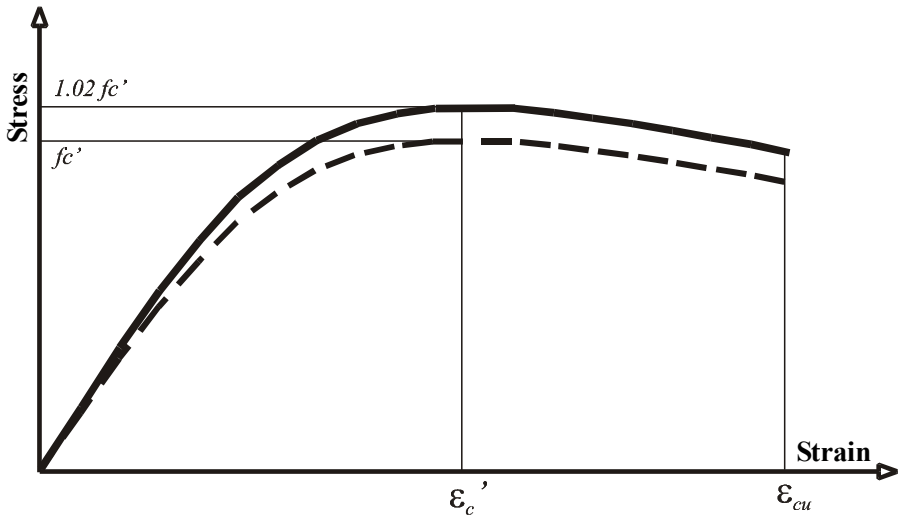

Fig. 5-2 Uniaxial Stress-Strain Relationship

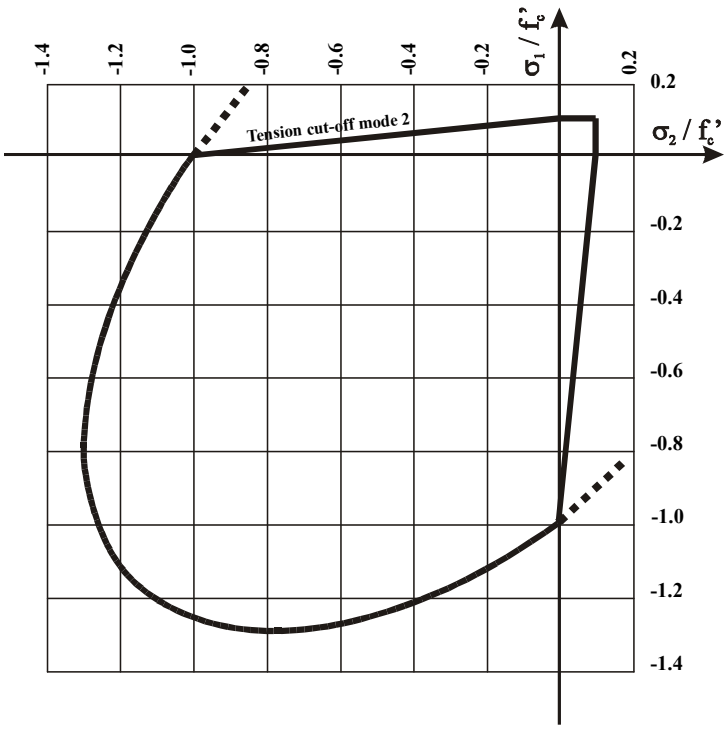

Fig. 5-3 Drucker-Prager Biaxial Failure Envelope with Tension Cut-Off

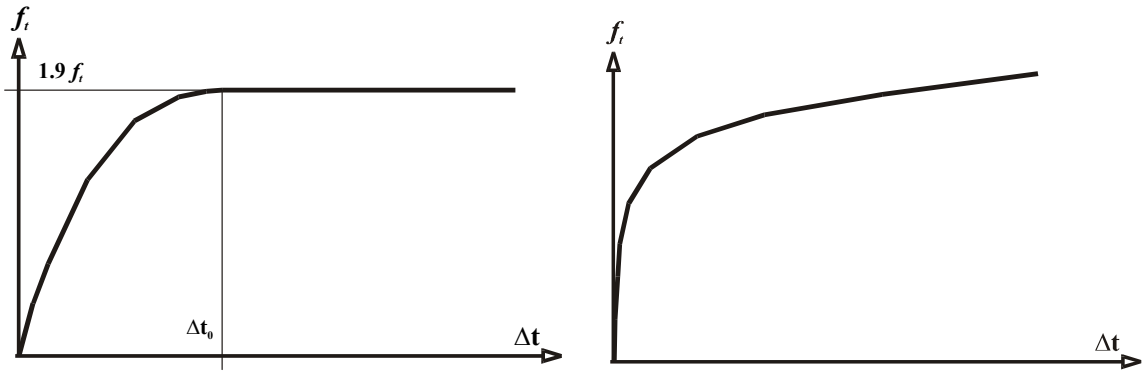

(a) **(b)**

Fig. 5-4 Shear-Traction Relationship Models (a) Dörr's Model (b) Noakowski Model

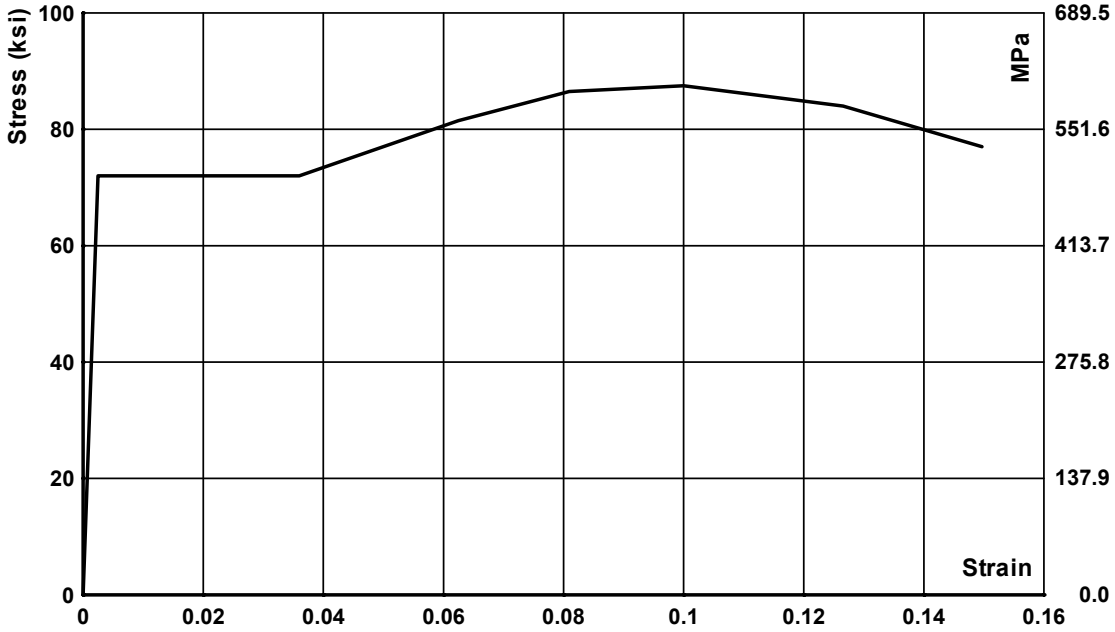

Fig. 5-5 Stress-Strain Curve for Steel Including Strain Rate Effect

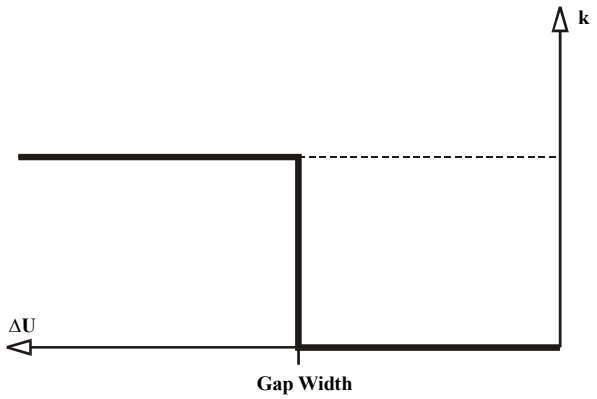

Fig. 5-6 Spring Elements Material Model

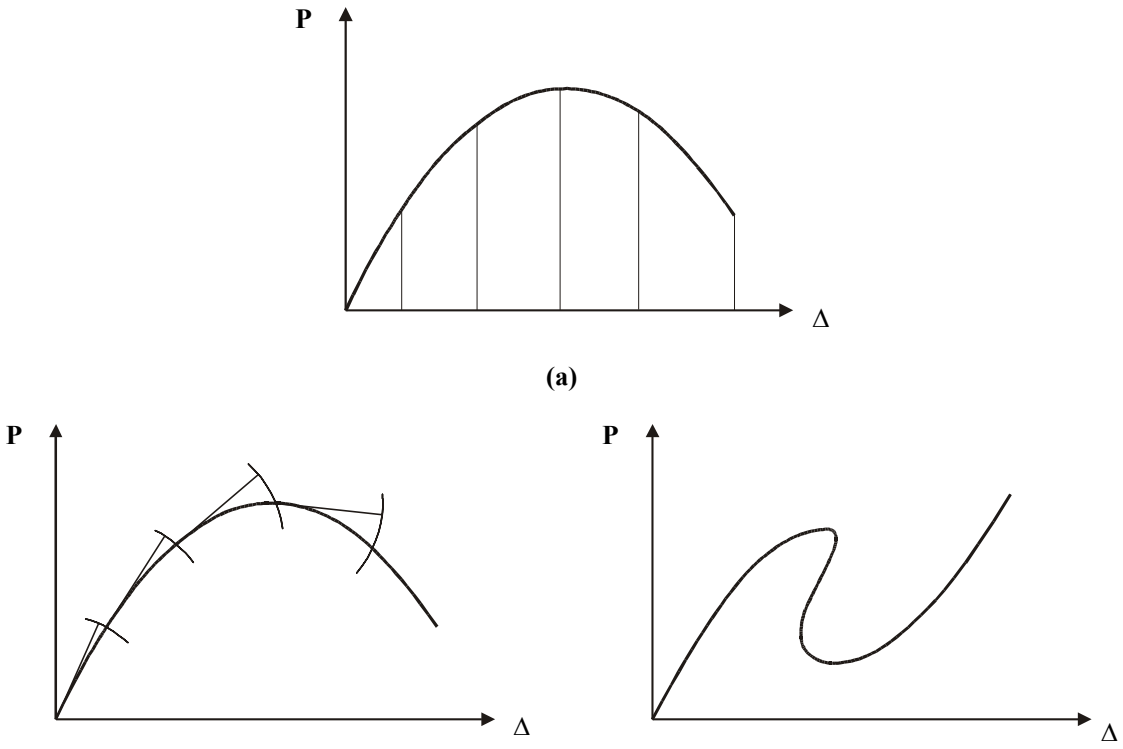

Fig. 5-7 Solver Technique (a) Displacement Controlled (b) Snap Through Arc-Length Method (c) Snap Back Arc-Length Method

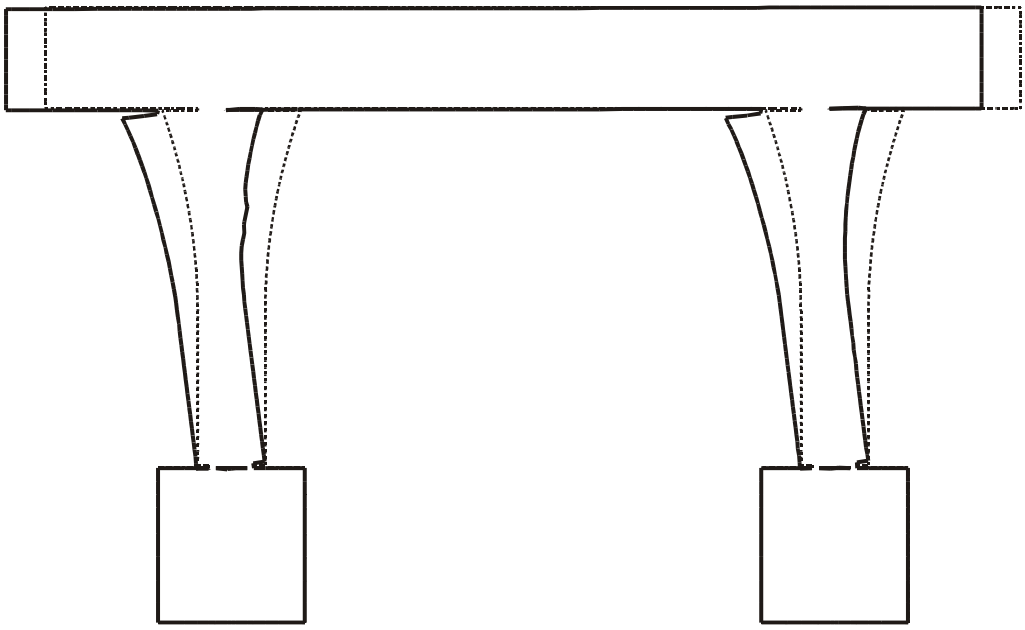

Fig. 5-8 Deformed Shape of LFCD1 at Horizontal Load level of 66.0 Kips

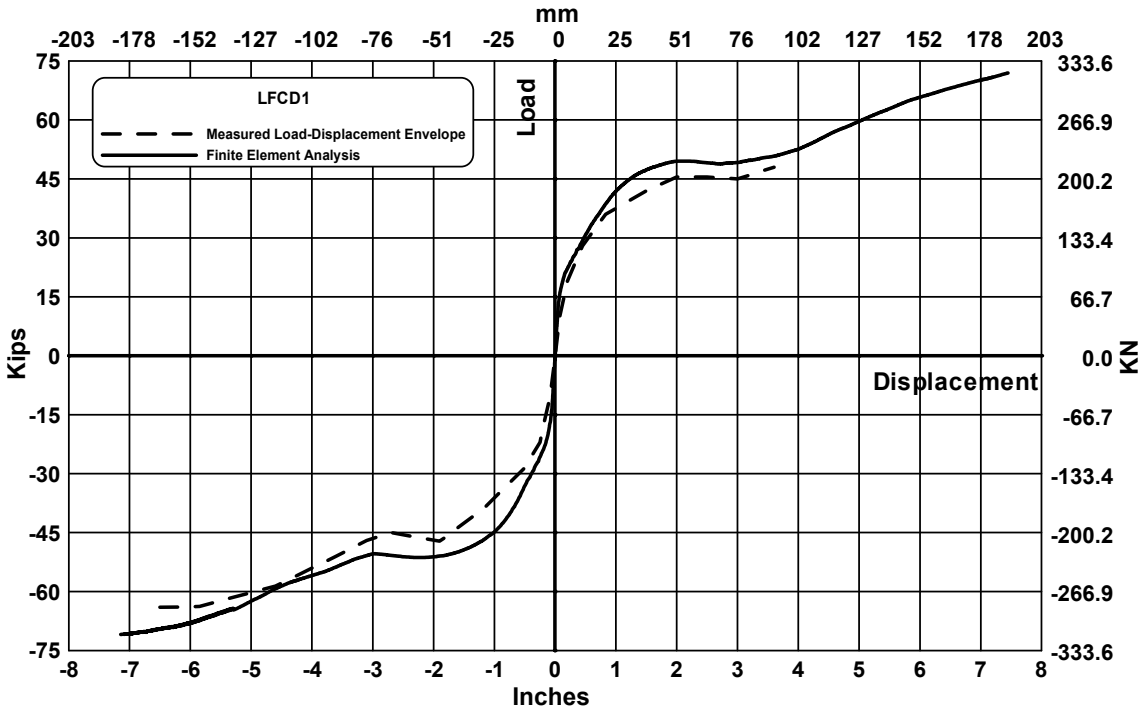

Fig. 5-9 Analytical Results versus Experimental Results for LFCD1

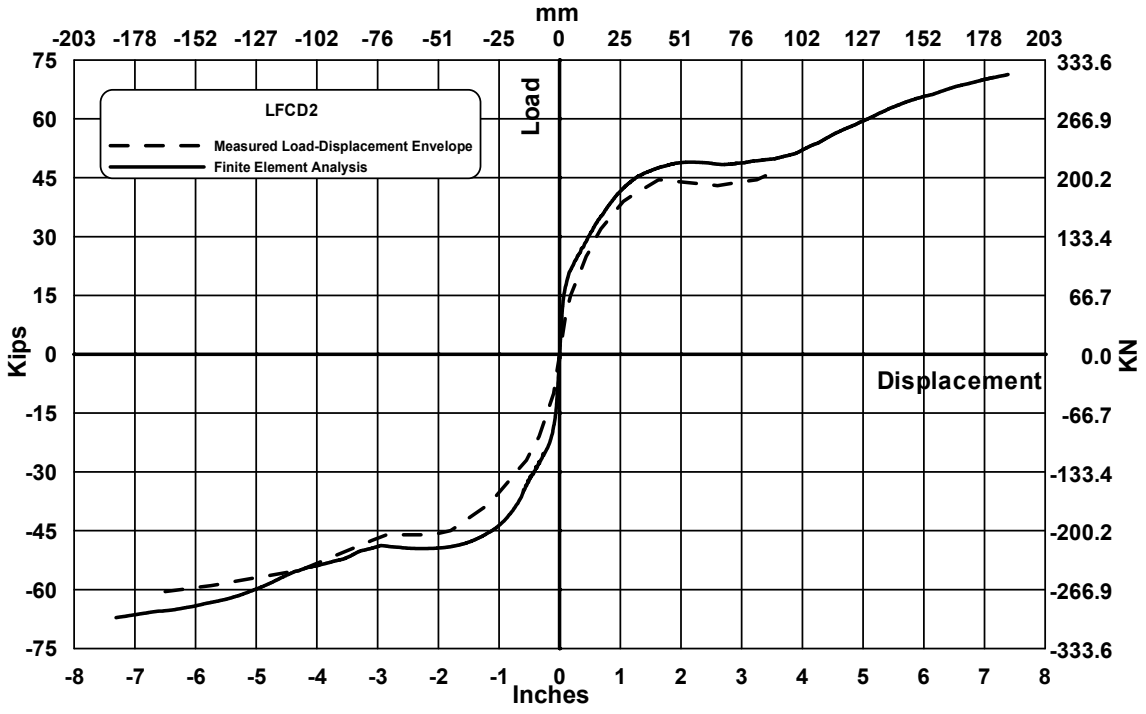

Fig. 5-10 Analytical Results versus Experimental Results for LFCD2

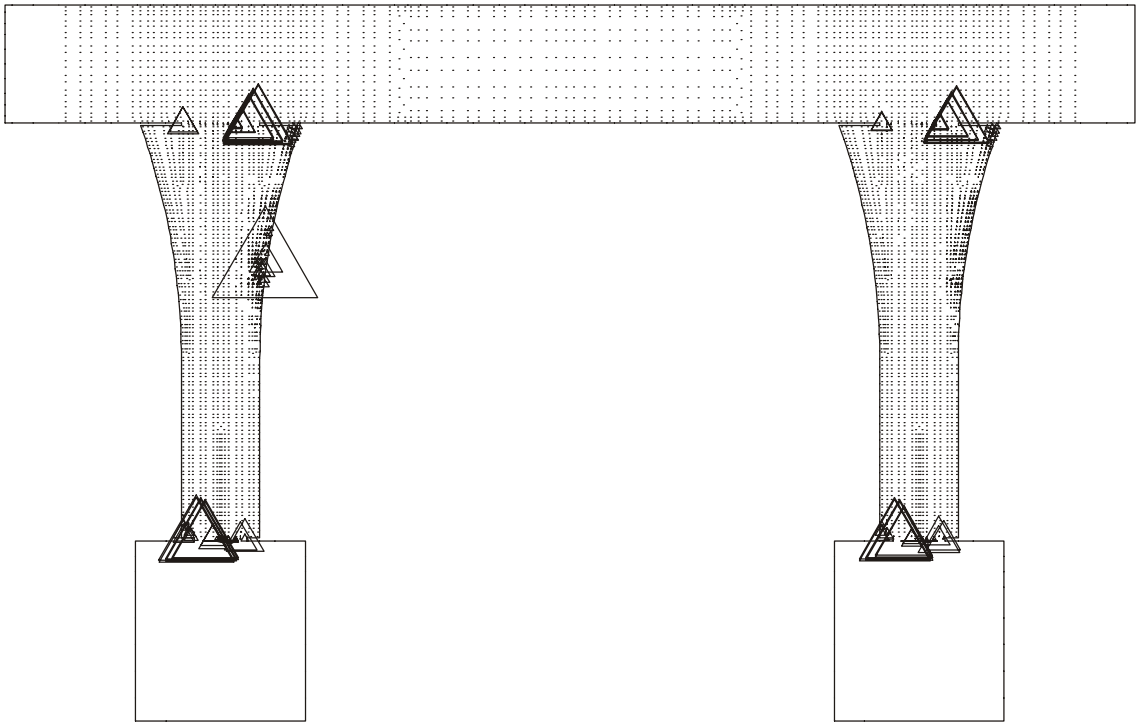

Fig. 5-11 Concrete Plasticity for LFCD1 Load = 67.9 K

(a) **(b)**

Fig. 5-12 Concrete Spalling Locations (a) West Column, Circles Looking from an Inside Angle (b) East Column, Looking from an outside angle

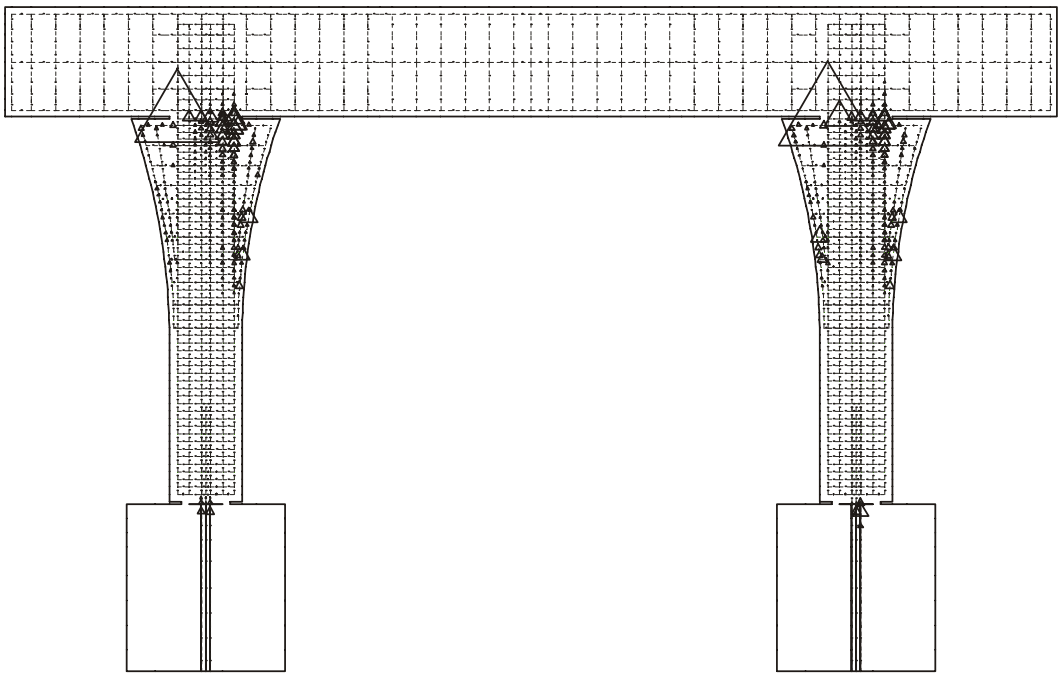

Fig. 5-13 Steel Plasticity Status limit for LFCD2 at Load = 67.9 K

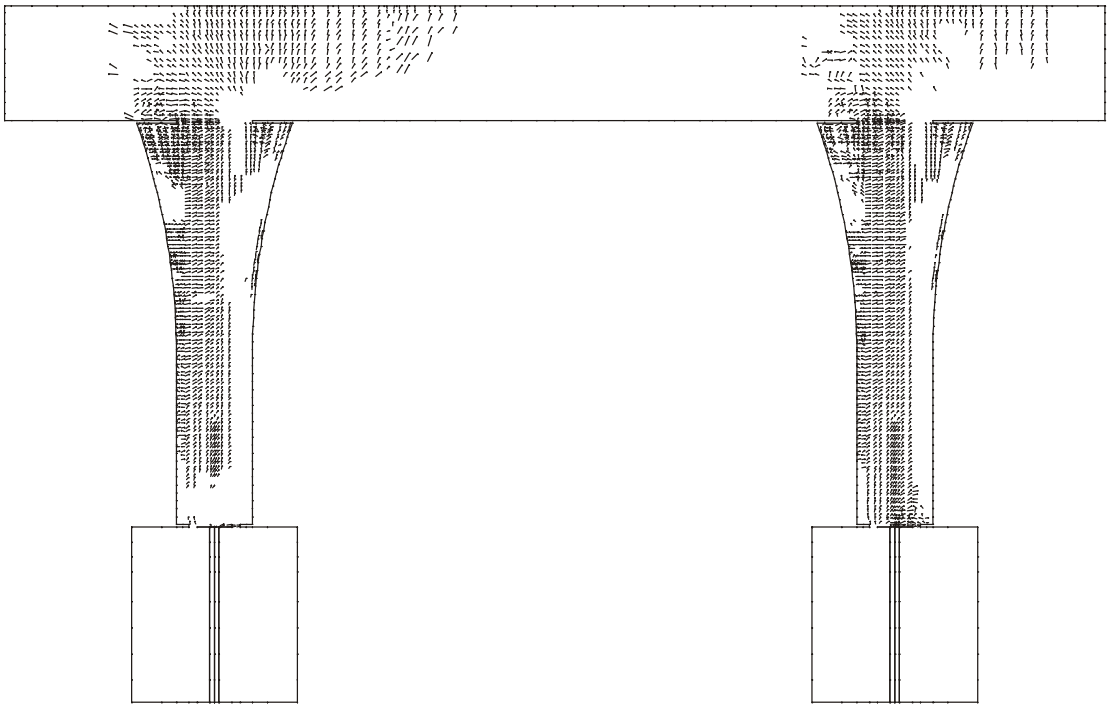

Fig. 5-14 LFCD2 DIANA Crack Pattern at Load = -53.3 K (Load in West Direction)

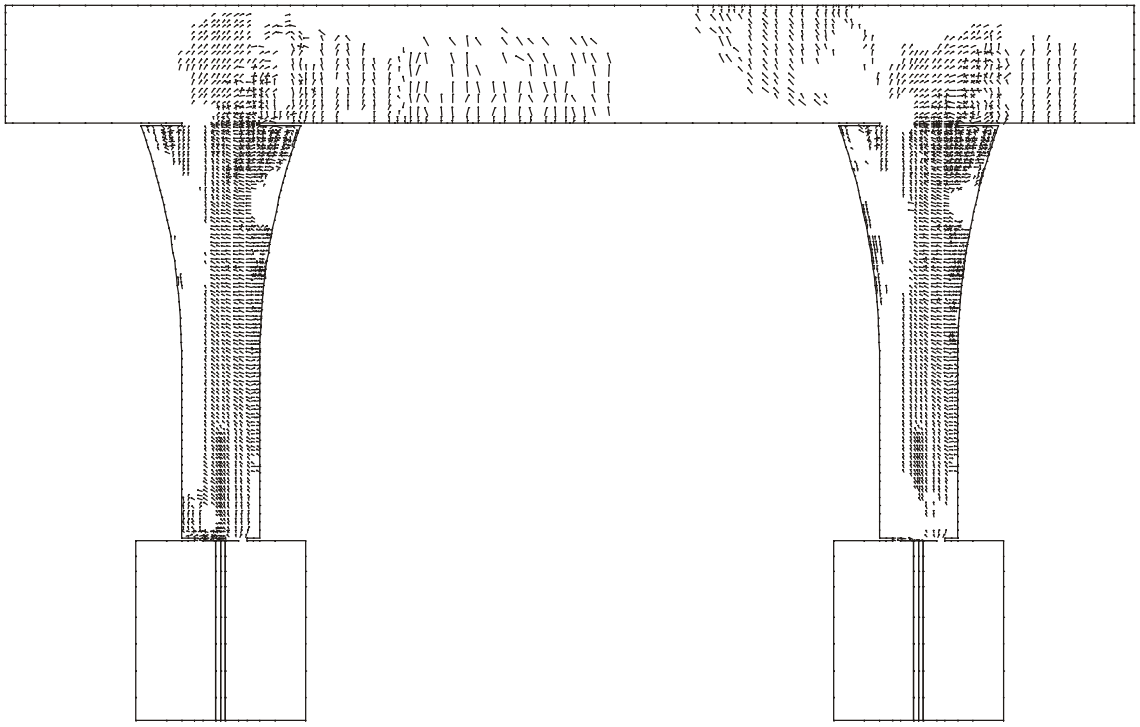

Fig. 5-15 LFCD2 DIANA Crack Pattern at Load = 53.9 K (Load in East Direction)

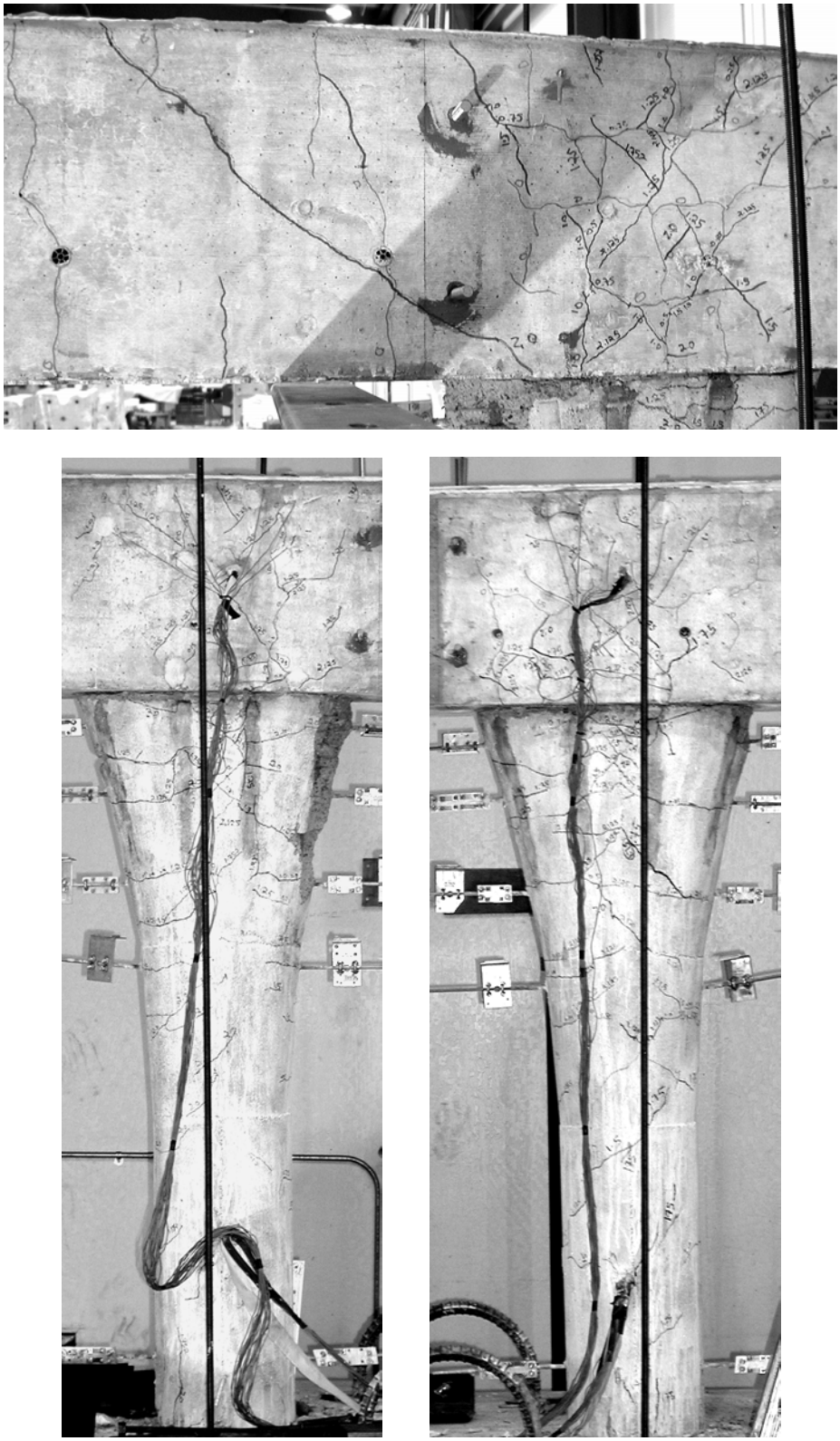

Fig. 5-16 LFCD2 Crack Pattern after Bucket Removal

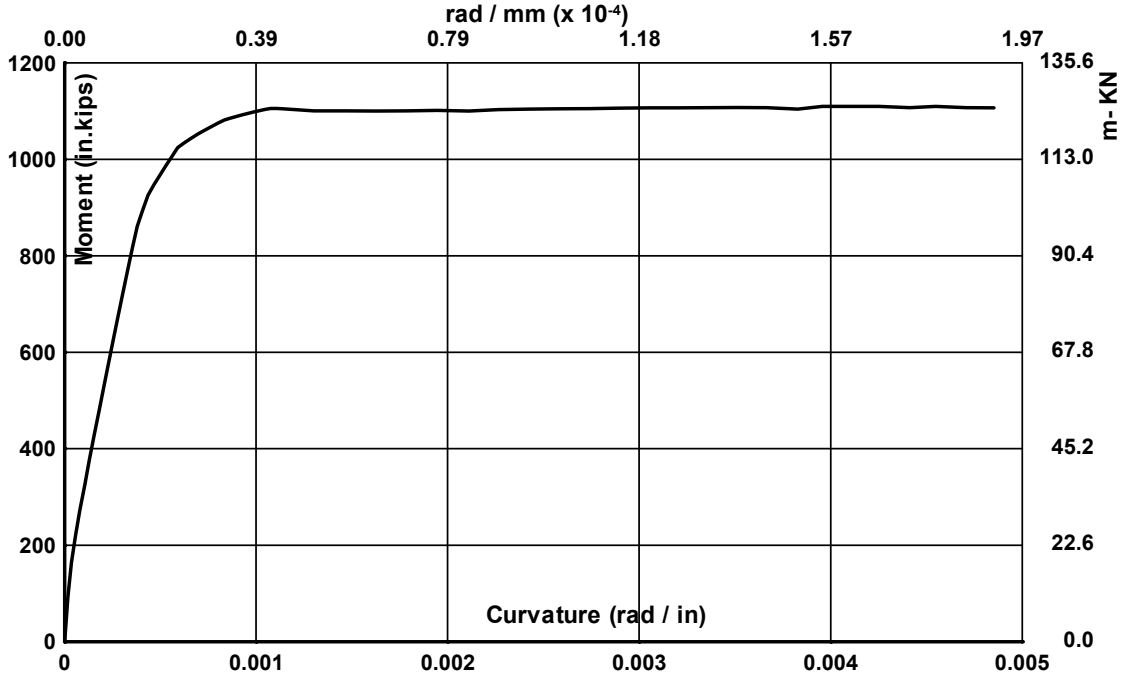

Fig. 5-17 Moment-Curvature Relationship for the Column Core

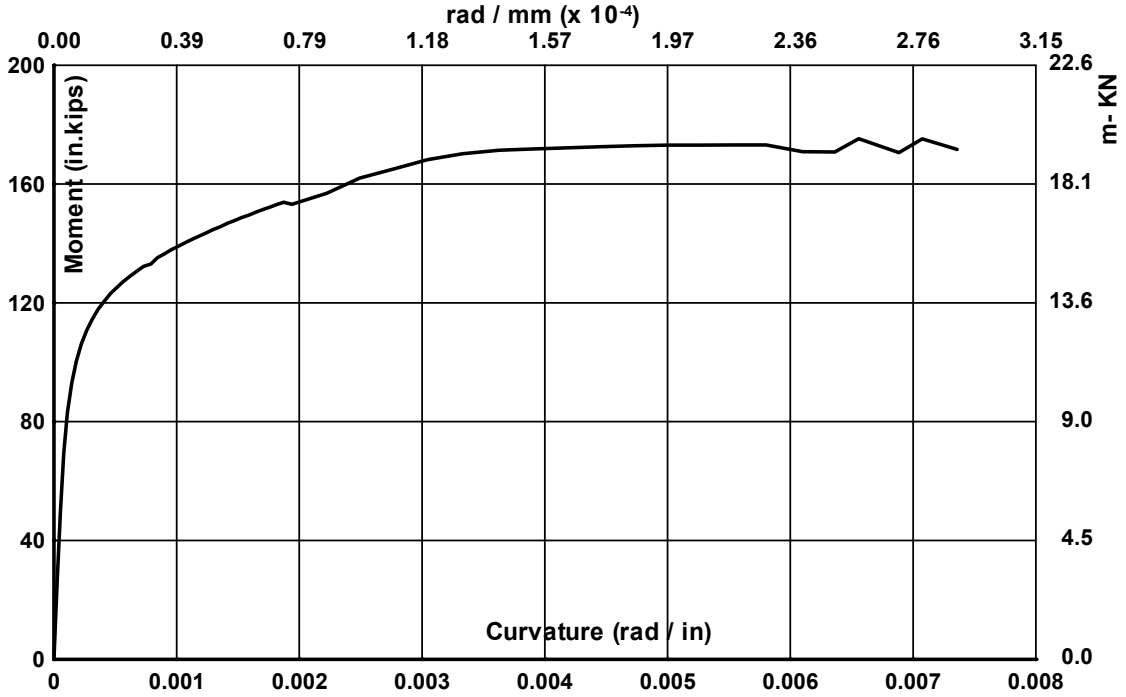

Fig. 5-18 Moment-Curvature Relationship for Base Hinge Section

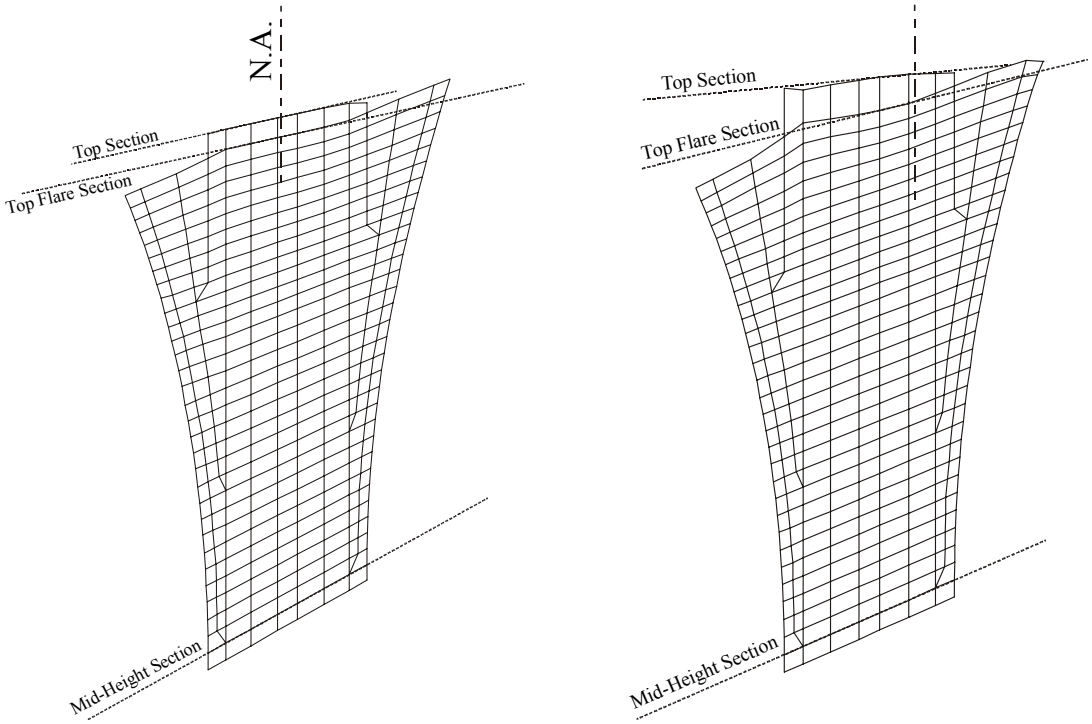

Fig. 5-19 Scaled Vertical Deformation (a) Before Gap Closure (b) After Gap Closure

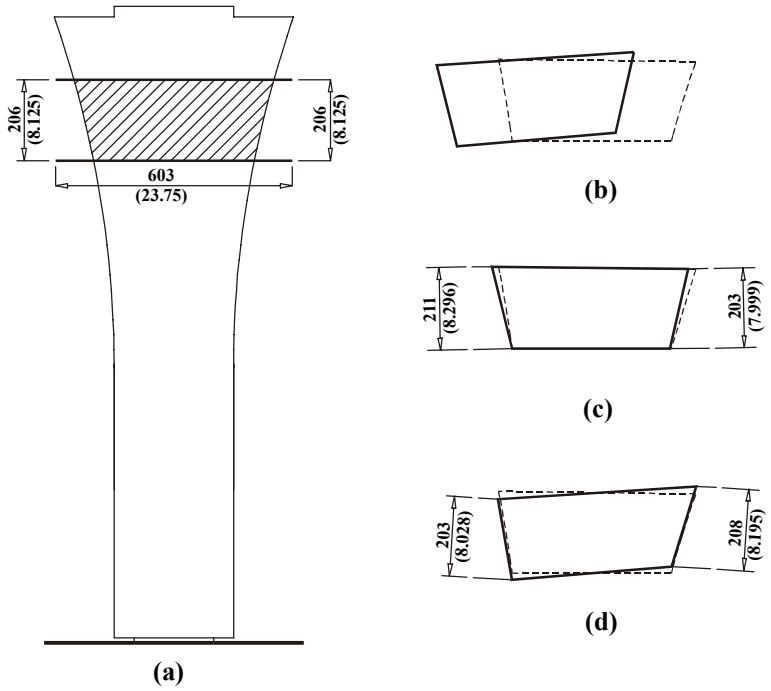

Fig. 5-20 Curvature Calculations (a) Section 3 for East Column (b) Final Deformed Shape (c) Horizontal Deformations (d) Vertical Deformations

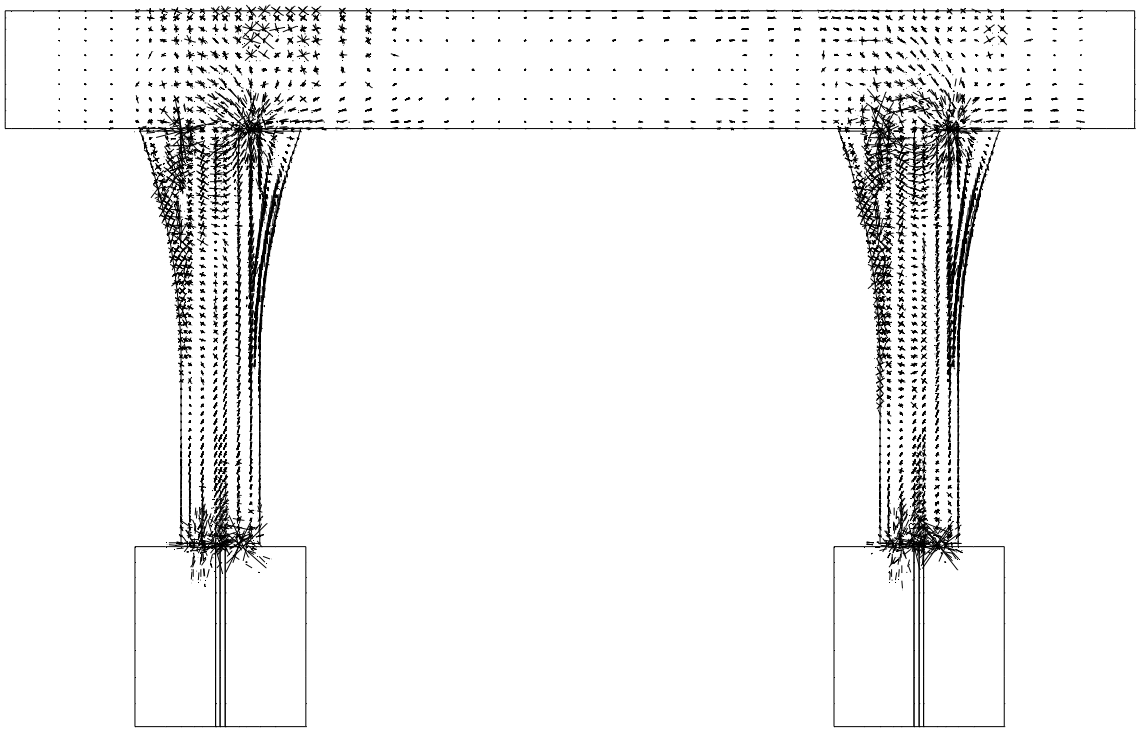

Fig. 5-21 LFCD2 Principal Stress Trajectories for LFCD2 at Load = 38.7 K

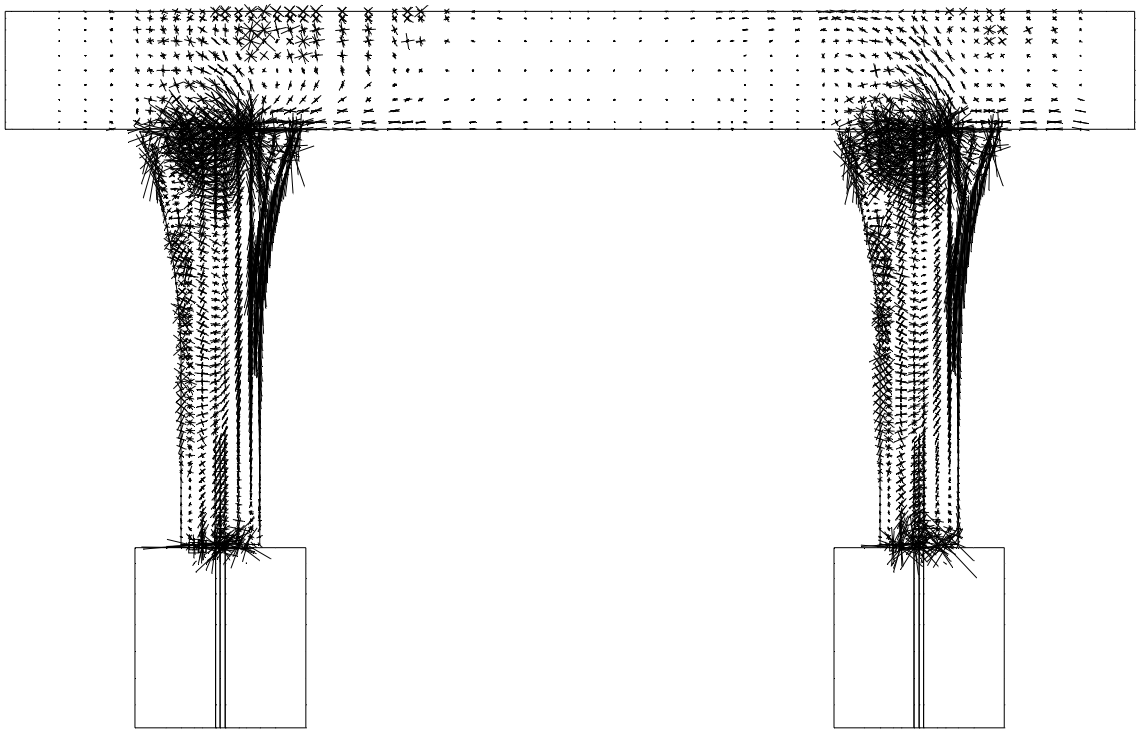

Fig. 5-22 Principal Stress Trajectories for LFCD2 at Load = 53.3 K

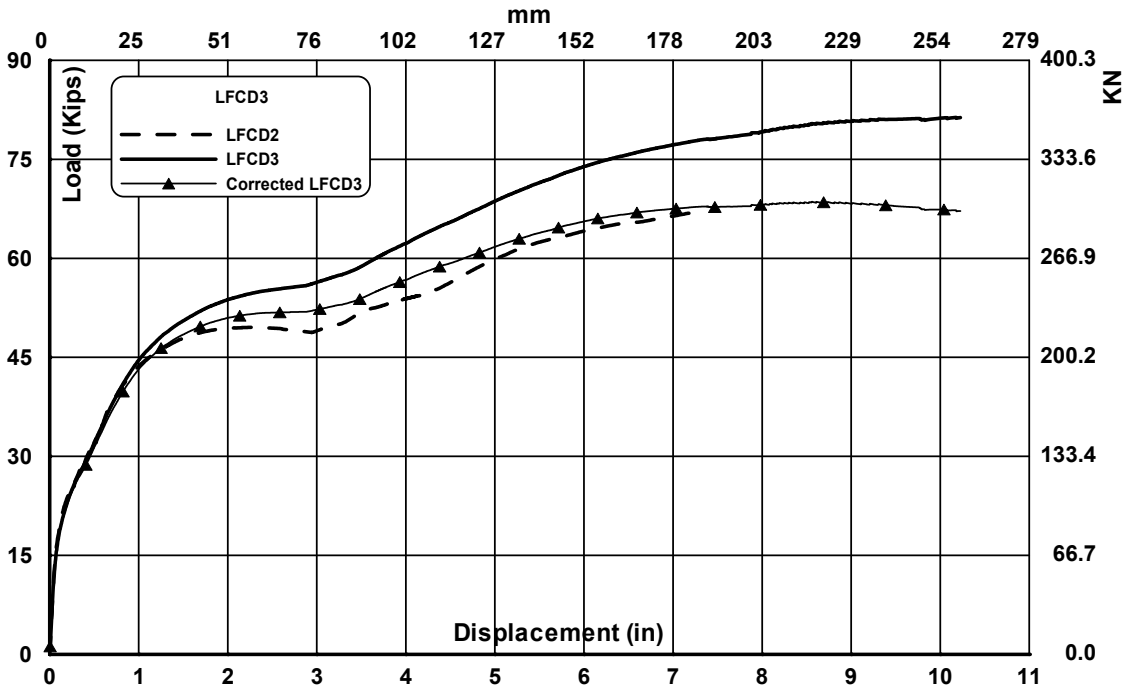

Fig. 5-23 Analytical Results versus Experimental Results for LFCD3

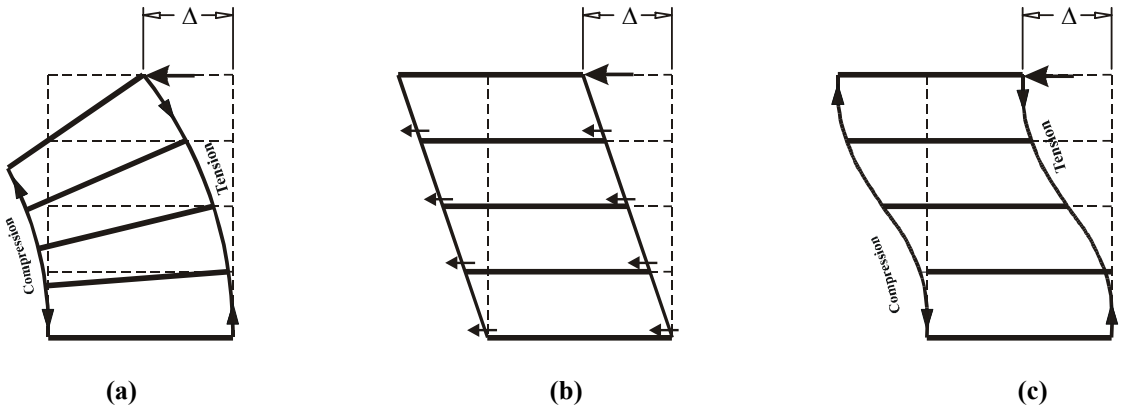

(a) **(b)** **(c)**

Fig. 5-24 Lateral Deflection Modes (a) Flexural Mode (b) Shear Mode (c) Combined Mode

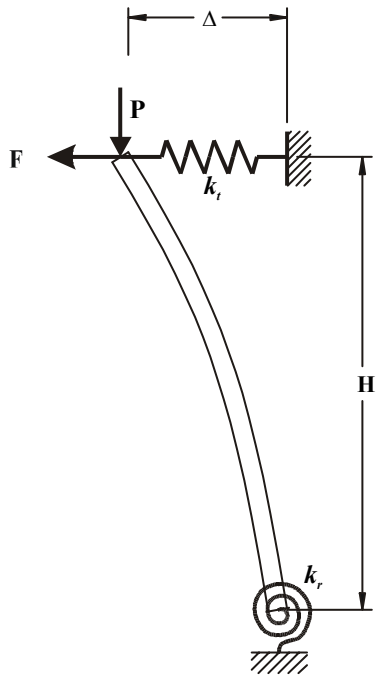

Fig. 5-25 Idealized Structure

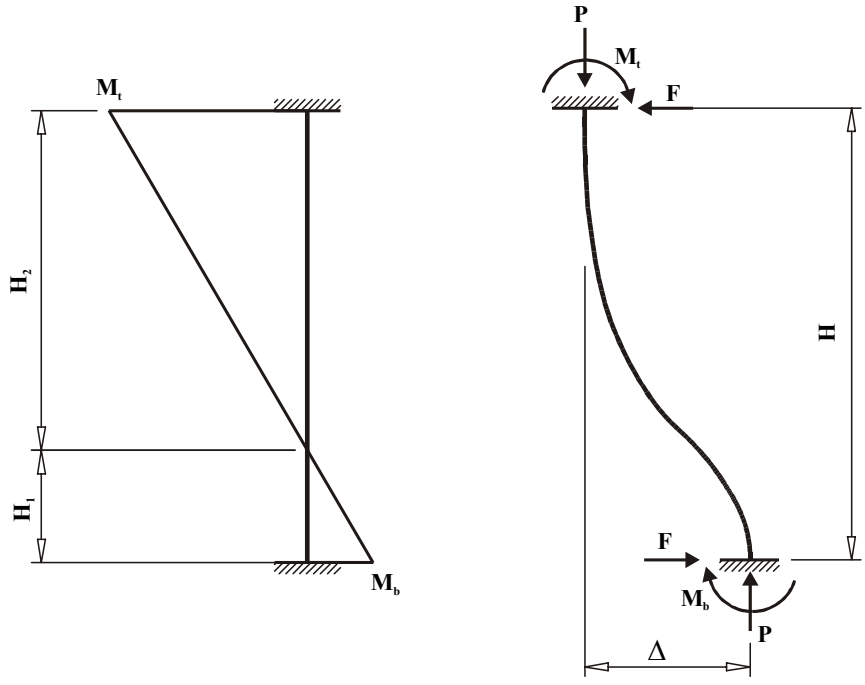

Fig. 5-26 Double Curvature (a) Bending Moment Diagram for Columns (b) Column Deformed Shape

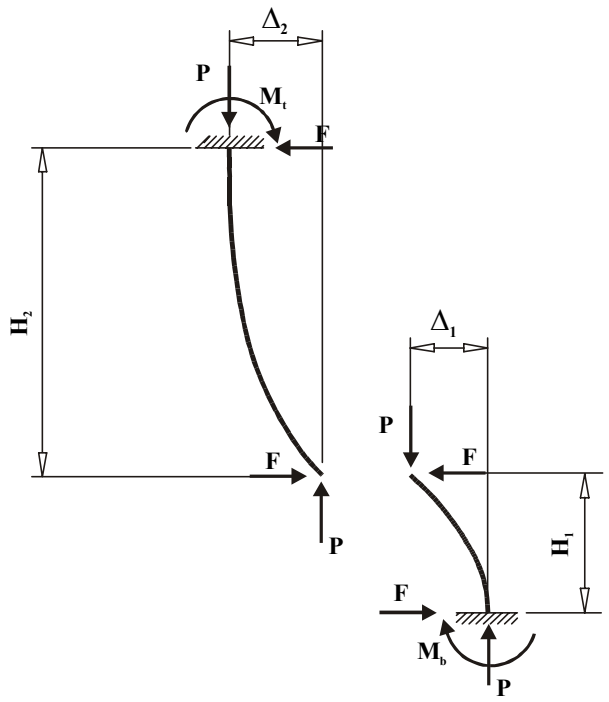

Fig. 5-27 Column Separated at Zero Moment

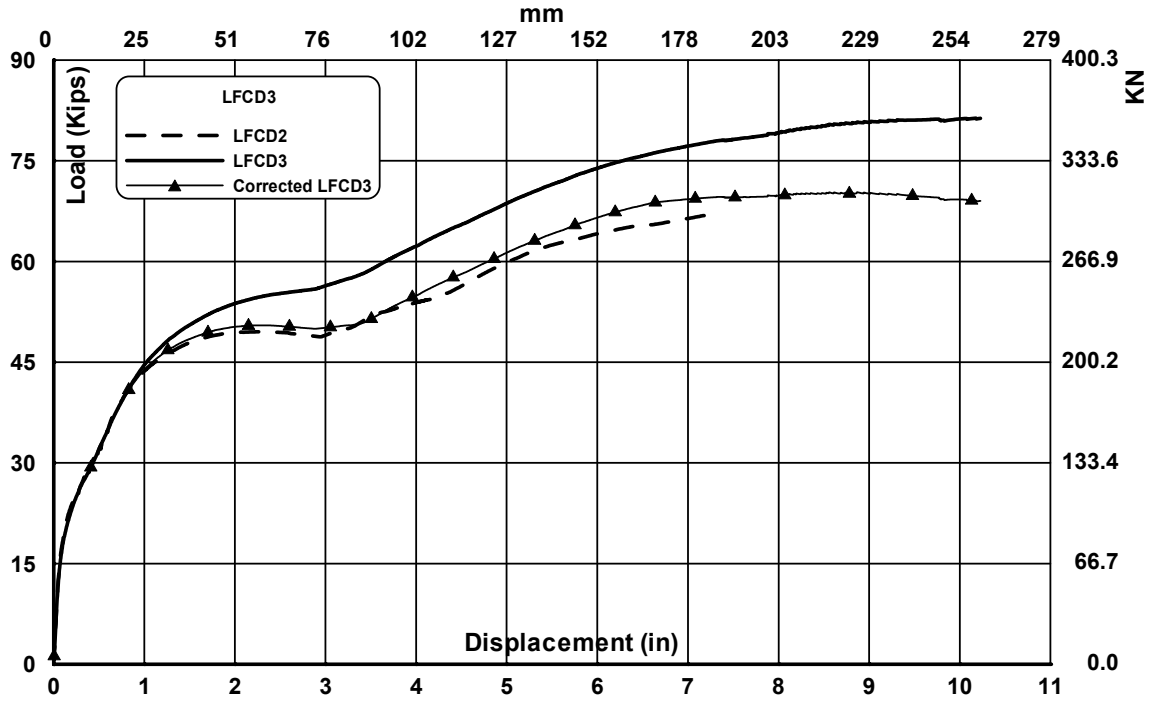

Fig. 5-28 Corrected LFCD3 Considering Double Curvature Correction

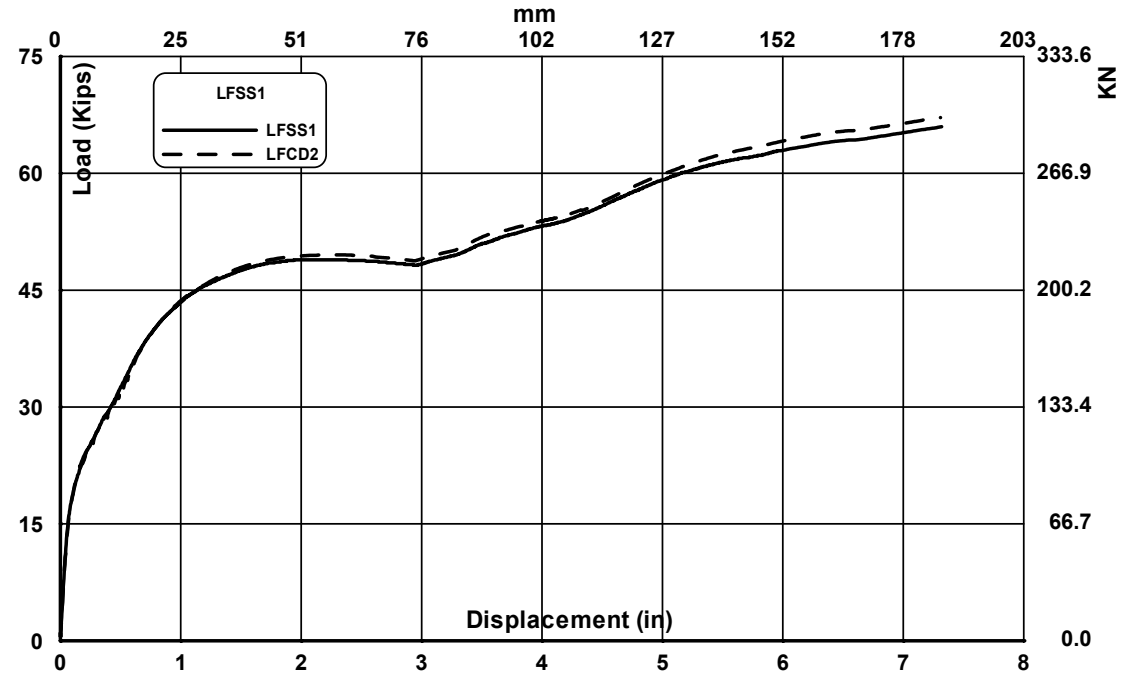

Fig. 5-29 Analytical Results for LFSS1

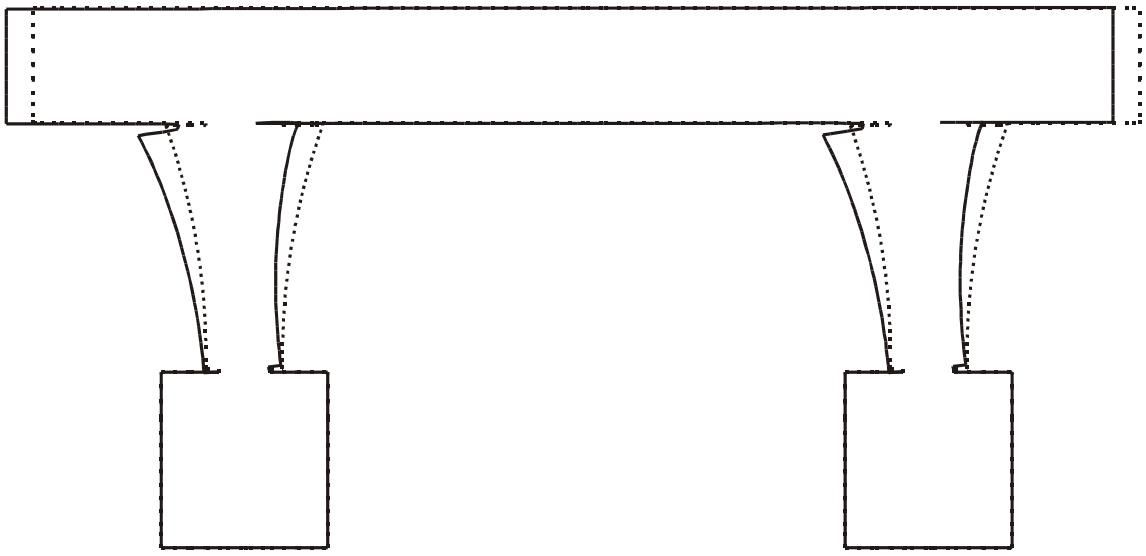

Fig. 5-30 Deformed Shape of SFCD2 at Horizontal Load level of 97.4 Kips

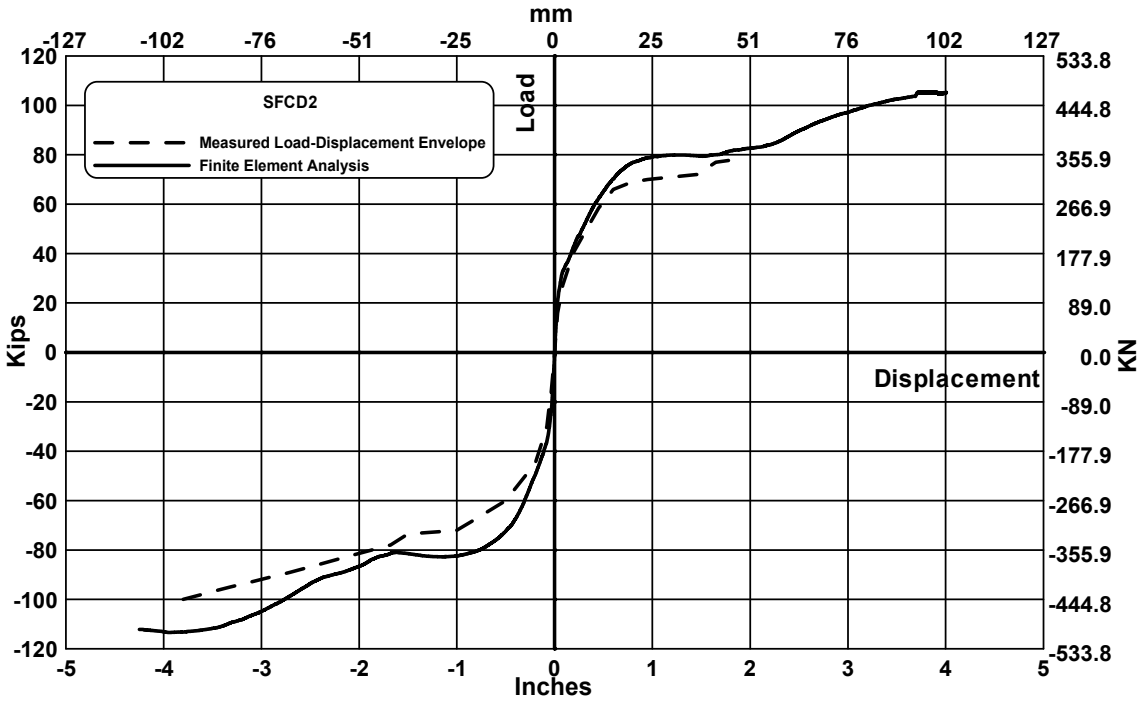

Fig. 5-31 Analytical Results versus Experimental Results for SFCD2

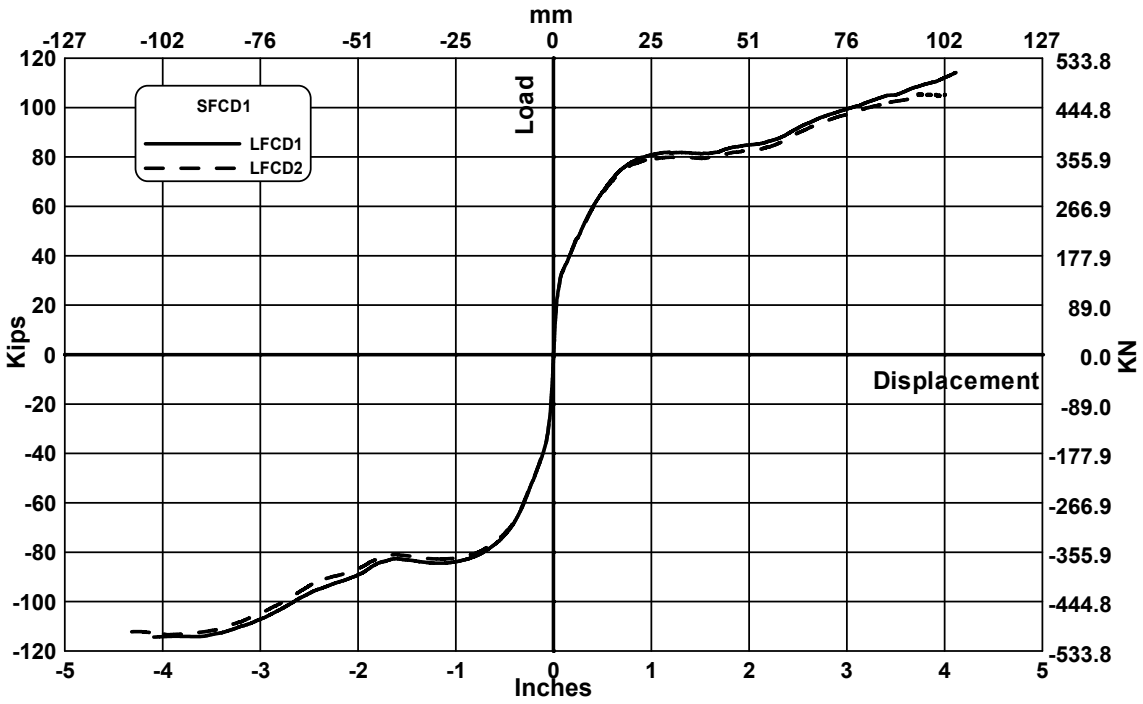

Fig. 5-32 Analytical Results versus Experimental Results for SFCD1

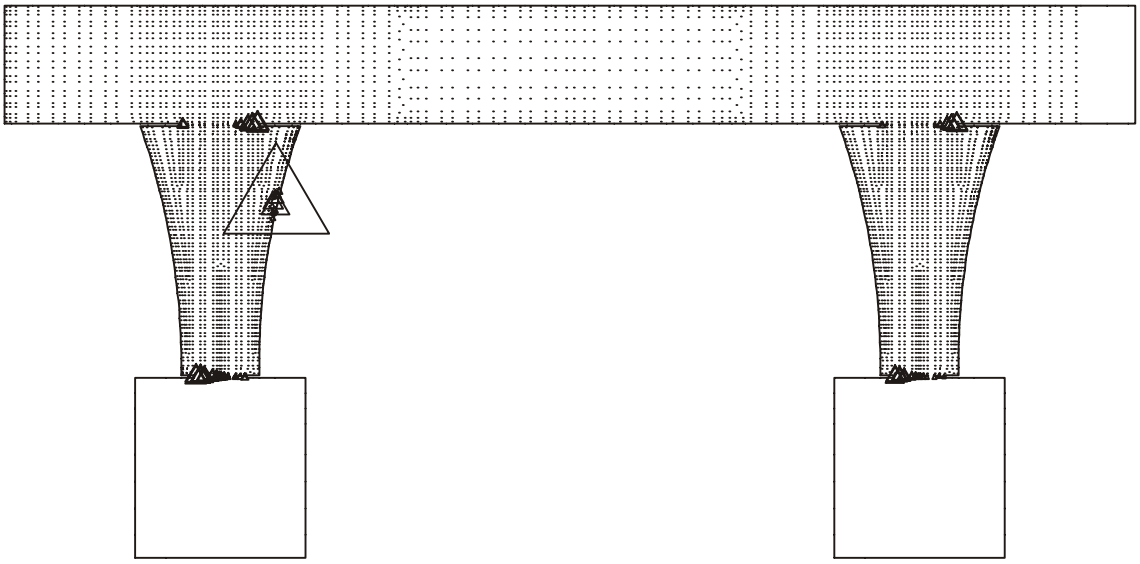

Fig. 5-33 Concrete Plasticity for SFCD2 Load = -115.3 K

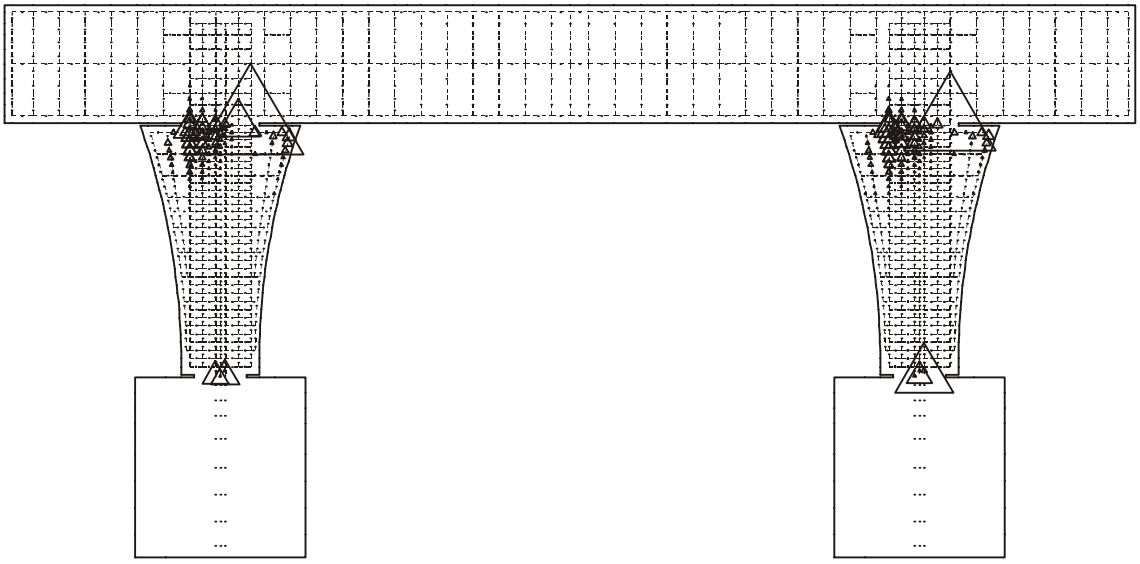

Fig. 5-34 Reinforcement Plasticity for SFCD2 Load = -115.3 K

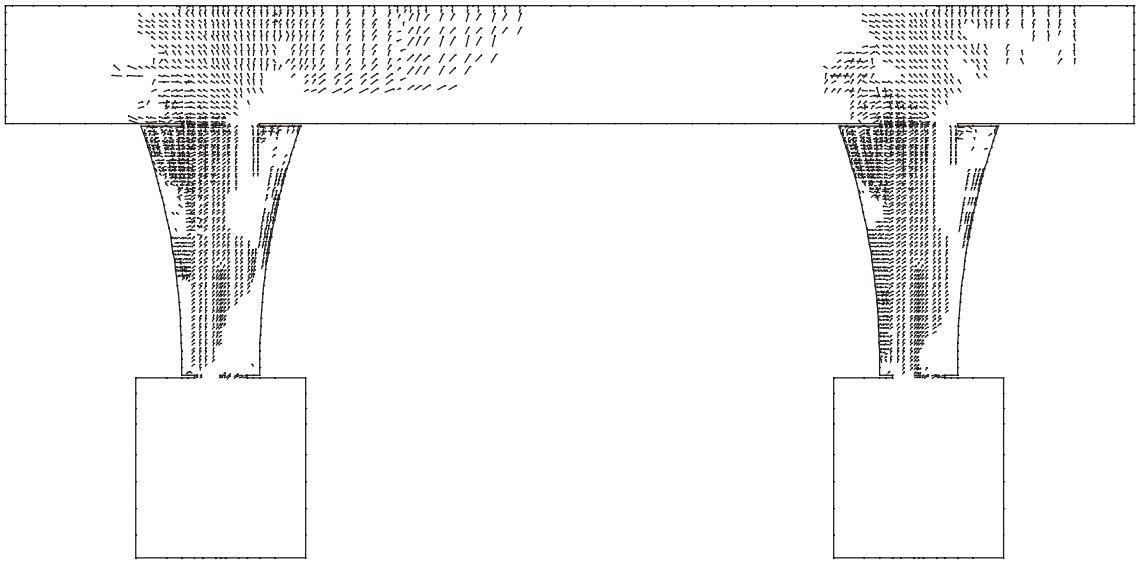

Fig. 5-35 SFCD2 DIANA Crack Pattern at Load = -115.3 K

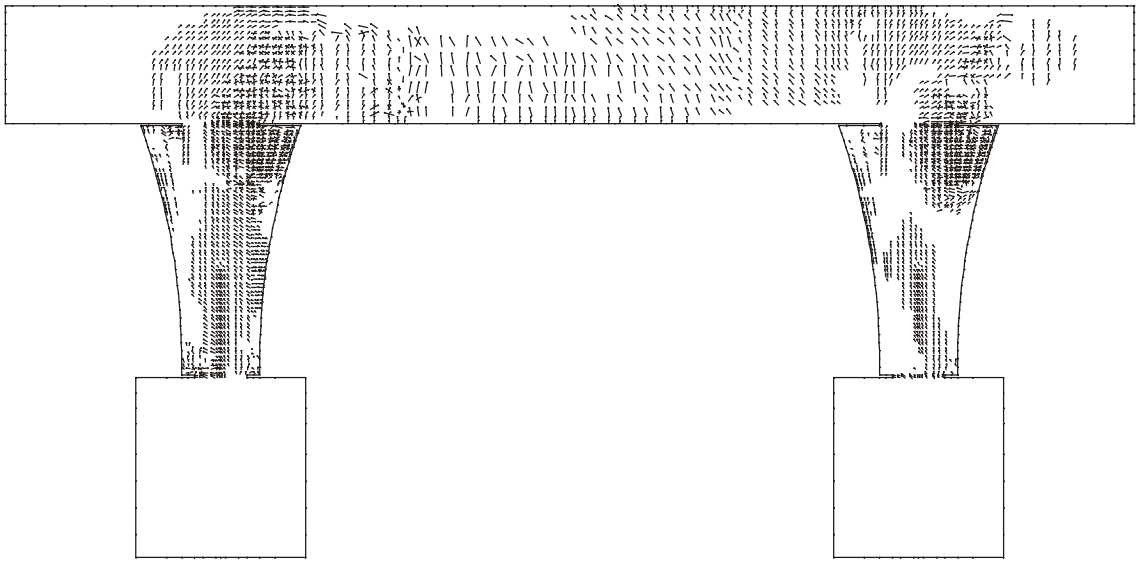

Fig. 5-36 SFCD2 DIANA Crack Pattern at Load = 114.0 K

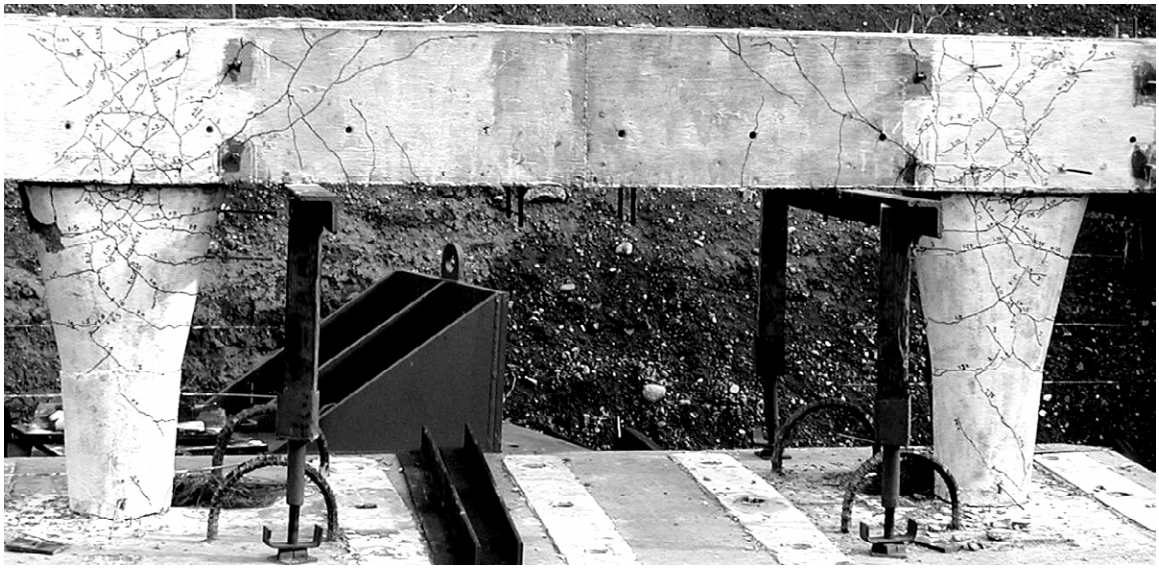

Fig. 5-37 SFCD2 Crack Pattern

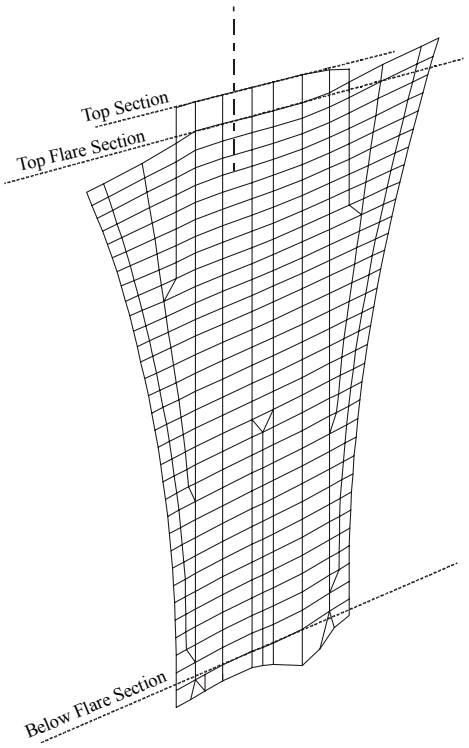

Fig. 5-38 Vertical Deformation at Load Level of 73.7 kips Scale of 60 SFCD2

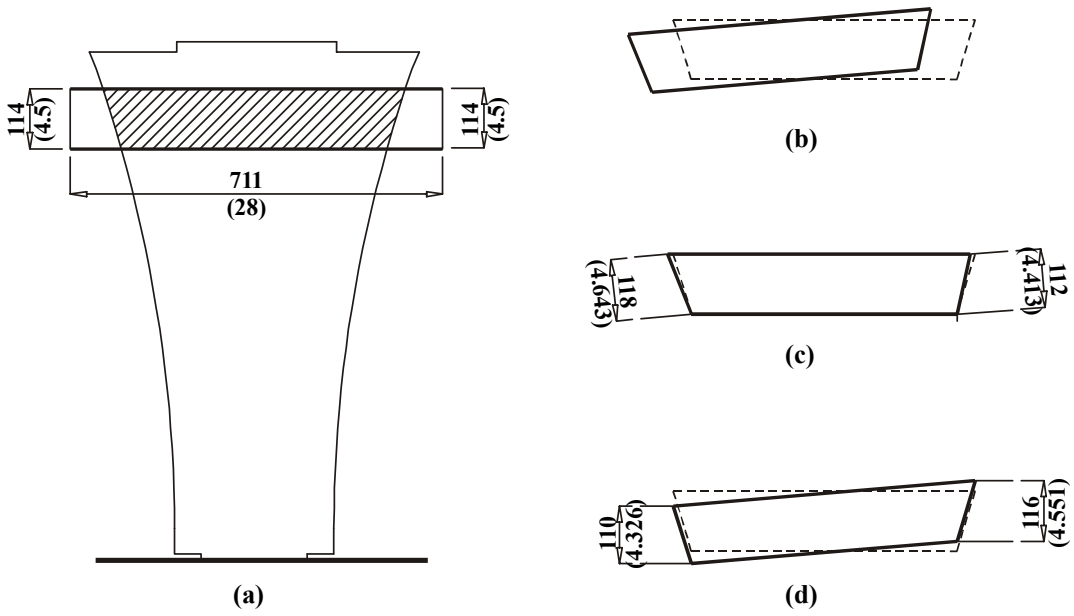

Fig. 5-39 Curvature Calculations (a) Section 4 for East Column (b) Final Deformed Shape (c) Horizontal Deformations (d) Vertical Deformations

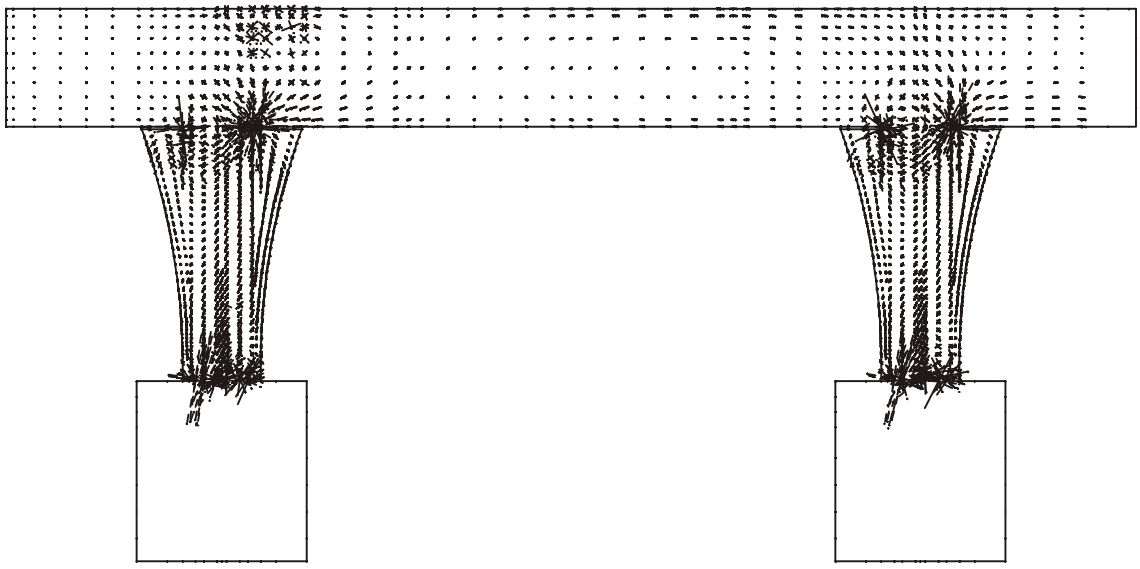

Fig. 5-40 Principal Stress Trajectories for SFCD2 at Load = -40.73 K

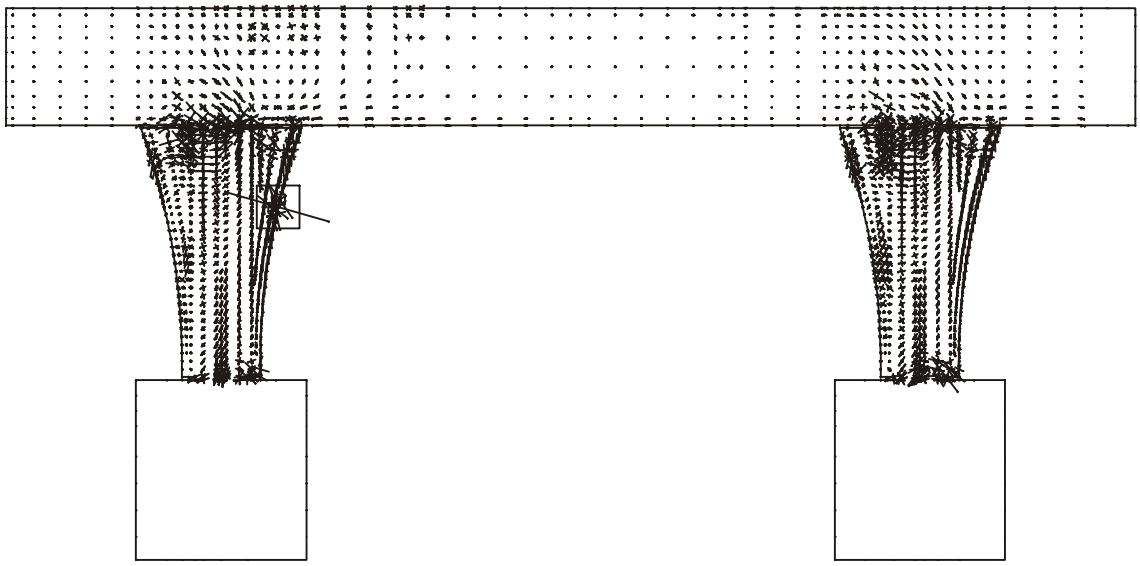

Fig. 5-41 Principal Stress Trajectories for SFCD2 at Load = -105.7 K

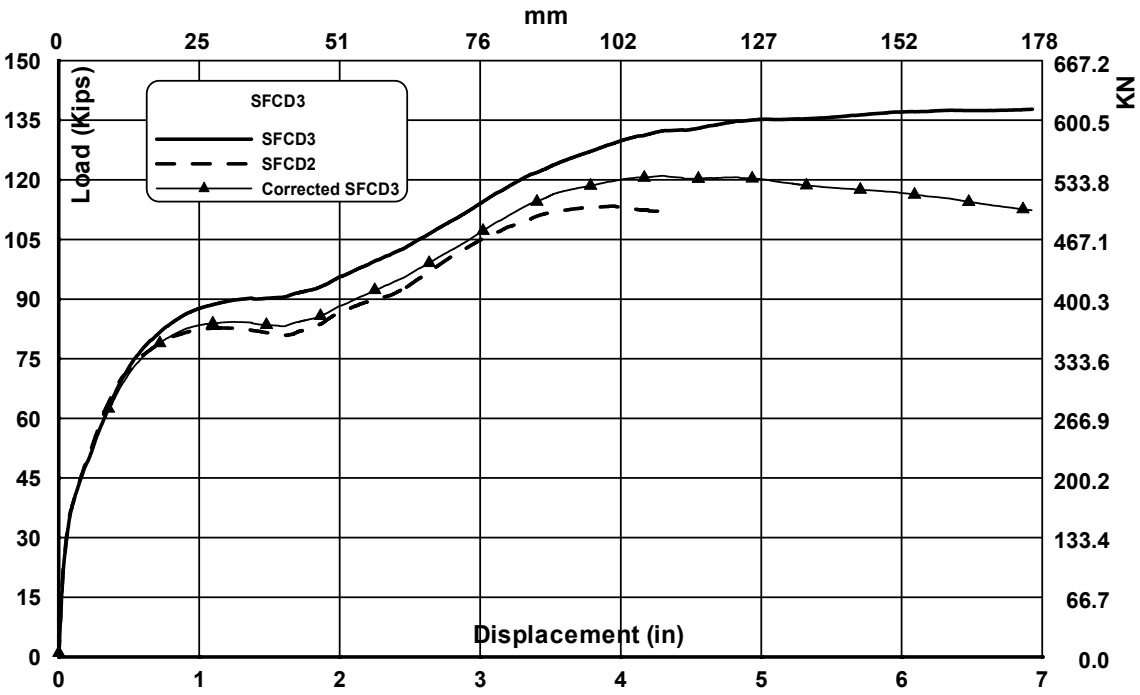

Fig. 5-42 Analytical Results for SFCD3

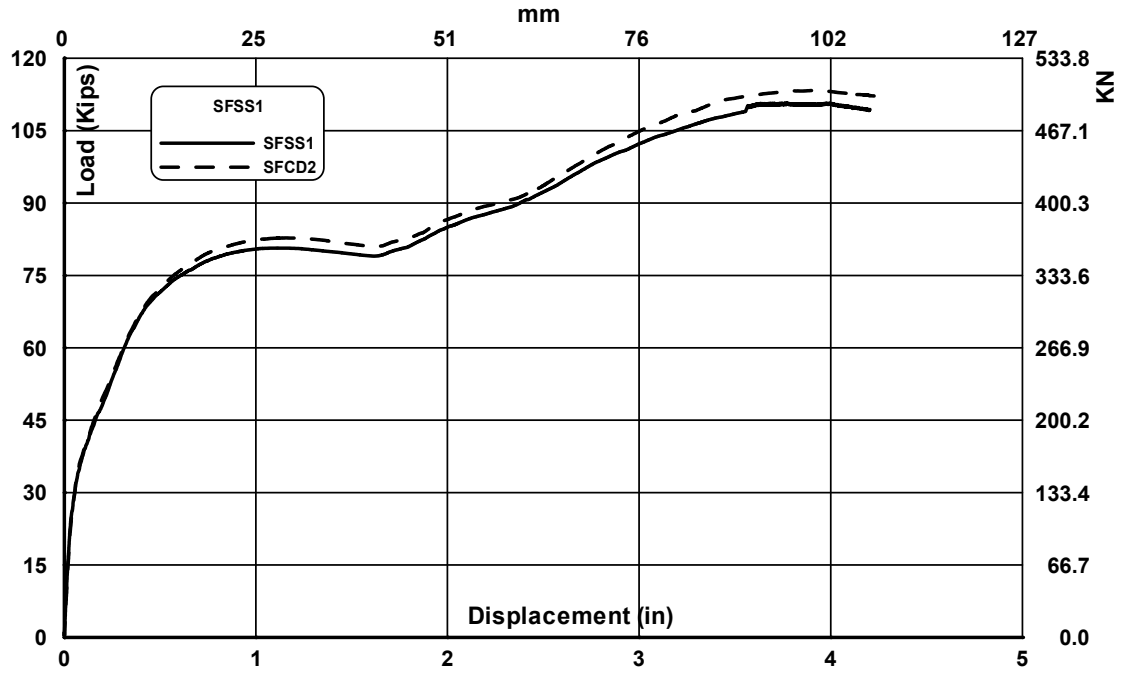

Fig. 5-43 Analytical Results for SFSS1

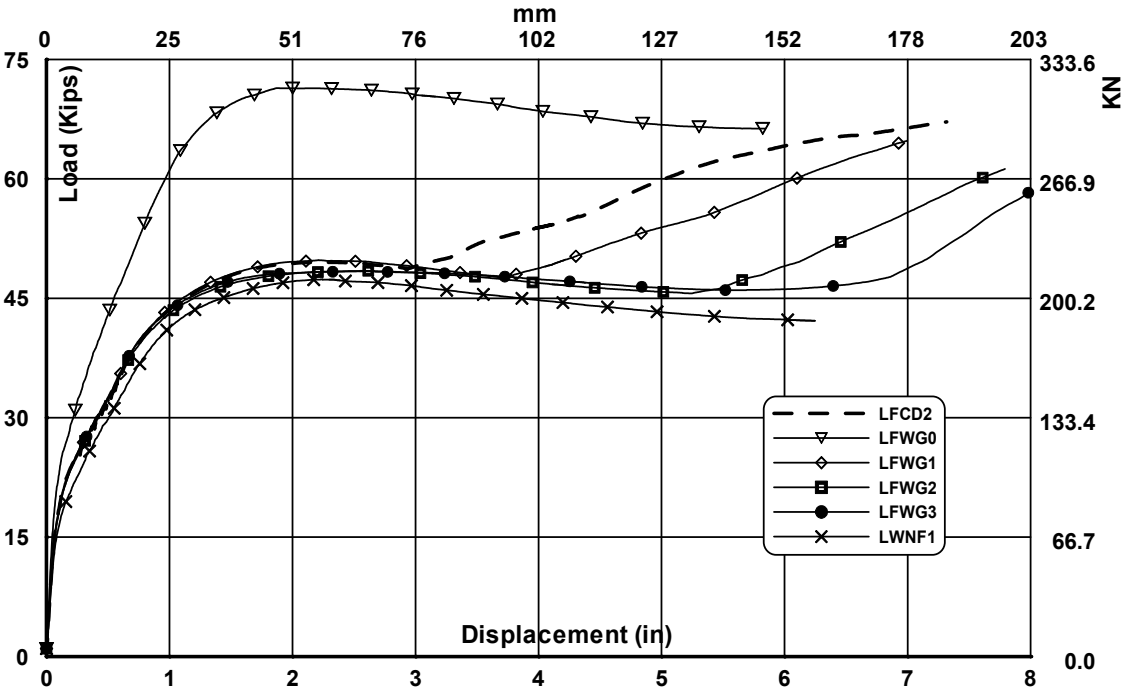

Fig. 5-44 Analytical Results for LFWG0 through LWNF1

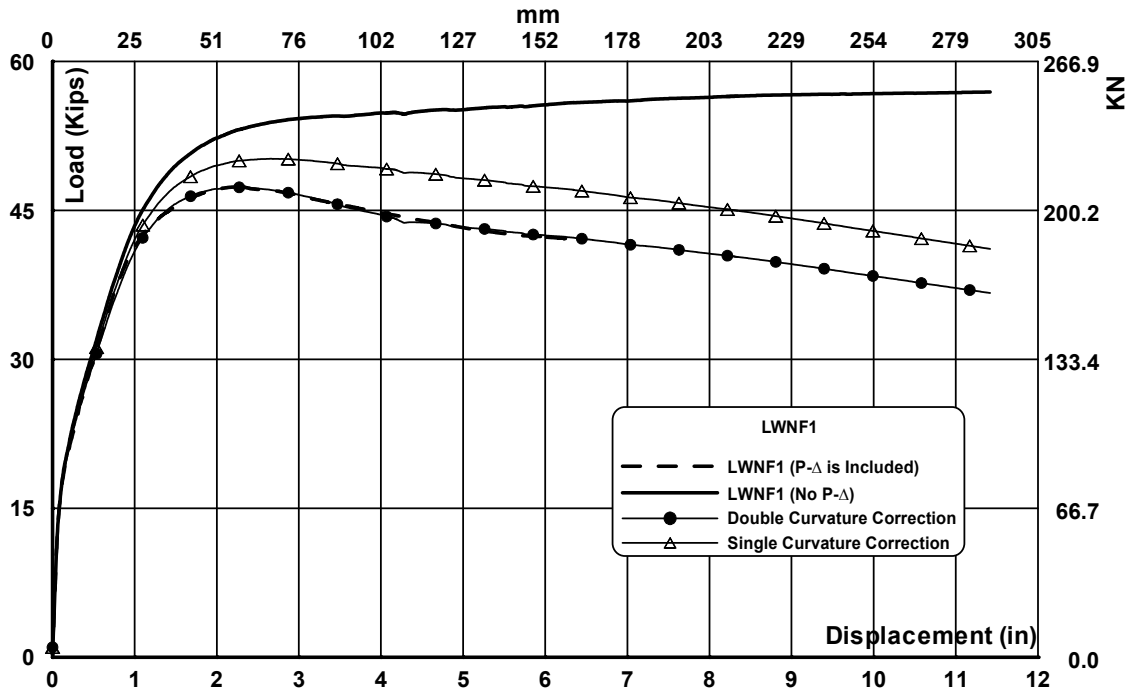

Fig. 5-45 P-Δ Effect Correction for LWNF1

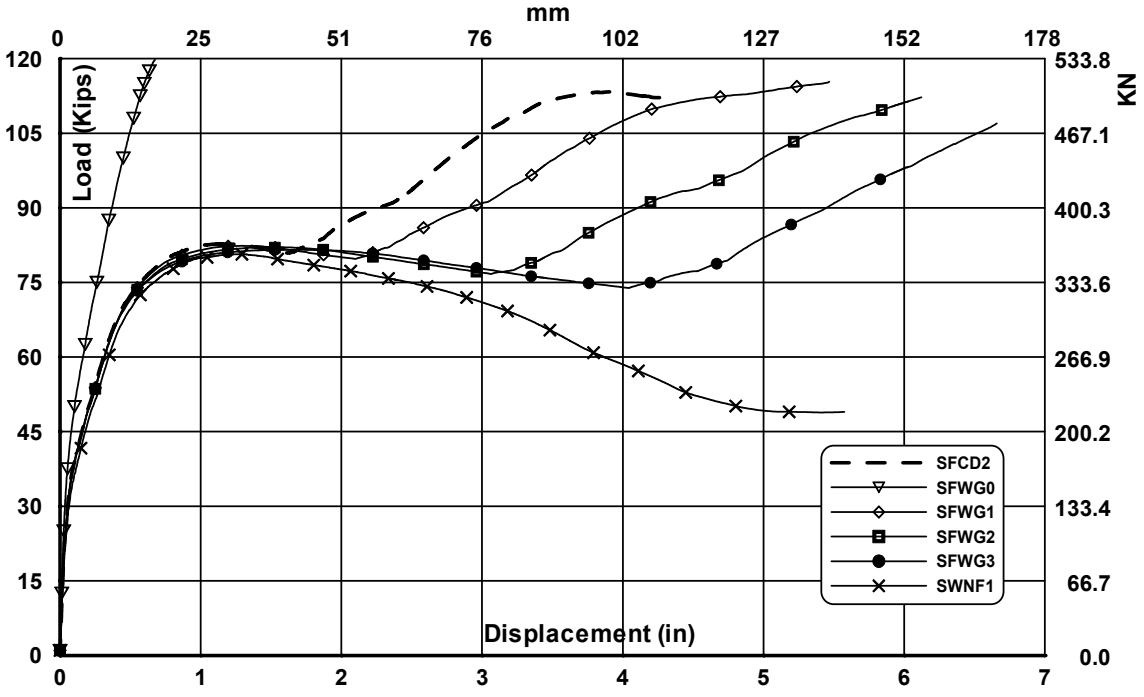

Fig. 5-46 Analytical Results for SFWG0 through SWNF1

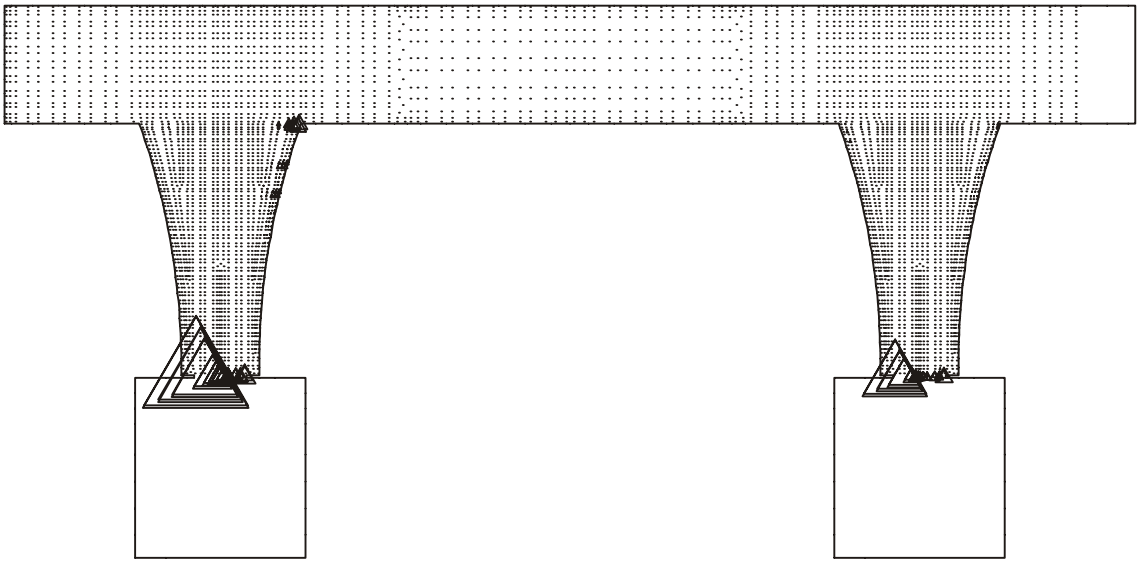

Fig. 5-47 Plasticity status of Concrete at for SFWG0 at Load level of 112.4 Kips

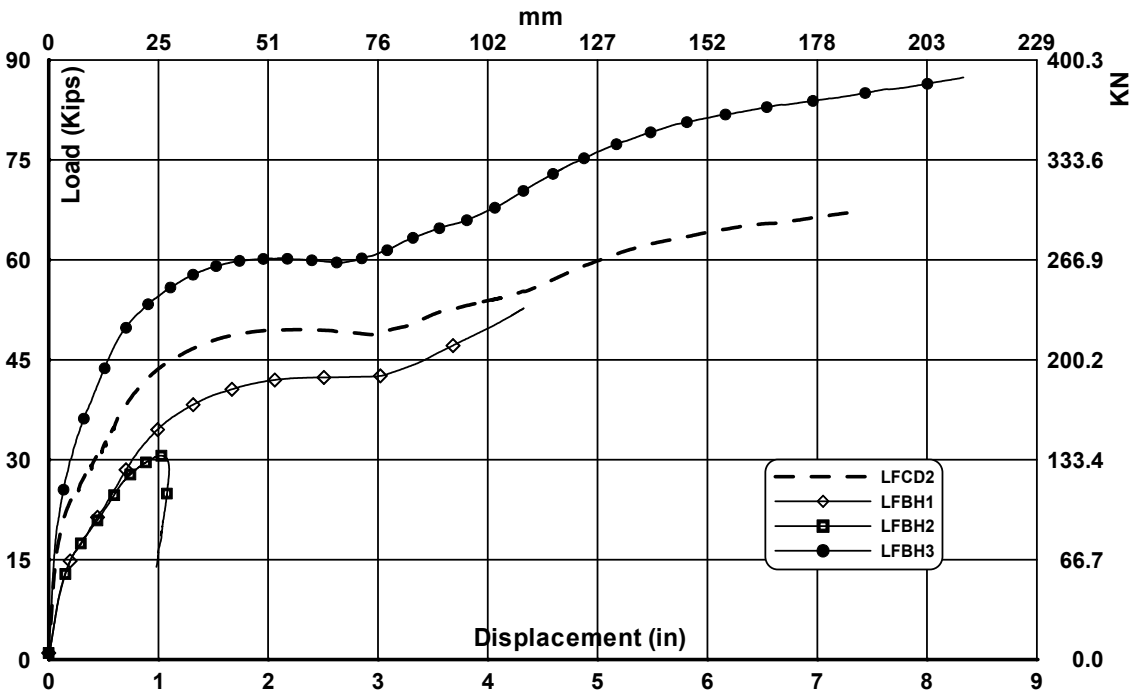

Fig. 5-48 Analytical Results for LFBH1 through LFBH3

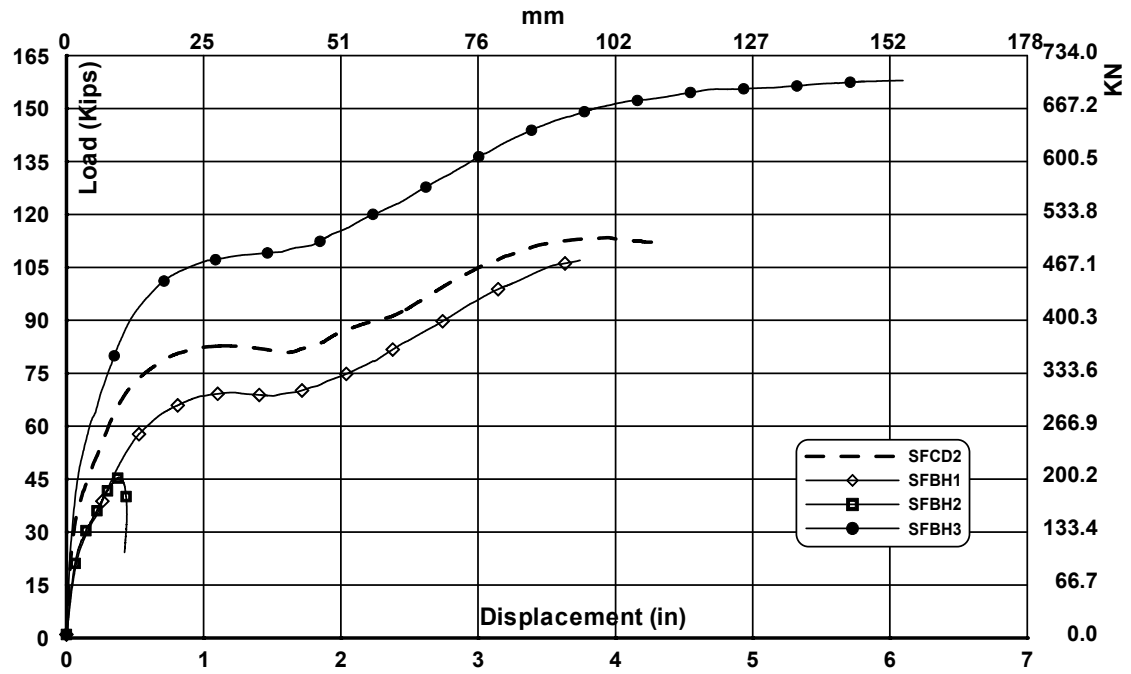

Fig. 5-49 Analytical Results for SFBH1 through SFBH3

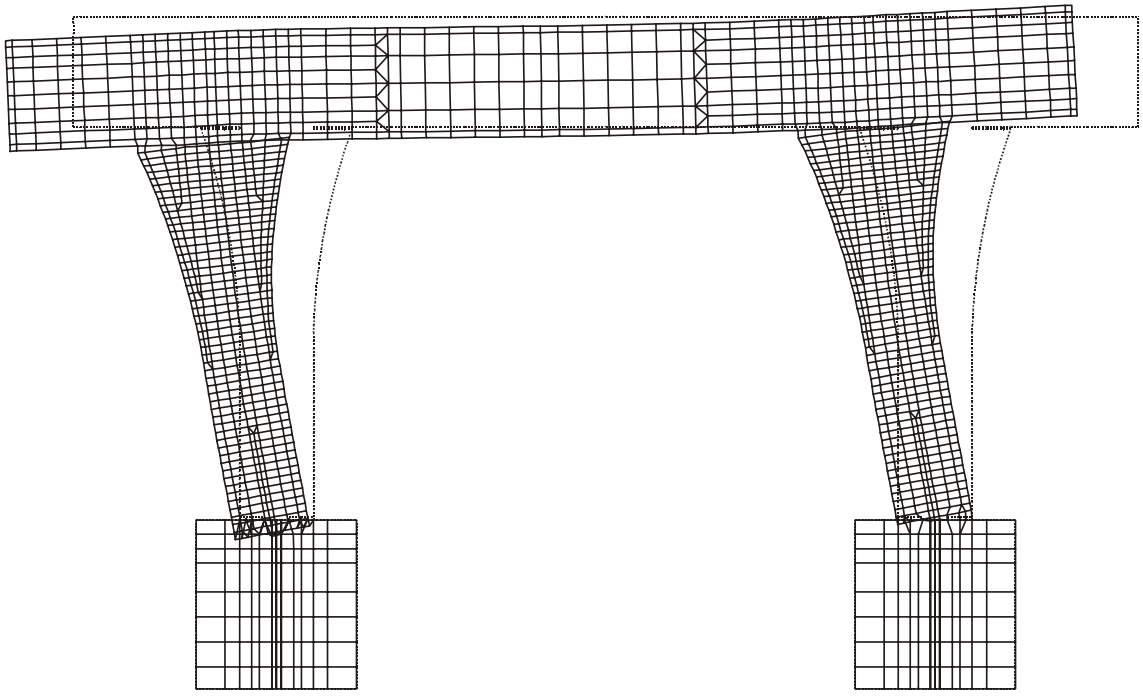

Fig. 5-50 Deformed Shape of LFBH1 at Load = 30.6 K

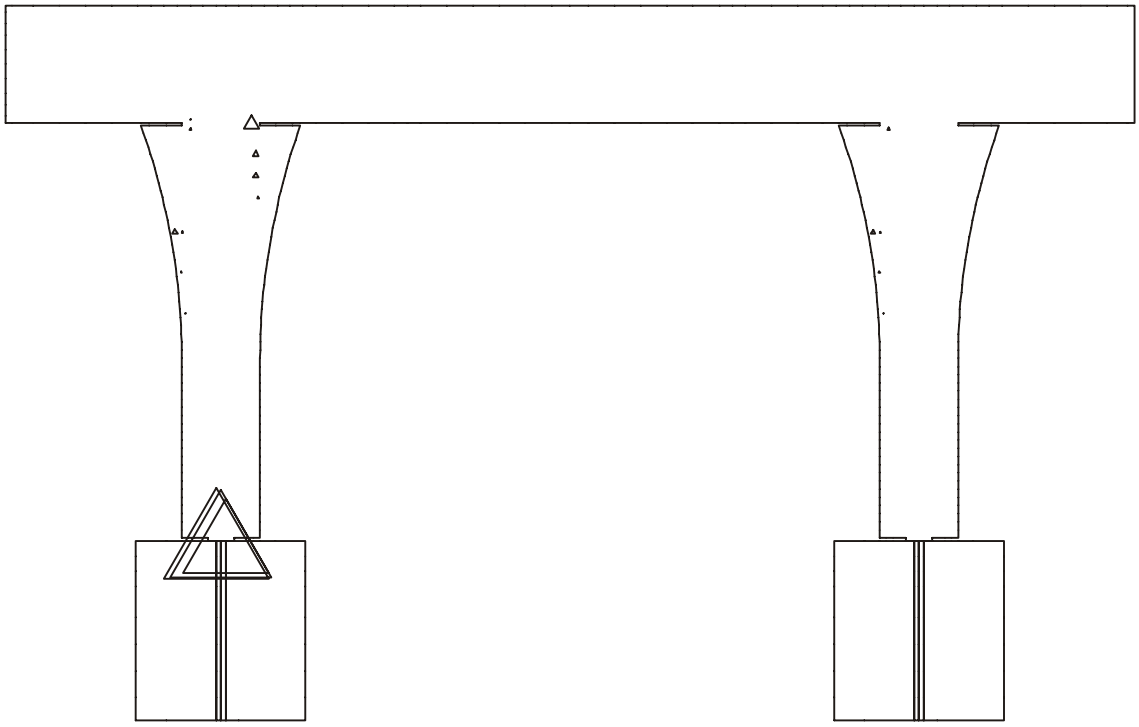

Fig. 5-51 Reinforcement Plasticity Status of LFBH1 at Load = 29.4 K

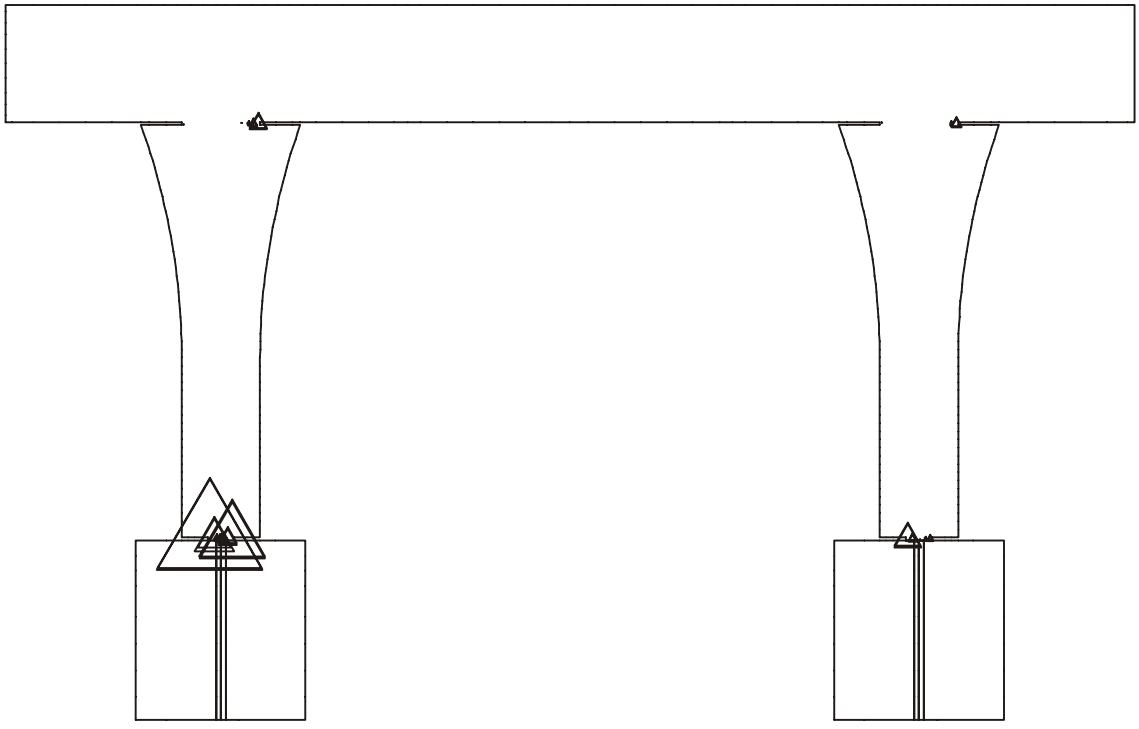

Fig. 5-52 Concrete Plasticity Status of LFBH1 at Load = 29.4 K

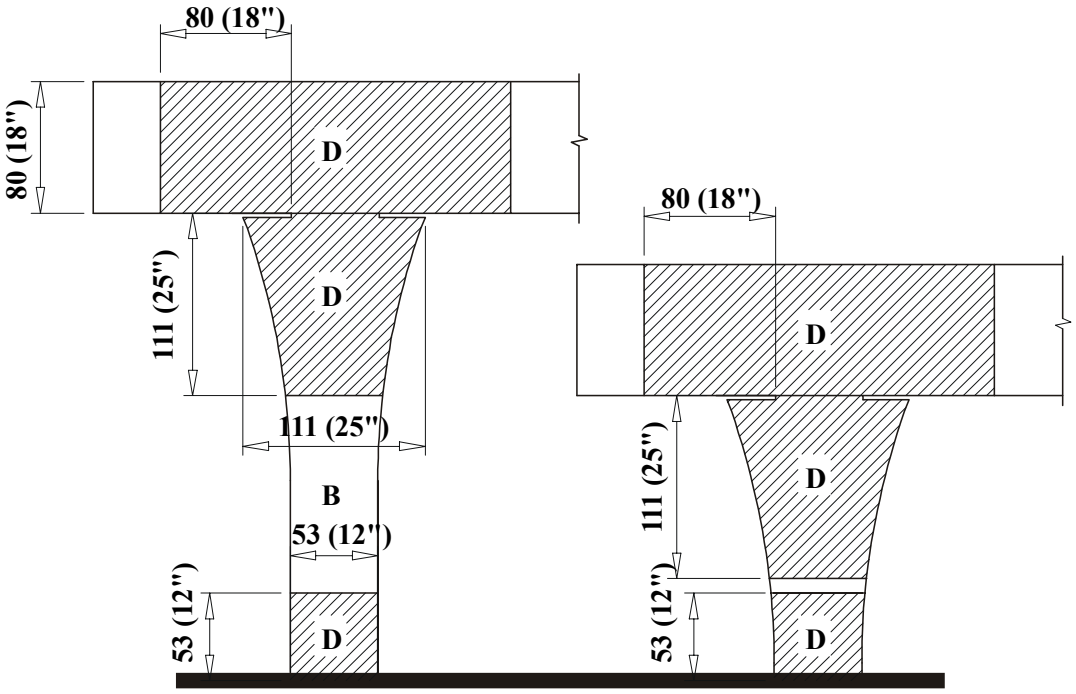

Fig. 6-1 D-Regions and B-Regions for flared columns with a gap (based on Saint Venant's principle)

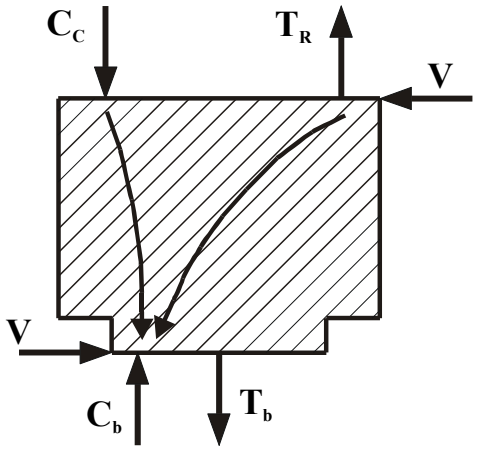

Fig. 6-2 Straining actions acting on the base hinge

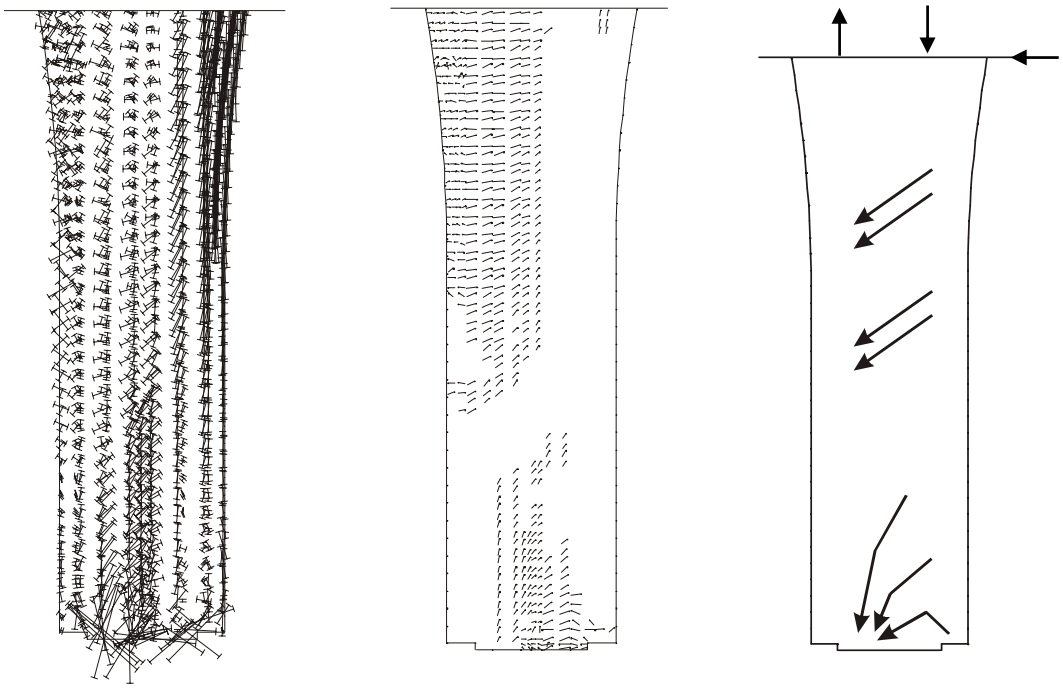

(a) (b) (c)

Fig. 6-3 Base Hinge Area (a) Principal Stresses Vectors (b) Cracking Pattern (c) Compression Fields

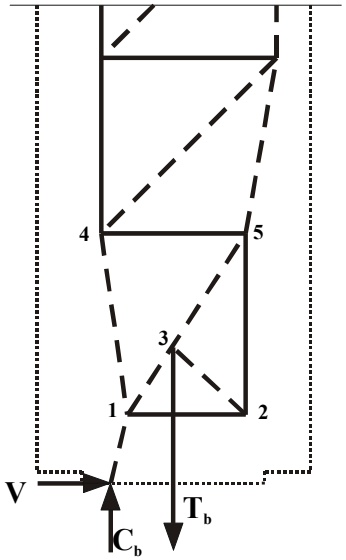

Fig. 6-4 Strut-and-tie model at the base hinge D-region

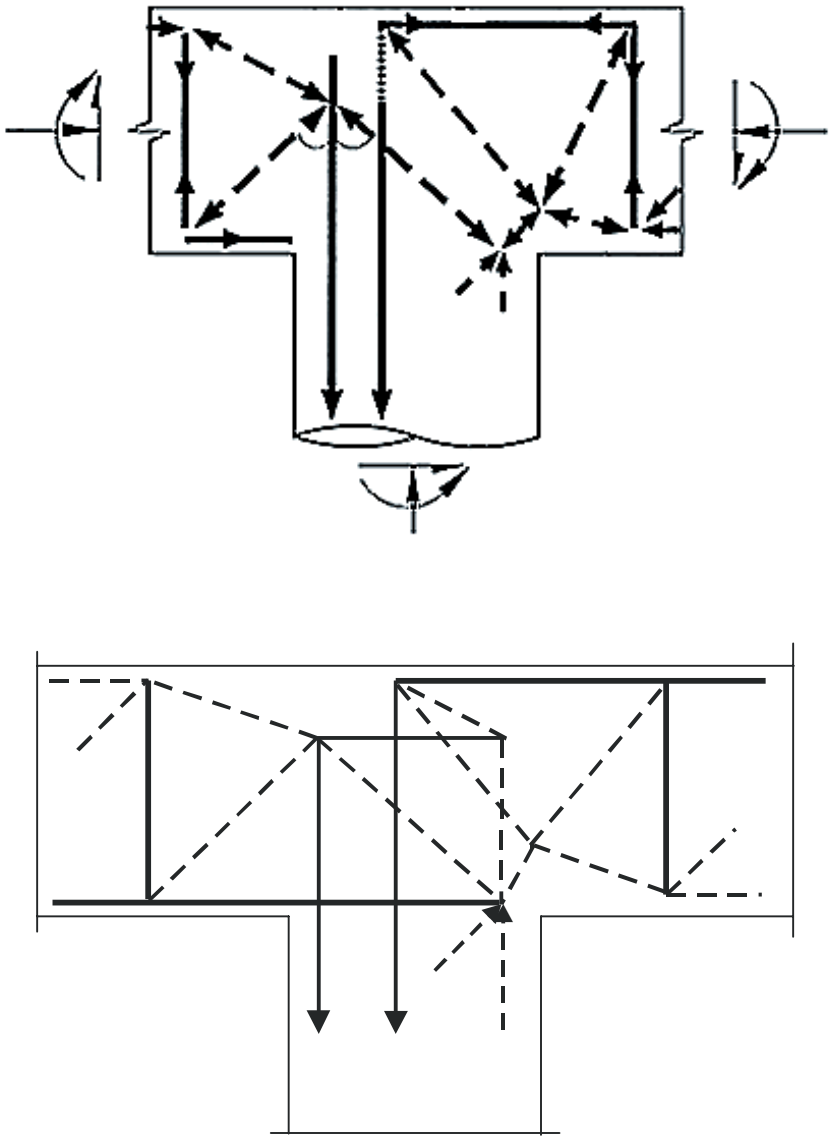

Fig. 6-5 Suggested Beam-Column Connection Strut-and-Tie Models form Previous Research

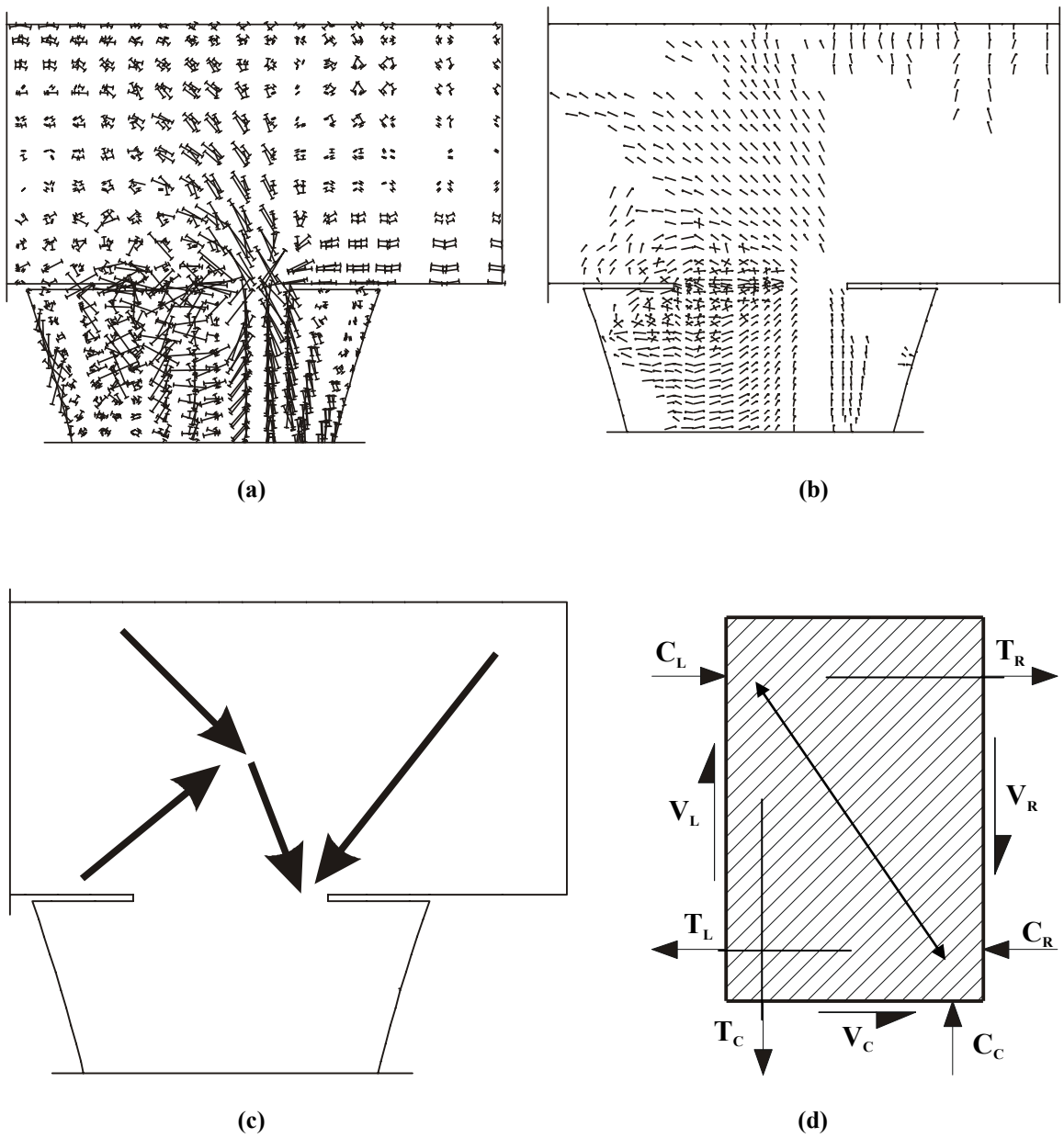

Fig. 6-6 East Beam-Column Connection (a) Principal Stresses Vectors (b) Cracking Pattern (c) Compression Fields (d) Straining Actions Acting on the East Beam-Column Connection

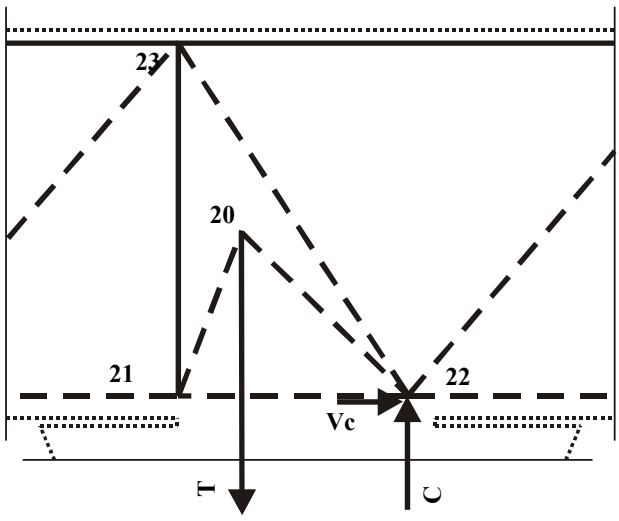

Fig. 6-7 Strut-And-Tie Model at the East Beam-Column Connection D-Region

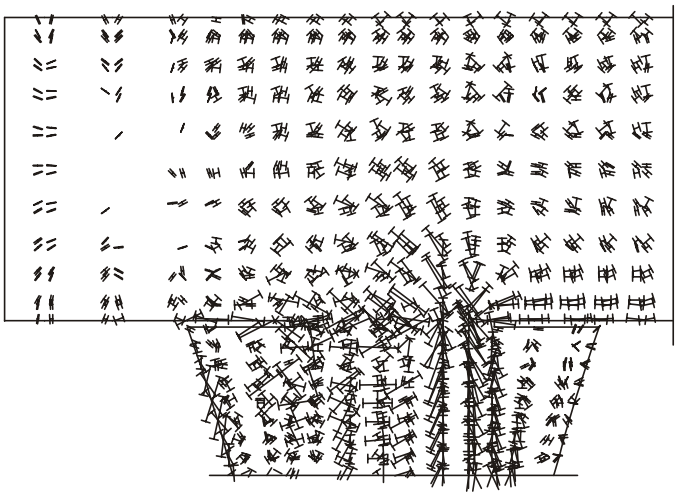

Fig. 6-8 West Beam-Column Connection Principal Stresses Vectors.

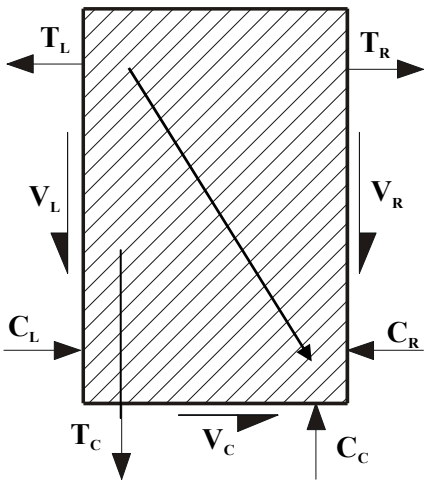

Fig. 6-9 Straining Actions Acting on the West Beam-Column Connection

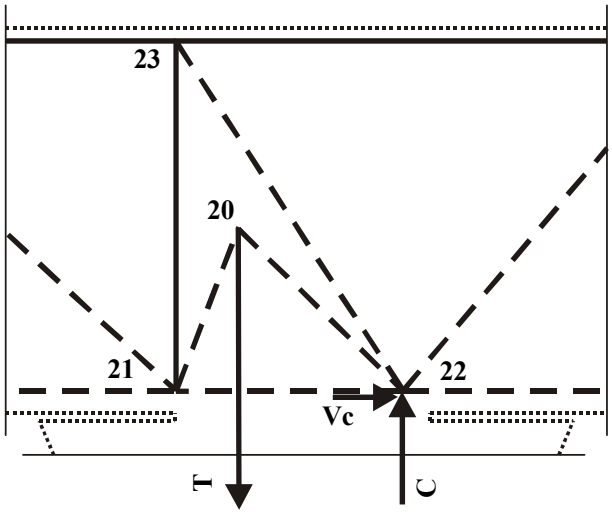

Fig. 6-10 Strut-And-Tie Model at the West Beam-Column Connection D-Region

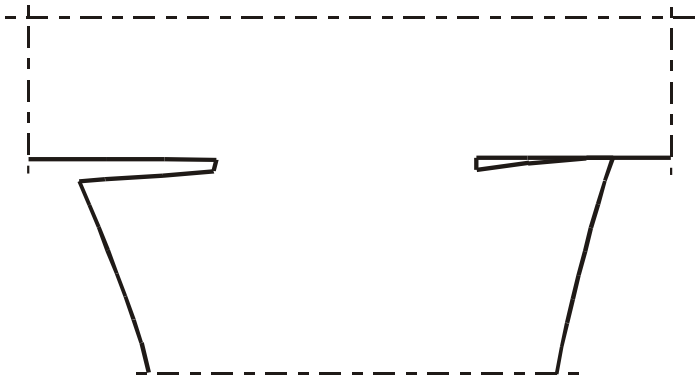

Fig. 6-11 Area in Contact at Gap Closure

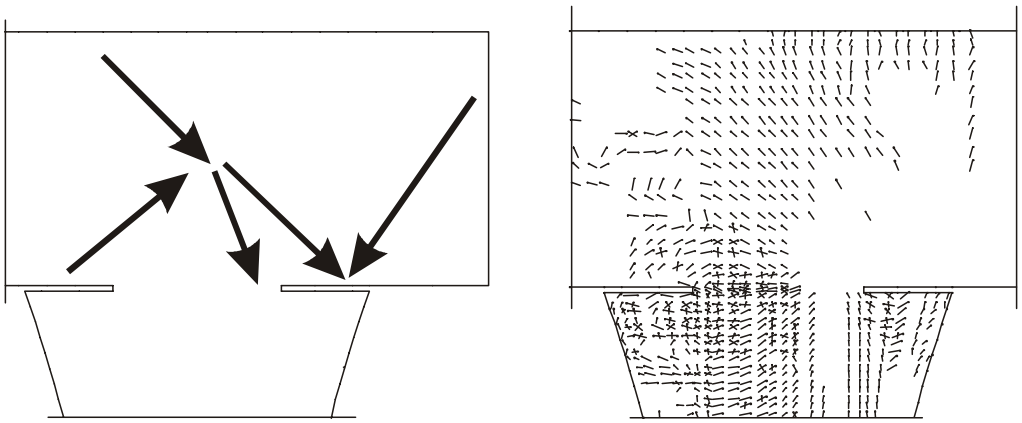

(a) **(b)**

Fig. 6-12 Beam-Column Connection after Gap Closure (a) Compression Fields (b) Cracking Pattern

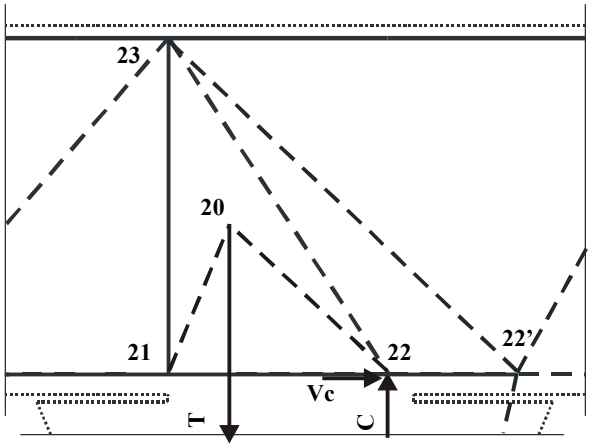

Fig. 6-13 Strut-And-Tie Model after Gap Closure

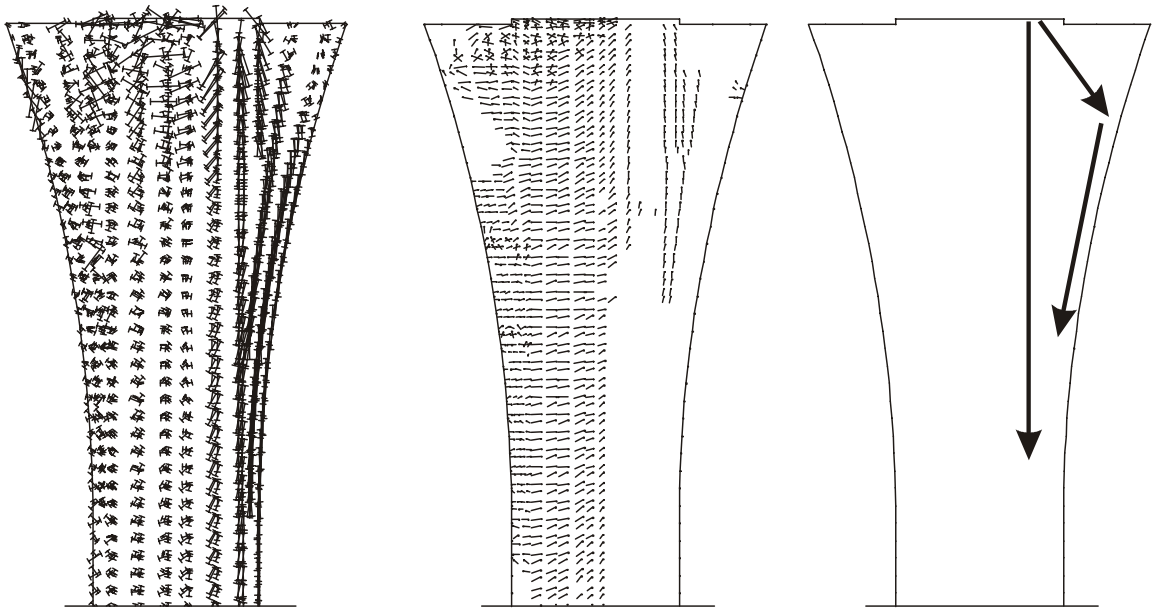

(a) **(b)** **(c)**

Fig. 6-14 Flare Region (a) Principal Stresses Vectors (b) Cracking Pattern (c) Compression Fields

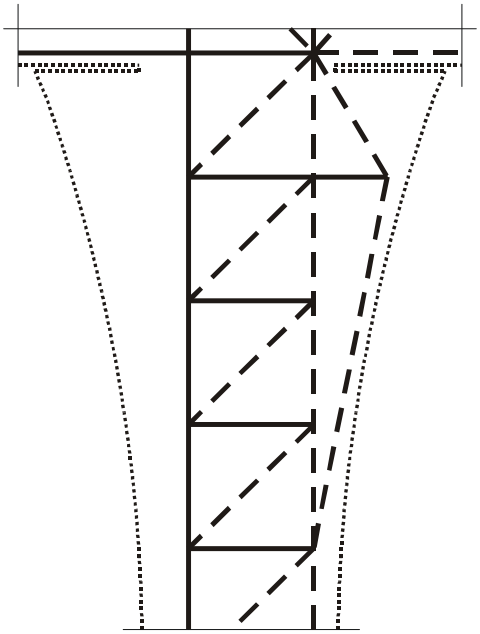

Fig. 6-15 Strut-And-Tie Model for the Flare D-Region before Gap Closure

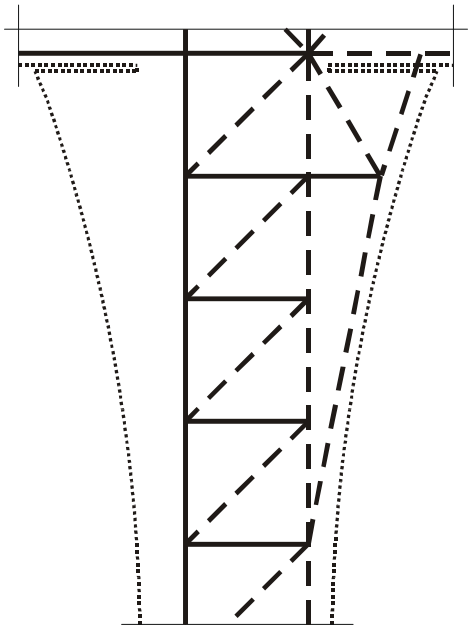

Fig. 6-16 Strut-And-Tie Model for the Flare D-Region after Gap Closure

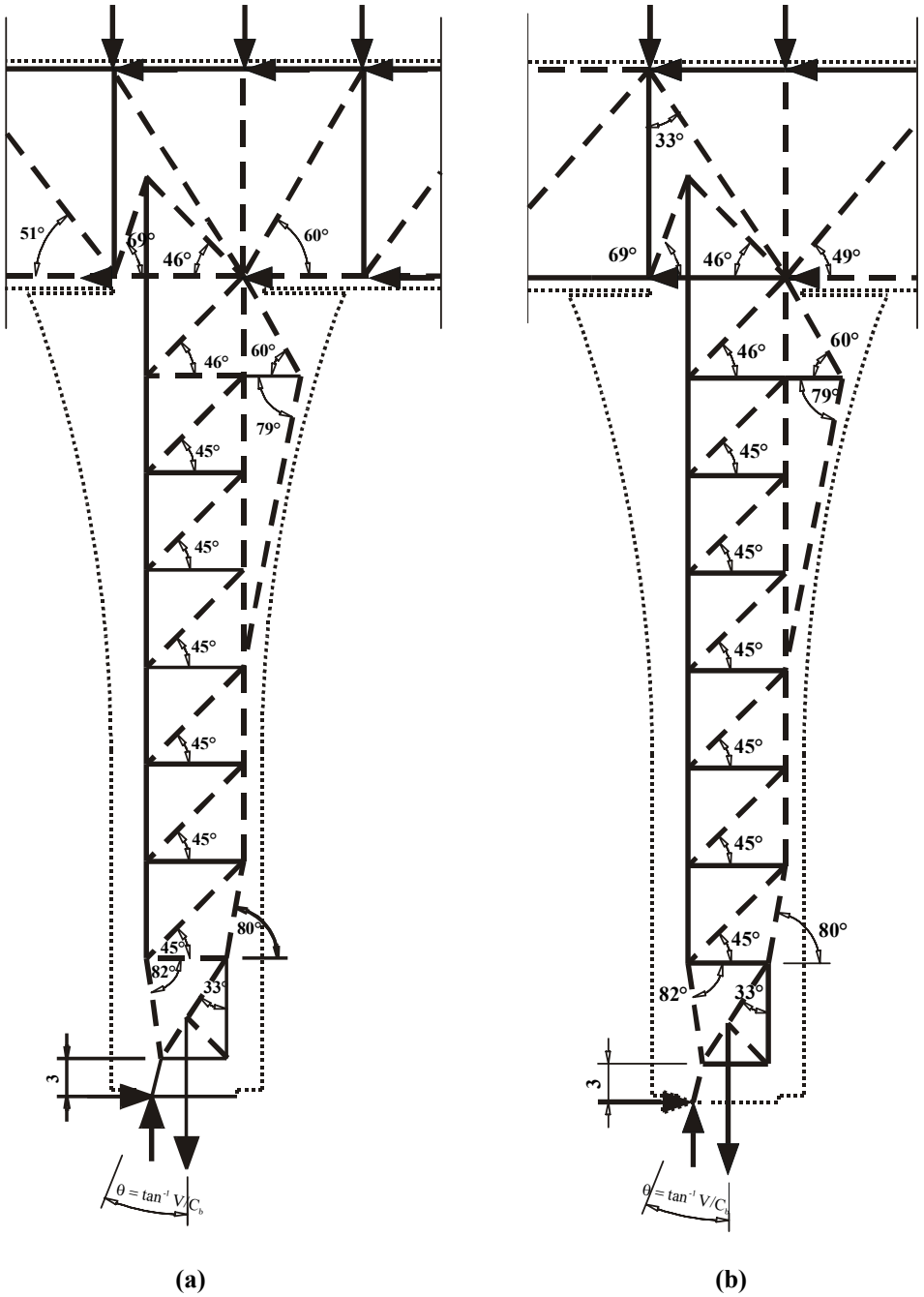

Fig. 6-17 Full Strut-and-Tie Model (a) West Column (b) East Column

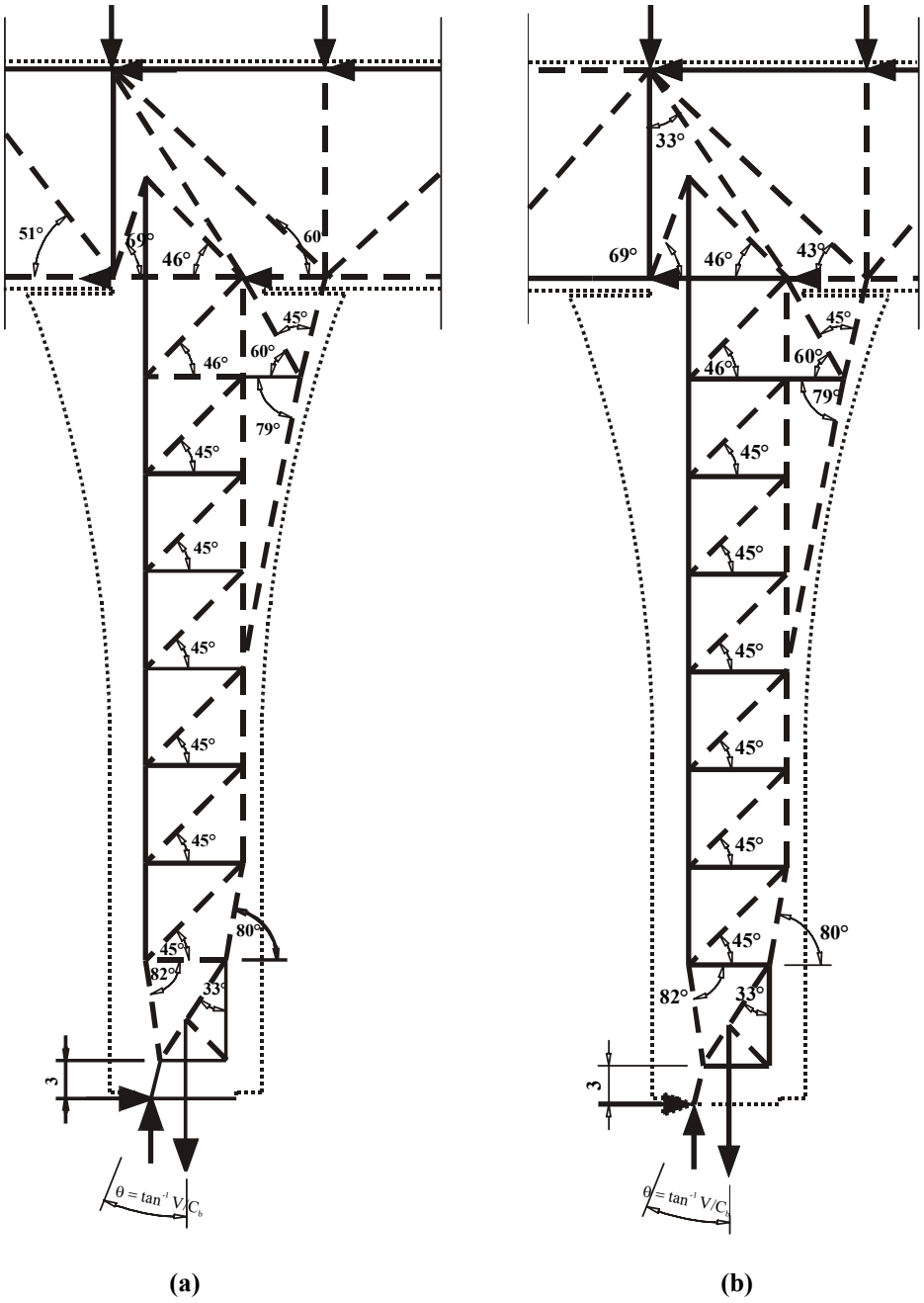

Fig. 6-18 Full Strut-and-Tie Model after Gap Closure (a) West Column (b) East Column

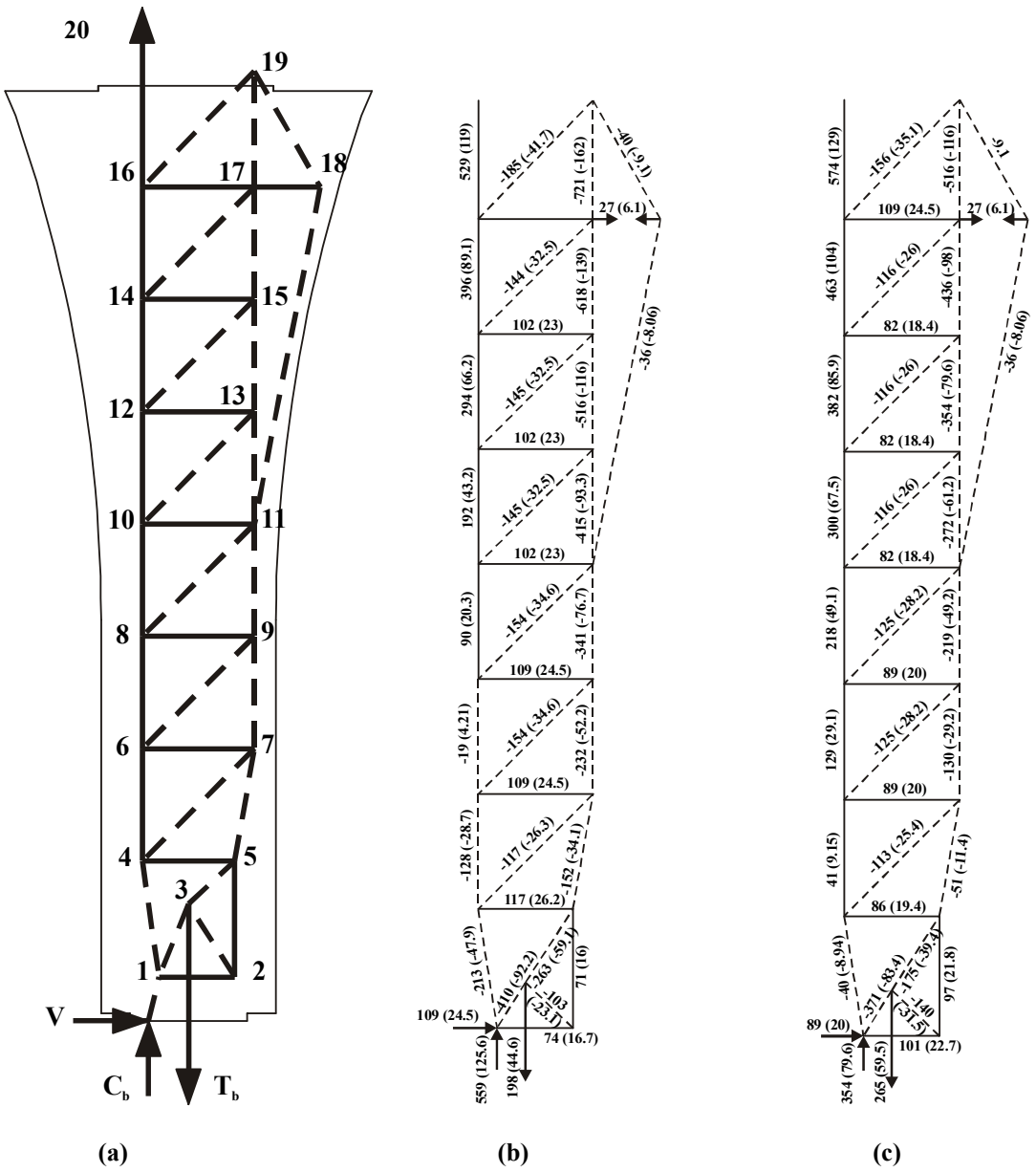

Fig. 6-19 Strut-and-tie model Results for Tall Columns (a) Node Numbering (b) West Column Internal Forces (c) East Column Internal Forces

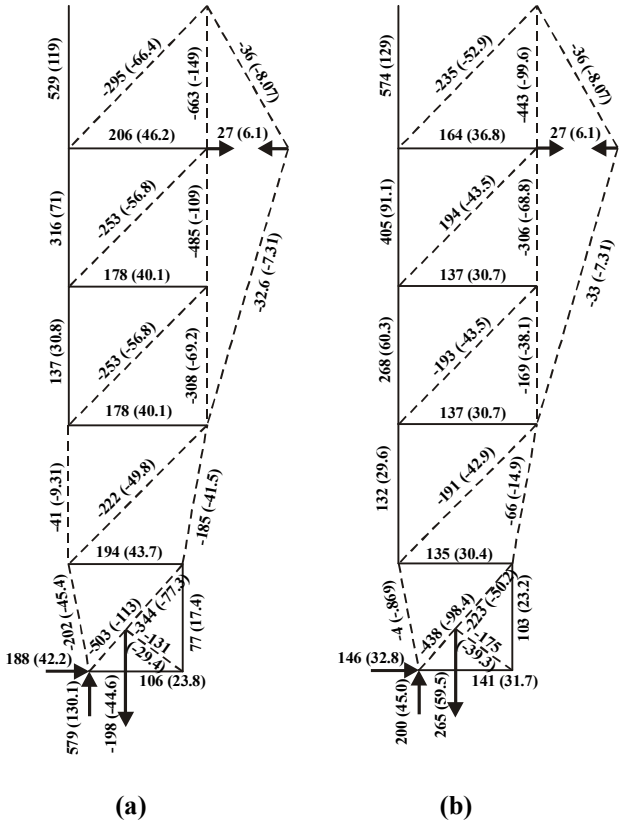

Fig. 6-20 Strut-and-tie model Results for Short Columns (a) West Column Internal Forces (b) East Column Internal Forces

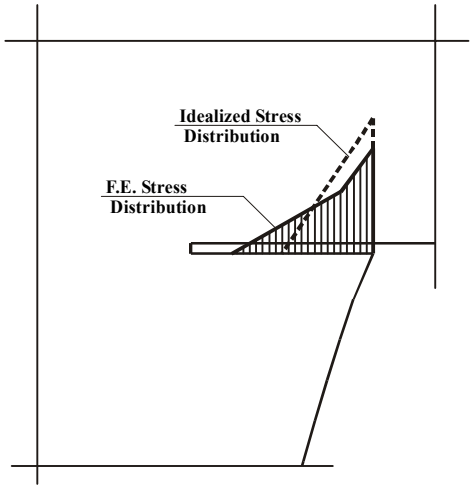

Fig. 6-21 Stress Distribution for the Area in Contact

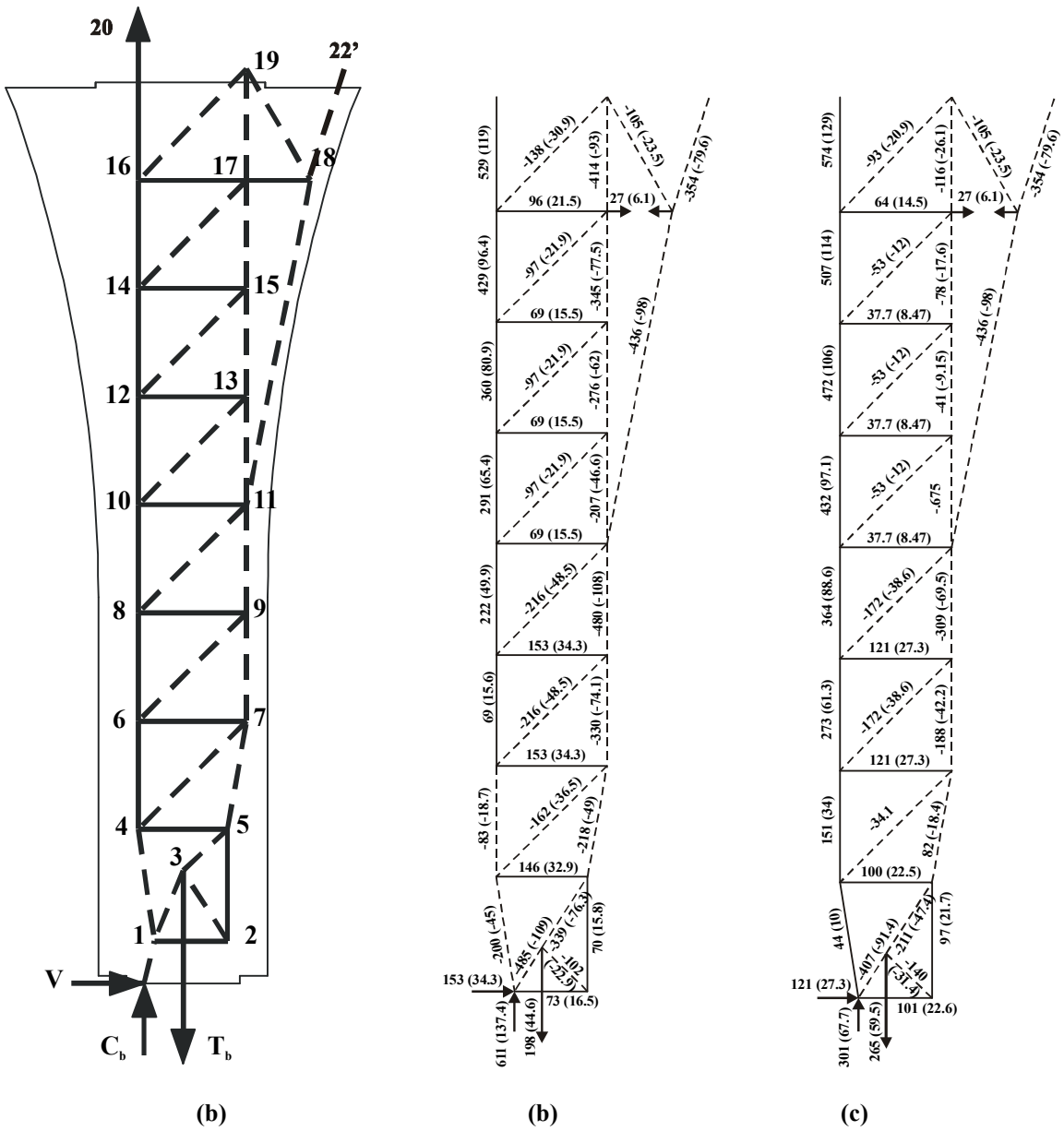

Fig. 6-22 Strut-and-tie model Results for Tall Columns with Gap Closed (a) Node Numbering

(b) West Column (c) East Column

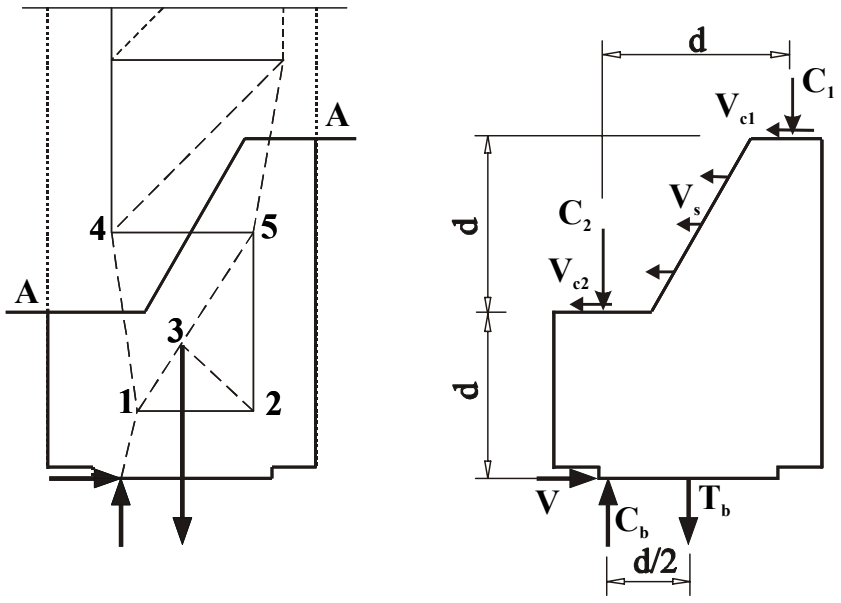

Fig. 6-23 Base Hinge Region (a) Location of Section (b) Internal Forces

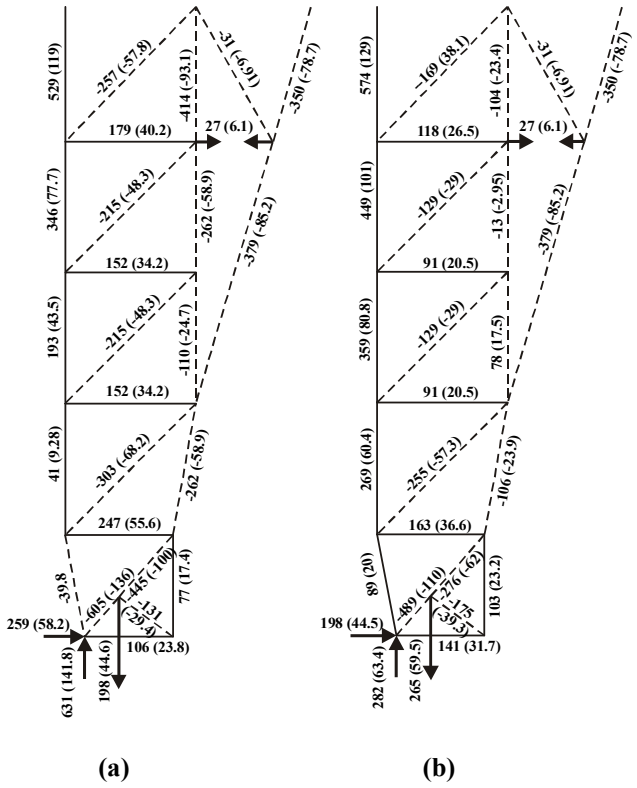

Fig. 6-24 Strut-and-tie model Results for Short Columns (a) West Column Internal Forces (b) East Column

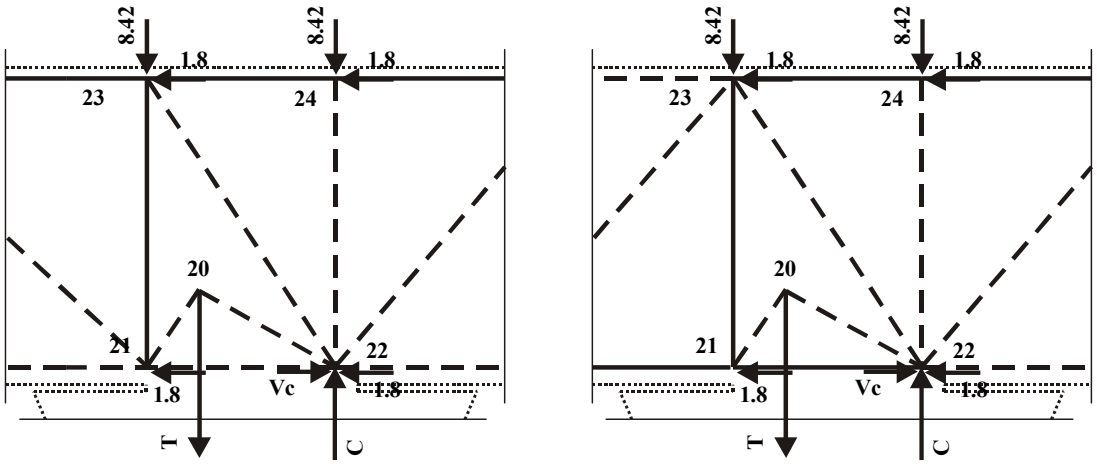

Fig. 6-25 Node Numbering for Beam-Column Connection Strut-and-Tie Model (a) West Joint

(b) East Joint

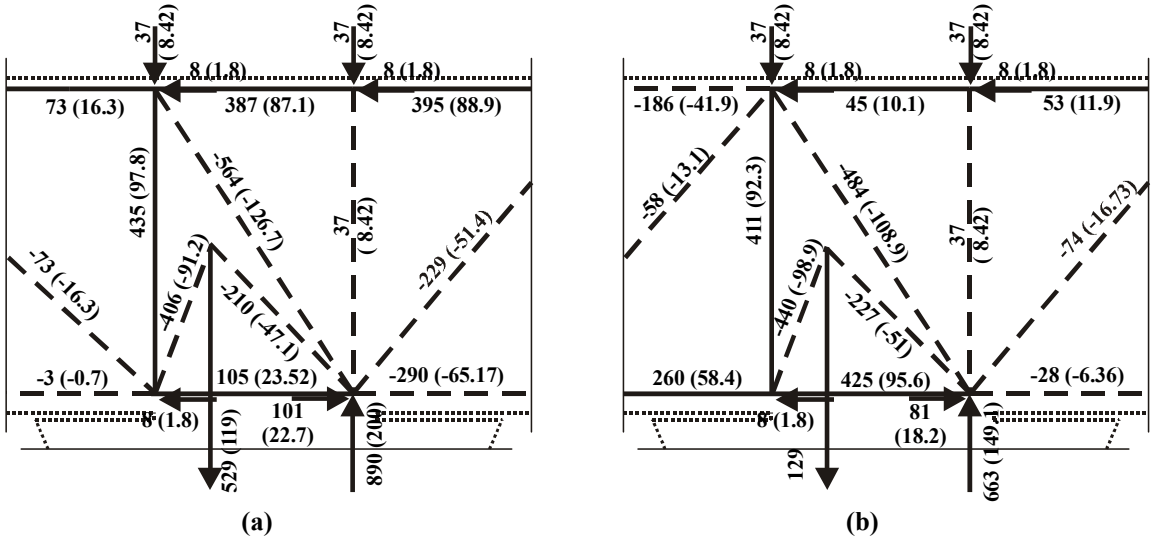

Fig. 6-26 Strut-and-tie model Results for Tall Columns' Beam-Column Connection (a) West Joint

(b) East Joint

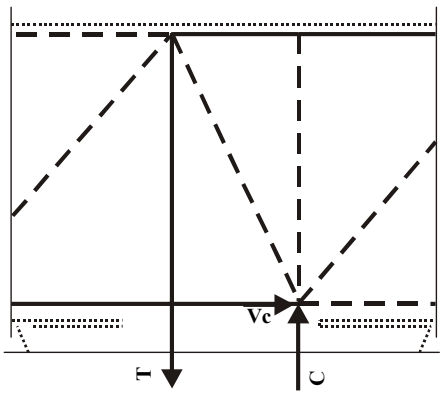

Fig. 6-27 Strut-and-Tie Model for Beam-Column Connections with Columns Reinforcement Extended Inside the Beam

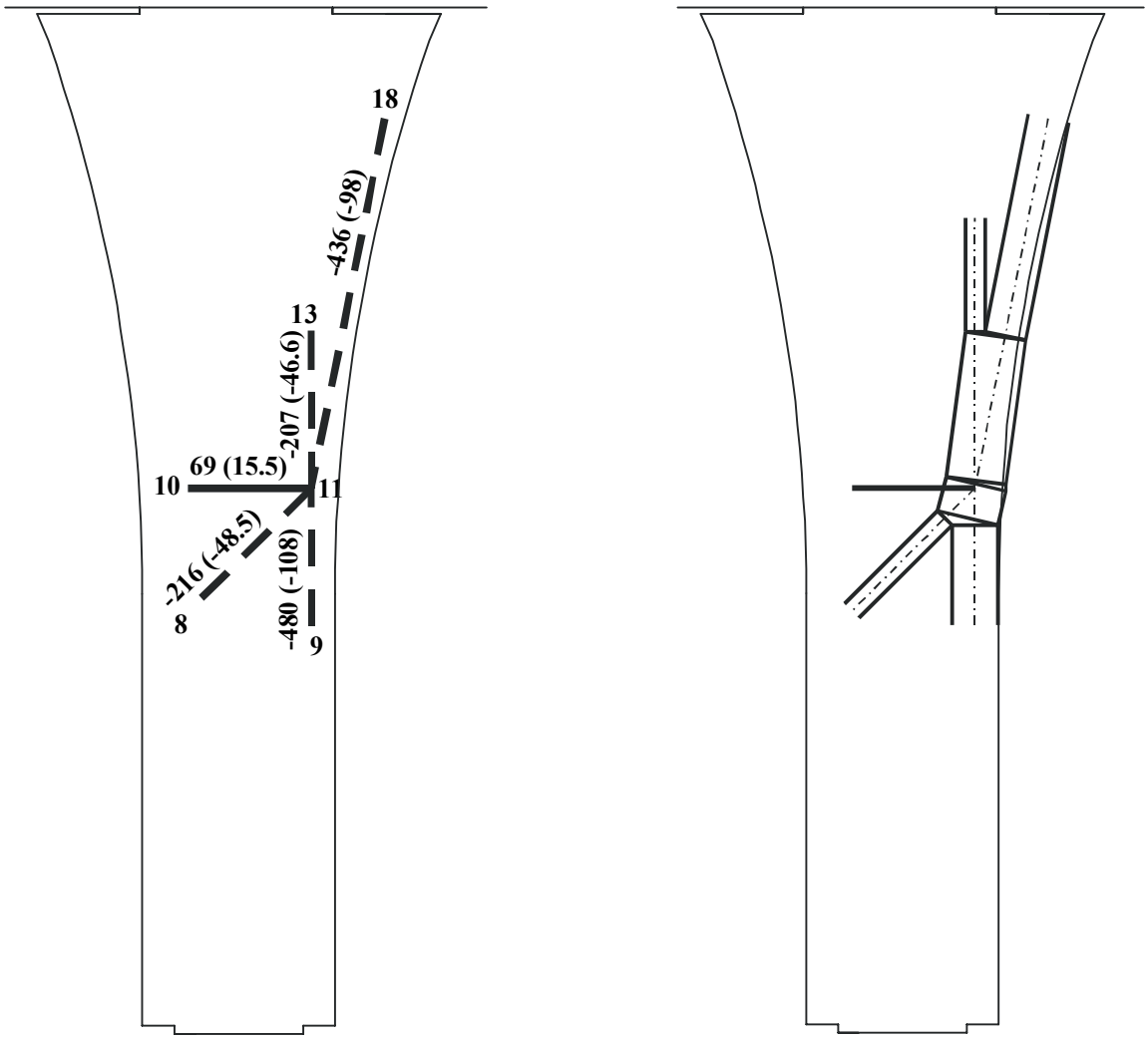

Fig. 6-28 Node location and struts widths

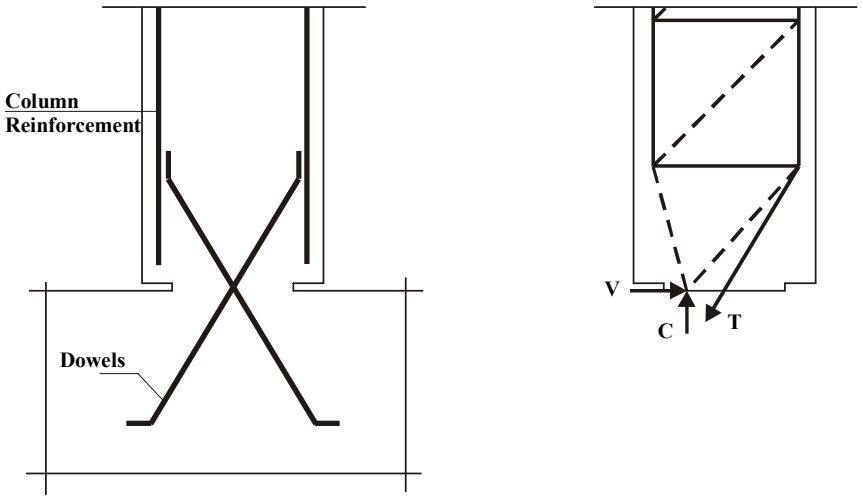

(a) **(b)**

Fig. 6-29 Alternative Base Hinge Detailing (a) Base Hinge Dowels (b) Strut-and-Tie Model

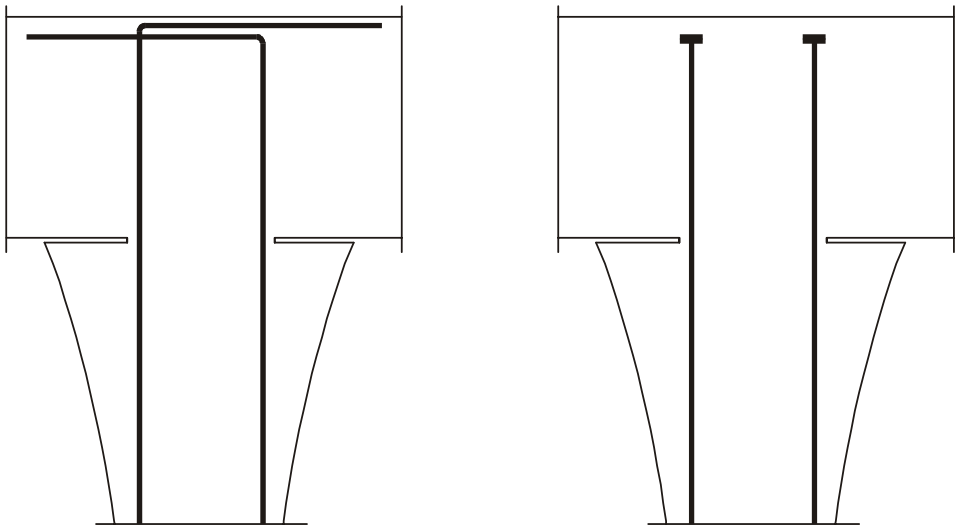

(a) **(b)**

Fig. 6-30 Alternative Beam-Column Connection Detailing (a) Column Reinforcement extended in the beam (b) Headed Bars

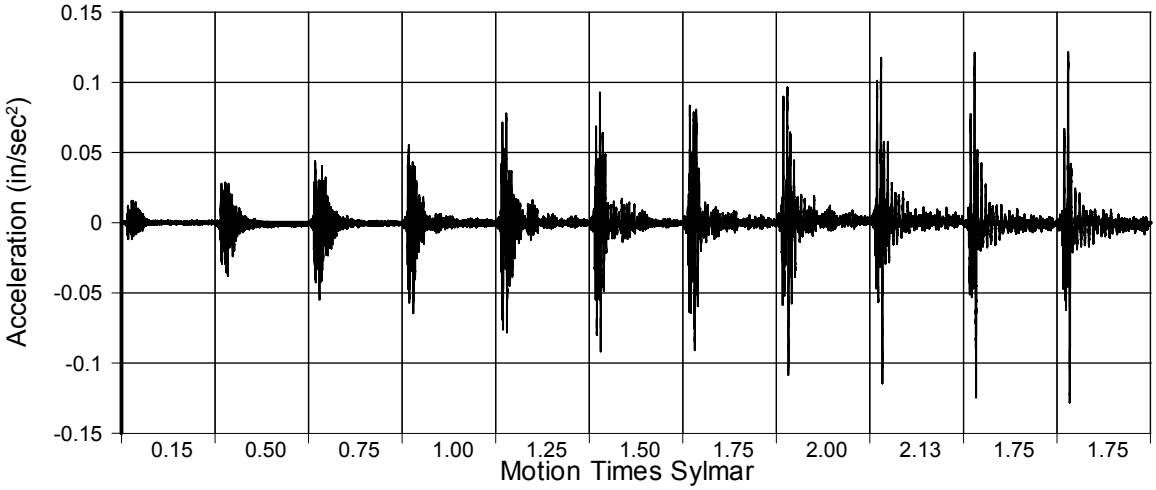

Fig. A-1 - Measured Transverse Acceleration for LFCD1

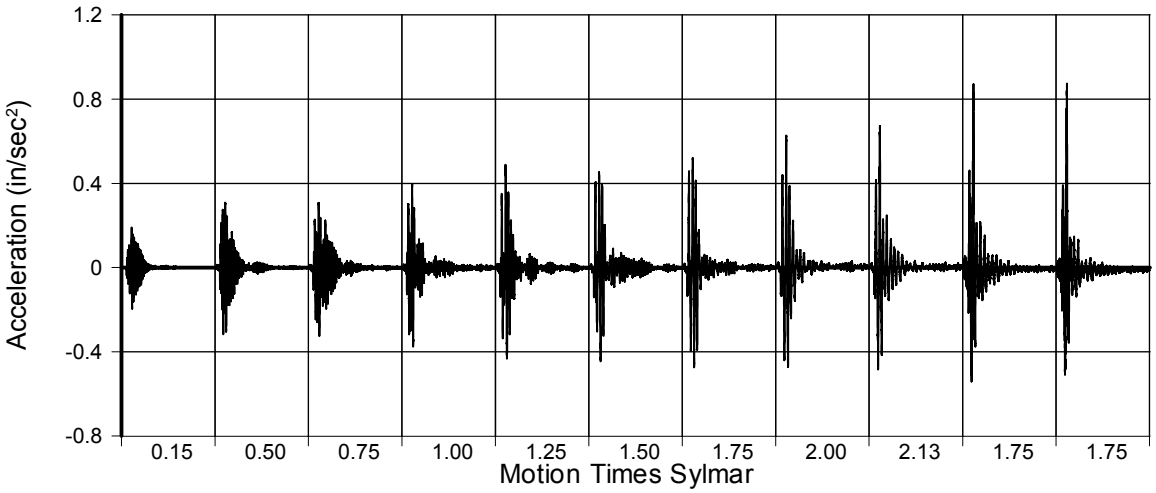

Fig. A-2 - Measured In-Plane Acceleration for LFCD1

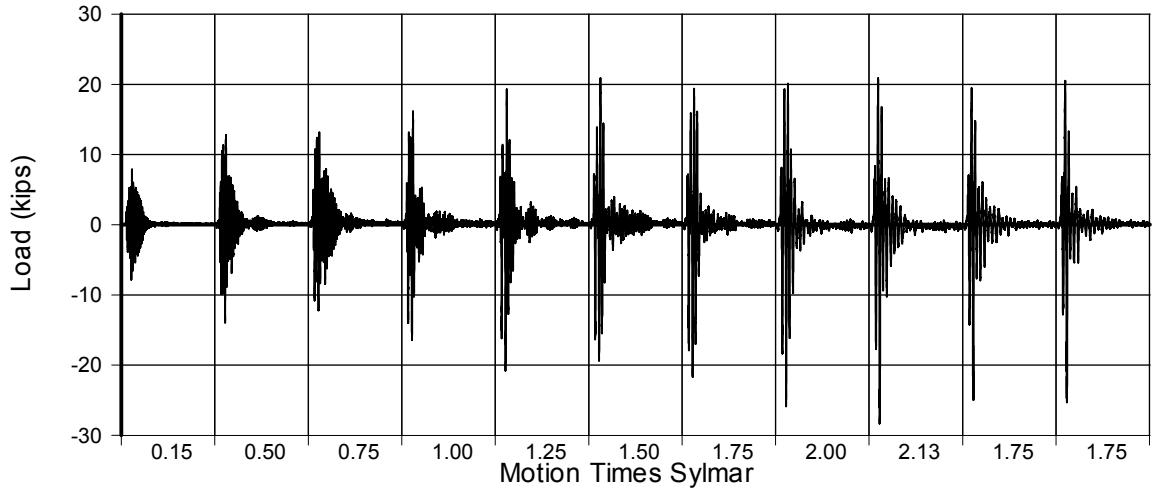

Fig. A-3 - Measured Link Load for LFCD1

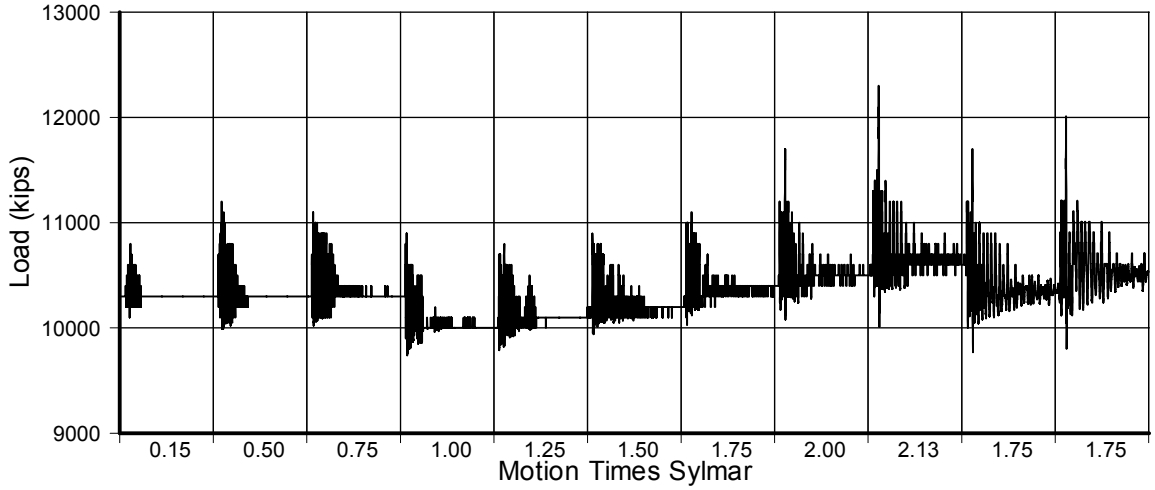

Fig. A-4 - Measured Vertical Load for LFCD1 (West Column)

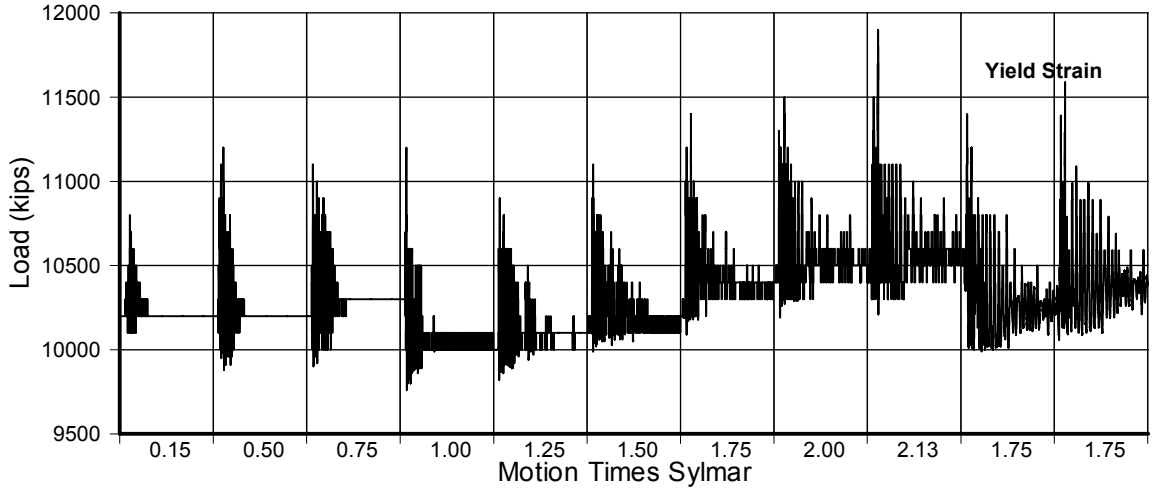

Fig. A-5 - Measured Vertical Load for LFCD1 (East Column))

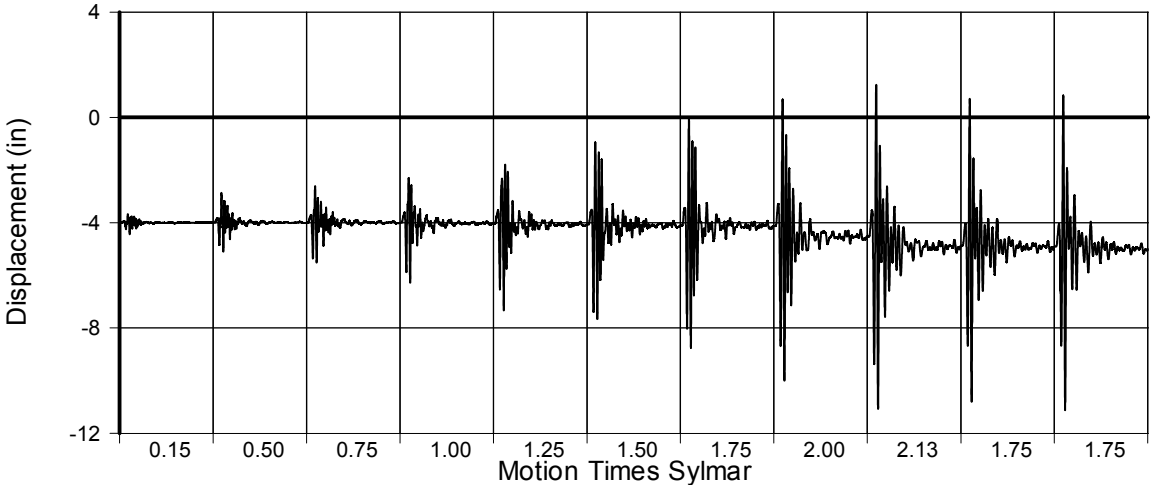

Fig. A-6 – Measured Absolute Displacement for LFCD1

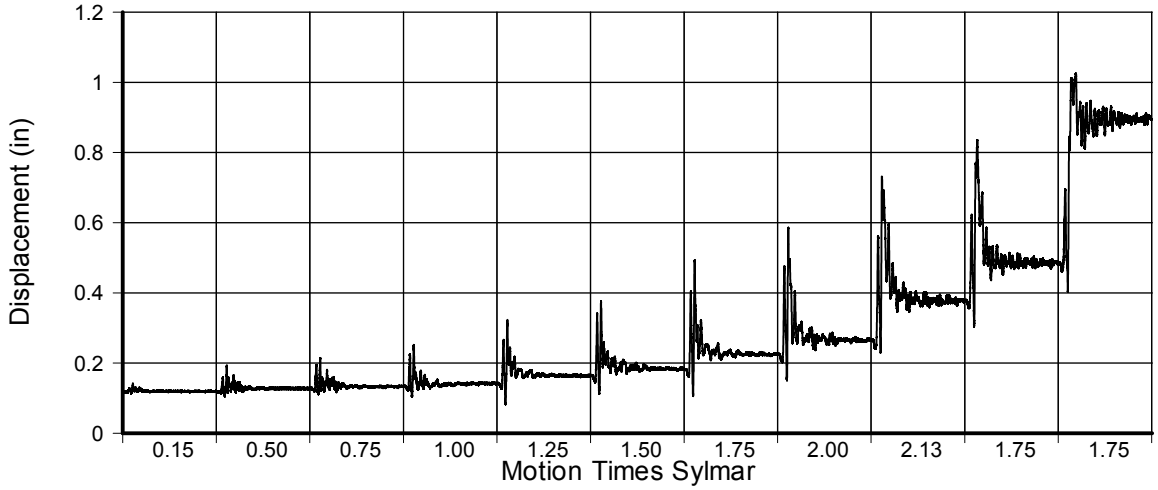

Fig. A-7 - Measured Transverse Disp. for LFCD1

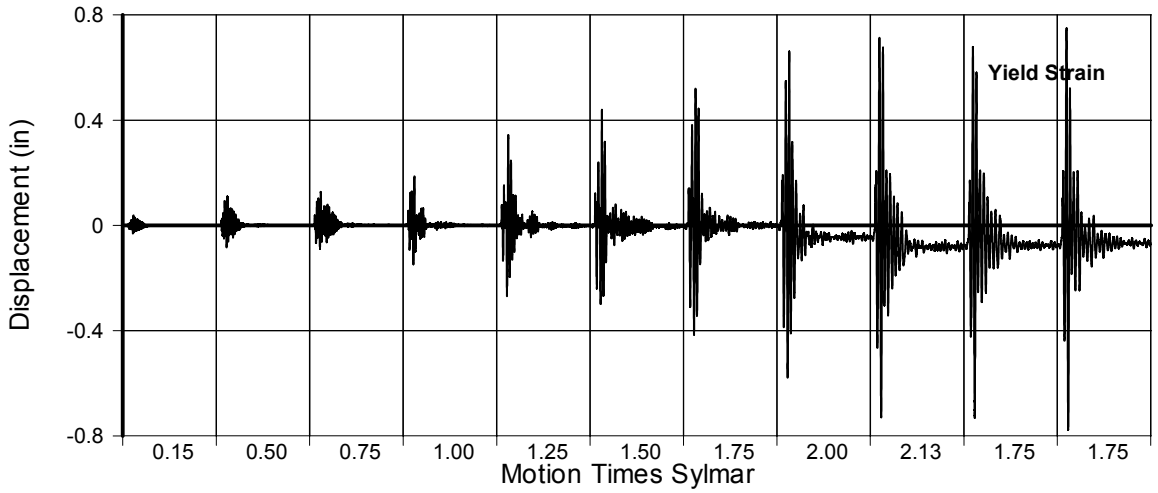

Fig. A-8 - Measured Disp. in Transducer No. 7 for LFCD1

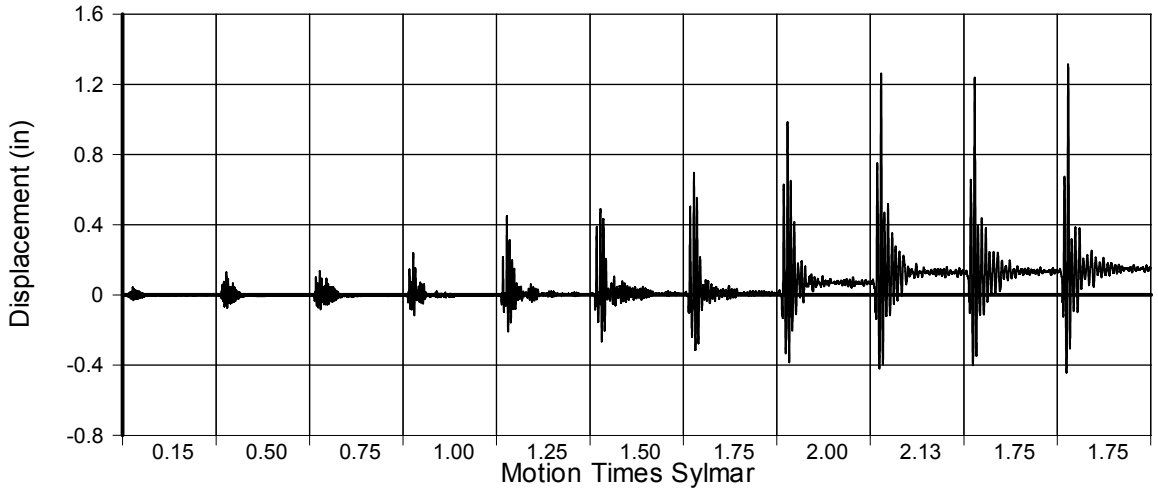

Fig. A-9 - Measured Disp. in Transducer No. 8 for LFCD1

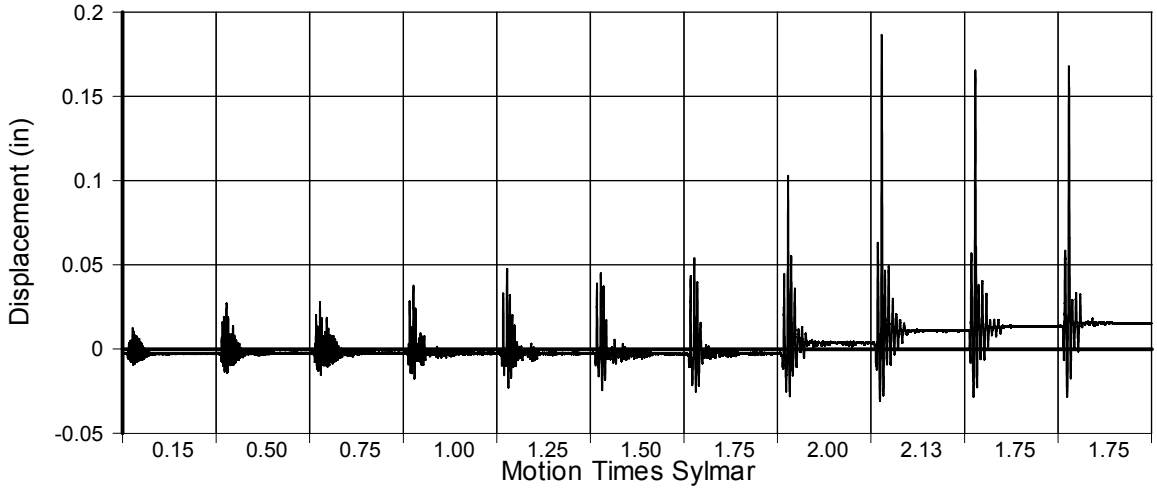

Fig. A-10 - Measured Disp. in Transducer No. 9 for LFCD1

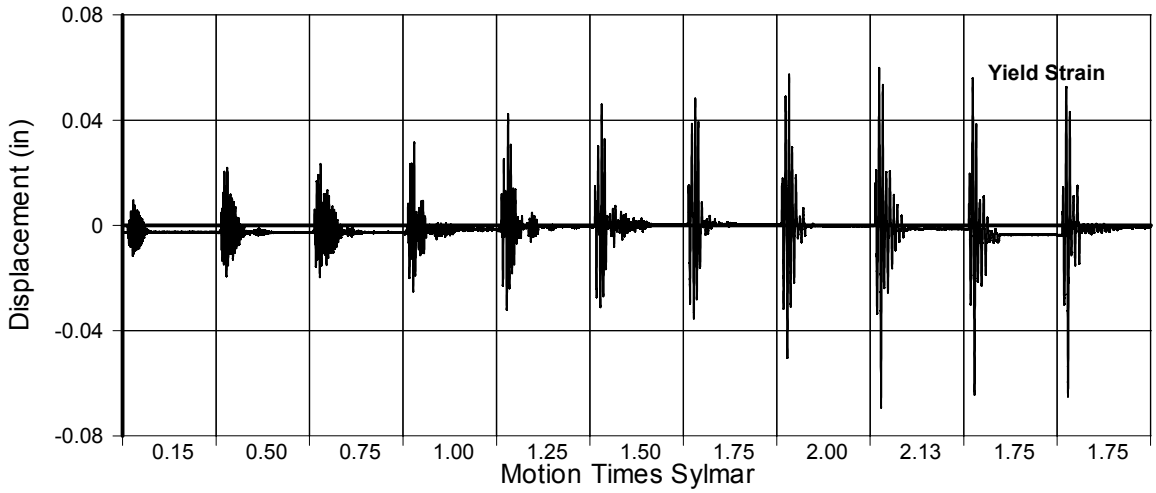

Fig. A-11 - Measured Disp. in Transducer No. 10 for LFCD1

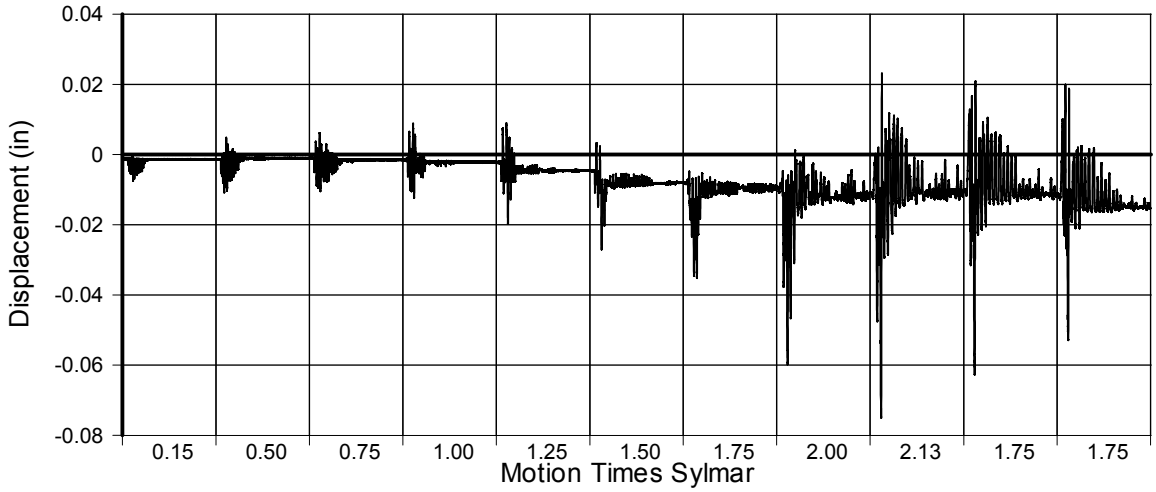

Fig. A-12 - Measured Disp. in Transducer No. 11 for LFCD1

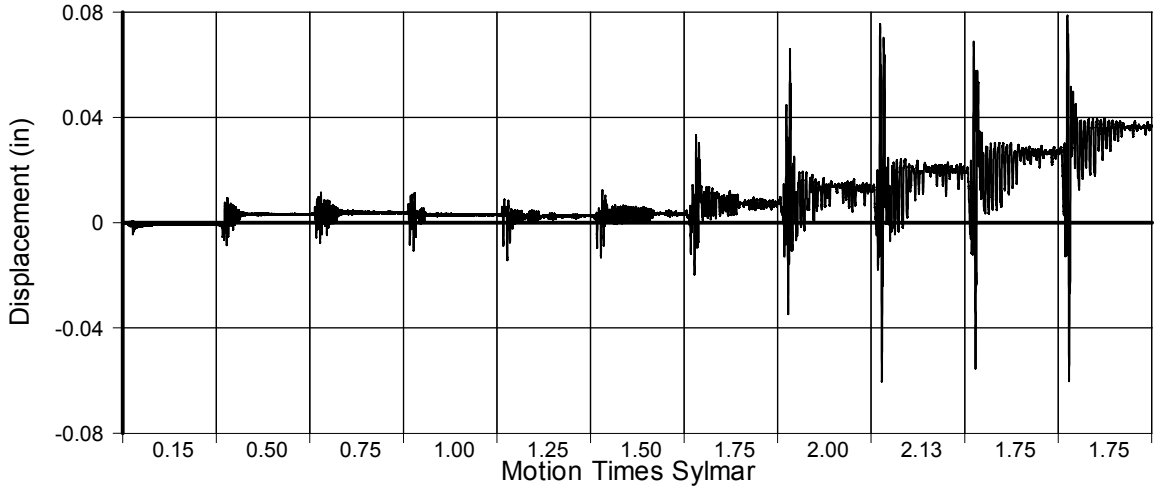

Fig. A-13 - Measured Disp. in Transducer No. 12 for LFCD1

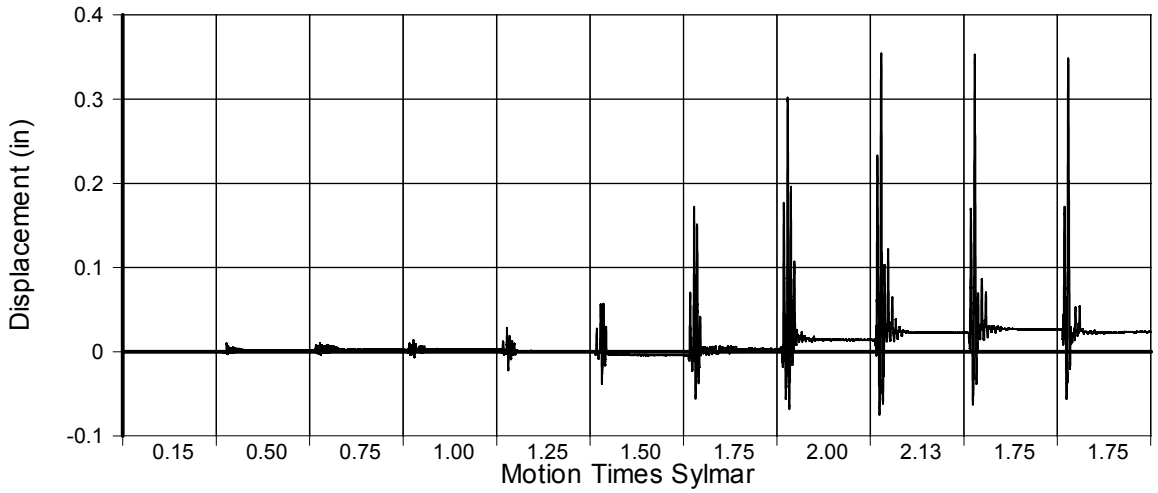

Fig. A-14 - Measured Disp. in Transducer No. 13 for LFCD1

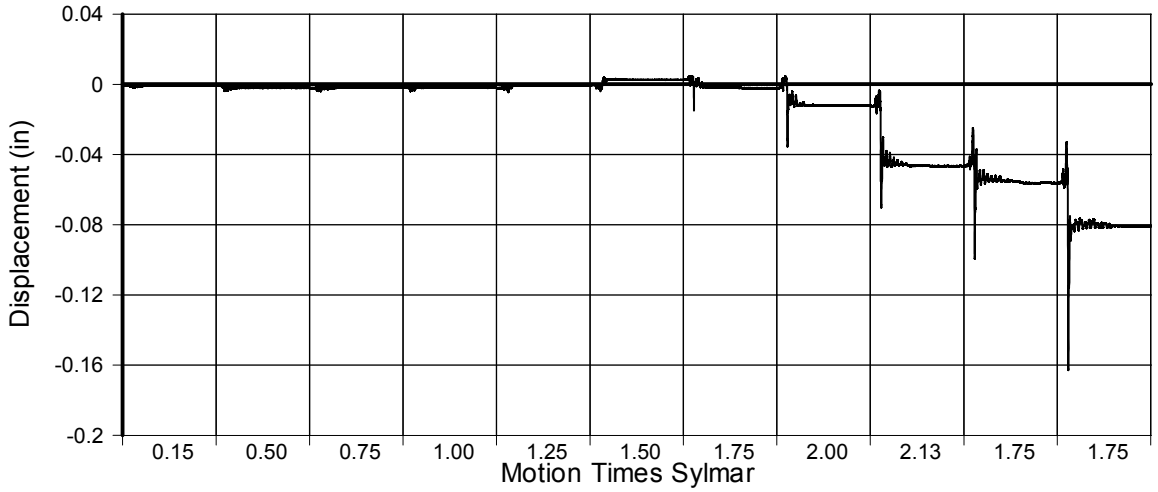

Fig. A-15 - Measured Disp. in Transducer No. 14 for LFCD1

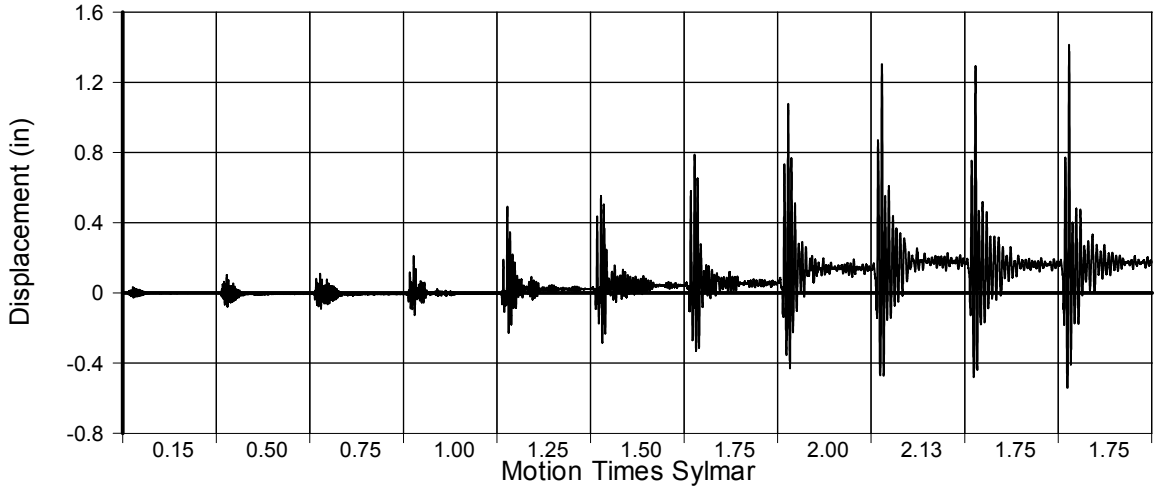

Fig. A-16 - Measured Disp. in Transducer No. 15 for LFCD1

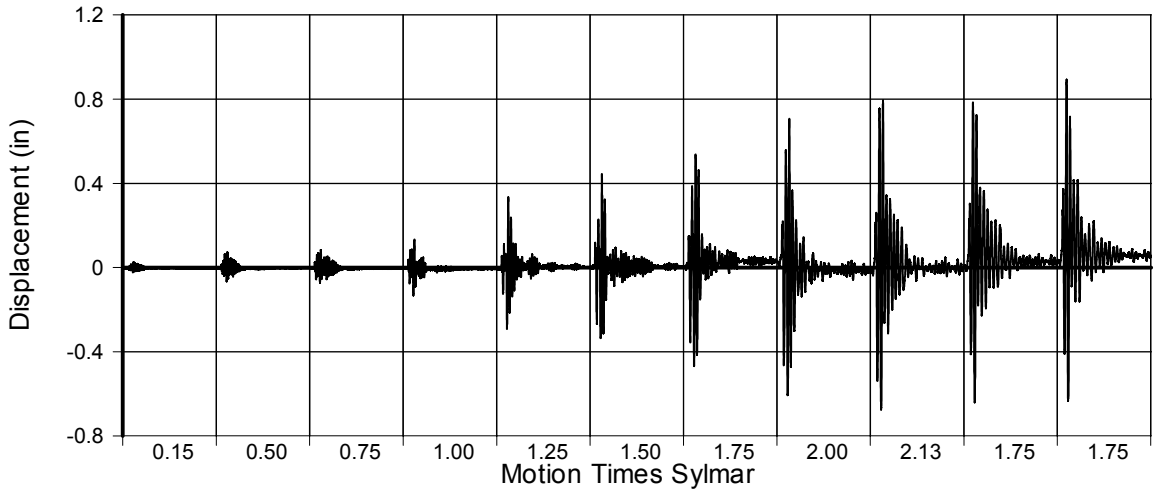

Fig. A-17 - Measured Disp. in Transducer No. 16 for LFCD1

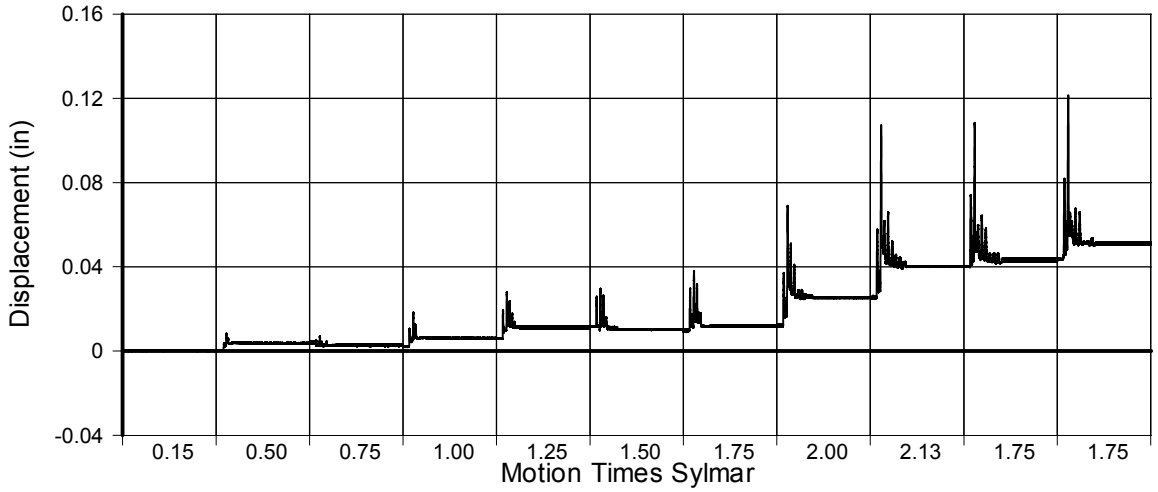

Fig. A-18 - Measured Disp. in Transducer No. 17 for LFCD1

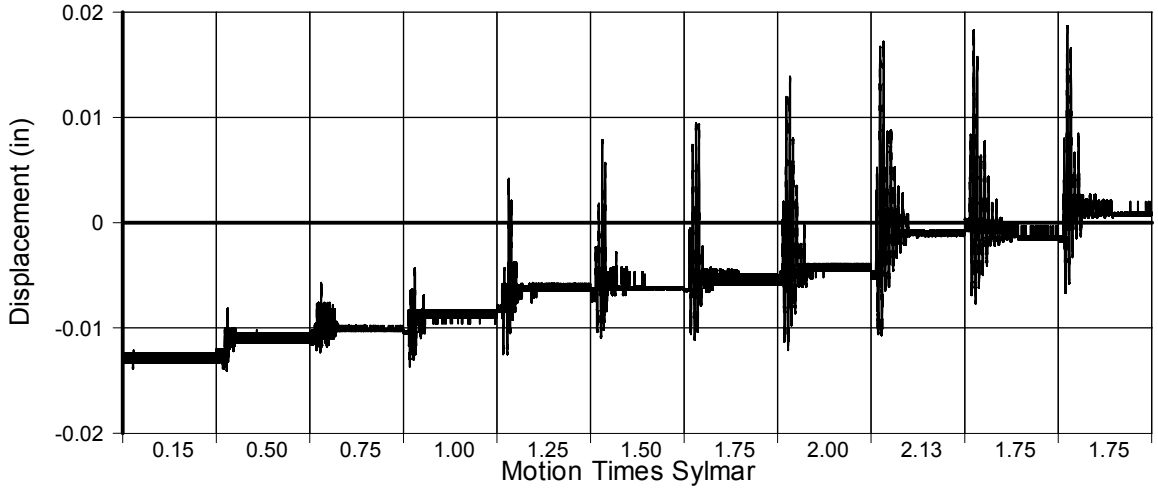

Fig. A-19 - Measured Disp. in Transducer No. 18 for LFCD1

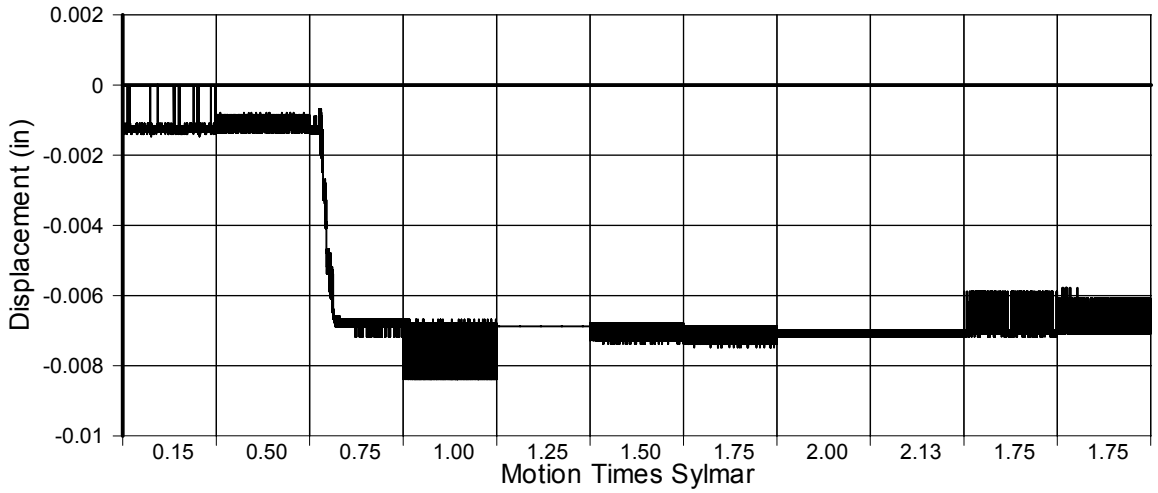

Fig. A-20 - Measured Disp. in Transducer No. 19 for LFCD1

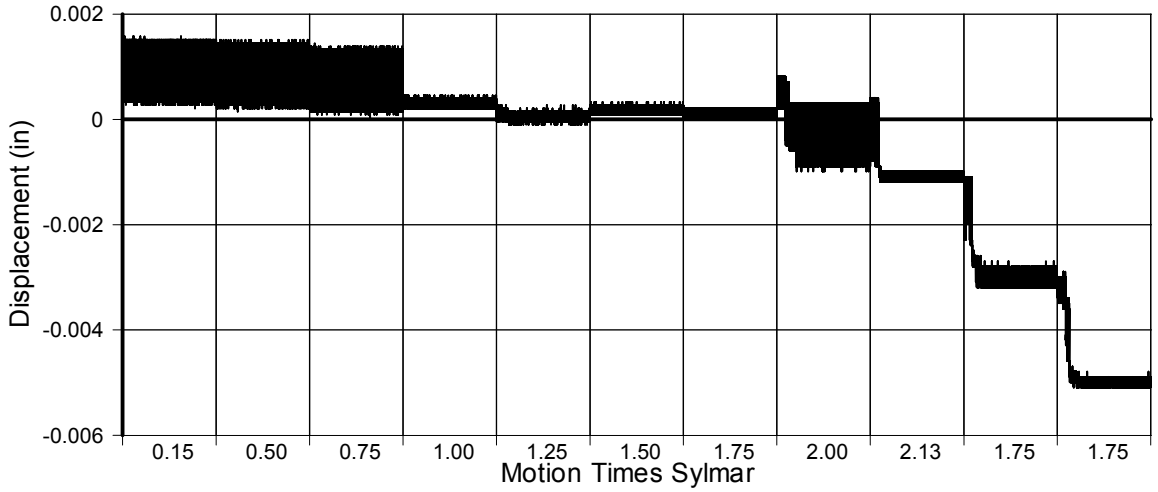

Fig. A-21 - Measured Disp. in Transducer No. 20 for LFCD1

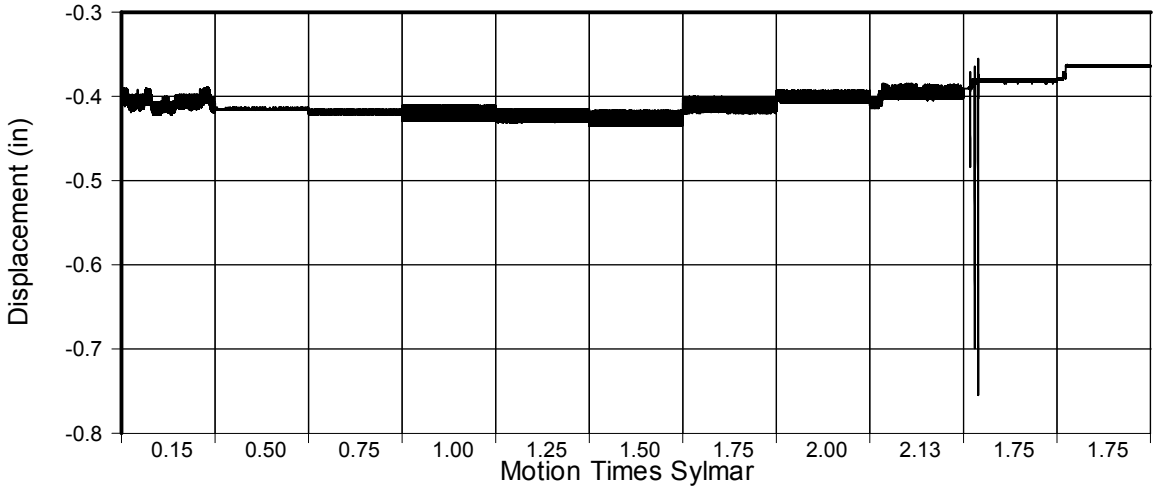

Fig. A-22 - Measured Disp. in Transducer No. 21 for LFCD1

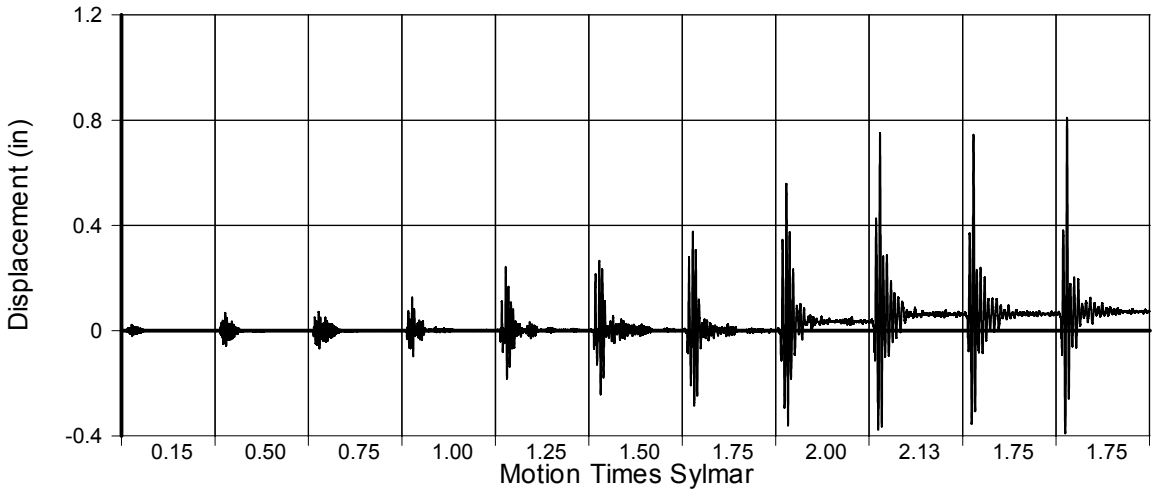

Fig. A-23 - Measured Disp. in Transducer No. 22 for LFCD1

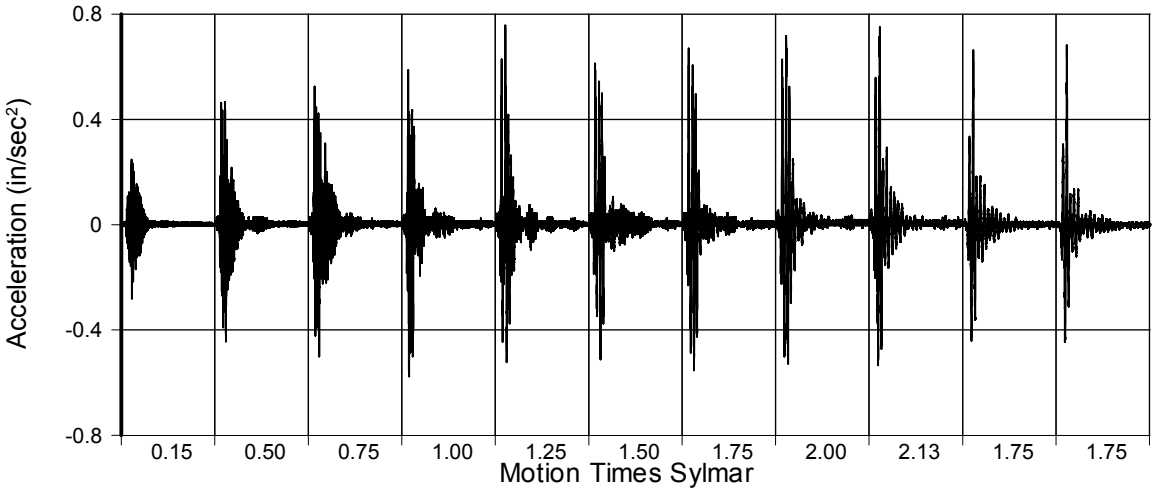

Fig. A-24 - Measured Beam Acceleration for LFCD1

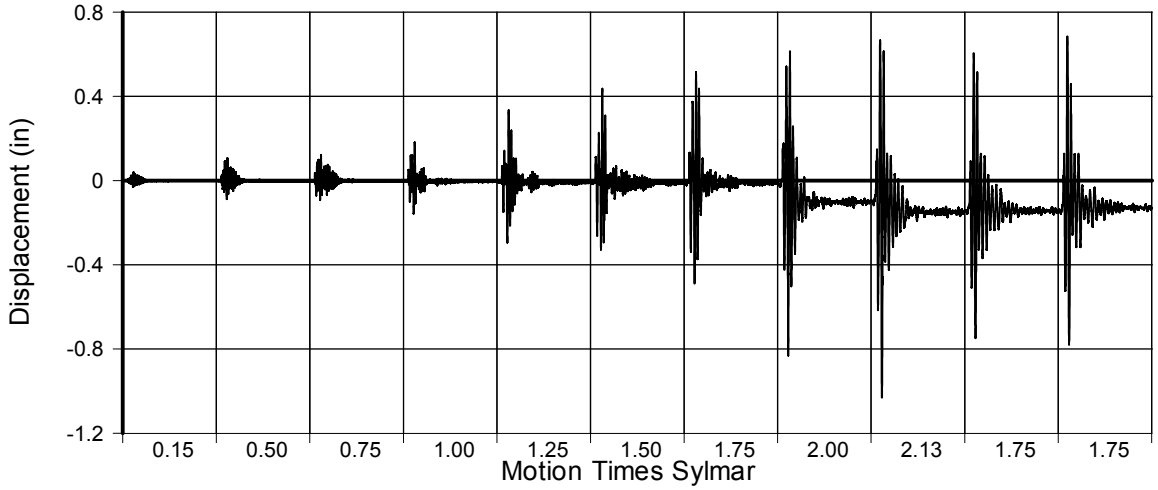

Fig. A-25 - Measured Disp. in Transducer No. 24 for LFCD1

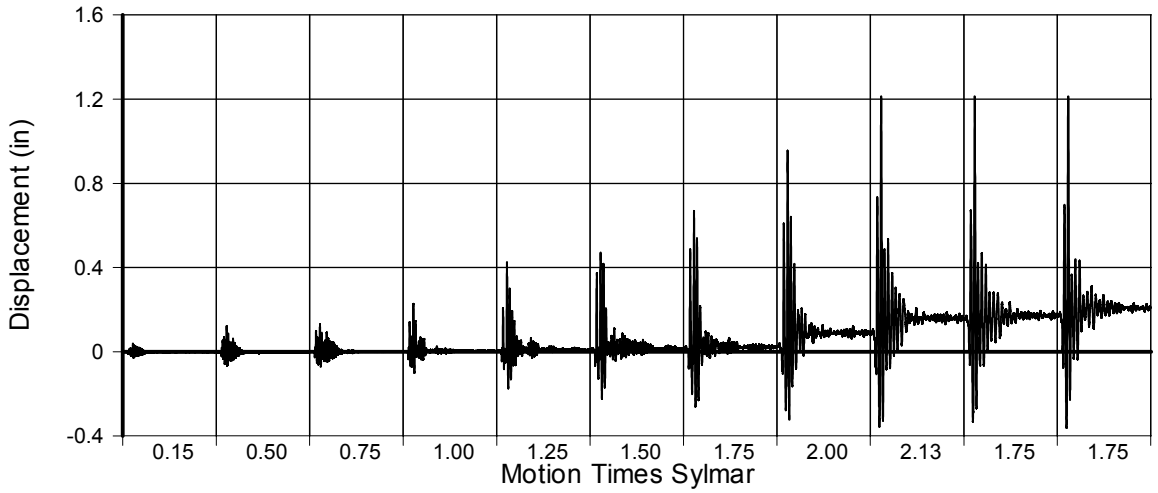

Fig. A-26 - Measured Disp. in Transducer No. 25 for LFCD1

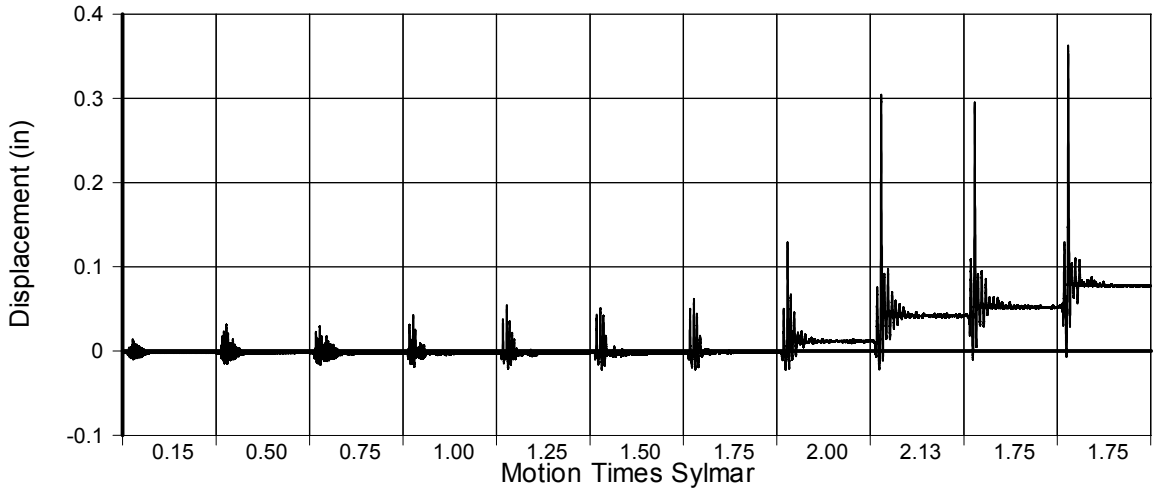

Fig. A-27 - Measured Disp. in Transducer No. 26 for LFCD1

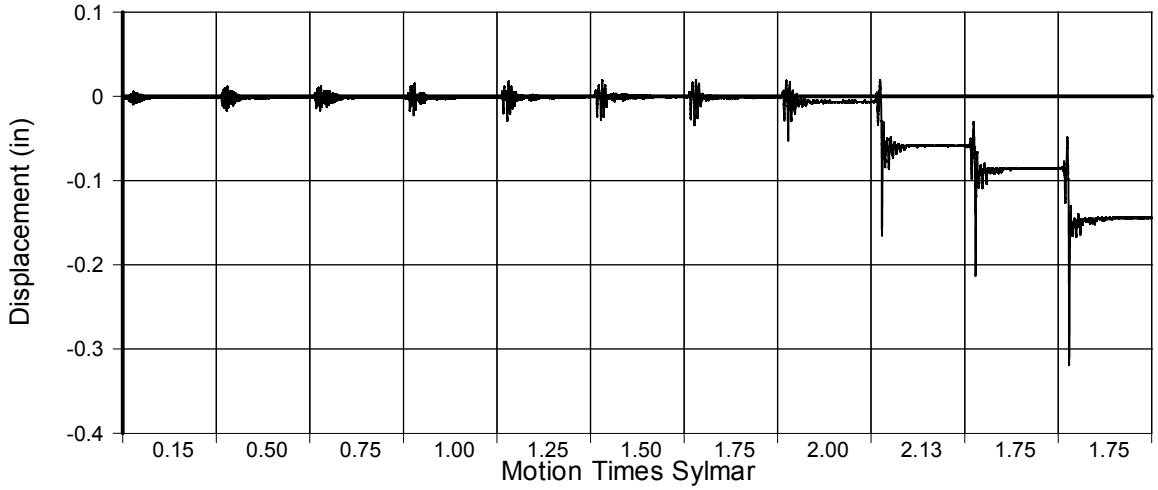

Fig. A-28 - Measured Disp. in Transducer No. 27 for LFCD1

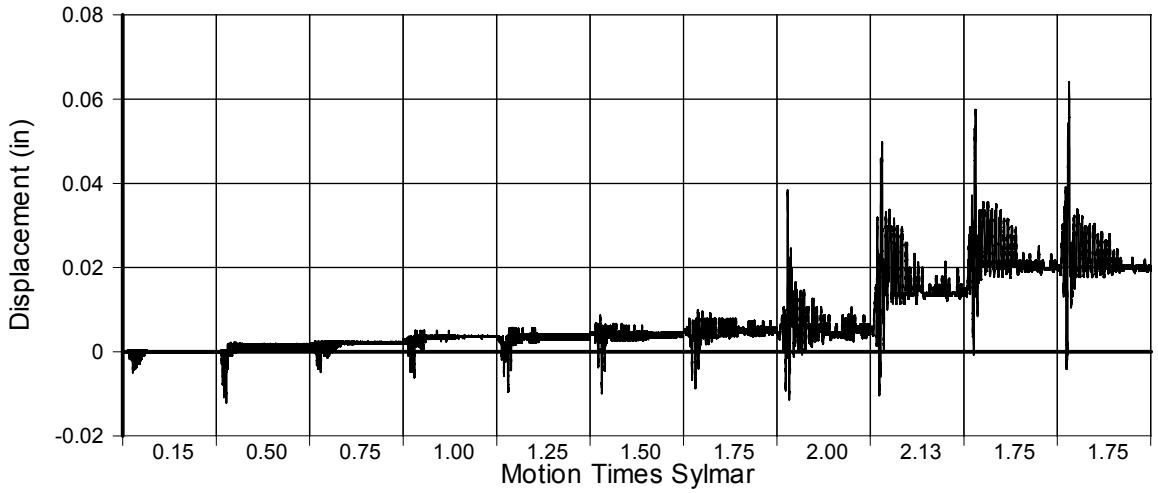

Fig. A-29 - Measured Disp. in Transducer No. 28 for LFCD1

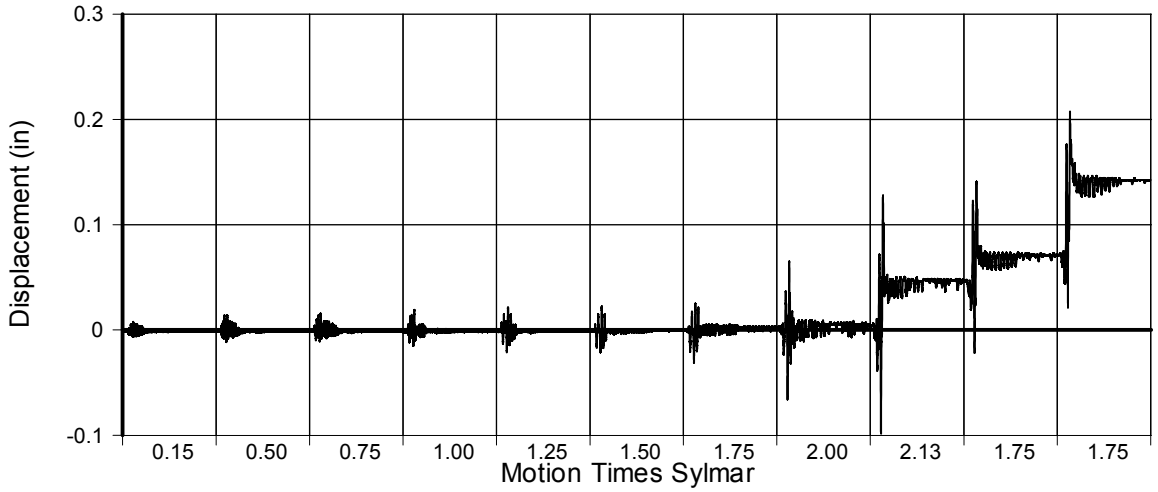

Fig. A-30 - Measured Disp. in Transducer No. 29 for LFCD1

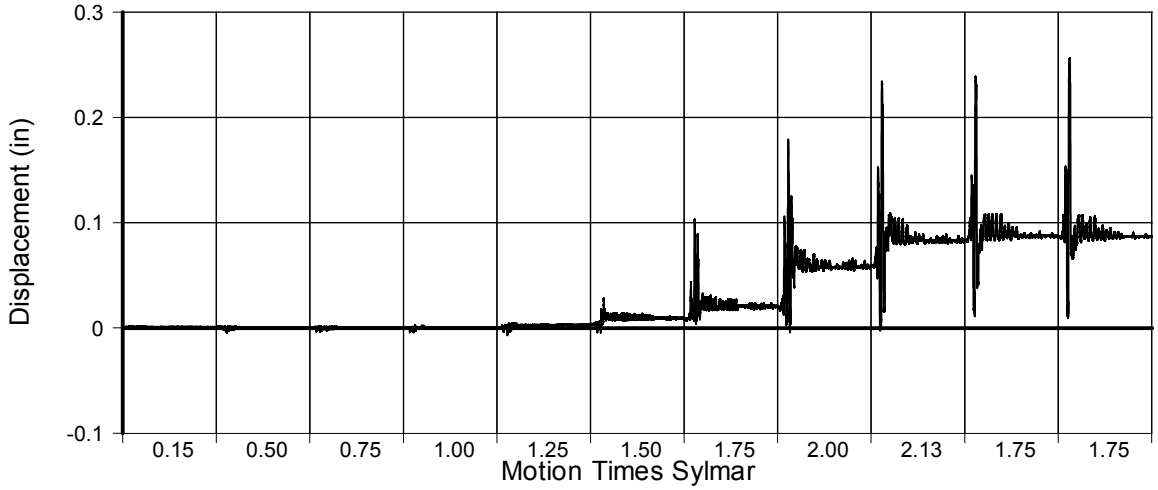

Fig. A-31 - Measured Disp. in Transducer No. 30 for LFCD1

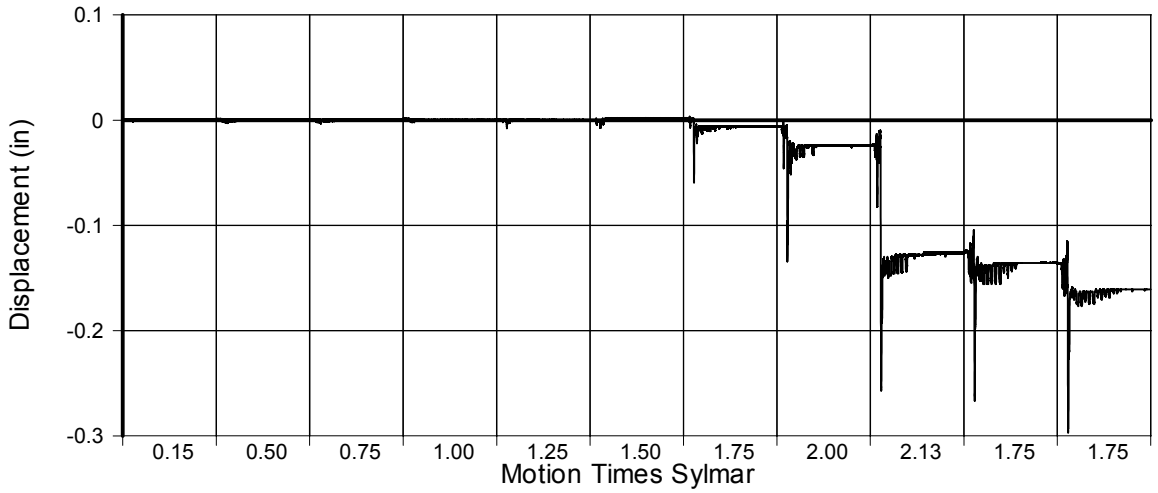

Fig. A-32 - Measured Disp. in Transducer No. 31 for LFCD1

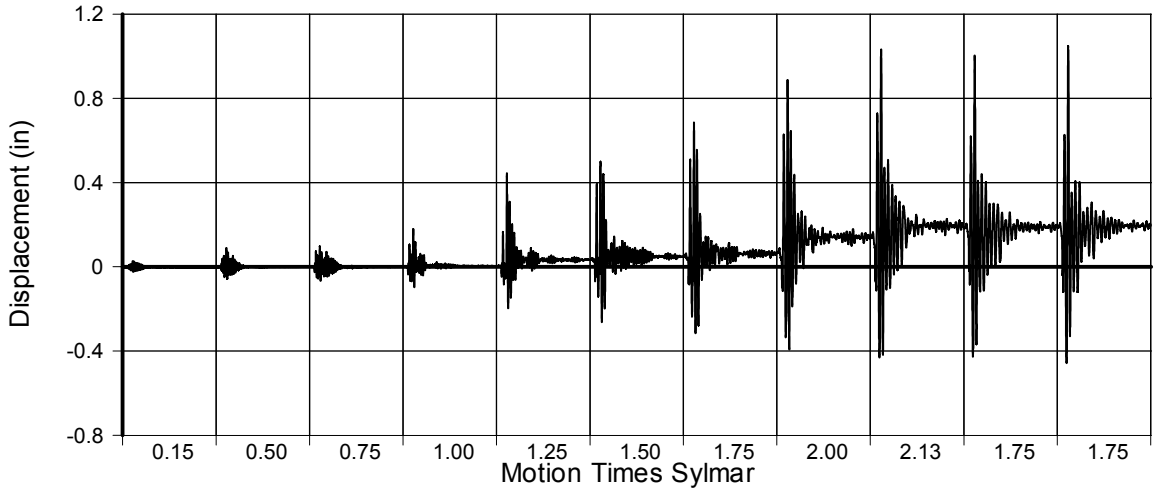

Fig. A-33 - Measured Disp. in Transducer No. 32 for LFCD1

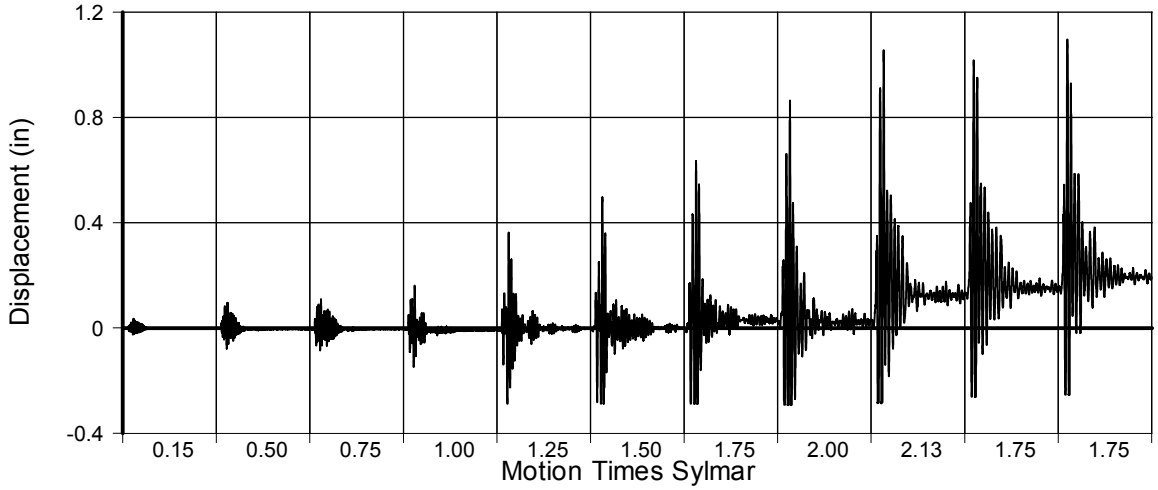

Fig. A-34 - Measured Disp. in Transducer No. 33 for LFCD1

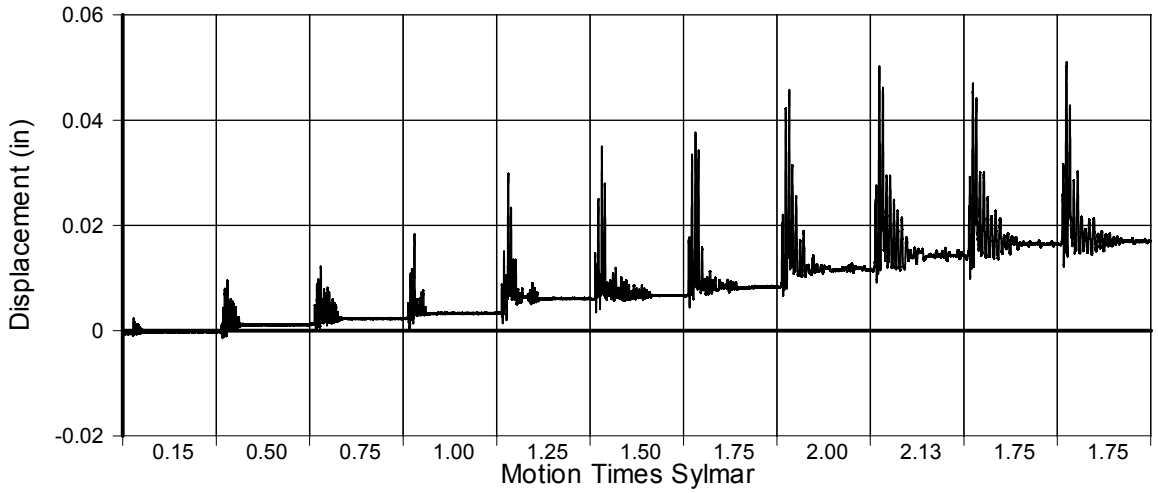

Fig. A-35 - Measured Disp. in Transducer No. 34 for LFCD1

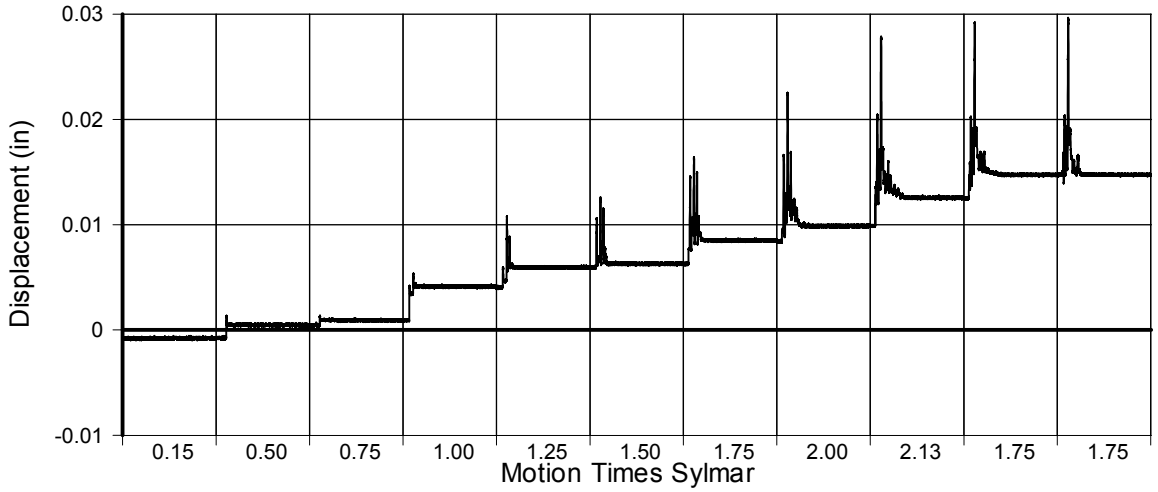

Fig. A-36 - Measured Disp. in Transducer No. 35 for LFCD1

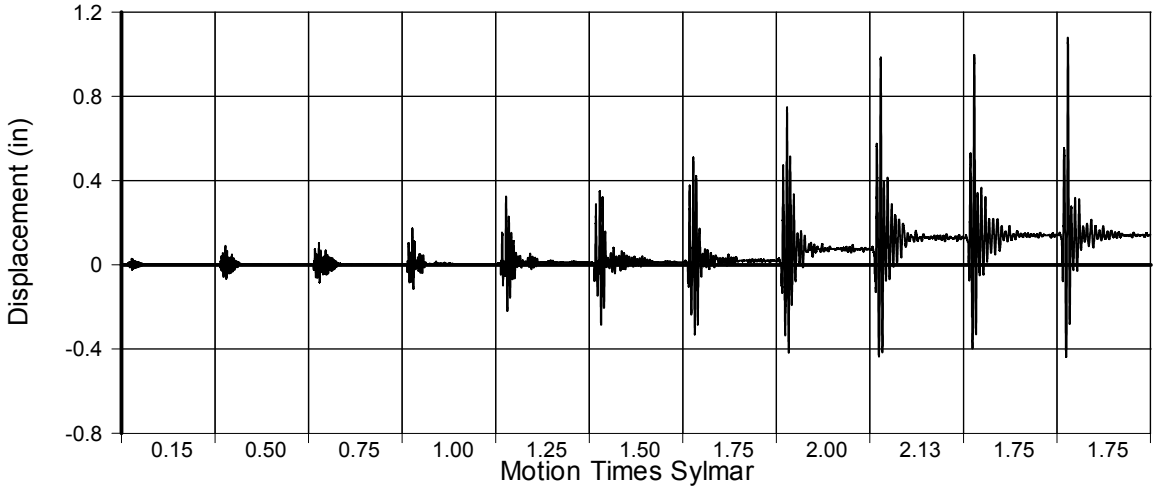

Fig. A-40 - Measured Disp. in Transducer No. 39 for LFCD1

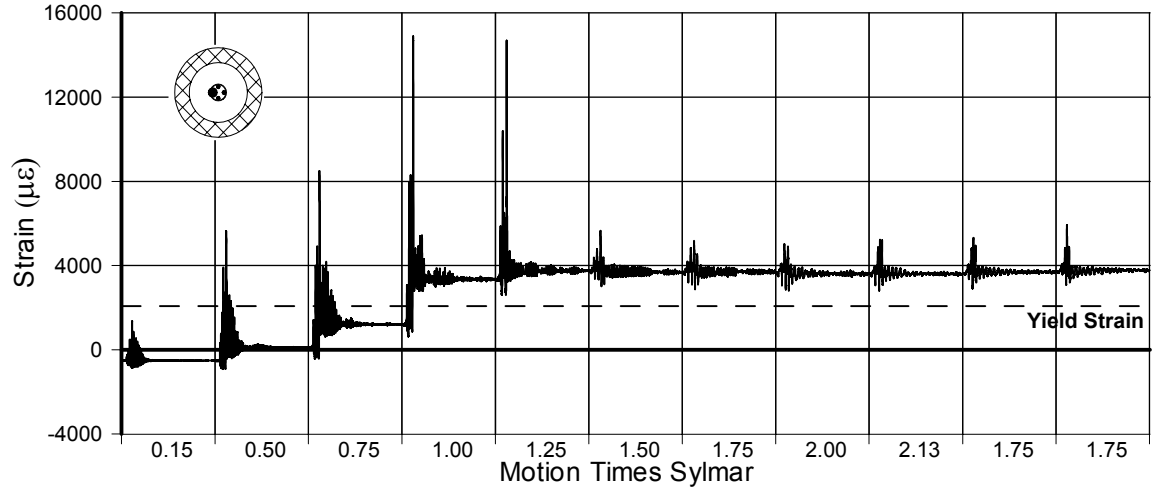

Fig. A-41 - Measured Strain in Gauge No. 40 for LFCD1

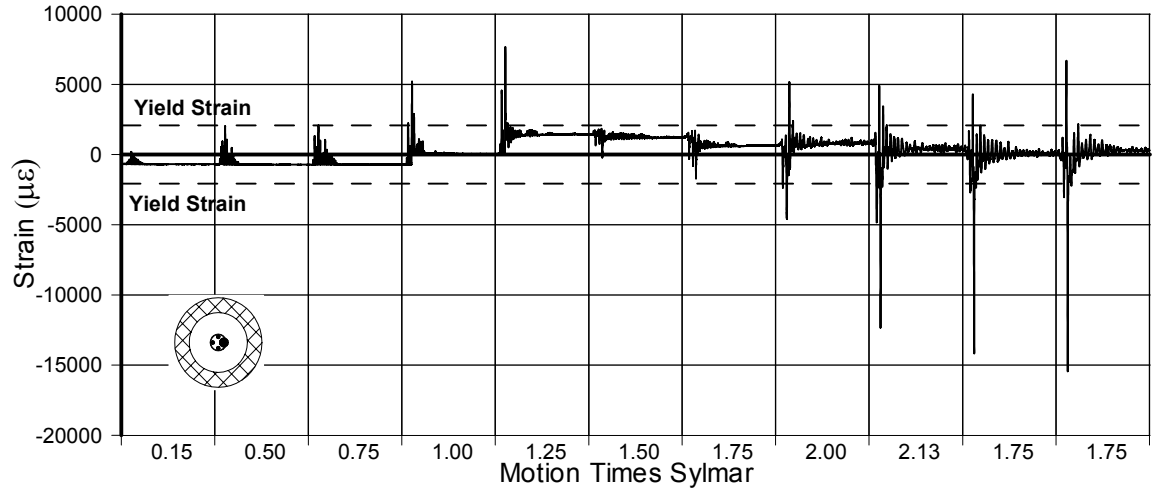

Fig. A-42 - Measured Strain in Gauge No. 41 for LFCD1

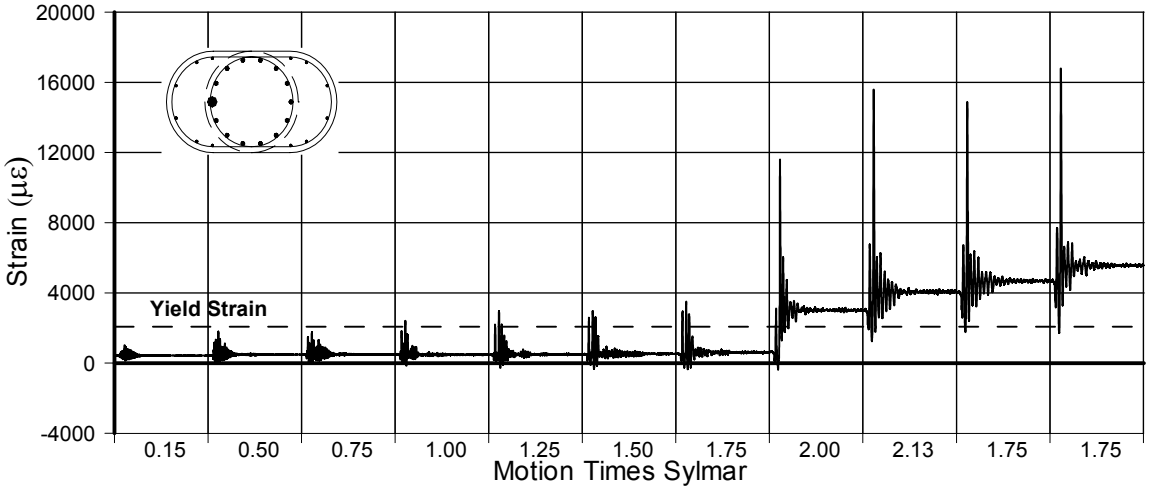

Fig. A-43 - Measured Strain in Gauge No. 43 for LFCD1

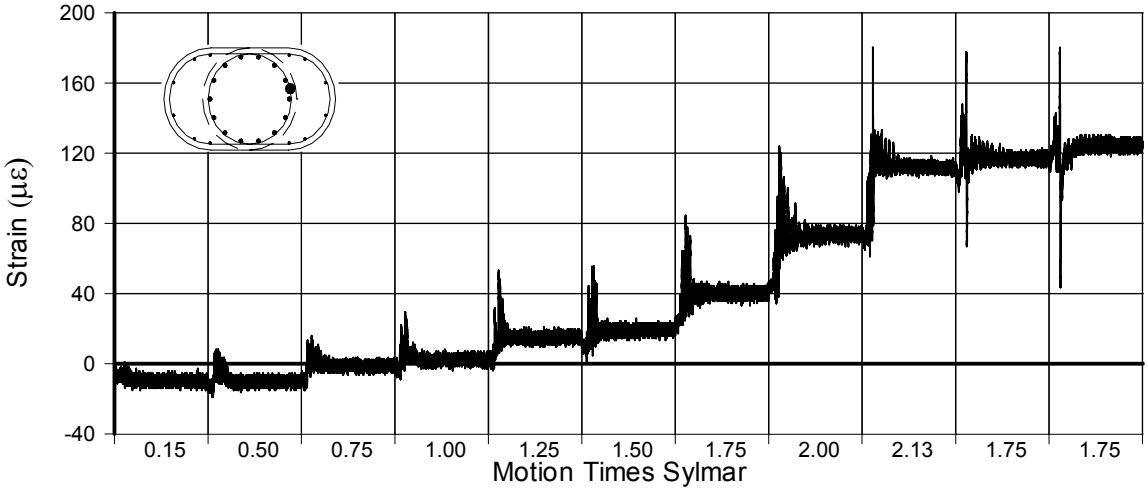

Fig. A-44 - Measured Strain in Gauge No. 48 for LFCD1

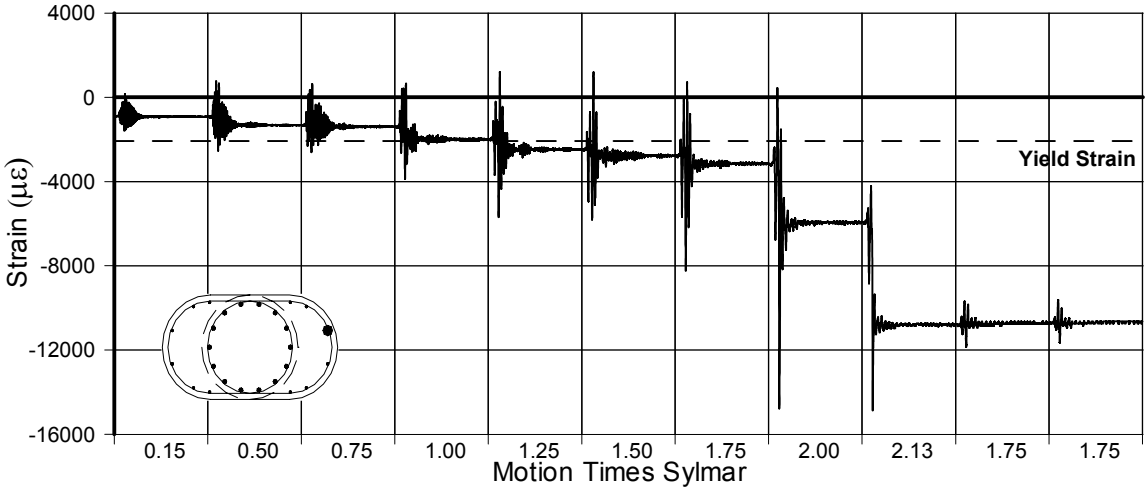

Fig. A-45 - Measured Strain in Gauge No. 49 for LFCD1

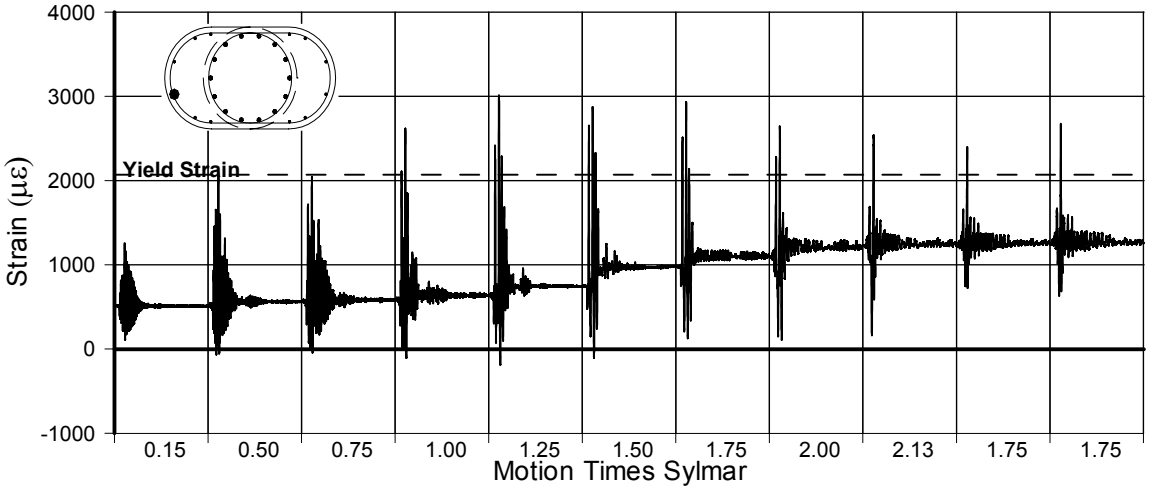

Fig. A-46 - Measured Strain in Gauge No. 51 for LFCD1

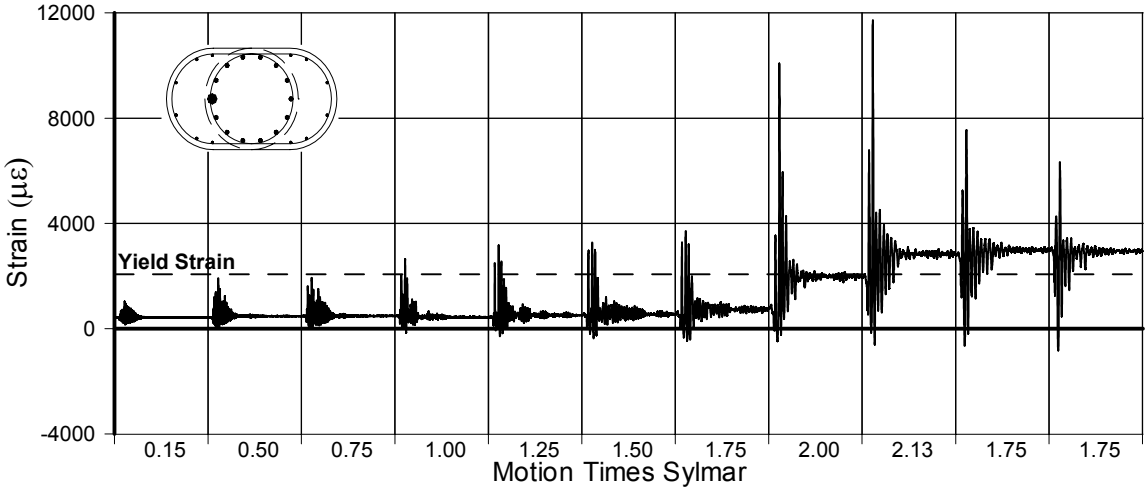

Fig. A-47 - Measured Strain in Gauge No. 52 for LFCD1

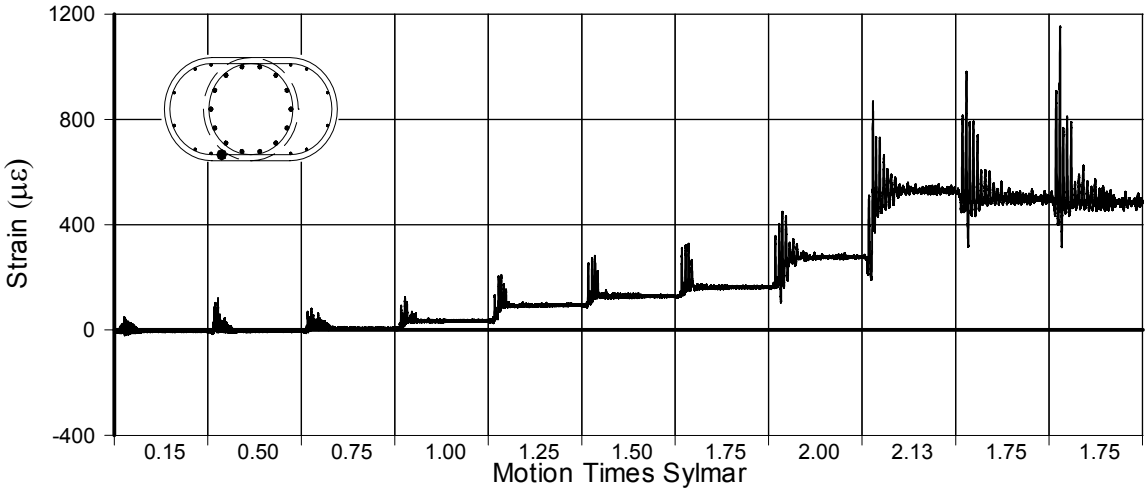

Fig. A-48 - Measured Strain in Gauge No. 53 for LFCD1

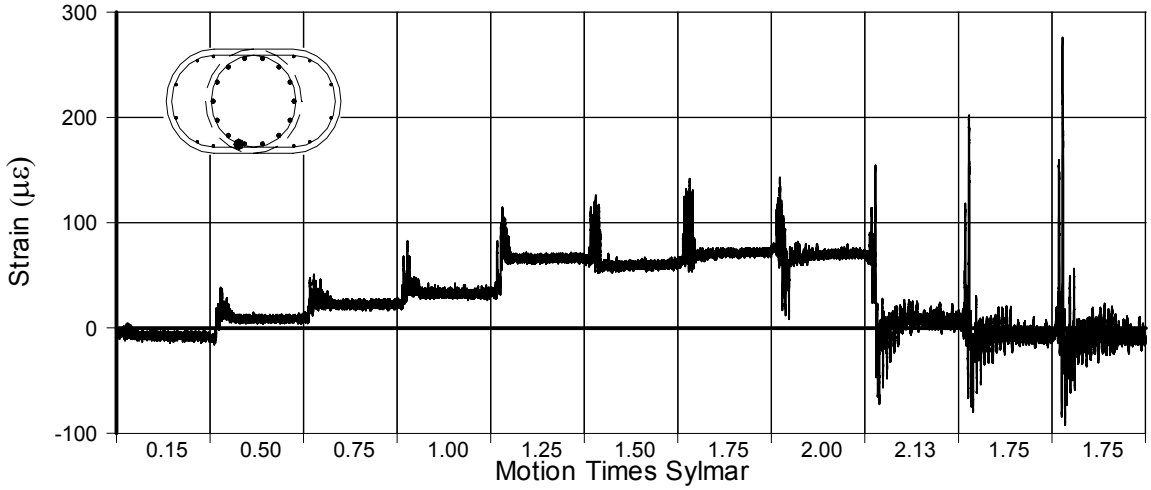

Fig. A-49 - Measured Strain in Gauge No. 54 for LFCD1

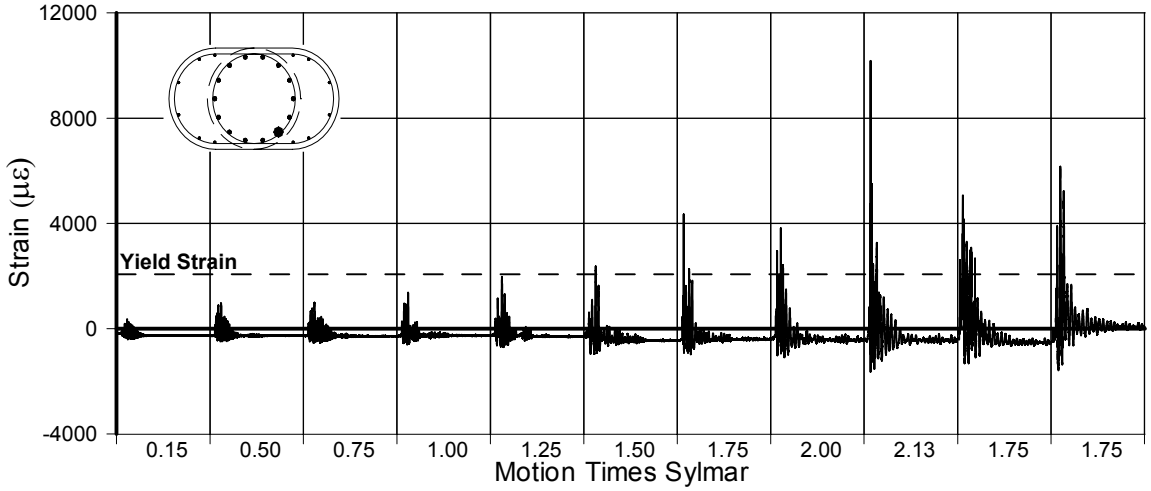

Fig. A-50 - Measured Strain in Gauge No. 55 for LFCD1

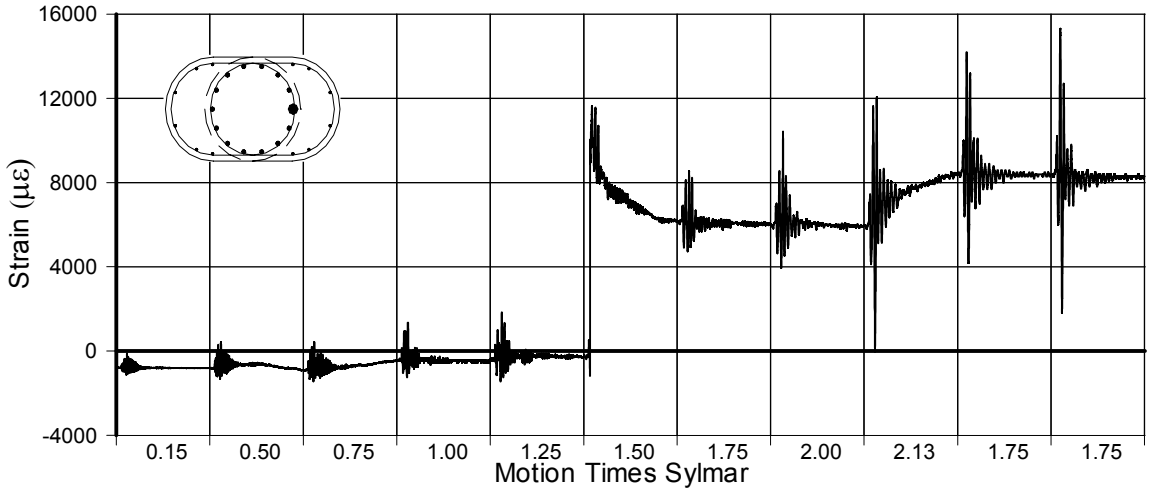

Fig. A-51 - Measured Strain in Gauge No. 56 for LFCD1

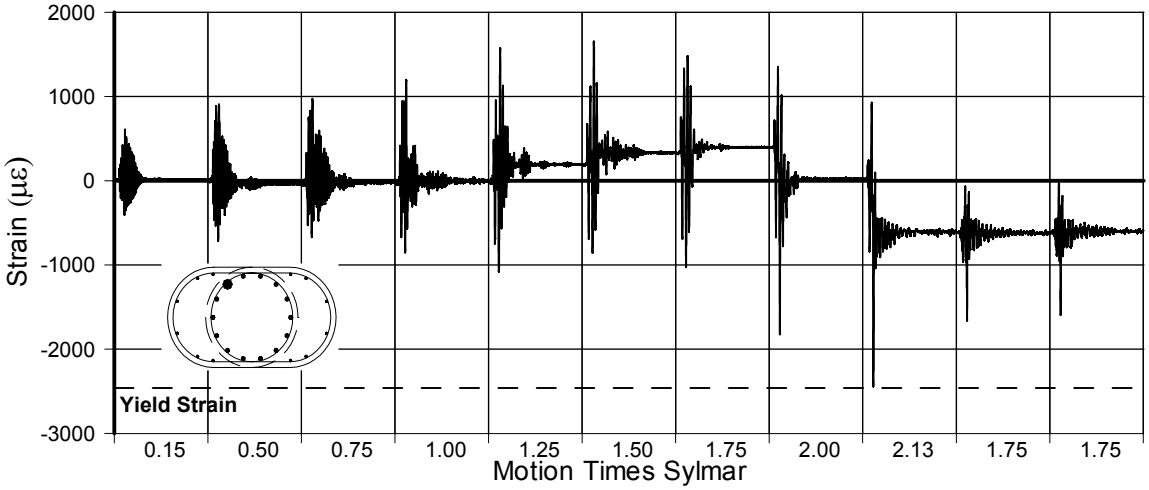

Fig. A-52 - Measured Strain in Gauge No. 57 for LFCD1

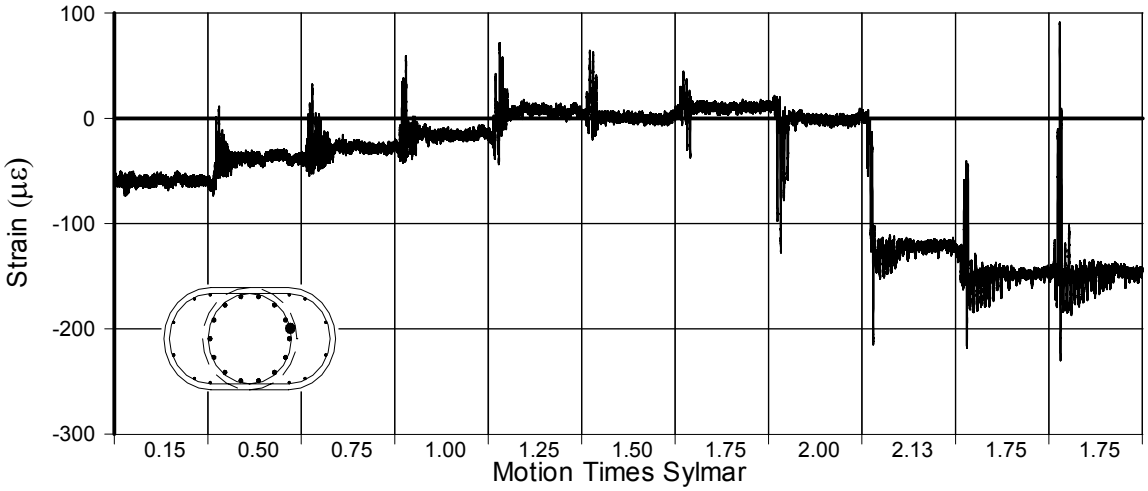

Fig. A-53 - Measured Strain in Gauge No. 58 for LFCD1

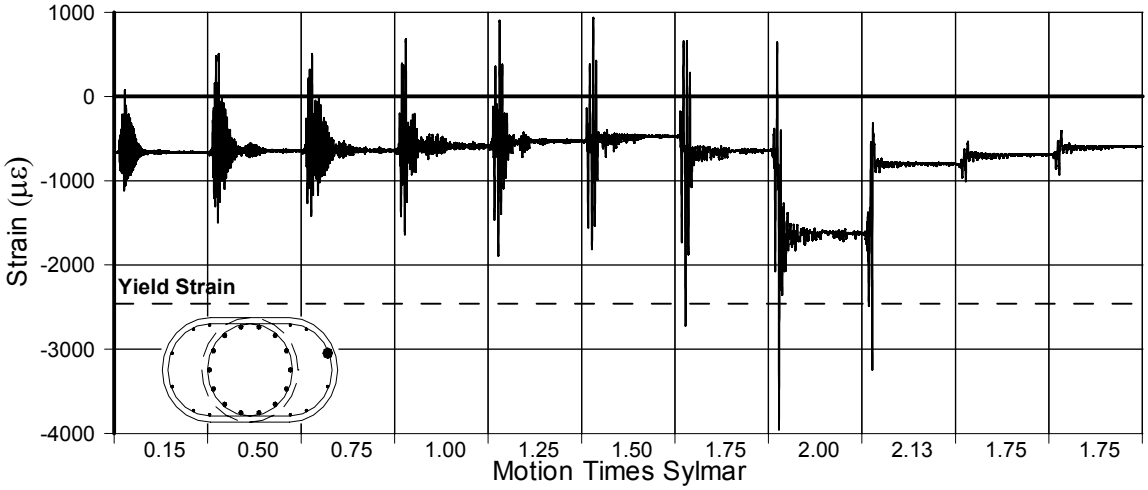

Fig. A-54 - Measured Strain in Gauge No. 59 for LFCD1

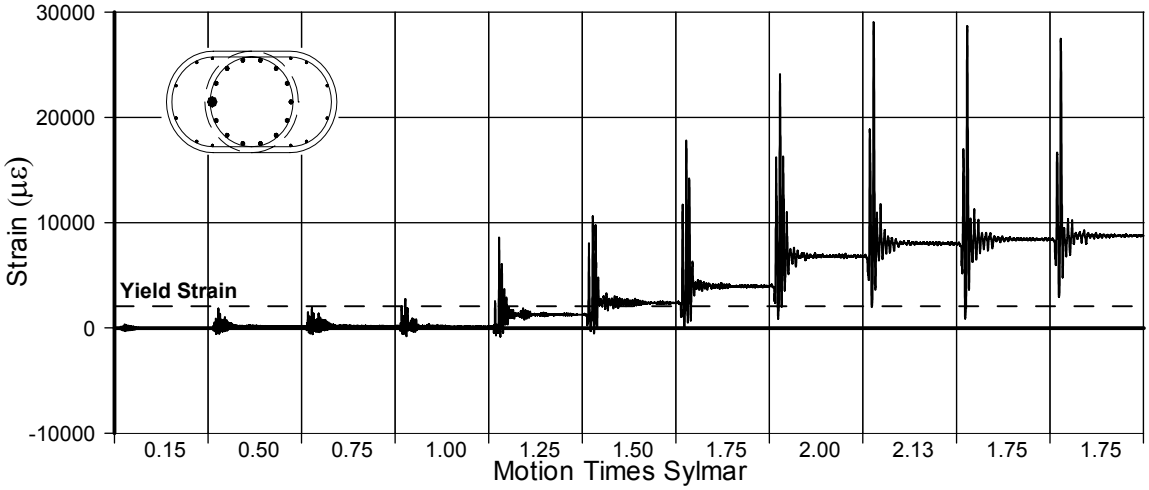

Fig. A-55 - Measured Strain in Gauge No. 62 for LFCD1

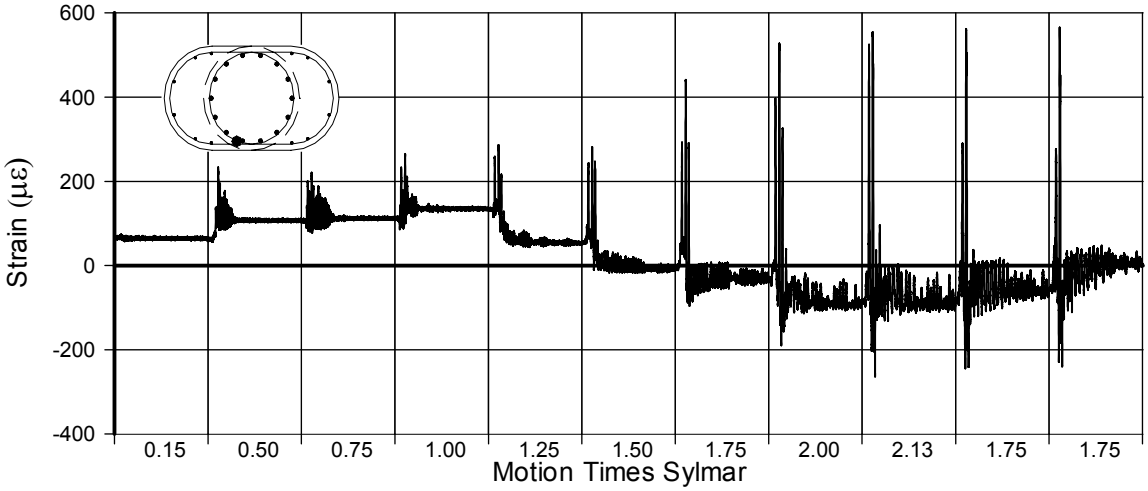

Fig. A-56 - Measured Strain in Gauge No. 64 for LFCD1

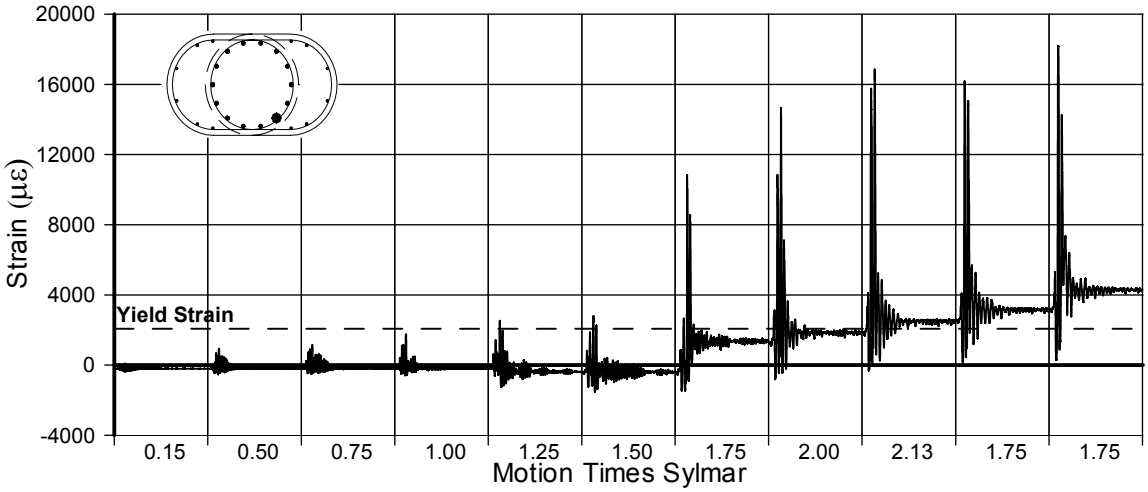

Fig. A-57 - Measured Strain in Gauge No. 65 for LFCD1

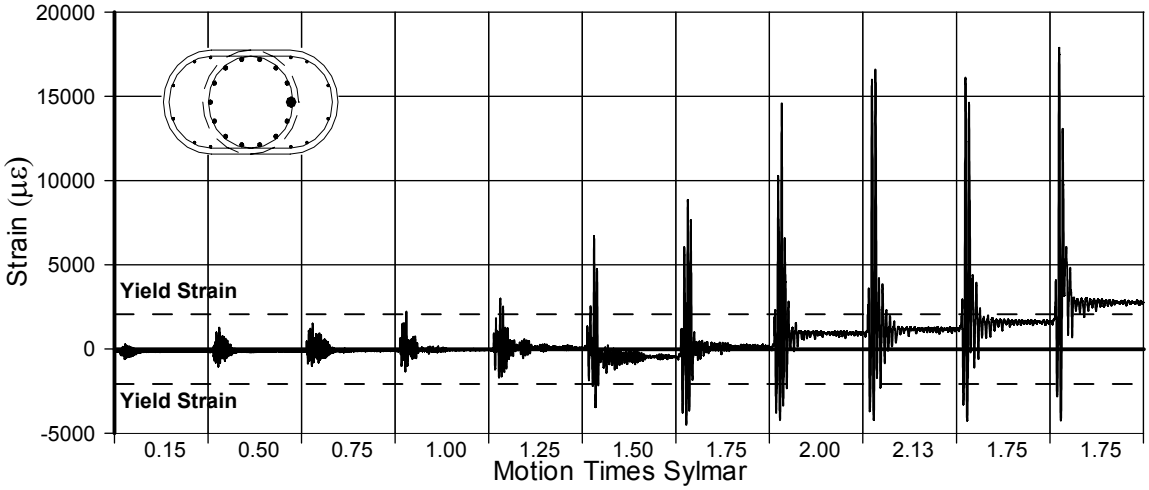

Fig. A-58 - Measured Strain in Gauge No. 66 for LFCD1

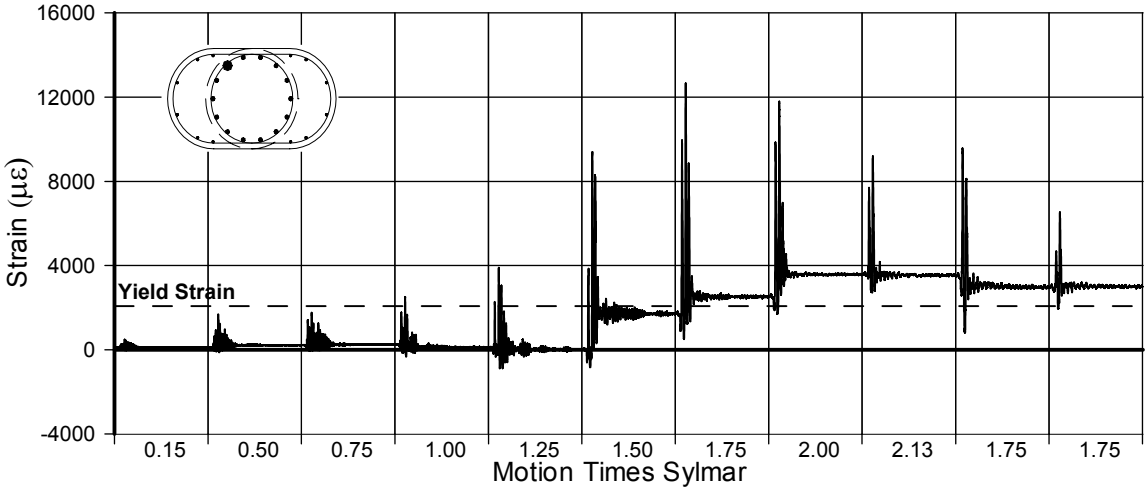

Fig. A-59 - Measured Strain in Gauge No. 67 for LFCD1

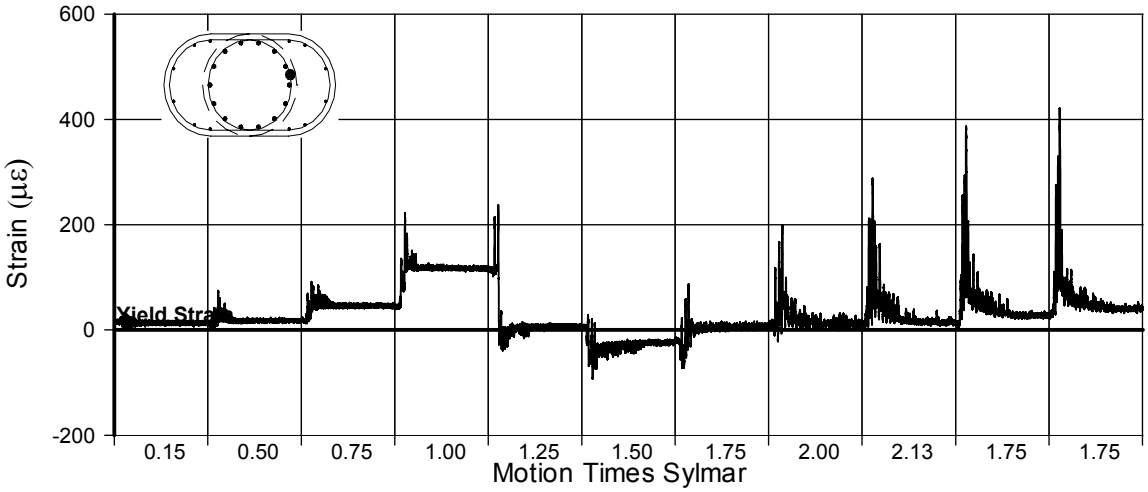

Fig. A-60 - Measured Strain in Gauge No. 68 for LFCD1

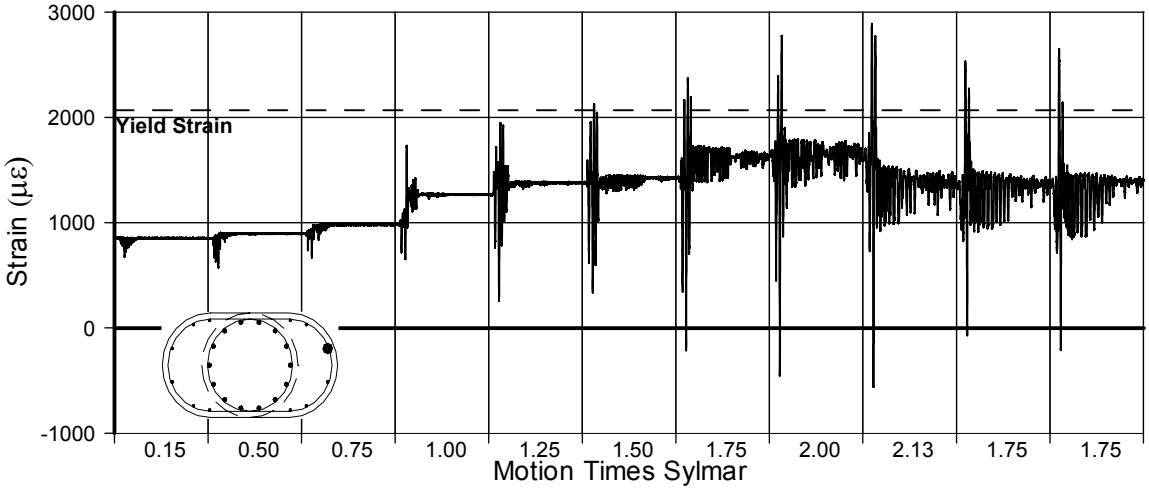

Fig. A-61 - Measured Strain in Gauge No. 69 for LFCD1

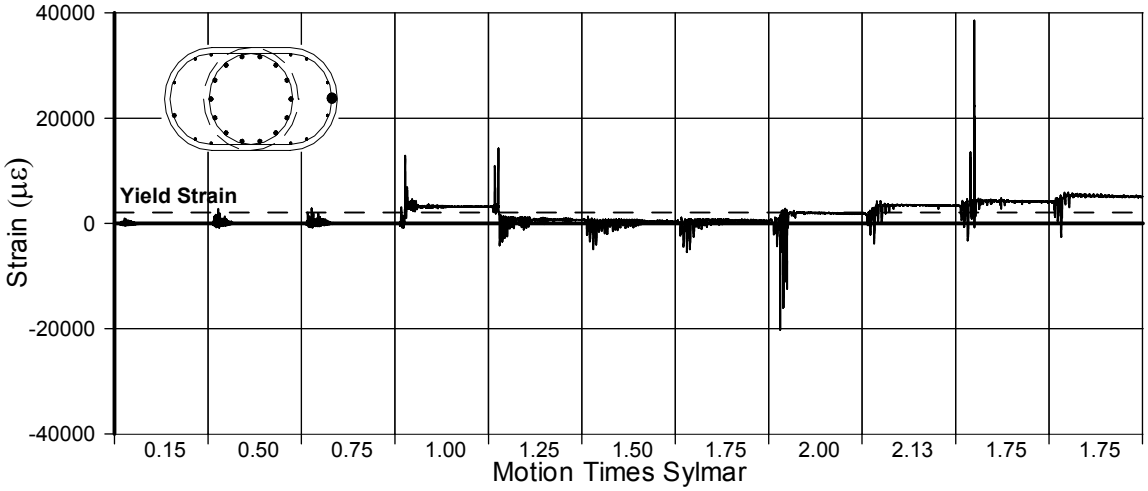

Fig. A-62 - Measured Strain in Gauge No. 71 for LFCD1

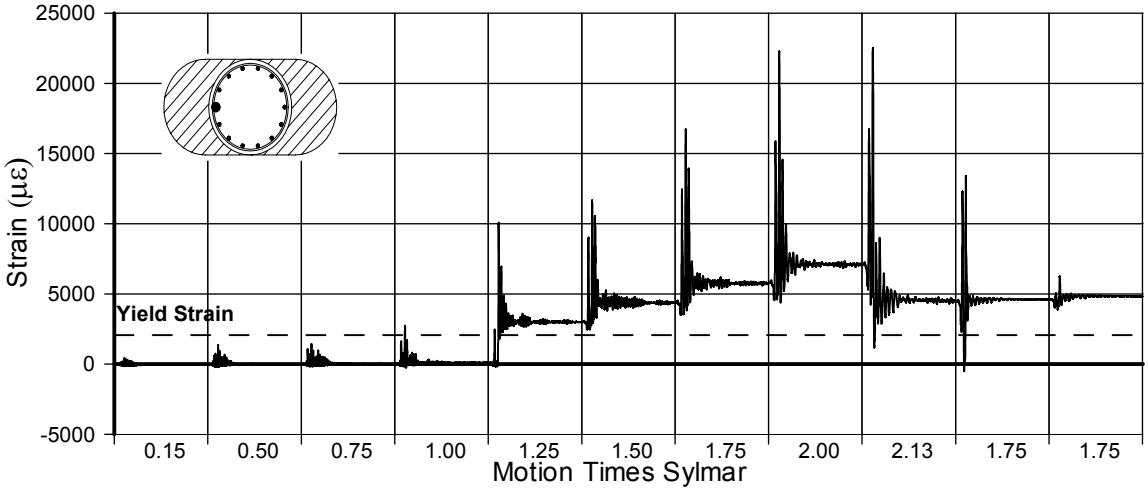

Fig. A-63 - Measured Strain in Gauge No. 72 for LFCD1

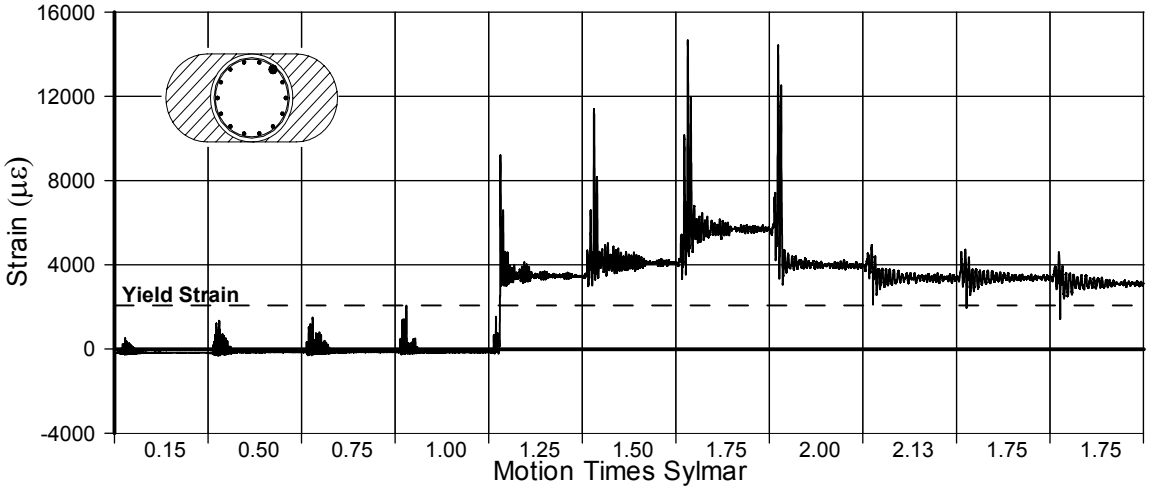

Fig. A-64 - Measured Strain in Gauge No. 74 for LFCD1

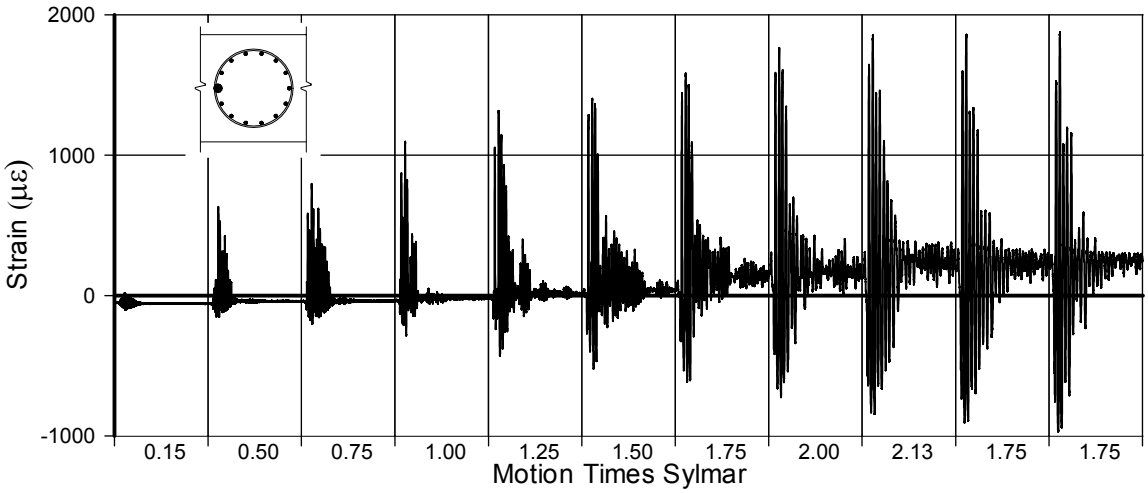

Fig. A-65 - Measured Strain in Gauge No. 75 for LFCD1

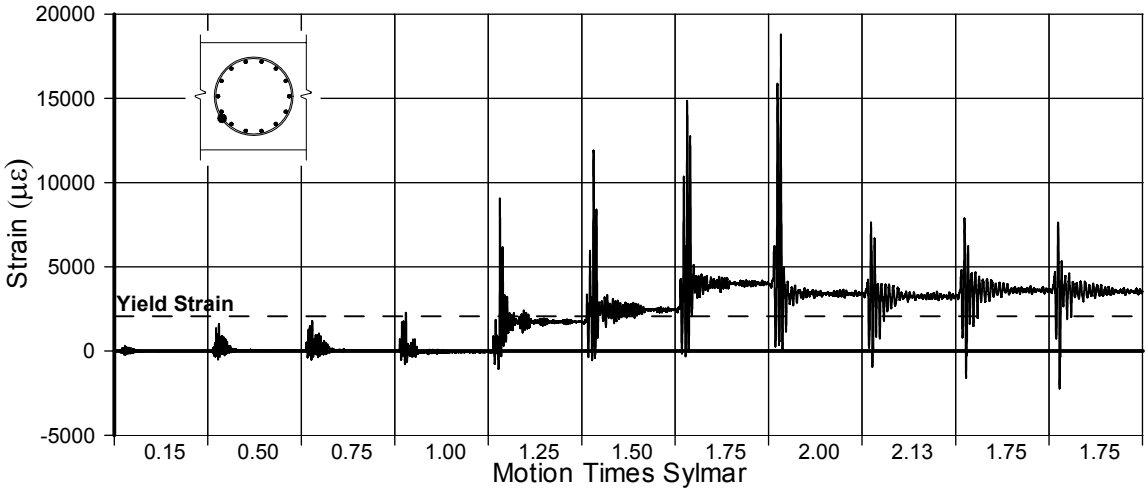

Fig. A-66 - Measured Strain in Gauge No. 76 for LFCD1

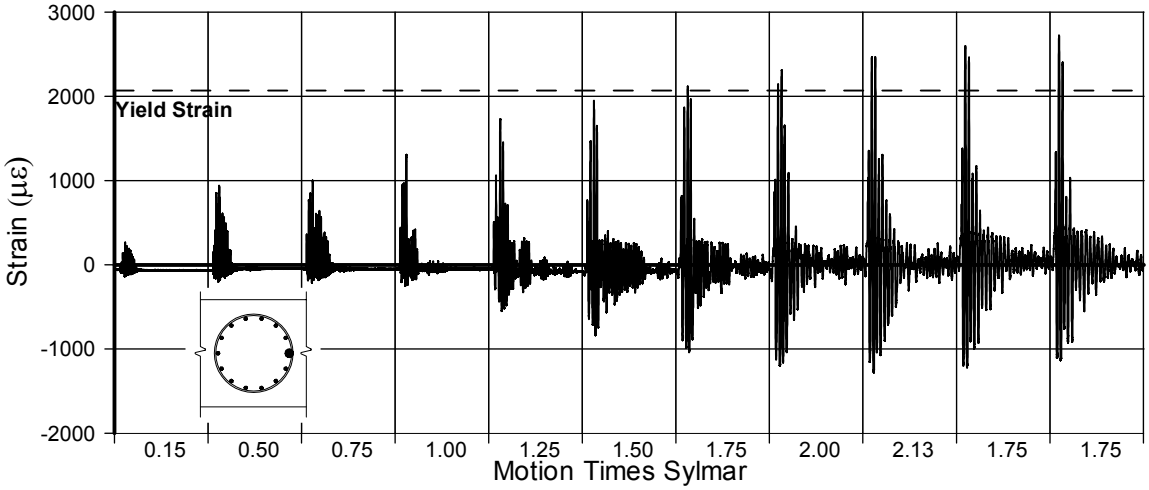

Fig. A-67 - Measured Strain in Gauge No. 77 for LFCD1

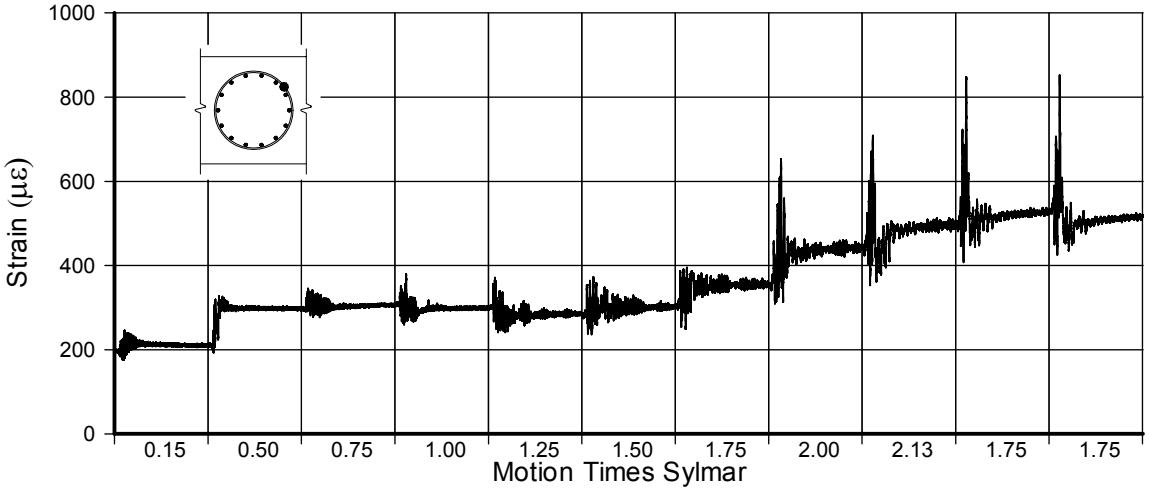

Fig. A-68 - Measured Strain in Gauge No. 78 for LFCD1

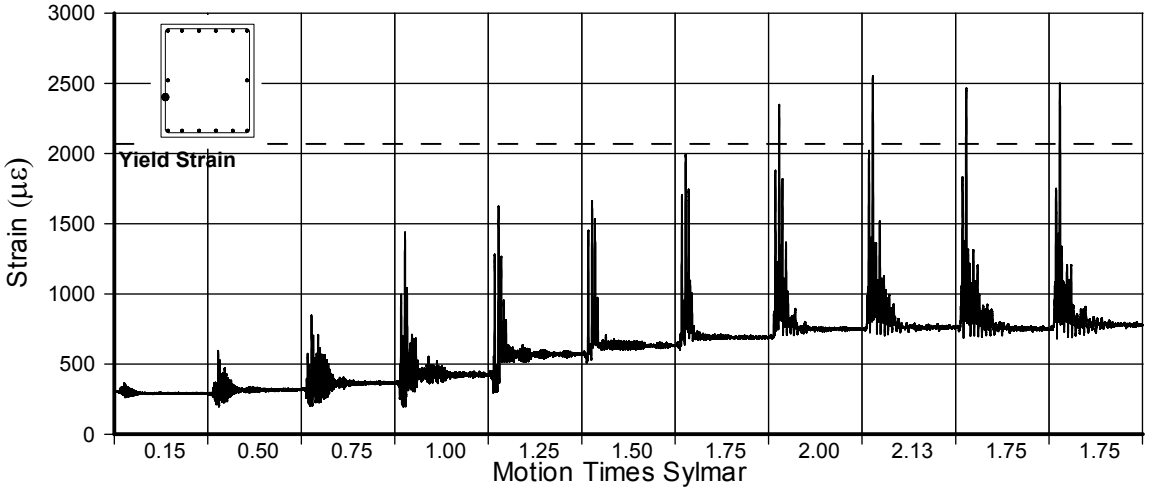

Fig. A-69 - Measured Strain in Gauge No. 80 for LFCD1

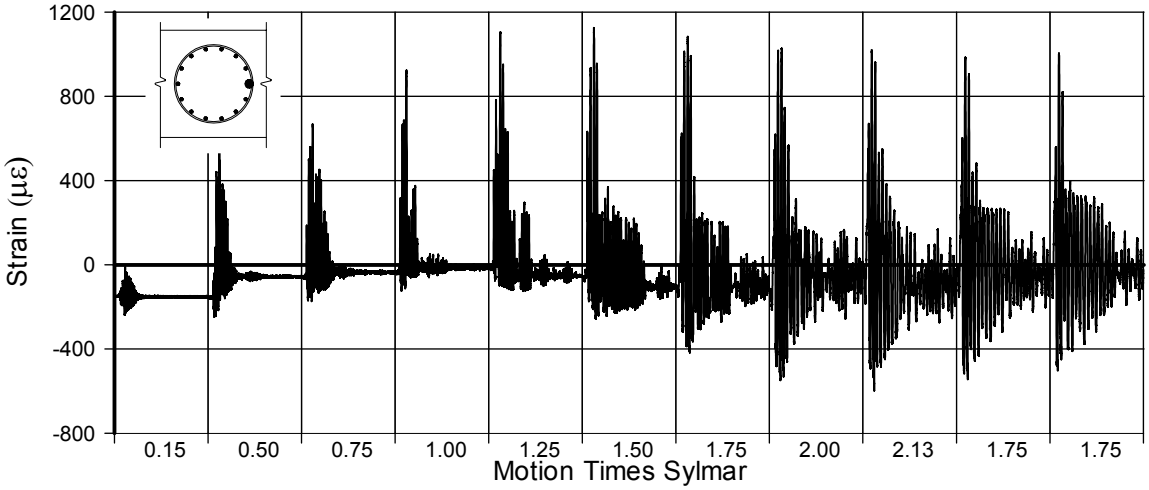

Fig. A-70 - Measured Strain in Gauge No. 81 for LFCD1

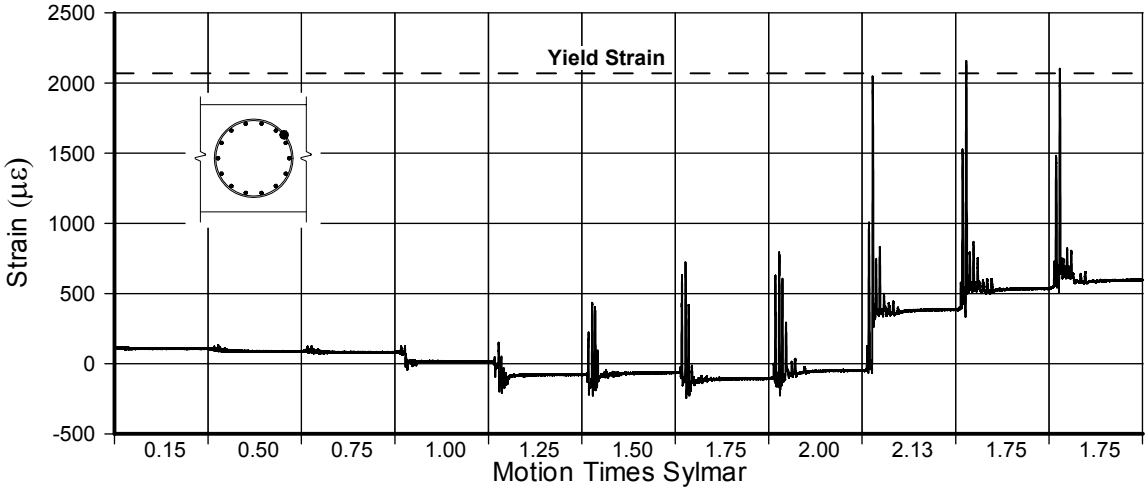

Fig. A-71 - Measured Strain in Gauge No. 82 for LFCD1

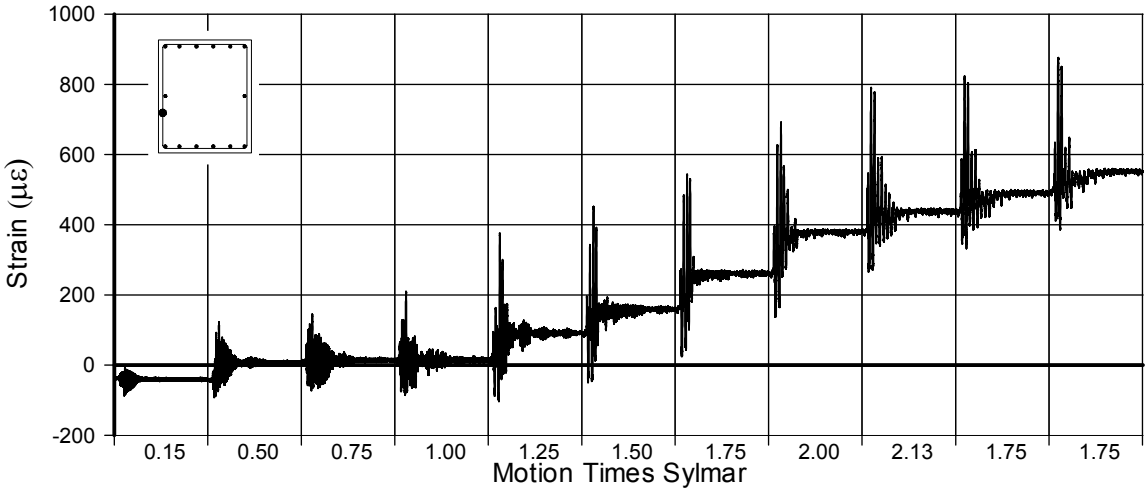

Fig. A-72 - Measured Strain in Gauge No. 83 for LFCD1

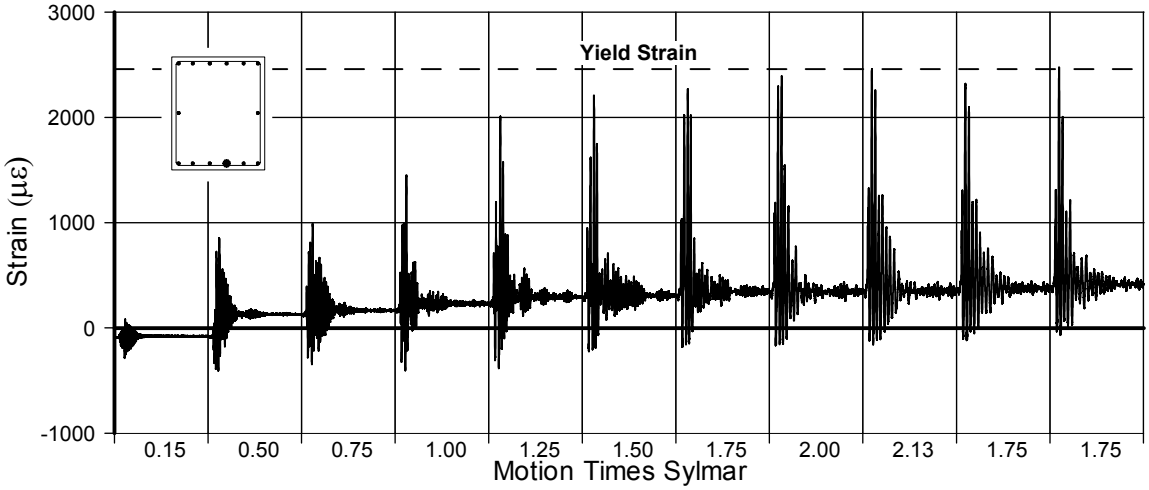

Fig. A-73 - Measured Strain in Gauge No. 85 for LFCD1

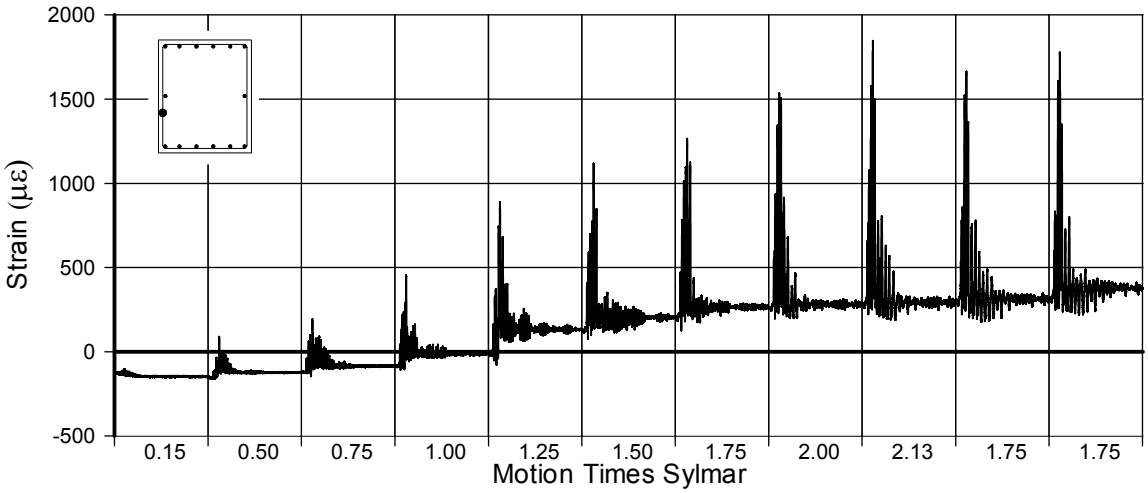

Fig. A-74 - Measured Strain in Gauge No. 86 for LFCD1

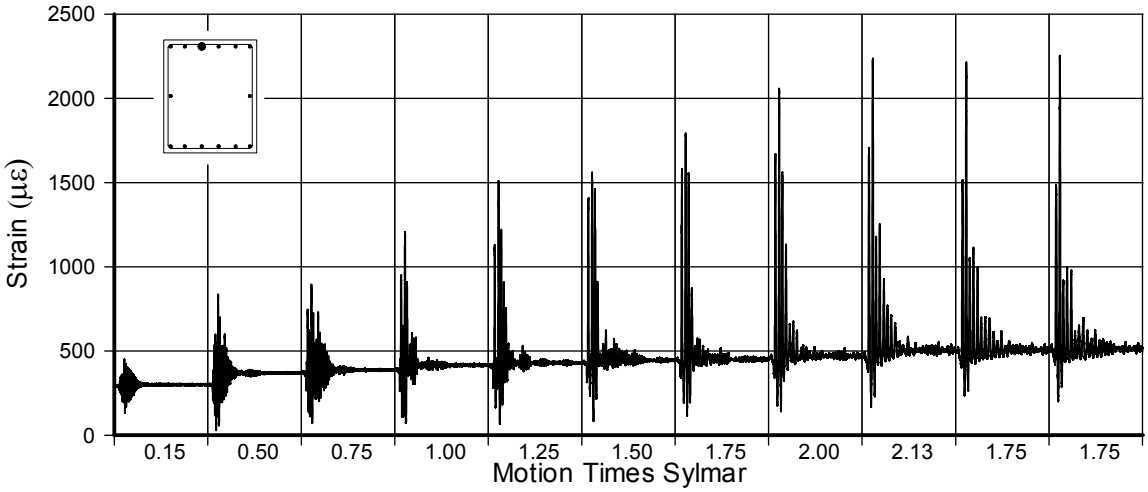

Fig. A-75 - Measured Strain in Gauge No. 87 for LFCD1

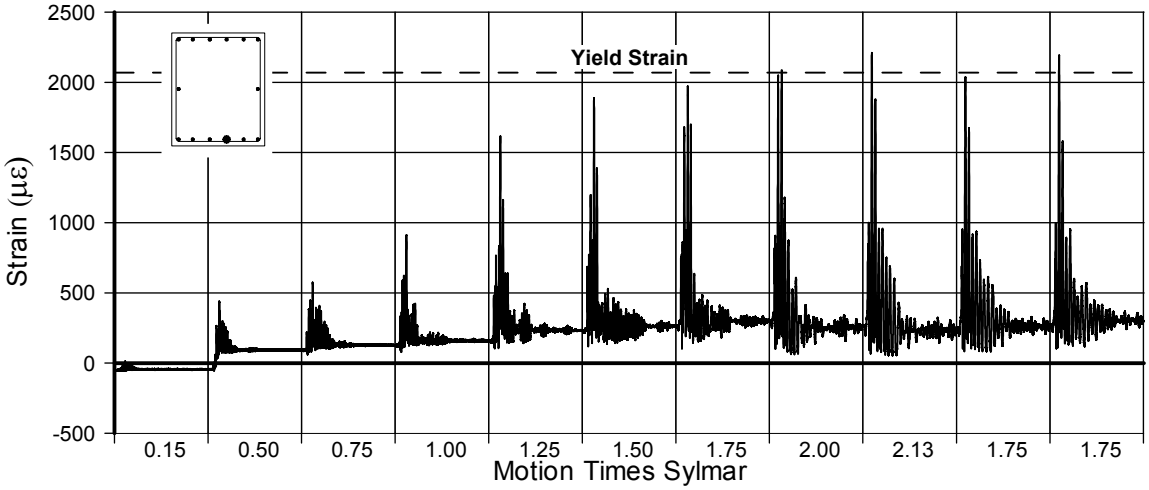

Fig. A-76 - Measured Strain in Gauge No. 91 for LFCD1

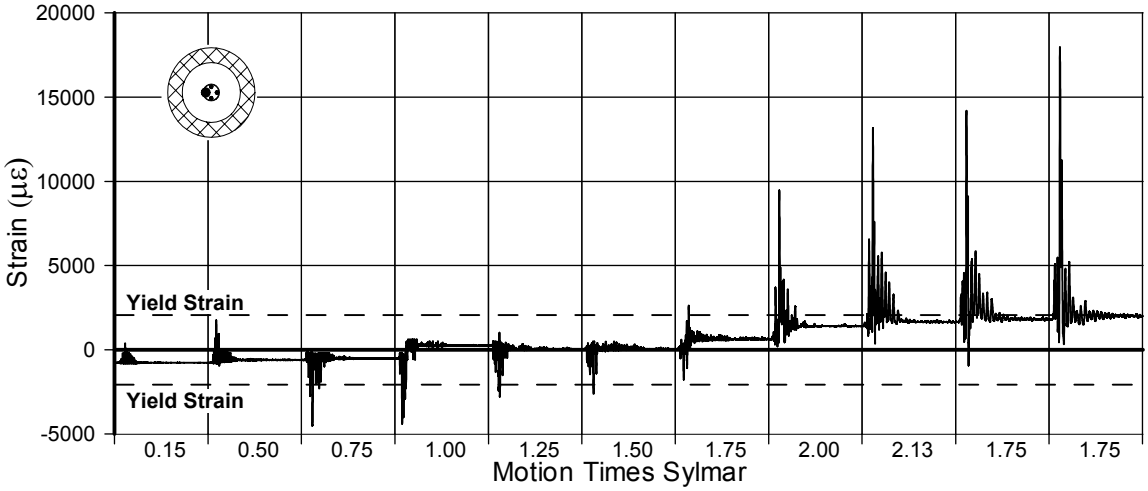

Fig. A-77 - Measured Strain in Gauge No. 92 for LFCD1

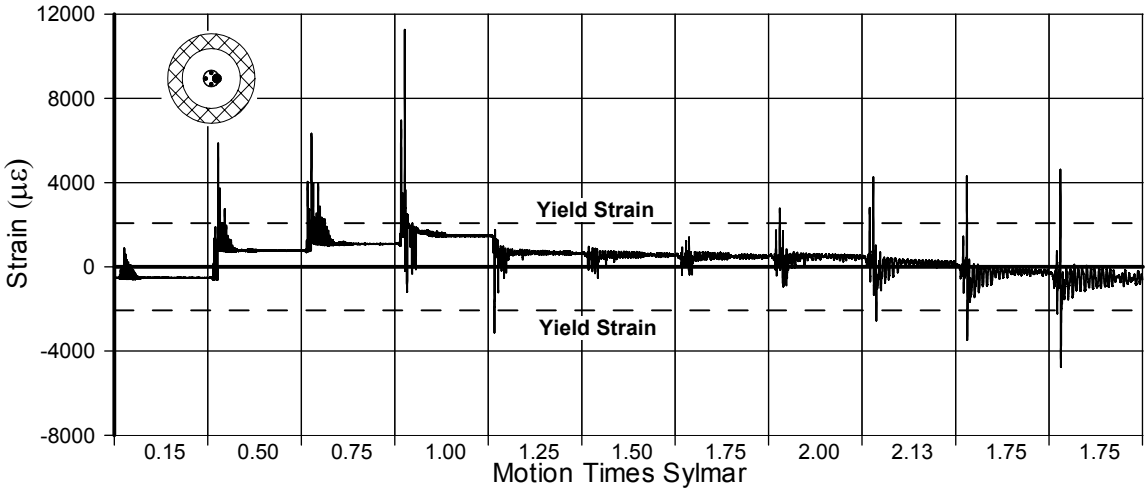

Fig. A-78 - Measured Strain in Gauge No. 93 for LFCD1

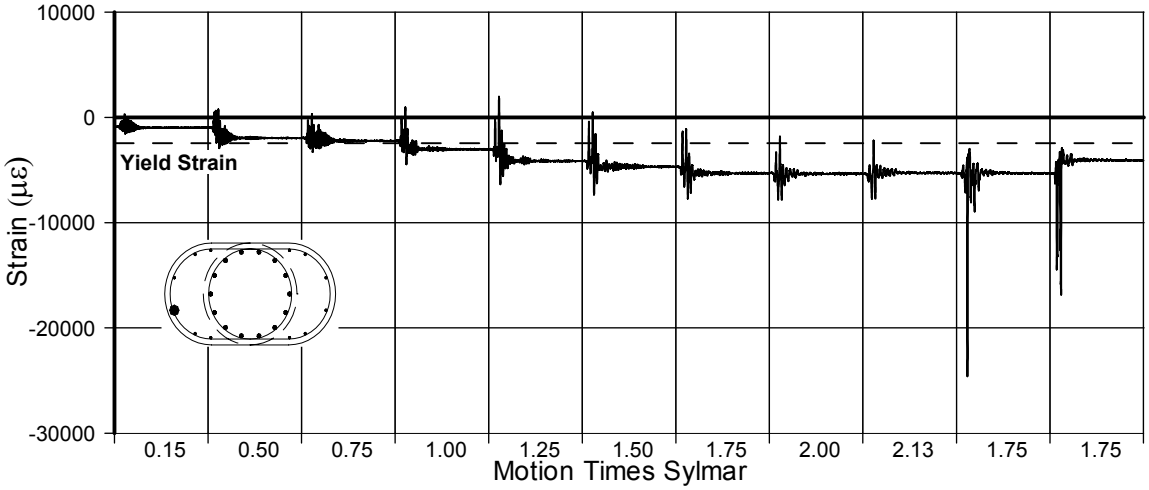

Fig. A-79 - Measured Strain in Gauge No. 94 for LFCD1

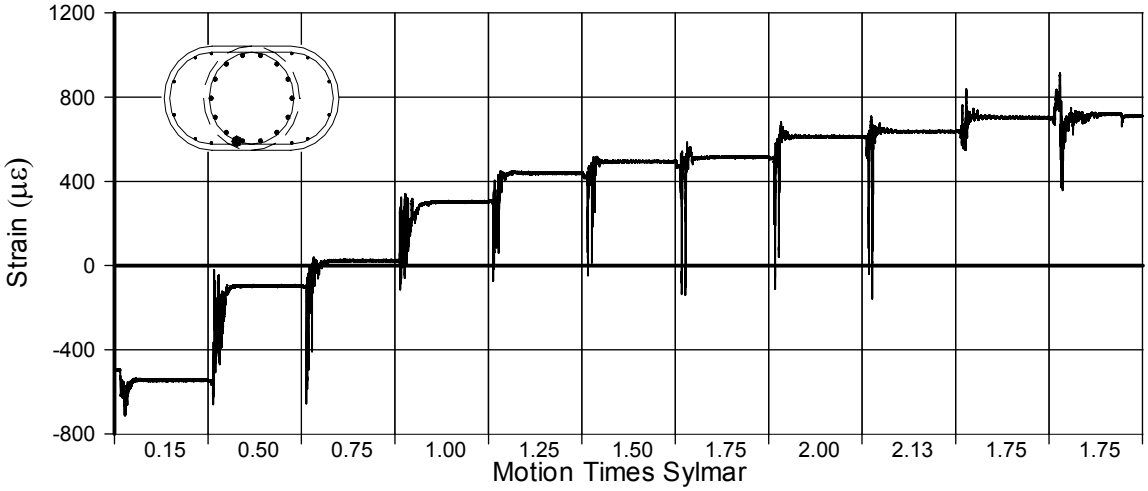

Fig. A-80 - Measured Strain in Gauge No. 97 for LFCD1

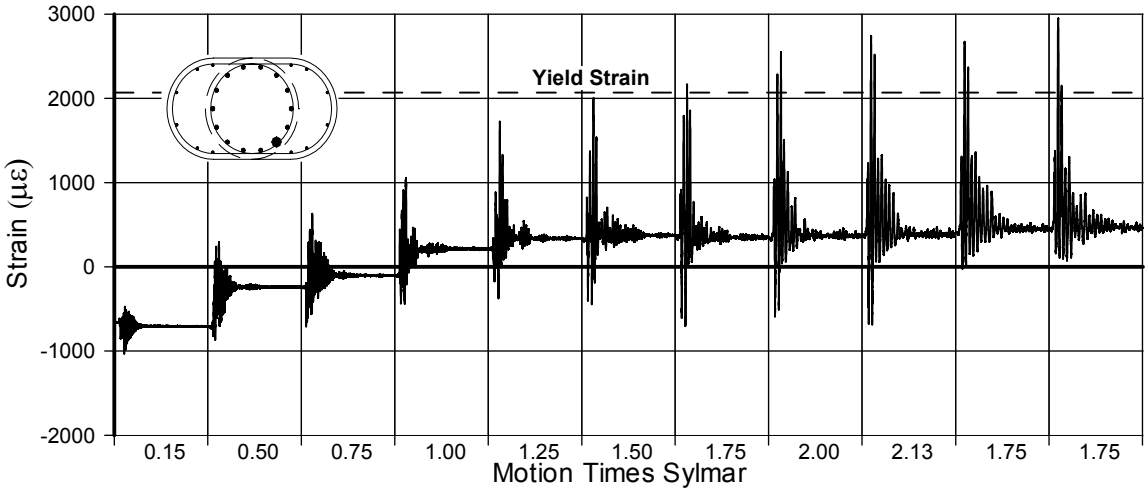

Fig. A-81 - Measured Strain in Gauge No. 98 for LFCD1

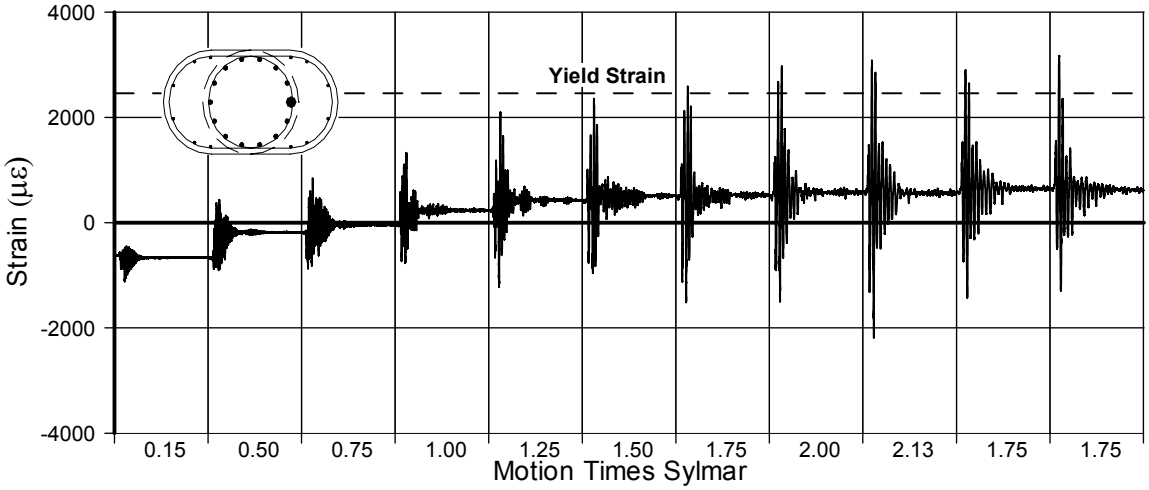

Fig. A-82 - Measured Strain in Gauge No. 99 for LFCD1

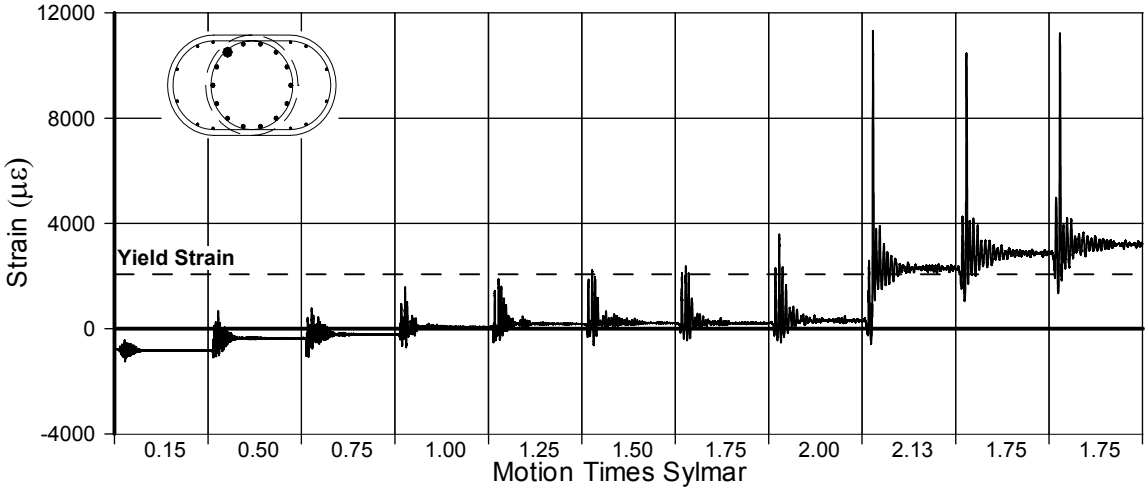

Fig. A-83 - Measured Strain in Gauge No. 100 for LFCD1

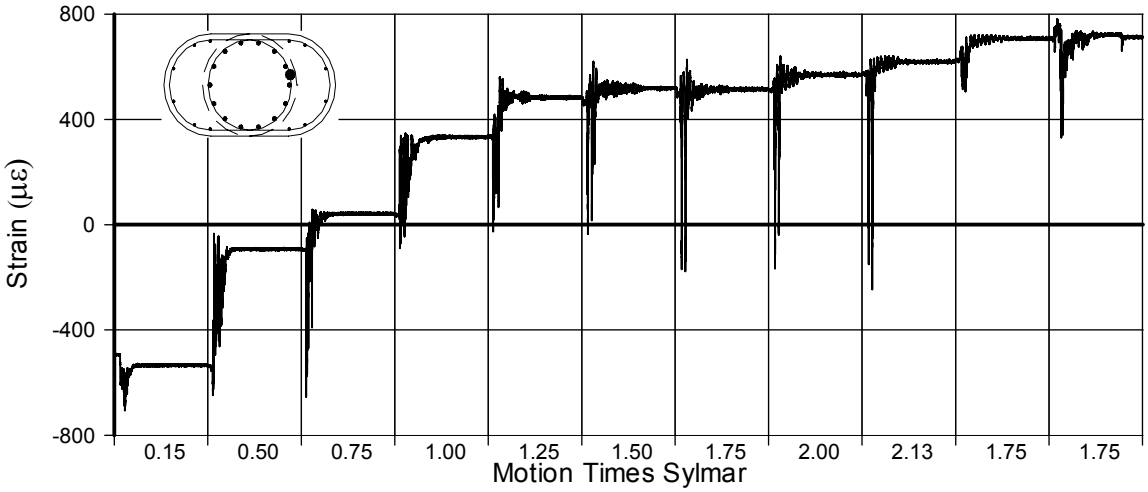

Fig. A-84 - Measured Strain in Gauge No. 101 for LFCD1

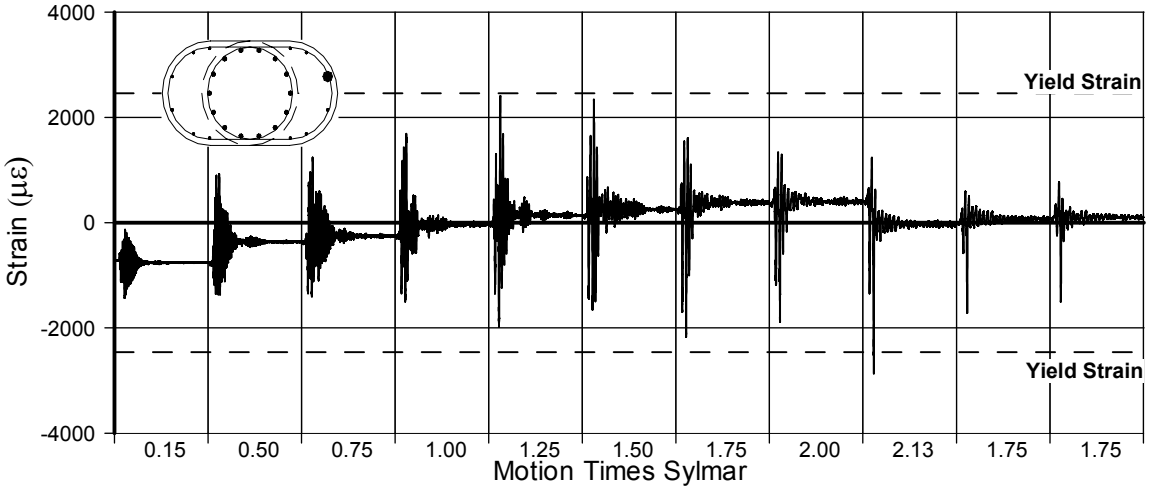

Fig. A-85 - Measured Strain in Gauge No. 102 for LFCD1

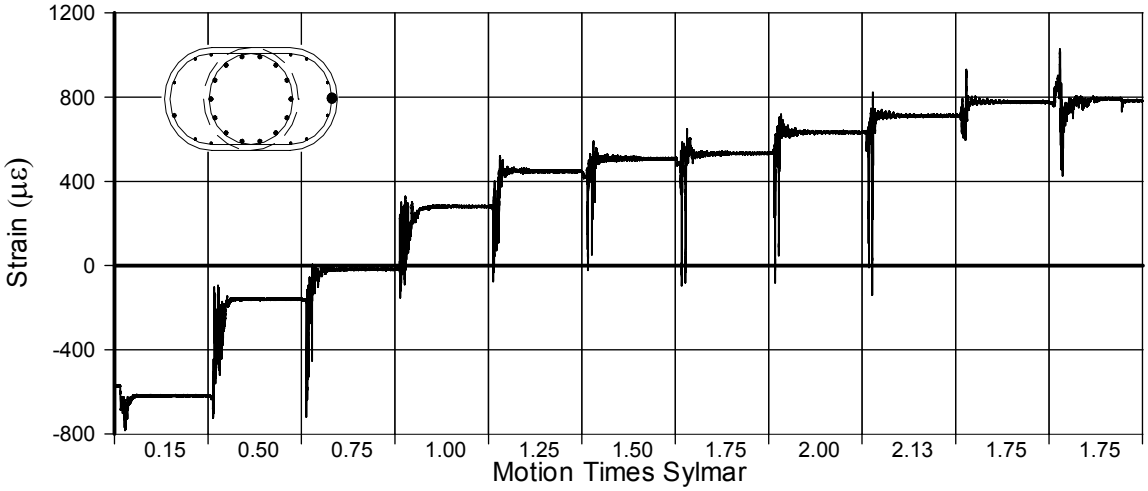

Fig. A-86 - Measured Strain in Gauge No. 103 for LFCD1

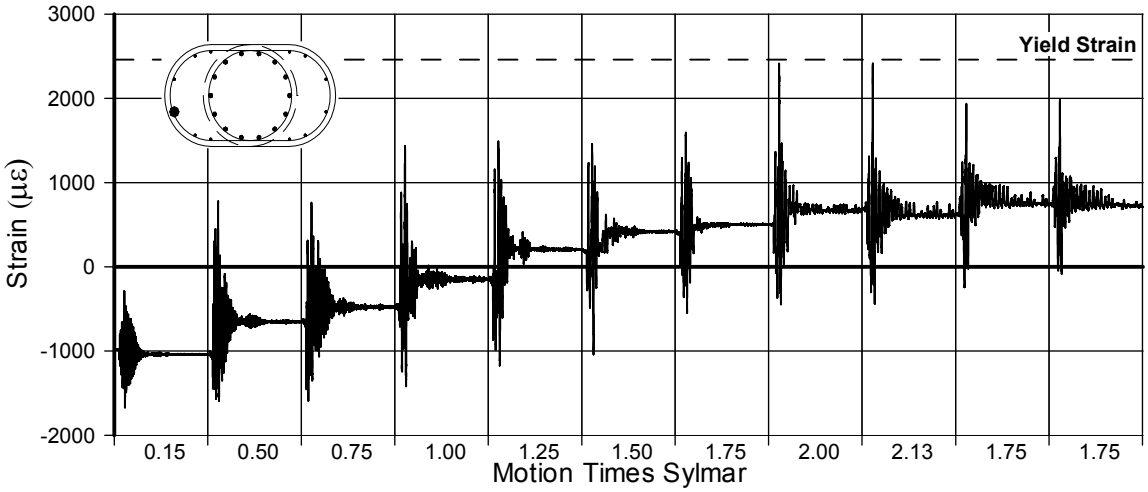

Fig. A-87 - Measured Strain in Gauge No. 104 for LFCD1

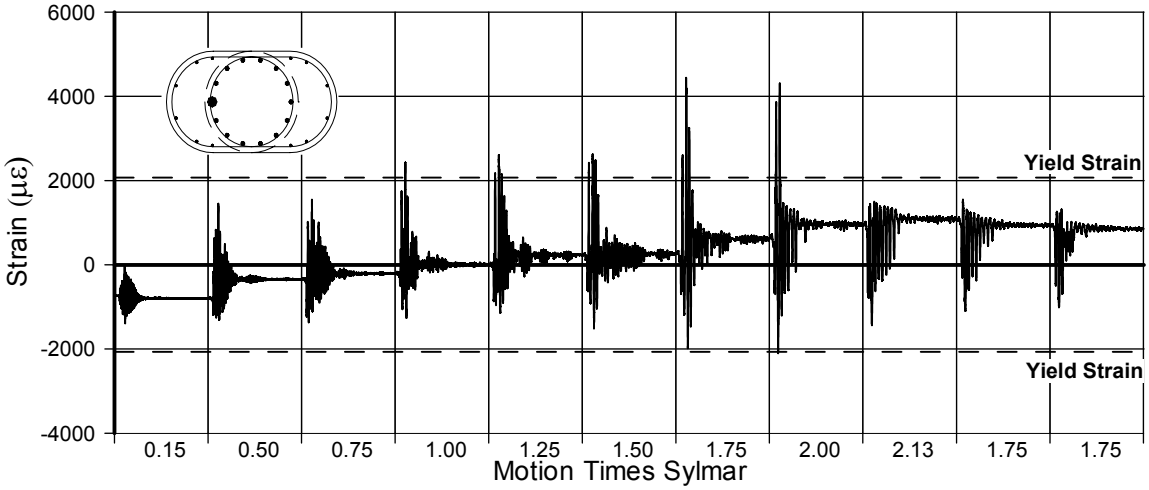

Fig. A-88 - Measured Strain in Gauge No. 105 for LFCD1

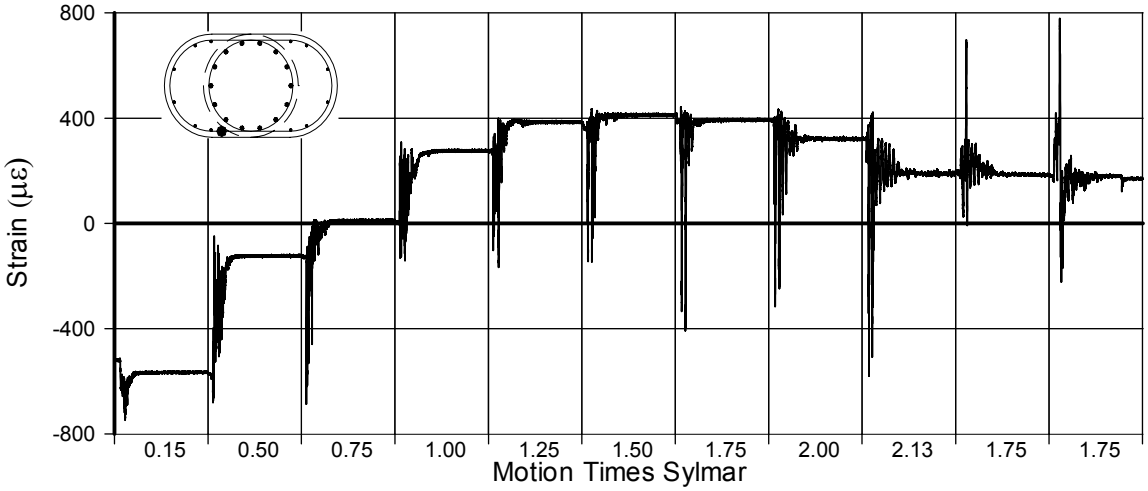

Fig. A-89 - Measured Strain in Gauge No. 106 for LFCD1

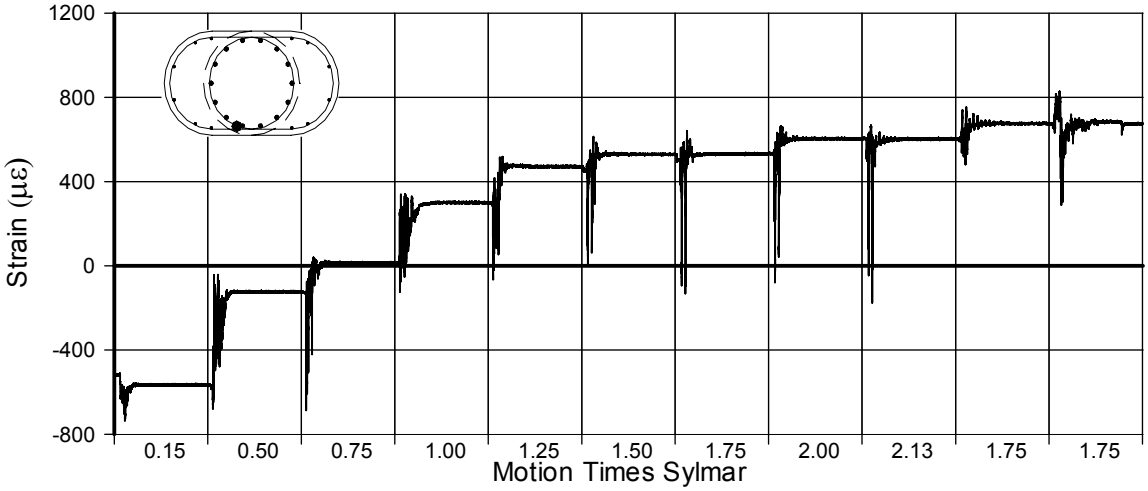

Fig. A-90 - Measured Strain in Gauge No. 107 for LFCD1

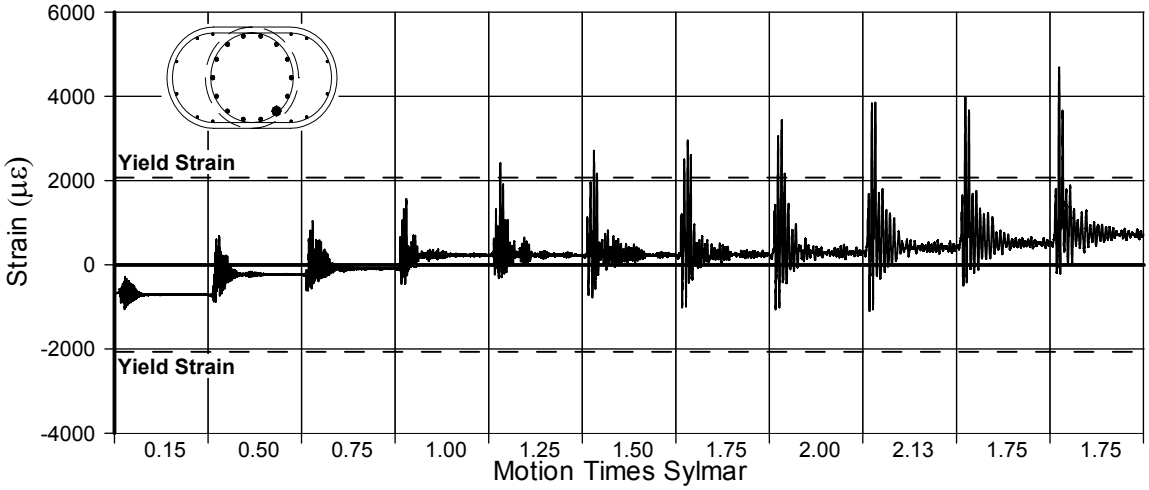

Fig. A-91 - Measured Strain in Gauge No. 108 for LFCD1

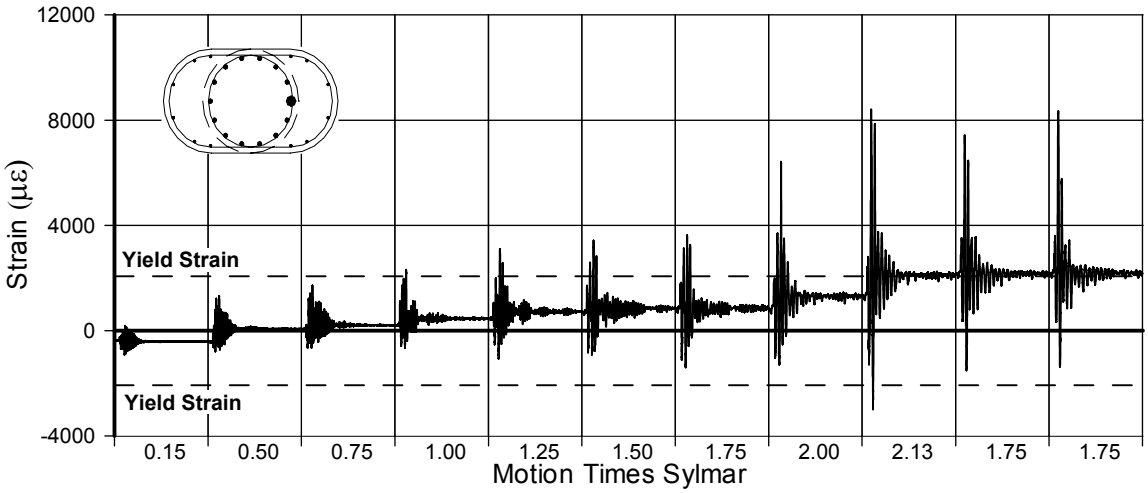

Fig. A-92 - Measured Strain in Gauge No. 109 for LFCD1

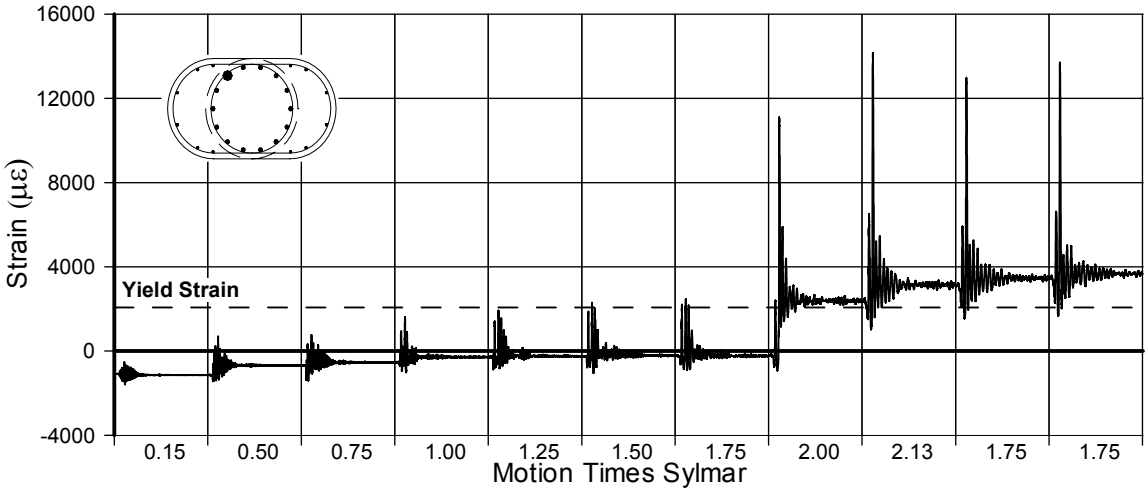

Fig. A-93 - Measured Strain in Gauge No. 110 for LFCD1

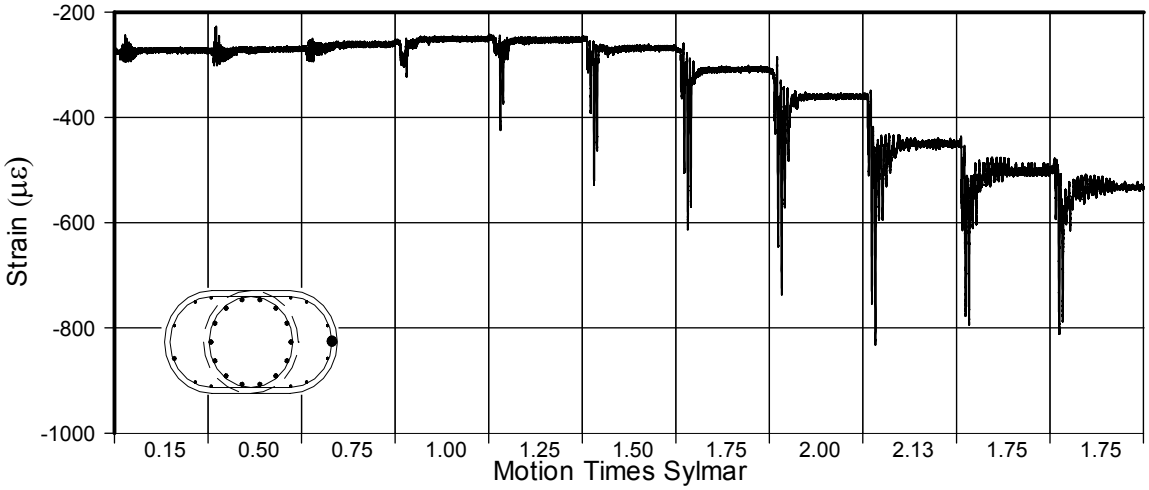

Fig. A-94 - Measured Strain in Gauge No. 113 for LFCD1

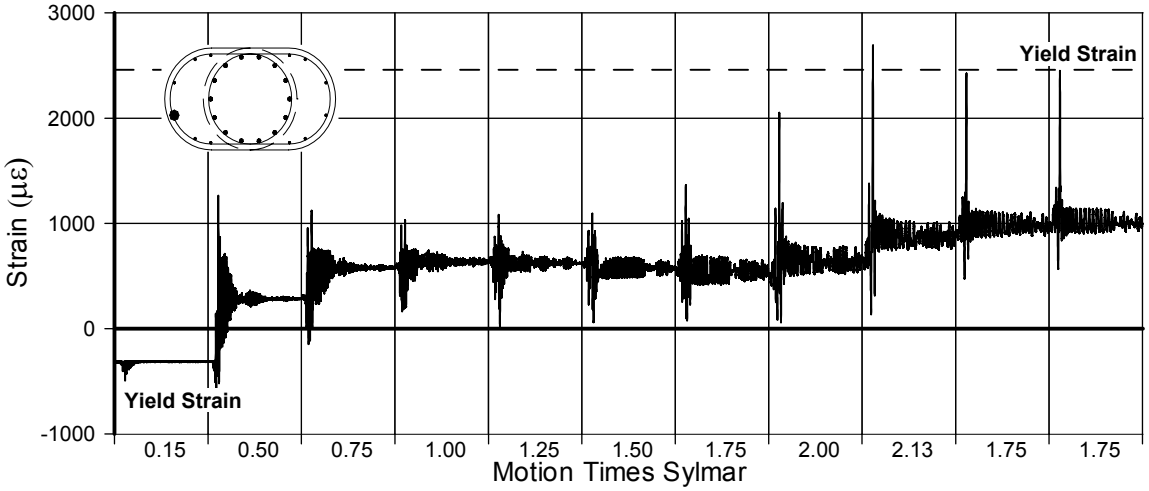

Fig. A-95 - Measured Strain in Gauge No. 114 for LFCD1

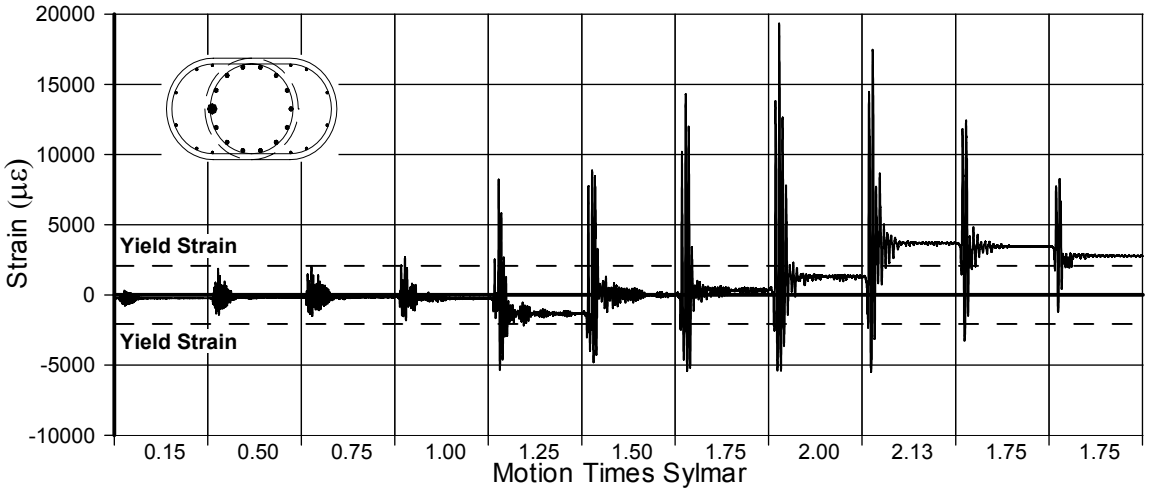

Fig. A-96 - Measured Strain in Gauge No. 115 for LFCD1

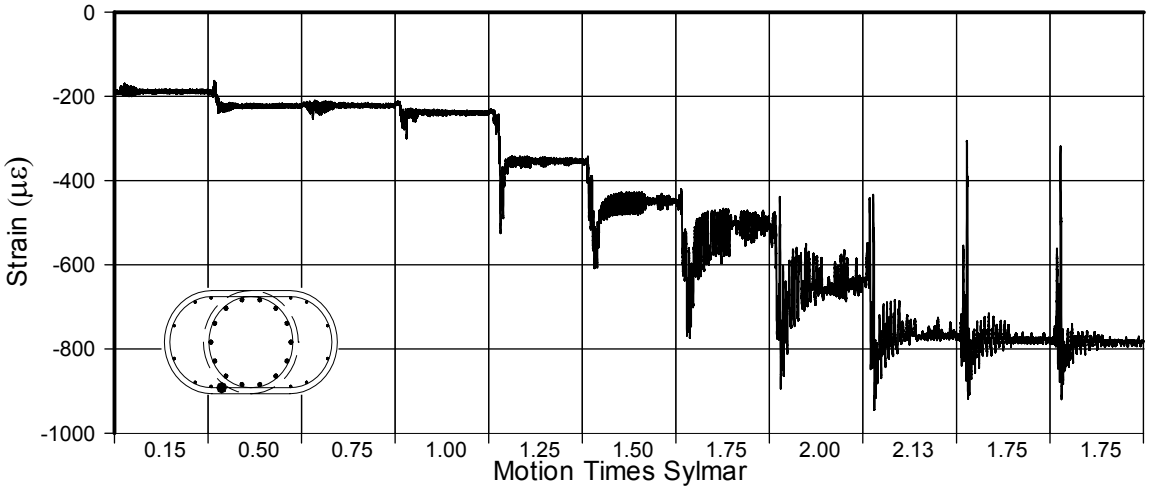

Fig. A-97 - Measured Strain in Gauge No. 116 for LFCD1

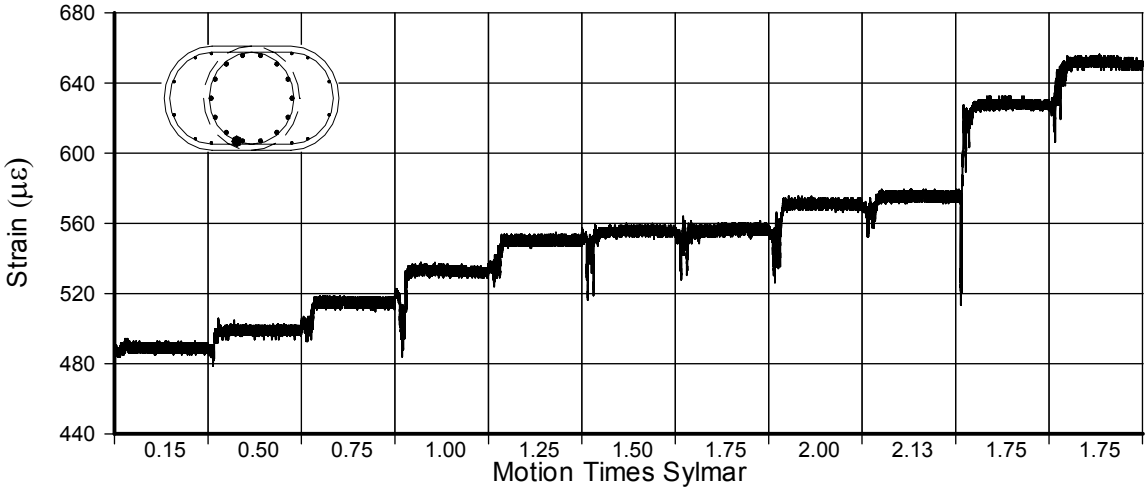

Fig. A-98 - Measured Strain in Gauge No. 117 for LFCD1

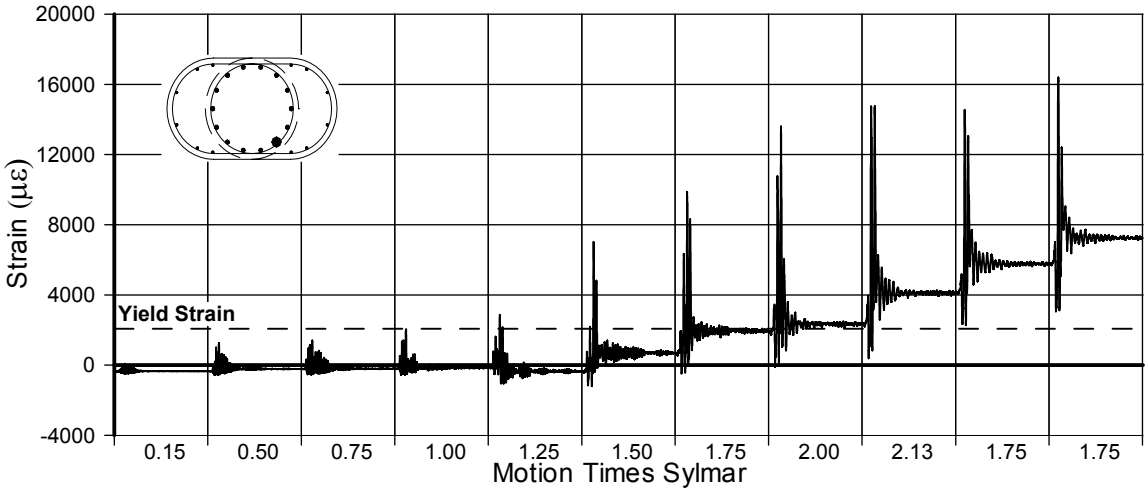

Fig. A-99 - Measured Strain in Gauge No. 118 for LFCD1

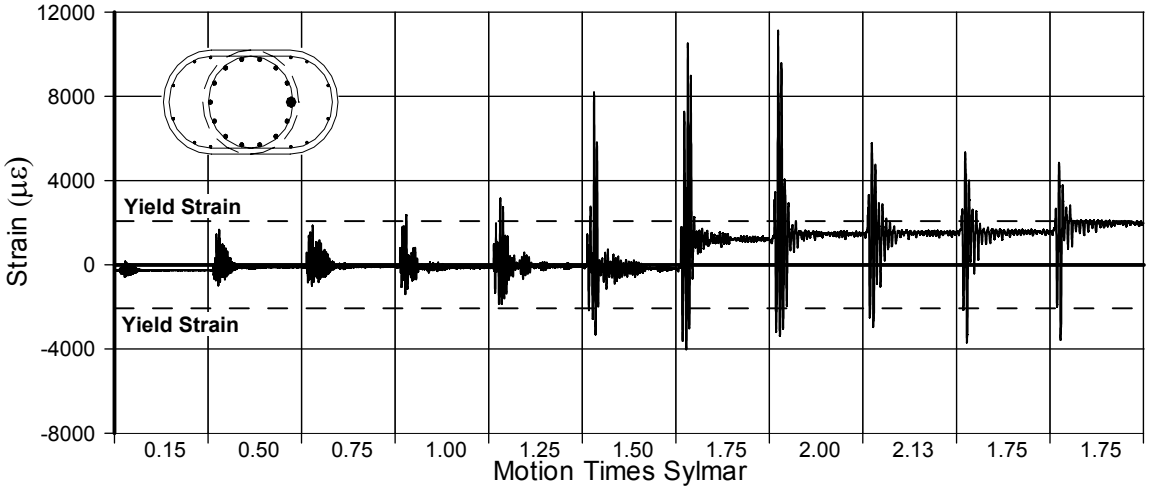

Fig. A-100 - Measured Strain in Gauge No. 119 for LFCD1

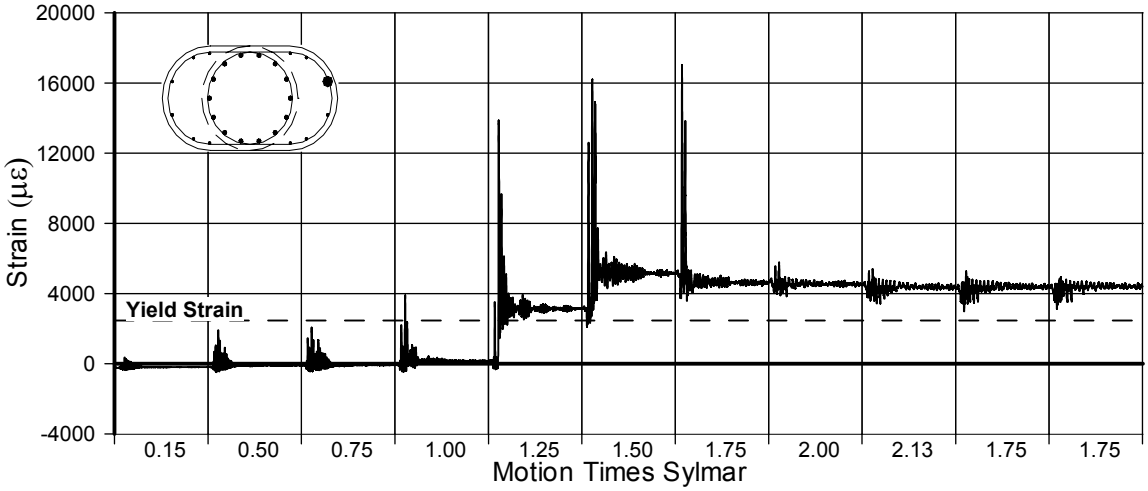

Fig. A-101 - Measured Strain in Gauge No. 122 for LFCD1

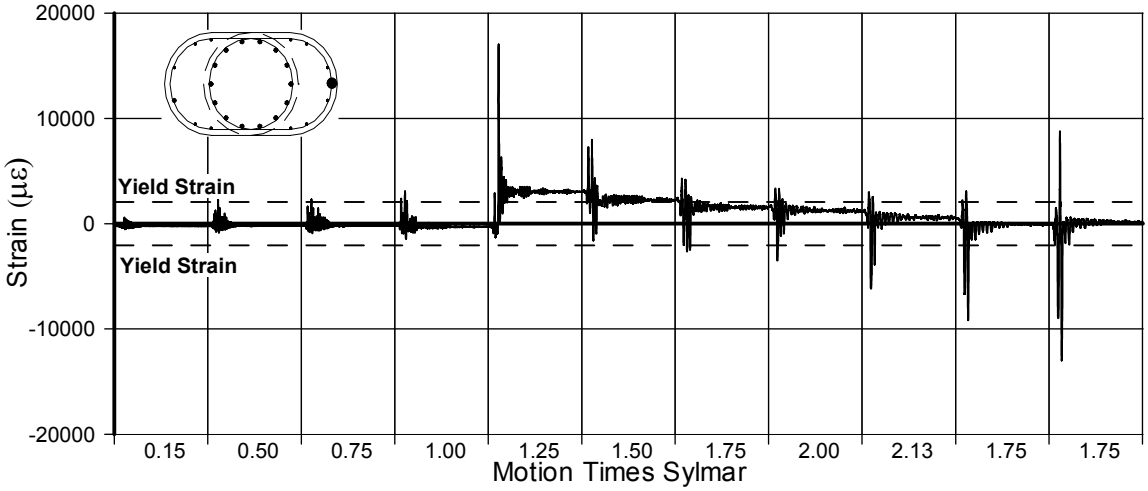

Fig. A-102 - Measured Strain in Gauge No. 123 for LFCD1

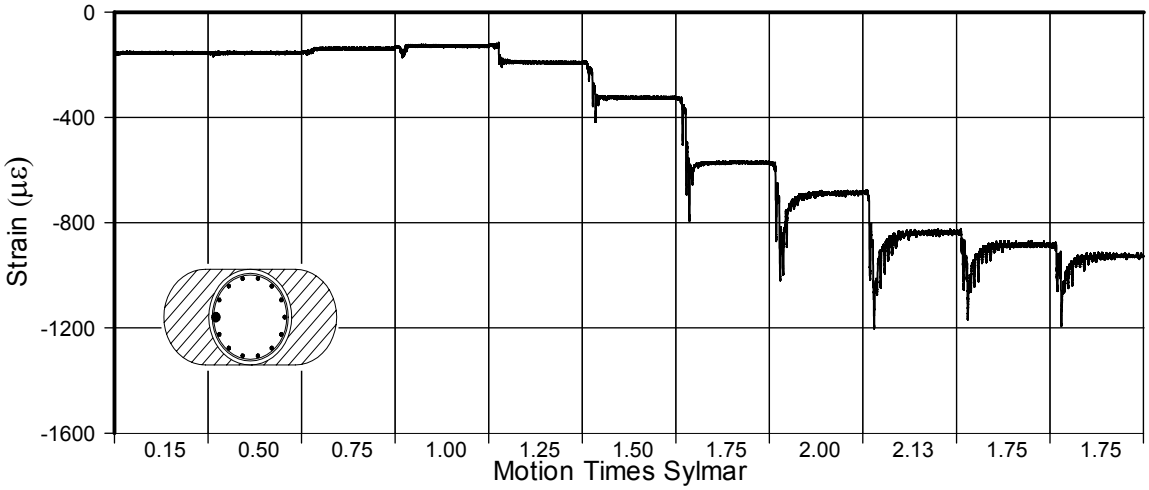

Fig. A-103 - Measured Strain in Gauge No. 124 for LFCD1

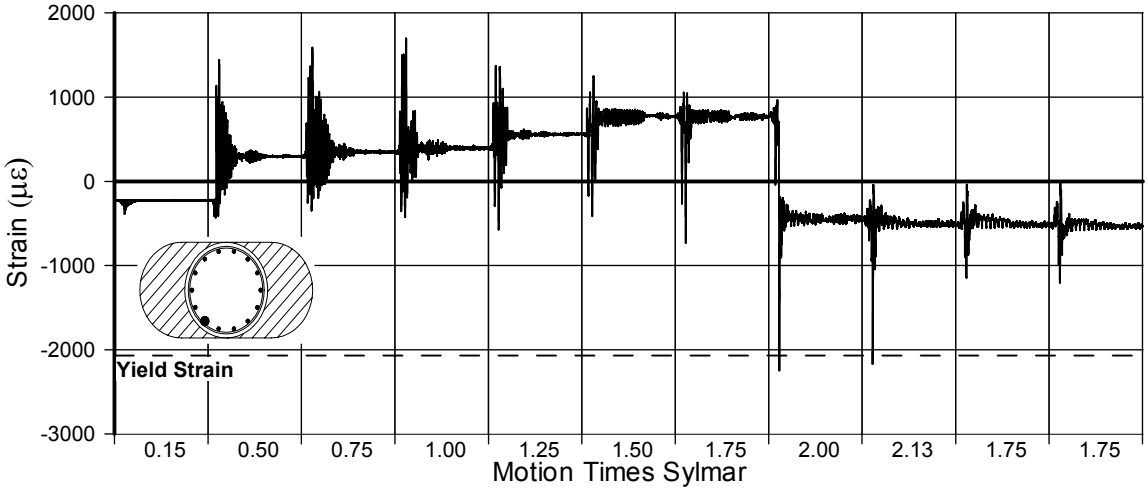

Fig. A-104 - Measured Strain in Gauge No. 125 for LFCD1

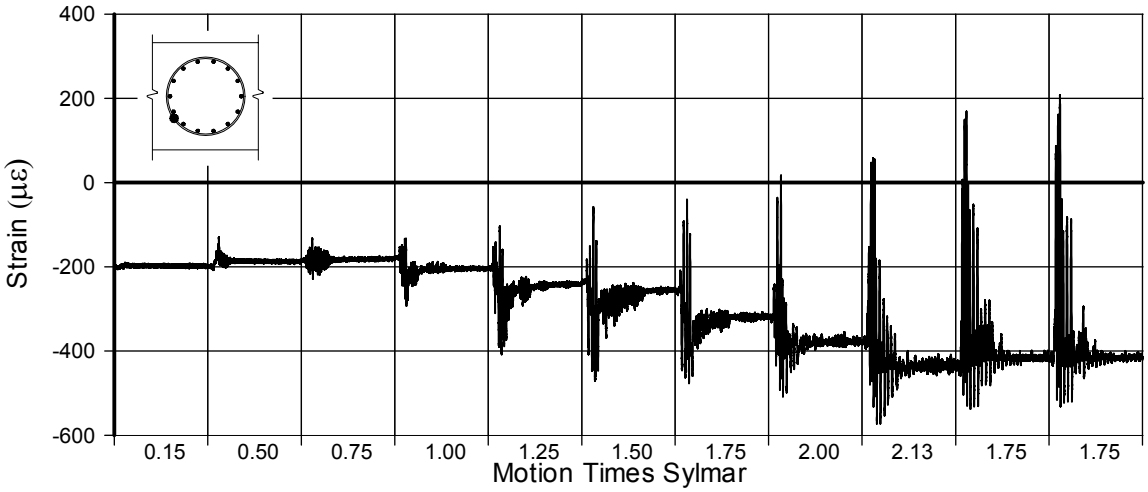

Fig. A-105 - Measured Strain in Gauge No. 129 for LFCD1

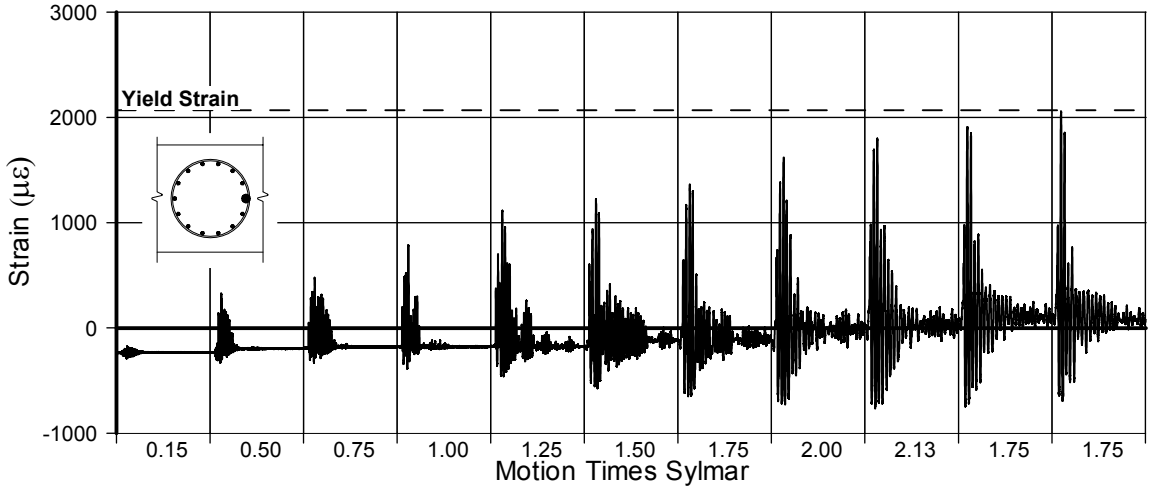

Fig. A-106 - Measured Strain in Gauge No. 130 for LFCD1

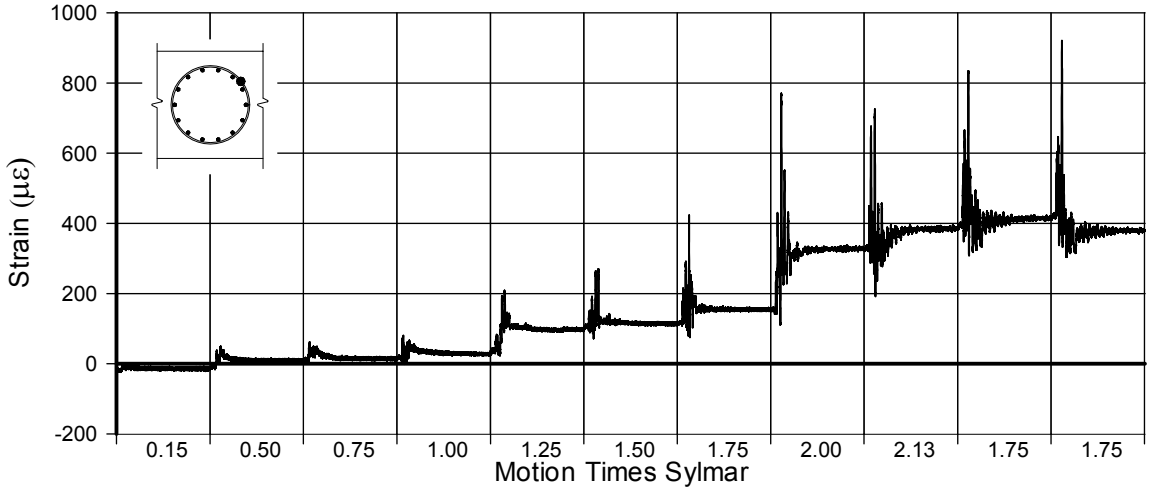

Fig. A-107 - Measured Strain in Gauge No. 131 for LFCD1

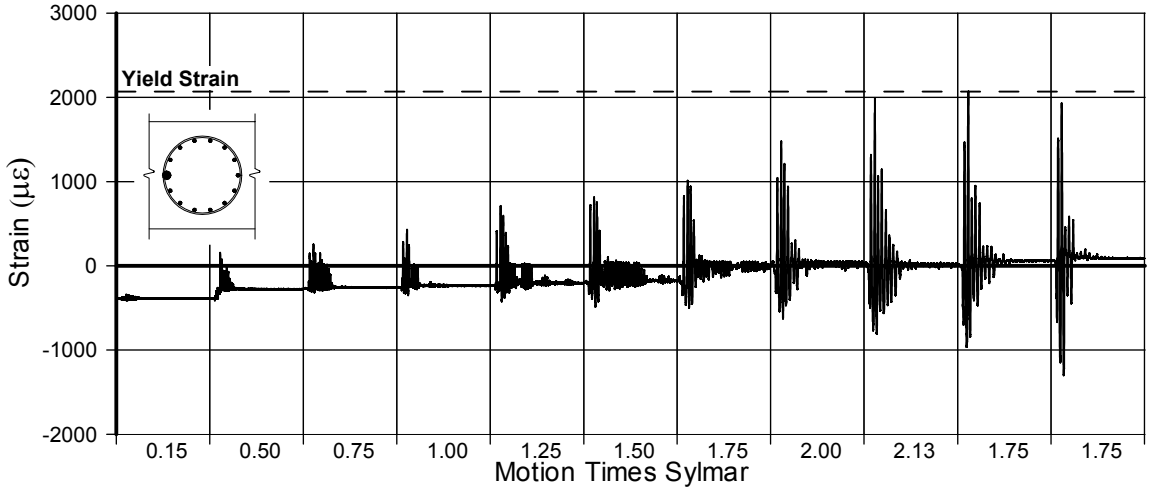

Fig. A-108 - Measured Strain in Gauge No. 132 for LFCD1

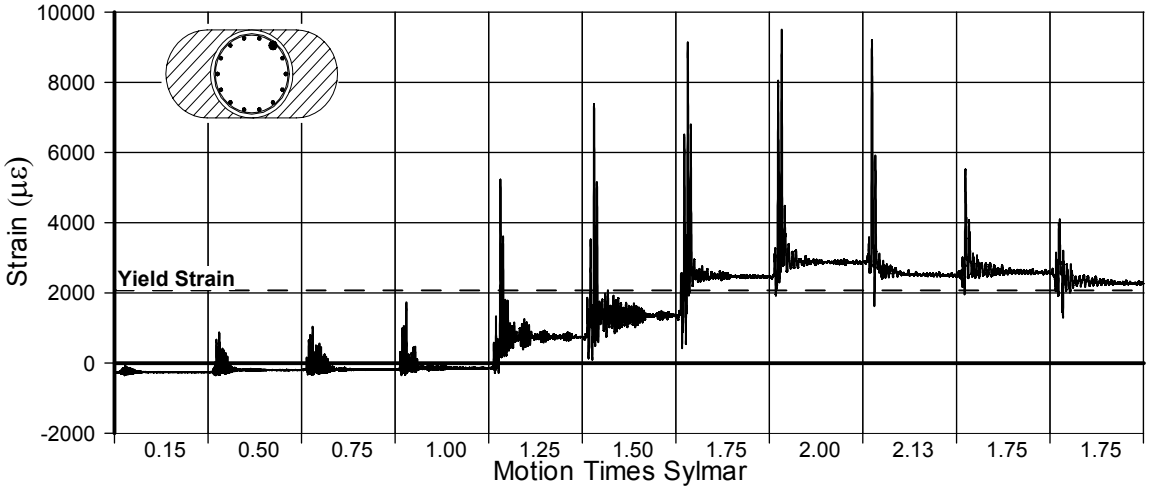

Fig. A-109 - Measured Strain in Gauge No. 133 for LFCD1

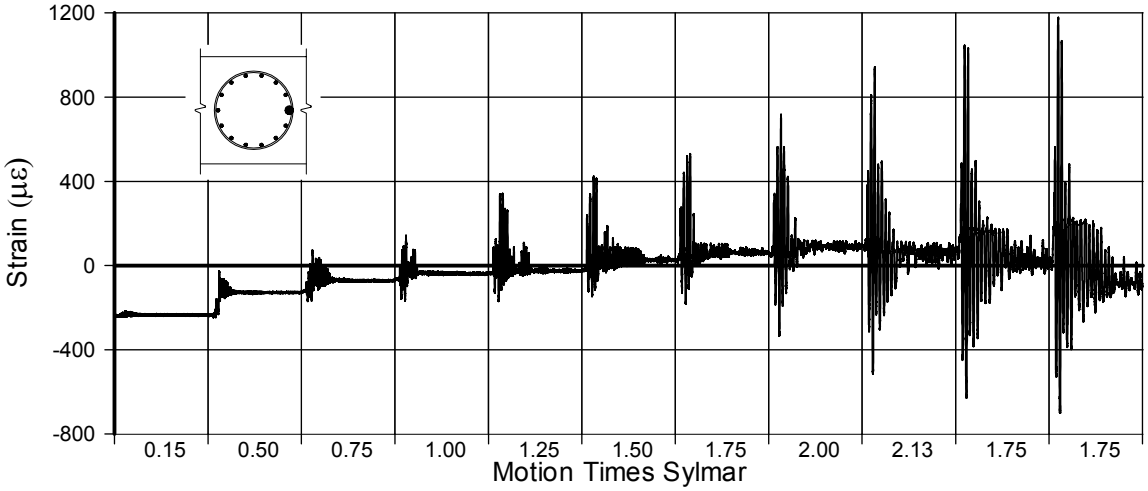

Fig. A-110 - Measured Strain in Gauge No. 134 for LFCD1

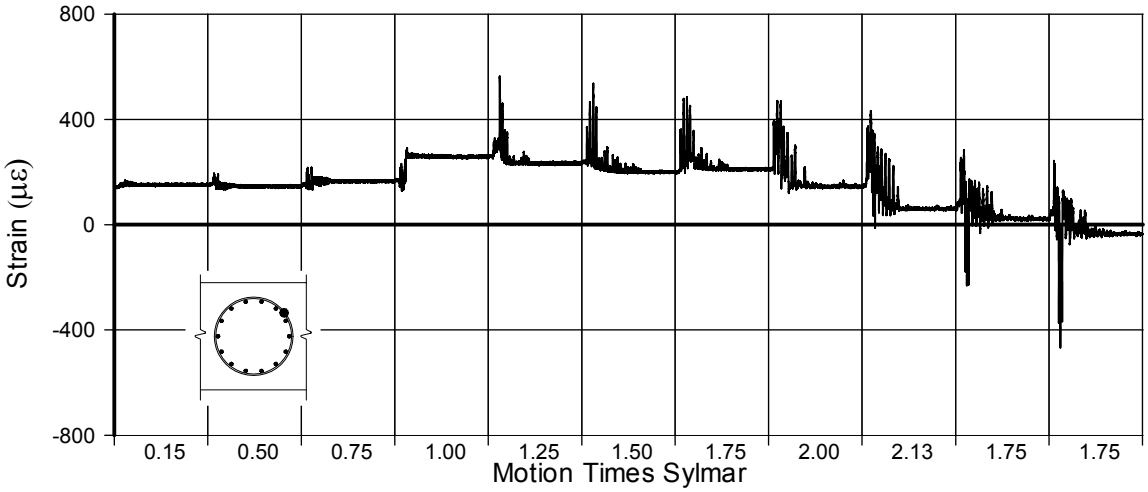

Fig. A-111 - Measured Strain in Gauge No. 135 for LFCD1

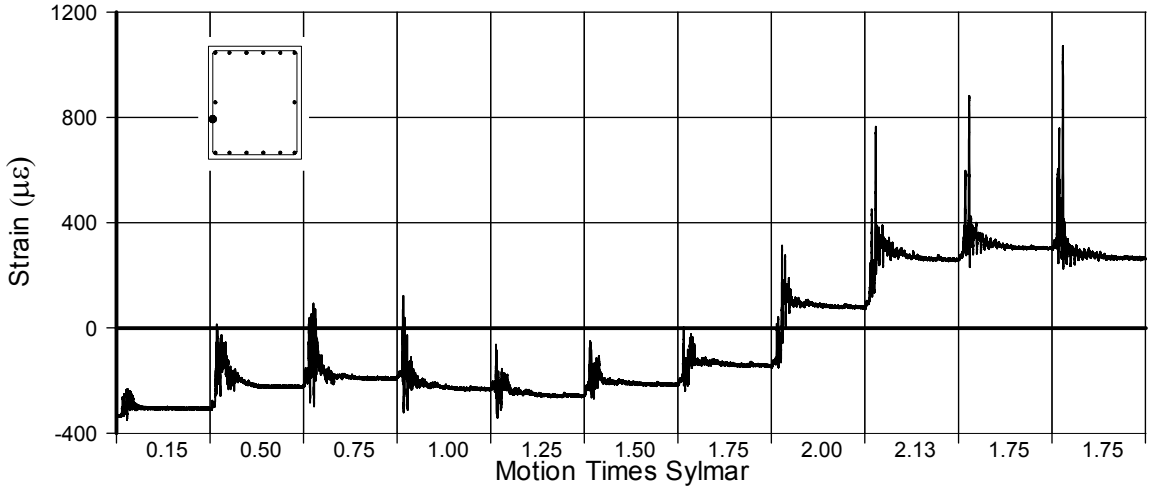

Fig. A-112 - Measured Strain in Gauge No. 136 for LFCD1

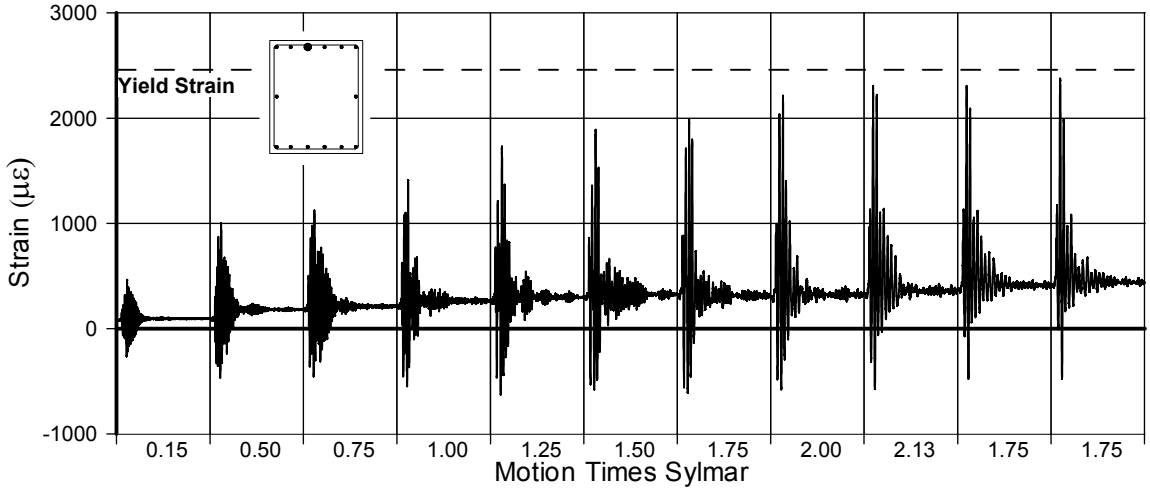

Fig. A-113 - Measured Strain in Gauge No. 137 for LFCD1

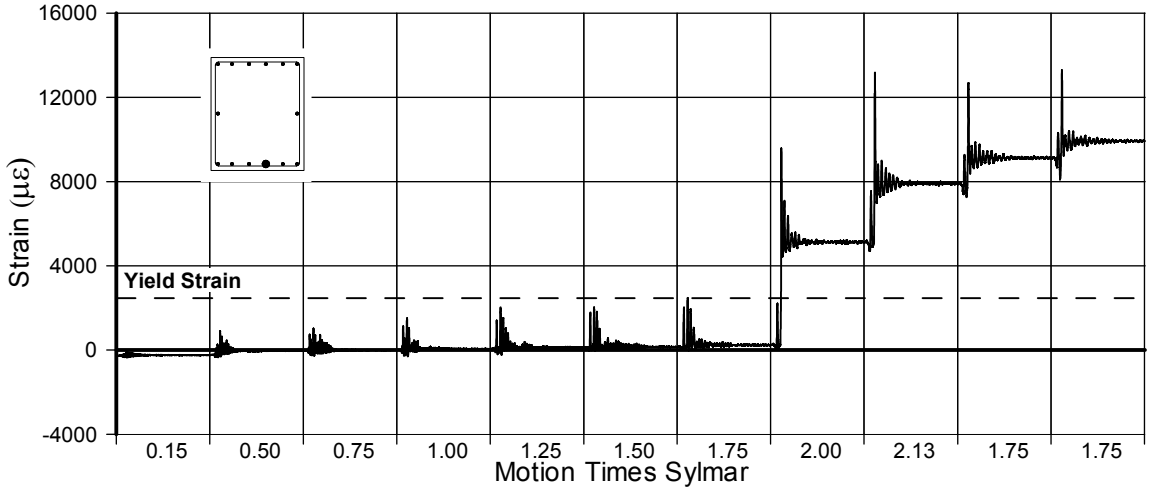

Fig. A-114 - Measured Strain in Gauge No. 138 for LFCD1

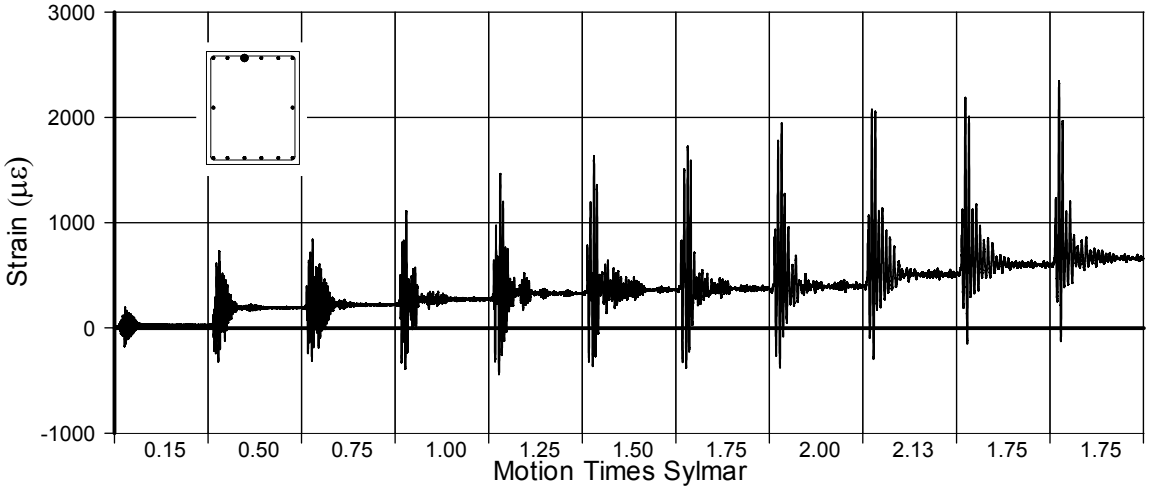

Fig. A-115 - Measured Strain in Gauge No. 140 for LFCD1

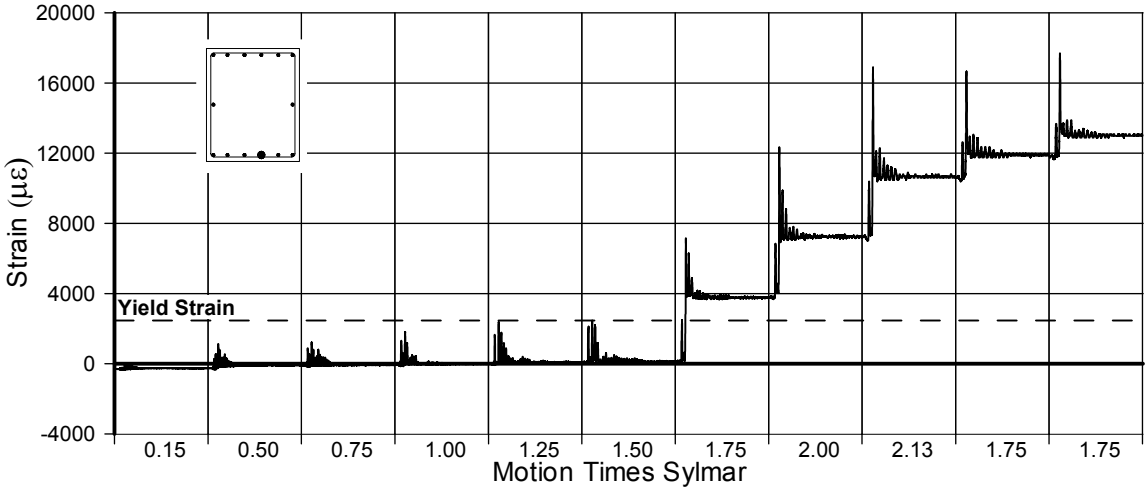

Fig. A-116 - Measured Strain in Gauge No. 141 for LFCD1

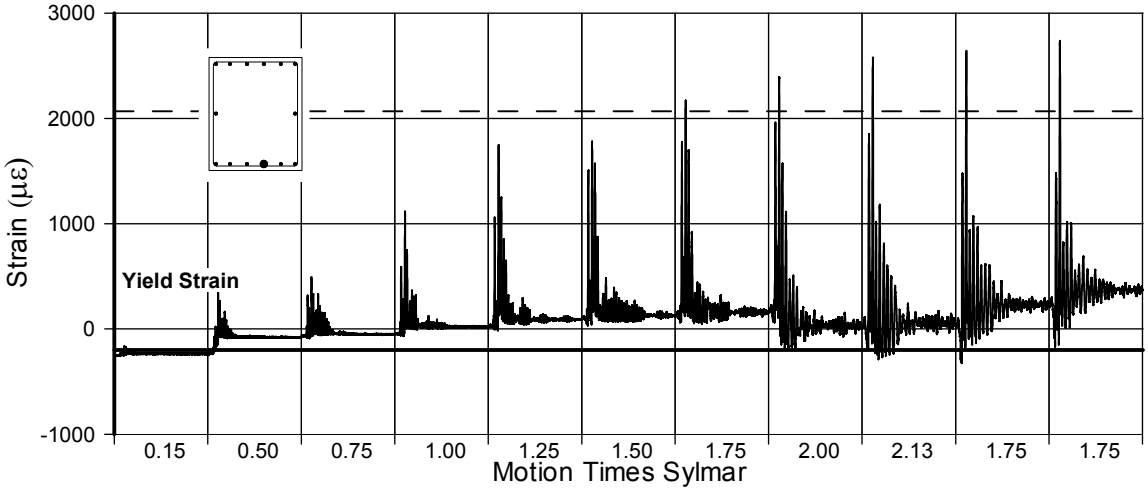

Fig. A-117 - Measured Strain in Gauge No. 144 for LFCD1

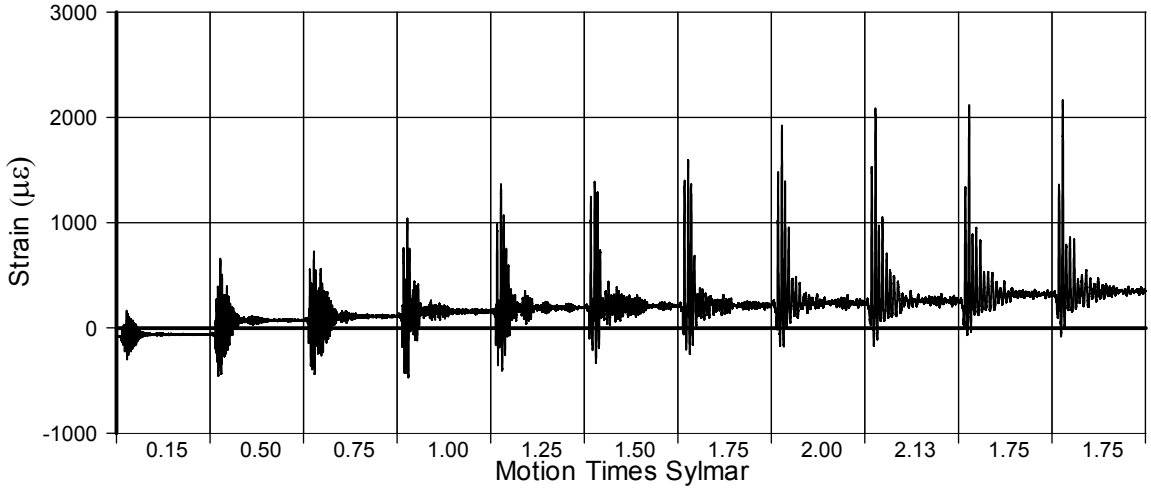

Fig. A-118 - Measured Strain in Gauge No. 145 for LFCD1

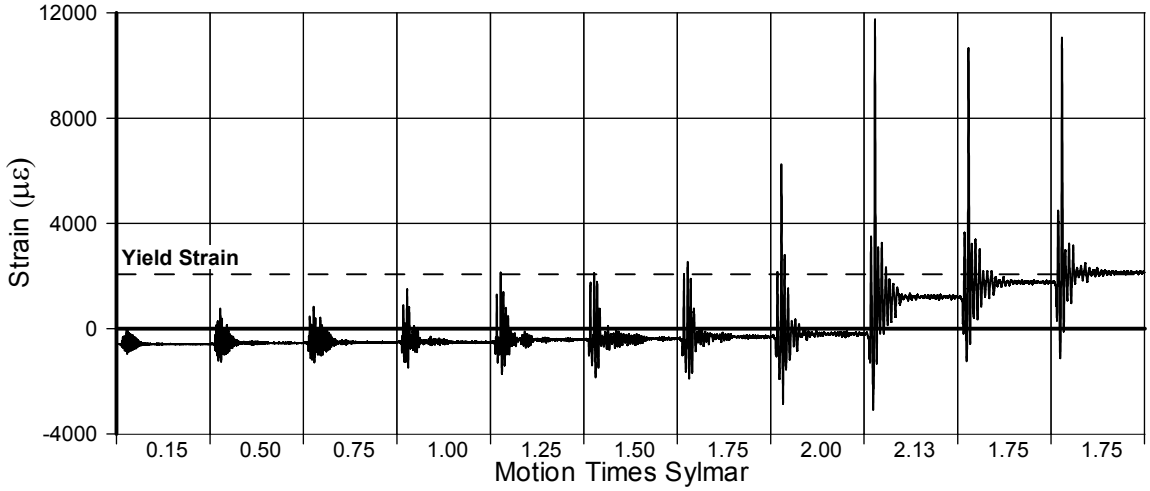

Fig. A-119 - Measured Strain in Gauge No. 147 for LFCD1

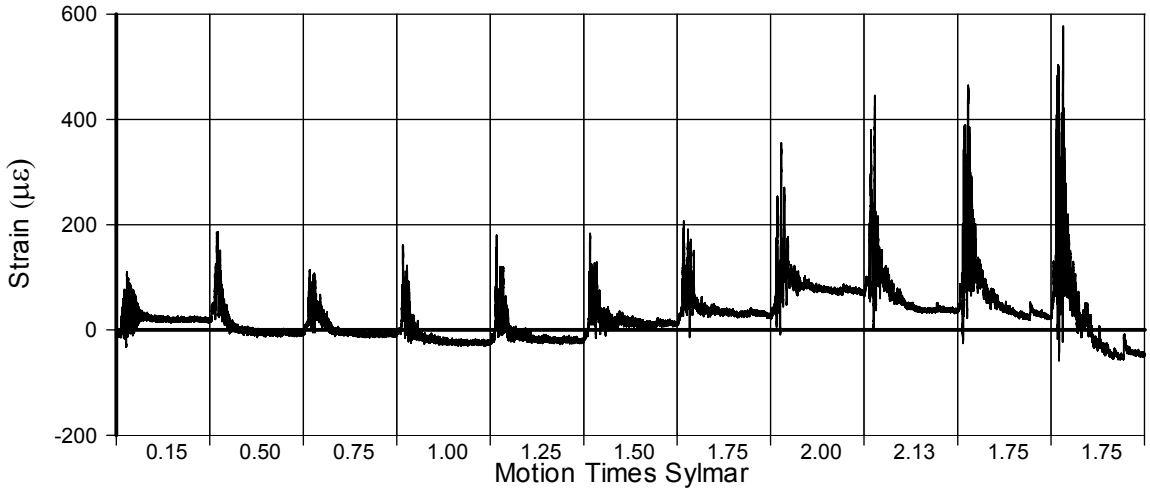

Fig. A-120 - Measured Strain in Gauge No. 148 for LFCD1

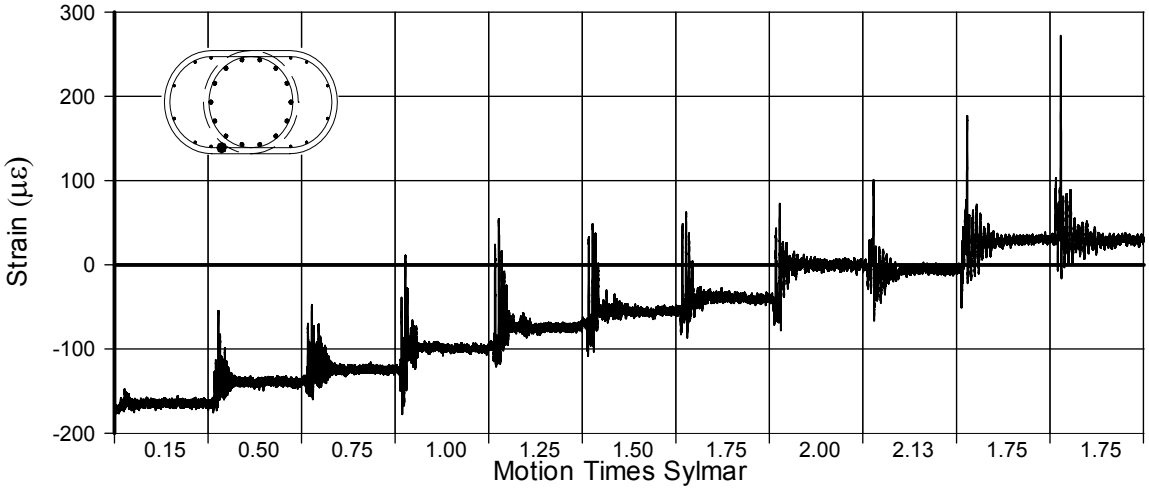

Fig. A-121 - Measured Strain in Gauge No. 149 for LFCD1

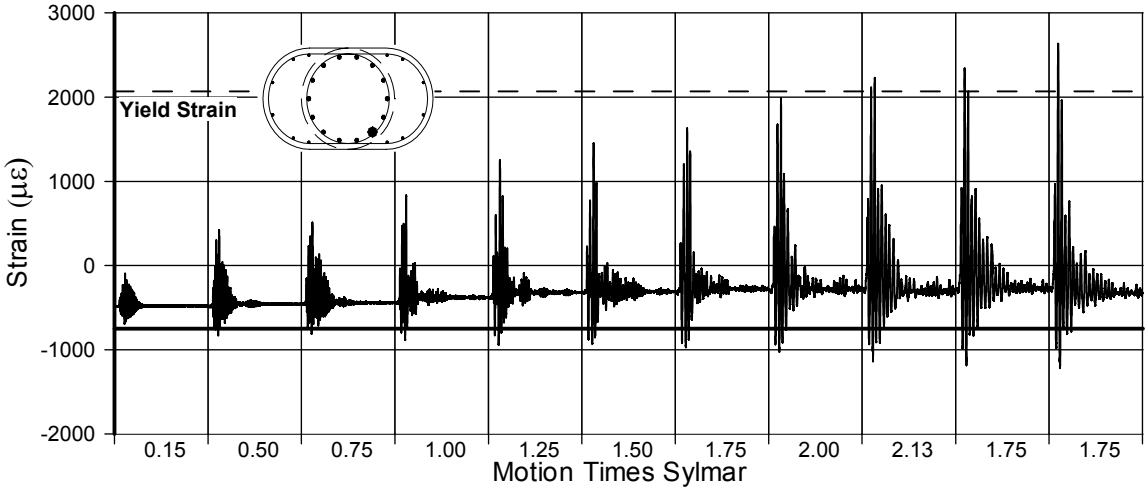

Fig. A-122 - Measured Strain in Gauge No. 150 for LFCD1

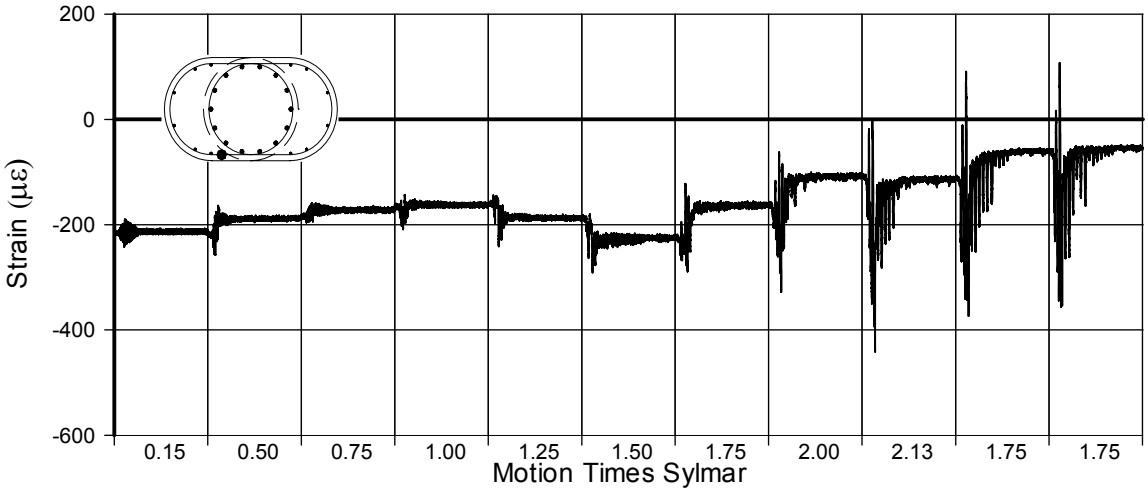

Fig. A-123 - Measured Strain in Gauge No. 152 for LFCD1

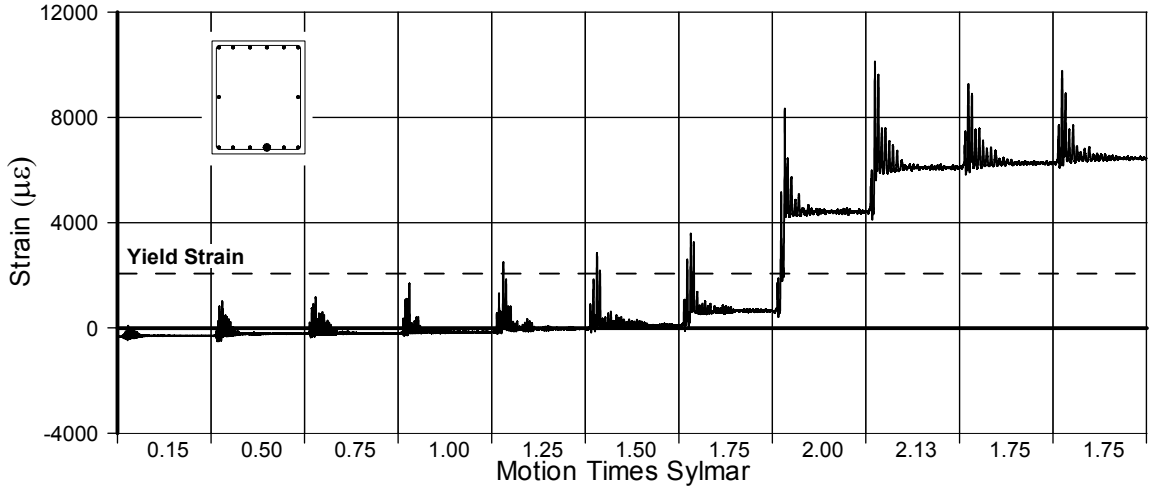

Fig. A-124 - Measured Strain in Gauge No. 153 for LFCD1

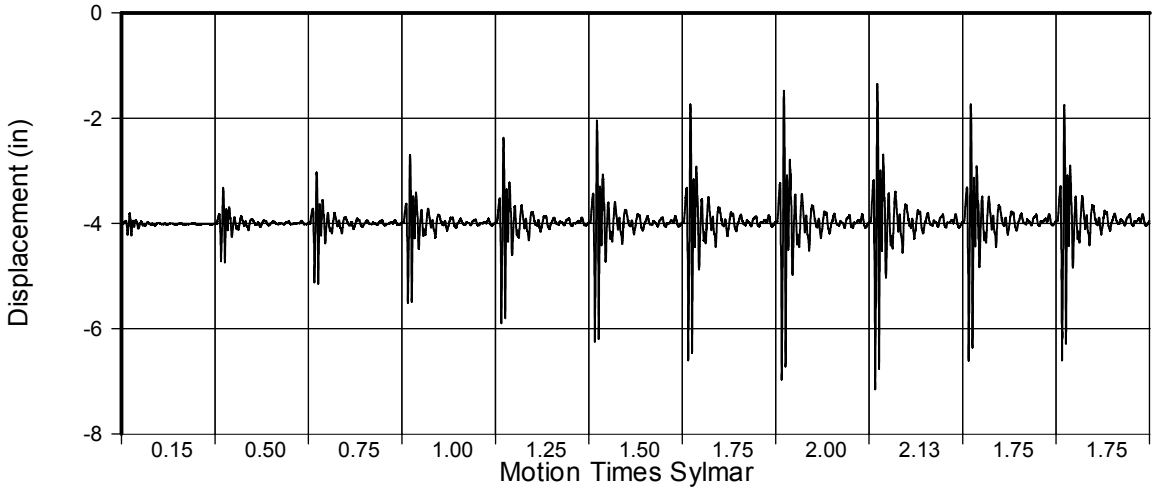

Fig. A-125 - Measured Shake Table Displacement for LFCD1

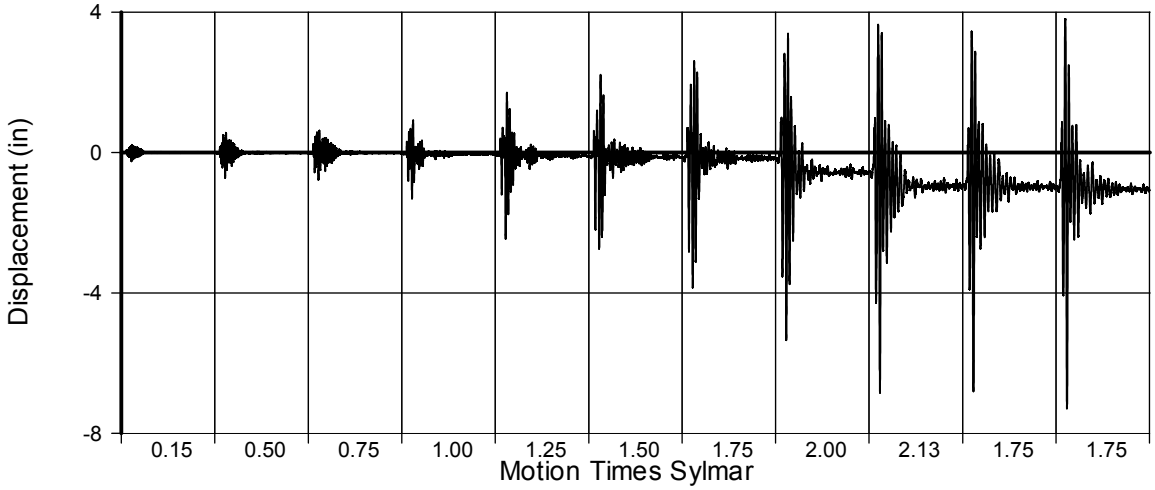

Fig. A-126 - Measured Beam's Relative Dispalcement for LFCD1

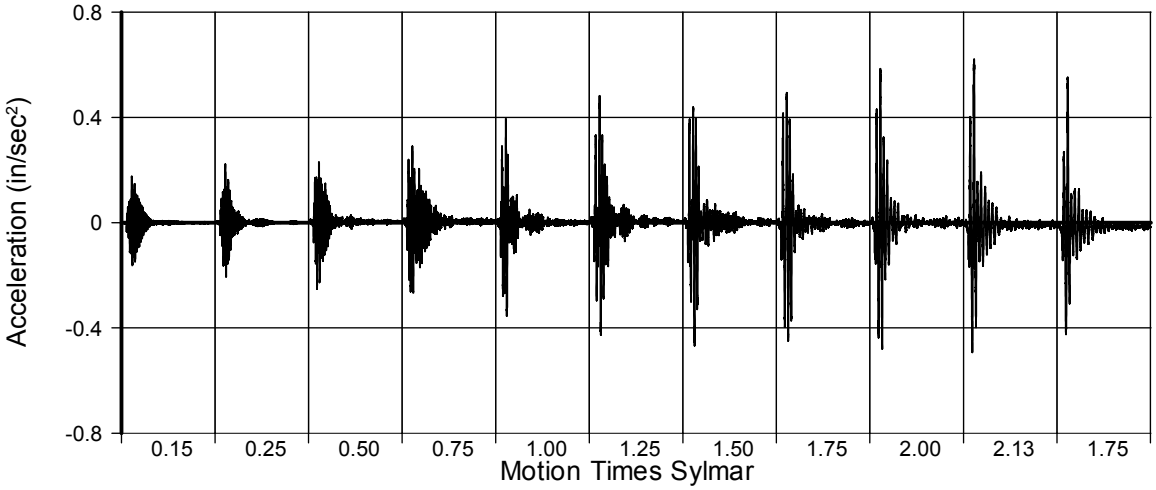

Fig. A-127 - Measured In-Plane Acceleration for LFCD2

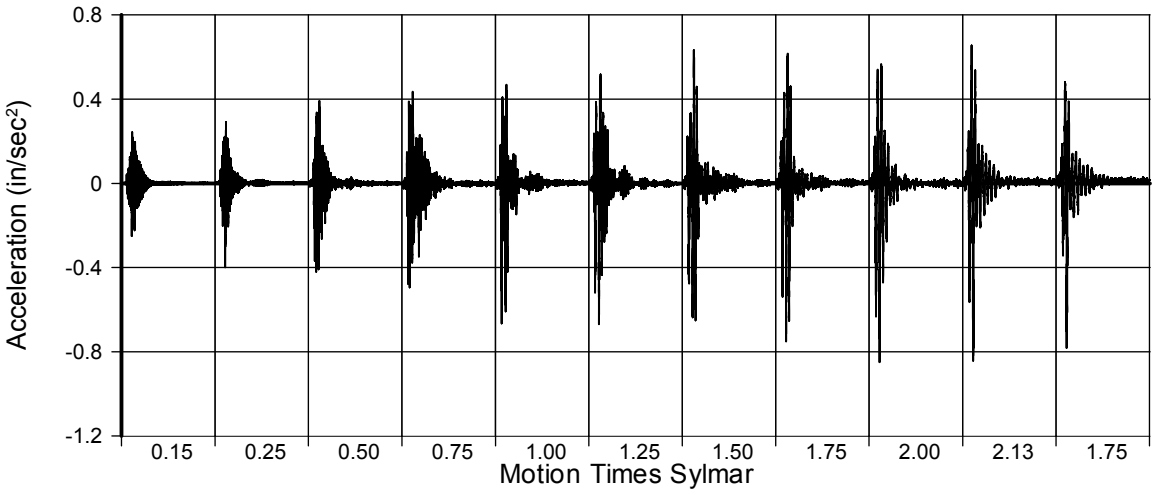

Fig. A-128 - Measured In-Plane Acceleration for LFCD2 (Bucket Mounted)

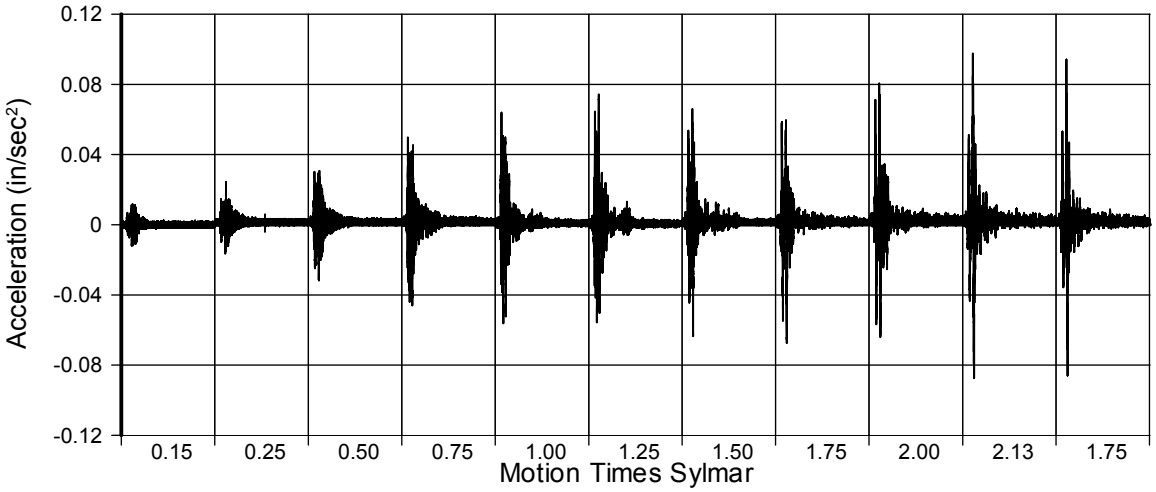

Fig. A-129 - Measured Transverse Acceleration for LFCD1

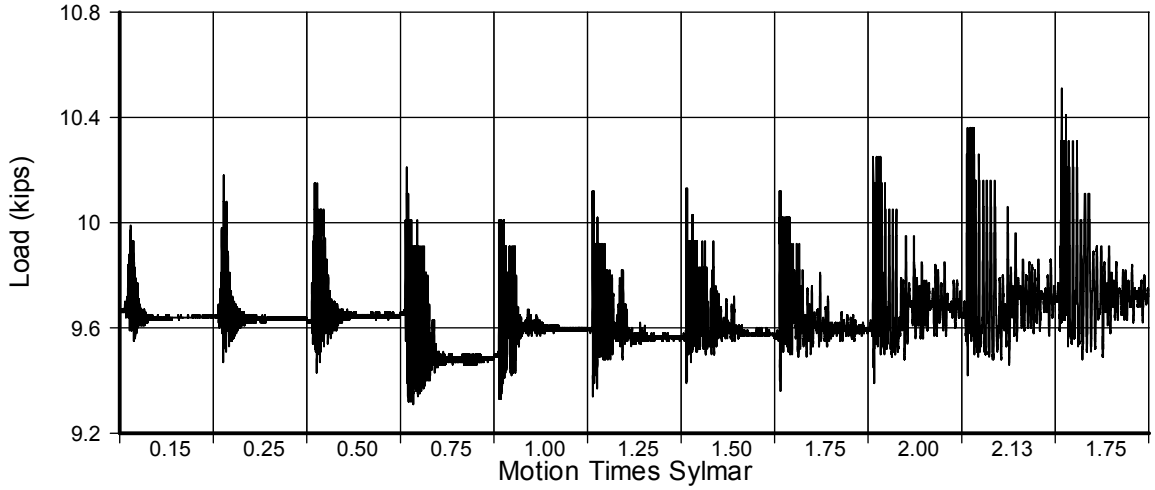

Fig. A-130 - Measured Vertical Load for LFCD2 (West Column)

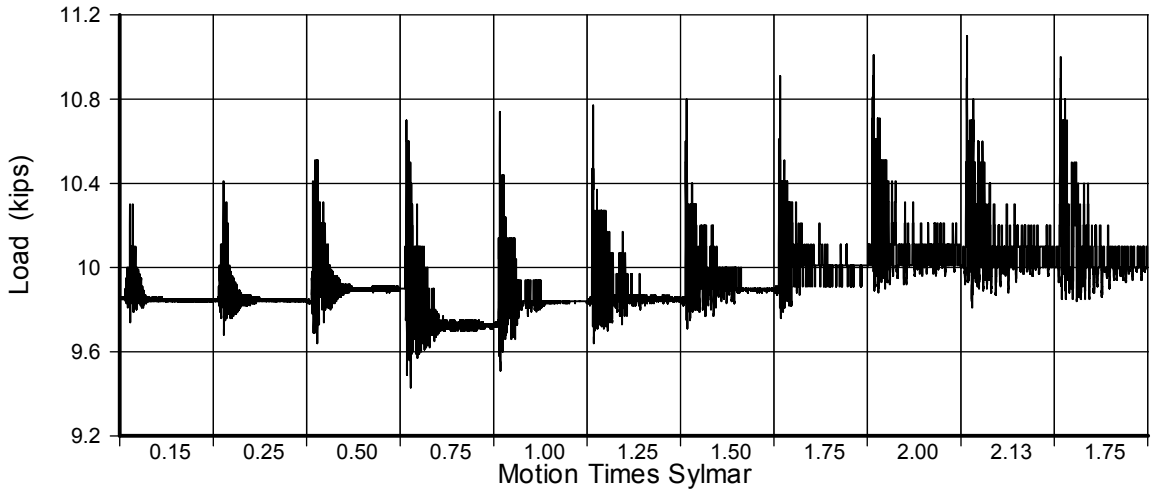

Fig. A-131 - Measured Vertical Load for LFCD2 (East Column)

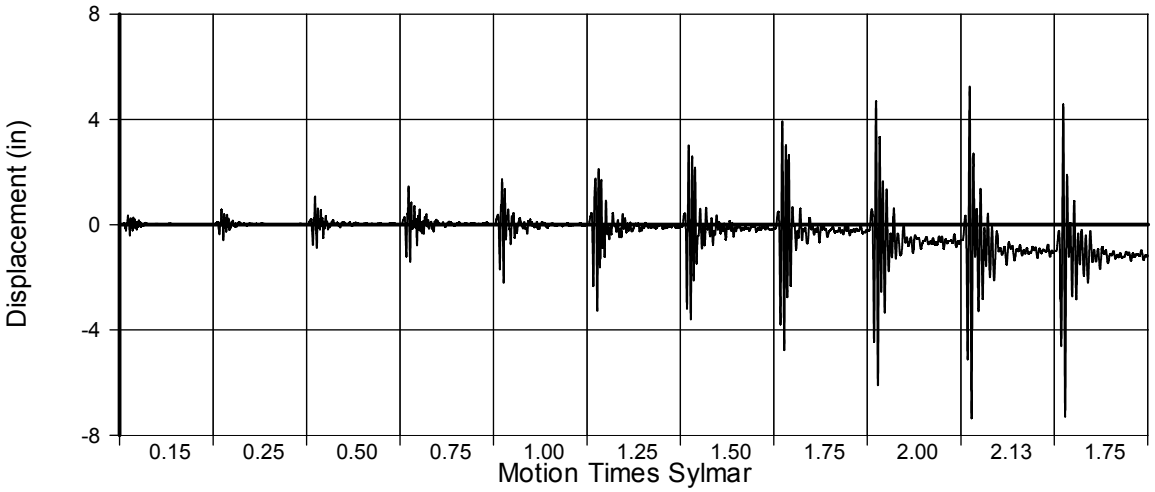

Fig. A-132 - Measured Absoulte Displacement for LFCD1

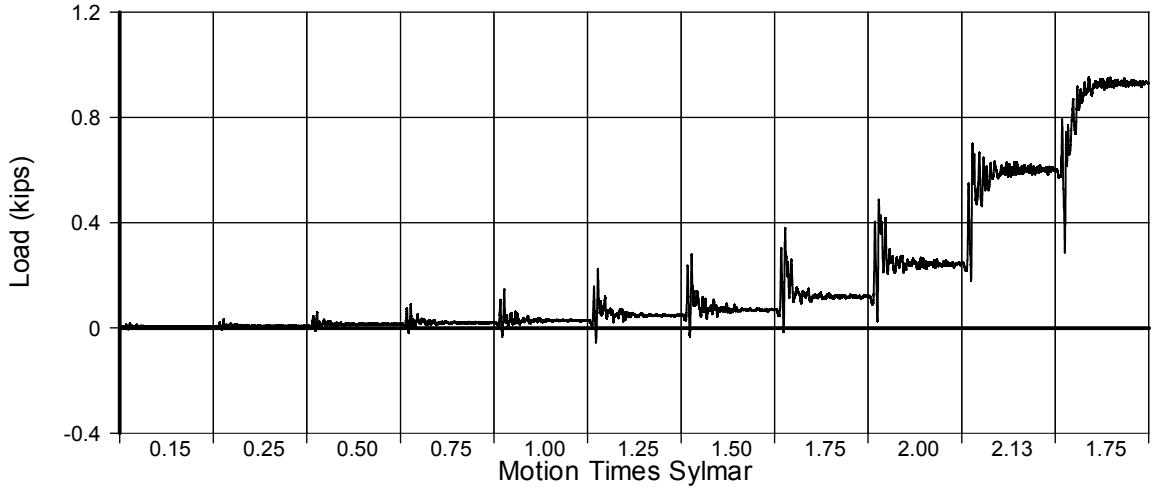

Fig. A-133 - Measured Transverse Disp. for LFCD2

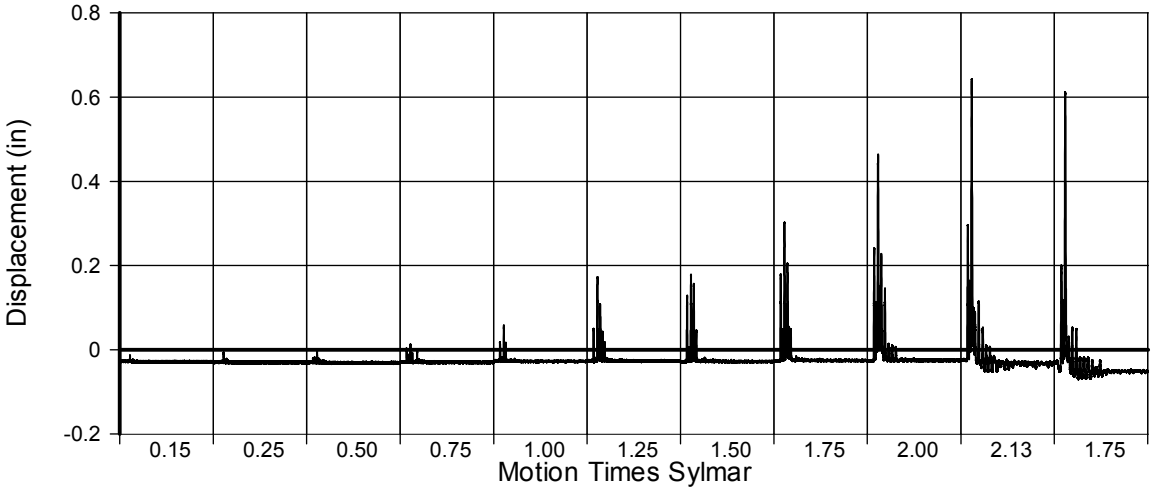

Fig. A-134 - Measured Vertical Mid-Span Deflection for LFCD2

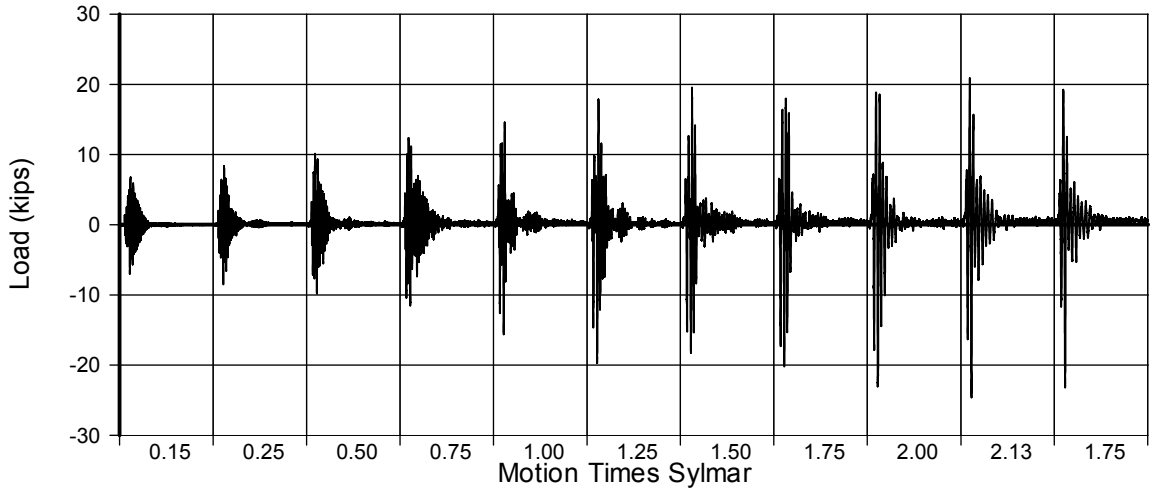

Fig. A-135 - Measured Link Load for LFCD1

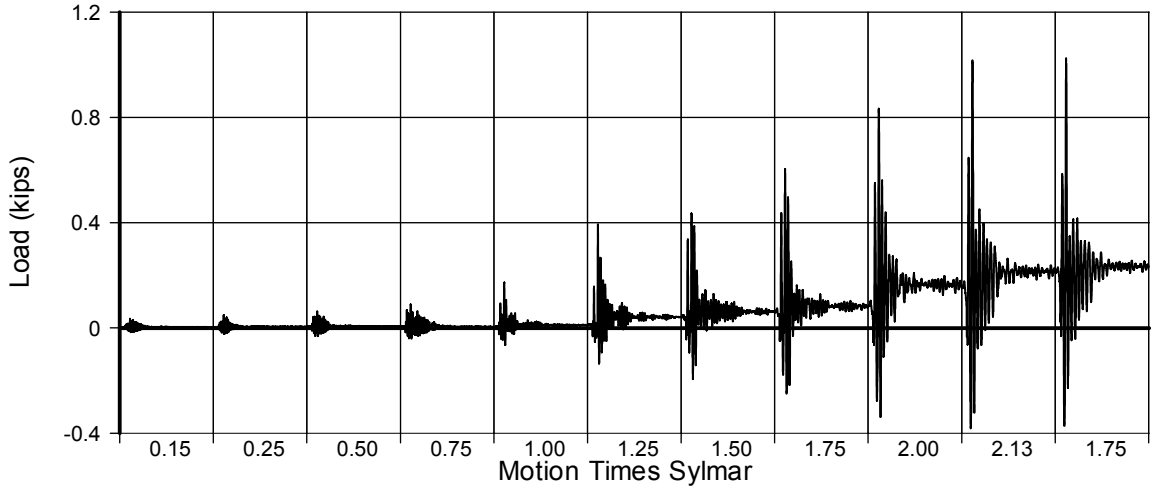

Fig. A-136 - Measured Disp. in Transducer No. 9 for LFCD2

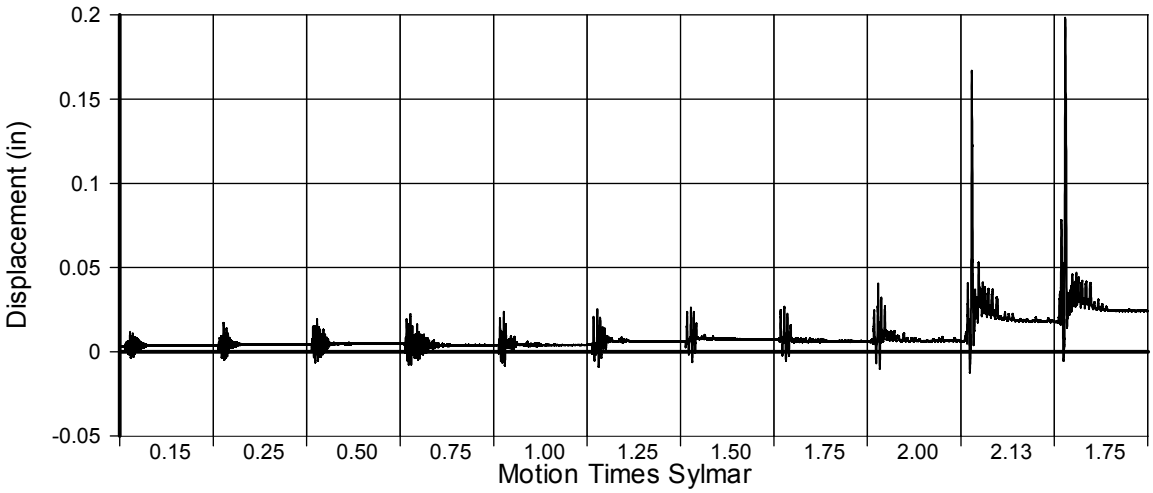

Fig. A-137 - Measured Disp. in Transducer No. 10 for LFCD2

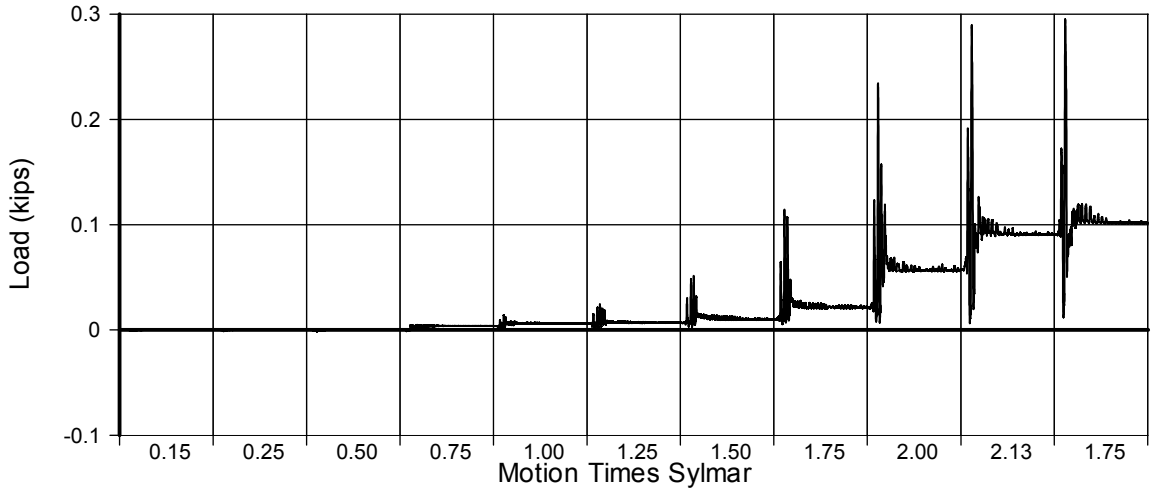

Fig. A-138 - Measured Disp. in Transducer No. 11 for LFCD1

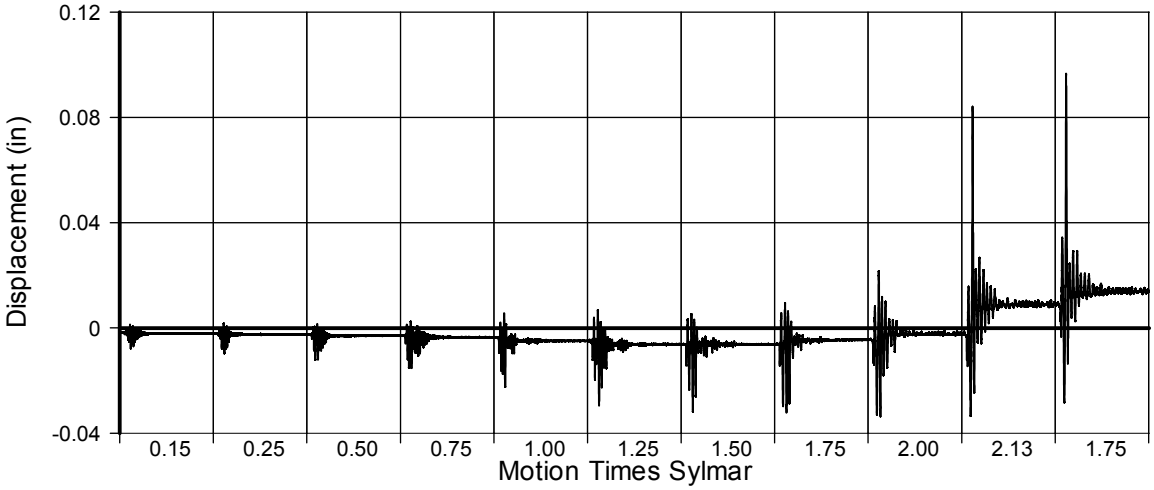

Fig. A-139 - Measured Disp. in Transducer No. 12 for LFCD2

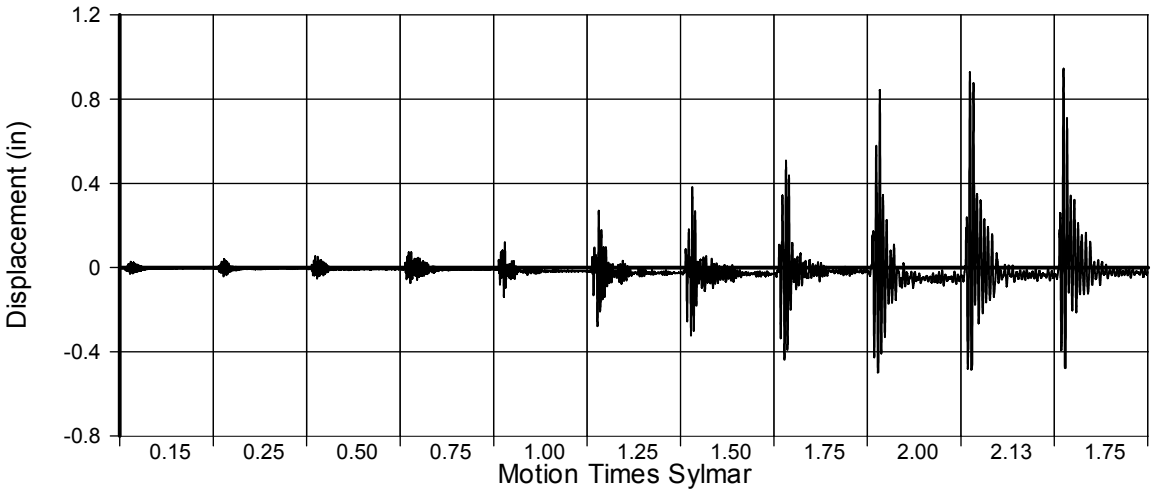

Fig. A-140 - Measured Disp. in Transducer No. 13 for LFCD2

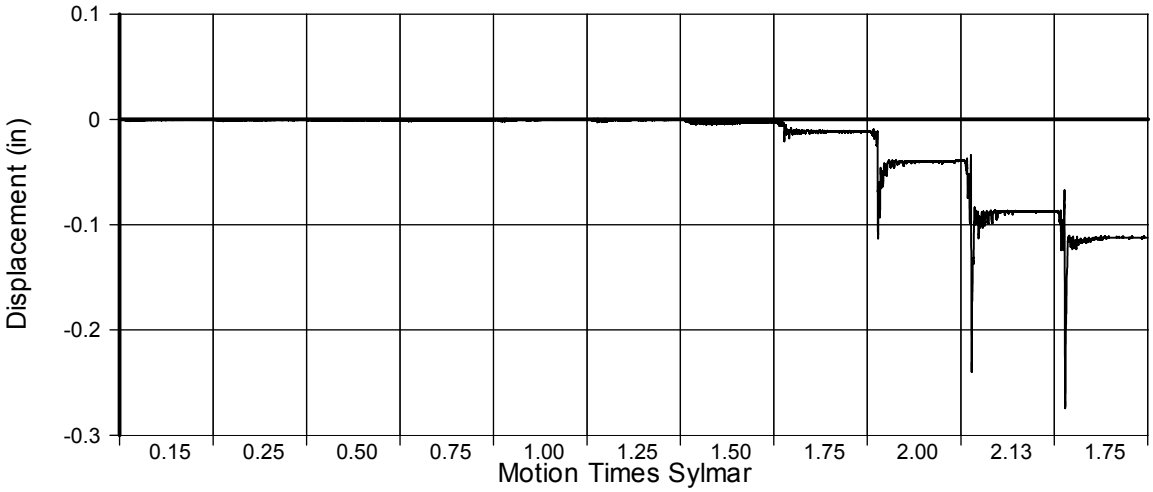

Fig. A-141 - Measured Disp. in Transducer No. 14 for LFCD1

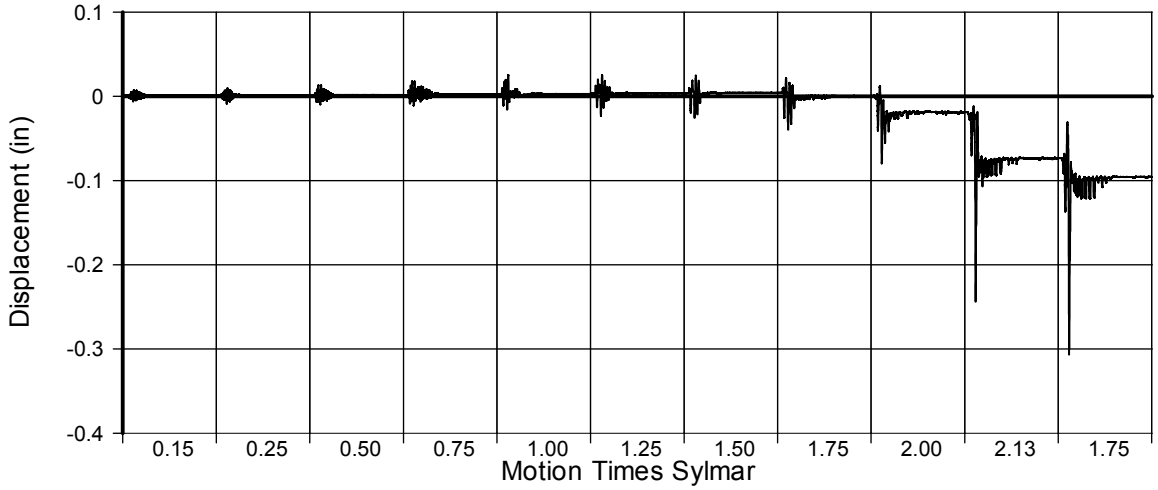

Fig. A-142 - Measured Disp. in Transducer No. 15 for LFCD2

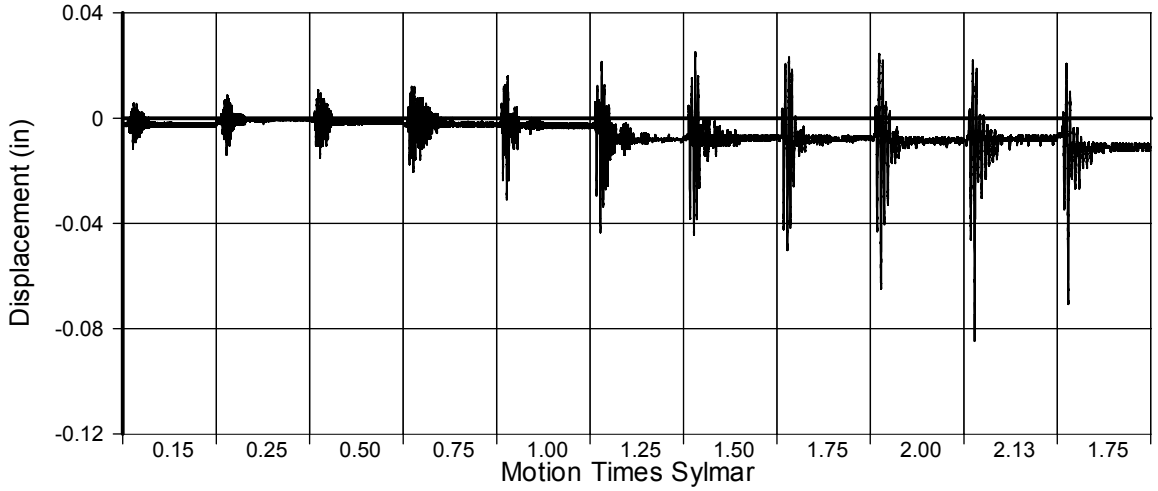

Fig. A-143 - Measured Disp. in Transducer No. 16 for LFCD2

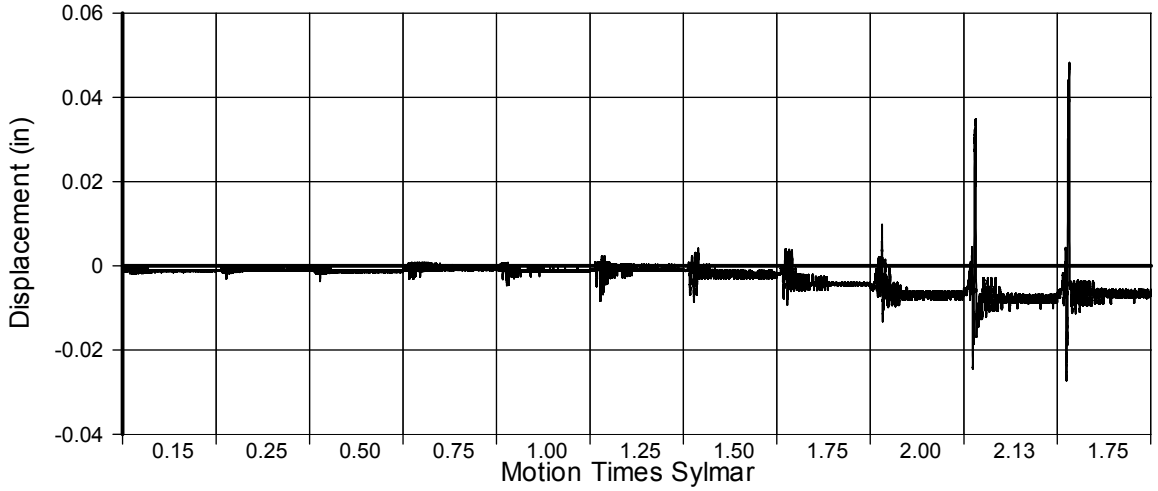

Fig. A-144 - Measured Disp. in Transducer No. 18 for LFCD1

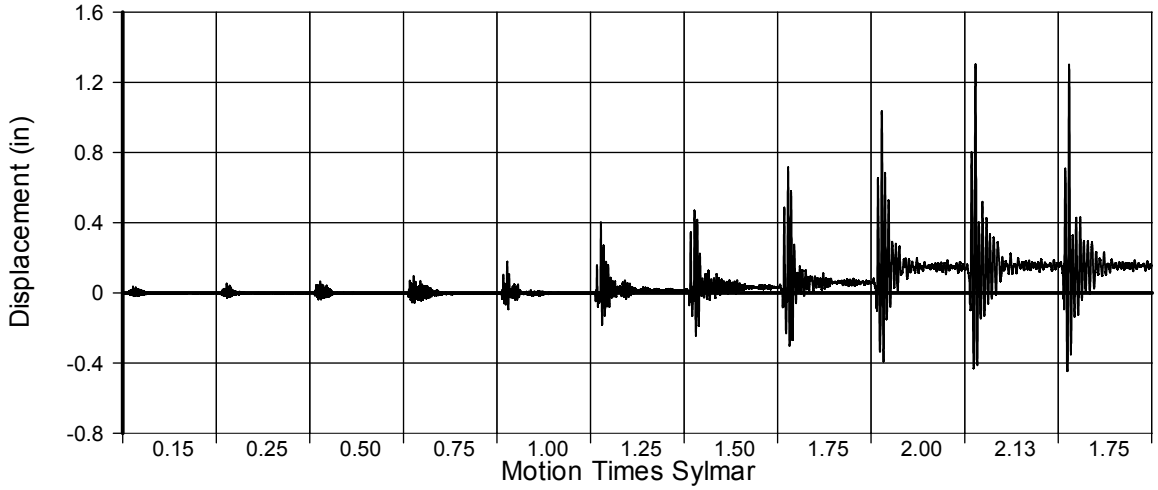

Fig. A-145 - Measured Disp. in Transducer No. 19 for LFCD2

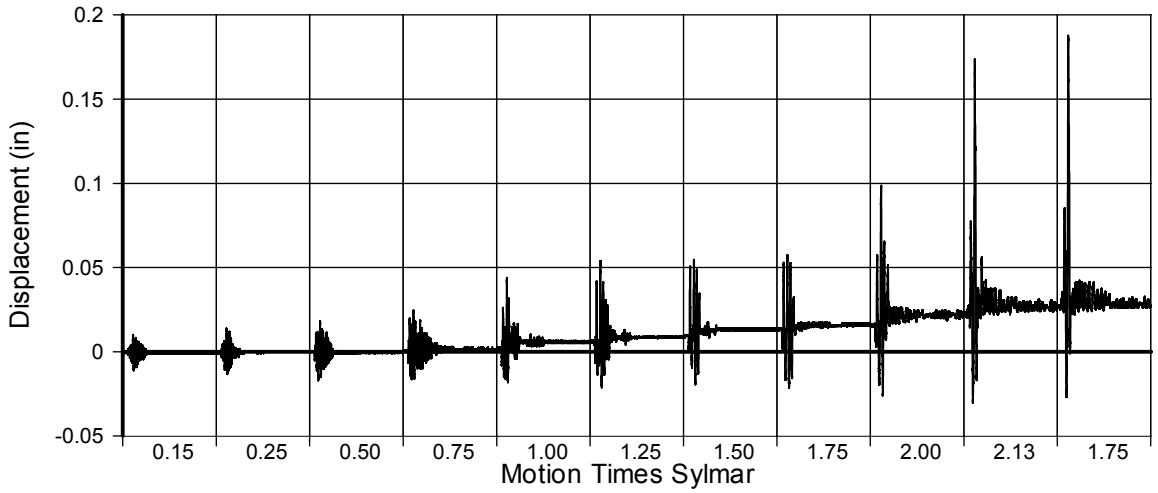

Fig. A-146 - Measured Disp. in Transducer No. 20 for LFCD2

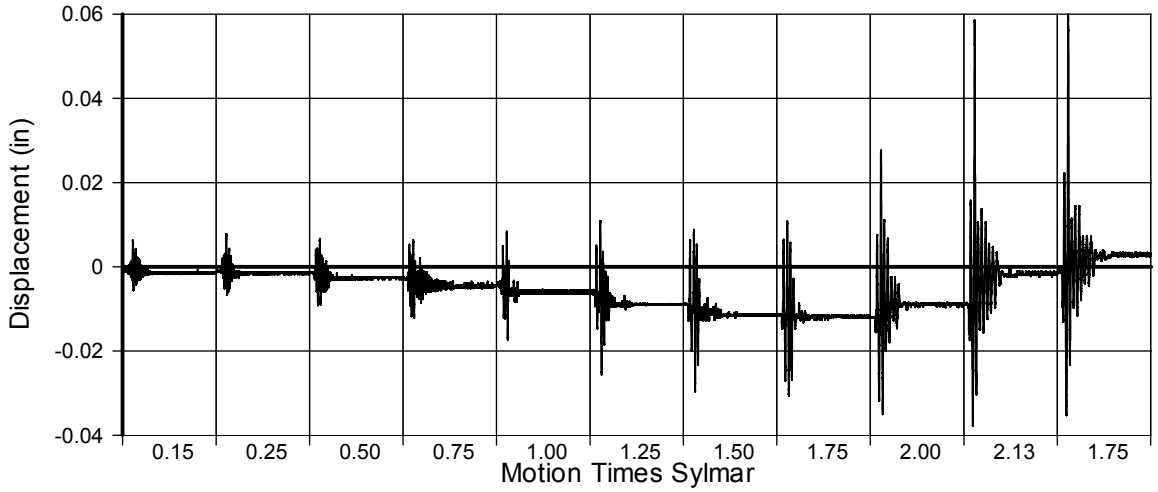

Fig. A-147 - Measured Disp. in Transducer No. 21 for LFCD1

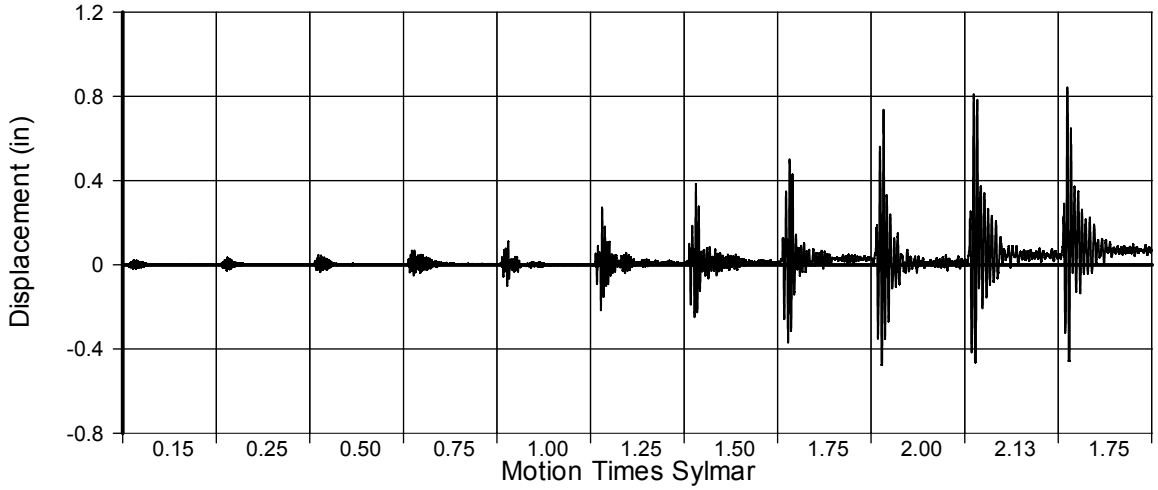

Fig. A-148 - Measured Disp. in Transducer No. 22 for LFCD2

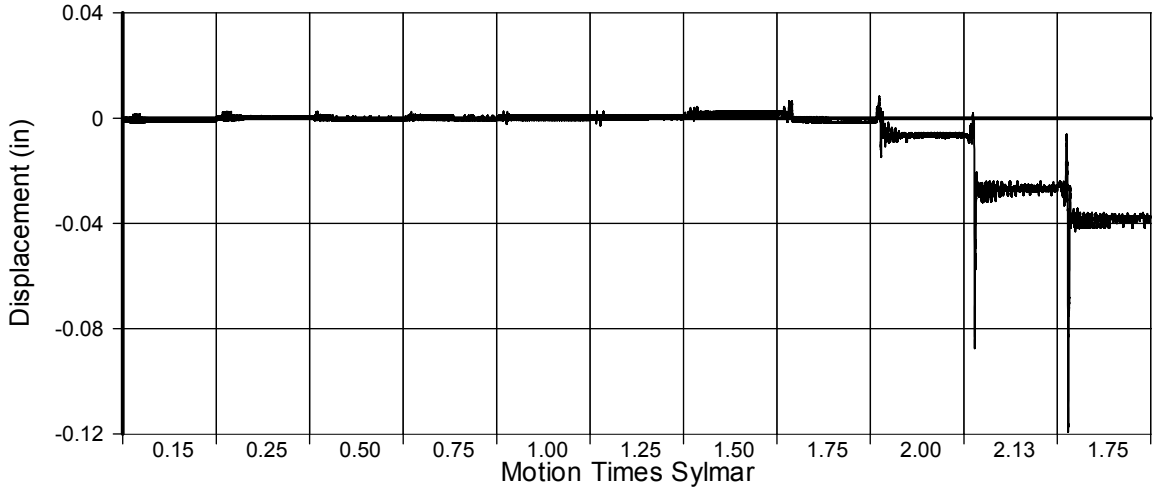

Fig. A-149 - Measured Disp. in Transducer No. 23 for LFCD2

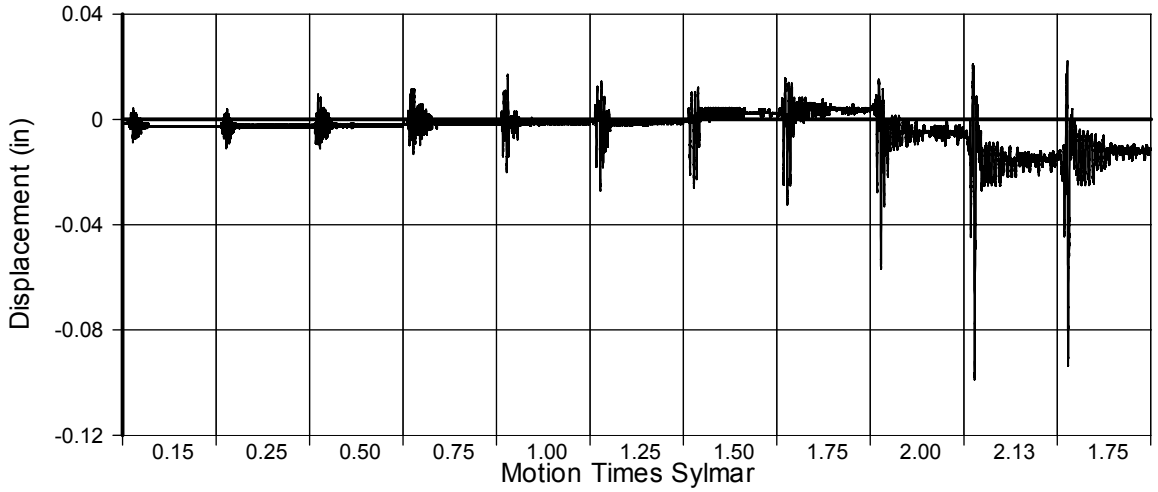

Fig. A-150 - Measured Disp. in Transducer No. 24 for LFCD1

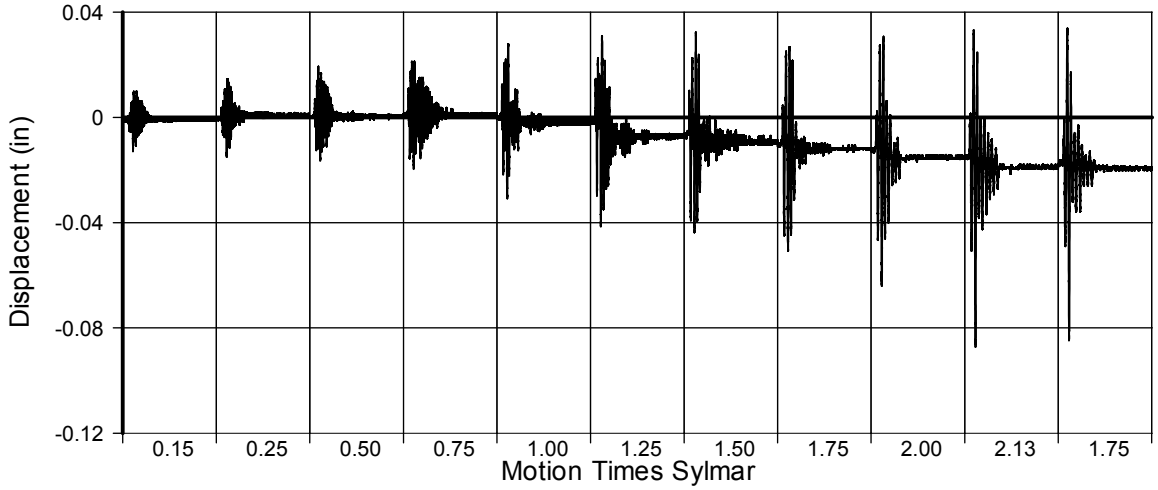

Fig. A-151 - Measured Disp. in Transducer No. 25 for LFCD2

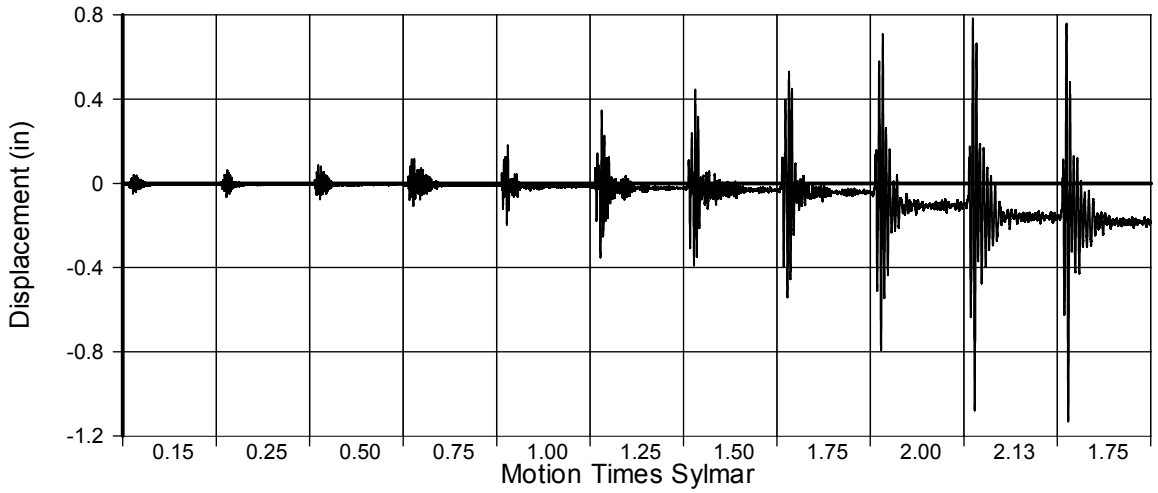

Fig. A-152 - Measured Disp. in Transducer No. 26 for LFCD2

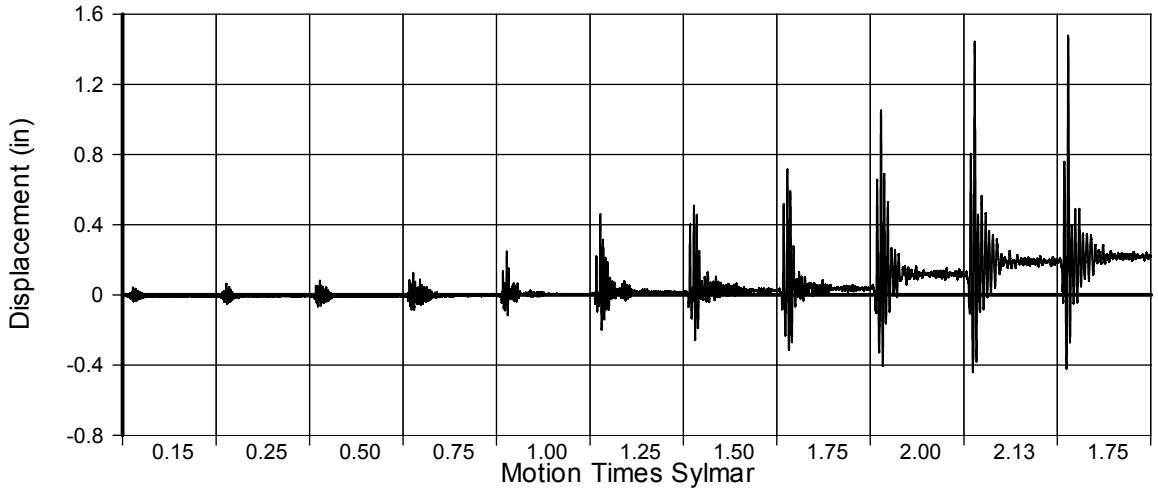

Fig. A-153 - Measured Disp. in Transducer No. 27 for LFCD1

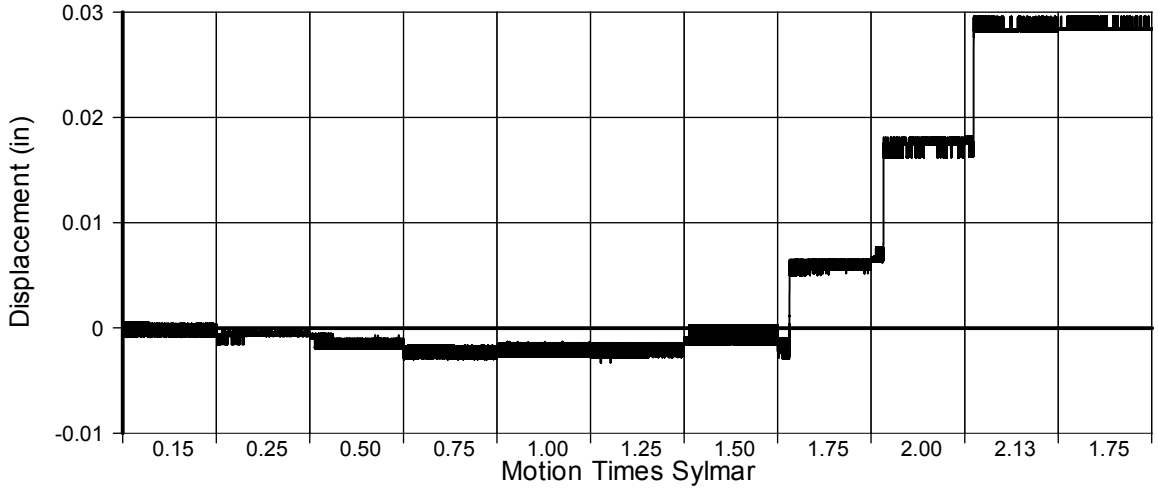

Fig. A-154 - Measured Disp. in Transducer No. 28 for LFCD2

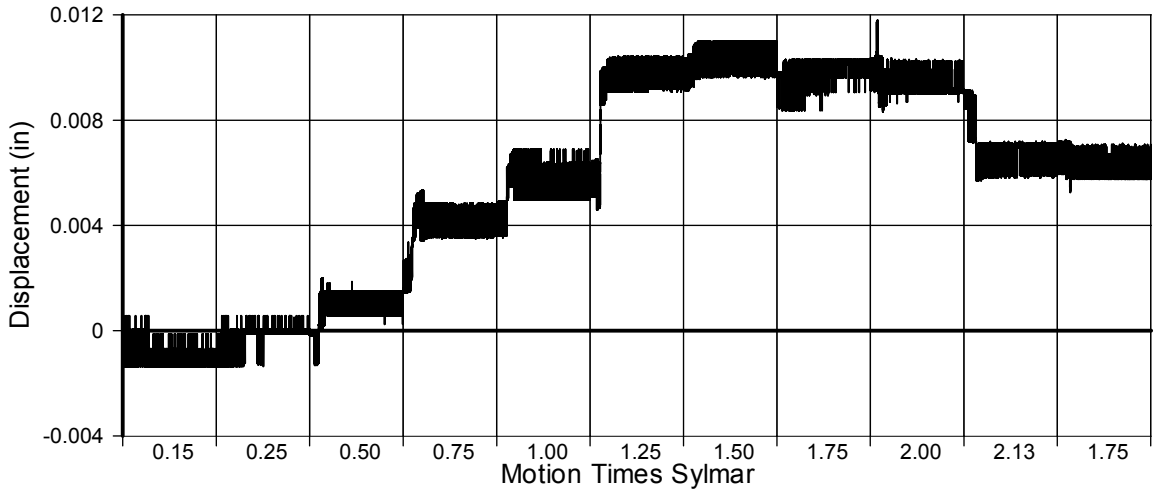

Fig. A-155 - Measured Disp. in Transducer No. 29 for LFCD2

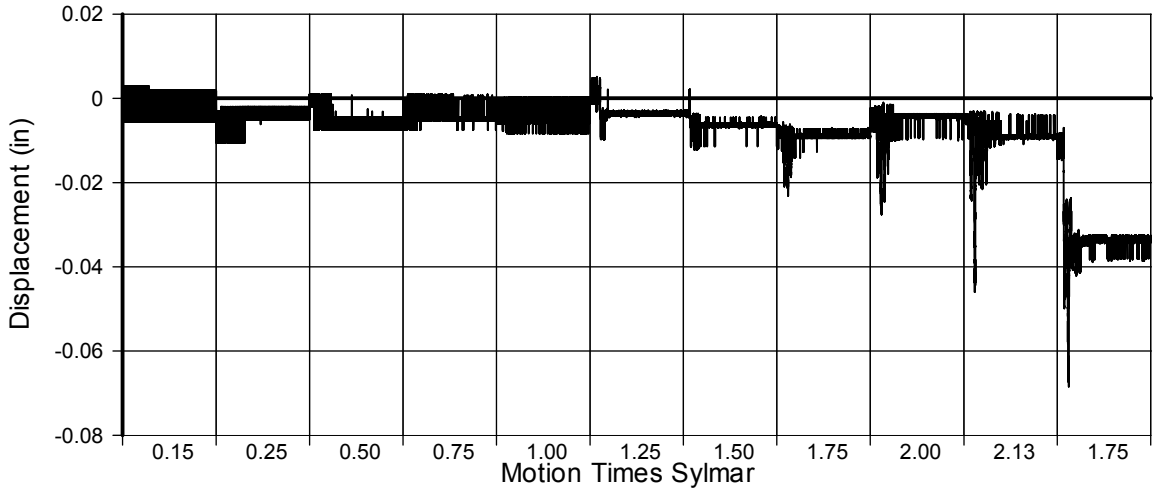

Fig. A-156 - Measured Disp. in Transducer No. 30 for LFCD1

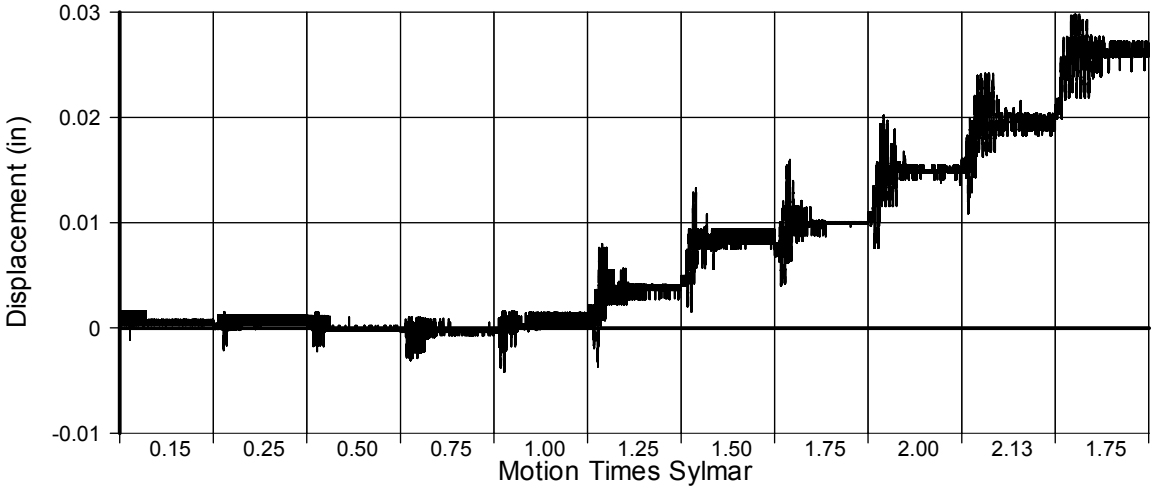

Fig. A-157 - Measured Disp. in Transducer No. 31 for LFCD2

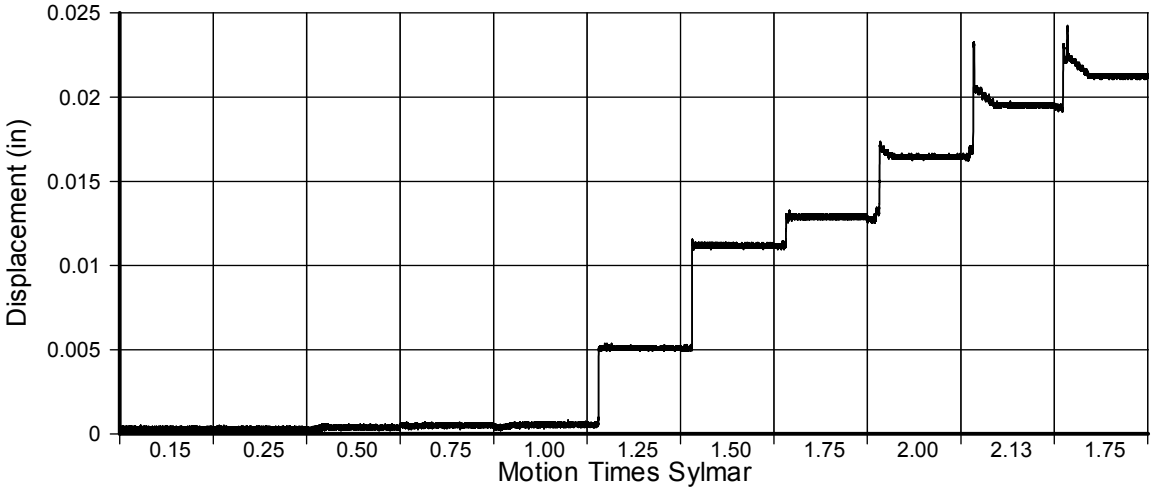

Fig. A-158 - Measured Disp. in Transducer No. 32 for LFCD2

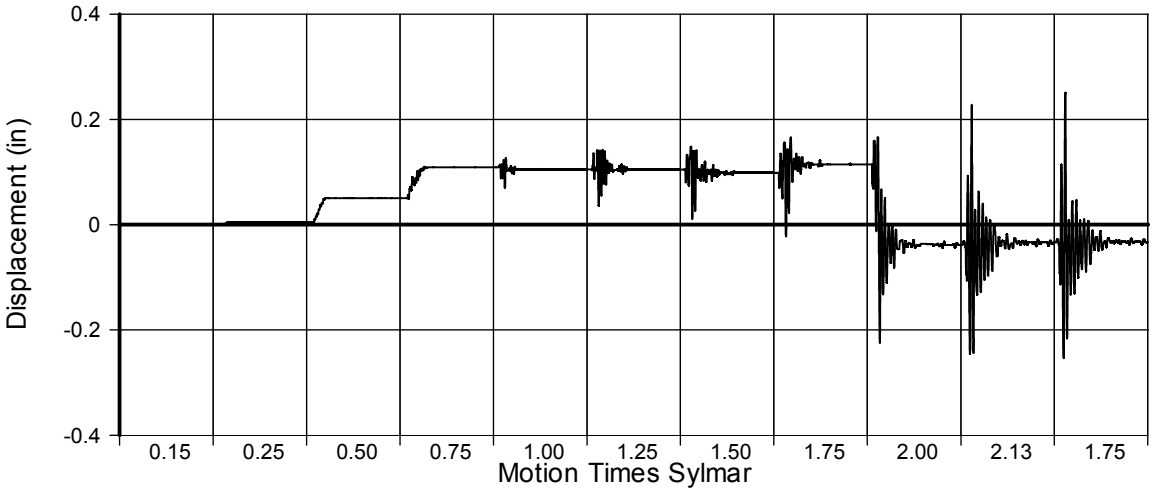

Fig. A-159 - Measured Disp. in Transducer No. 33 for LFCD1

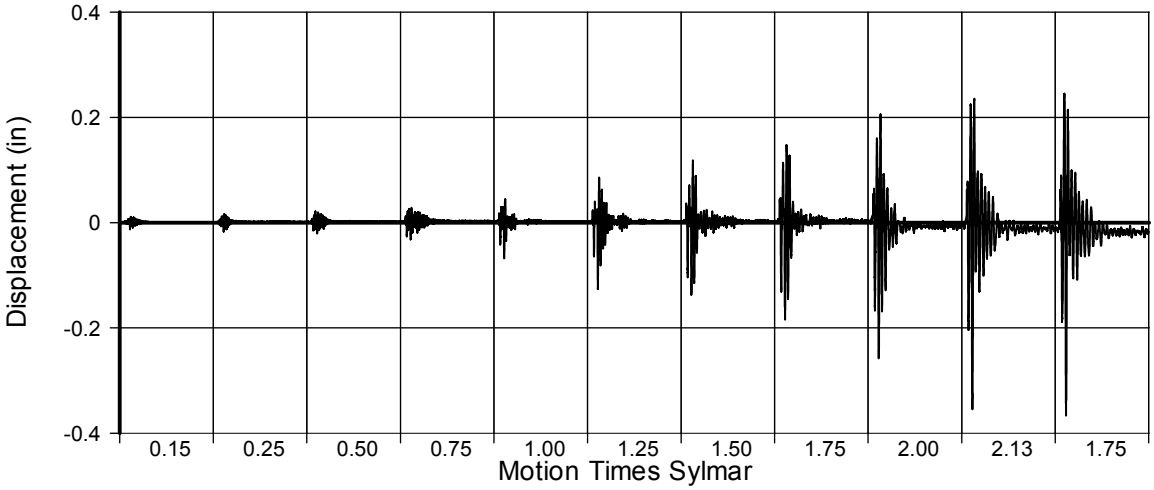

Fig. A-160 - Measured Disp. in Transducer No. 34 for LFCD2

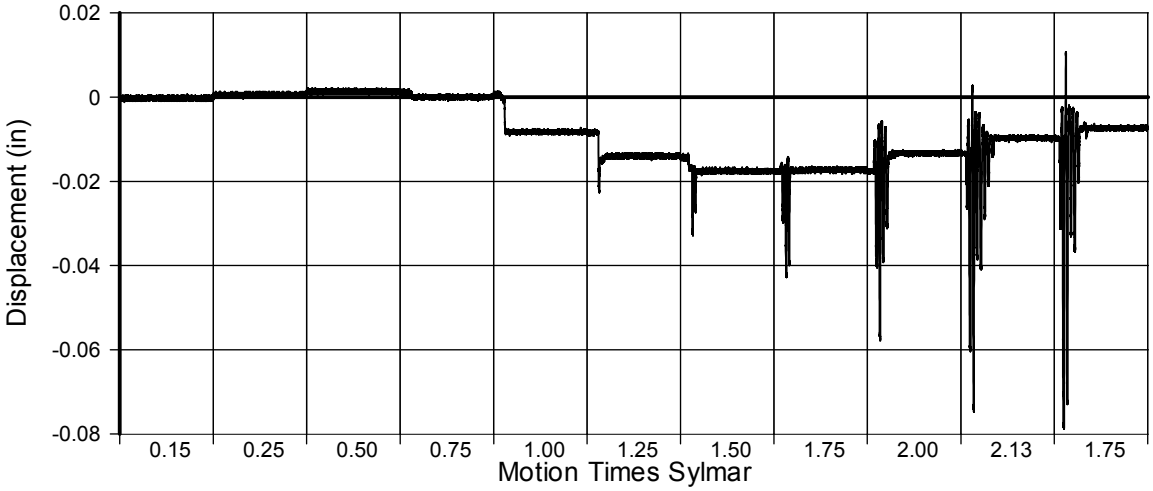

Fig. A-161 - Measured Disp. in Transducer No. 35 for LFCD2

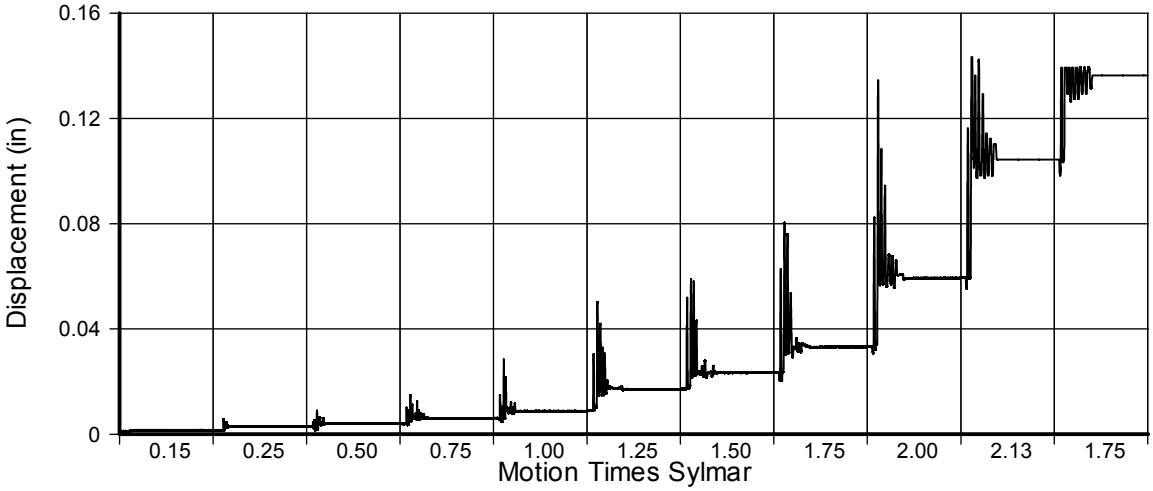

Fig. A-162 - Measured Disp. in Transducer No. 36 for LFCD1

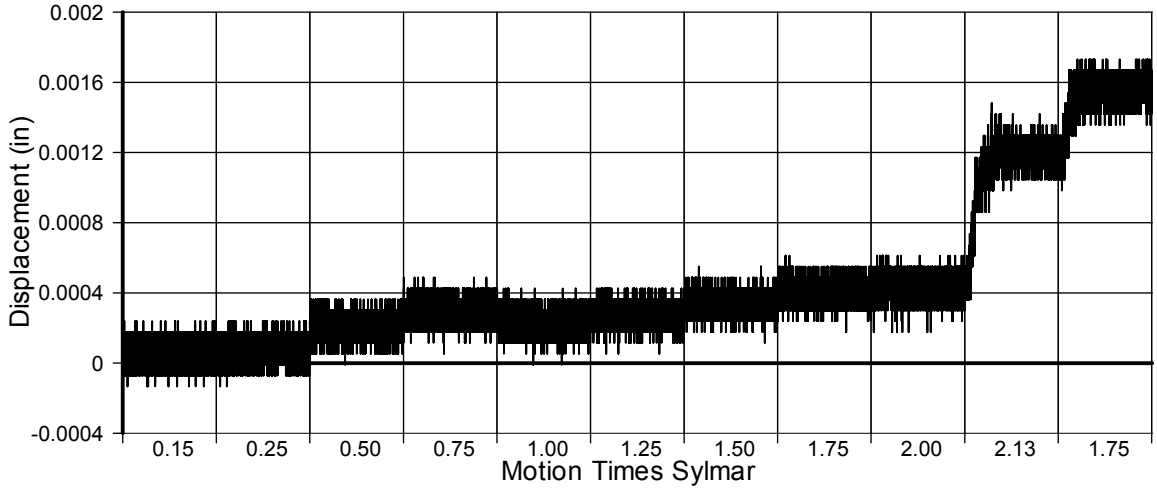

Fig. A-163 - Measured Disp. in Transducer No. 37 for LFCD2

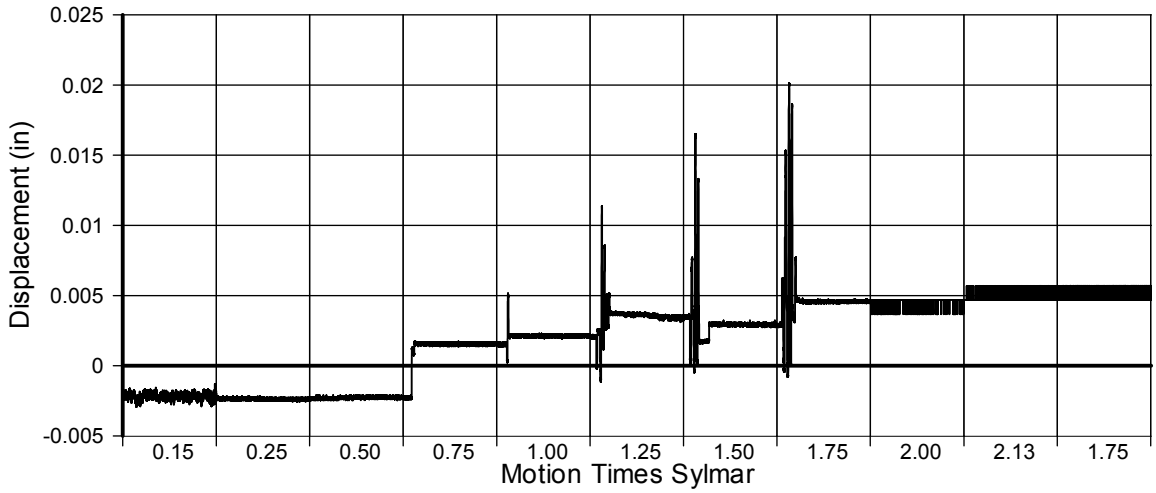

Fig. A-164 - Measured Disp. in Transducer No. 38 for LFCD2

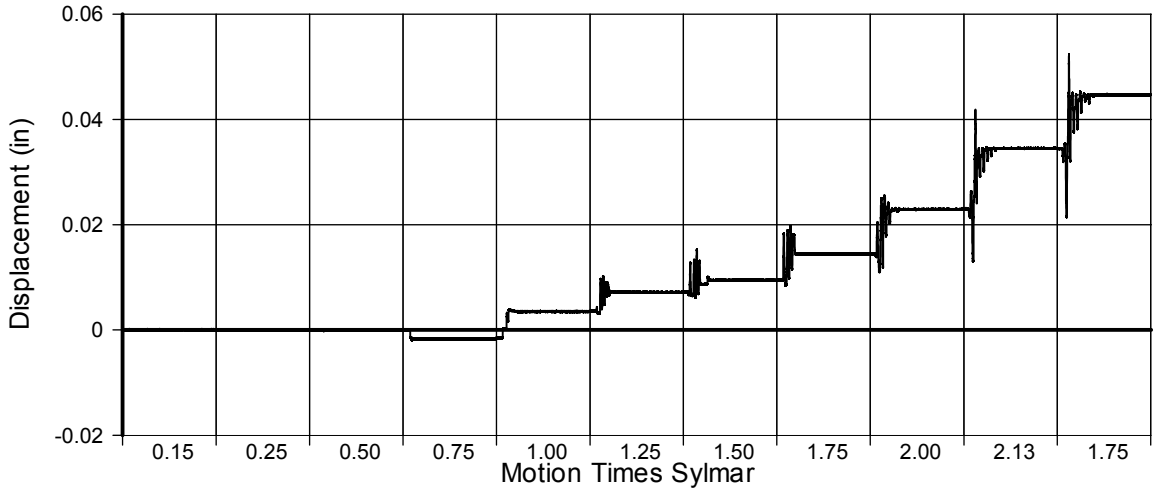

Fig. A-165 - Measured Disp. in Transducer No. 39 for LFCD1

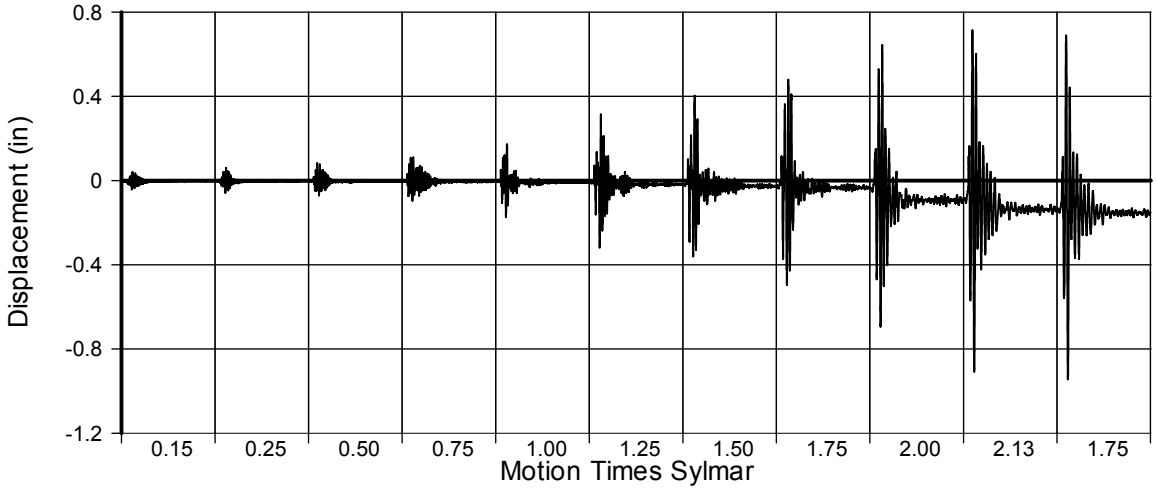

Fig. A-166 - Measured Disp. in Transducer No. 40 for LFCD2

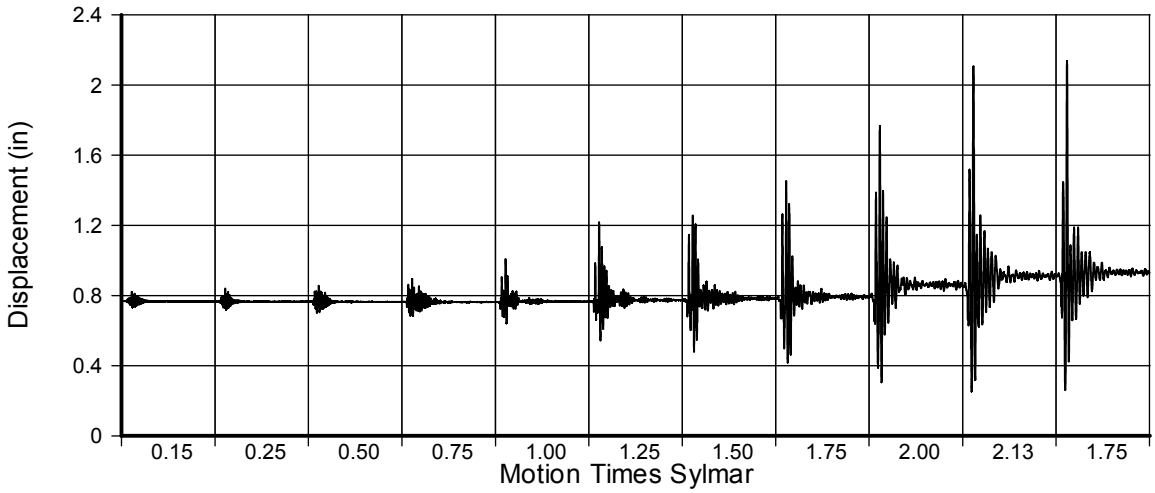

Fig. A-167 - Measured Disp. in Transducer No. 41 for LFCD2

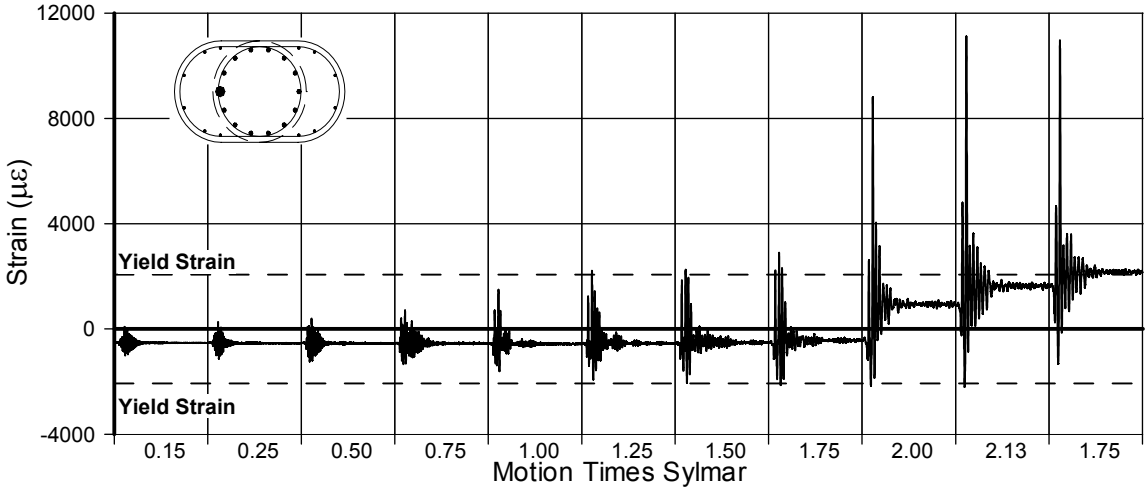

Fig. A-168 - Measured Strain in Gauge No. 43 for LFCD1

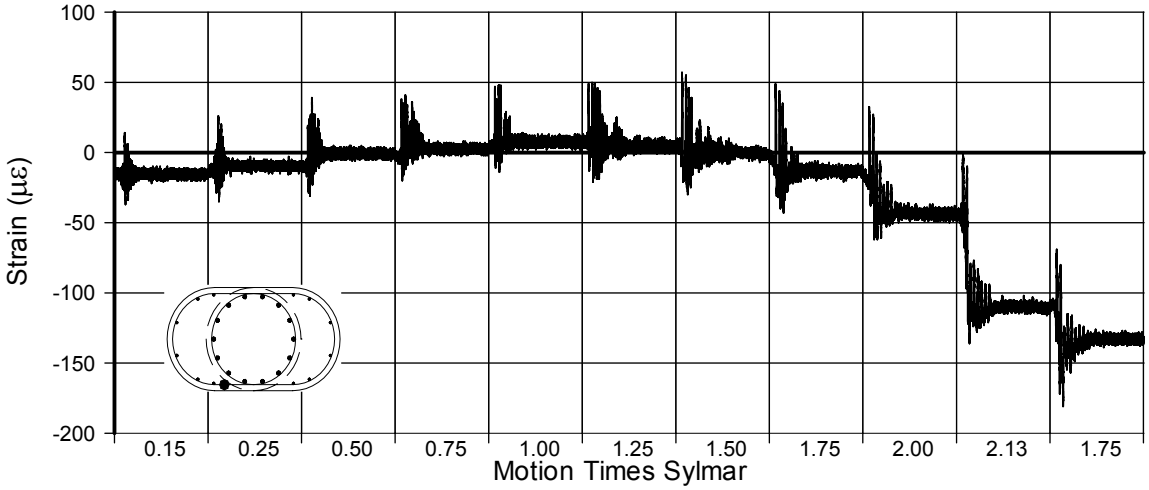

Fig. A-169 - Measured Strain in Gauge No. 44 for LFCD2

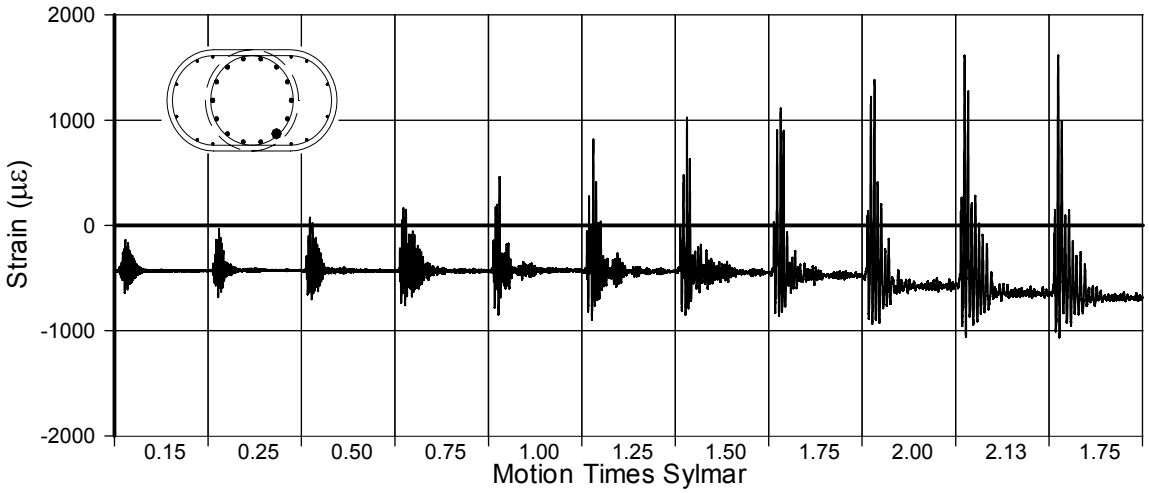

Fig. A-170 - Measured Strain in Gauge No. 45 for LFCD2

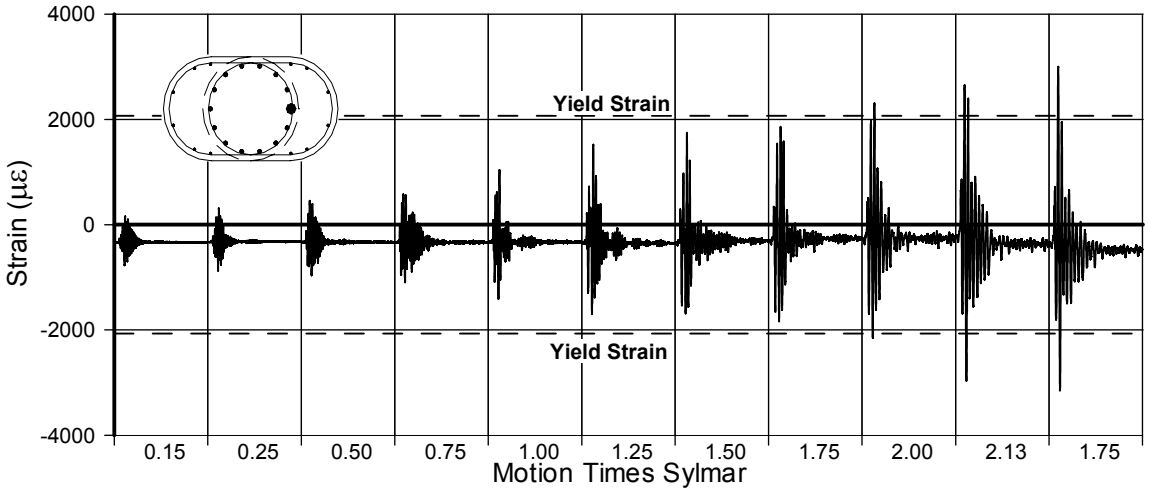

Fig. A-171 - Measured Strain in Gauge No. 46 for LFCD1

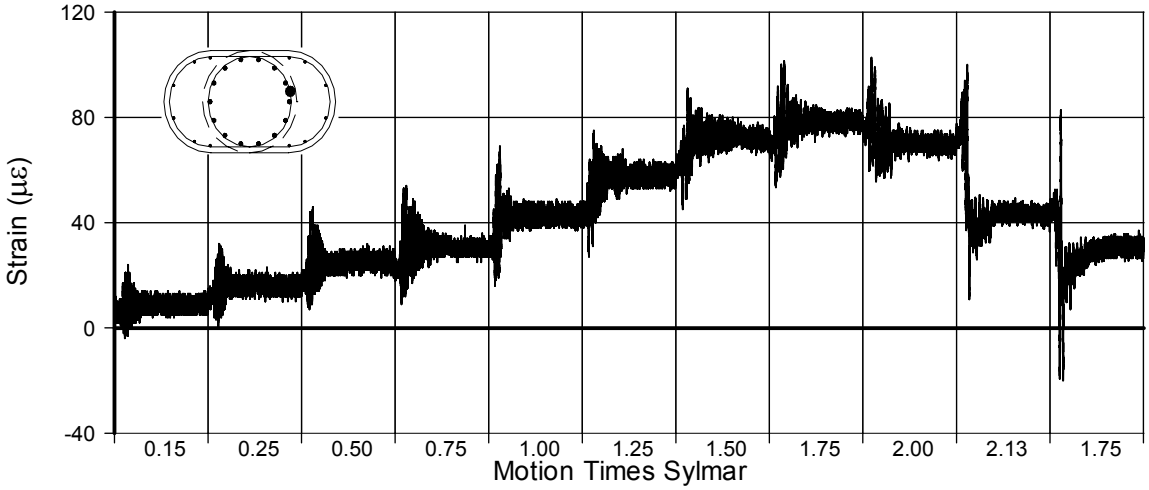

Fig. A-172 - Measured Strain in Gauge No. 48 for LFCD2

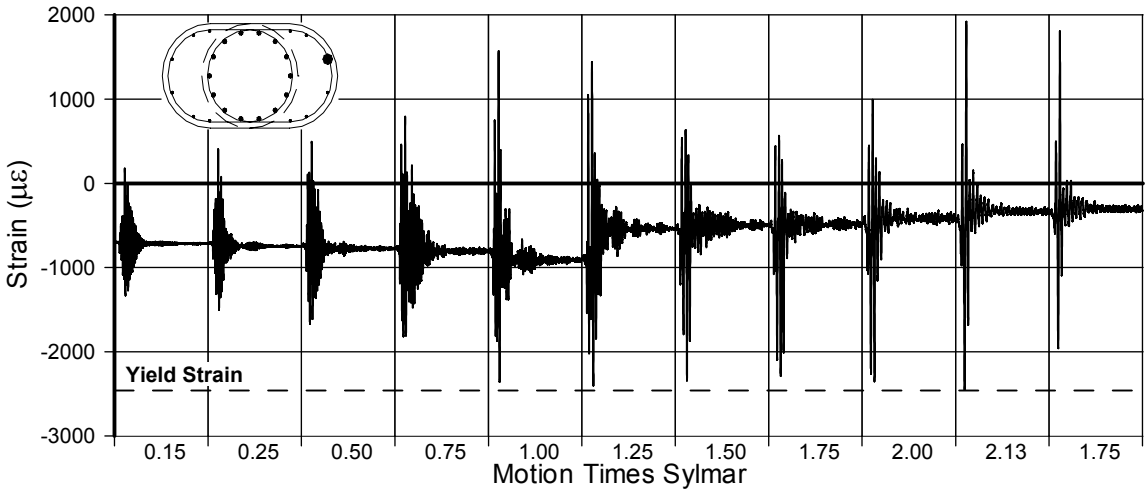

Fig. A-173 - Measured Strain in Gauge No. 49 for LFCD2

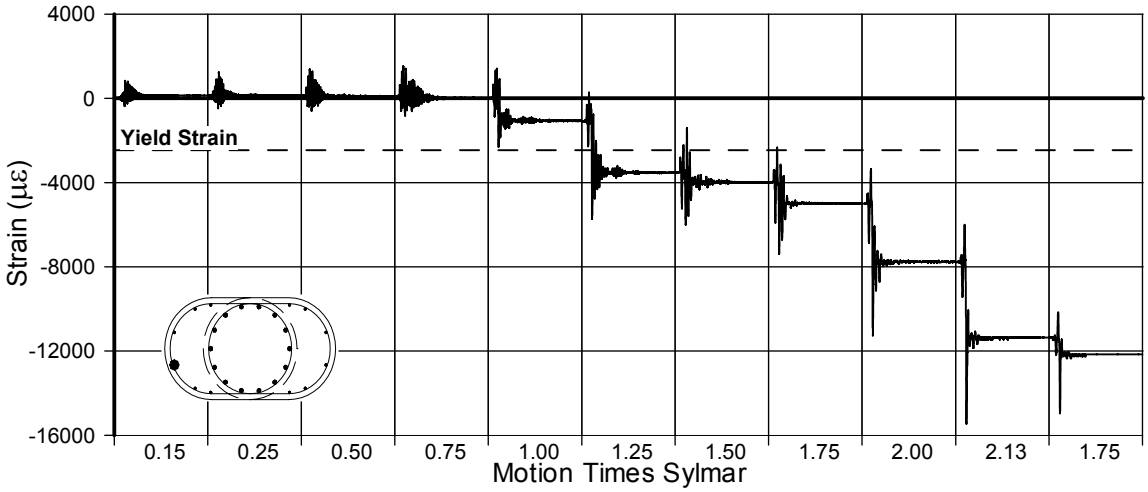

Fig. A-174 - Measured Strain in Gauge No. 50 for LFCD1

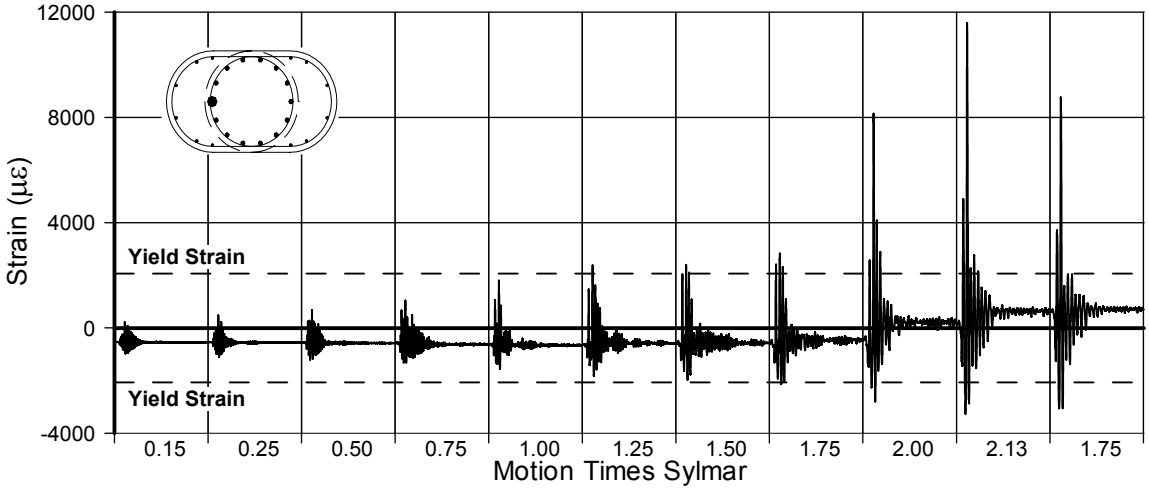

Fig. A-175 - Measured Strain in Gauge No. 51 for LFCD2

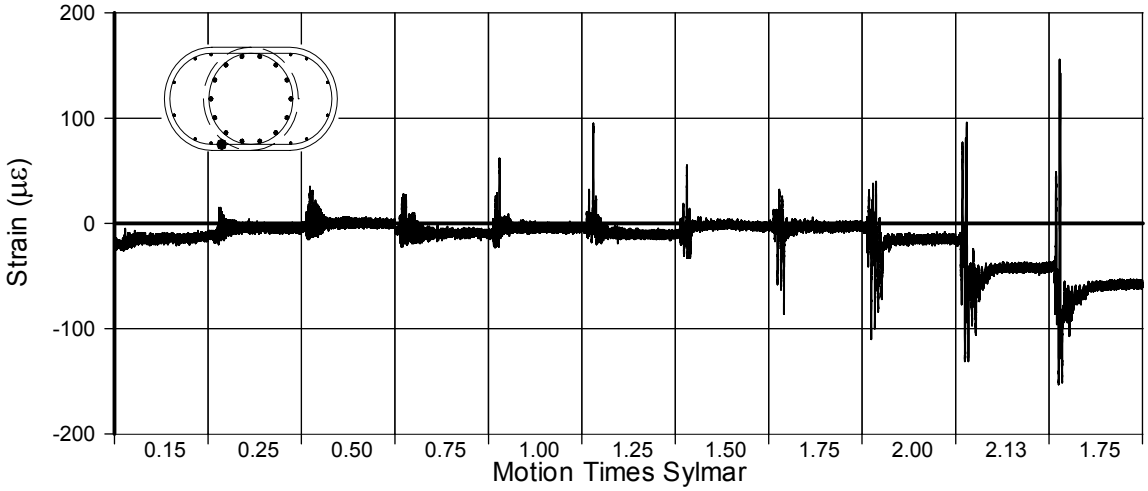

Fig. A-176 - Measured Strain in Gauge No. 52 for LFCD2

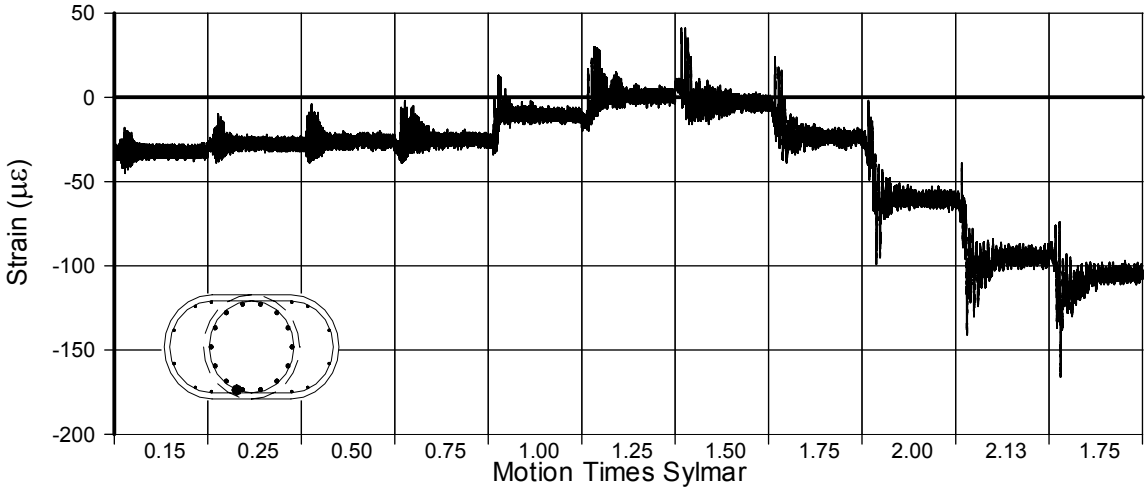

Fig. A-177 - Measured Strain in Gauge No. 53 for LFCD2

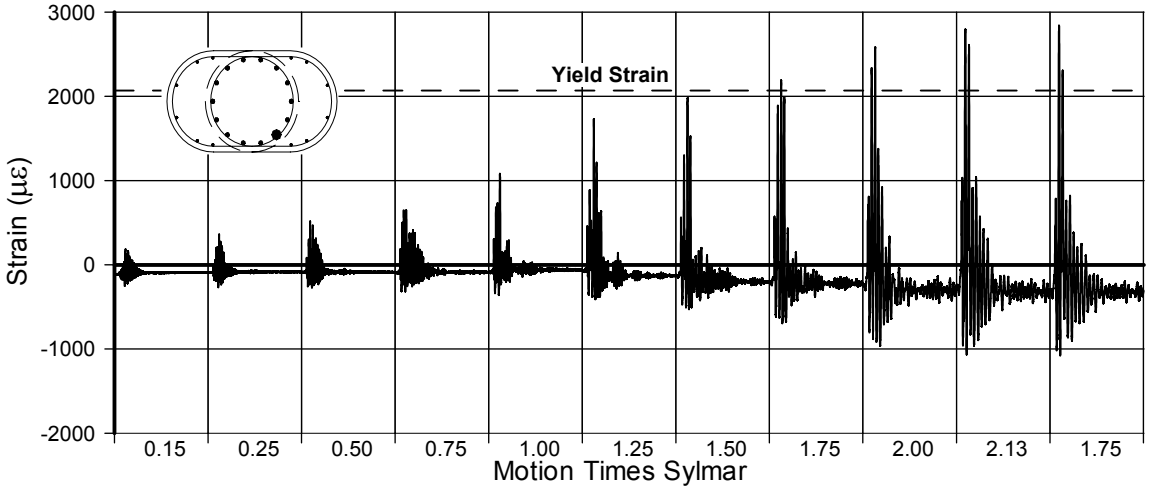

Fig. A-178 - Measured Strain in Gauge No. 54 for LFCD2

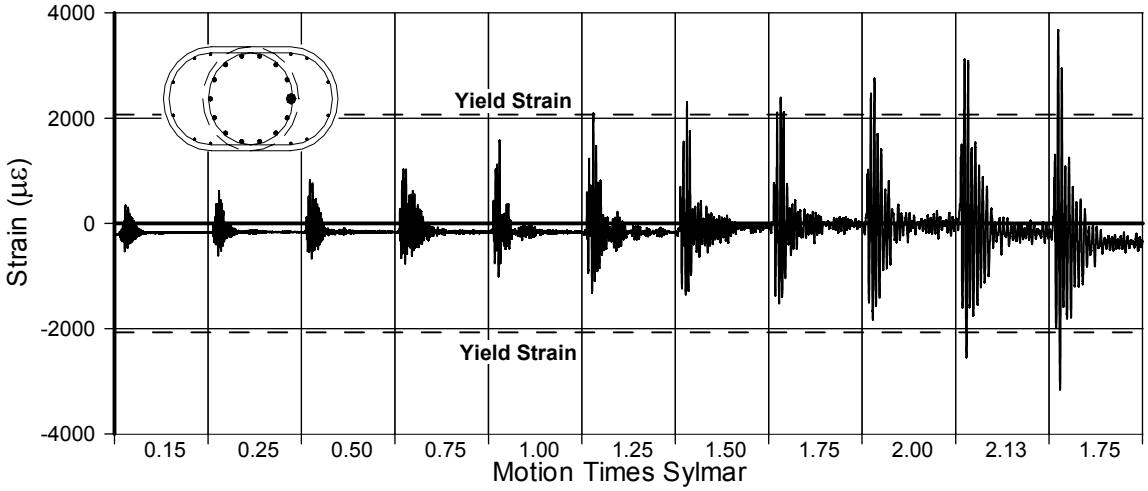

Fig. A-179 - Measured Strain in Gauge No. 55 for LFCD2

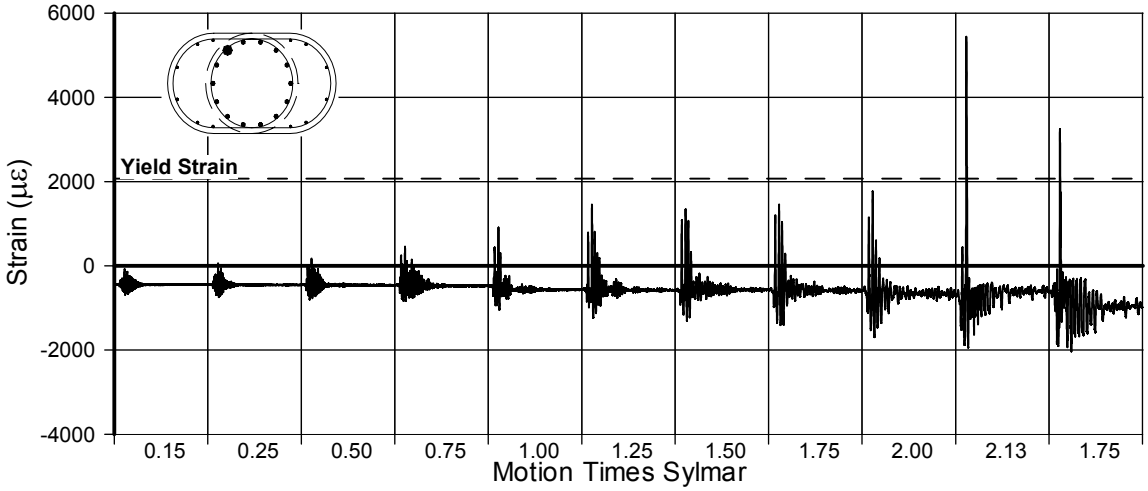

Fig. A-180 - Measured Strain in Gauge No. 56 for LFCD2

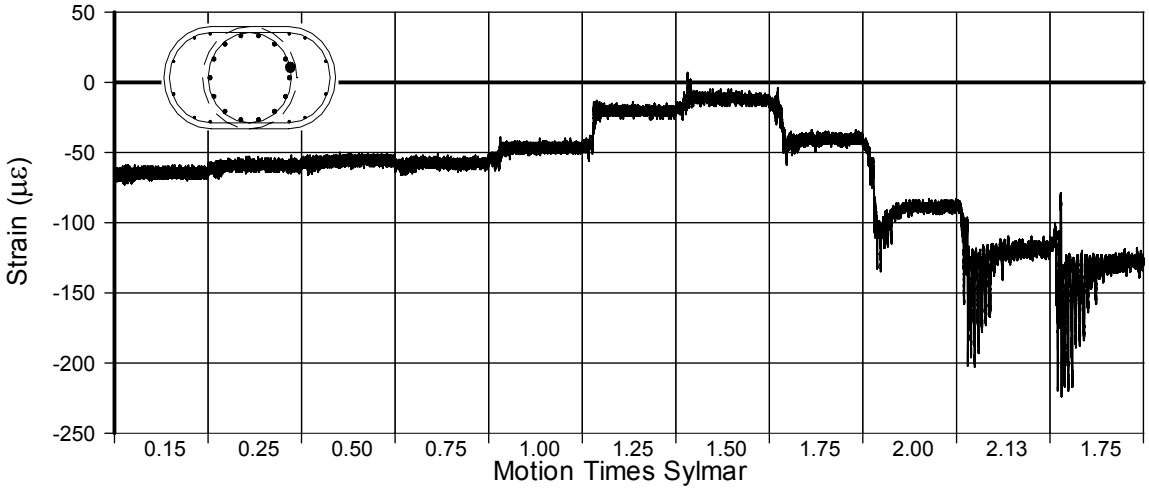

Fig. A-181 - Measured Strain in Gauge No. 57 for LFCD2

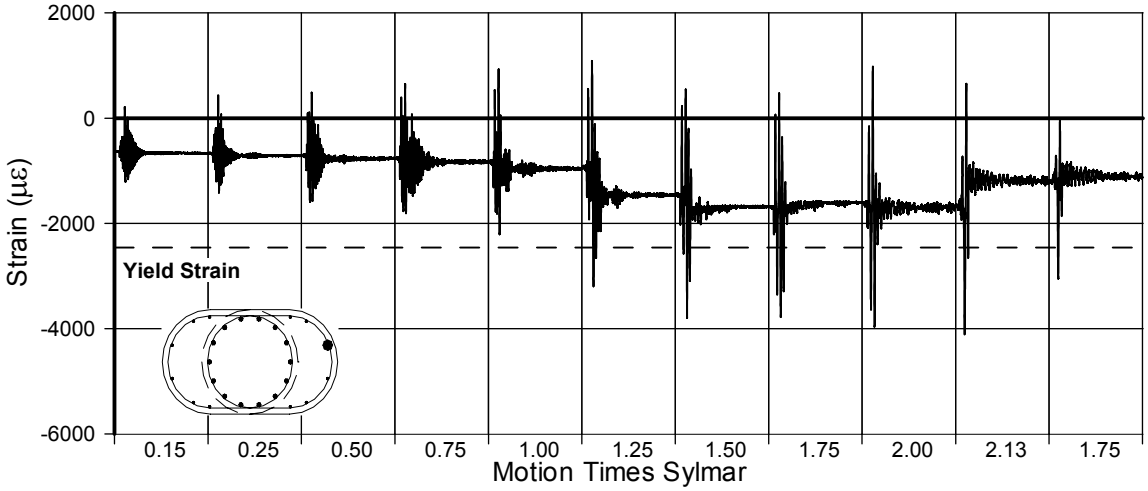

Fig. A-182 - Measured Strain in Gauge No. 58 for LFCD2

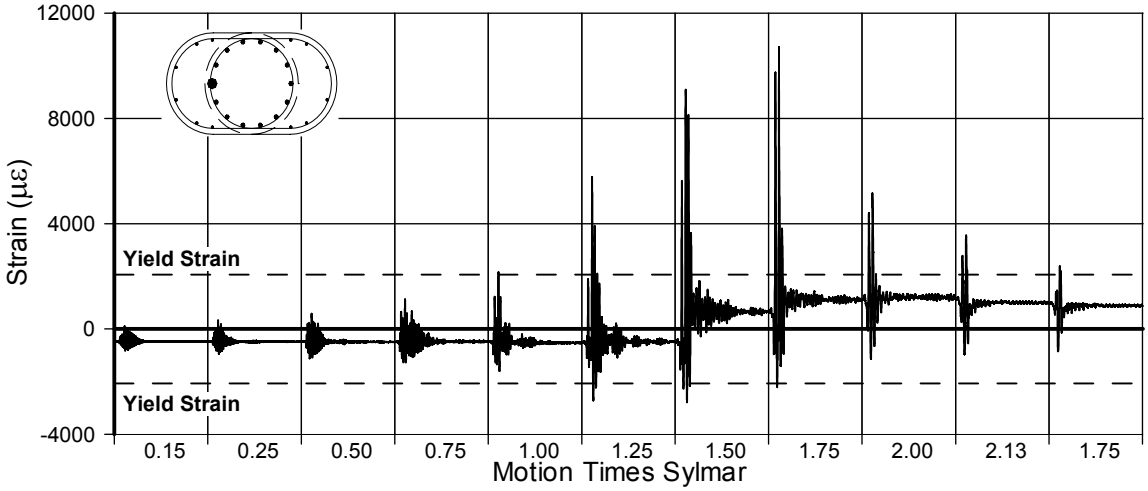

Fig. A-183 - Measured Strain in Gauge No. 59 for LFCD2

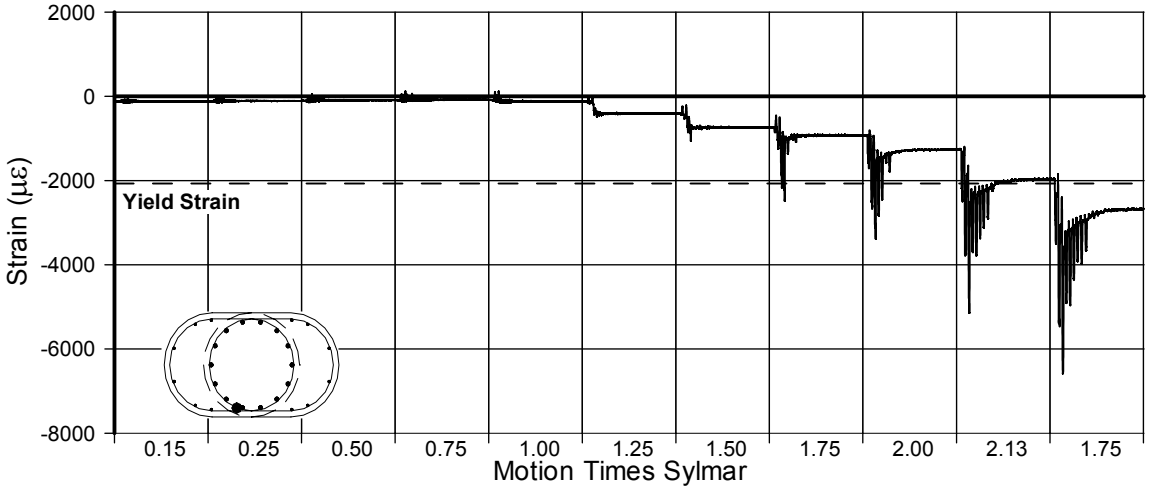

Fig. A-184 - Measured Strain in Gauge No. 61 for LFCD2

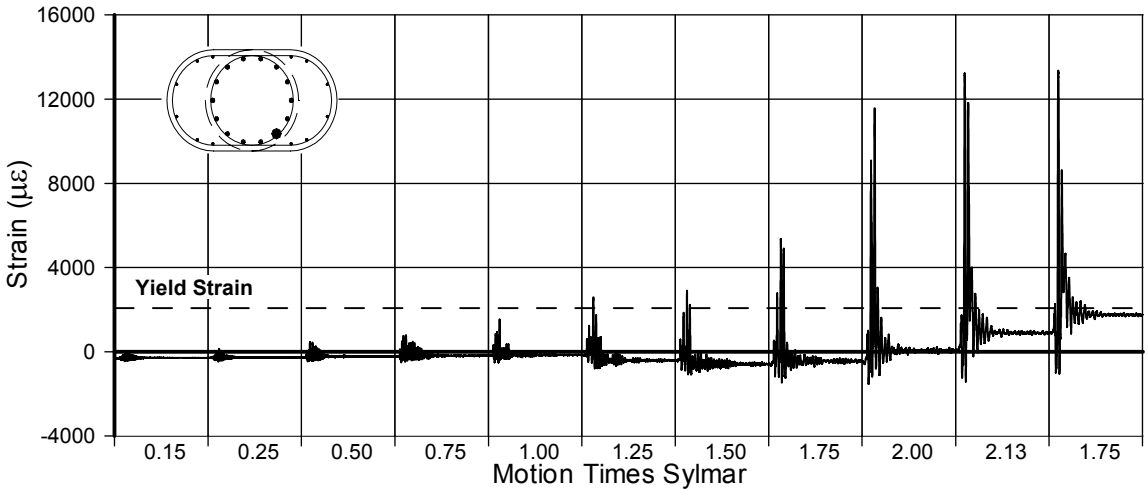

Fig. A-185 - Measured Strain in Gauge No. 62 for LFCD2

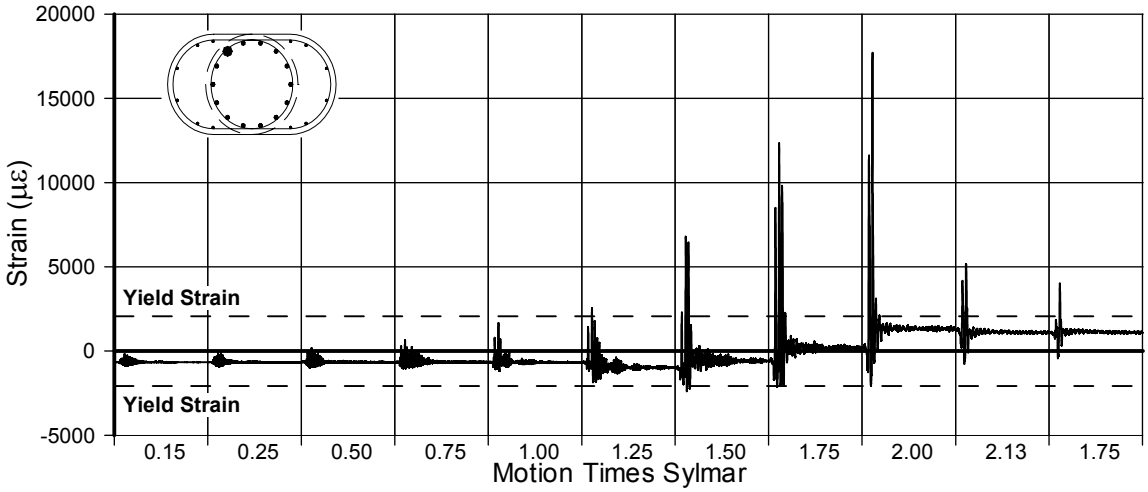

Fig. A-186 - Measured Strain in Gauge No. 64 for LFCD2

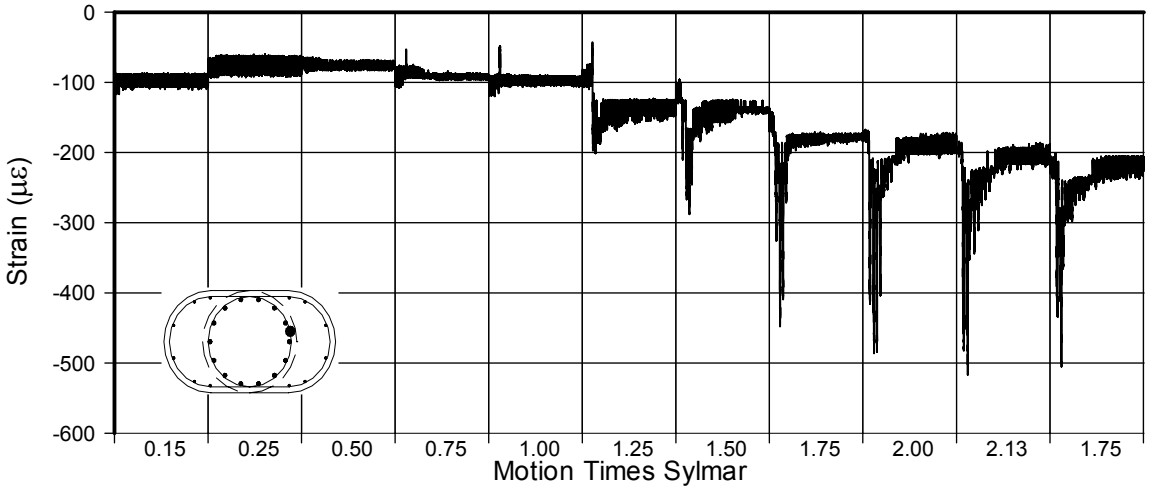

Fig. A-187 - Measured Strain in Gauge No. 65 for LFCD2

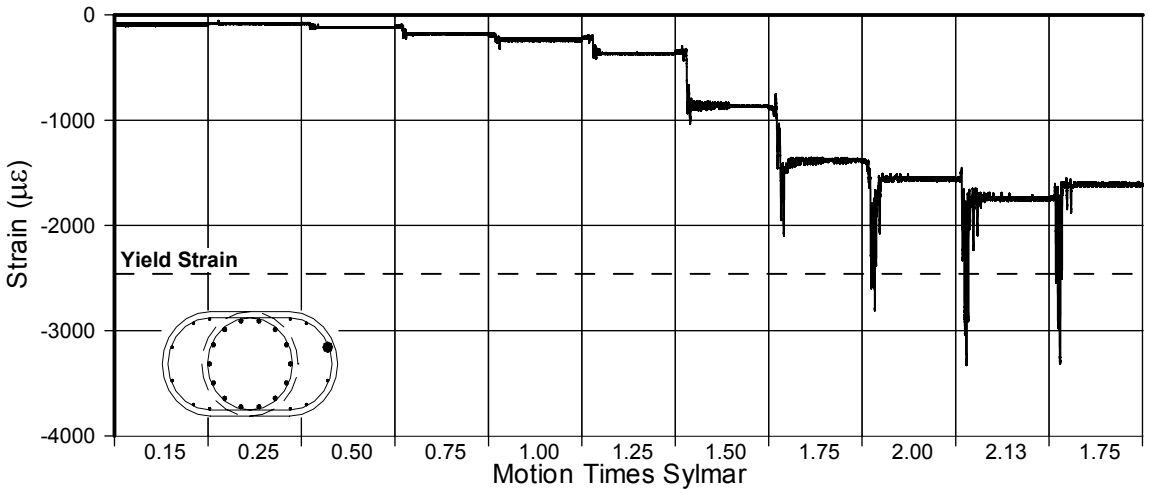

Fig. A-188 - Measured Strain in Gauge No. 67 for LFCD2

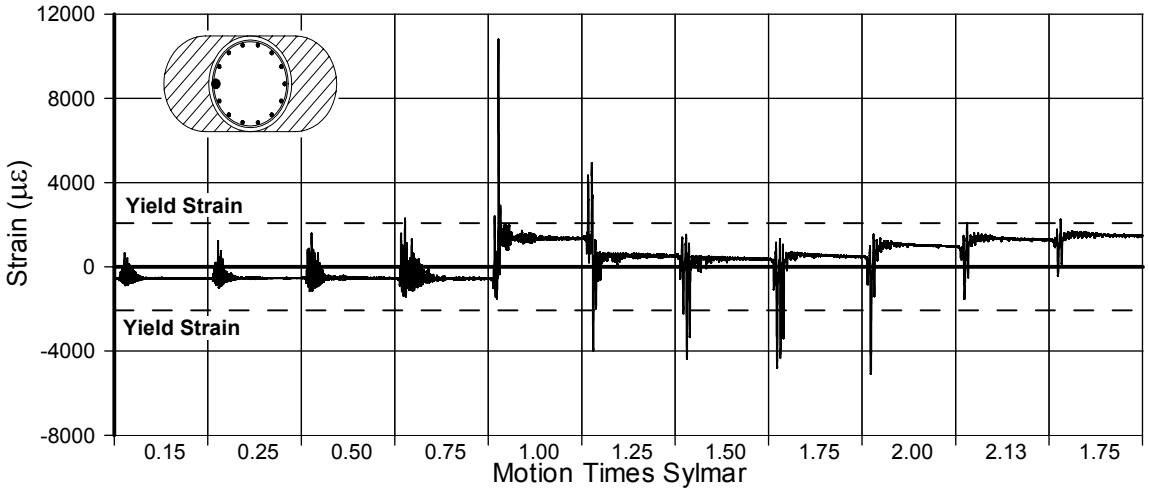

Fig. A-189 - Measured Strain in Gauge No. 68 for LFCD2

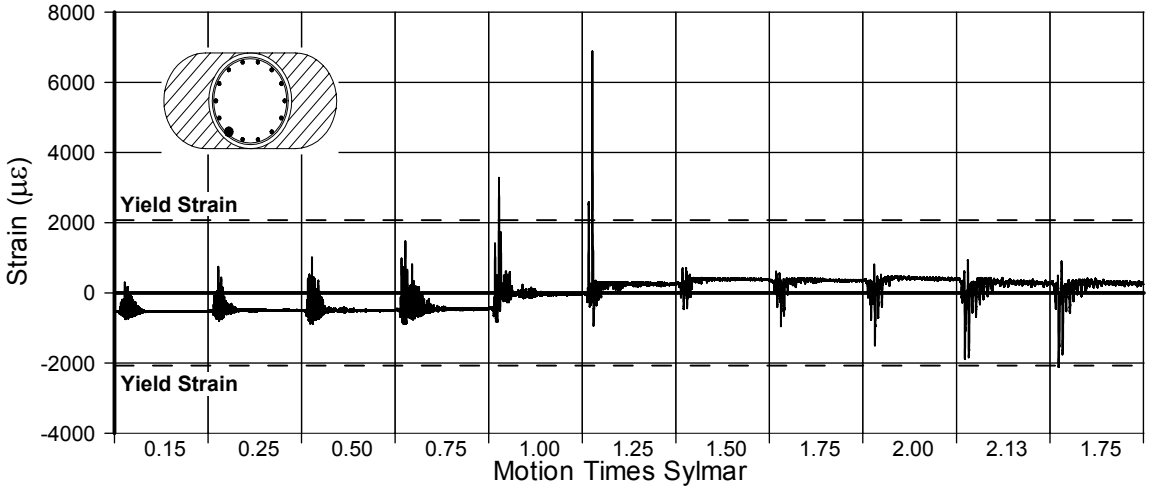

Fig. A-190 - Measured Strain in Gauge No. 69 for LFCD2

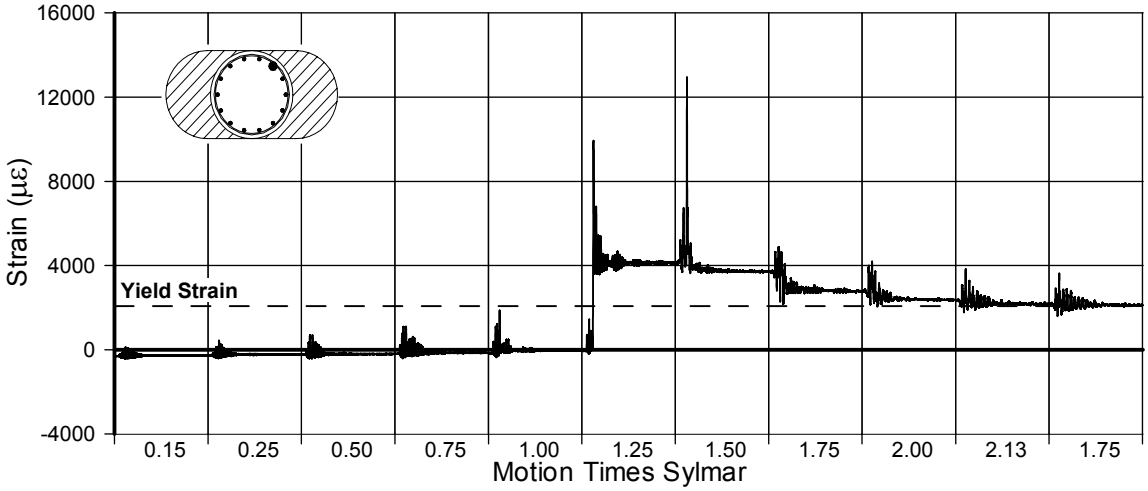

Fig. A-191 - Measured Strain in Gauge No. 71 for LFCD2

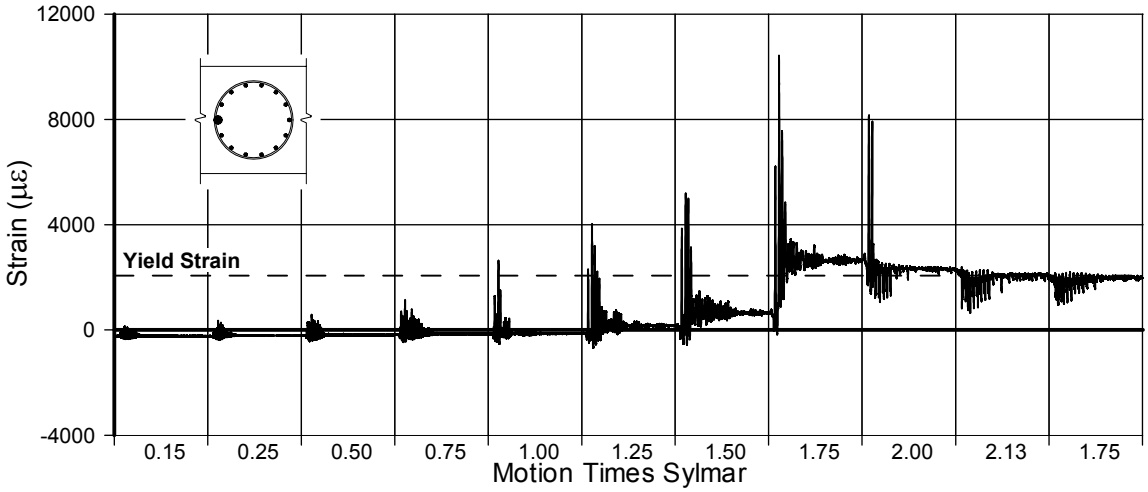

Fig. A-192 - Measured Strain in Gauge No. 72 for LFCD2

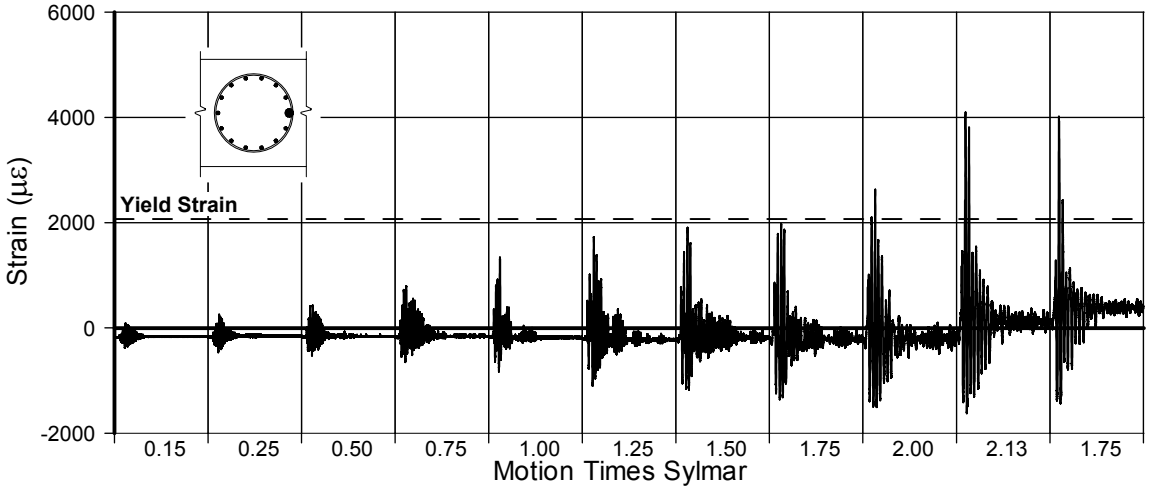

Fig. A-193 - Measured Strain in Gauge No. 74 for LFCD2

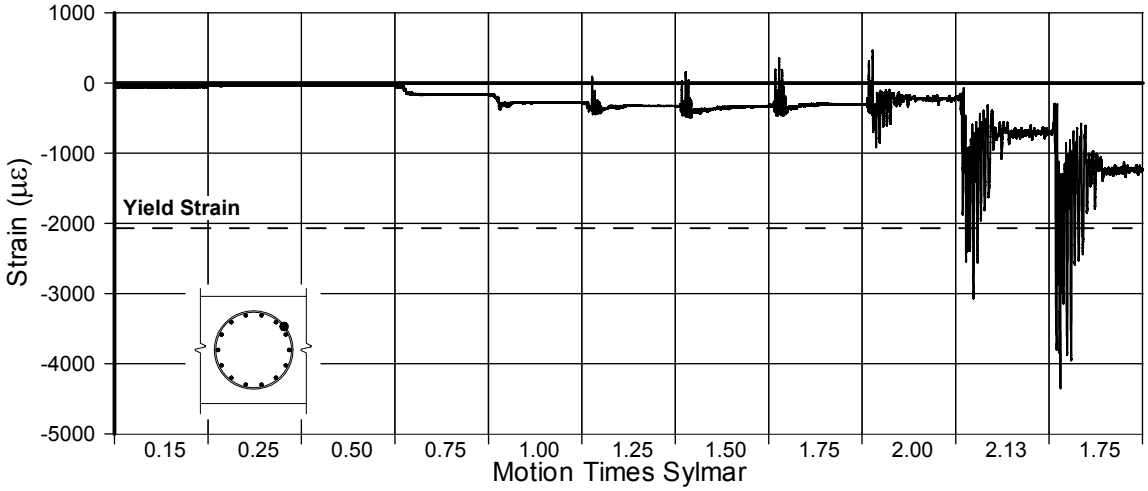

Fig. A-194 - Measured Strain in Gauge No. 75 for LFCD2

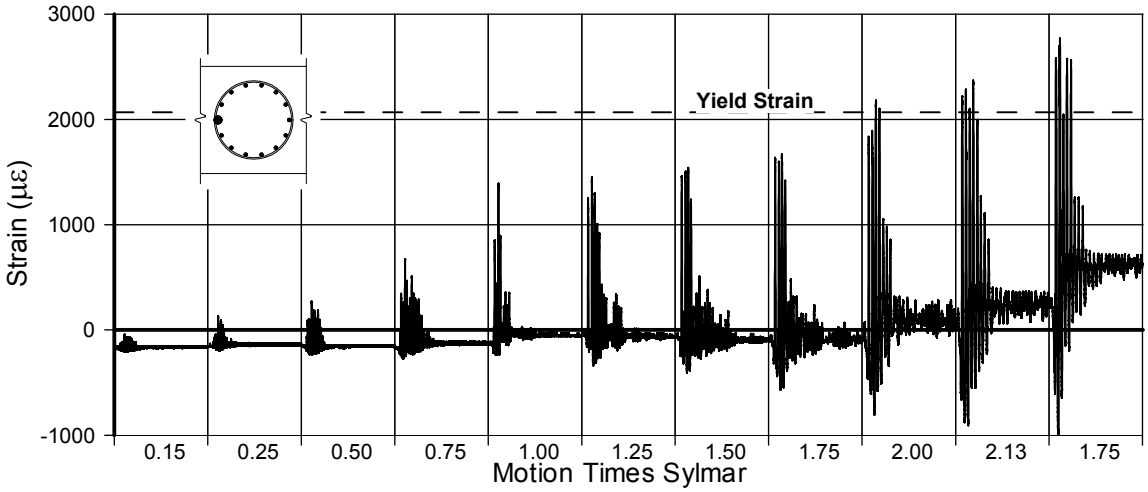

Fig. A-195 - Measured Strain in Gauge No. 76 for LFCD2

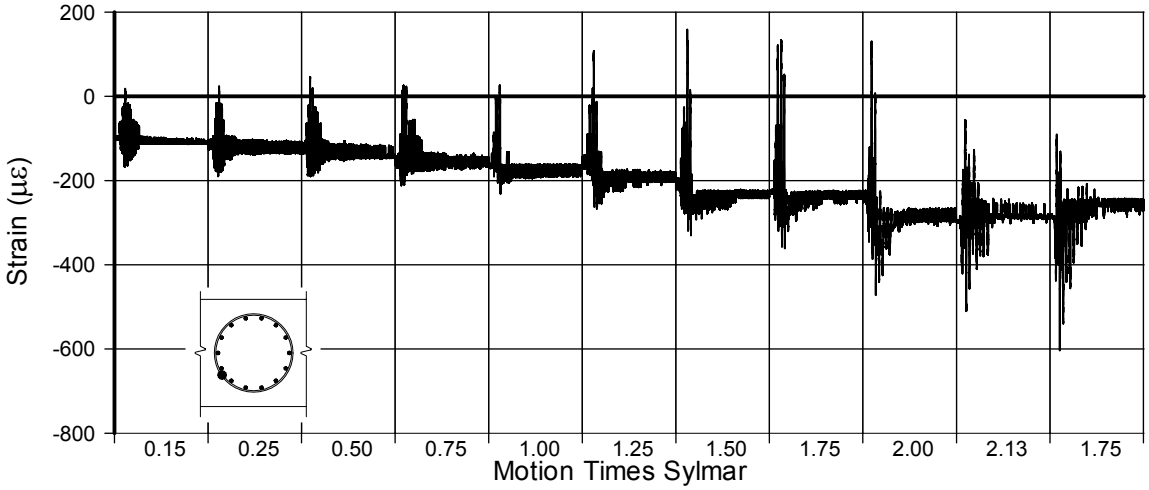

Fig. A-196 - Measured Strain in Gauge No. 77 for LFCD2

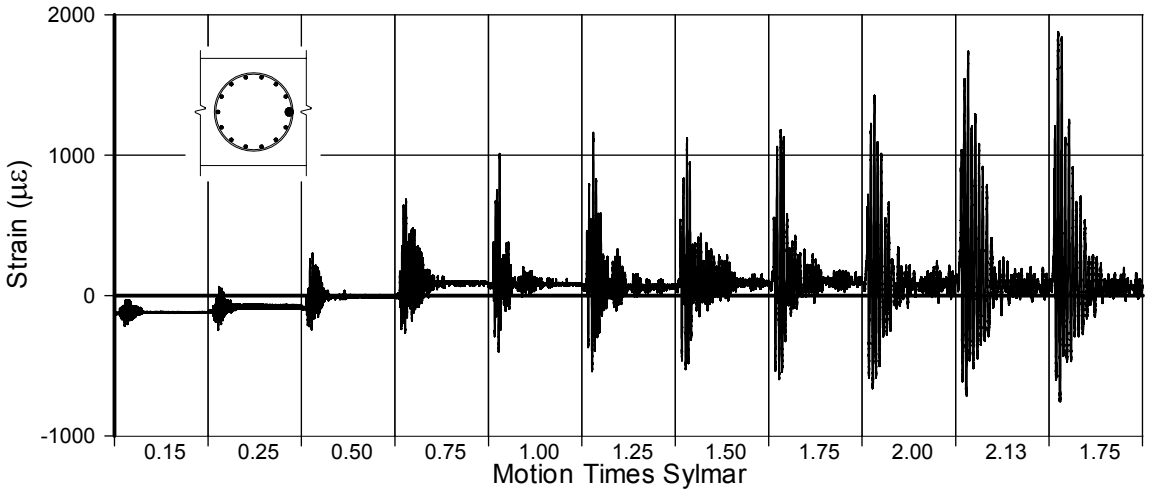

Fig. A-197 - Measured Strain in Gauge No. 78 for LFCD2

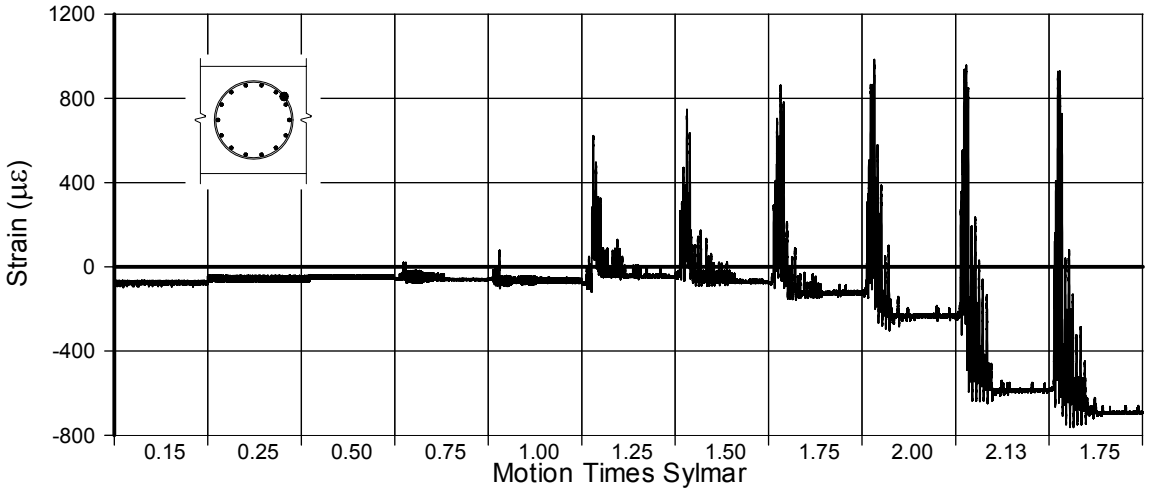

Fig. A-198 - Measured Strain in Gauge No. 79 for LFCD2

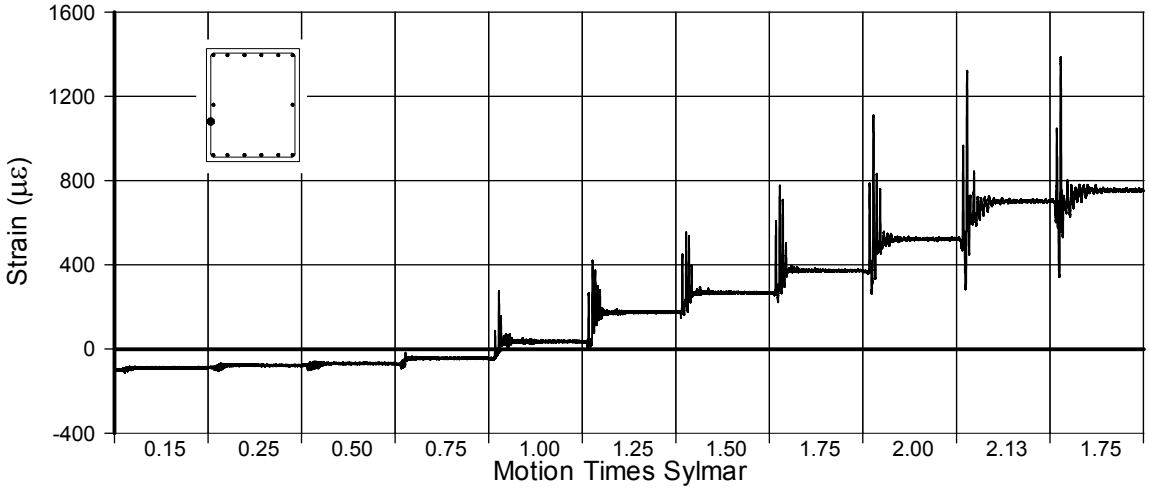

Fig. A-199 - Measured Strain in Gauge No. 80 for LFCD2

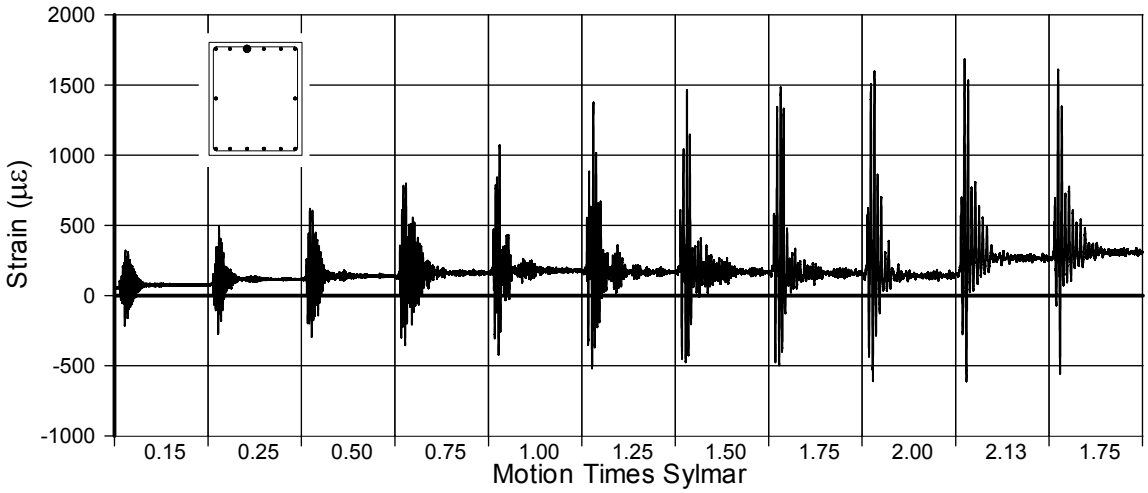

Fig. A-200 - Measured Strain in Gauge No. 81 for LFCD2

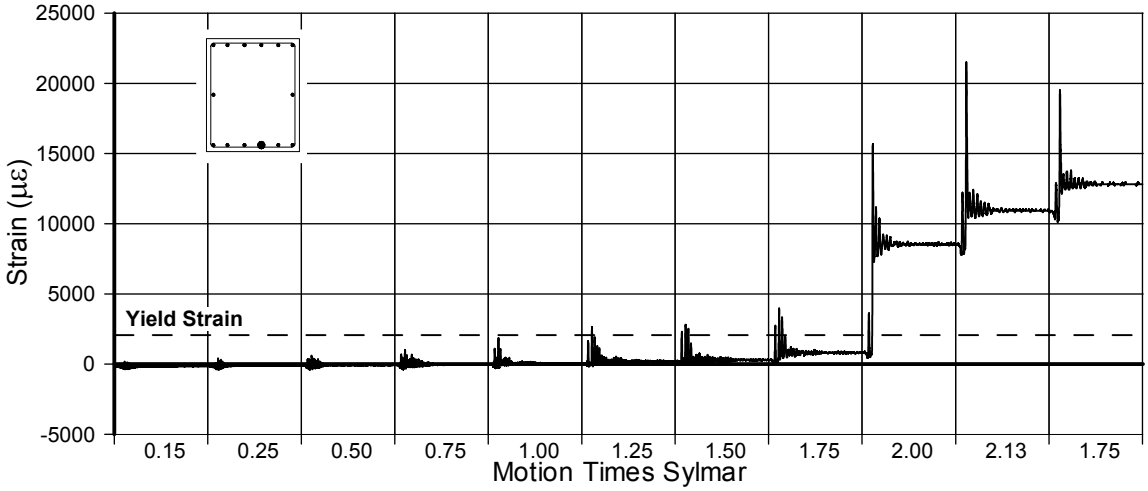

Fig. A-201 - Measured Strain in Gauge No. 82 for LFCD2

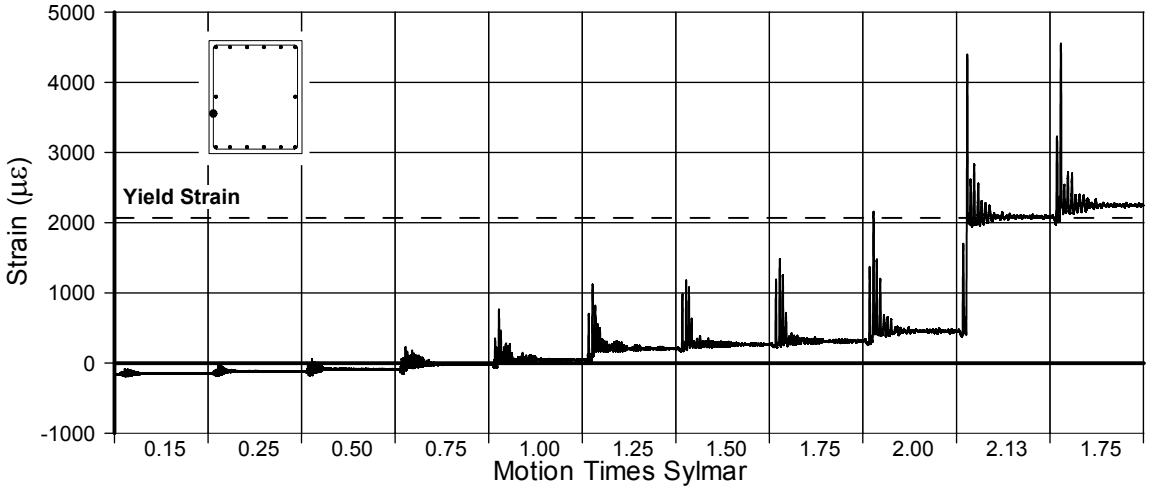

Fig. A-202 - Measured Strain in Gauge No. 83 for LFCD2

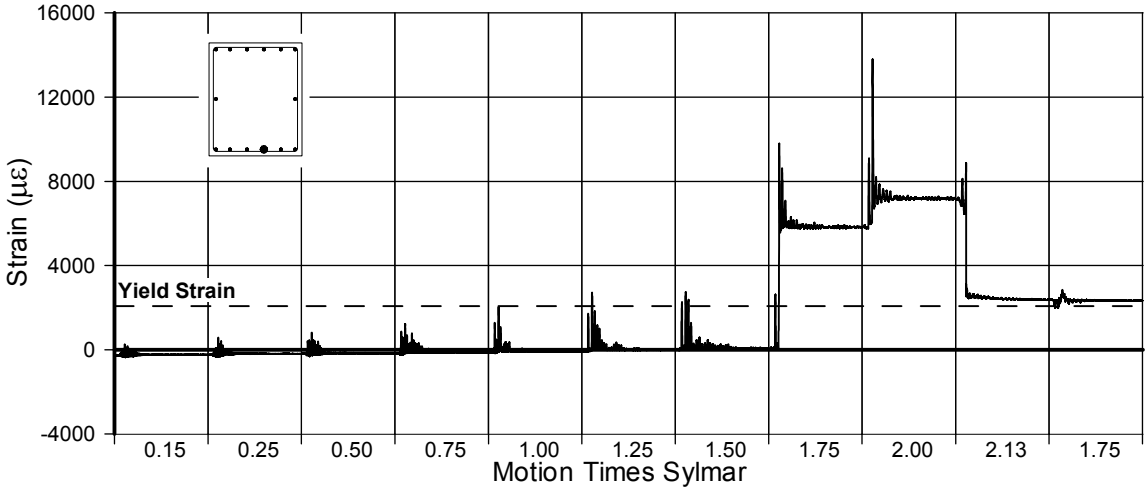

Fig. A-203 - Measured Strain in Gauge No. 85 for LFCD2

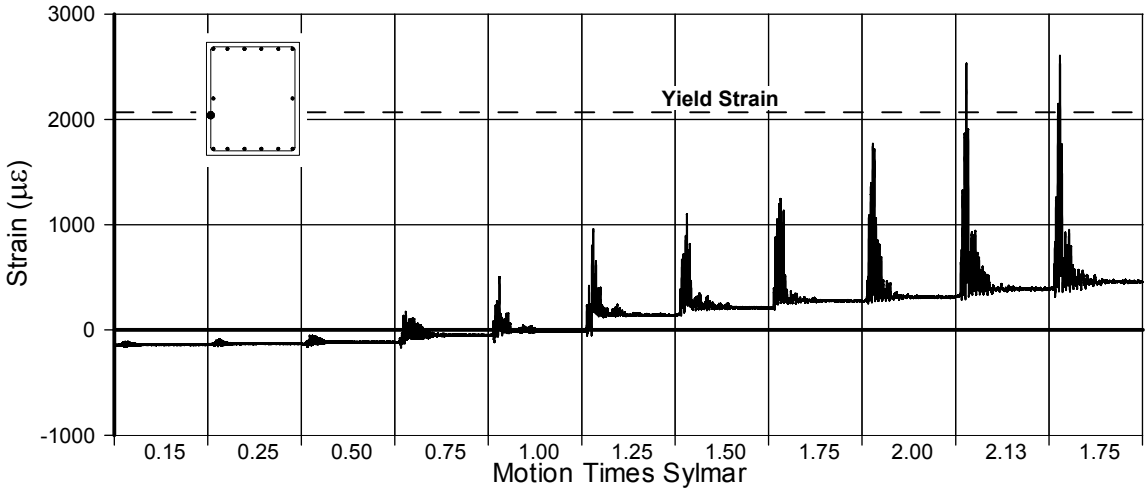

Fig. A-204 - Measured Strain in Gauge No. 86 for LFCD2

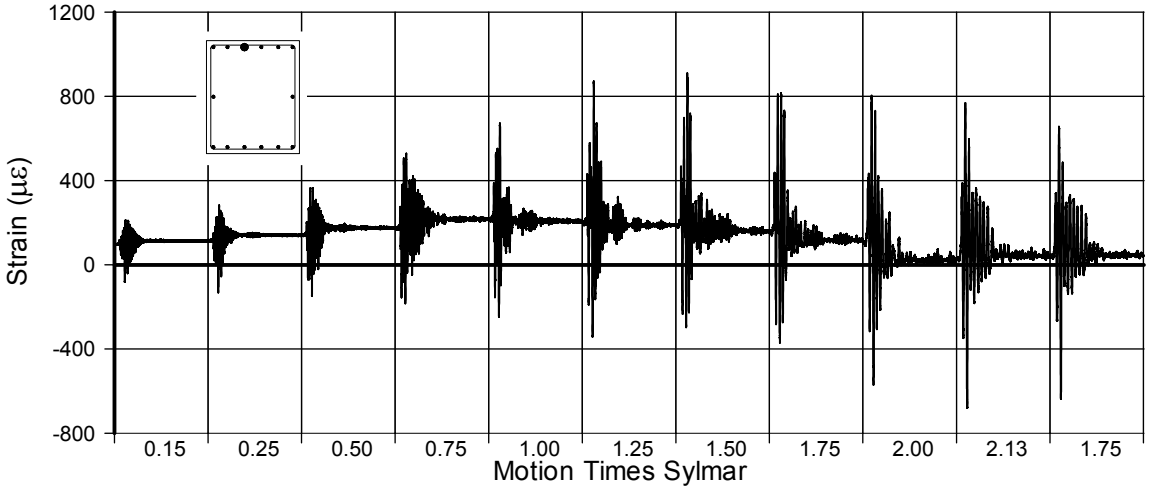

Fig. A-205 - Measured Strain in Gauge No. 87 for LFCD2

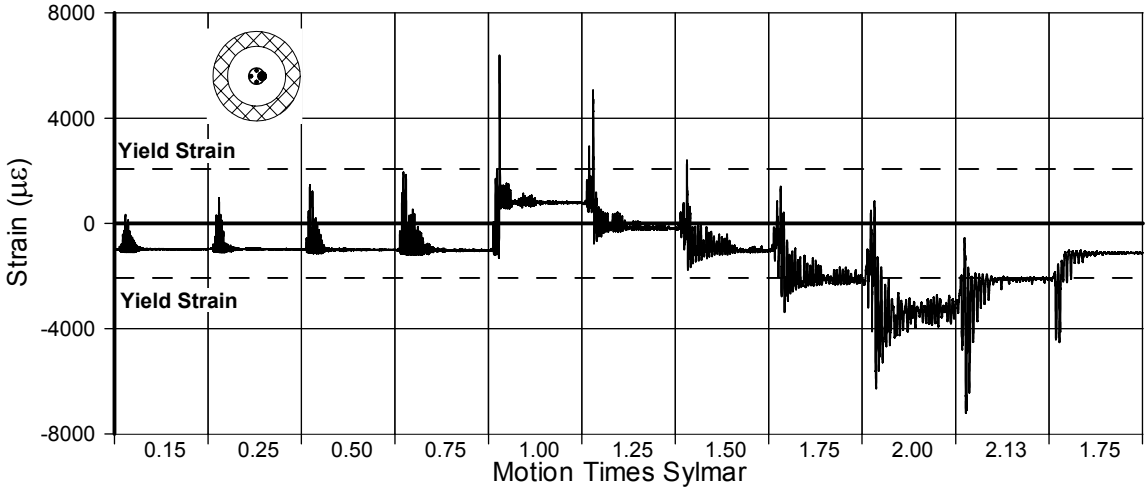

Fig. A-206 - Measured Strain in Gauge No. 89 for LFCD2

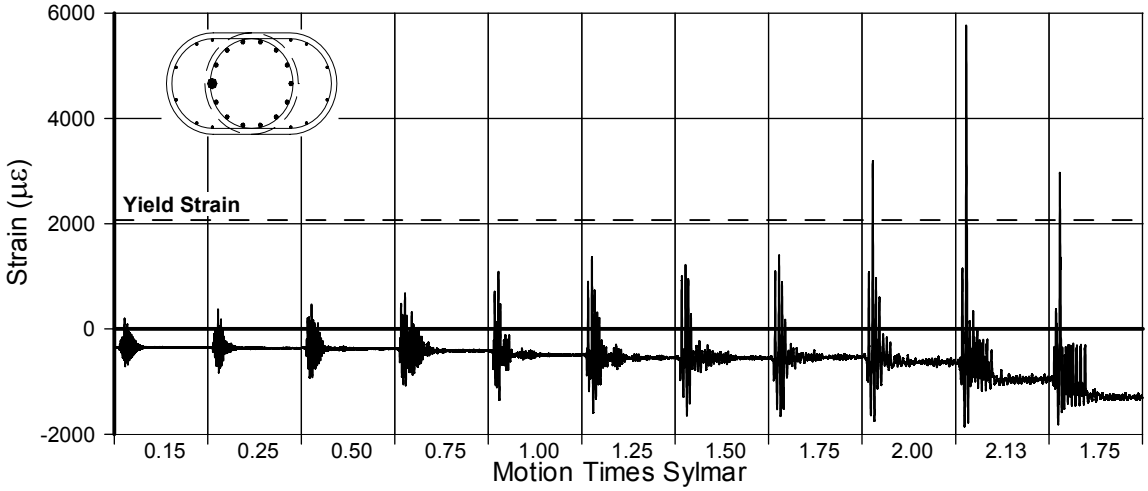

Fig. A-207 - Measured Strain in Gauge No. 91 for LFCD2

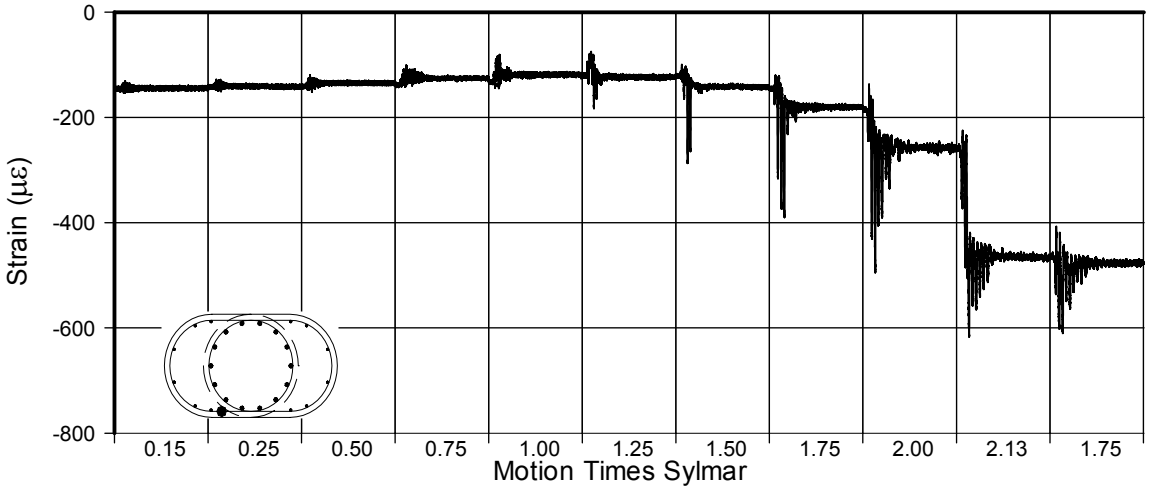

Fig. A-208 - Measured Strain in Gauge No. 92 for LFCD2

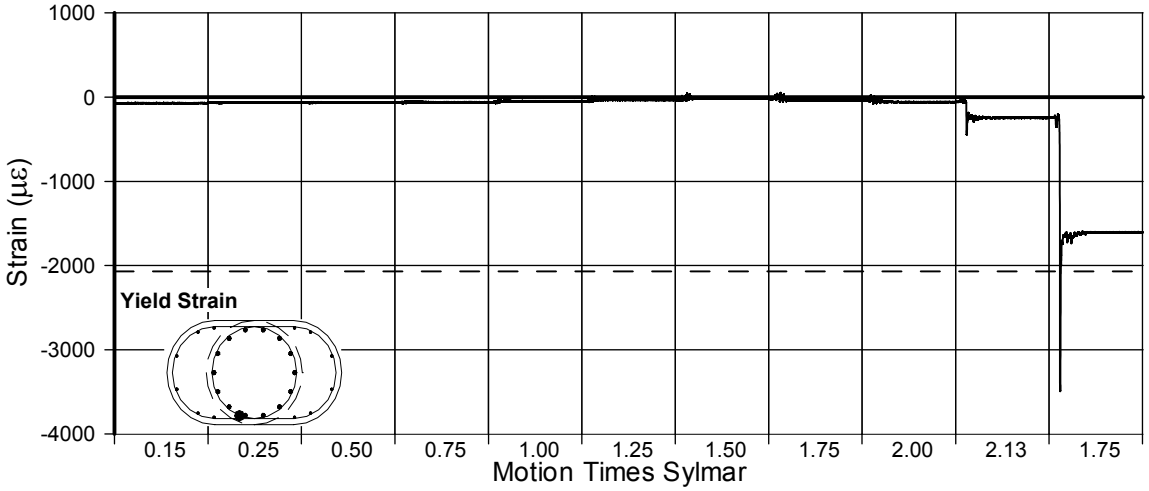

Fig. A-209 - Measured Strain in Gauge No. 93 for LFCD2

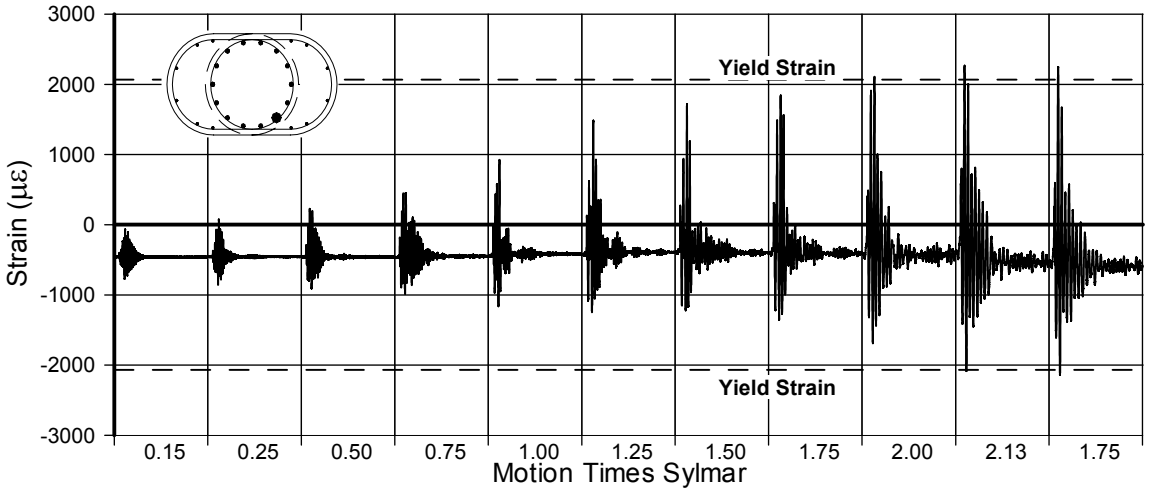

Fig. A-210 - Measured Strain in Gauge No. 94 for LFCD2

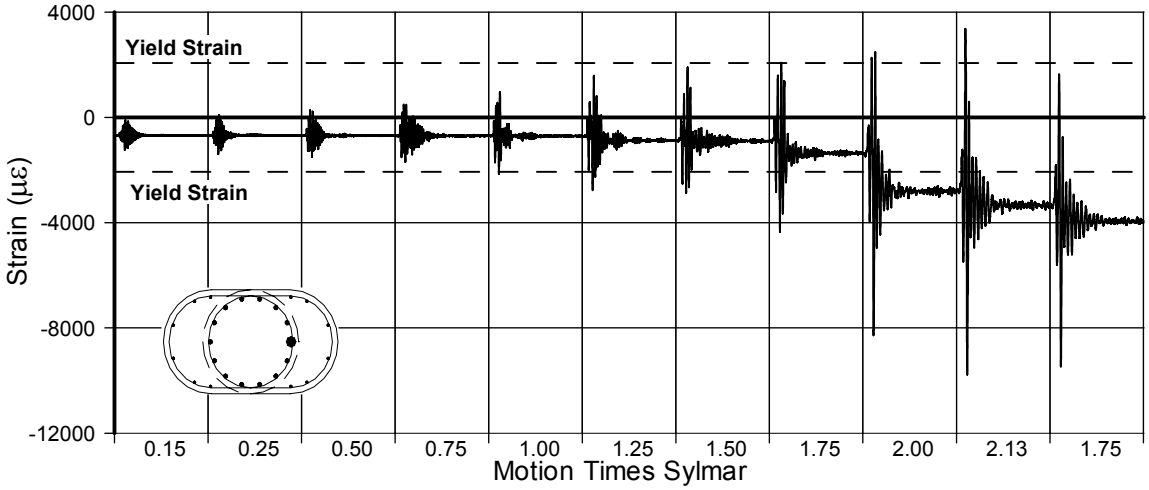

Fig. A-211 - Measured Strain in Gauge No. 95 for LFCD2

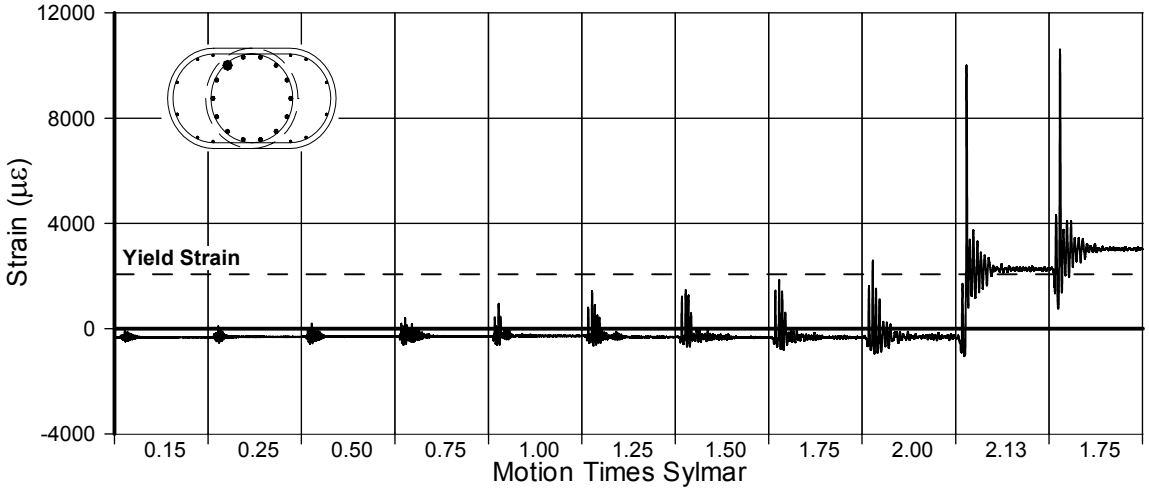

Fig. A-212 - Measured Strain in Gauge No. 96 for LFCD2

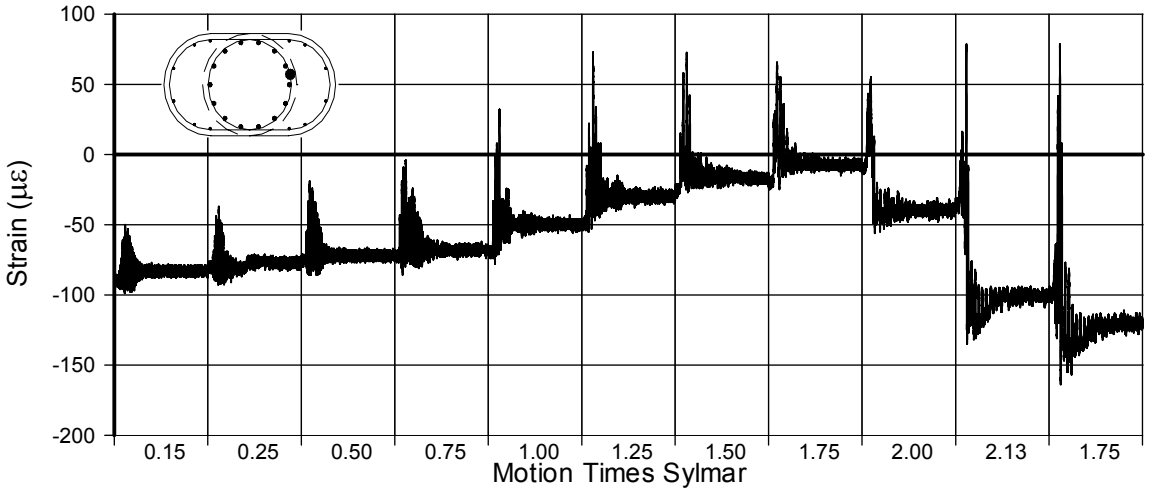

Fig. A-213 - Measured Strain in Gauge No. 97 for LFCD2

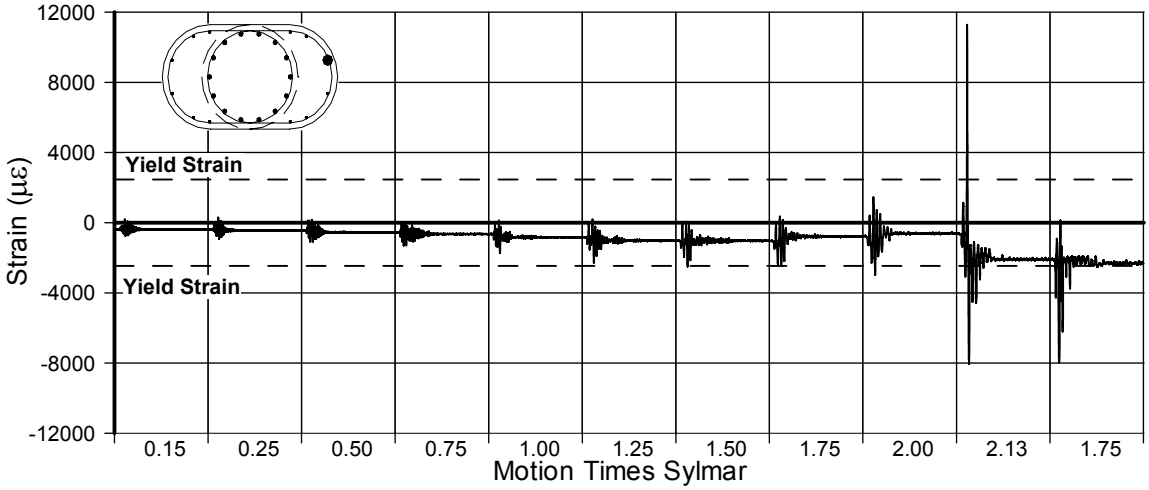

Fig. A-214 - Measured Strain in Gauge No. 98 for LFCD2

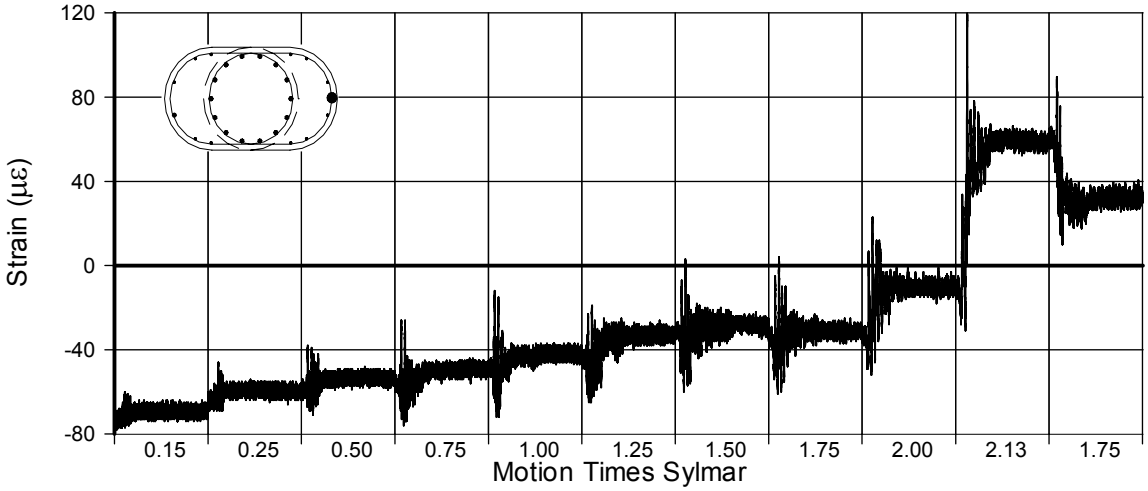

Fig. A-215 - Measured Strain in Gauge No. 99 for LFCD2

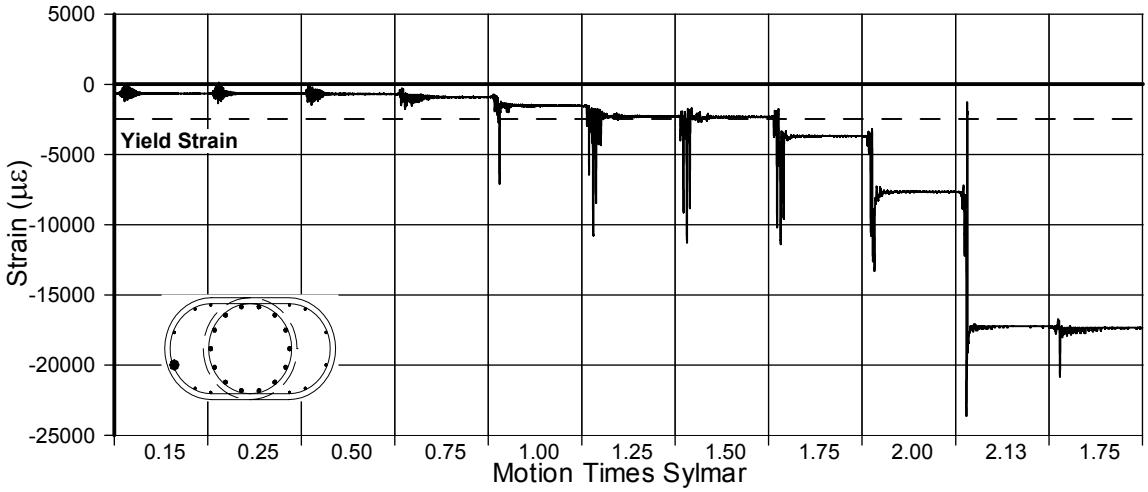

Fig. A-216 - Measured Strain in Gauge No. 100 for LFCD2

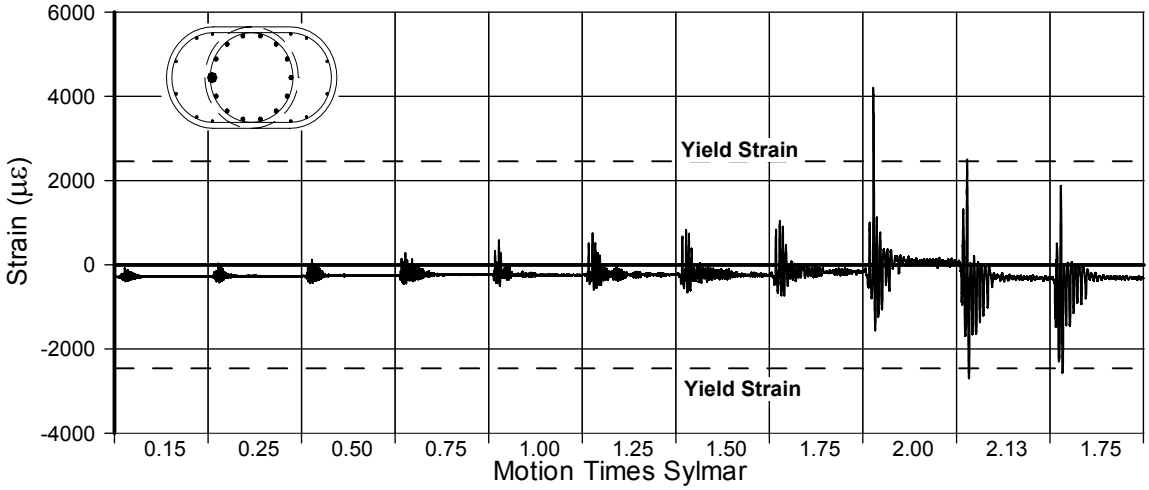

Fig. A-217 - Measured Strain in Gauge No. 101 for LFCD2

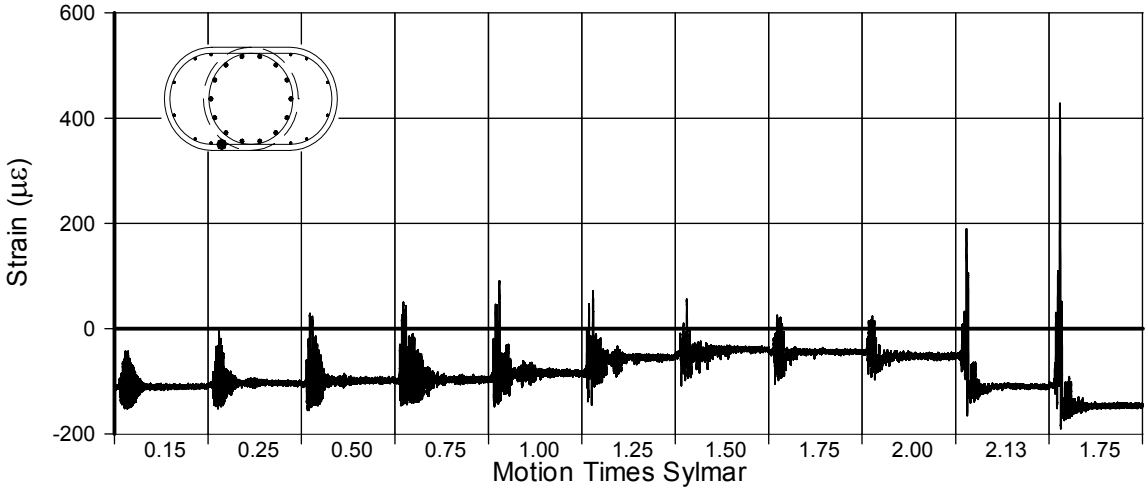

Fig. A-218 - Measured Strain in Gauge No. 102 for LFCD2

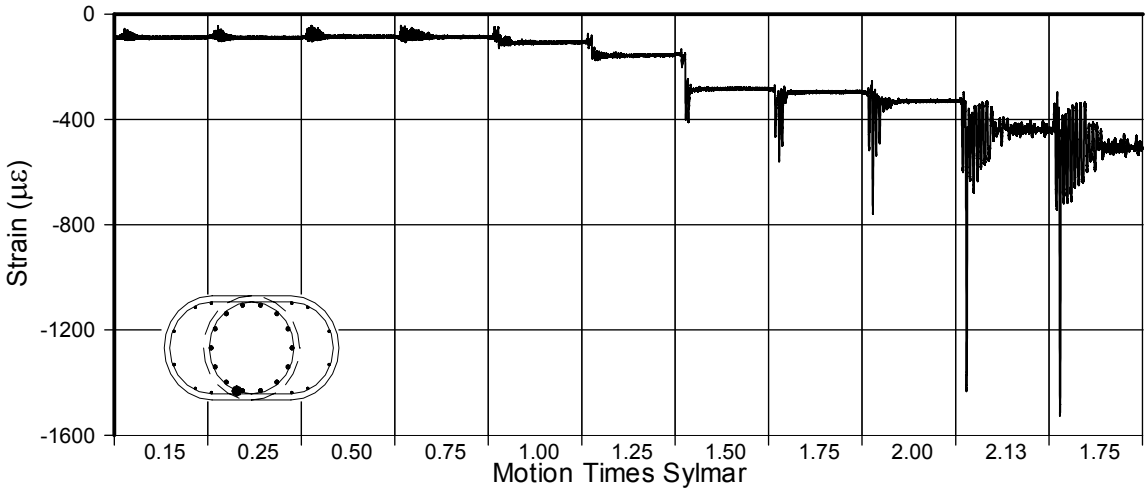

Fig. A-219 - Measured Strain in Gauge No. 103 for LFCD2

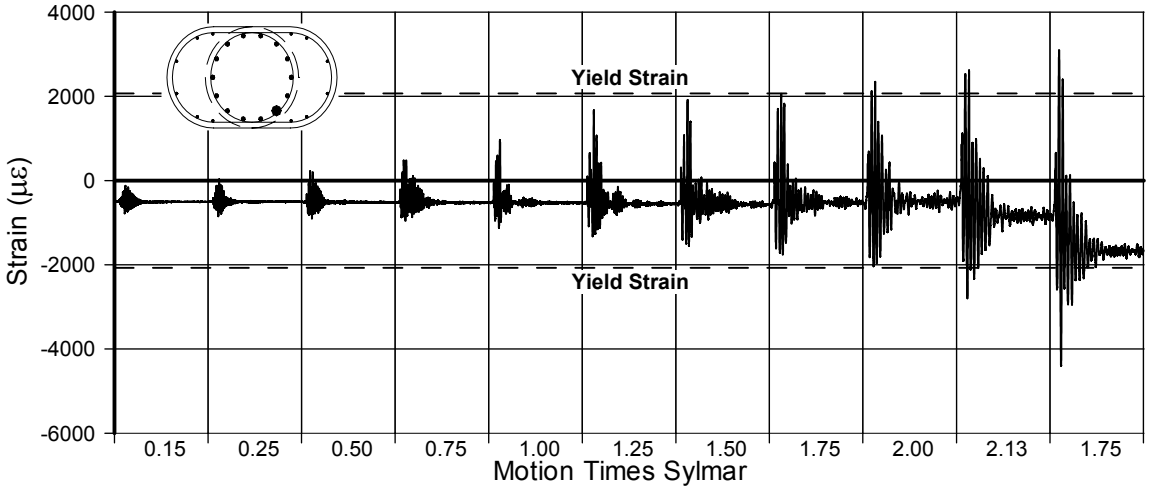

Fig. A-220 - Measured Strain in Gauge No. 104 for LFCD2

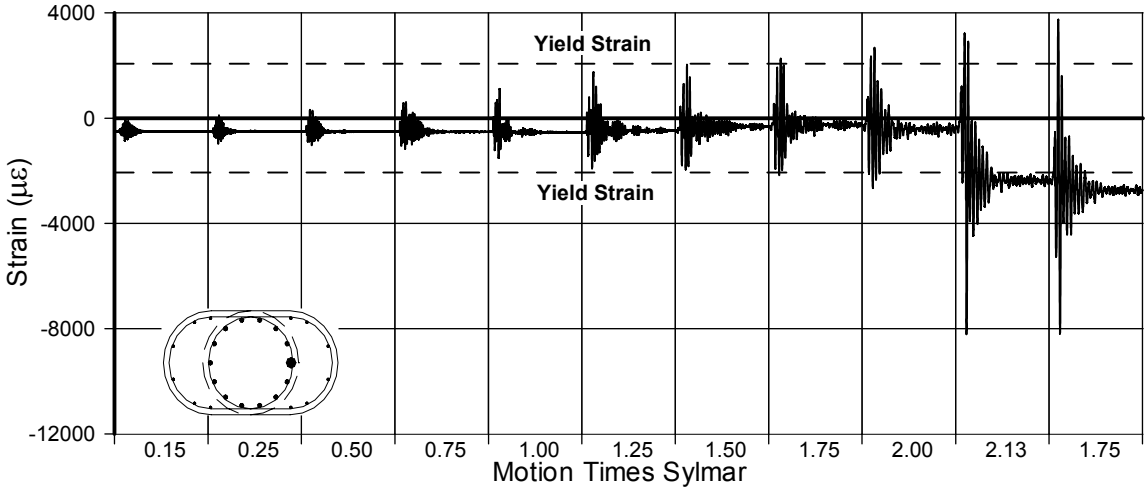

Fig. A-221 - Measured Strain in Gauge No. 105 for LFCD2

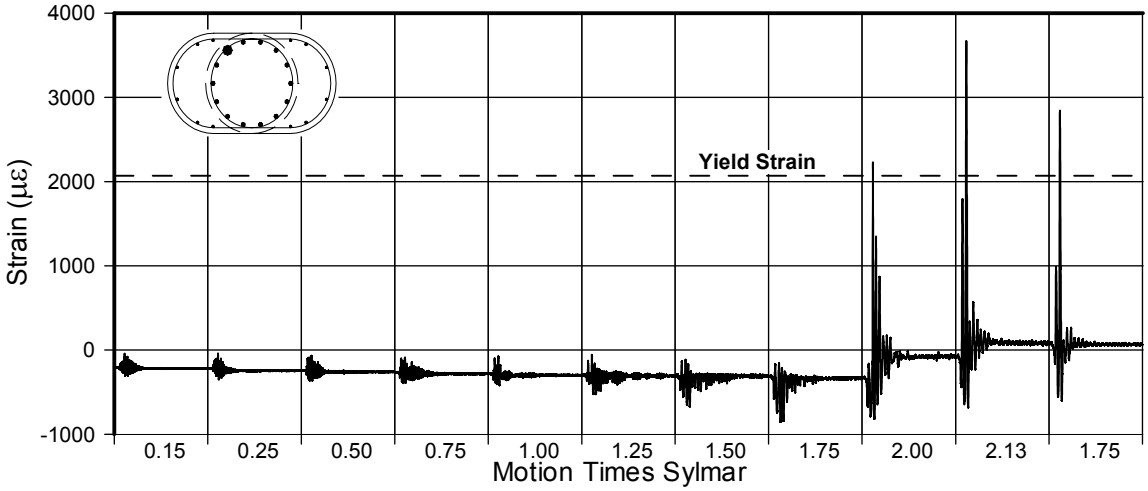

Fig. A-222 - Measured Strain in Gauge No. 106 for LFCD2

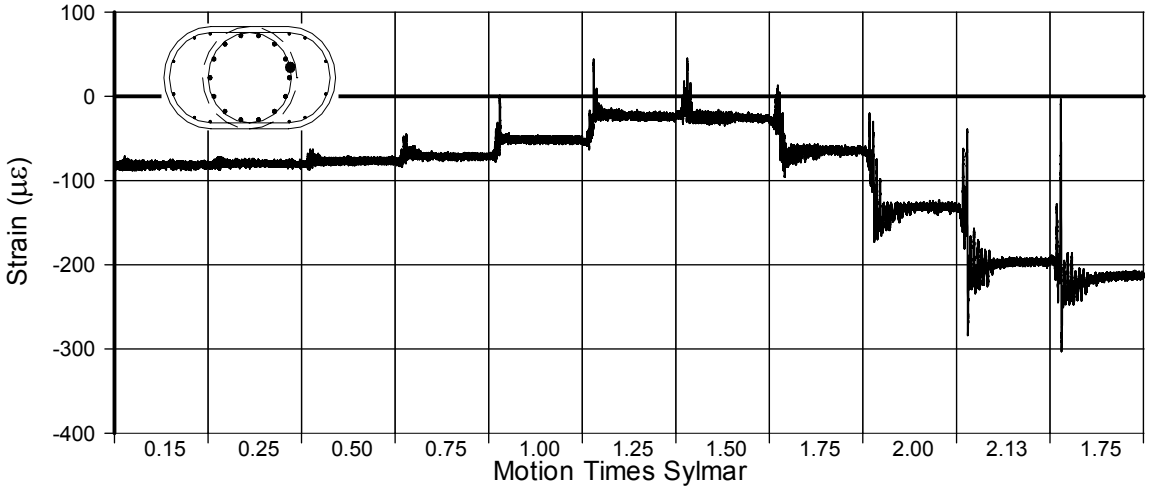

Fig. A-223 - Measured Strain in Gauge No. 107 for LFCD2

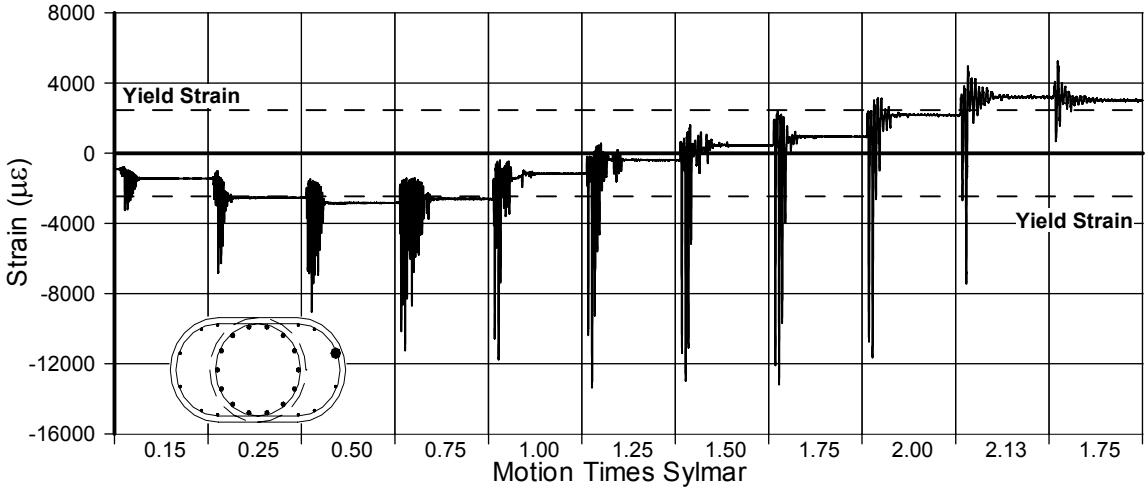

Fig. A-224 - Measured Strain in Gauge No. 108 for LFCD2

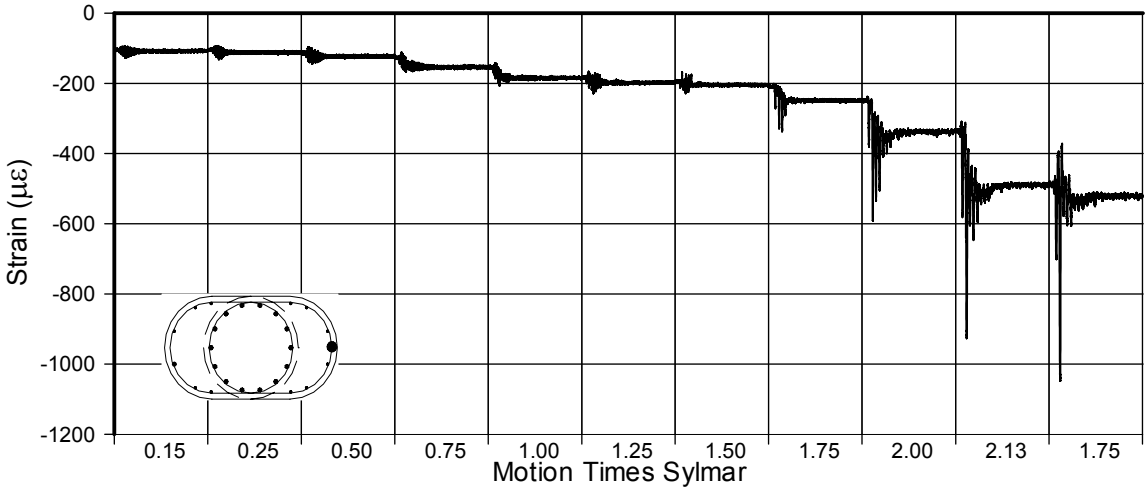

Fig. A-225 - Measured Strain in Gauge No. 109 for LFCD2

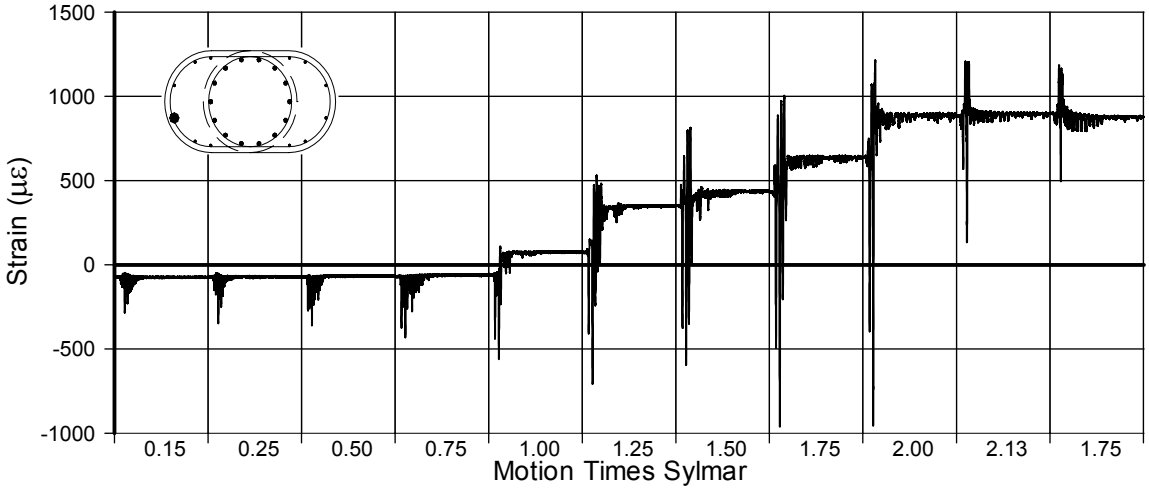

Fig. A-226 - Measured Strain in Gauge No. 110 for LFCD2

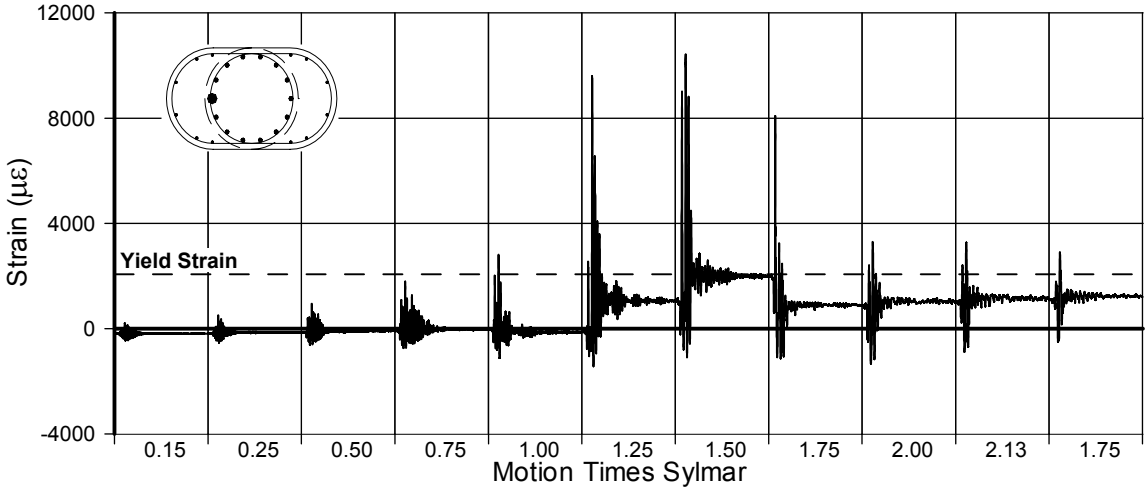

Fig. A-227 - Measured Strain in Gauge No. 111 for LFCD2

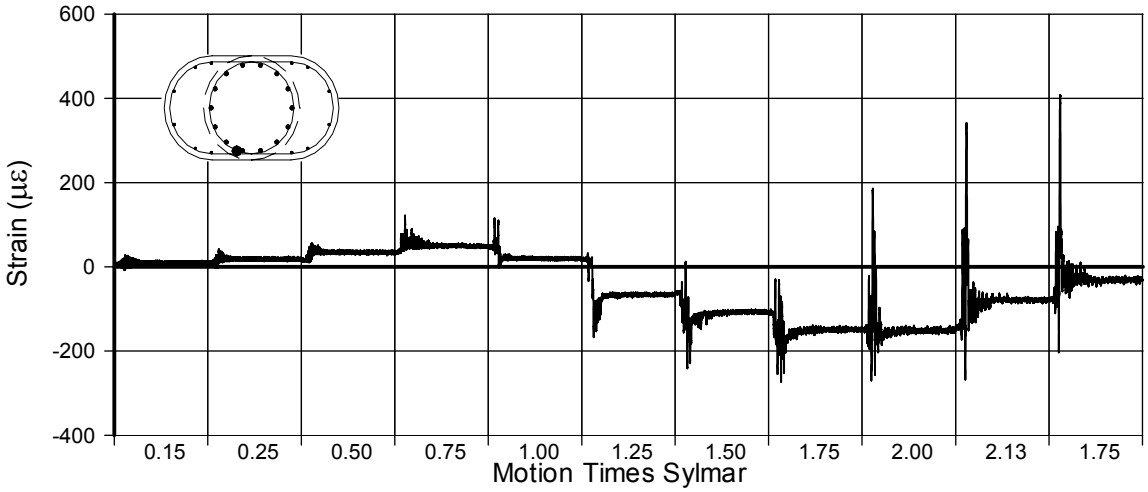

Fig. A-228 - Measured Strain in Gauge No. 112 for LFCD2

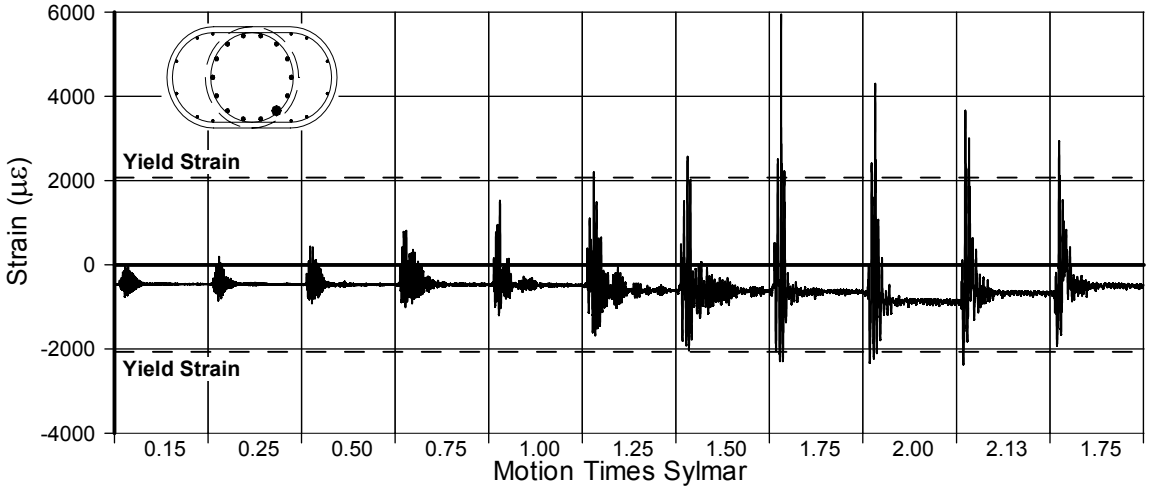

Fig. A-229 - Measured Strain in Gauge No. 113 for LFCD2

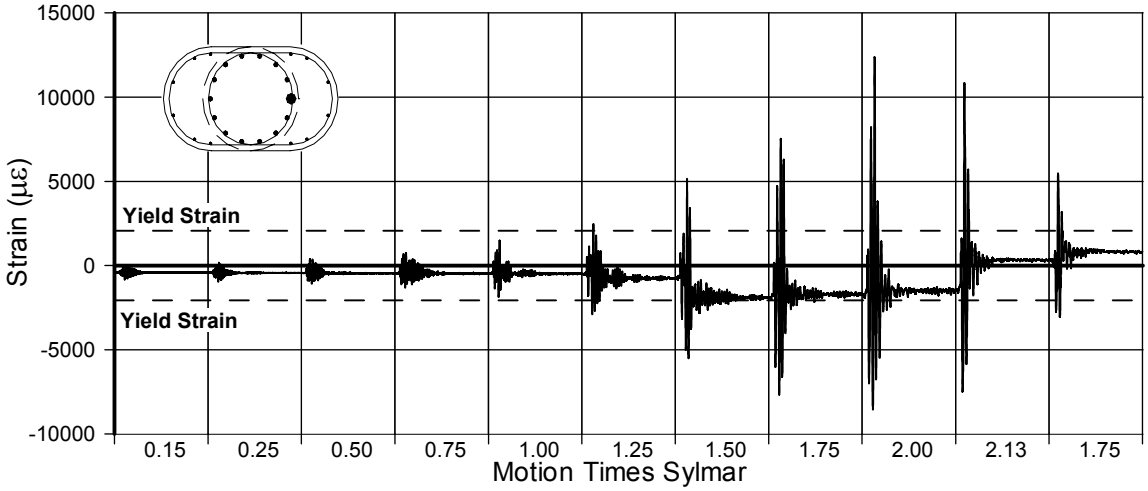

Fig. A-230 - Measured Strain in Gauge No. 114 for LFCD2

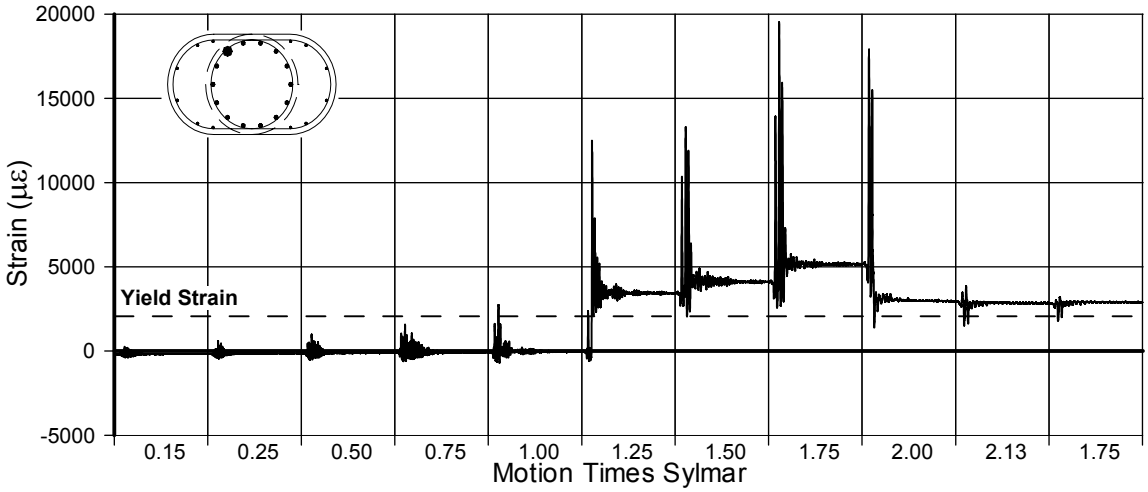

Fig. A-231 - Measured Strain in Gauge No. 115 for LFCD2

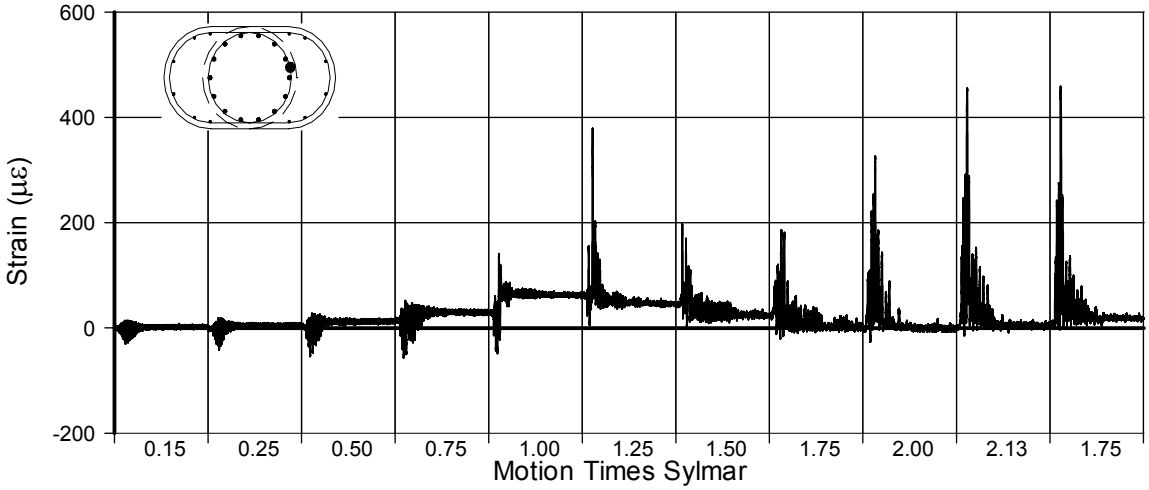

Fig. A-232 - Measured Strain in Gauge No. 116 for LFCD2

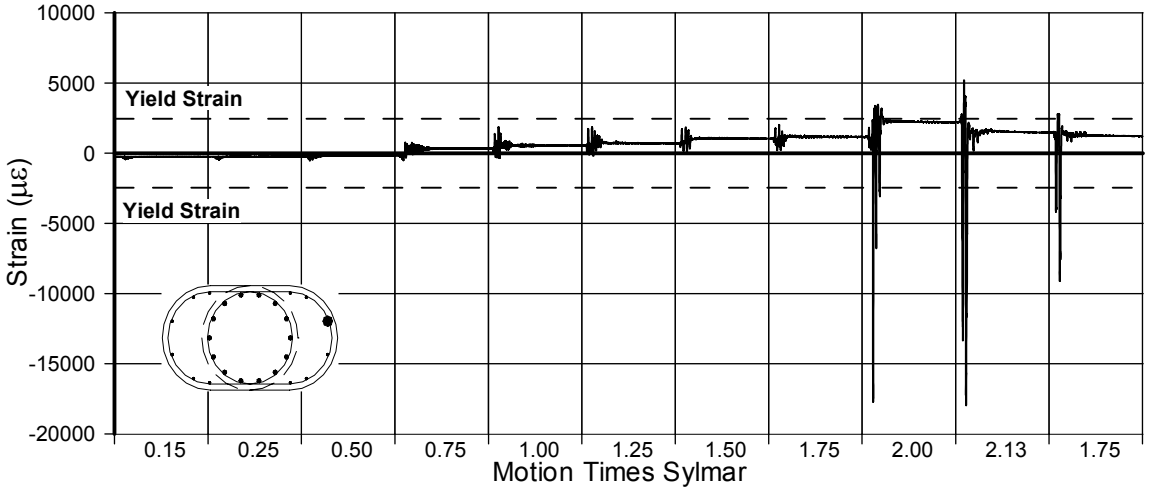

Fig. A-233 - Measured Strain in Gauge No. 117 for LFCD2

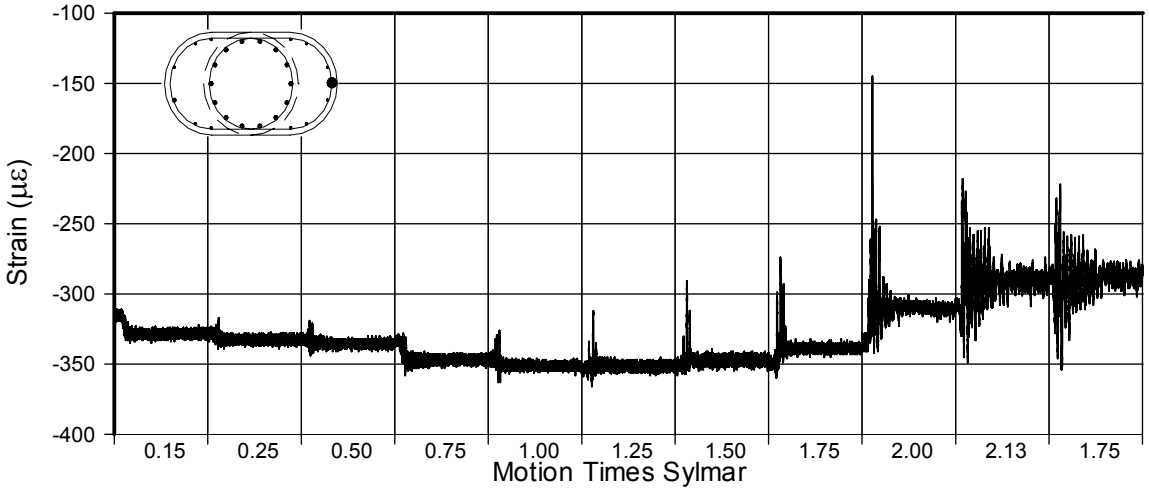

Fig. A-234 - Measured Strain in Gauge No. 118 for LFCD2

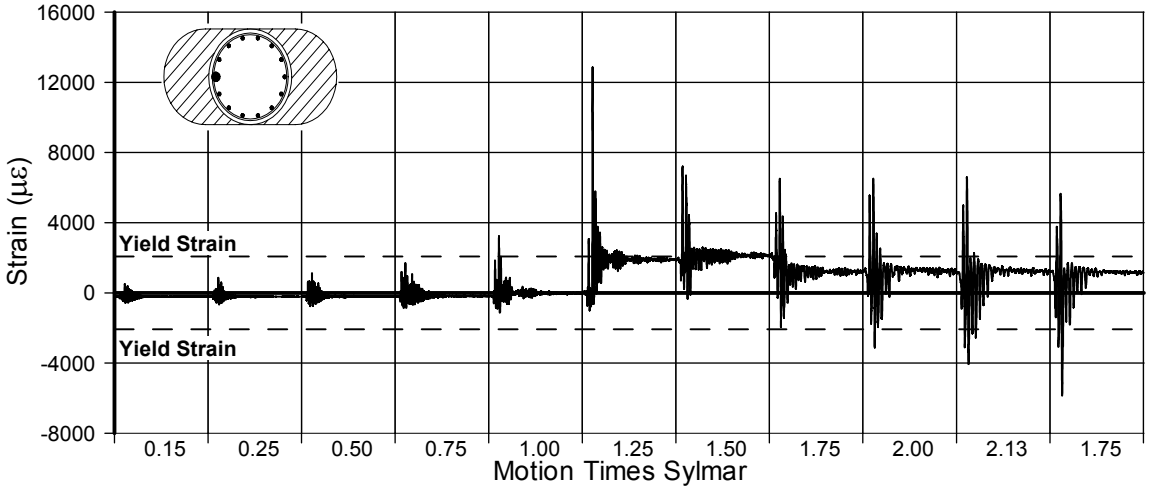

Fig. A-235 - Measured Strain in Gauge No. 119 for LFCD2

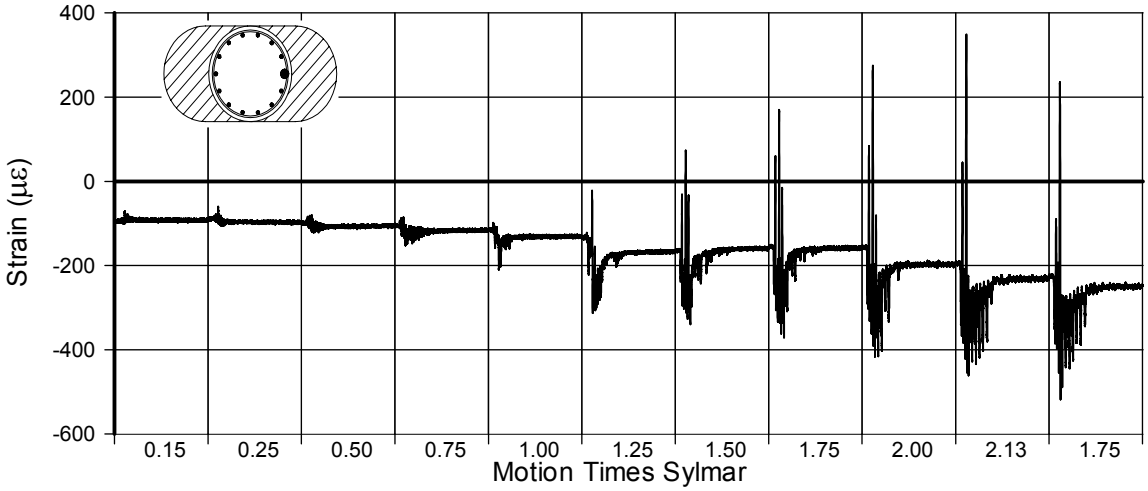

Fig. A-236 - Measured Strain in Gauge No. 121 for LFCD2

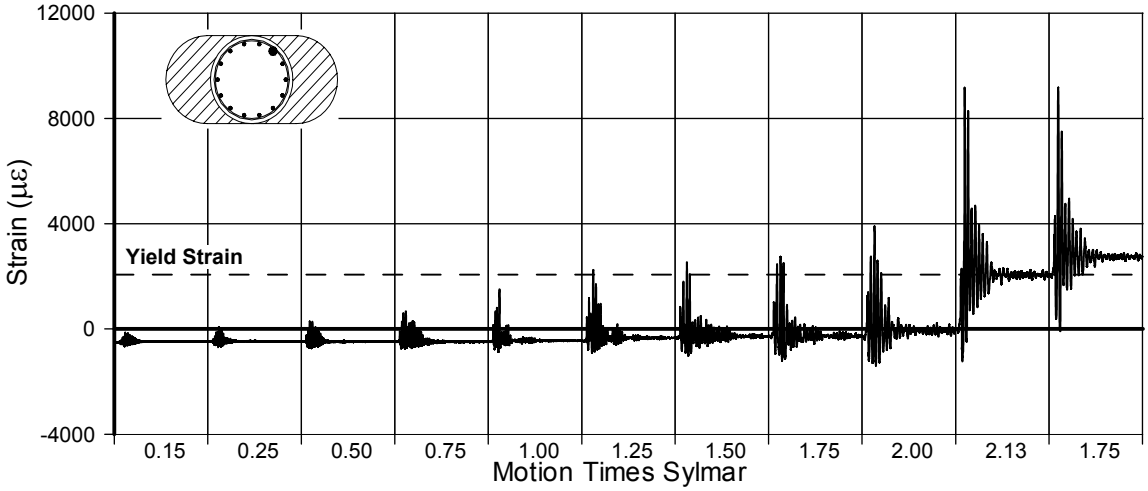

Fig. A-237 - Measured Strain in Gauge No. 122 for LFCD2

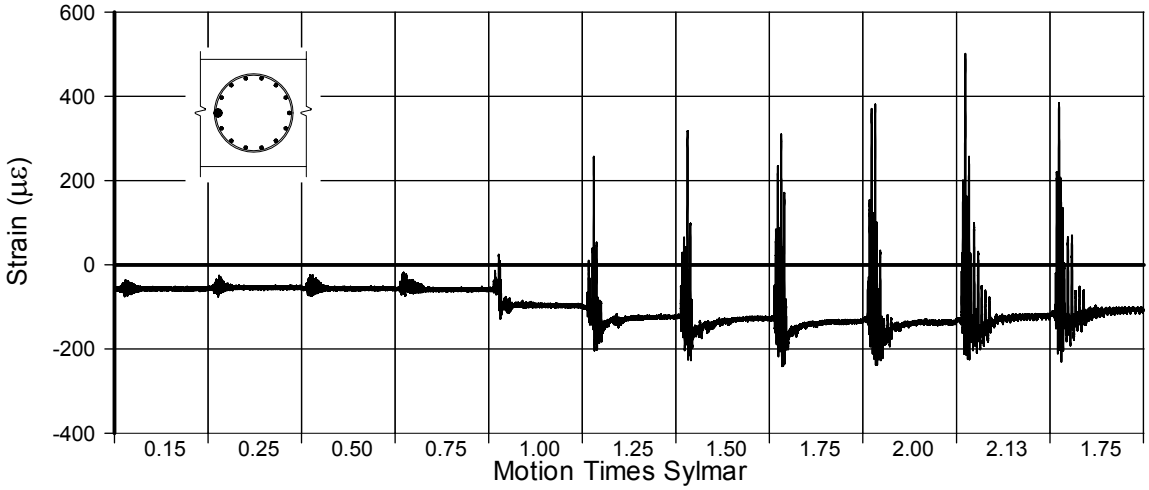

Fig. A-238 - Measured Strain in Gauge No. 123 for LFCD2

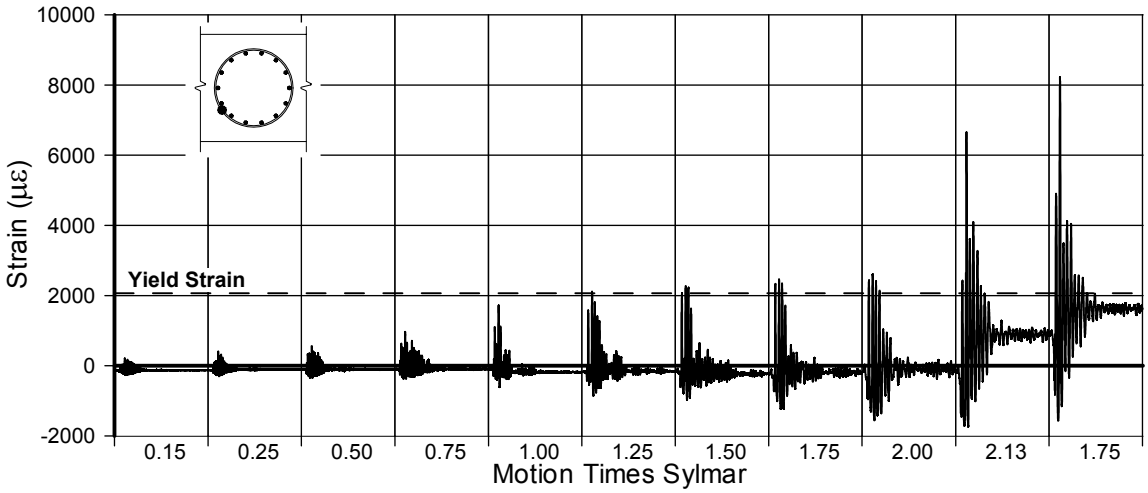

Fig. A-239 - Measured Strain in Gauge No. 124 for LFCD2

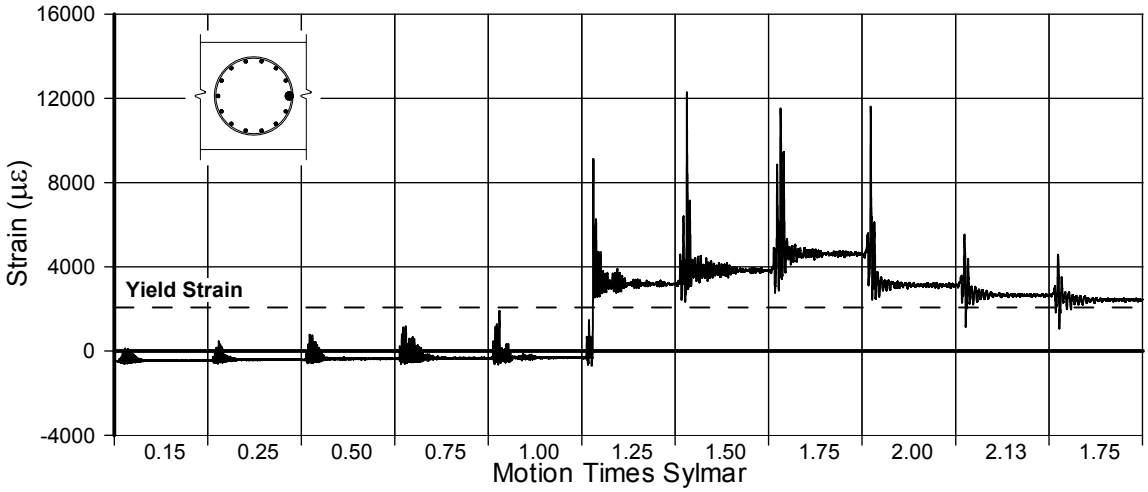

Fig. A-240 - Measured Strain in Gauge No. 125 for LFCD2

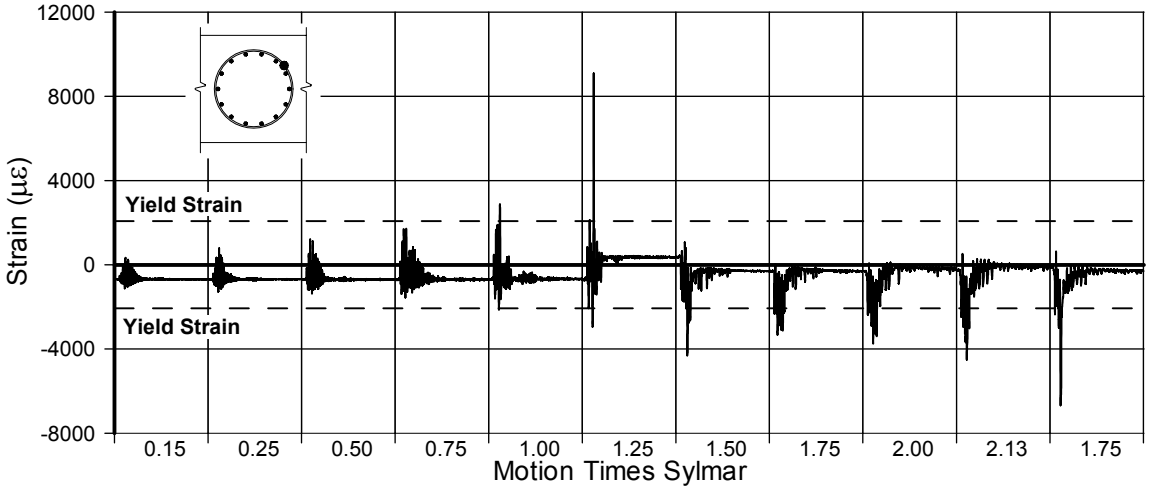

Fig. A-241 - Measured Strain in Gauge No. 126 for LFCD2

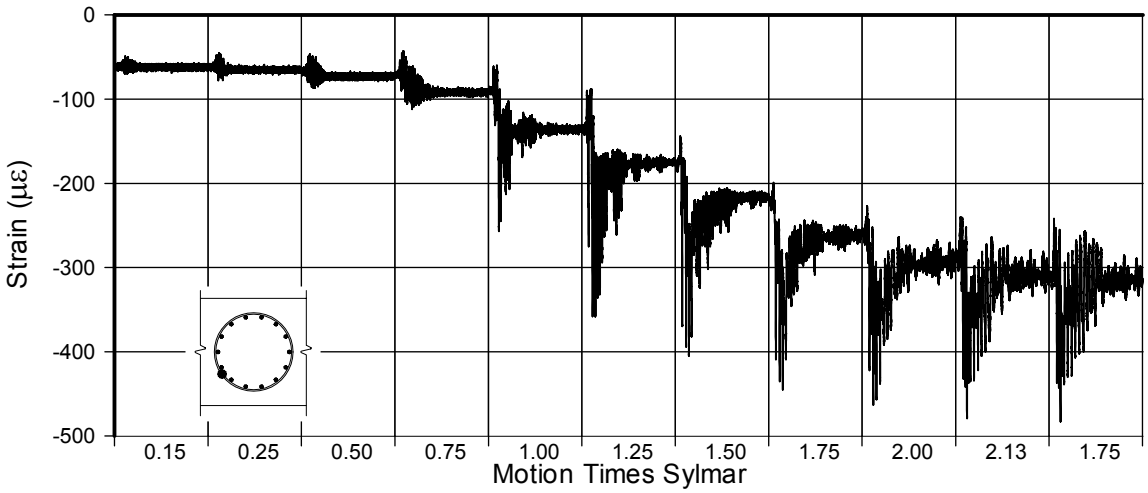

Fig. A-242 - Measured Strain in Gauge No. 129 for LFCD2

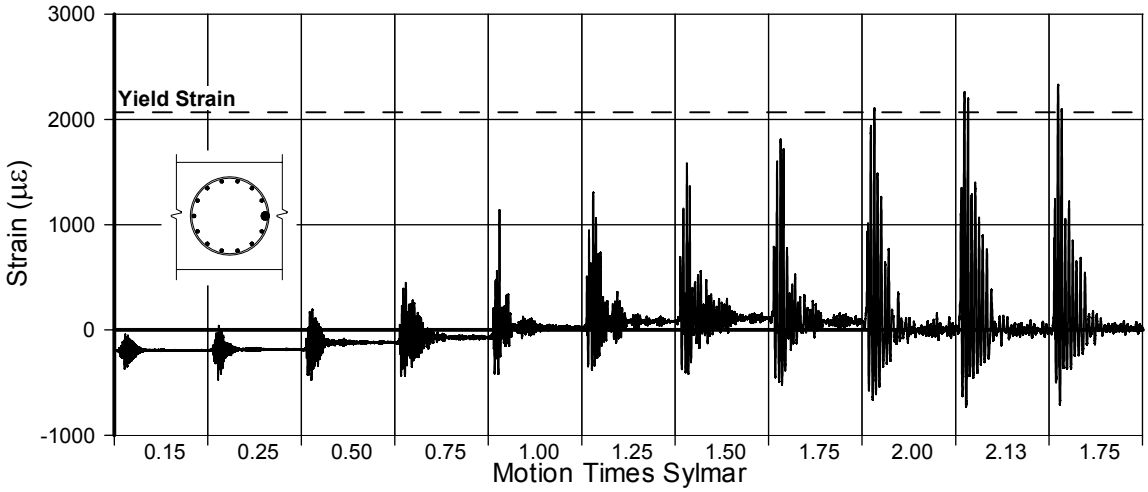

Fig. A-243 - Measured Strain in Gauge No. 130 for LFCD2

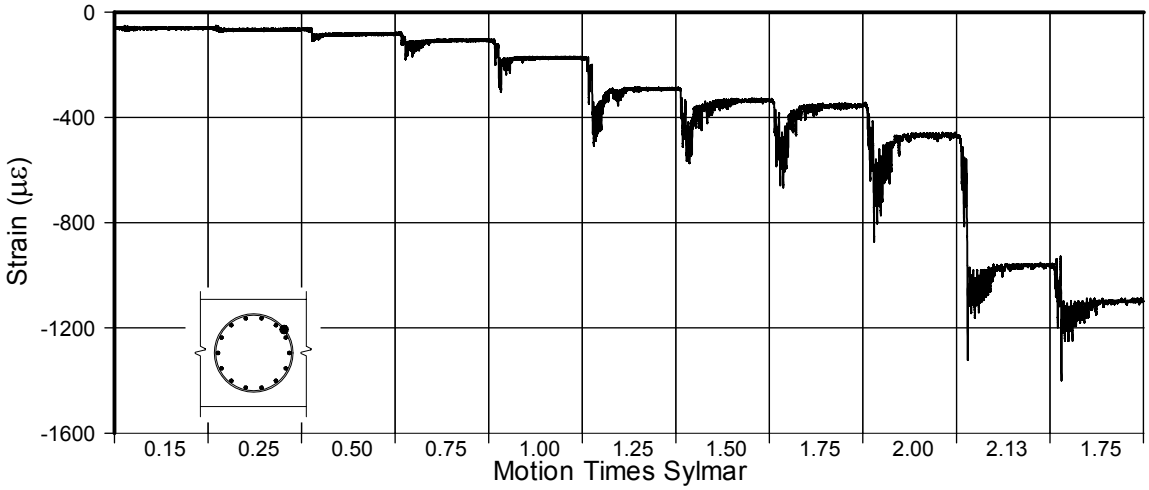

Fig. A-244 - Measured Strain in Gauge No. 131 for LFCD2

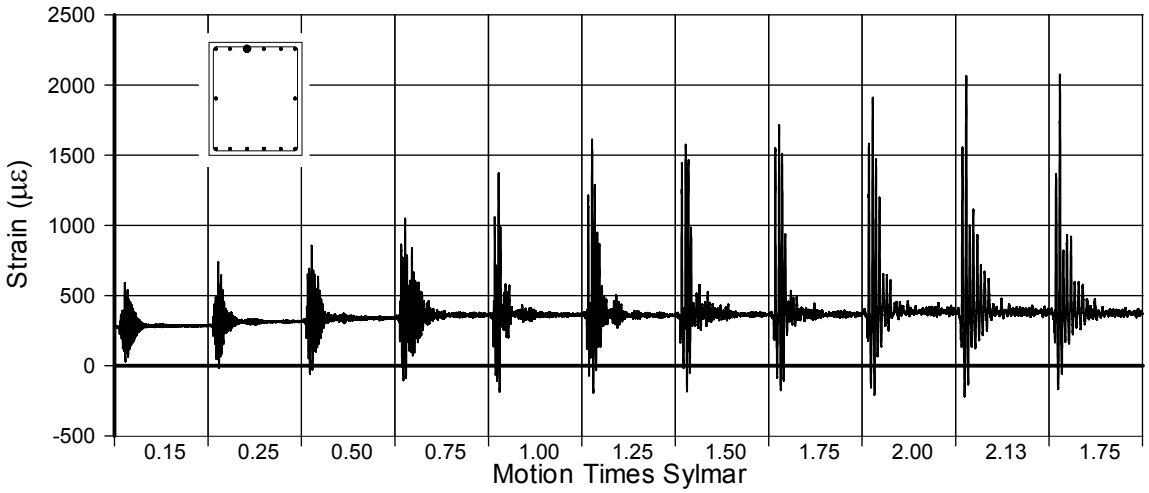

Fig. A-245 - Measured Strain in Gauge No. 133 for LFCD2

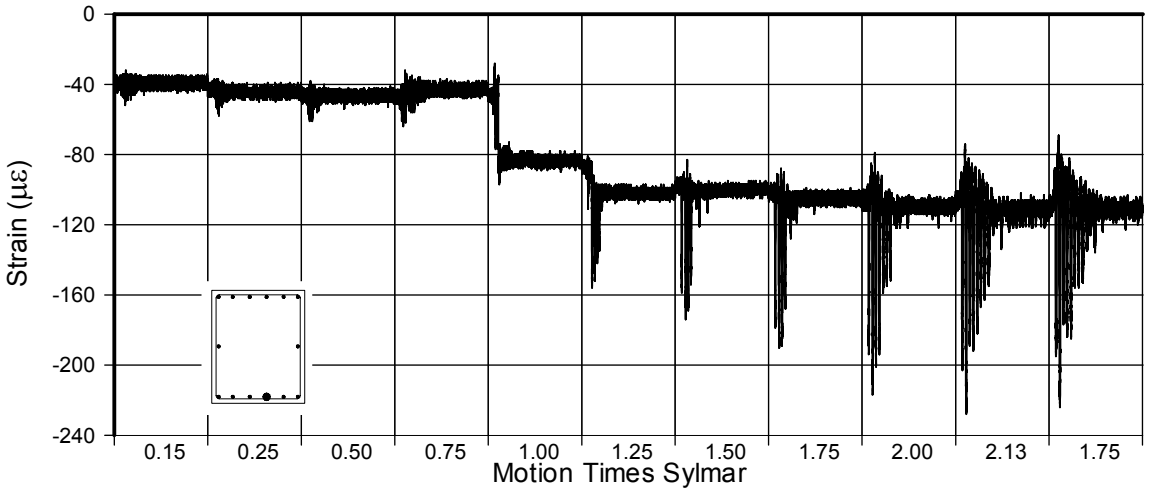

Fig. A-246 - Measured Strain in Gauge No. 134 for LFCD2

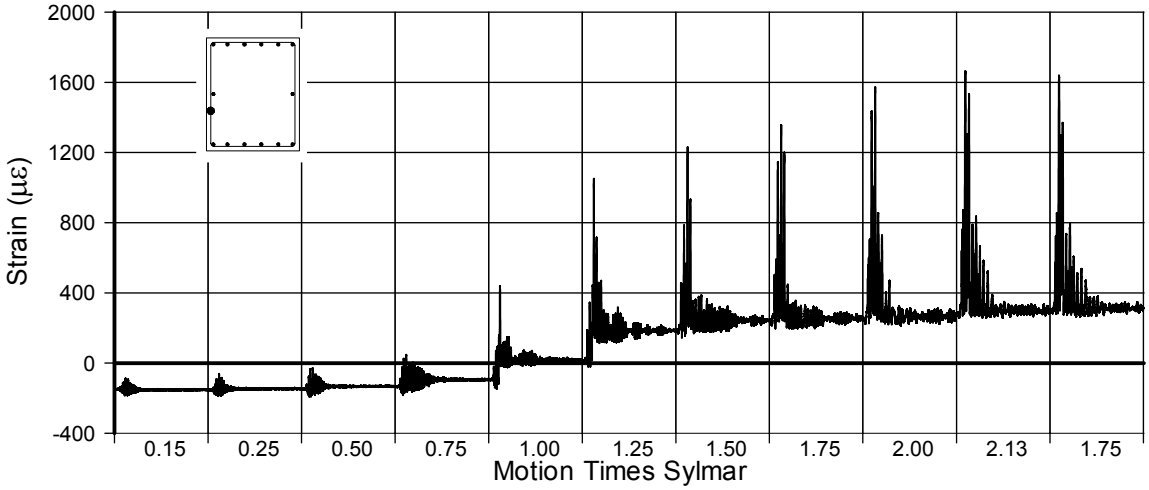

Fig. A-247 - Measured Strain in Gauge No. 135 for LFCD2

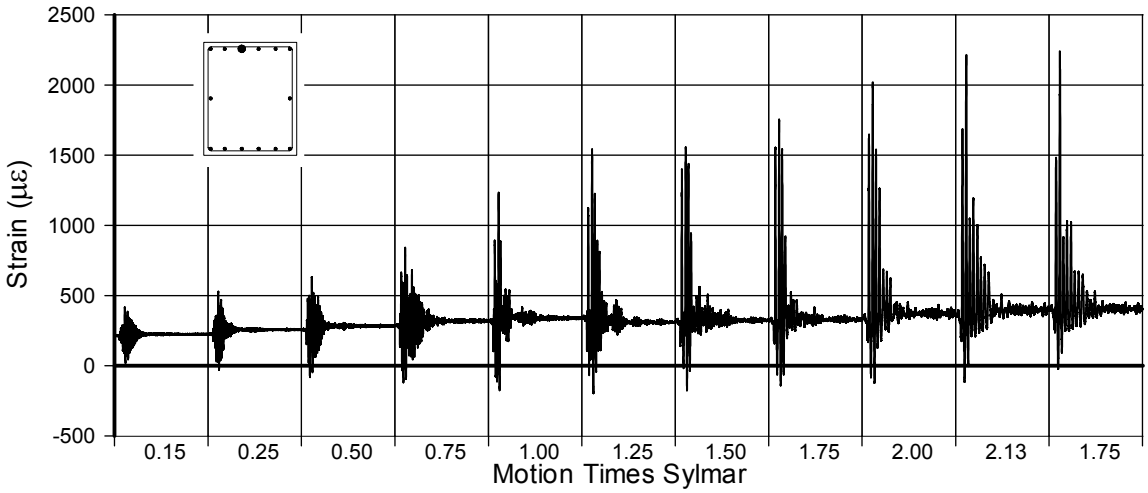

Fig. A-248 - Measured Strain in Gauge No. 136 for LFCD2

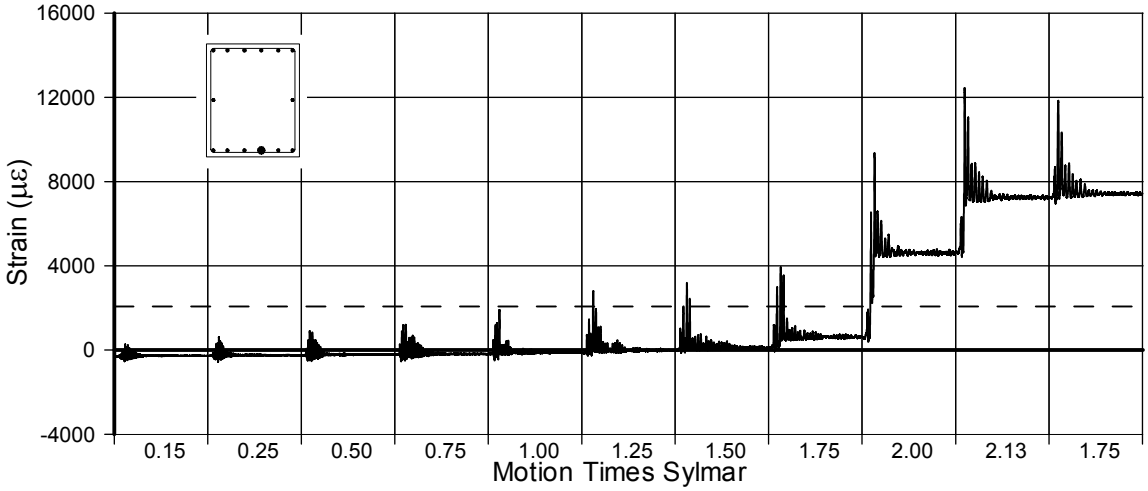

Fig. A-249 - Measured Strain in Gauge No. 137 for LFCD2

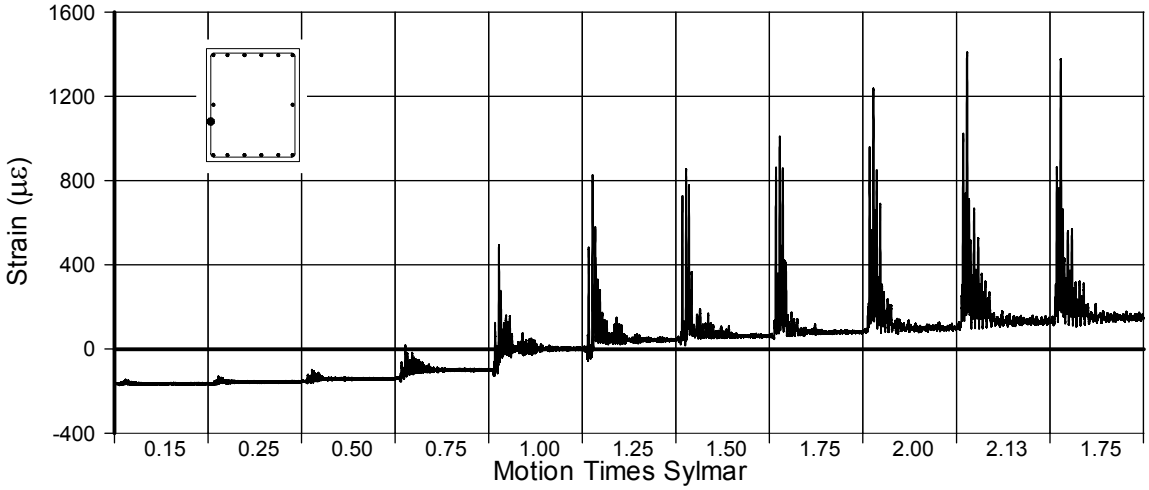

Fig. A-250 - Measured Strain in Gauge No. 138 for LFCD2

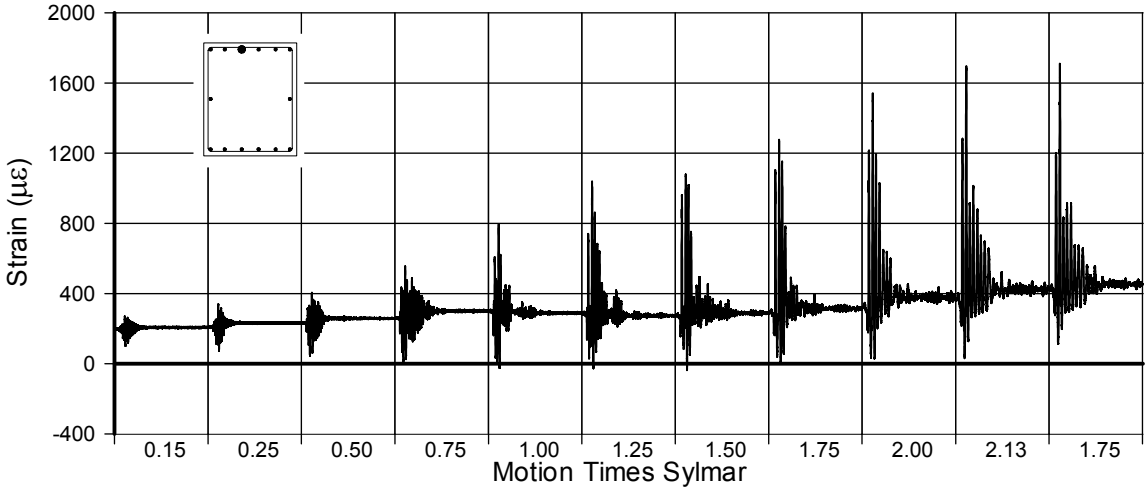

Fig. A-251 - Measured Strain in Gauge No. 139 for LFCD2

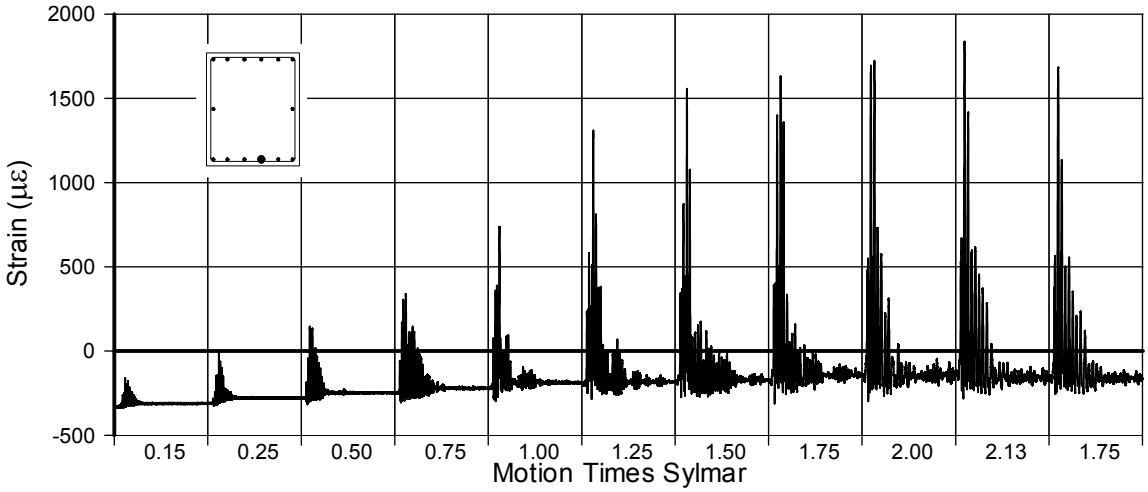

Fig. A-252 - Measured Strain in Gauge No. 140 for LFCD2

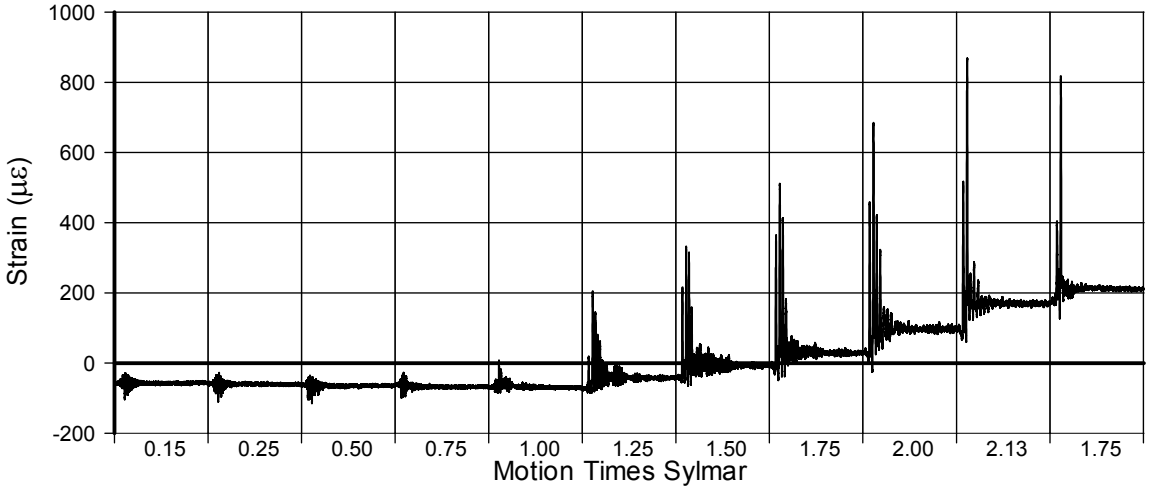

Fig. A-253 - Measured Strain in Gauge No. 141 for LFCD2

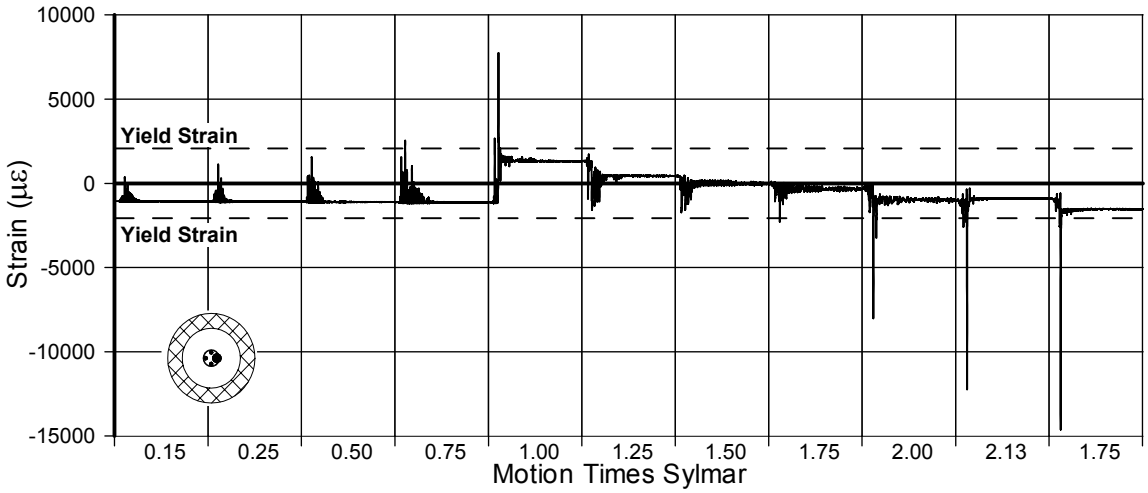

Fig. A-254 - Measured Strain in Gauge No. 144 for LFCD2

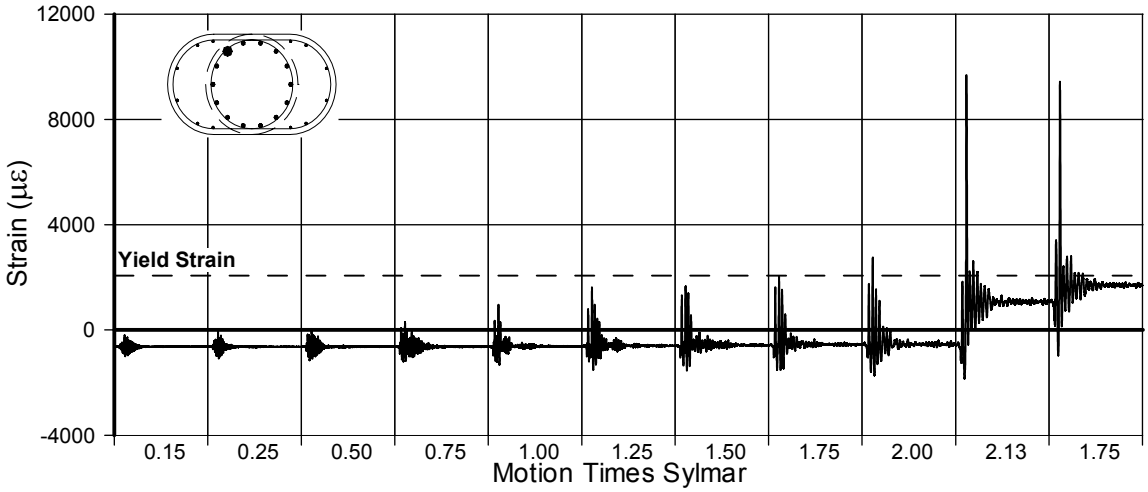

Fig. A-255 - Measured Strain in Gauge No. 145 for LFCD2

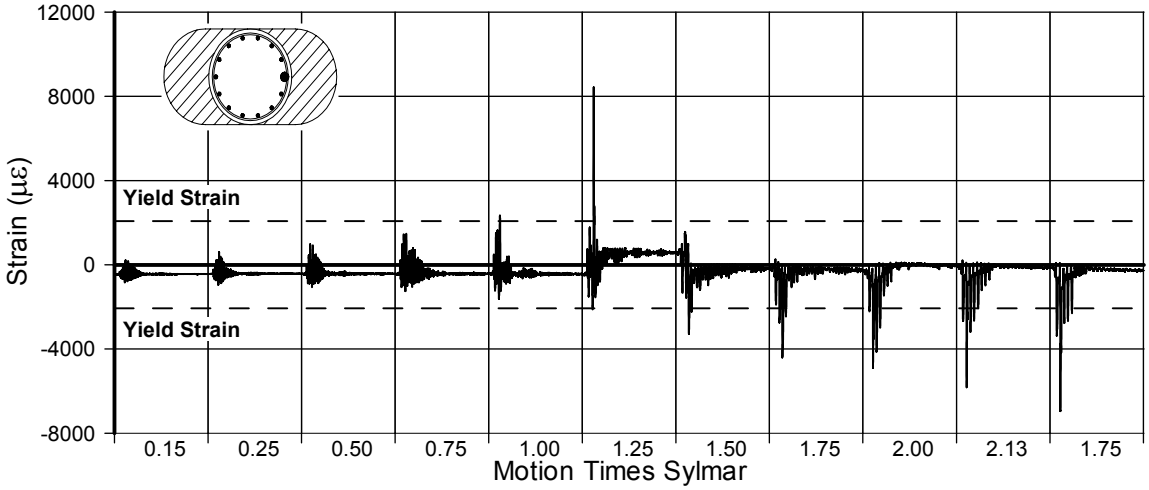

Fig. A-256 - Measured Strain in Gauge No. 146 for LFCD2

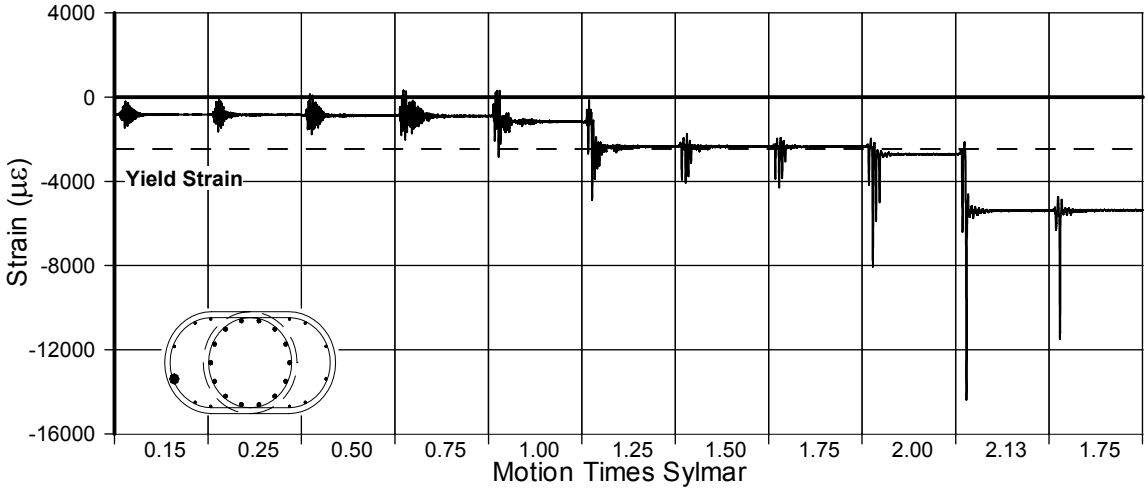

Fig. A-257 - Measured Strain in Gauge No. 148 for LFCD2

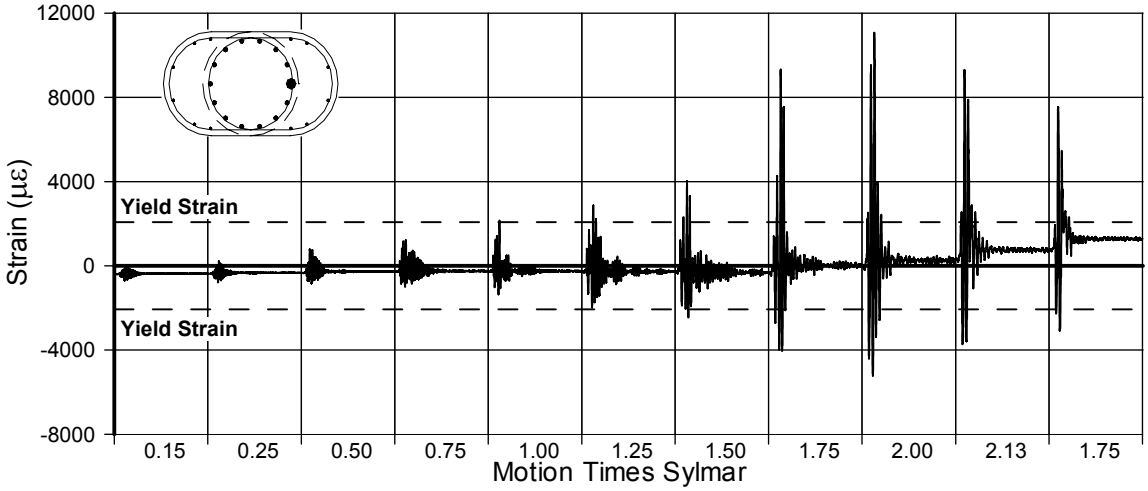

Fig. A-258 - Measured Strain in Gauge No. 149 for LFCD2

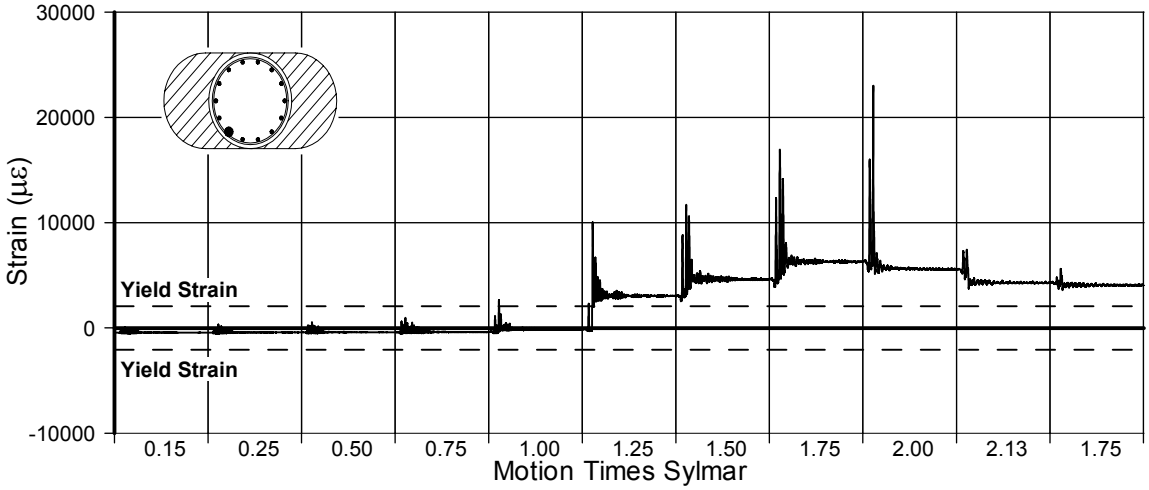

Fig. A-259 - Measured Strain in Gauge No. 150 for LFCD2

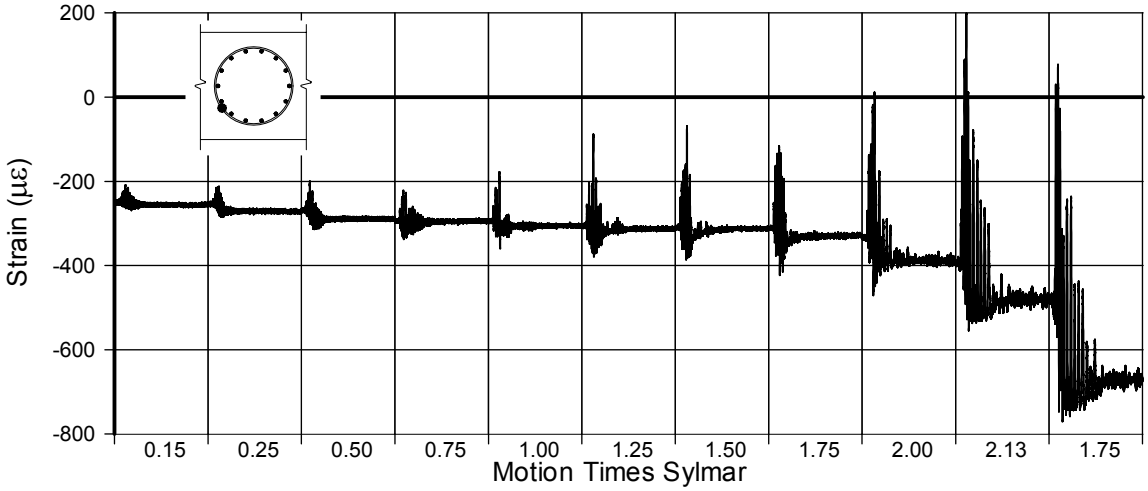

Fig. A-260 - Measured Strain in Gauge No. 151 for LFCD2

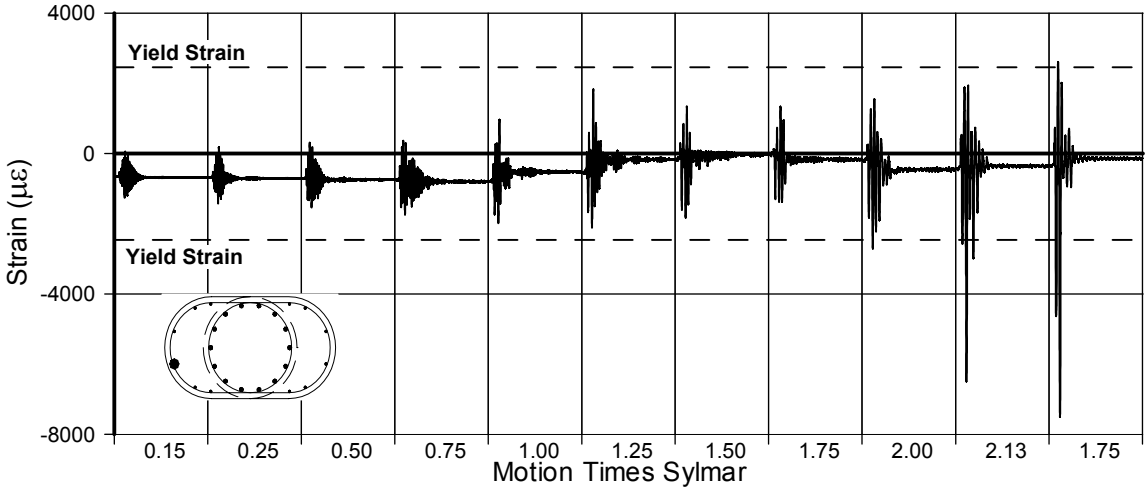

Fig. A-261 - Measured Strain in Gauge No. 152 for LFCD2

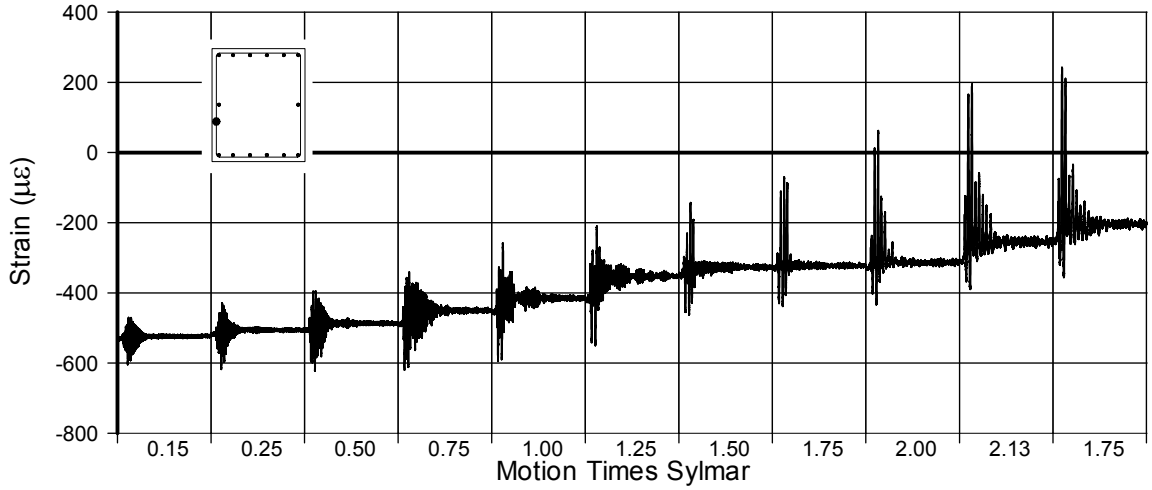

Fig. A-262 - Measured Strain in Gauge No. 153 for LFCD2

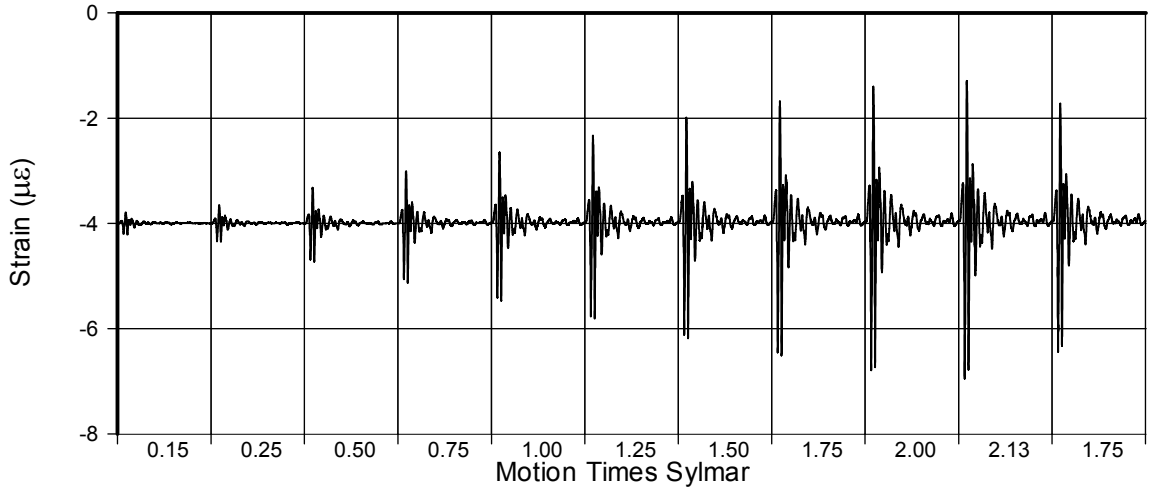

Fig. A-263 - Measured Shake Table Displacement for LFCD2

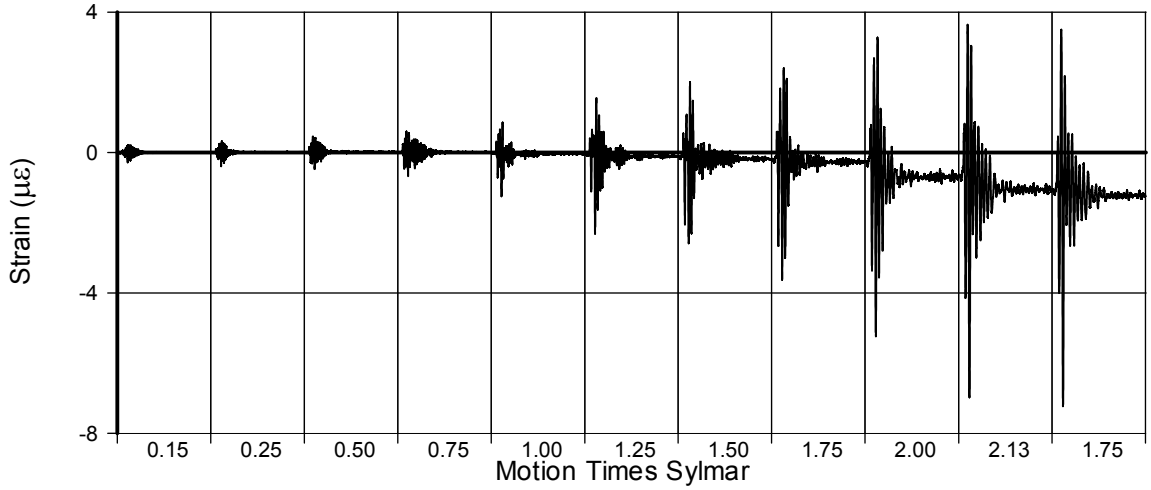

Fig. A-264 - Measured Measured Beam's Relative Dispalcement for LFCD2

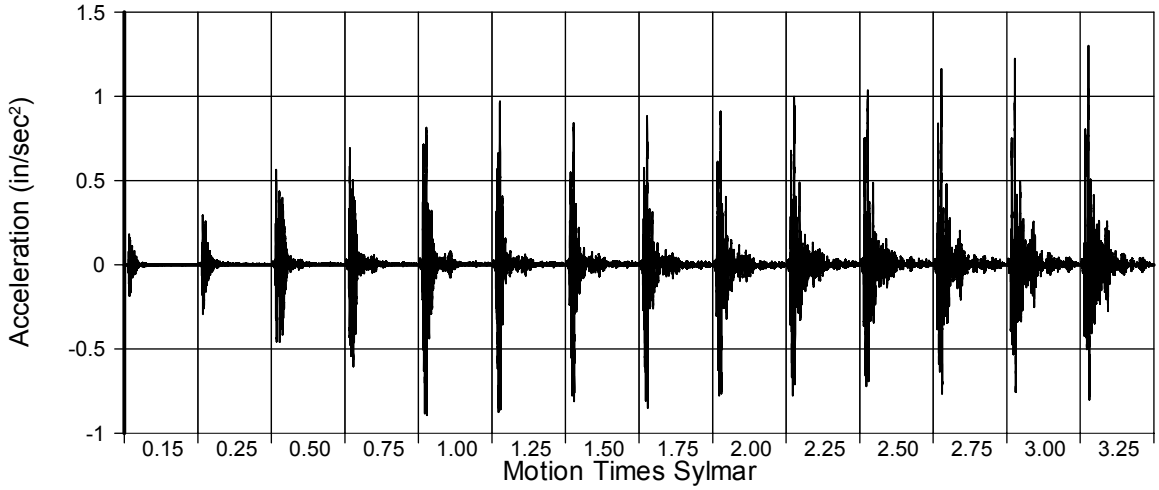

Fig. A-265 - Measured In-Plane Acceleration for SFCD2

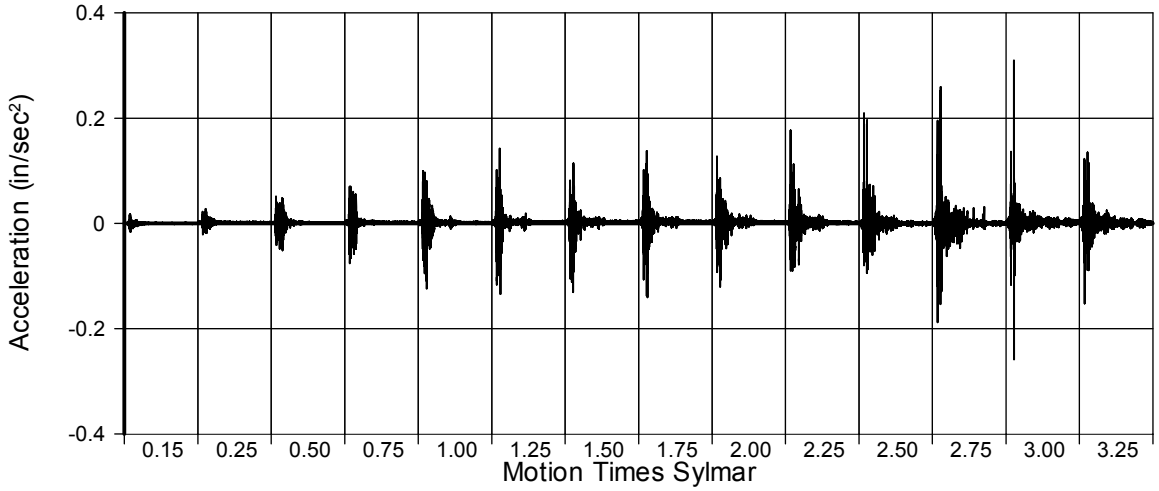

Fig. A-266 - Measured Transverse Acceleration for SFCD2

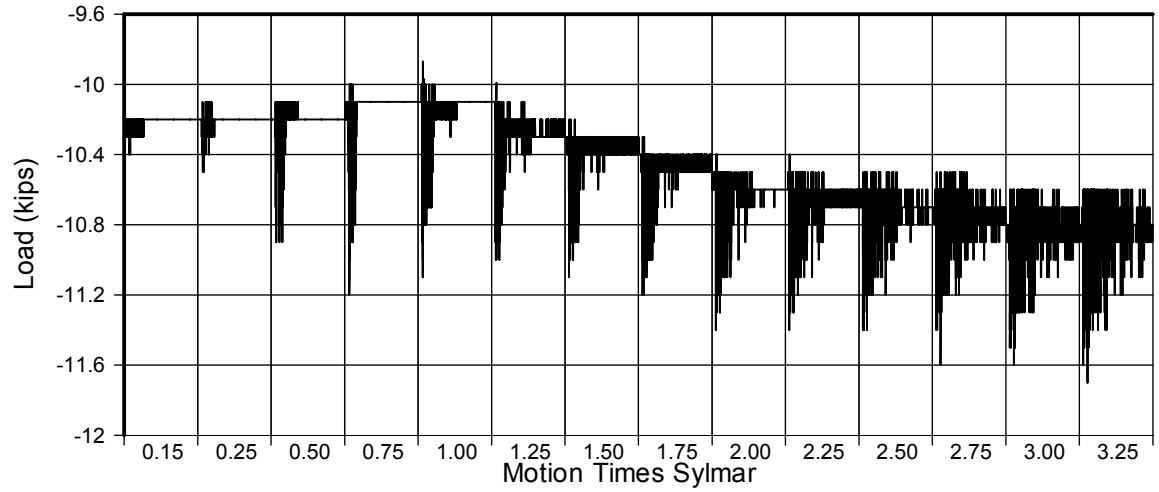

Fig. A-267 - Measured Vertical Load for SFCD2 (West Column)

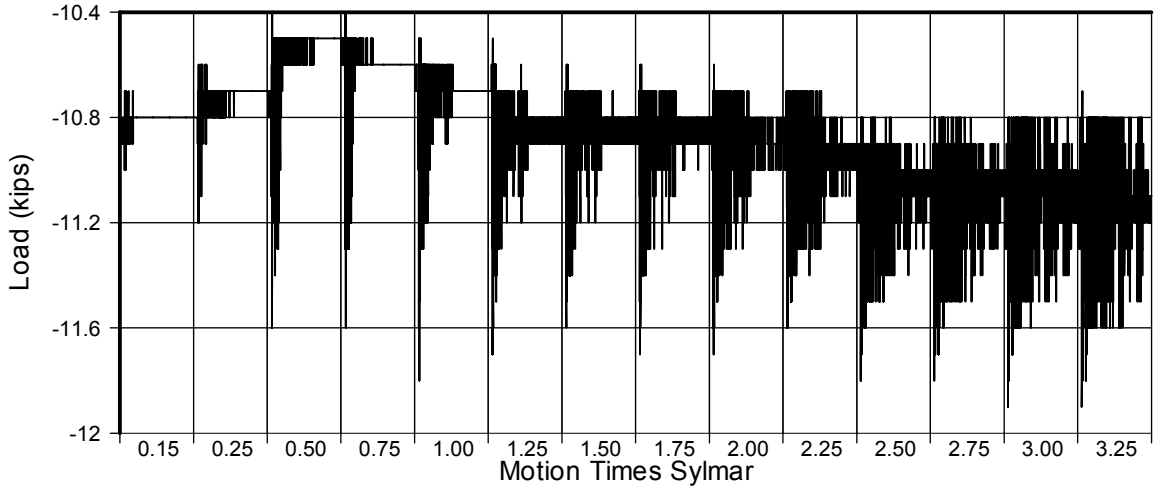

Fig. A-268 - Measured Vertical Load for SFCD2 (East Column)

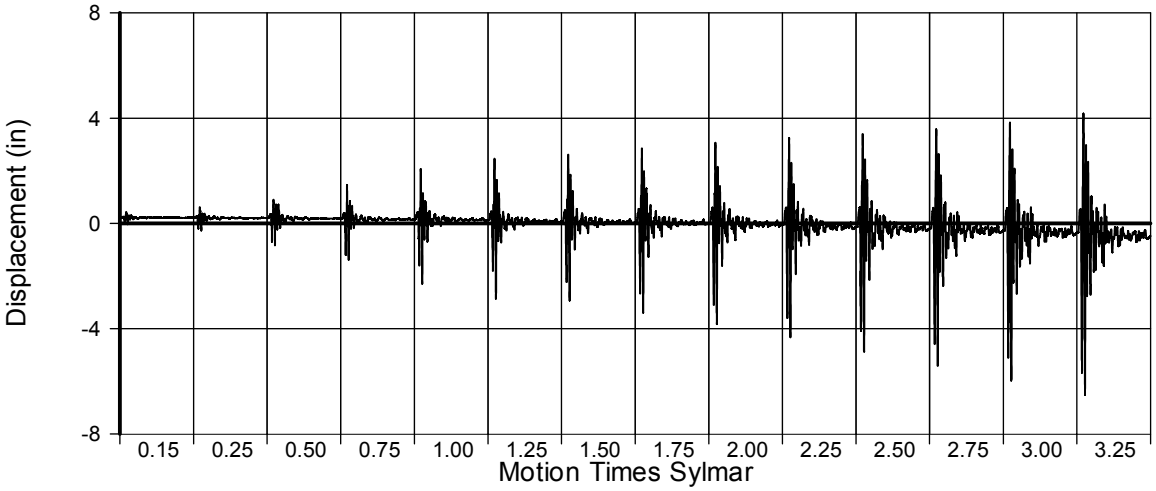

Fig. A-269 - Measured Absolute Displacement for SFCD2

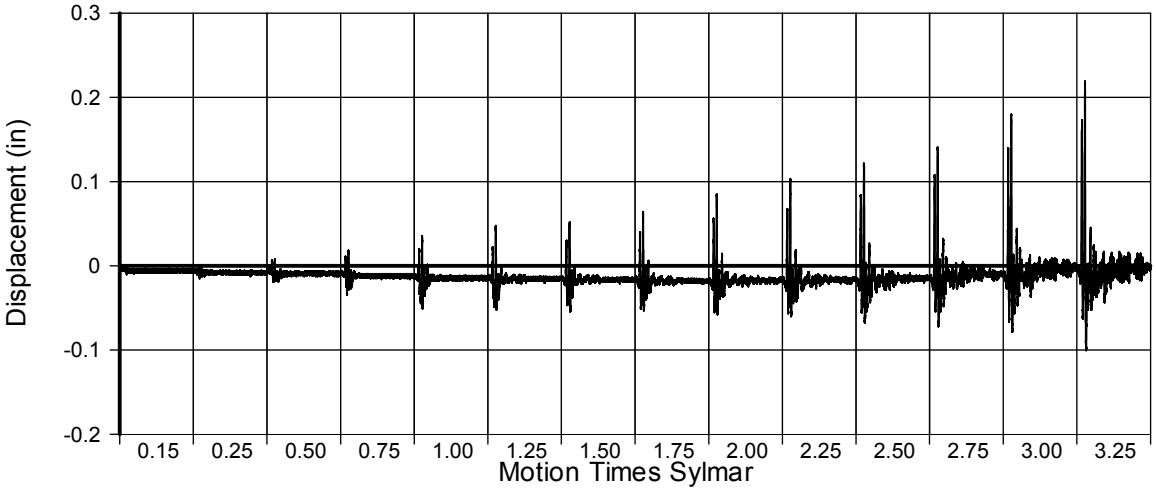

Fig. A-270 - Measured Transeverse Displacement for SFCD2

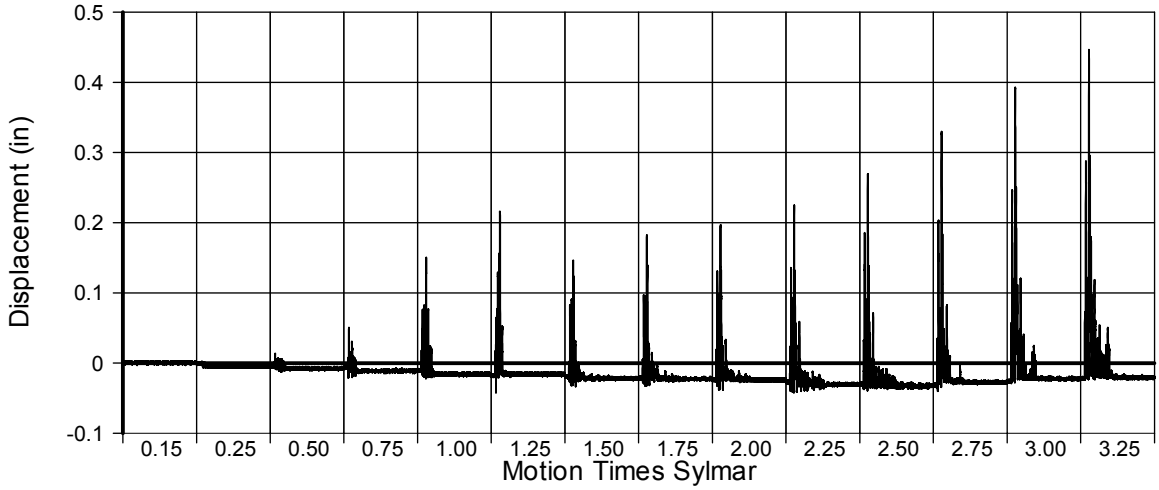

Fig. A-271 - Measured Mid-Span Deflection for SFCD2

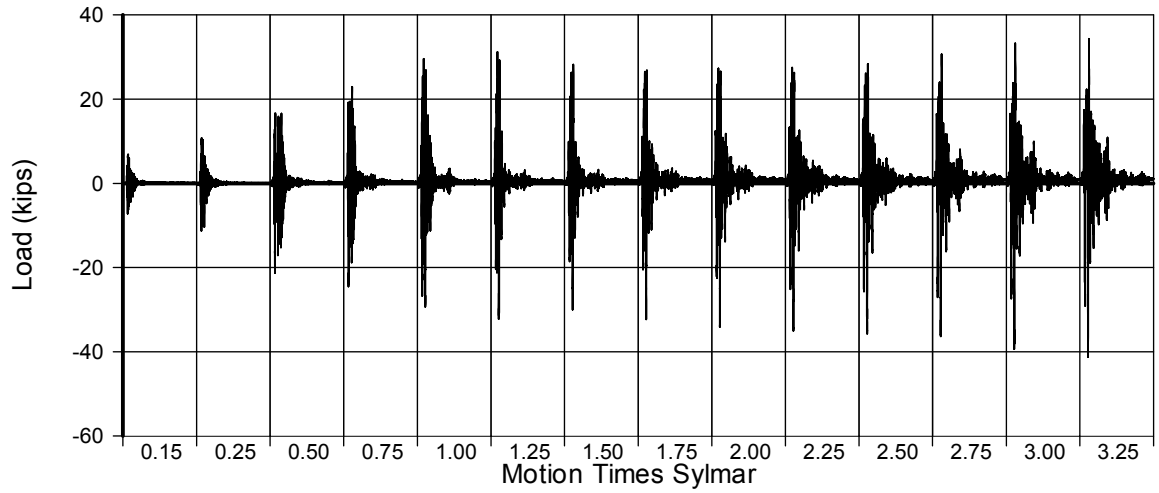

Fig. A-272 - Measured Link Load for SFCD2

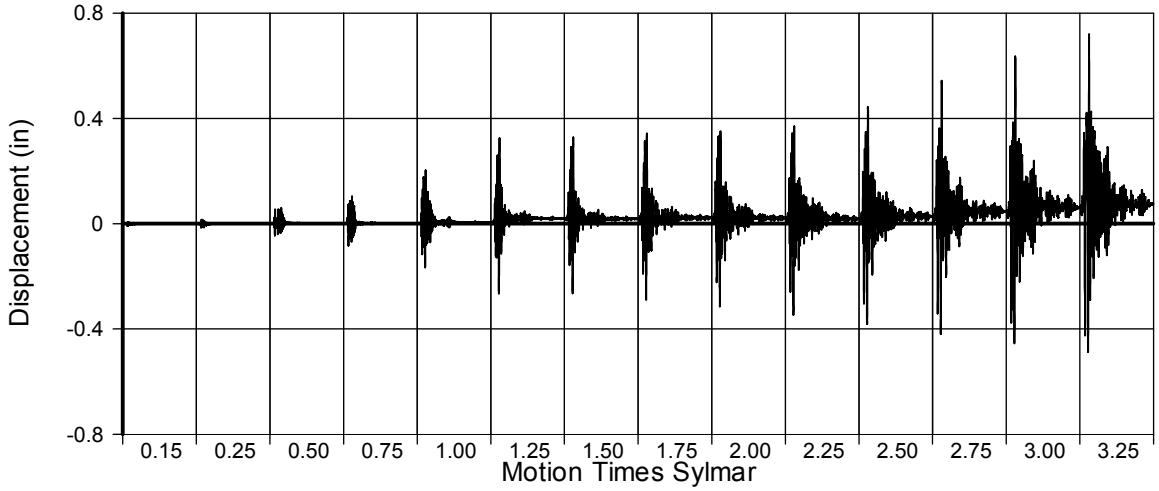

Fig. A-273 - Measured Disp. in Transeducer No. 9 for SFCD2

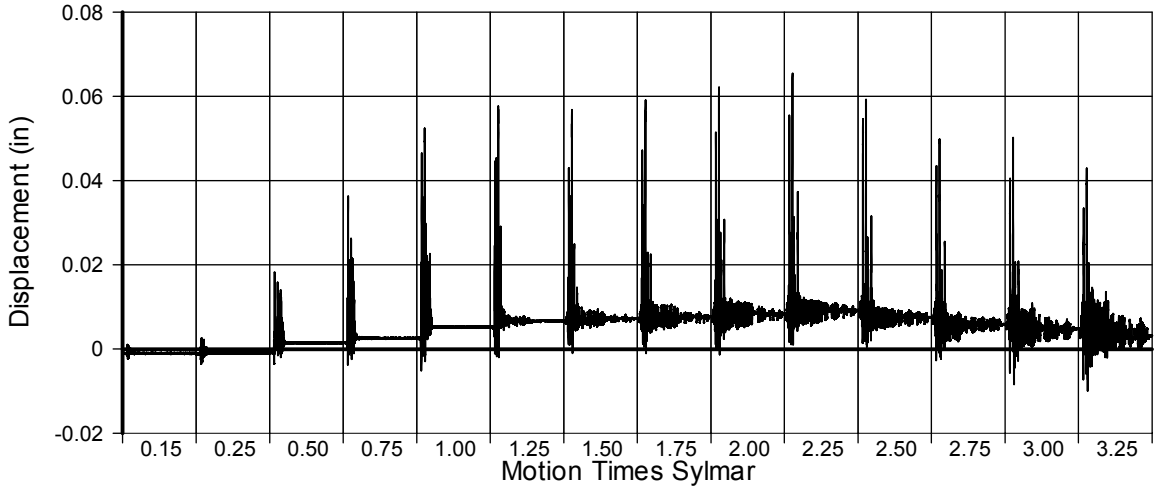

Fig. A-274 - Measured Disp. in Transeducer No. 10 for SFCD2

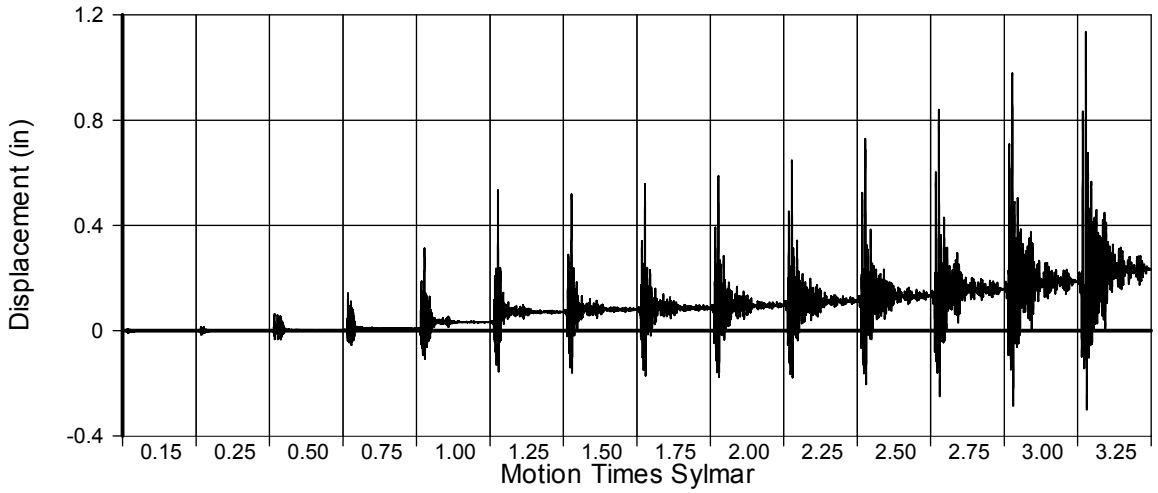

Fig. A-275 - Measured Disp. in Transeducer No. 11 for SFCD2

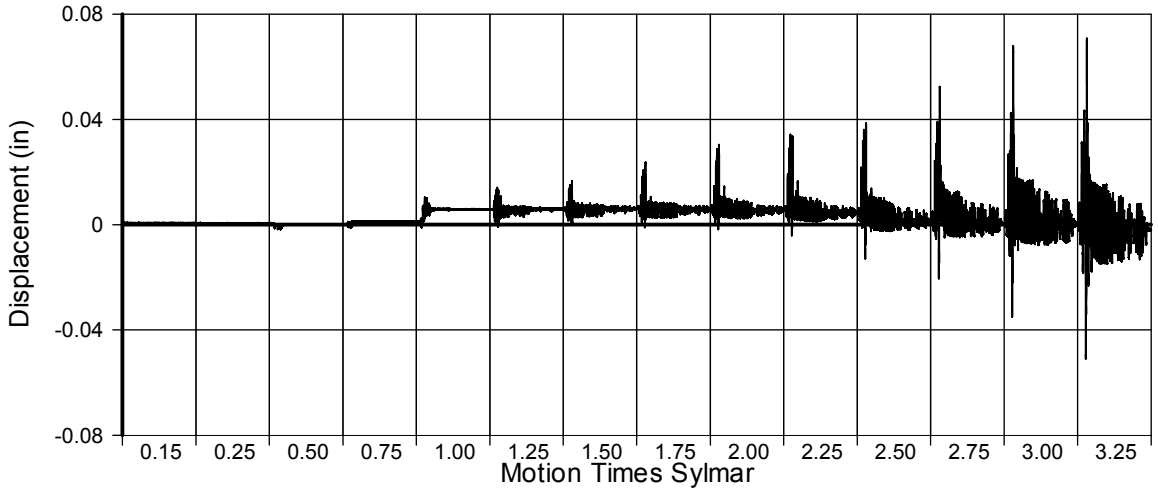

Fig. A-276 - Measured Disp. in Transeducer No. 12 for SFCD2

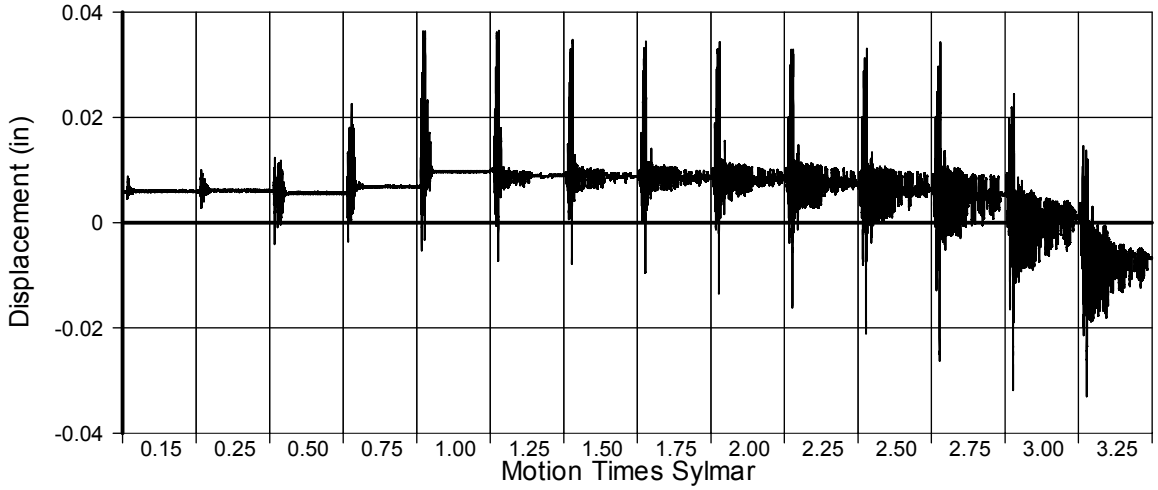

Fig. A-277 - Measured Disp. in Transeducer No. 13 for SFCD2

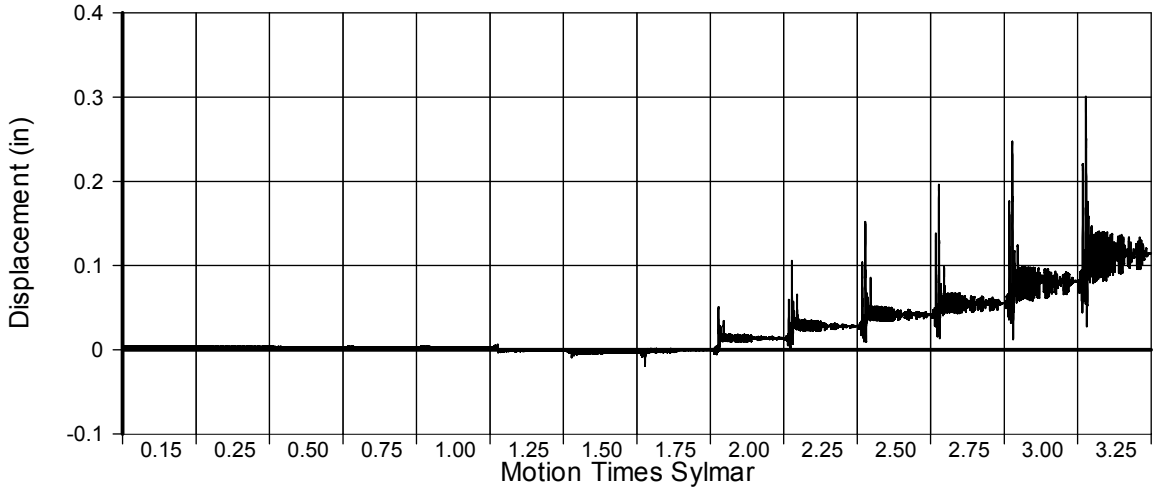

Fig. A-278 - Measured Disp. in Transeducer No. 14 for SFCD2

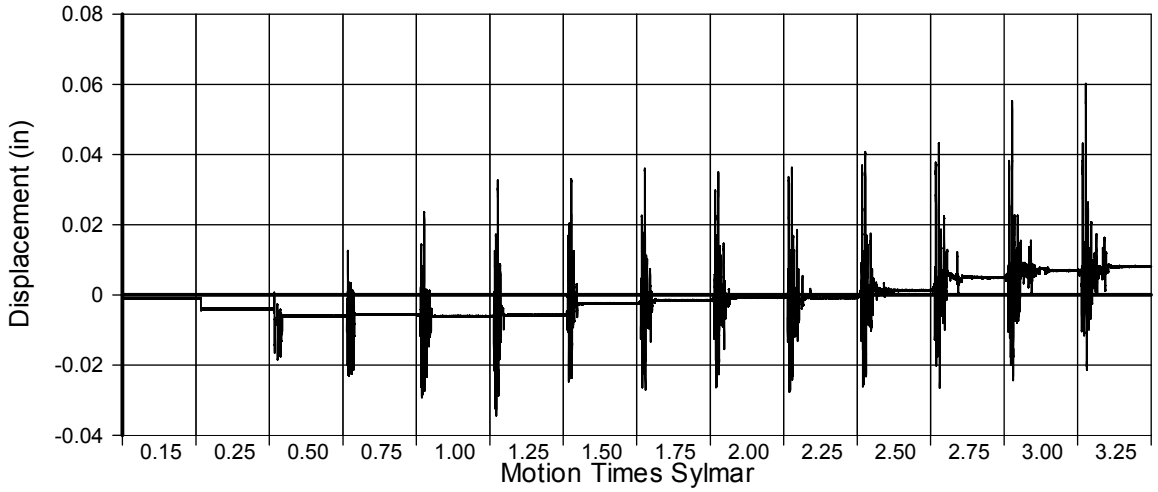

Fig. A-279 - Measured Disp. in Transeducer No. 15 for SFCD2

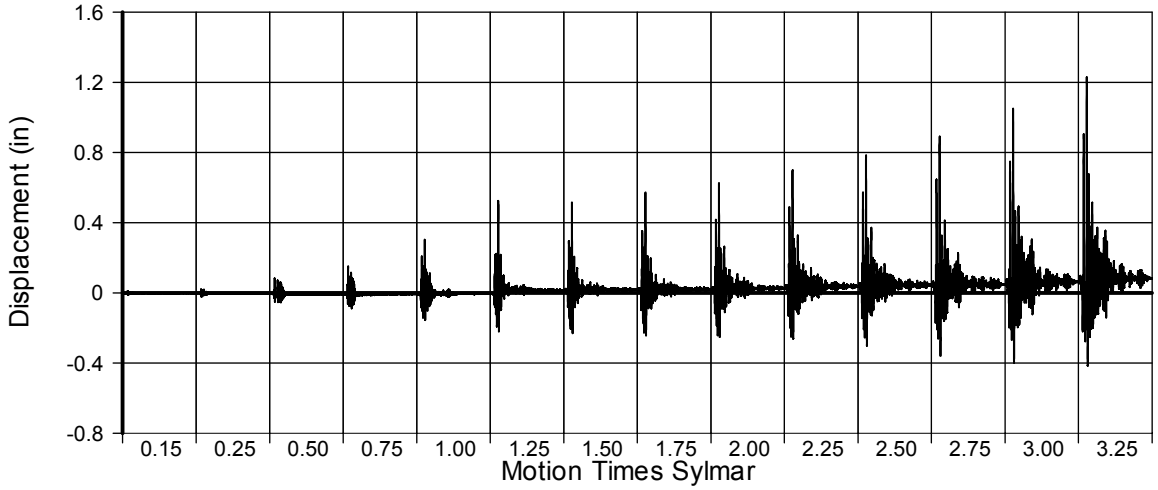

Fig. A-280 - Measured Disp. in Transeducer No. 16 for SFCD2

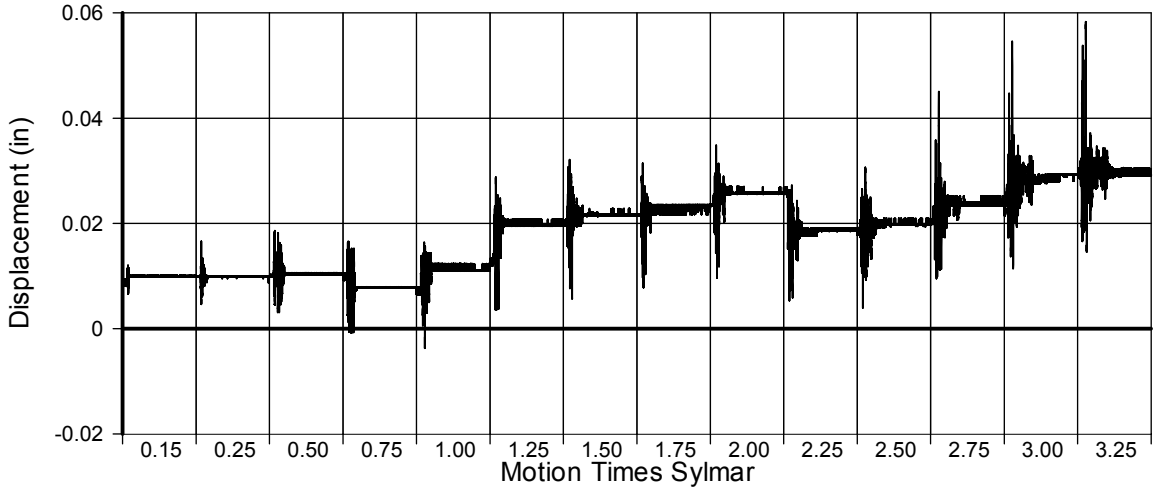

Fig. A-281 - Measured Disp. in Transeducer No. 18 for SFCD2

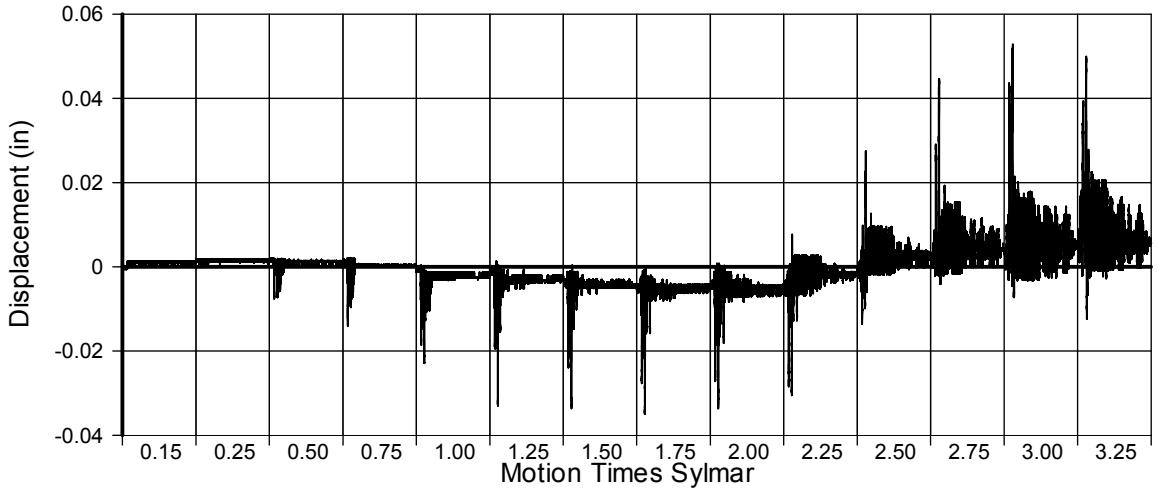

Fig. A-282 - Measured Disp. in Transeducer No. 20 for SFCD2

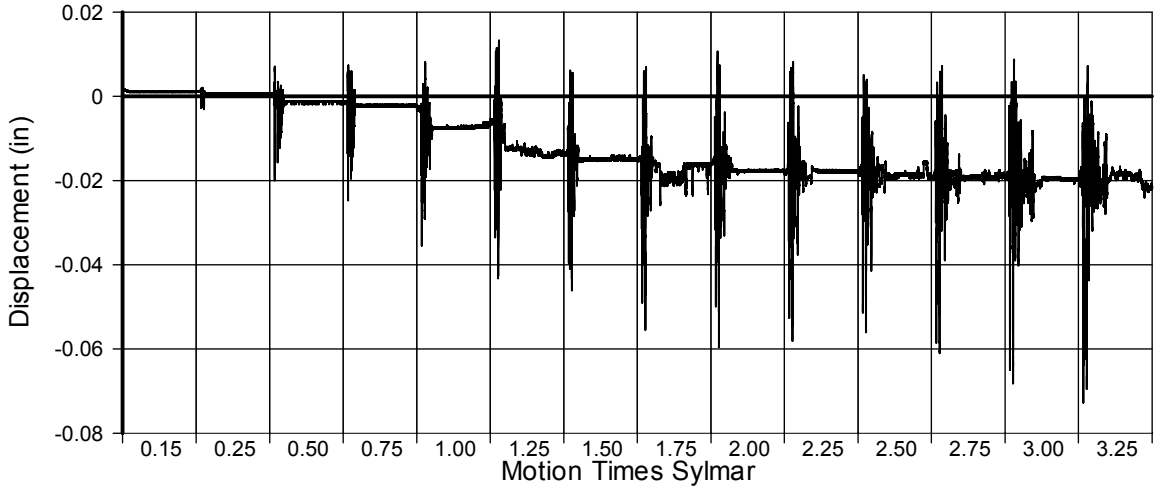

Fig. A-283 - Measured Disp. in Transeducer No. 21 for SFCD2

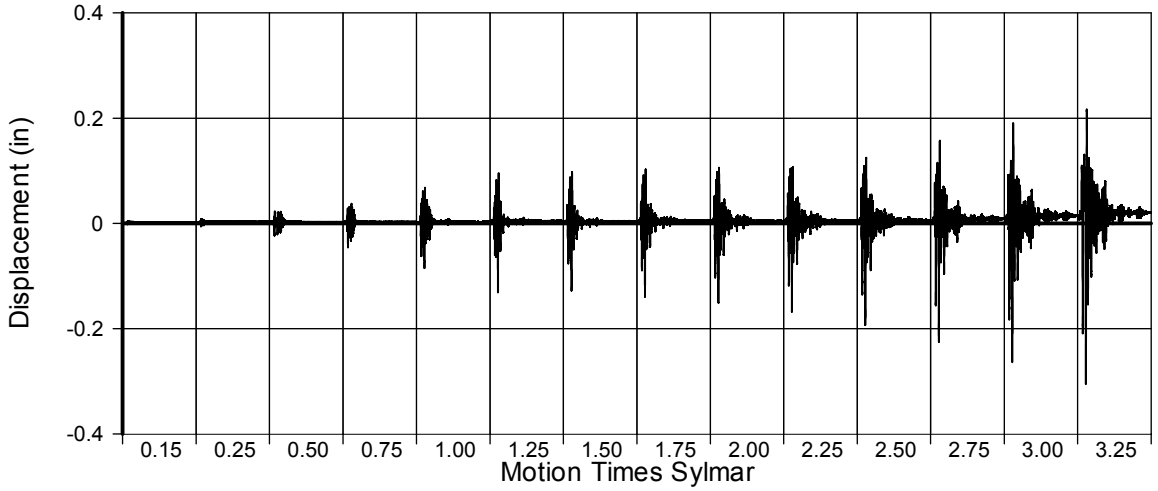

Fig. A-284 - Measured Disp. in Transeducer No. 22 for SFCD2

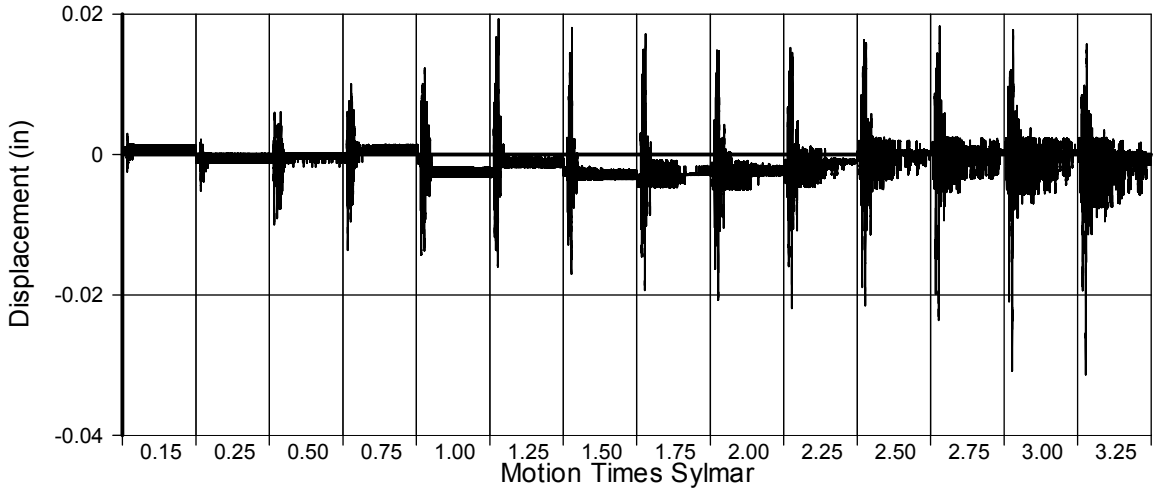

Fig. A-285 - Measured Disp. in Transeducer No. 23 for SFCD2

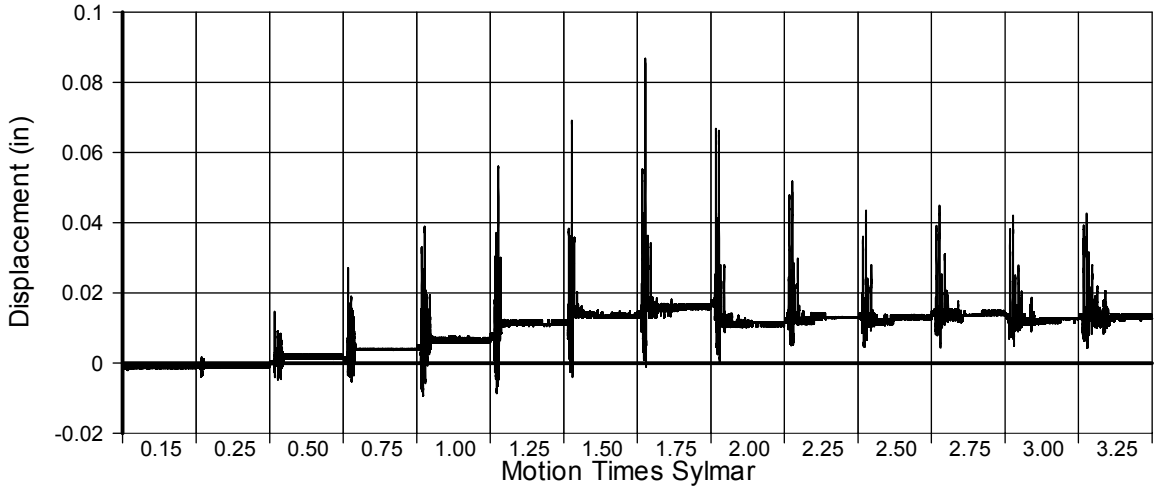

Fig. A-286 - Measured Disp. in Transeducer No. 24 for SFCD2

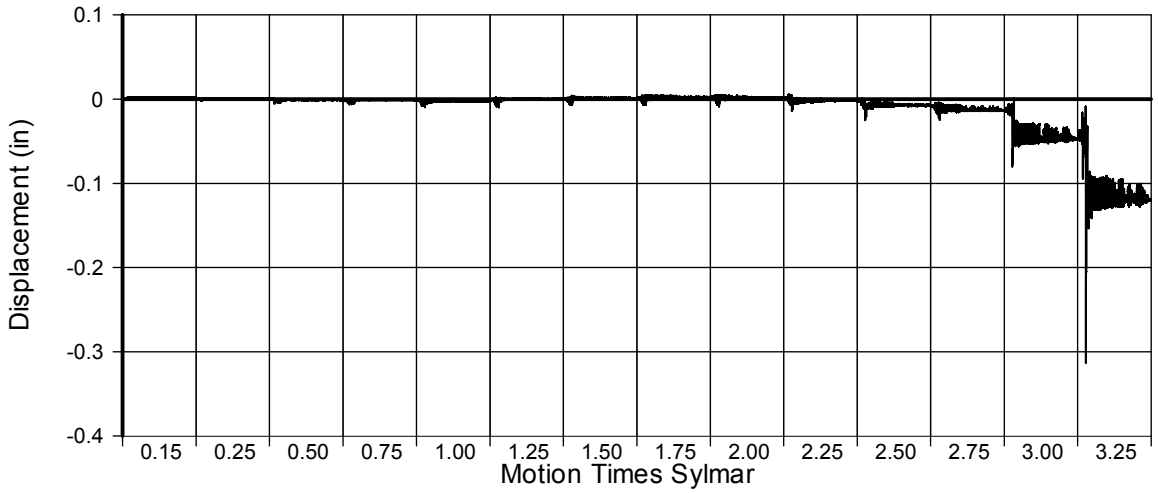

Fig. A-287 - Measured Disp. in Transeducer No. 25 for SFCD2

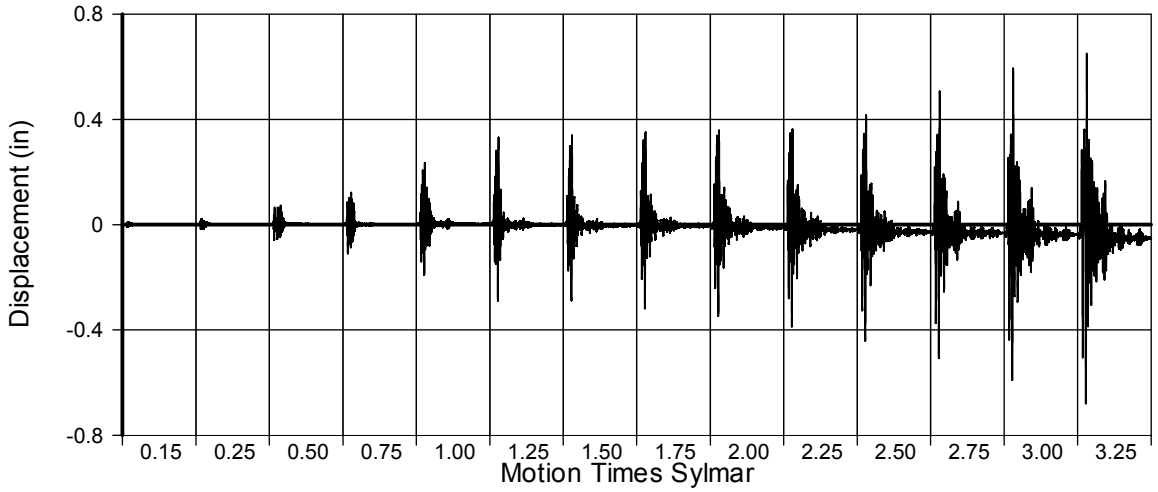

Fig. A-288 - Measured Disp. in Transeducer No. 26 for SFCD2

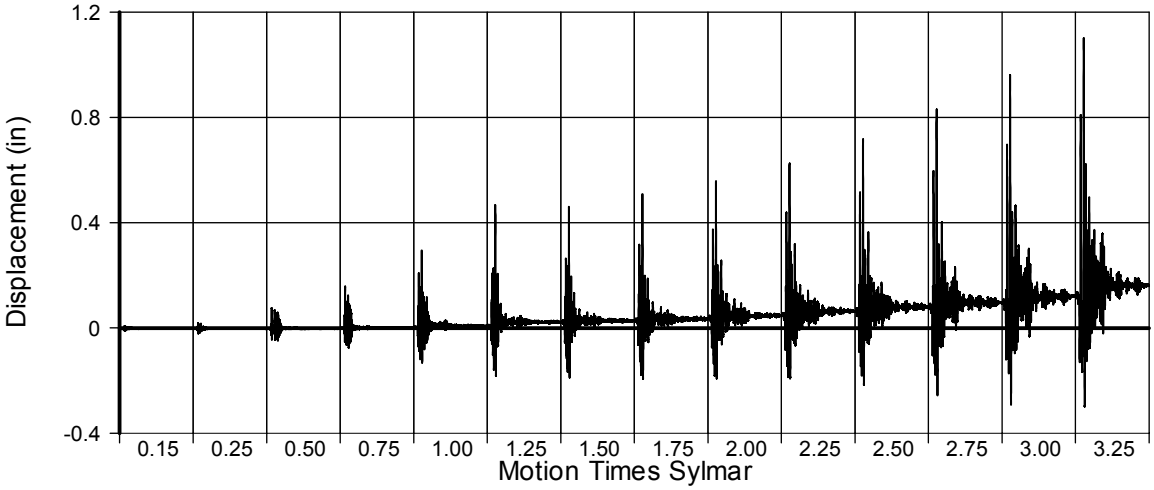

Fig. A-289 - Measured Disp. in Transeducer No. 27 for SFCD2

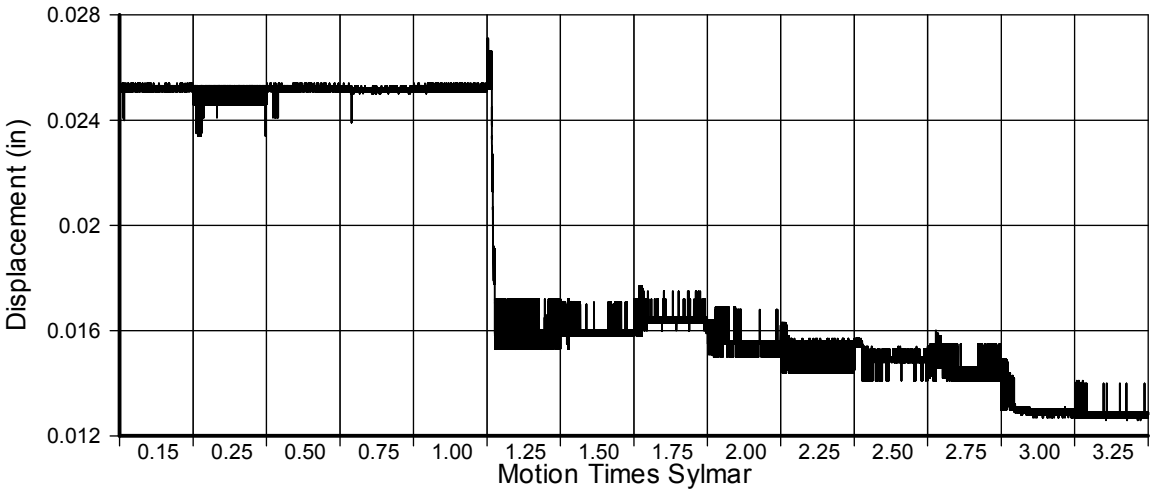

Fig. A-290 - Measured Disp. in Transeducer No. 28 for SFCD2

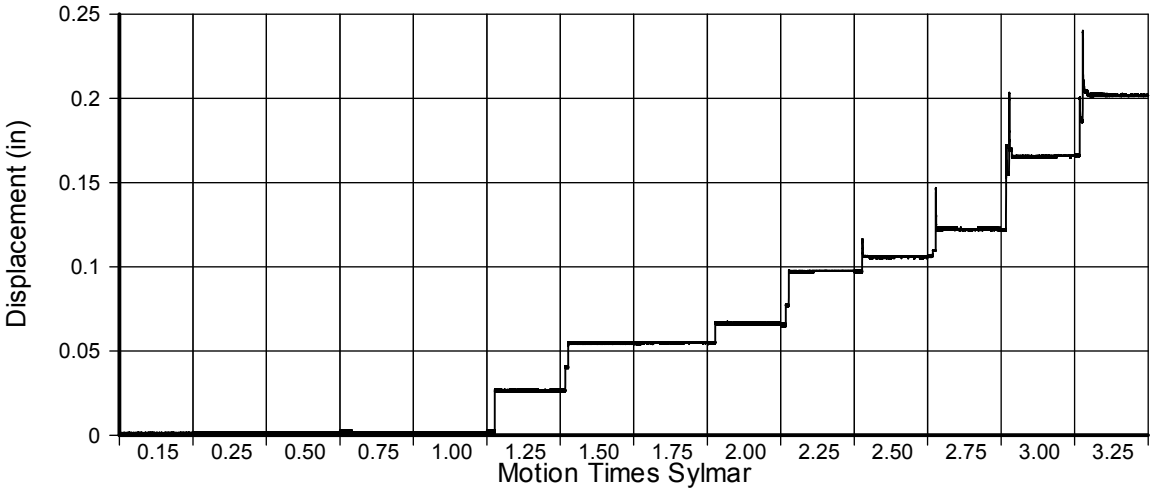

Fig. A-291 - Measured Disp. in Transeducer No. 29 for SFCD2

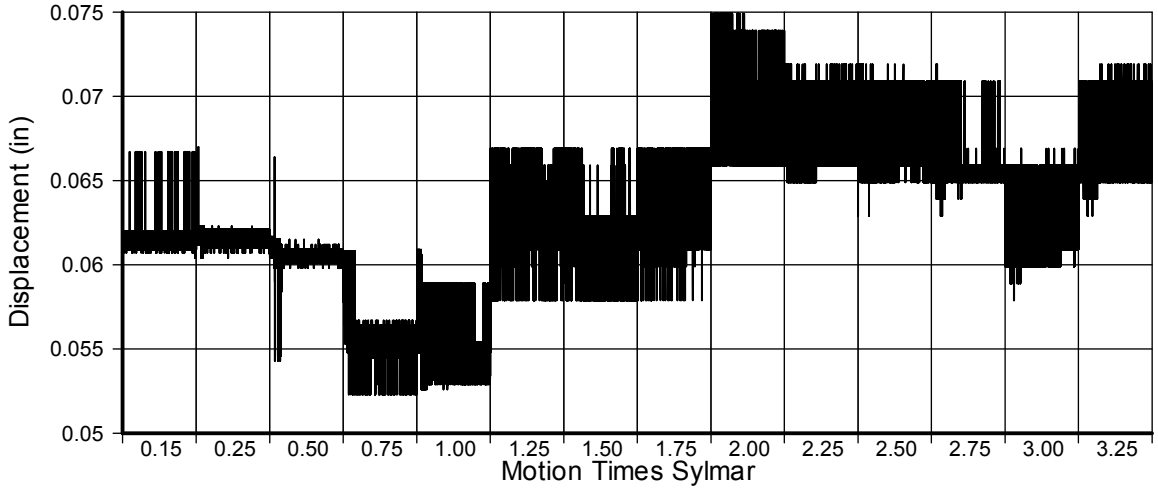

Fig. A-292 - Measured Disp. in Transeducer No. 30 for SFCD2

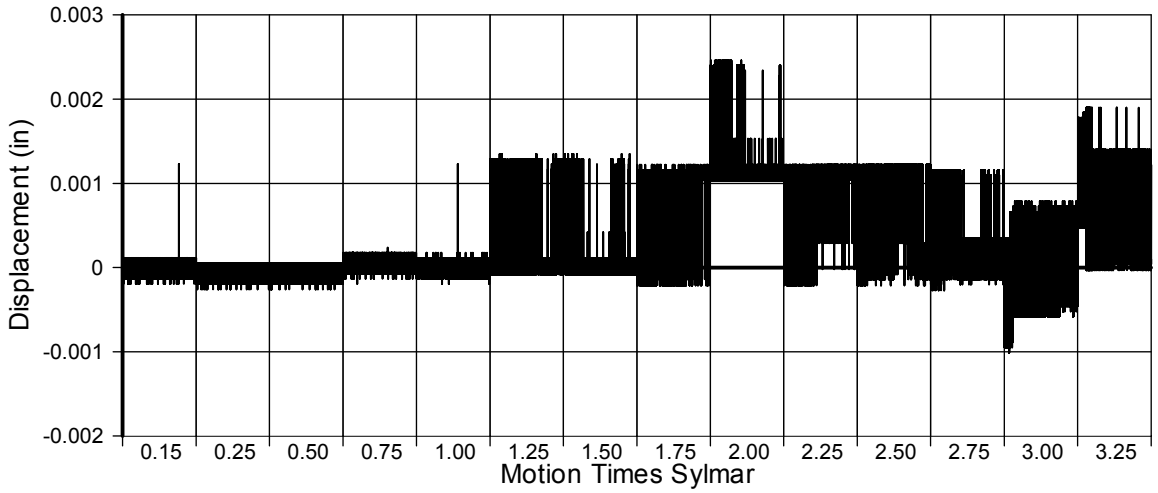

Fig. A-293 - Measured Disp. in Transeducer No. 31 for SFCD2

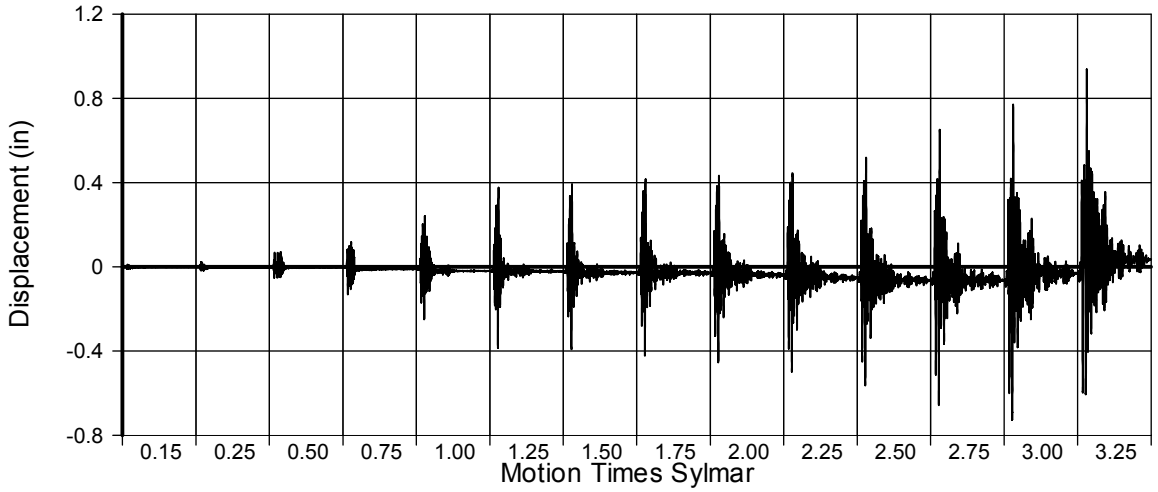

Fig. A-294 - Measured Disp. in Transeducer No. 32 for SFCD2

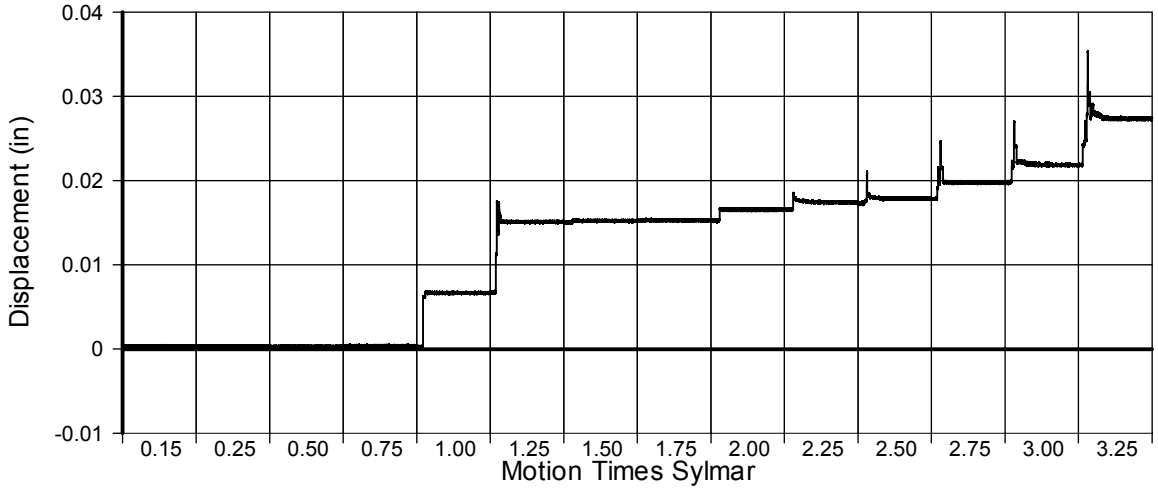

Fig. A-295 - Measured Disp. in Transeducer No. 33 for SFCD2

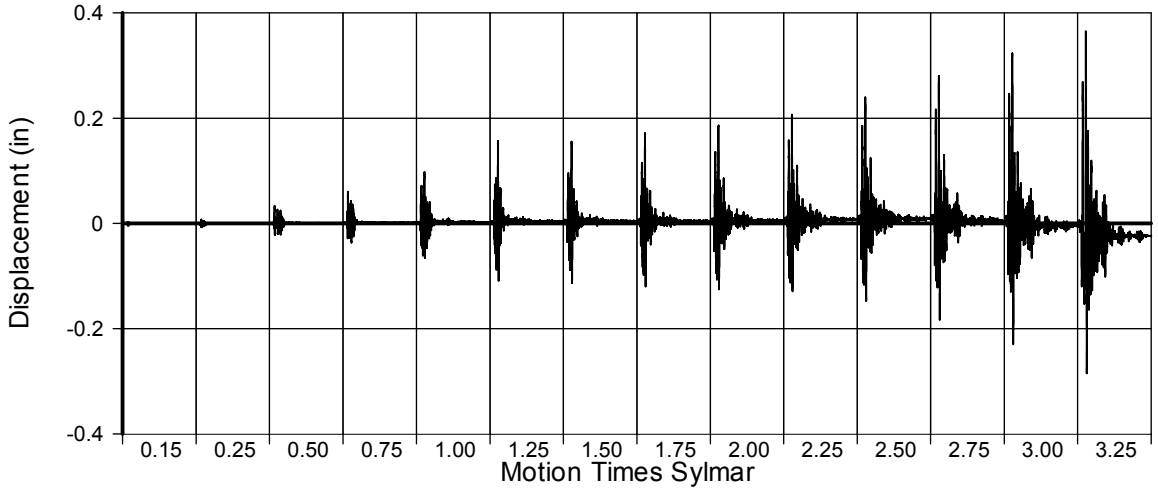

Fig. A-296 - Measured Disp. in Transeducer No. 34 for SFCD2

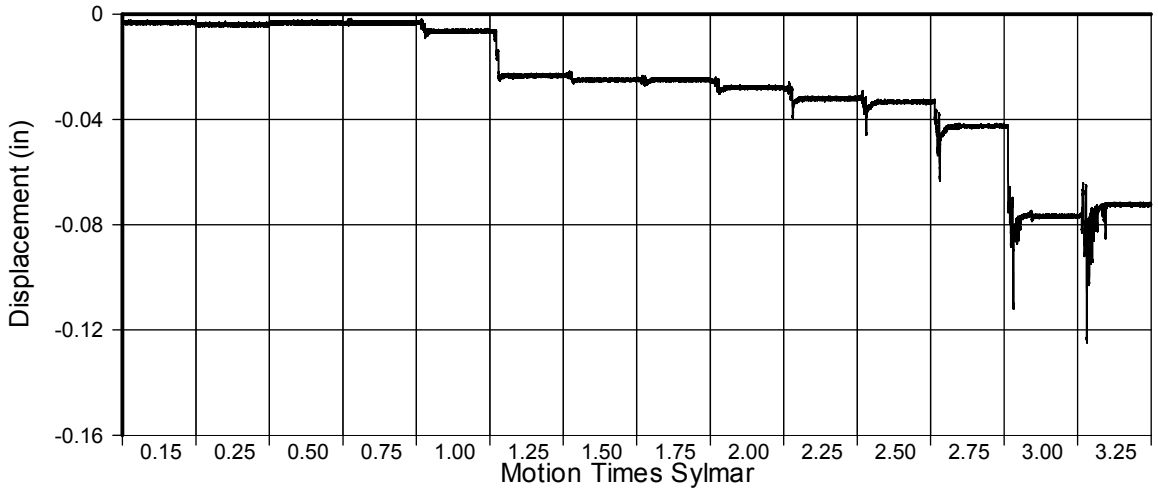

Fig. A-297 - Measured Disp. in Transeducer No. 35 for SFCD2

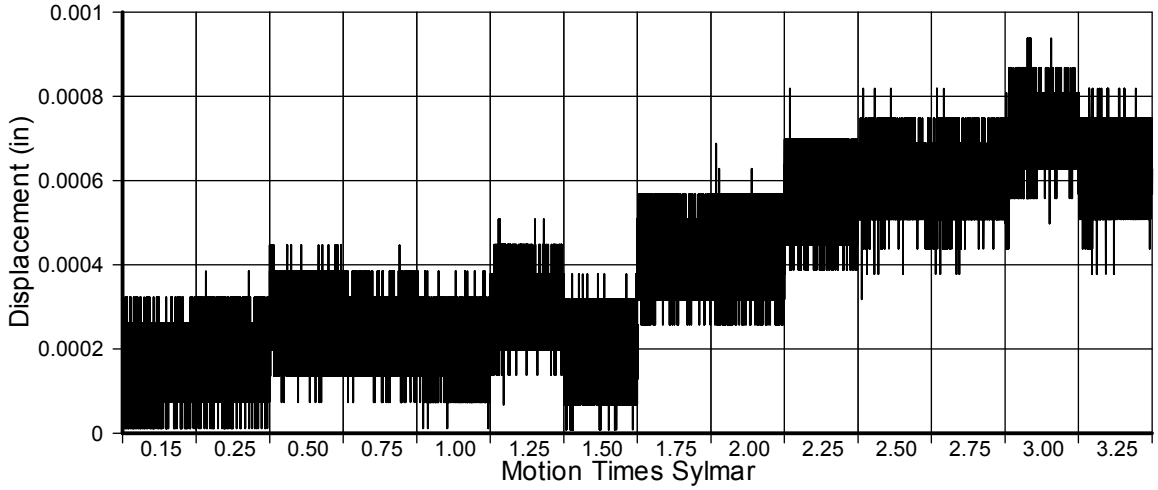

Fig. A-298 - Measured Disp. in Transeducer No. 36 for SFCD2

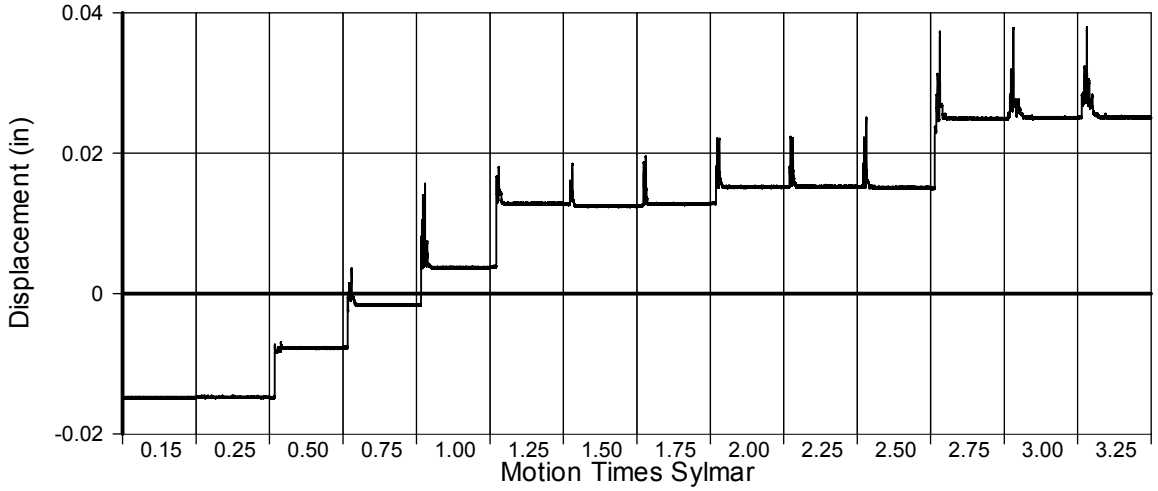

Fig. A-299 - Measured Disp. in Transeducer No. 37 for SFCD2

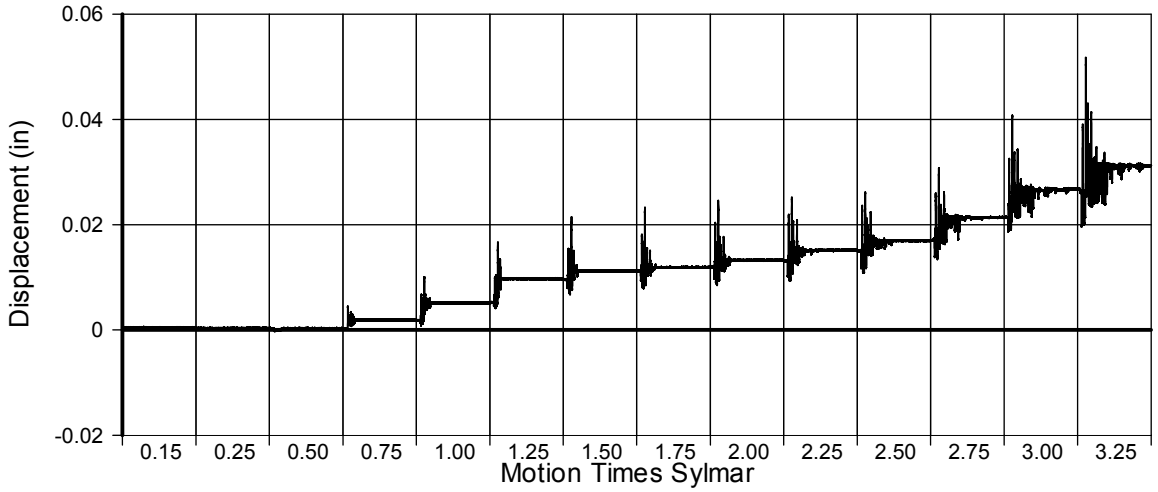

Fig. A-300 - Measured Disp. in Transeducer No. 39 for SFCD2

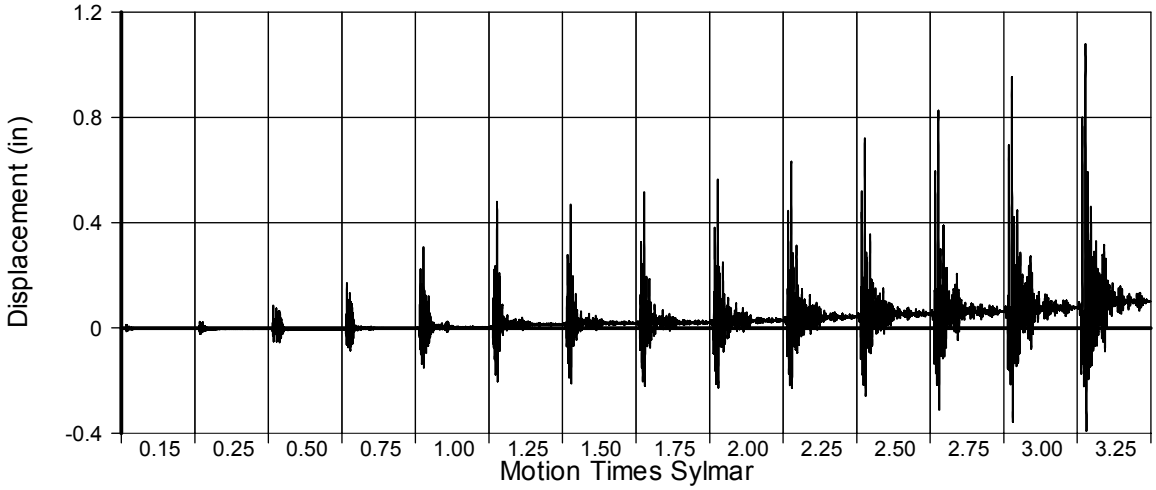

Fig. A-301 - Measured Disp. in Transeducer No. 40 for SFCD2

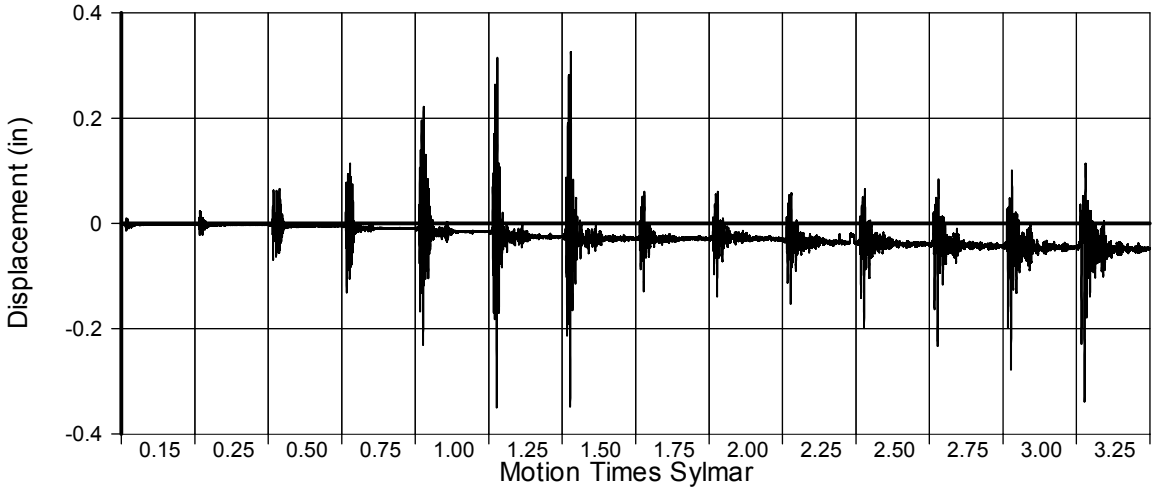

Fig. A-302 - Measured Disp. in Transeducer No. 41 for SFCD2

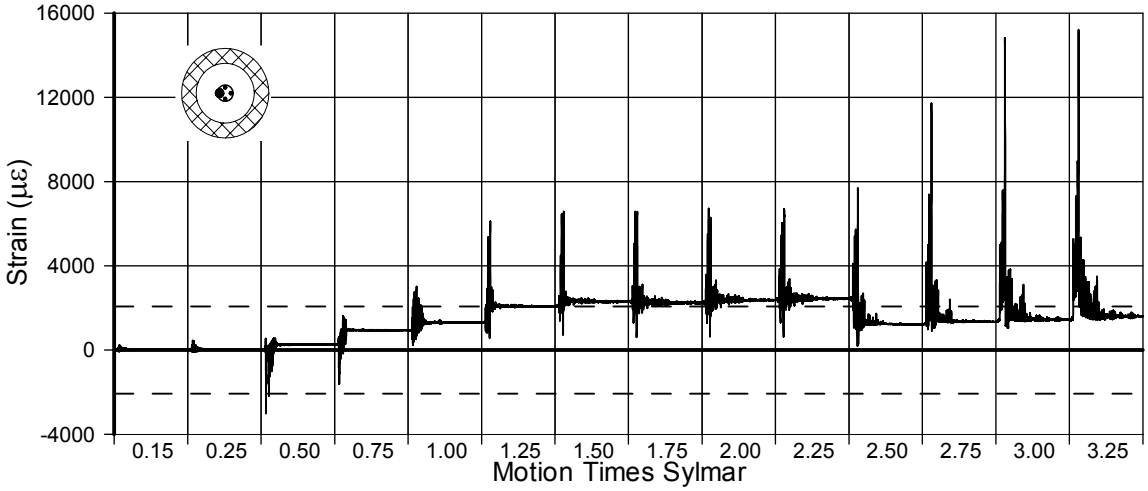

Fig. A-303 - Measured Strain in Gauge No. 43 for SFCD2

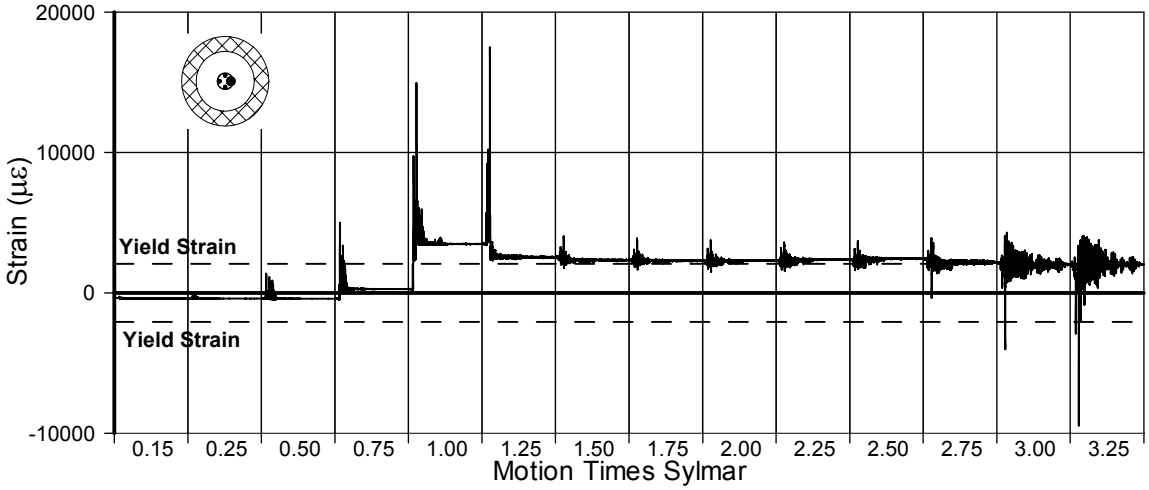

Fig. A-304 - Measured Strain in Gauge No. 44 for SFCD2

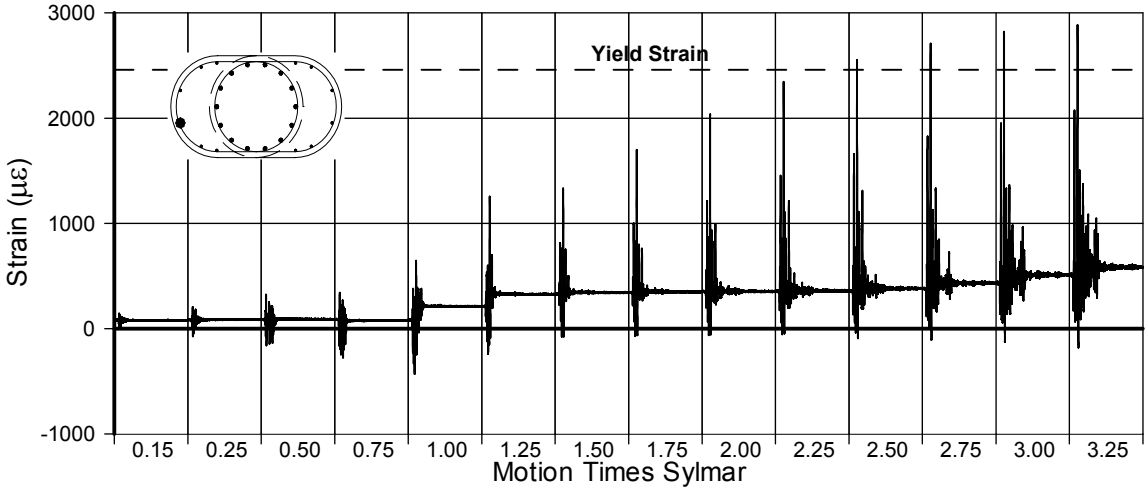

Fig. A-305 - Measured Strain in Gauge No. 45 for SFCD2

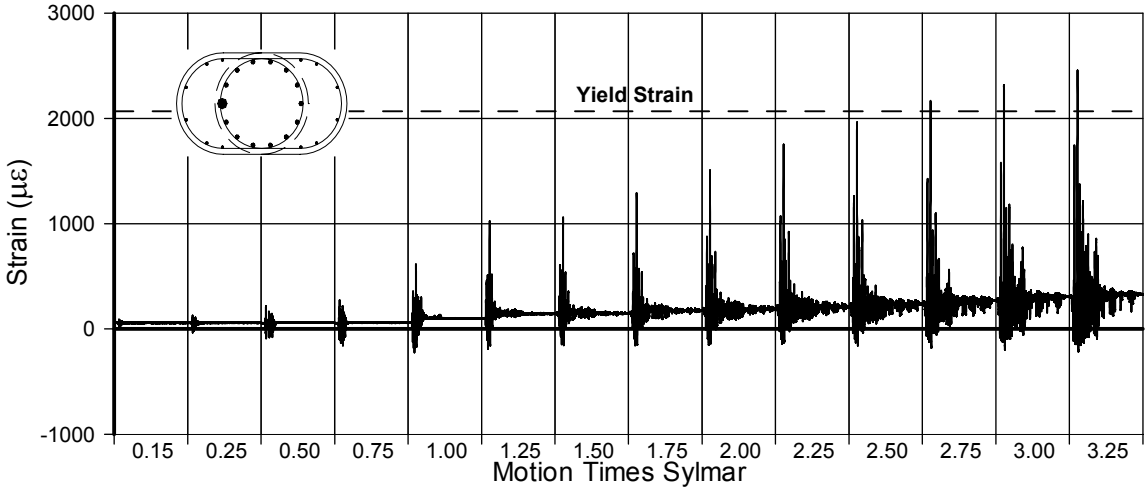

Fig. A-306 - Measured Strain in Gauge No. 46 for SFCD2

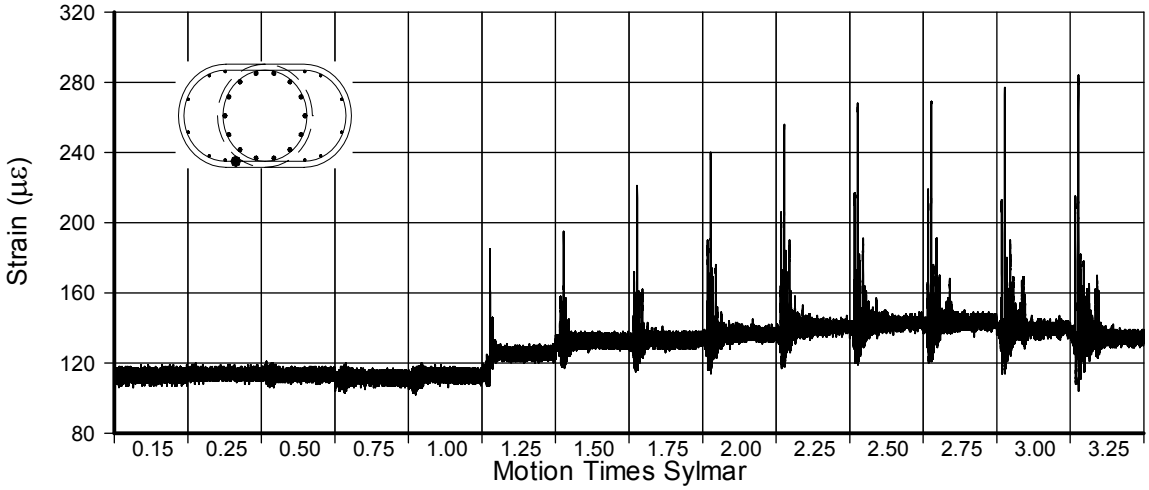

Fig. A-307 - Measured Strain in Gauge No. 48 for SFCD2

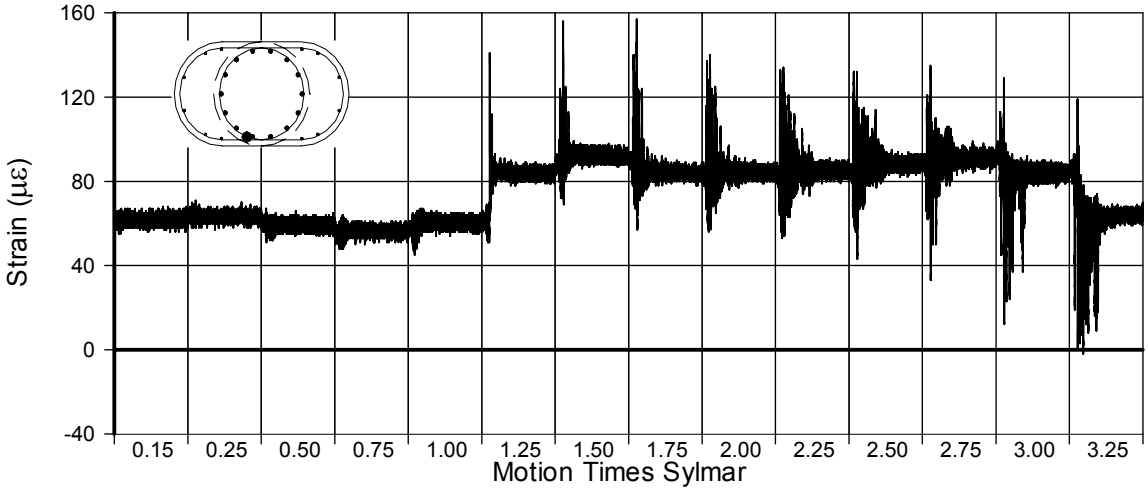

Fig. A-308 - Measured Strain in Gauge No. 49 for SFCD2

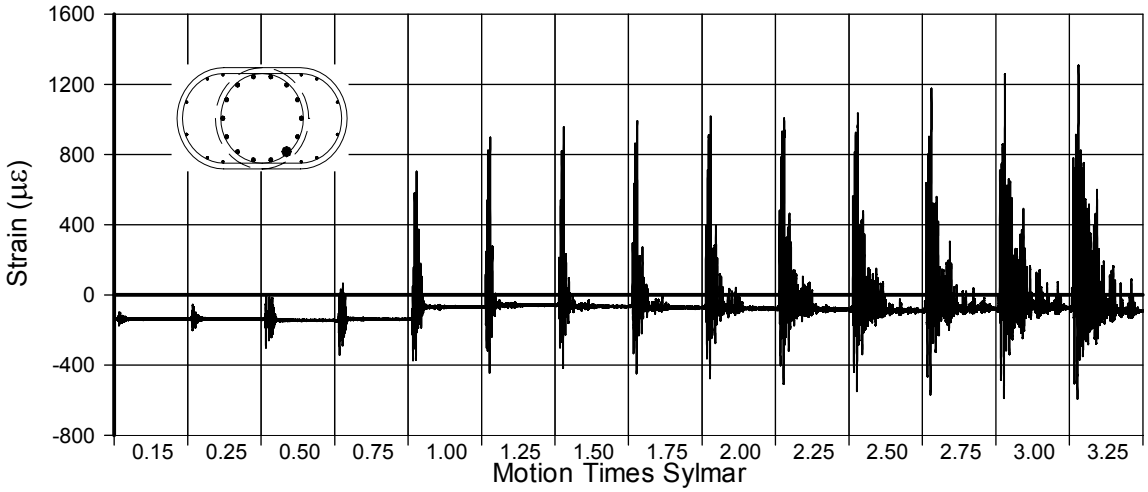

Fig. A-309 - Measured Strain in Gauge No. 50 for SFCD2

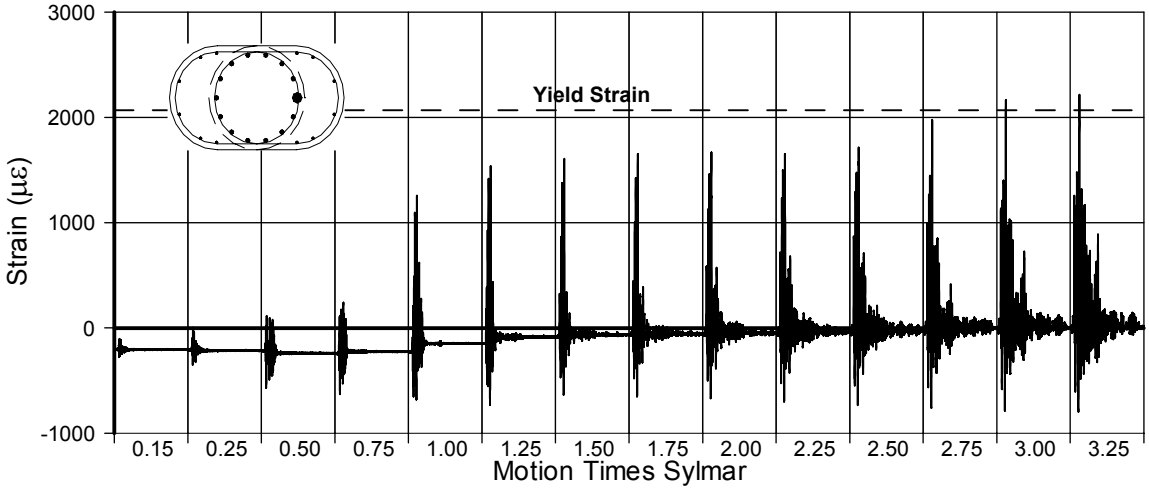

Fig. A-310 - Measured Strain in Gauge No. 51 for SFCD2

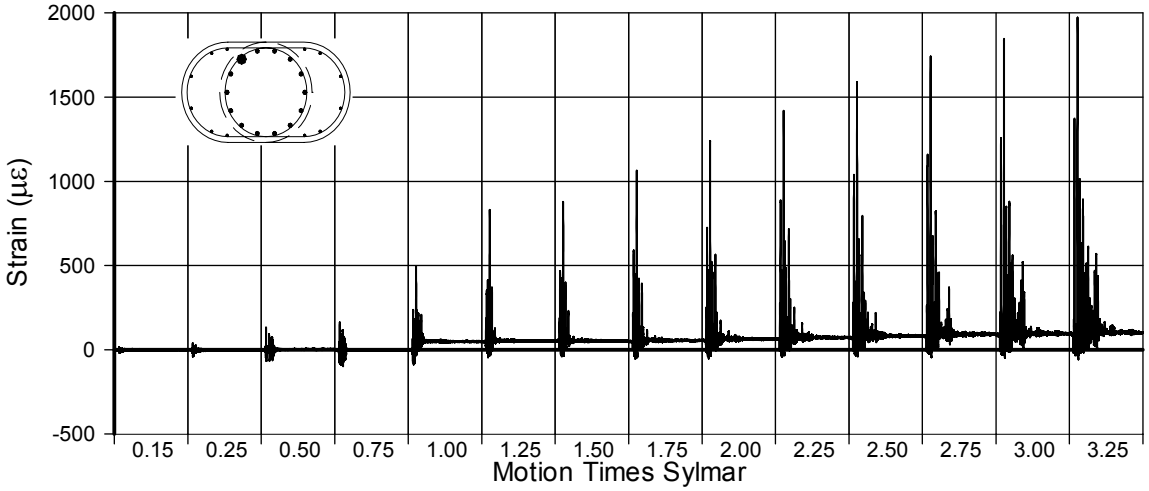

Fig. A-311 - Measured Strain in Gauge No. 52 for SFCD2

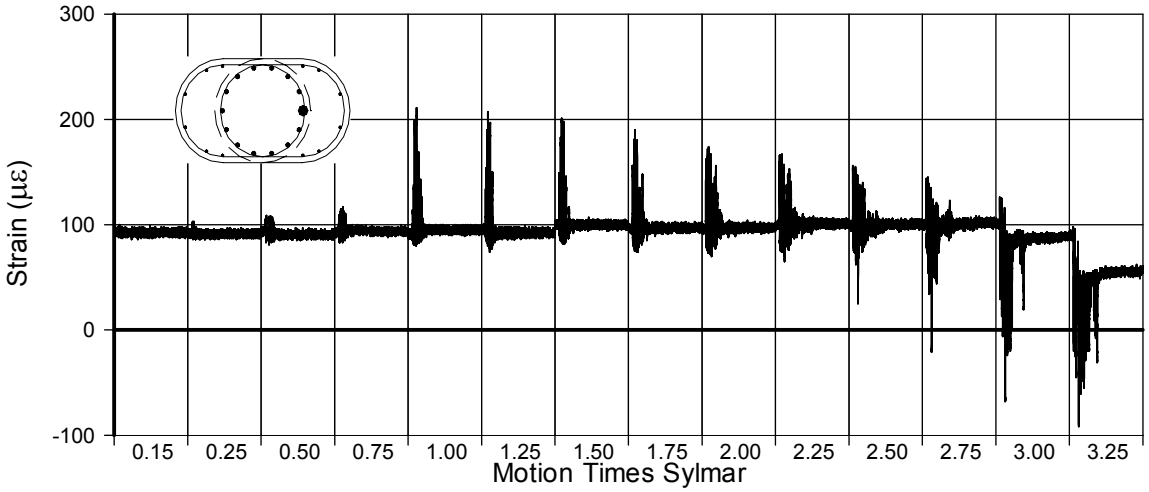

Fig. A-312 - Measured Strain in Gauge No. 53 for SFCD2

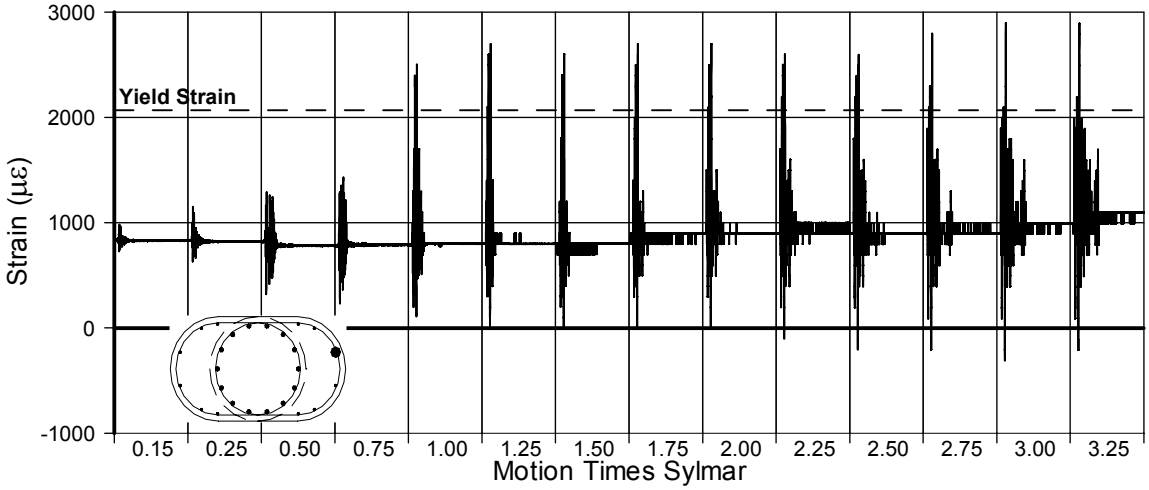

Fig. A-313 - Measured Strain in Gauge No. 54 for SFCD2

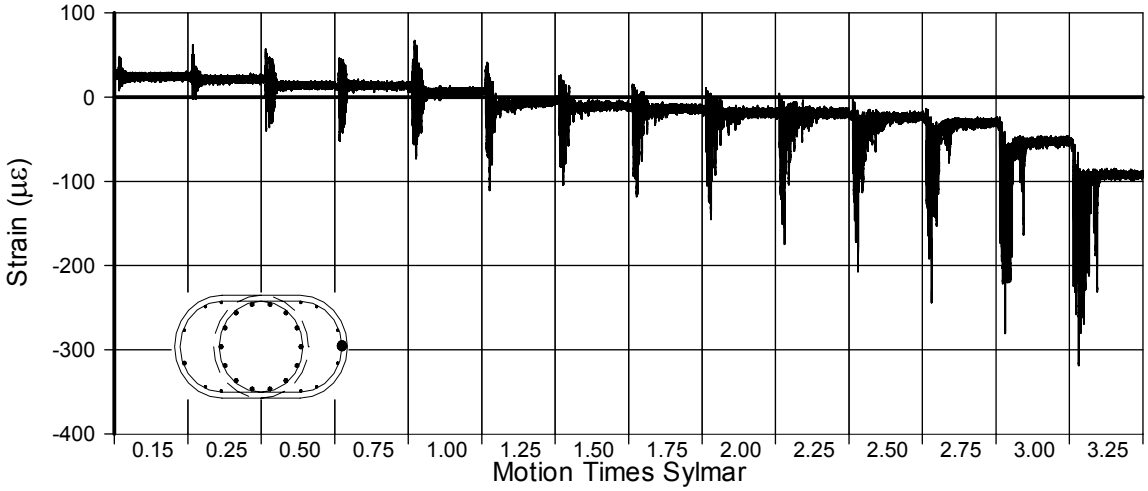

Fig. A-314 - Measured Strain in Gauge No. 55 for SFCD2

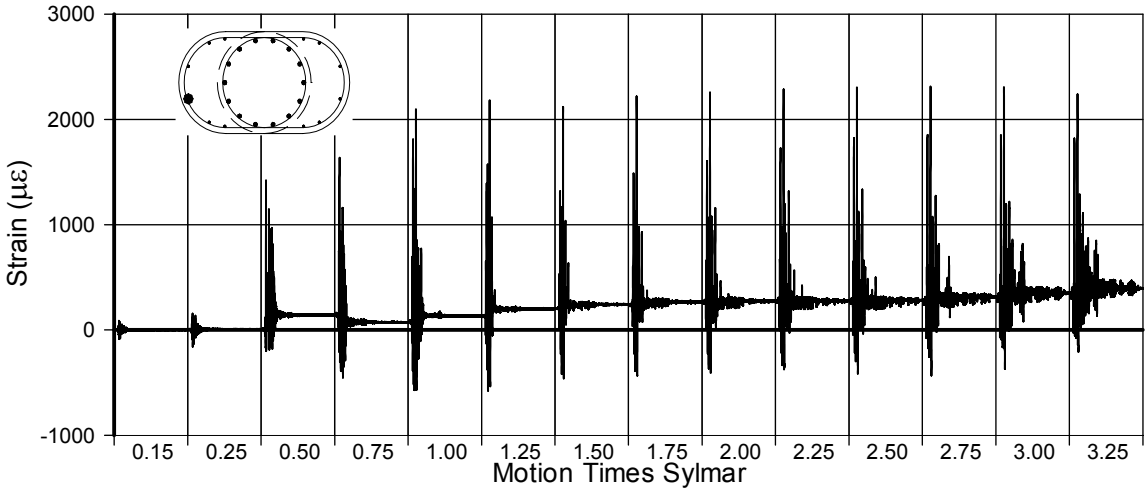

Fig. A-315 - Measured Strain in Gauge No. 56 for SFCD2

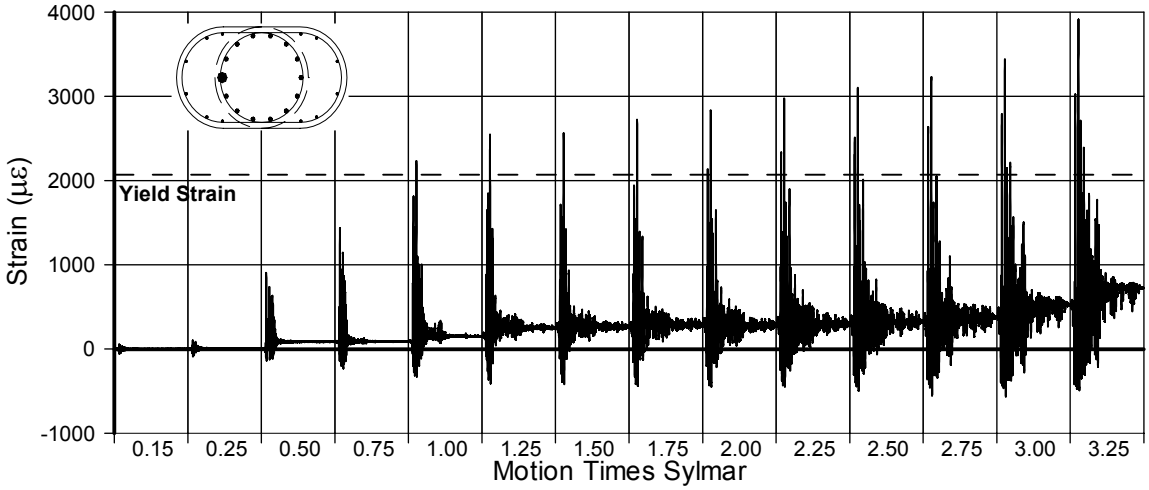

Fig. A-316 - Measured Strain in Gauge No. 57 for SFCD2

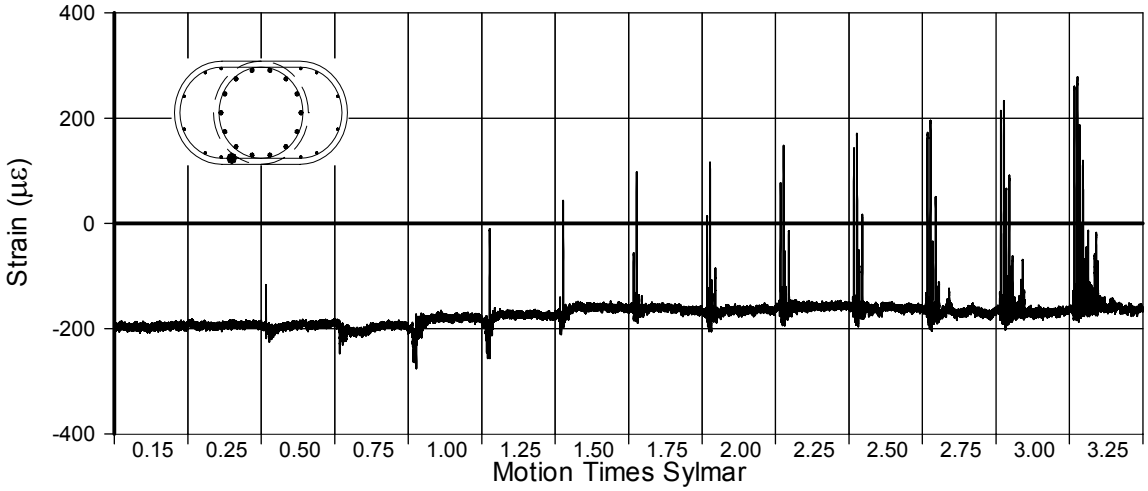

Fig. A-317 - Measured Strain in Gauge No. 58 for SFCD2

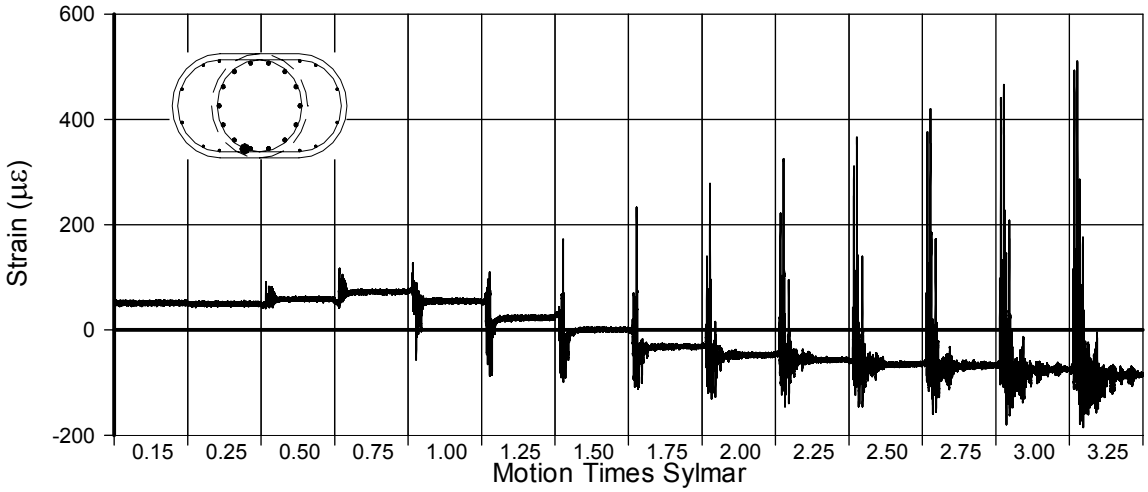

Fig. A-318 - Measured Strain in Gauge No. 59 for SFCD2

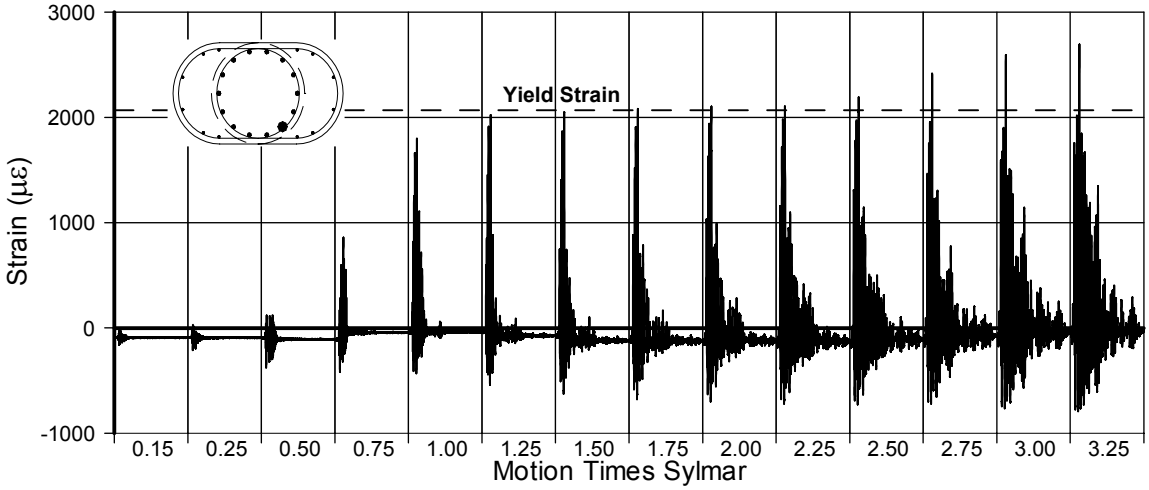

Fig. A-319 - Measured Strain in Gauge No. 60 for SFCD2

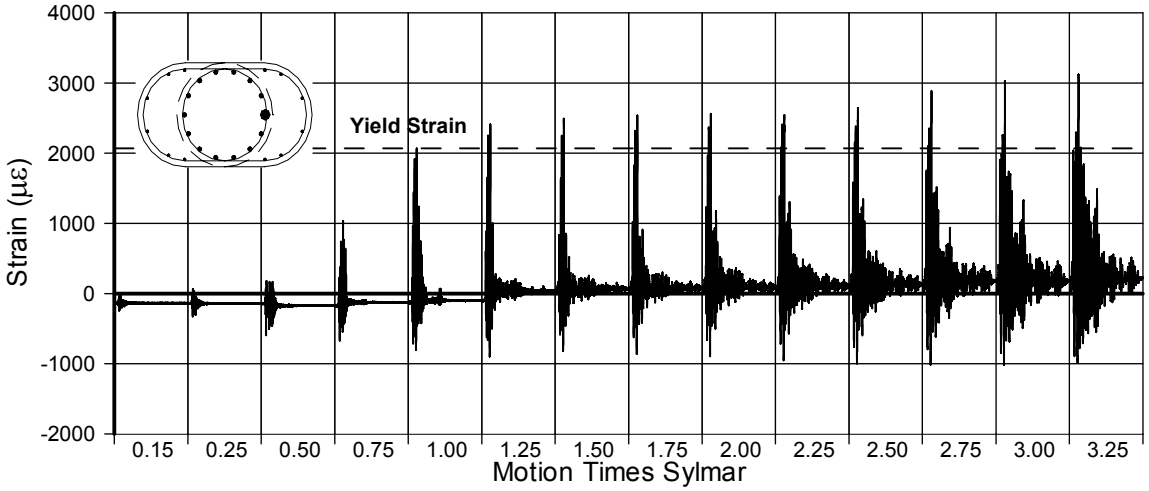

Fig. A-320 - Measured Strain in Gauge No. 61 for SFCD2

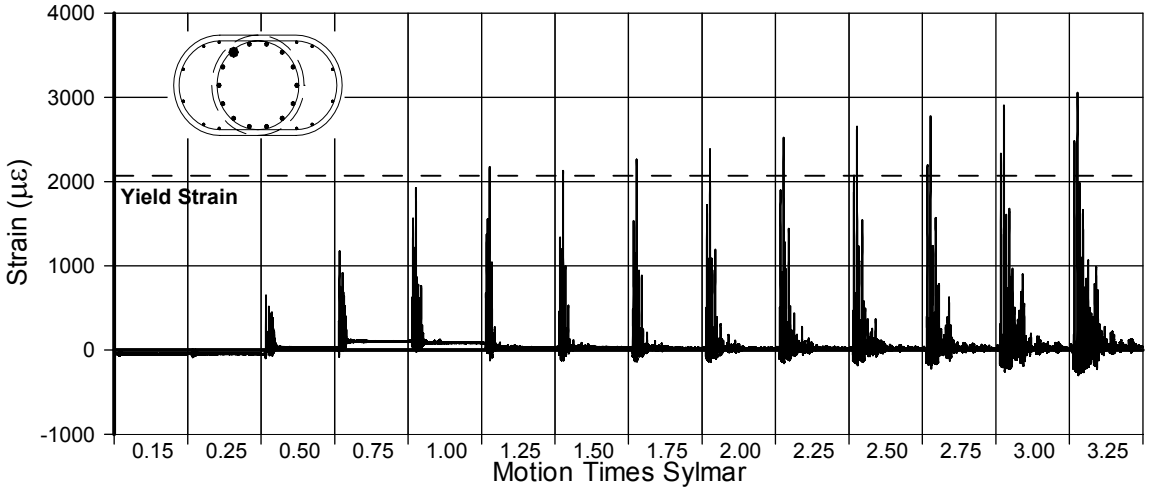

Fig. A-321 - Measured Strain in Gauge No. 62 for SFCD2

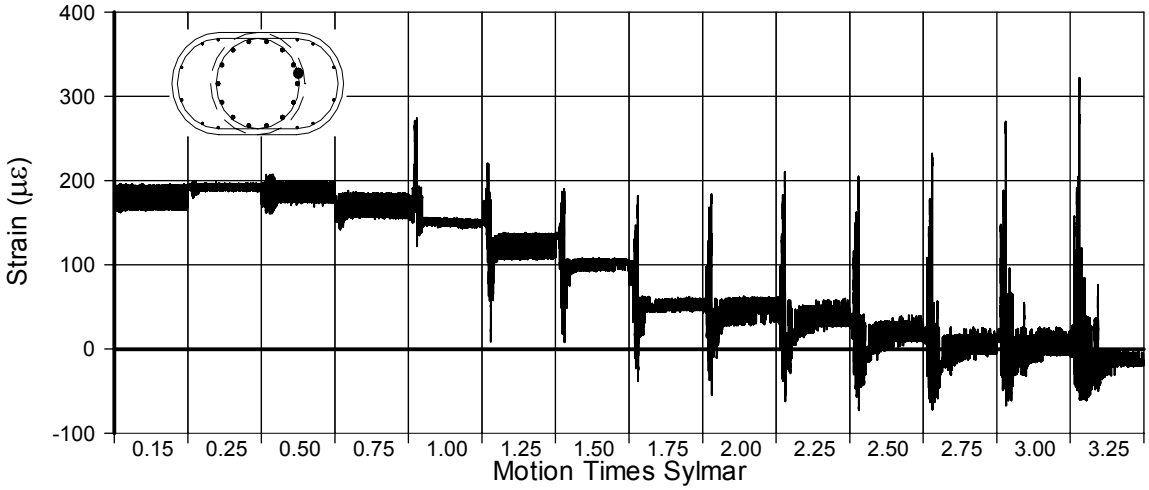

Fig. A-322 - Measured Strain in Gauge No. 64 for SFCD2

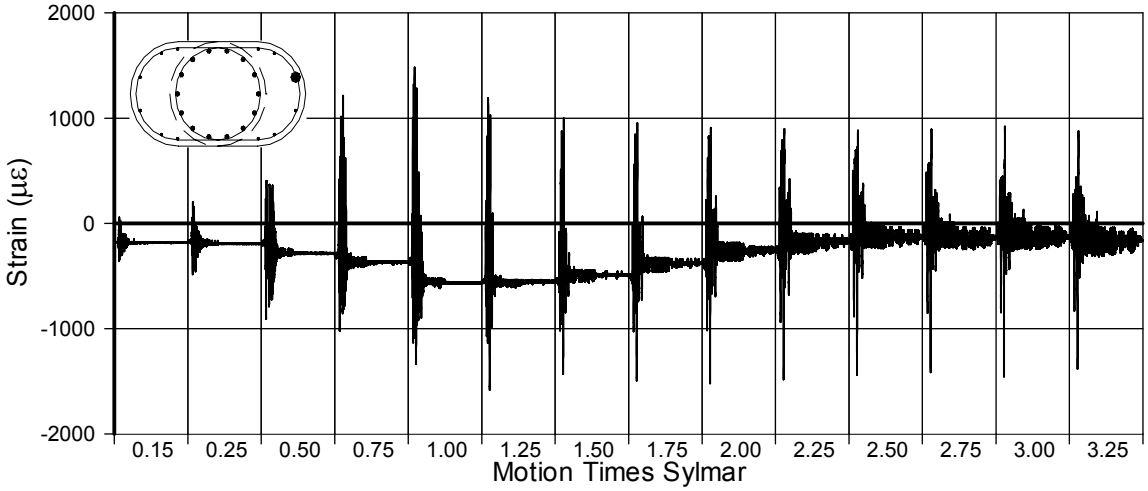

Fig. A-323 - Measured Strain in Gauge No. 65 for SFCD2

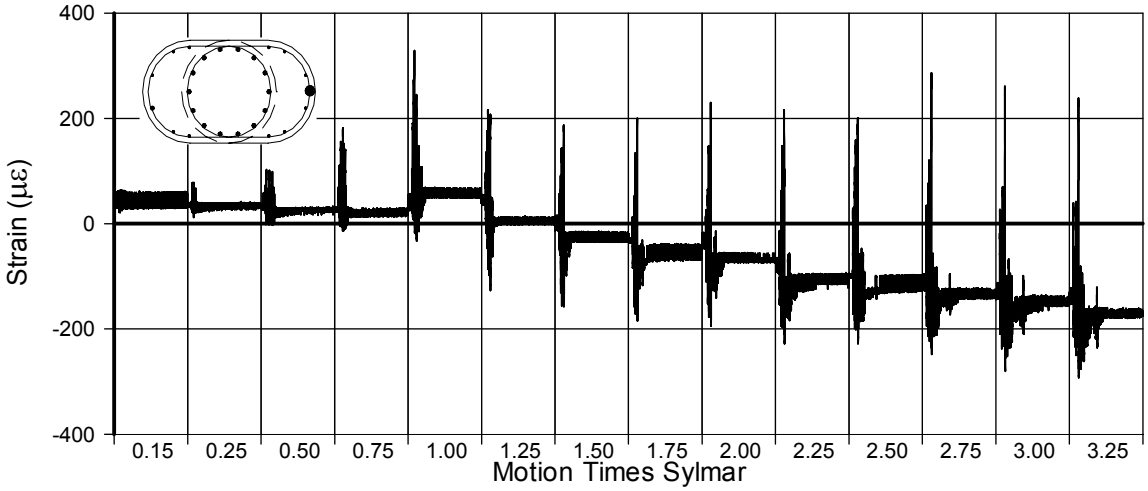

Fig. A-324 - Measured Strain in Gauge No. 66 for SFCD2

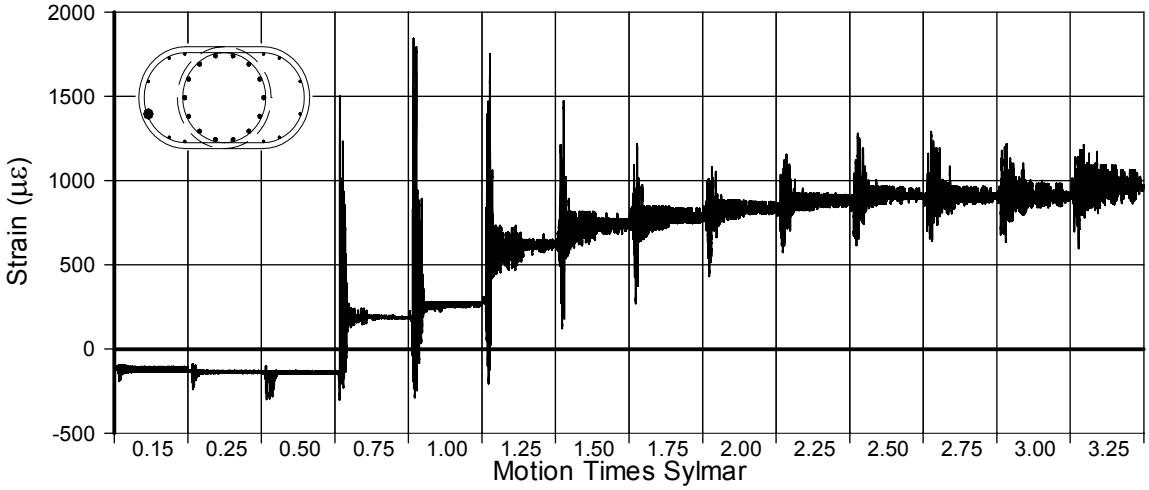

Fig. A-325 - Measured Strain in Gauge No. 67 for SFCD2

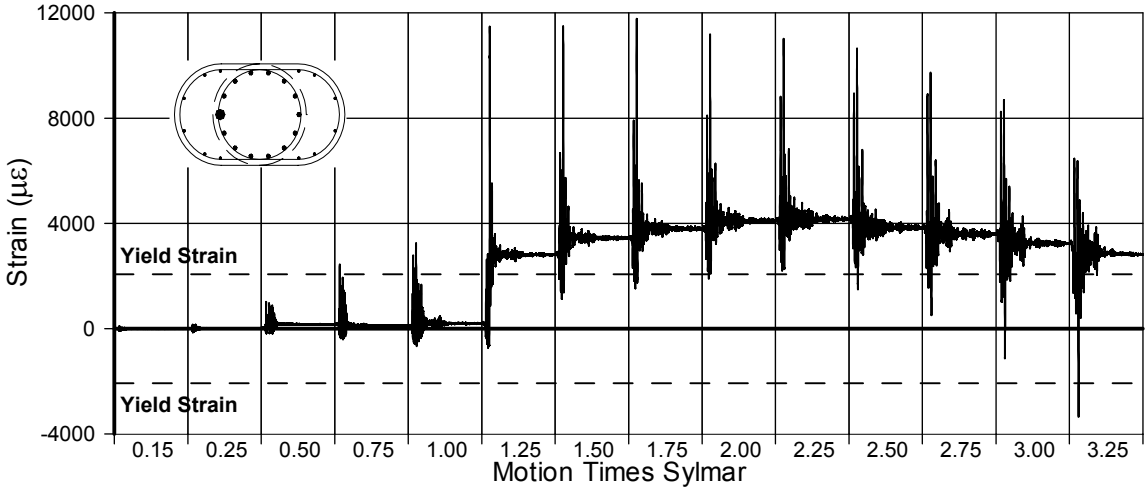

Fig. A-326 - Measured Strain in Gauge No. 68 for SFCD2

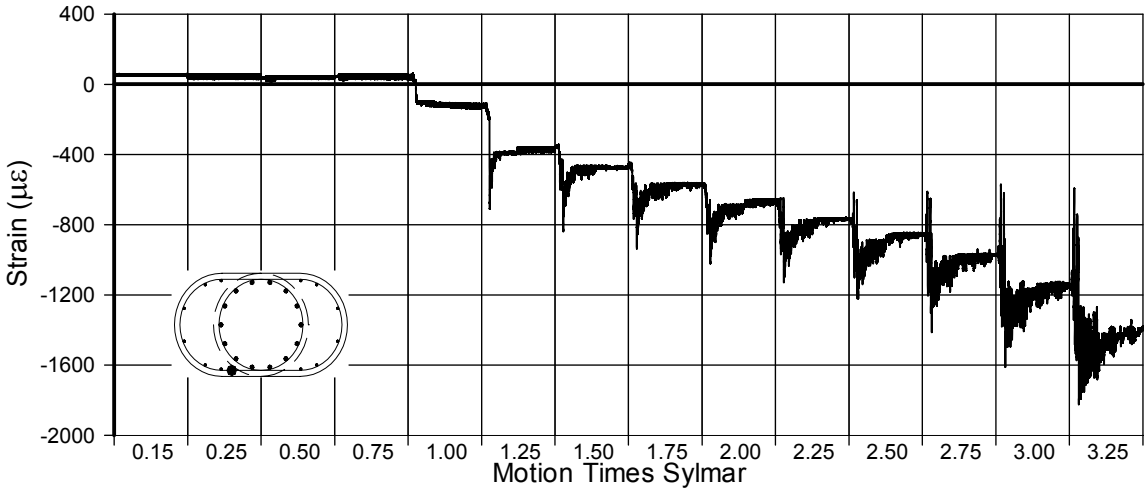

Fig. A-327 - Measured Strain in Gauge No. 69 for SFCD2

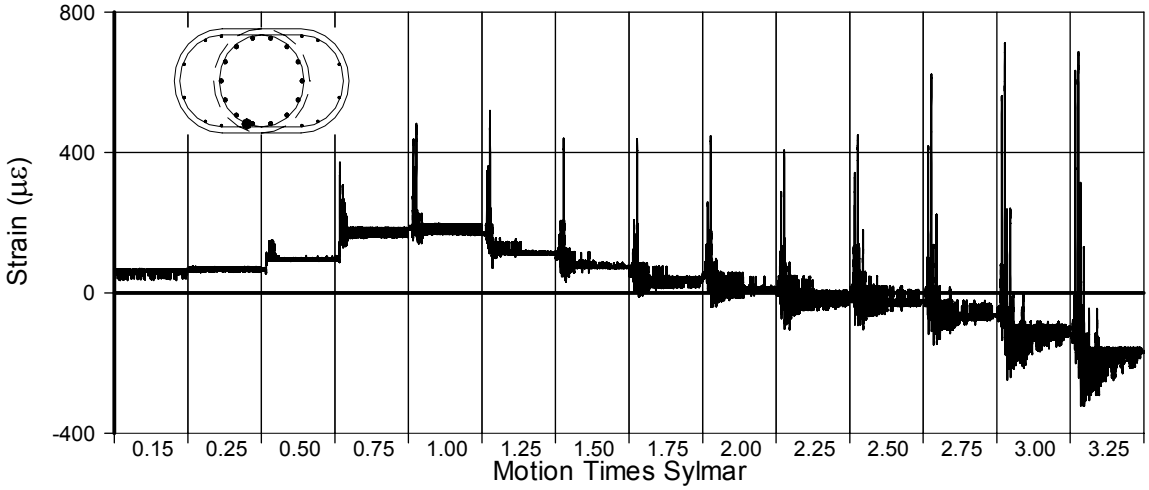

Fig. A-328 - Measured Strain in Gauge No. 71 for SFCD2

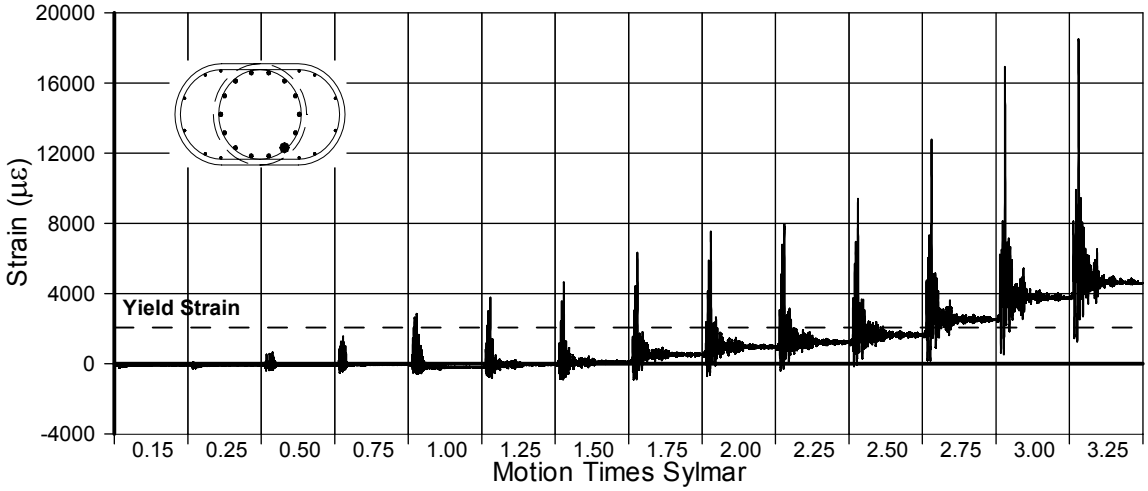

Fig. A-329 - Measured Strain in Gauge No. 72 for SFCD2

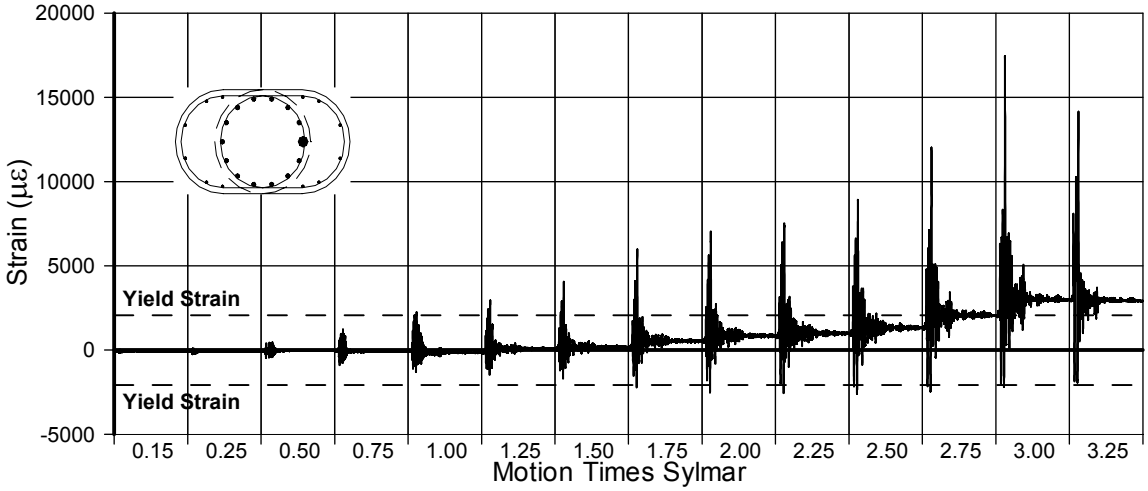

Fig. A-330 - Measured Strain in Gauge No. 74 for SFCD2

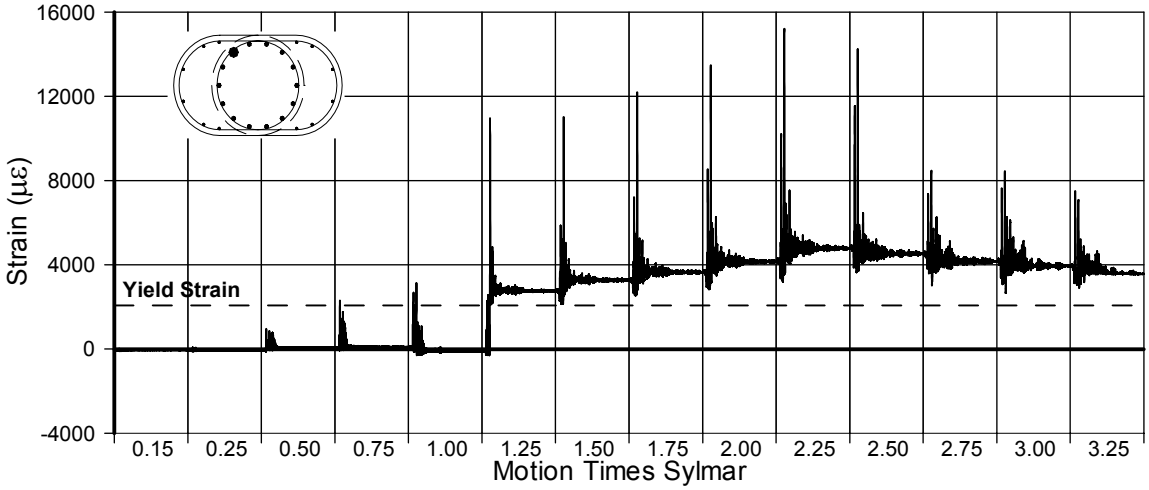

Fig. A-331 - Measured Strain in Gauge No. 75 for SFCD2

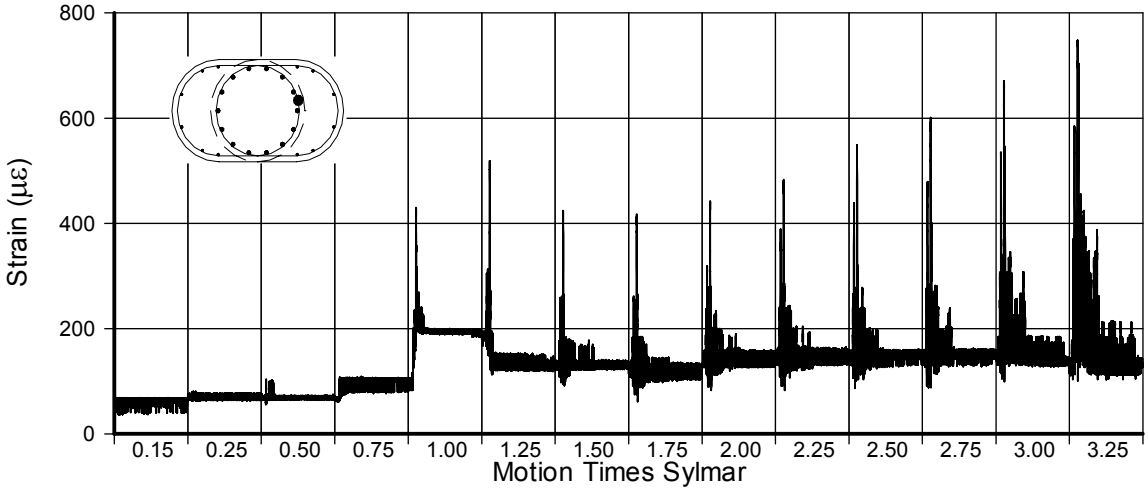

Fig. A-332 - Measured Strain in Gauge No. 76 for SFCD2

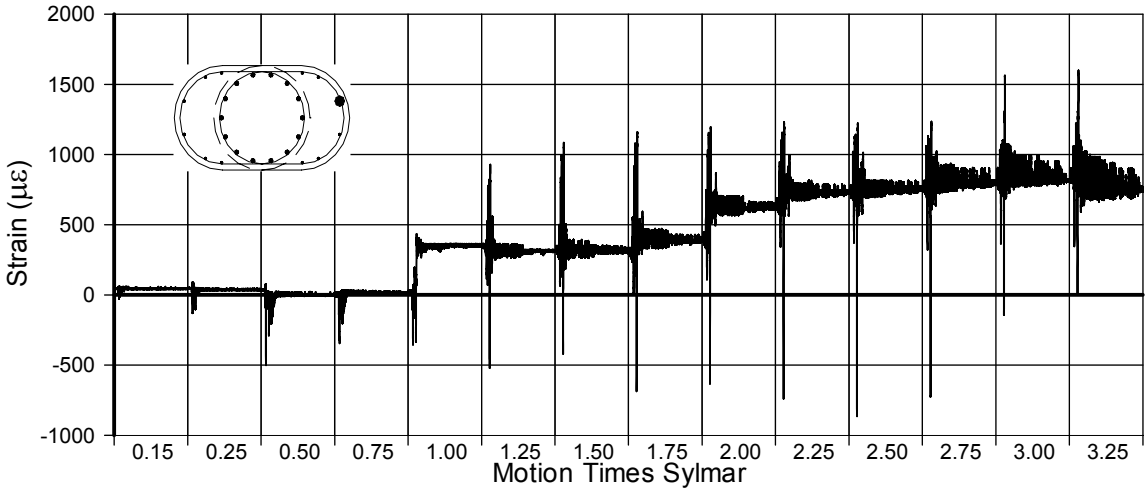

Fig. A-333 - Measured Strain in Gauge No. 77 for SFCD2

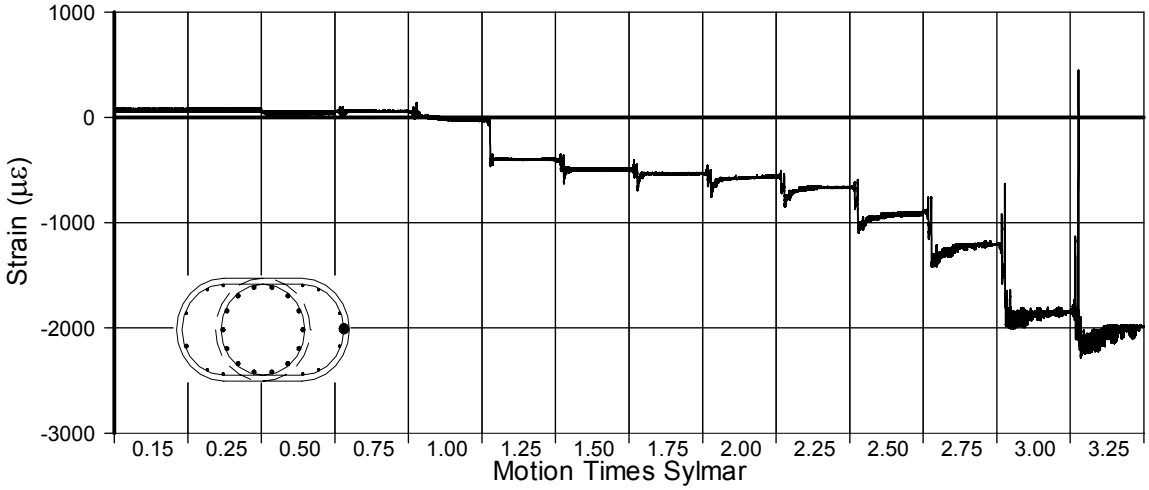

Fig. A-334 - Measured Strain in Gauge No. 78 for SFCD2

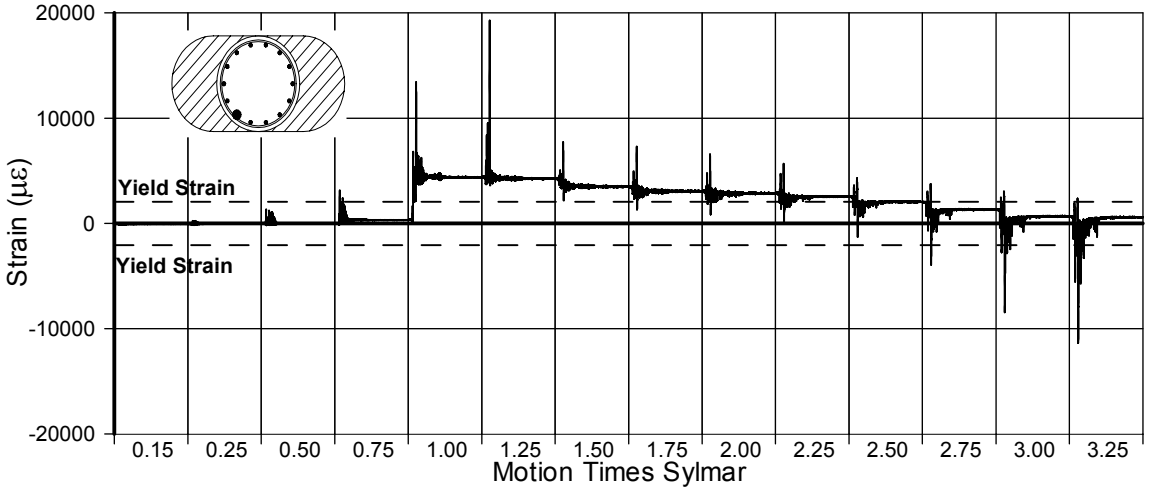

Fig. A-335 - Measured Strain in Gauge No. 79 for SFCD2

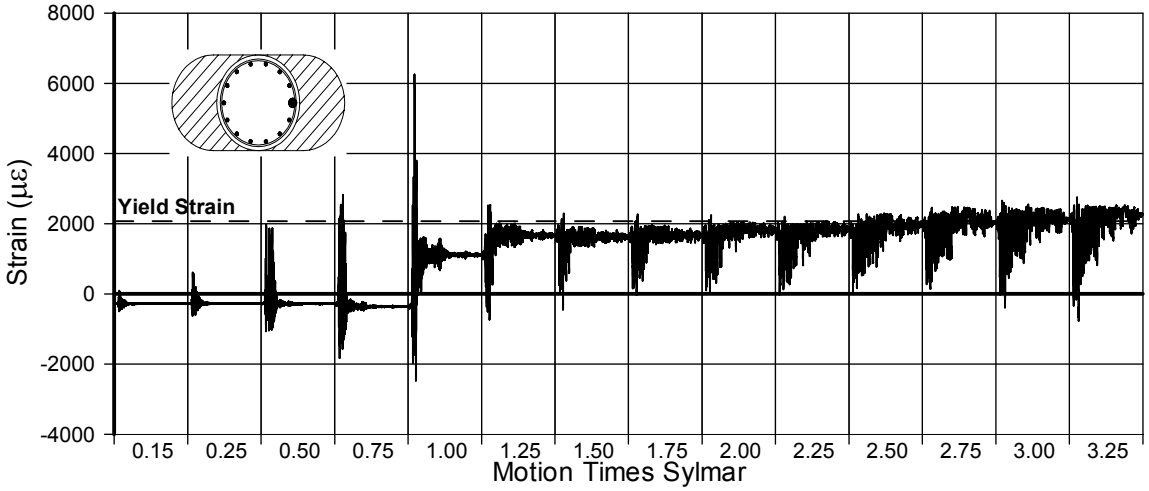

Fig. A-336 - Measured Strain in Gauge No. 80 for SFCD2

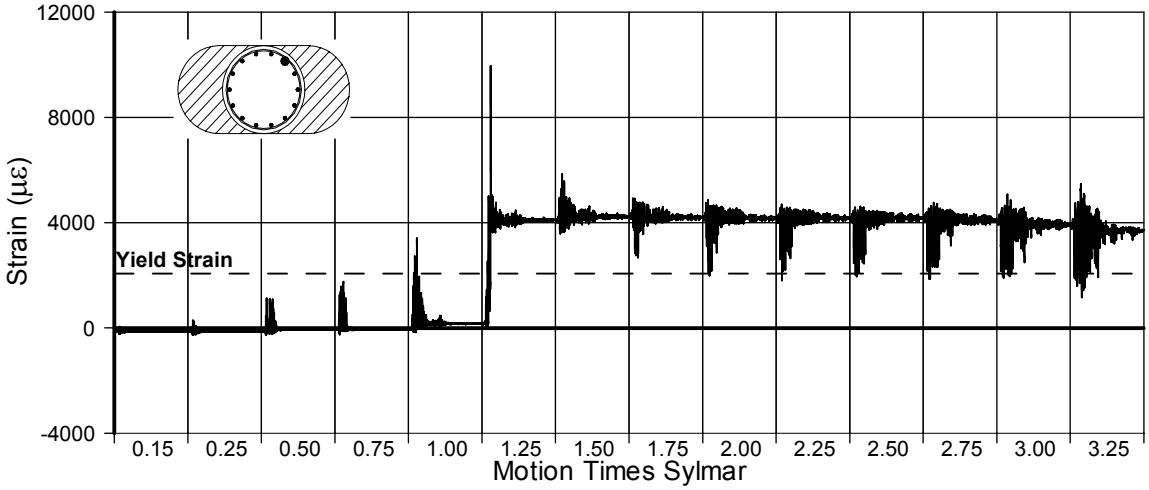

Fig. A-337 - Measured Strain in Gauge No. 81 for SFCD2

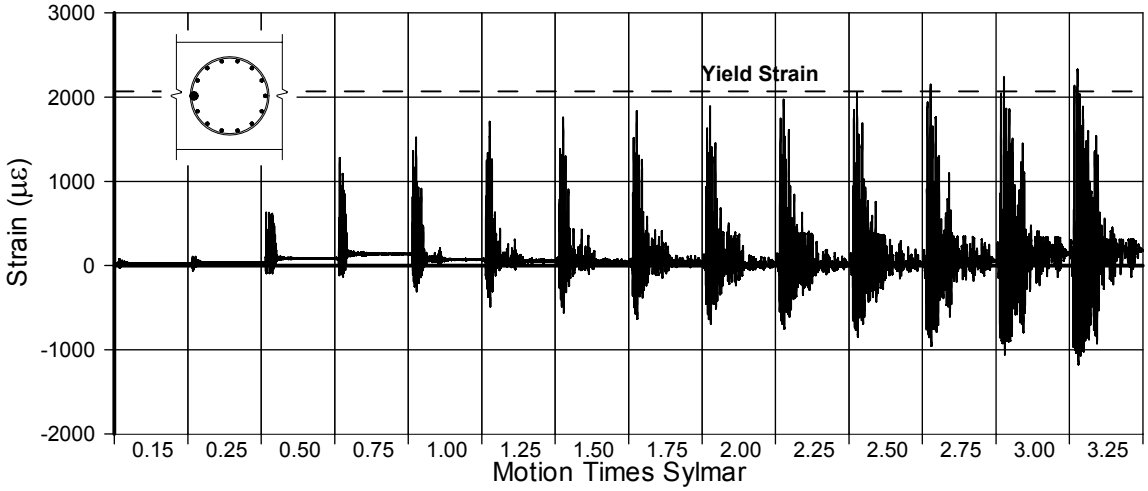

Fig. A-338 - Measured Strain in Gauge No. 82 for SFCD2

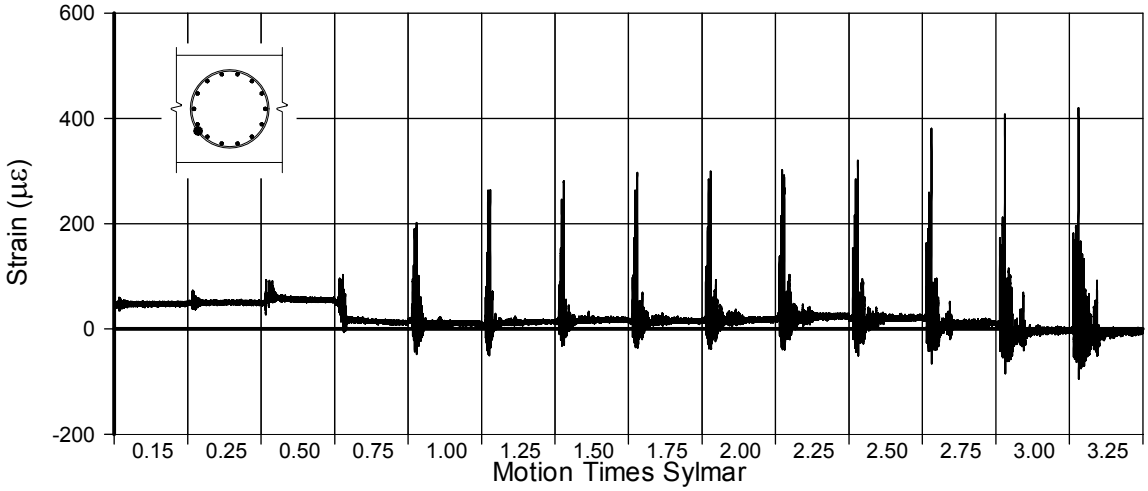

Fig. A-339 - Measured Strain in Gauge No. 83 for SFCD2

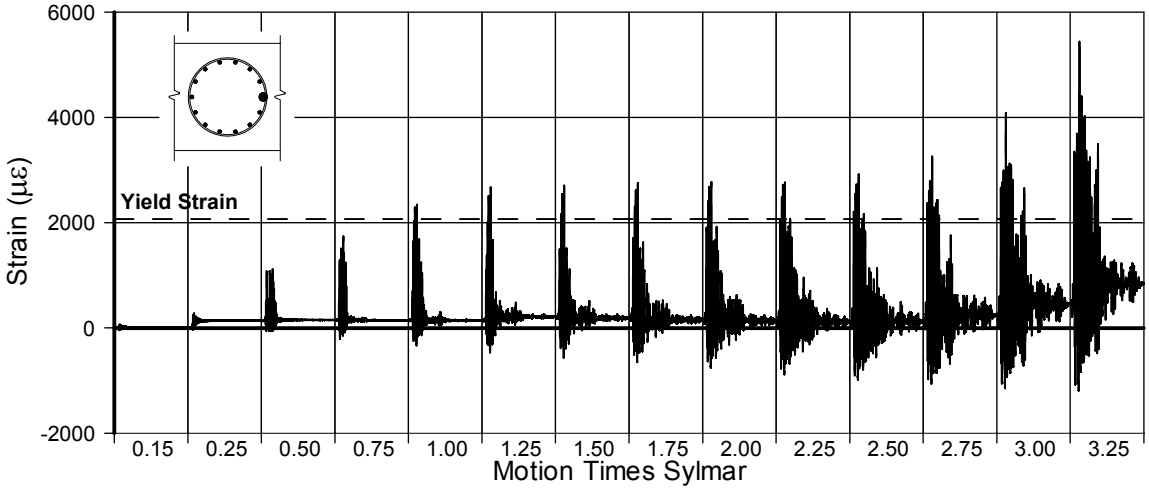

Fig. A-340 - Measured Strain in Gauge No. 85 for SFCD2

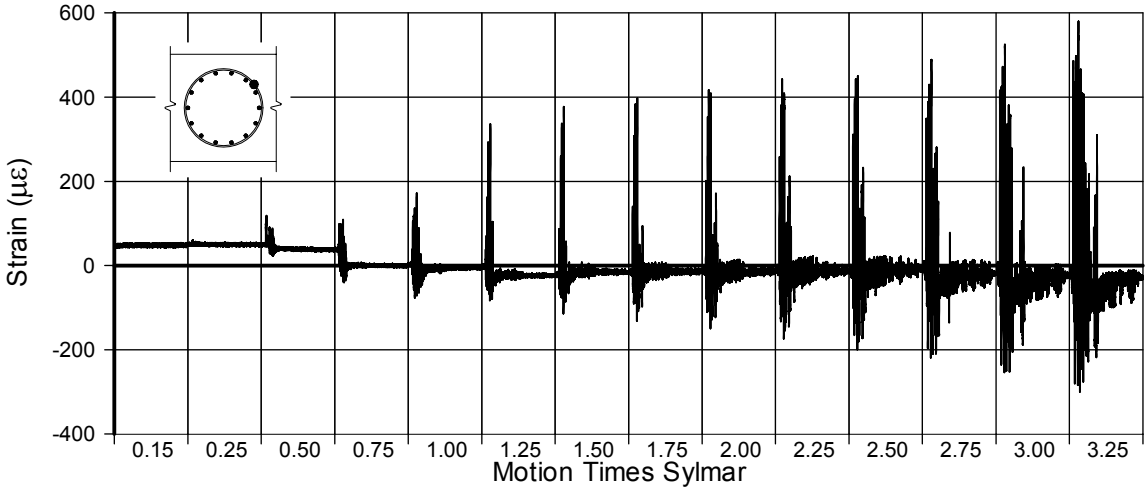

Fig. A-341 - Measured Strain in Gauge No. 86 for SFCD2

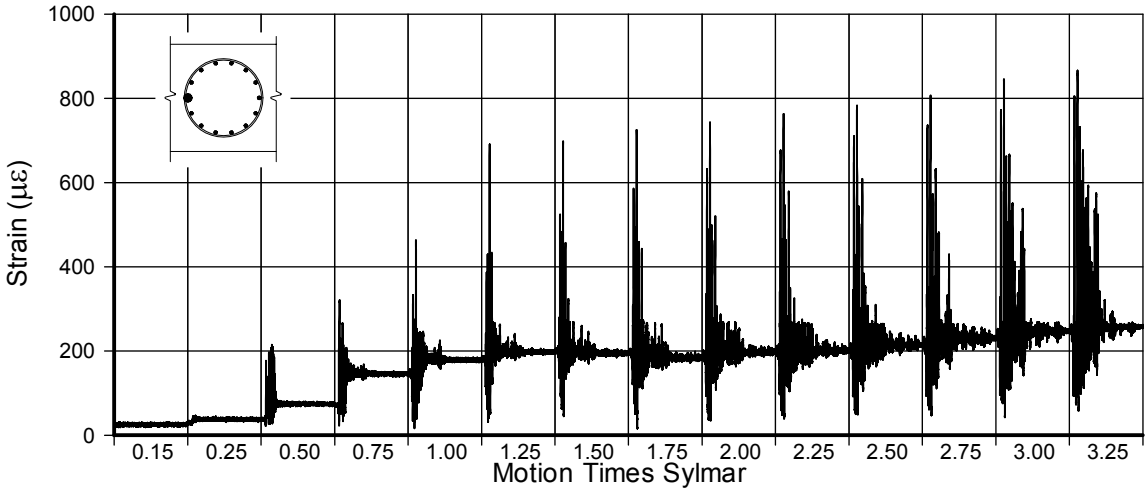

Fig. A-342 - Measured Strain in Gauge No. 87 for SFCD2

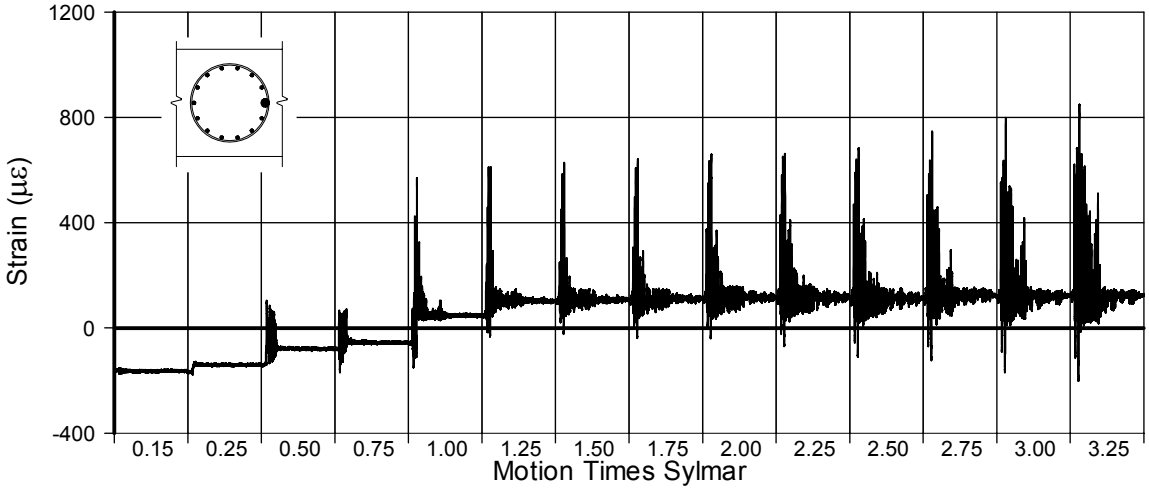

Fig. A-343 - Measured Strain in Gauge No. 89 for SFCD2

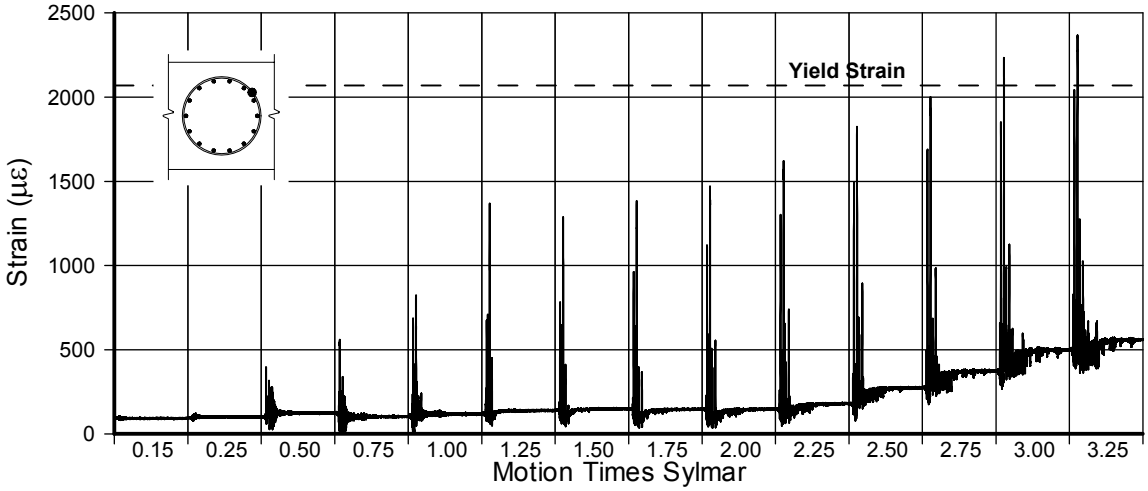

Fig. A-344 - Measured Strain in Gauge No. 91 for SFCD2

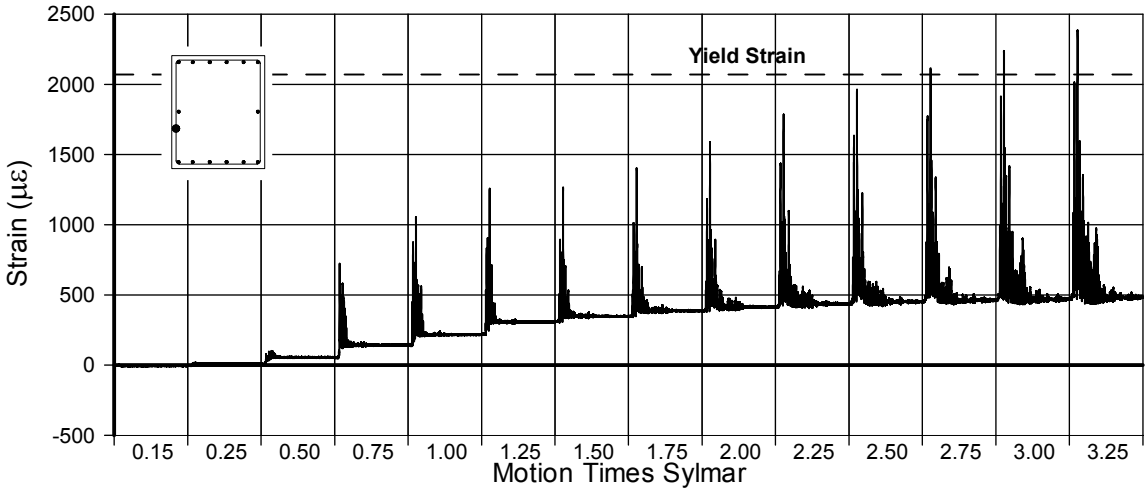

Fig. A-345 - Measured Strain in Gauge No. 92 for SFCD2

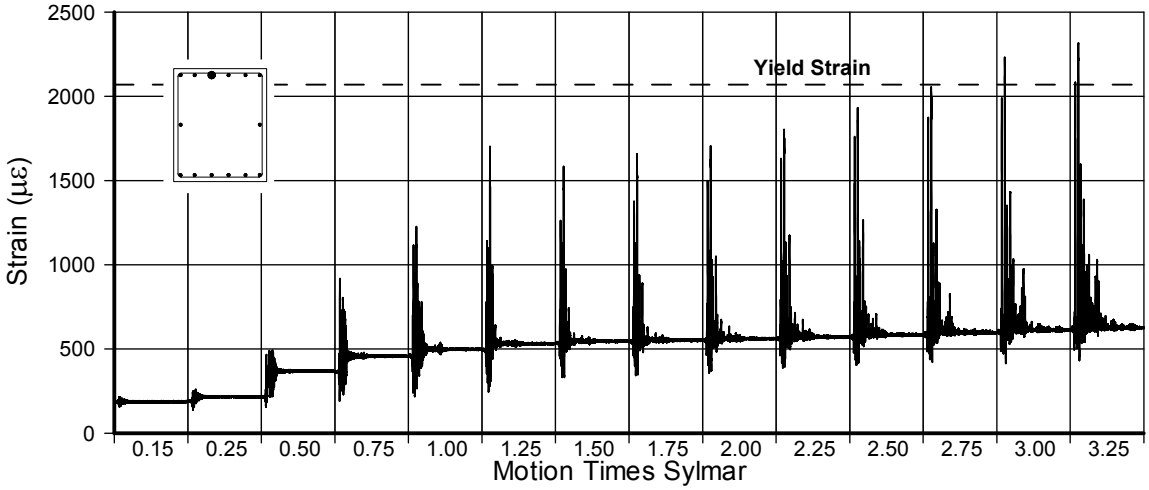

Fig. A-346 - Measured Strain in Gauge No. 93 for SFCD2

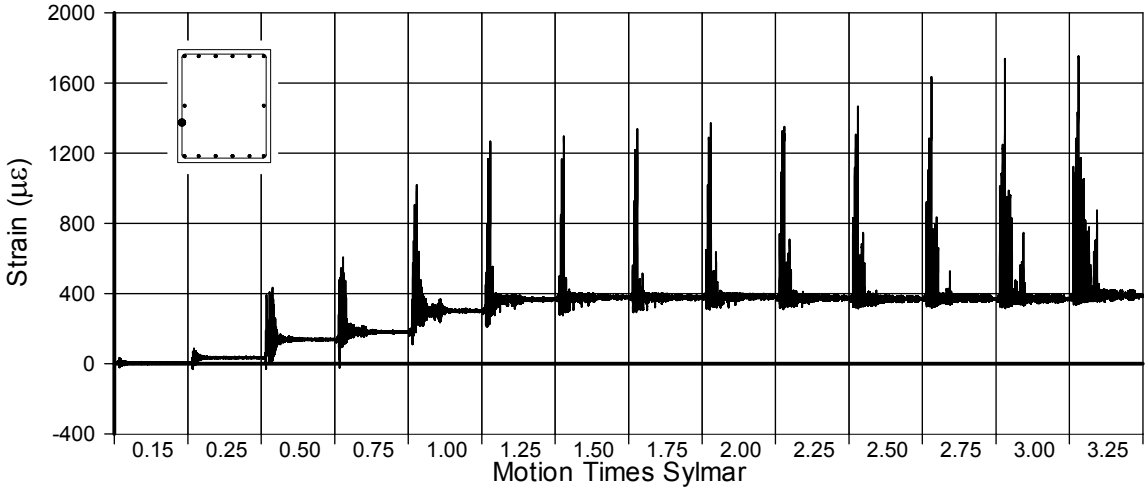

Fig. A-347 - Measured Strain in Gauge No. 95 for SFCD2

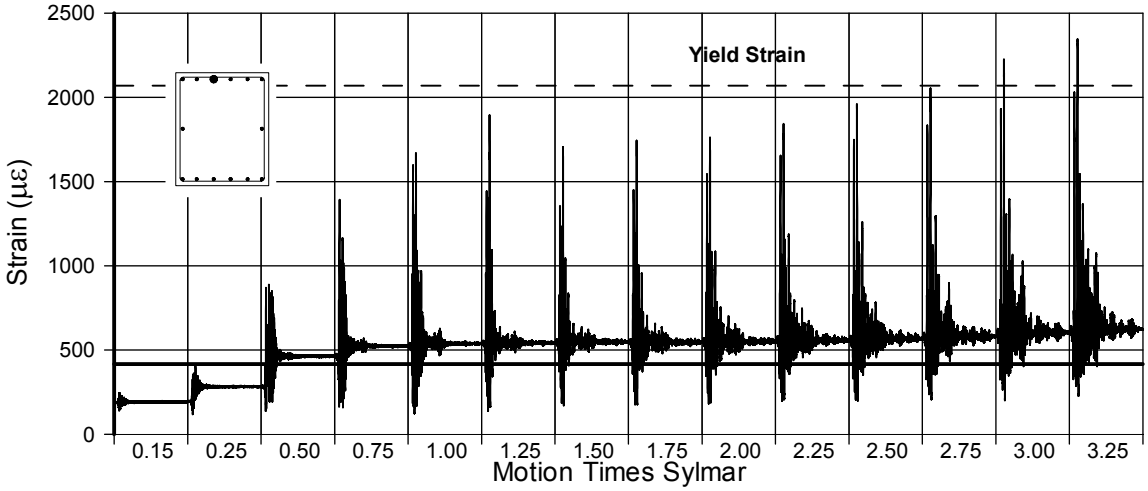

Fig. A-348 - Measured Strain in Gauge No. 96 for SFCD2

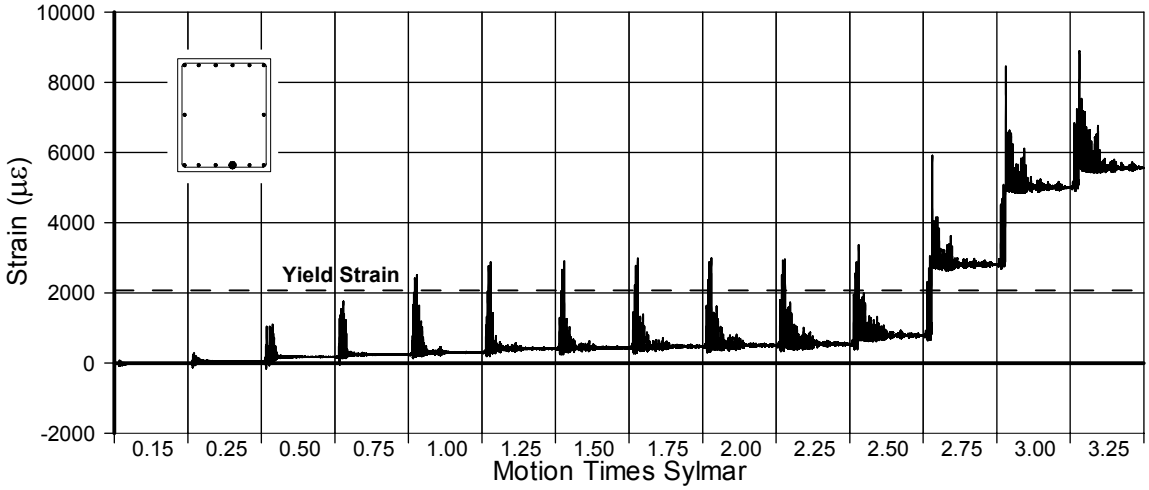

Fig. A-349 - Measured Strain in Gauge No. 97 for SFCD2

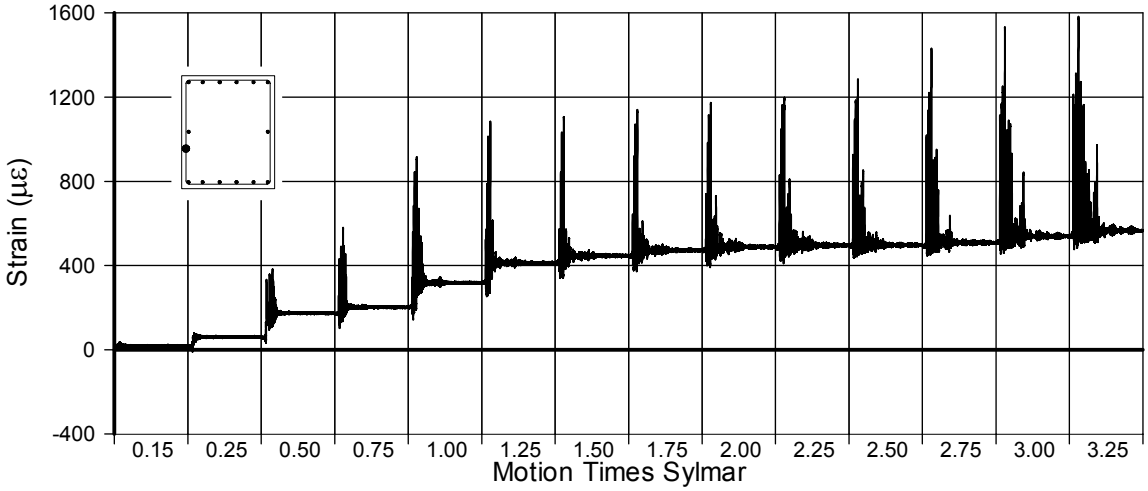

Fig. A-350 - Measured Strain in Gauge No. 98 for SFCD2

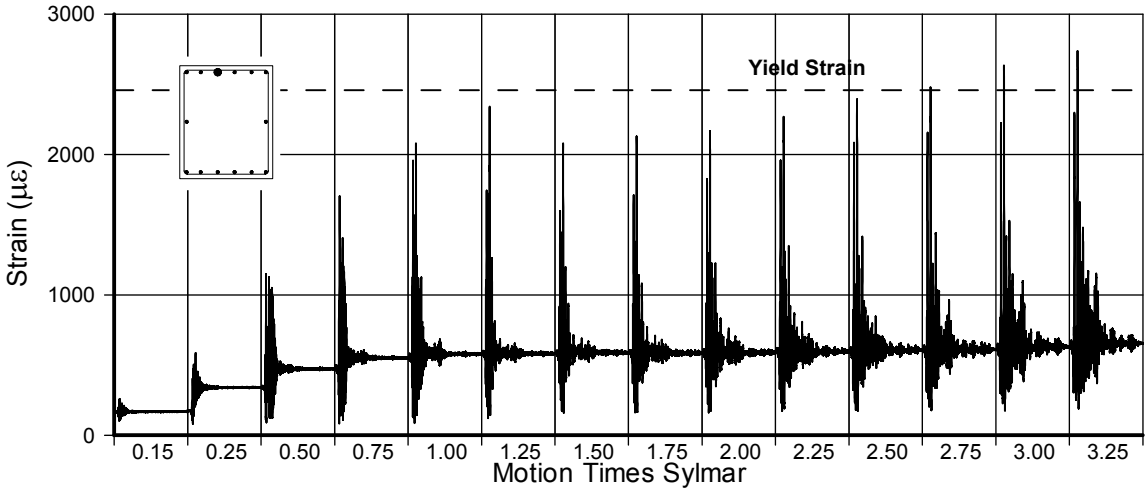

Fig. A-351 - Measured Strain in Gauge No. 99 for SFCD2

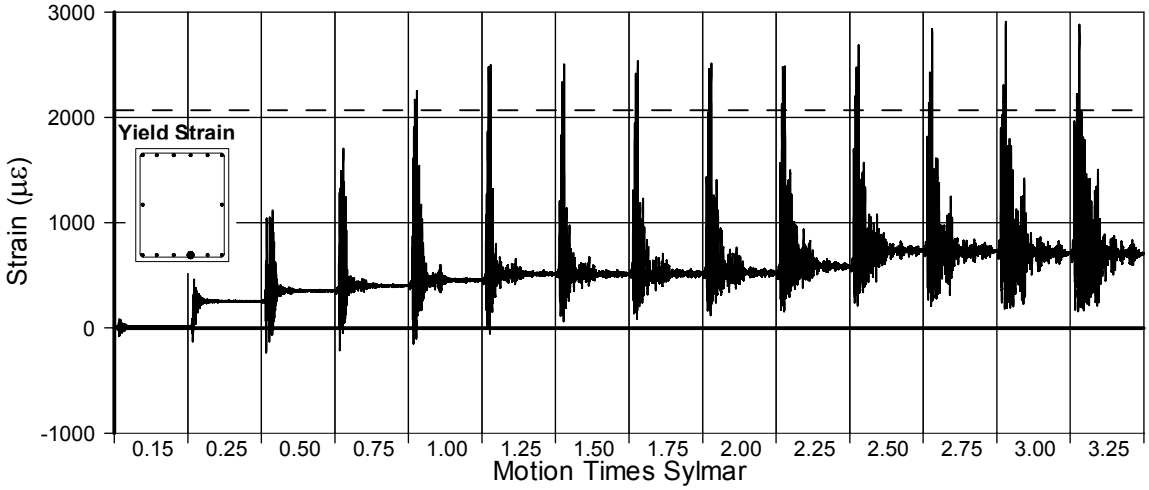

Fig. A-352 - Measured Strain in Gauge No. 100 for SFCD2

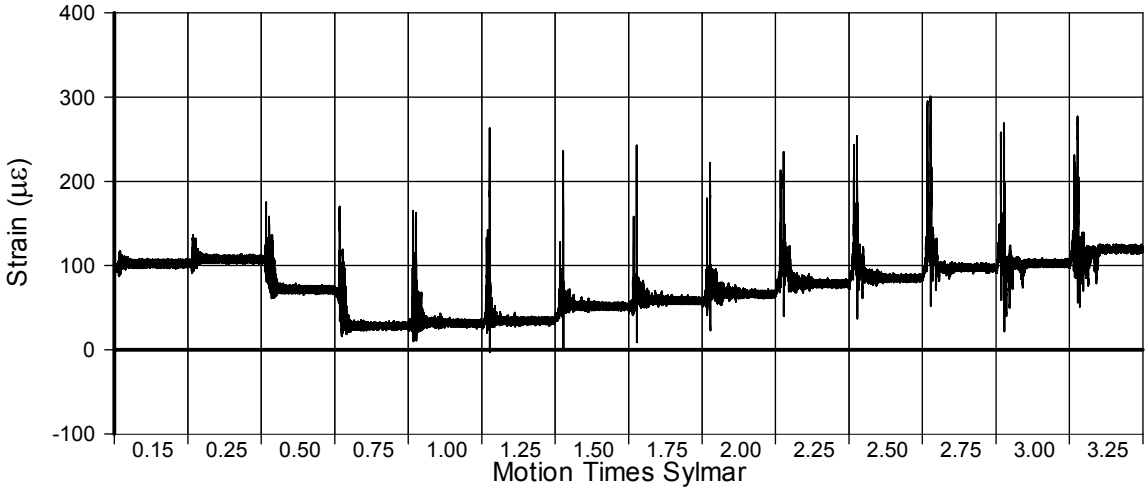

Fig. A-353 - Measured Strain in Gauge No. 101 for SFCD2

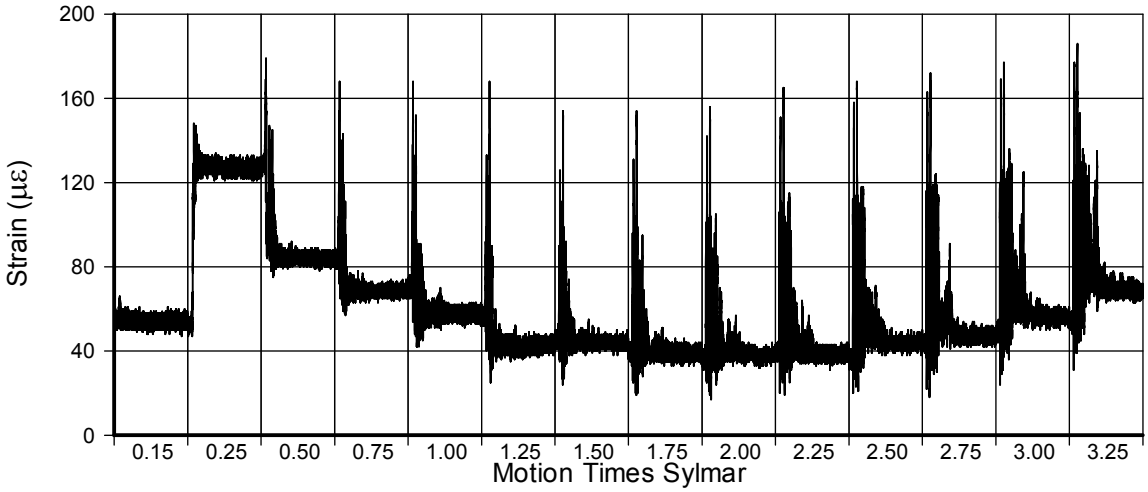

Fig. A-354 - Measured Strain in Gauge No. 102 for SFCD2

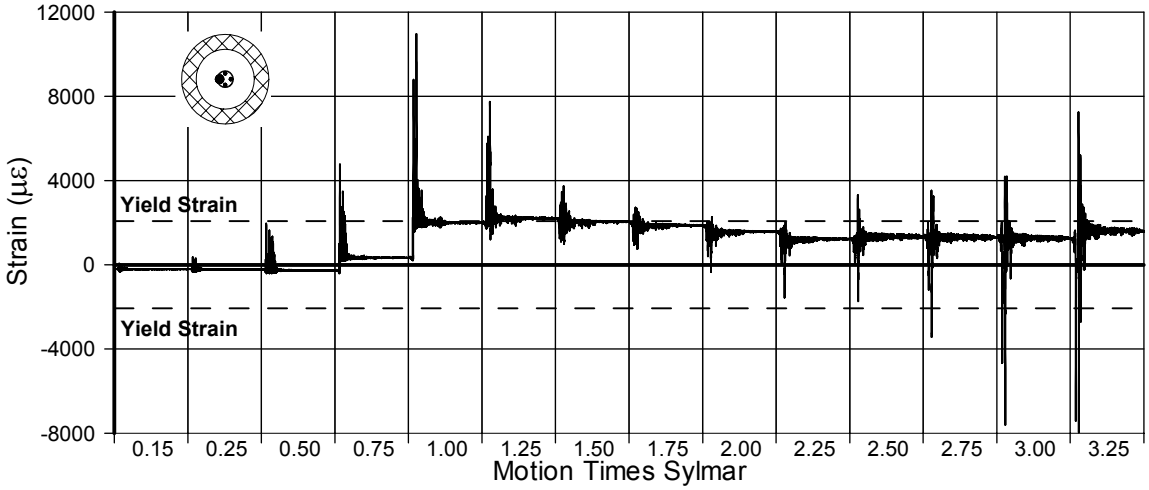

Fig. A-355 - Measured Strain in Gauge No. 103 for SFCD2

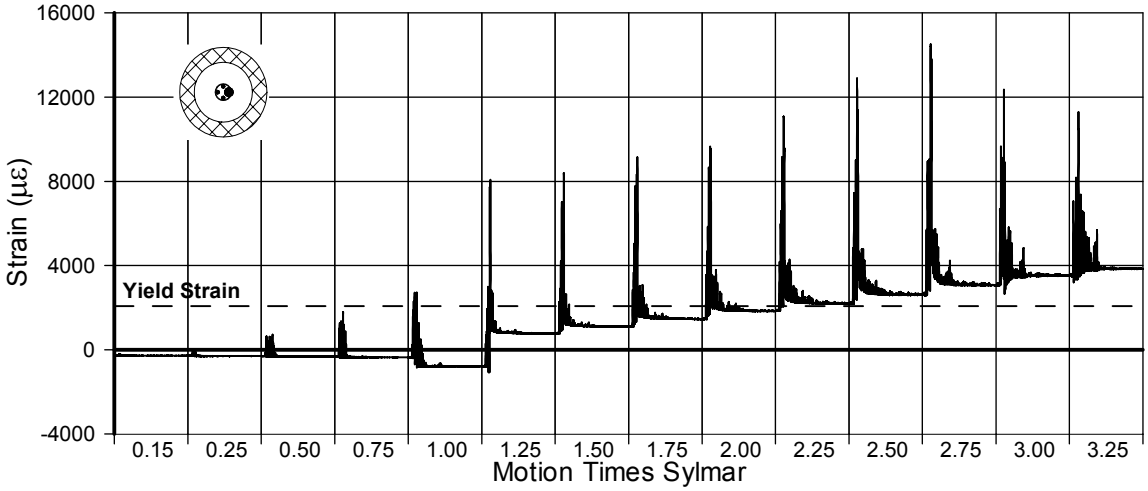

Fig. A-356 - Measured Strain in Gauge No. 104 for SFCD2

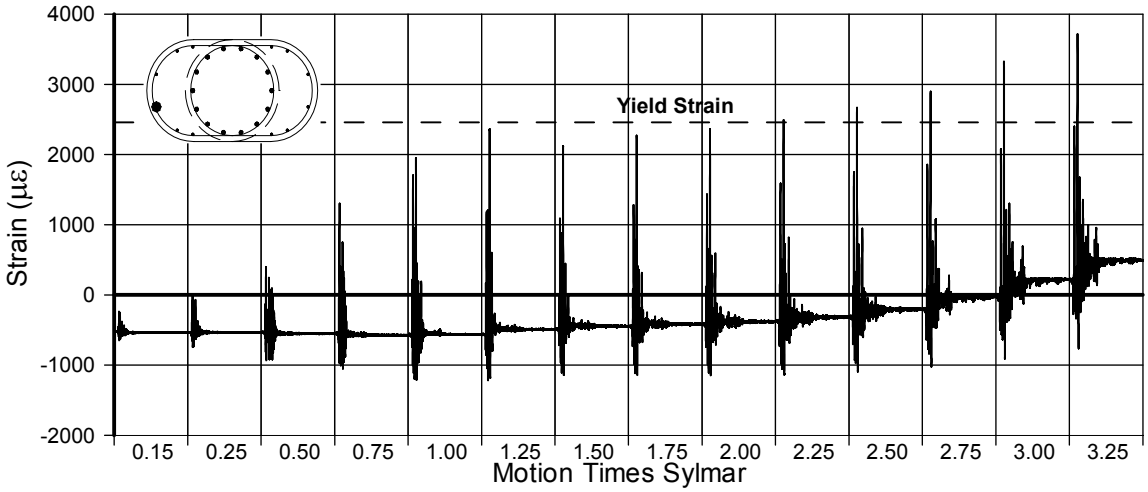

Fig. A-357 - Measured Strain in Gauge No. 105 for SFCD2

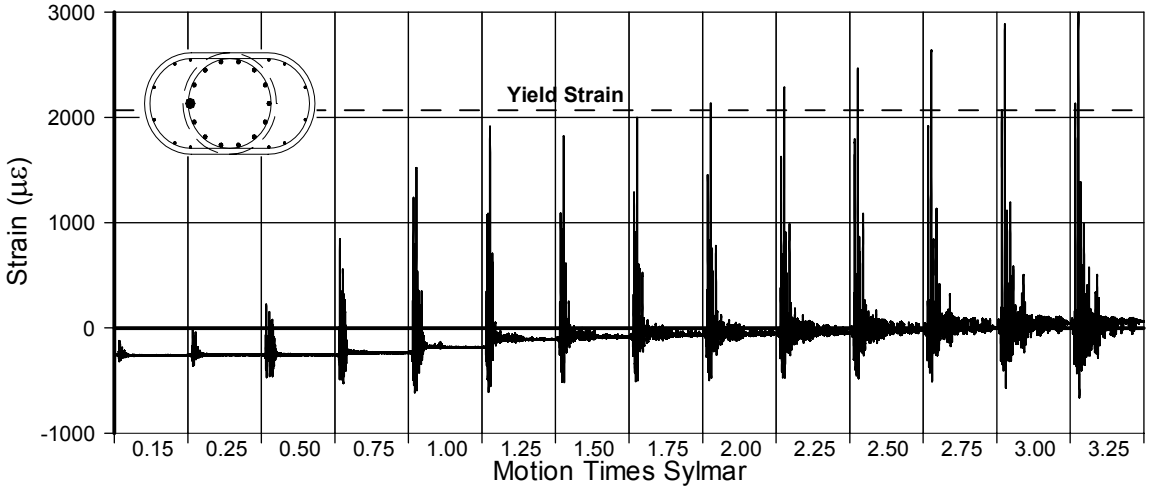

Fig. A-358 - Measured Strain in Gauge No. 106 for SFCD2

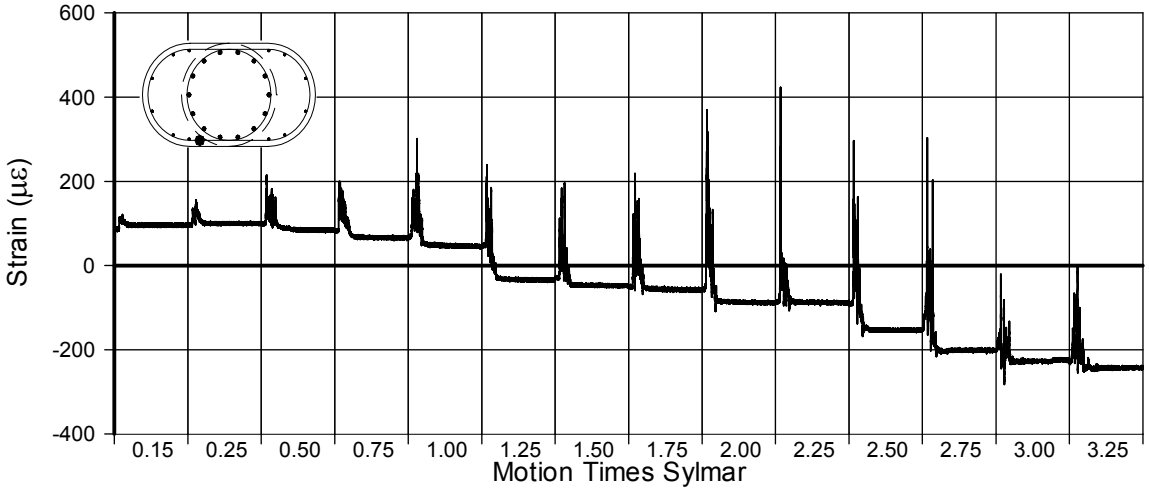

Fig. A-359 - Measured Strain in Gauge No. 107 for SFCD2

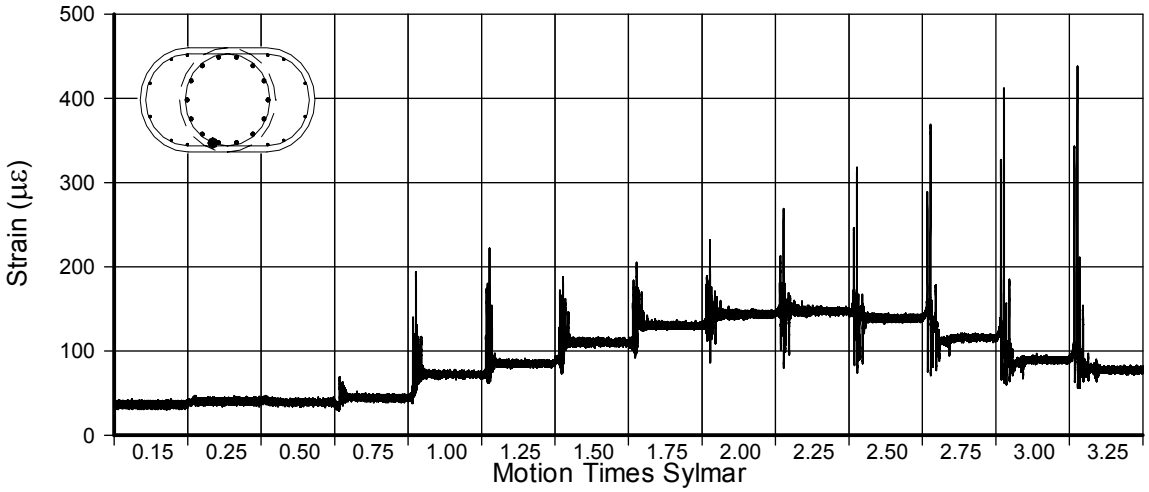

Fig. A-360 - Measured Strain in Gauge No. 108 for SFCD2

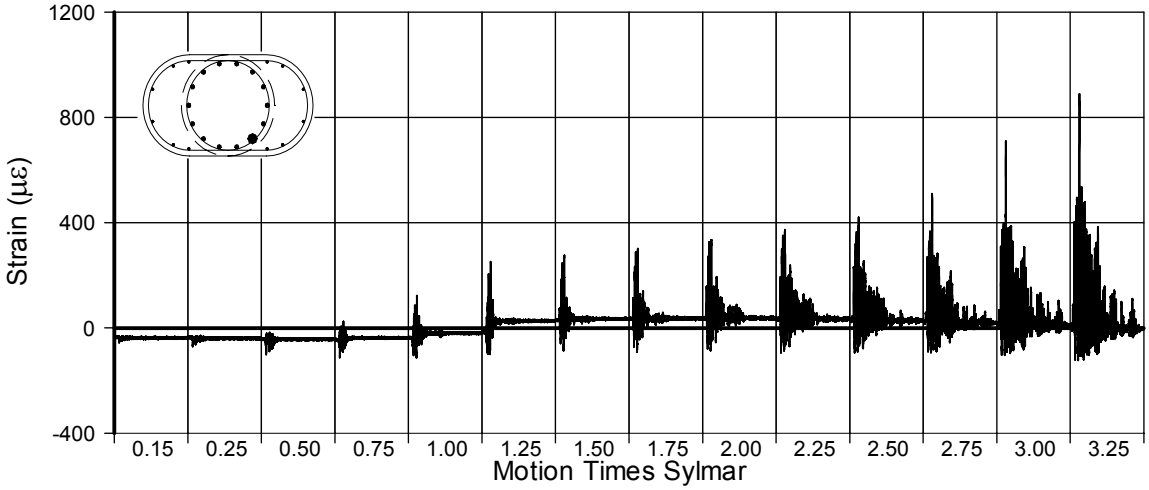

Fig. A-361 - Measured Strain in Gauge No. 109 for SFCD2

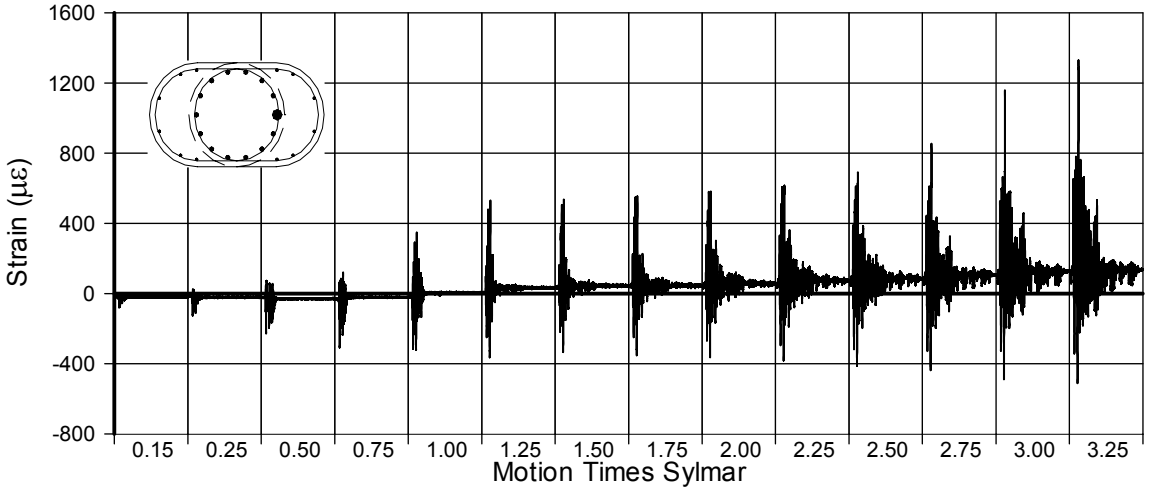

Fig. A-362 - Measured Strain in Gauge No. 110 for SFCD2

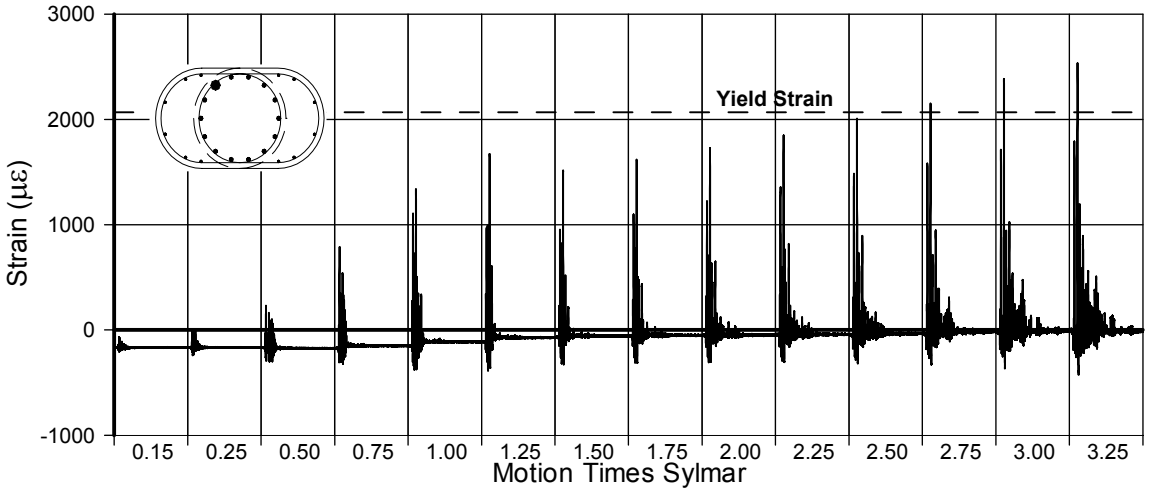

Fig. A-363 - Measured Strain in Gauge No. 111 for SFCD2

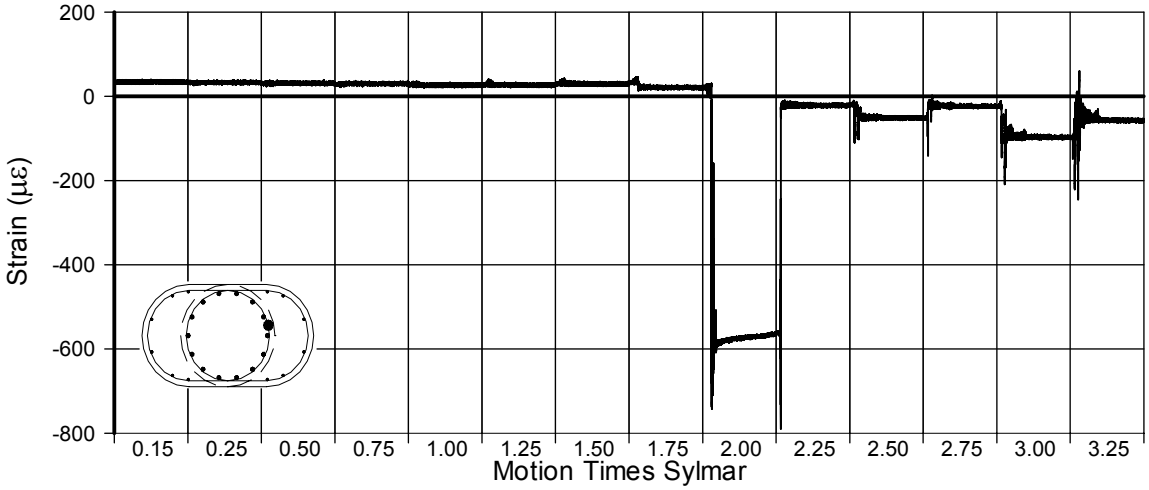

Fig. A-364 - Measured Strain in Gauge No. 112 for SFCD2

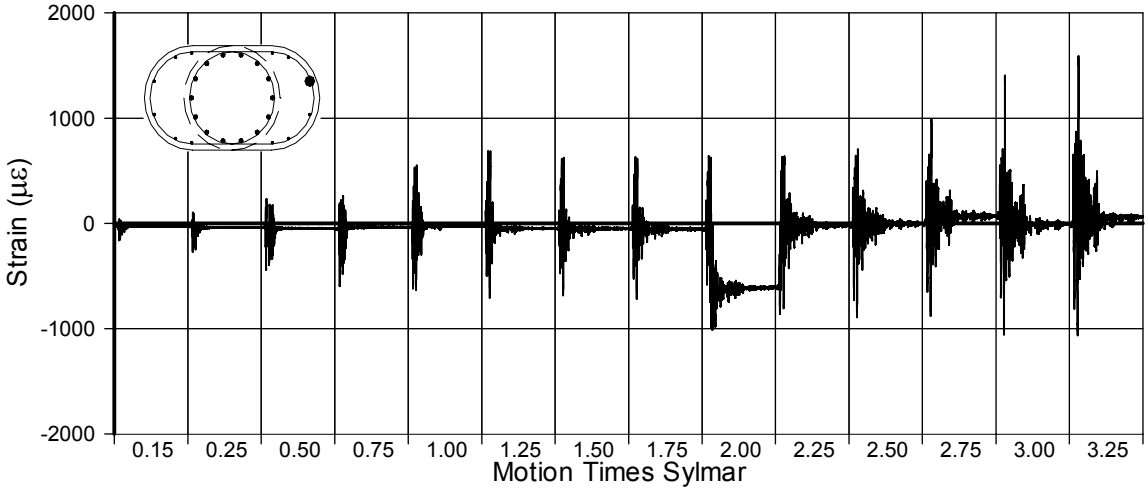

Fig. A-365 - Measured Strain in Gauge No. 113 for SFCD2

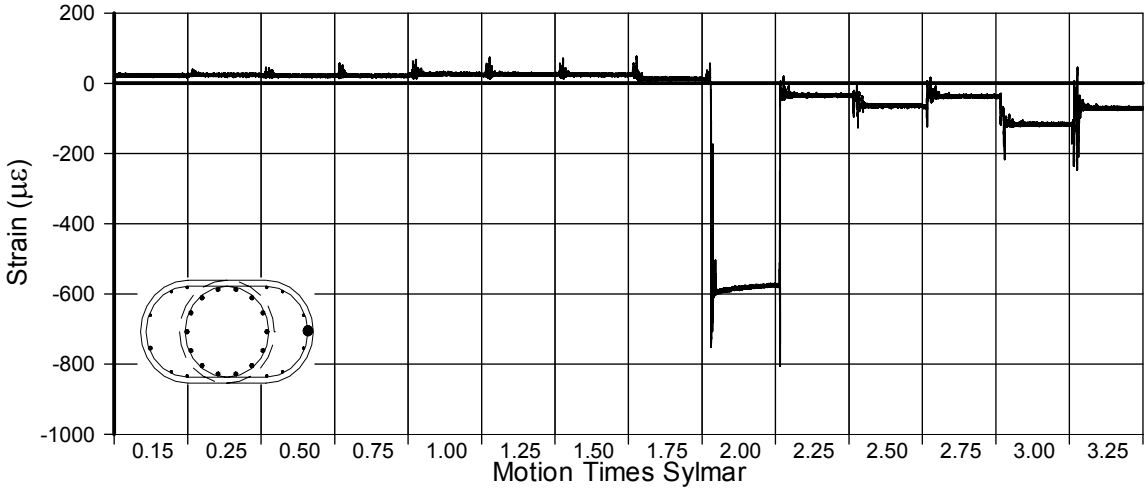

Fig. A-366 - Measured Strain in Gauge No. 114 for SFCD2

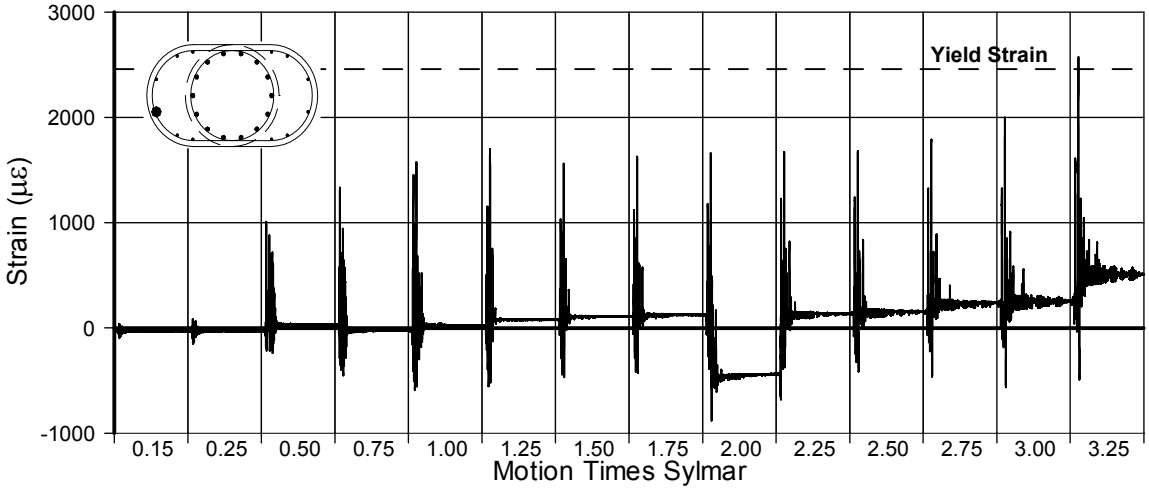

Fig. A-367 - Measured Strain in Gauge No. 115 for SFCD2

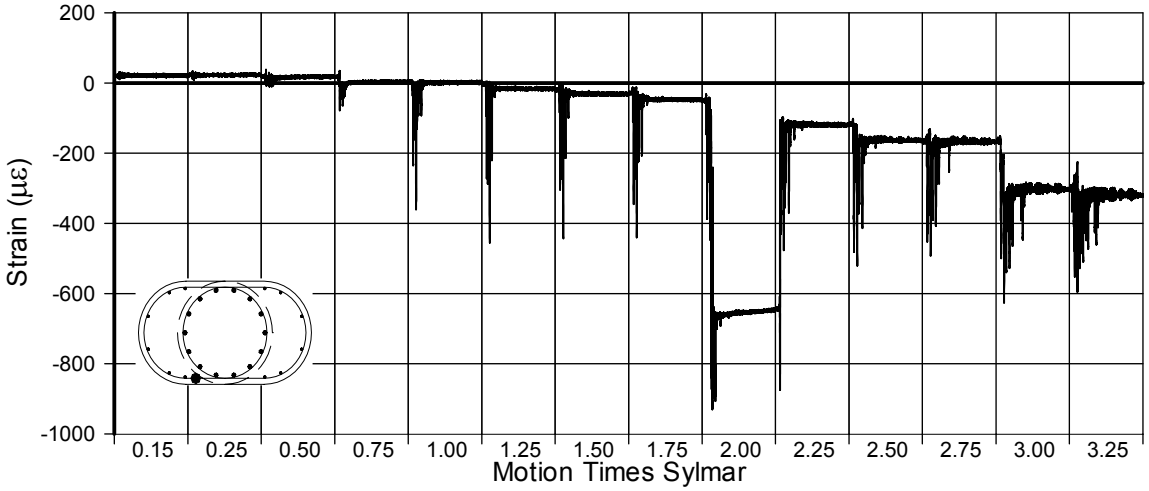

Fig. A-368 - Measured Strain in Gauge No. 116 for SFCD2

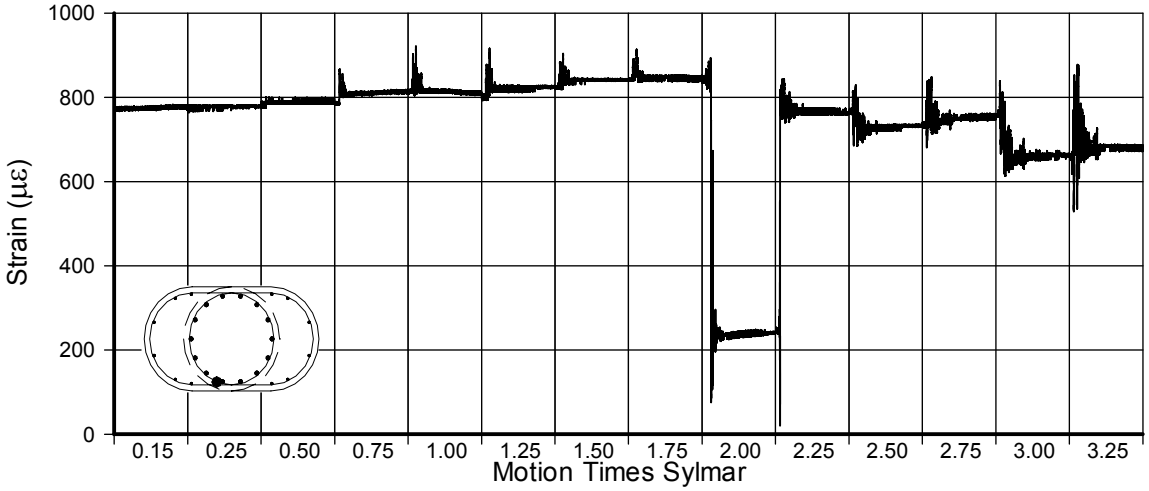

Fig. A-369 - Measured Strain in Gauge No. 117 for SFCD2

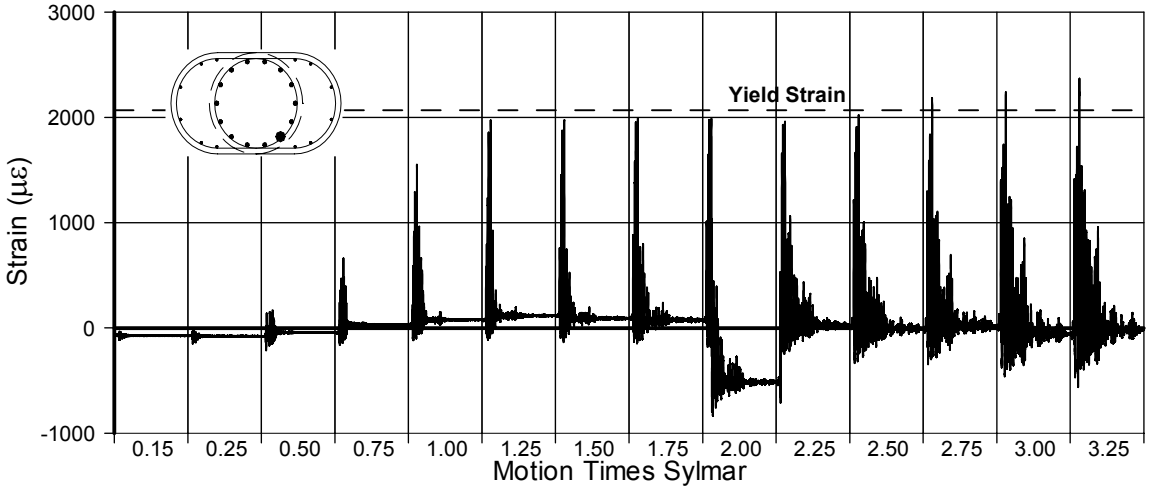

Fig. A-370 - Measured Strain in Gauge No. 118 for SFCD2

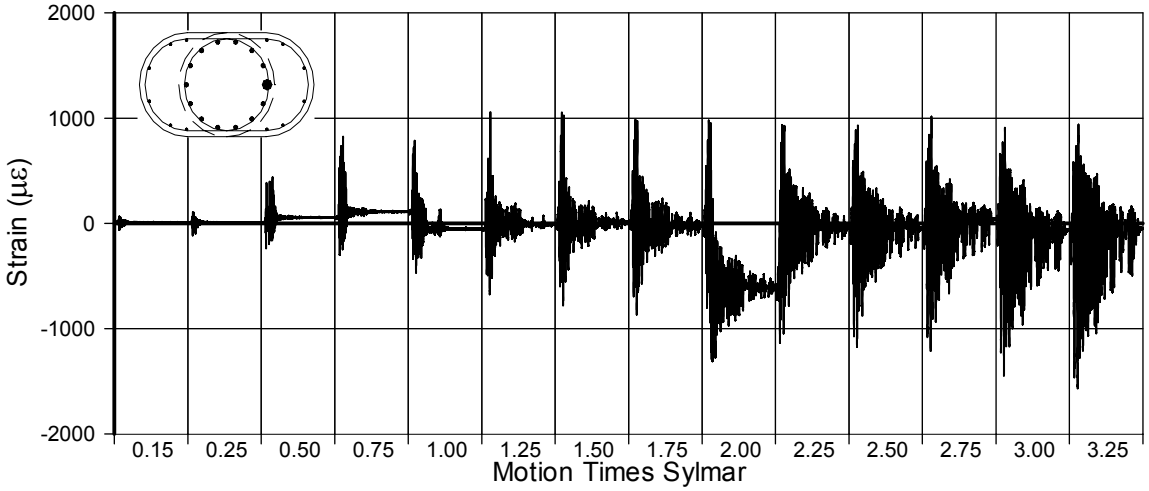

Fig. A-371 - Measured Strain in Gauge No. 119 for SFCD2

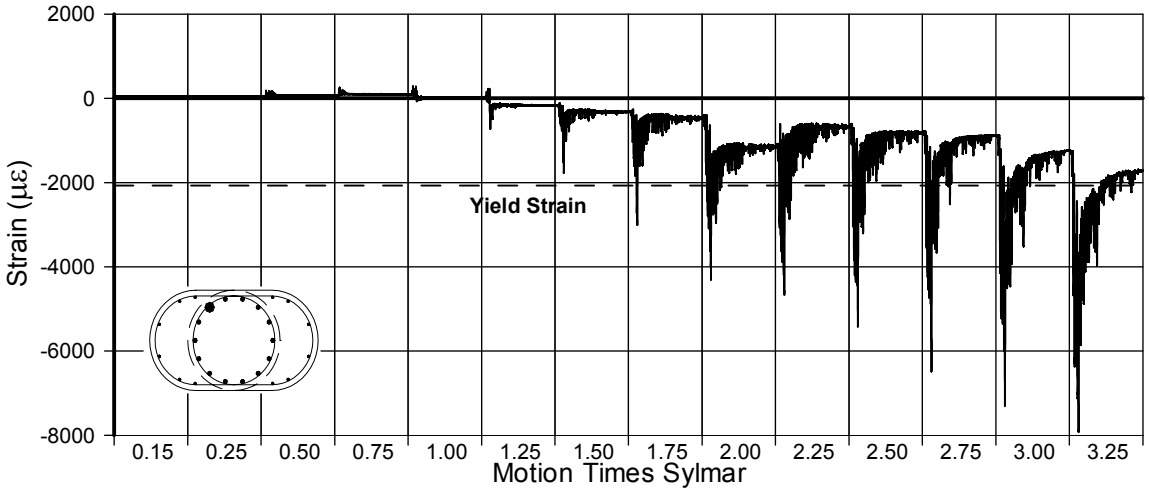

Fig. A-372 - Measured Strain in Gauge No. 121 for SFCD2

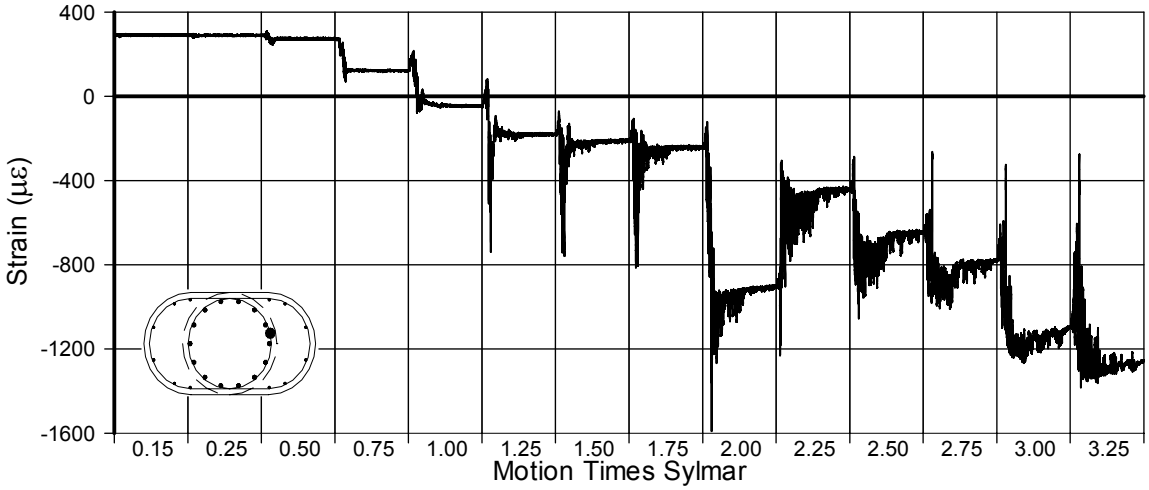

Fig. A-373 - Measured Strain in Gauge No. 122 for SFCD2

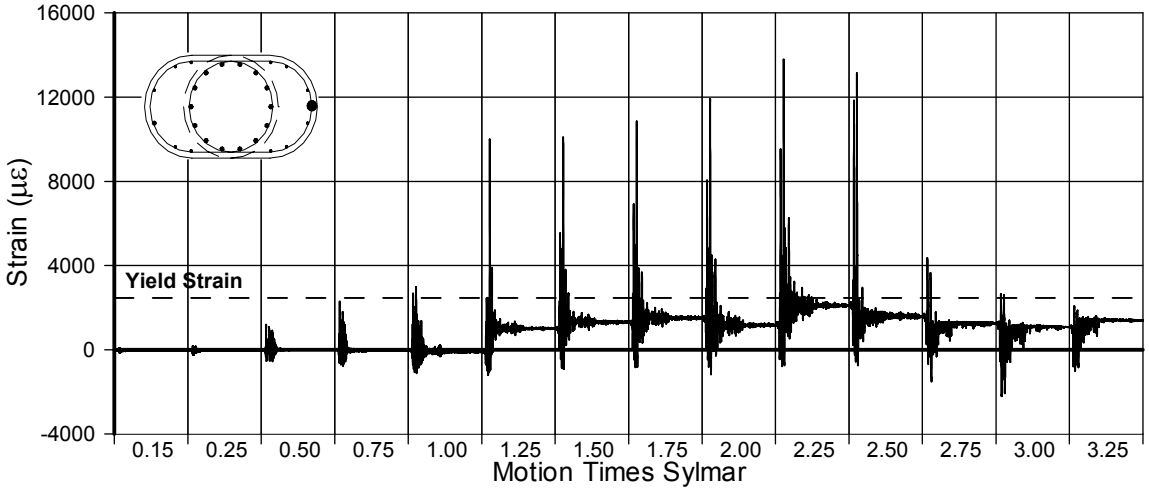

Fig. A-374 - Measured Strain in Gauge No. 123 for SFCD2

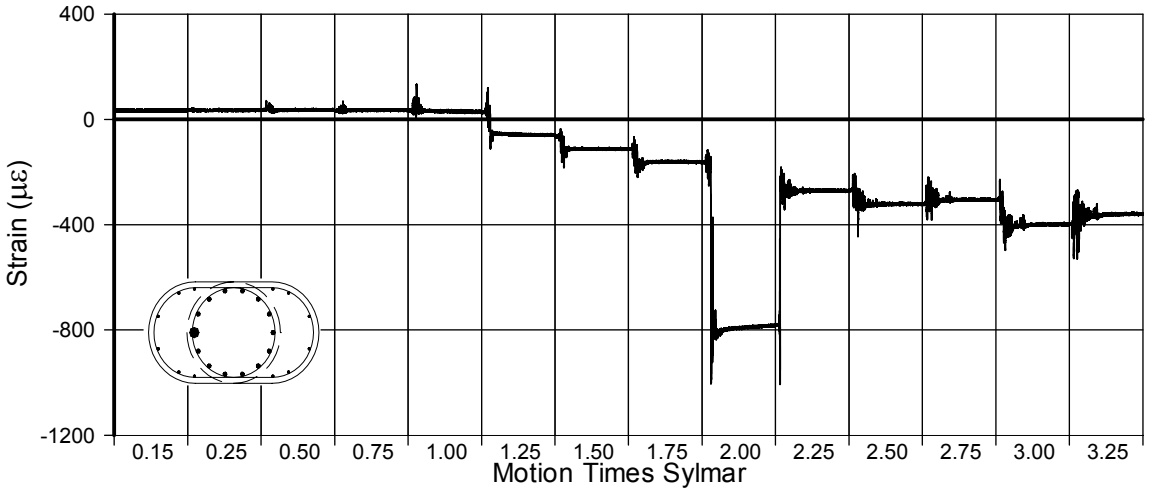

Fig. A-375 - Measured Strain in Gauge No. 124 for SFCD2

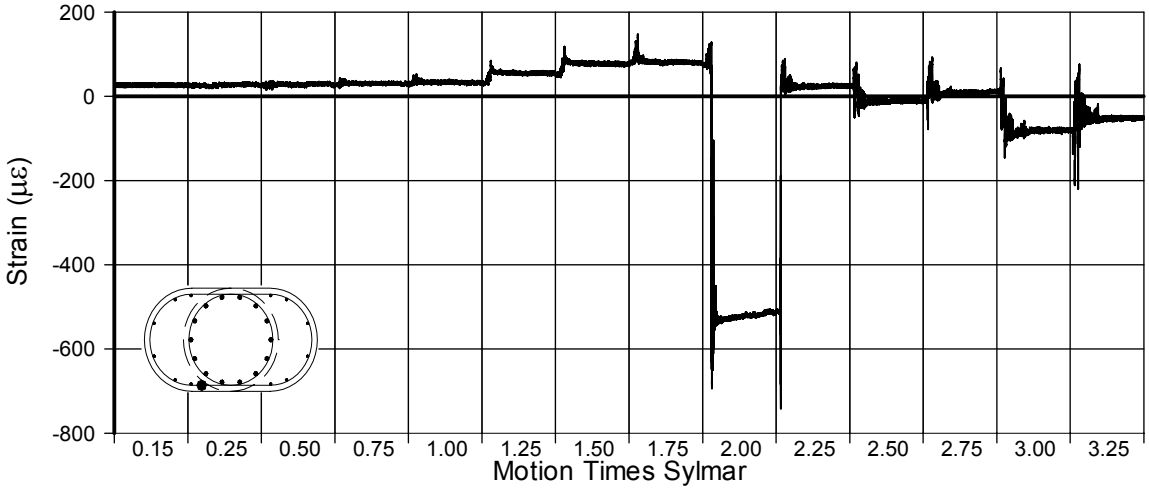

Fig. A-376 - Measured Strain in Gauge No. 125 for SFCD2

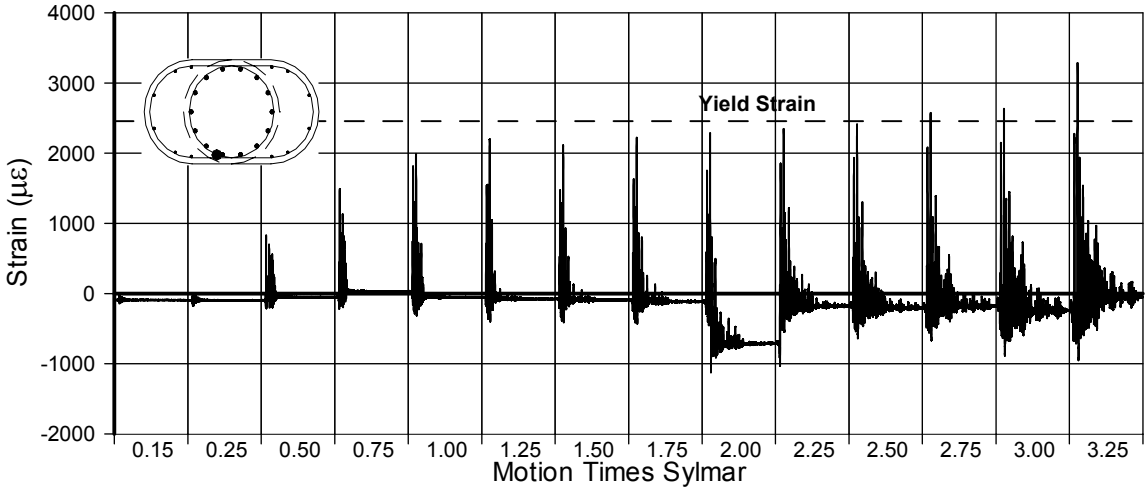

Fig. A-377 - Measured Strain in Gauge No. 126 for SFCD2

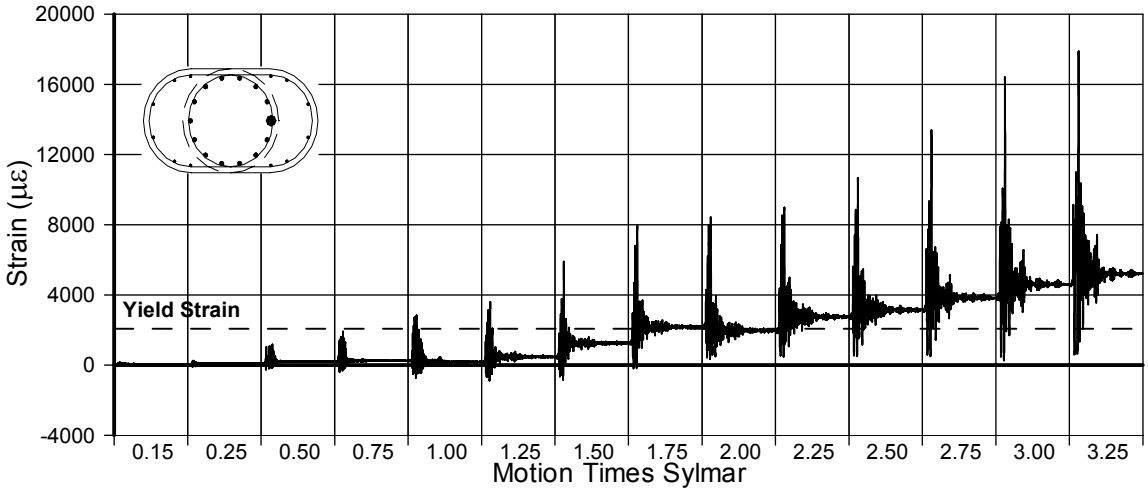

Fig. A-378 - Measured Strain in Gauge No. 128 for SFCD2

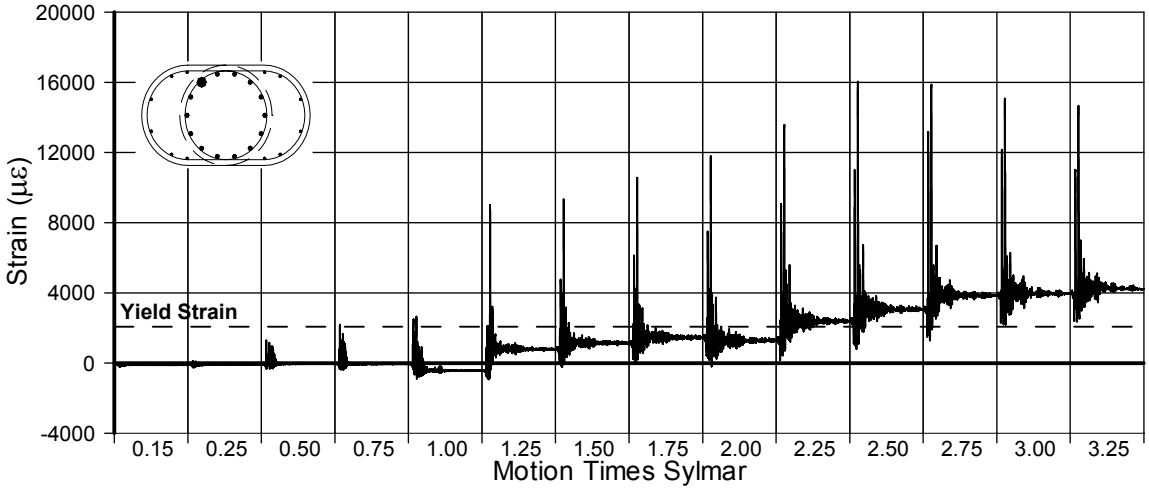

Fig. A-379 - Measured Strain in Gauge No. 129 for SFCD2

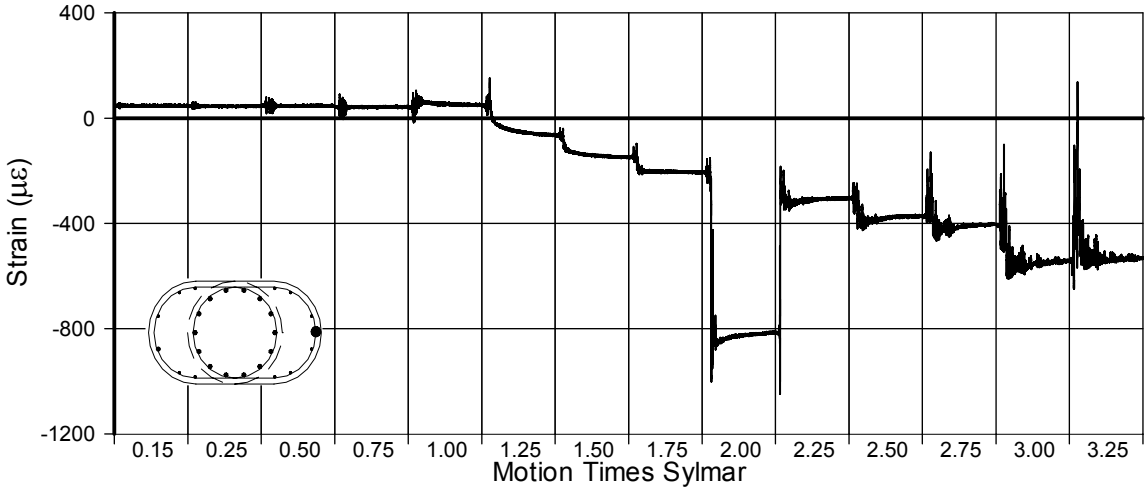

Fig. A-380 - Measured Strain in Gauge No. 130 for SFCD2

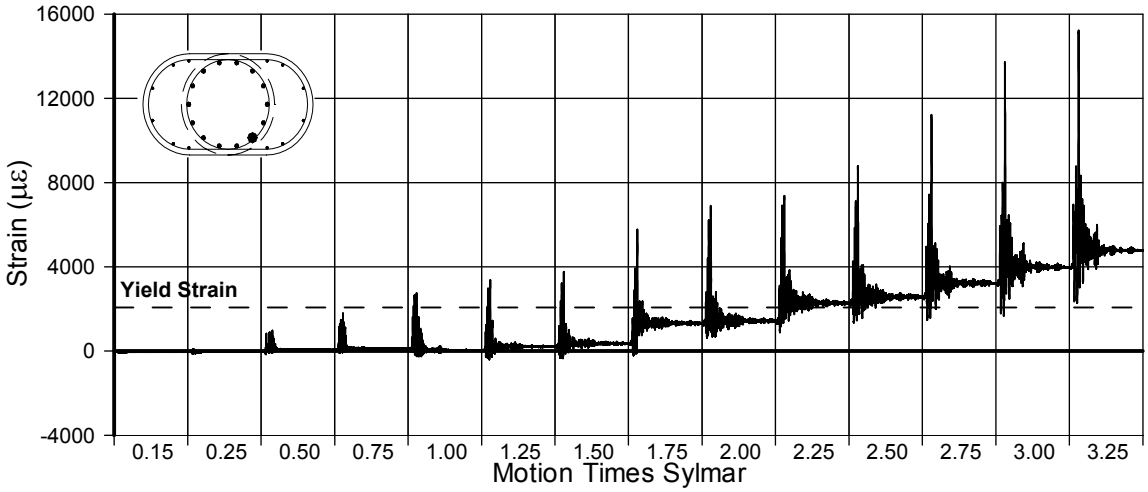

Fig. A-381 - Measured Strain in Gauge No. 131 for SFCD2

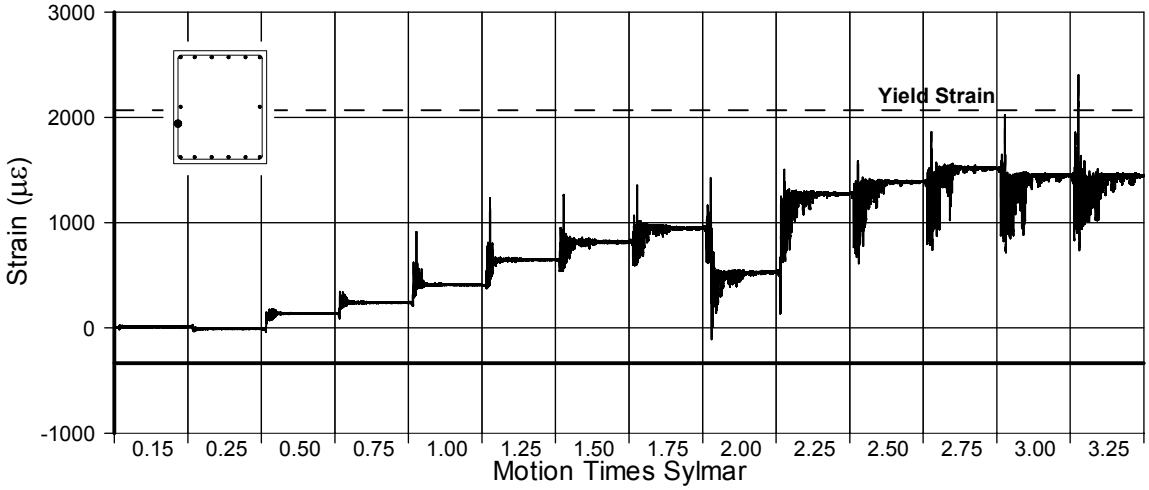

Fig. A-382 - Measured Strain in Gauge No. 133 for SFCD2

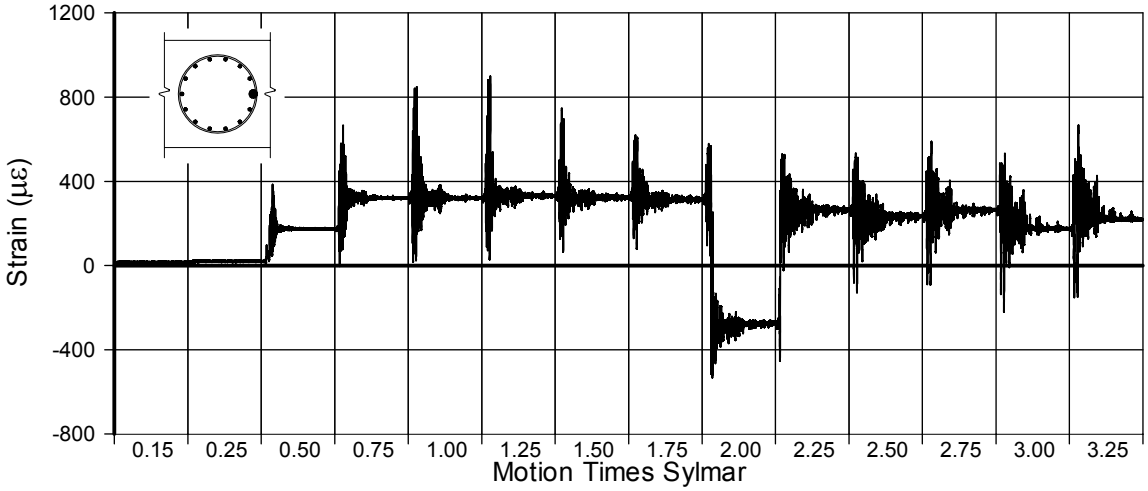

Fig. A-383 - Measured Strain in Gauge No. 134 for SFCD2

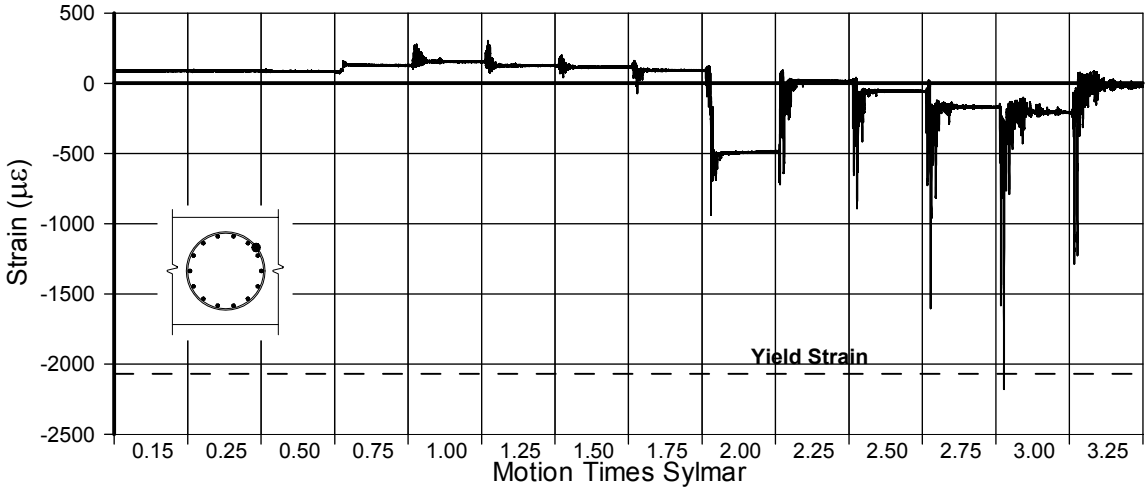

Fig. A-384 - Measured Strain in Gauge No. 135 for SFCD2

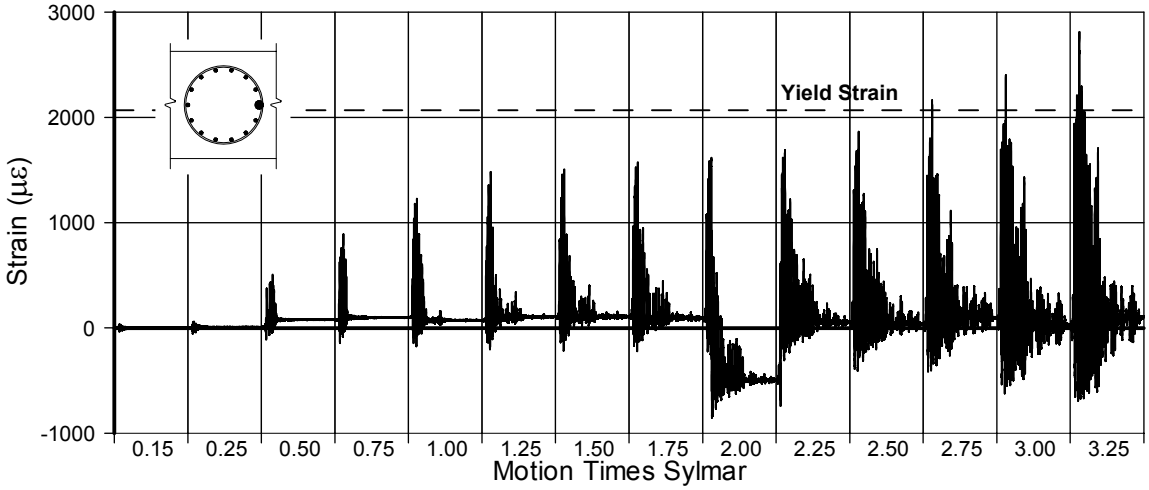

Fig. A-385 - Measured Strain in Gauge No. 136 for SFCD2

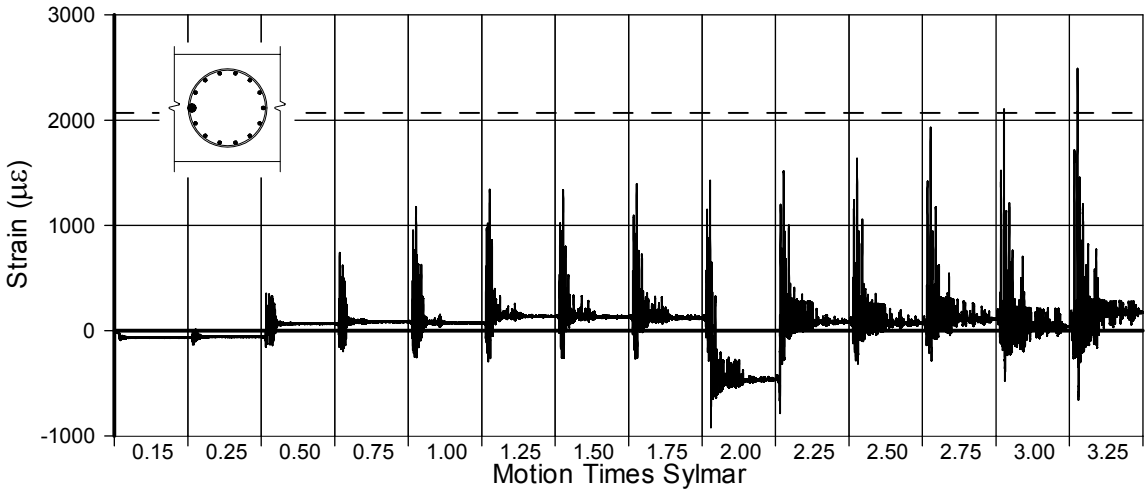

Fig. A-386 - Measured Strain in Gauge No. 137 for SFCD2

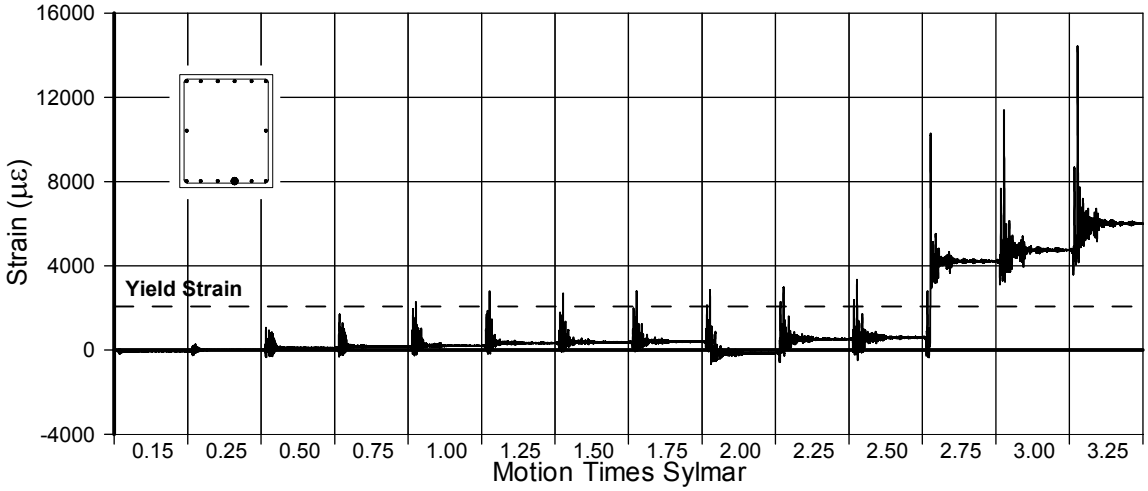

Fig. A-387 - Measured Strain in Gauge No. 138 for SFCD2

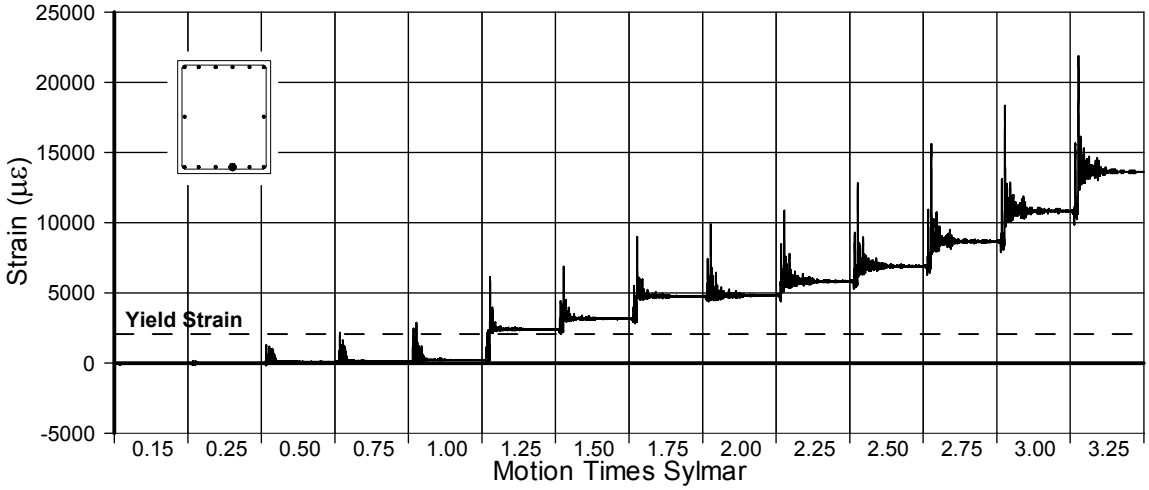

Fig. A-388 - Measured Strain in Gauge No. 139 for SFCD2

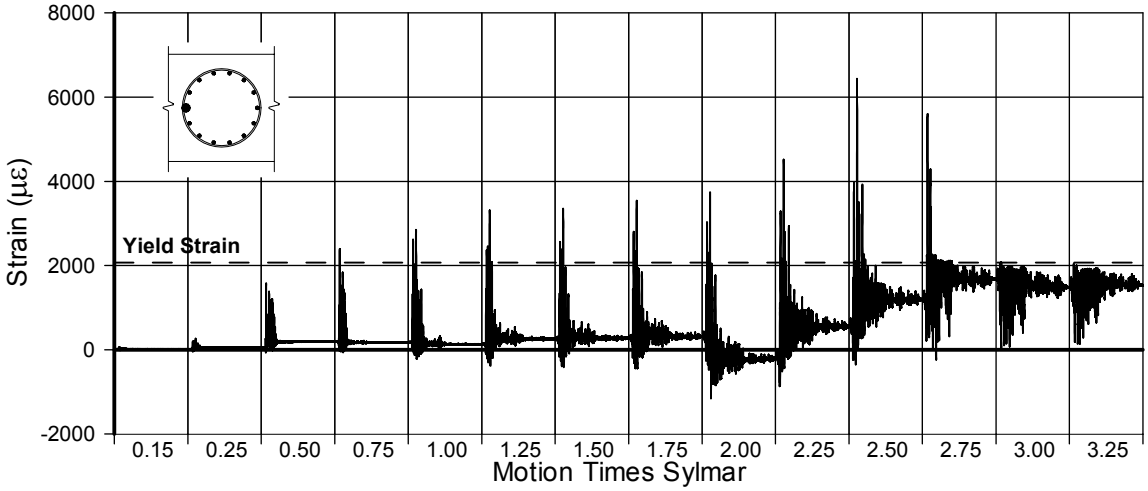

Fig. A-389 - Measured Strain in Gauge No. 140 for SFCD2

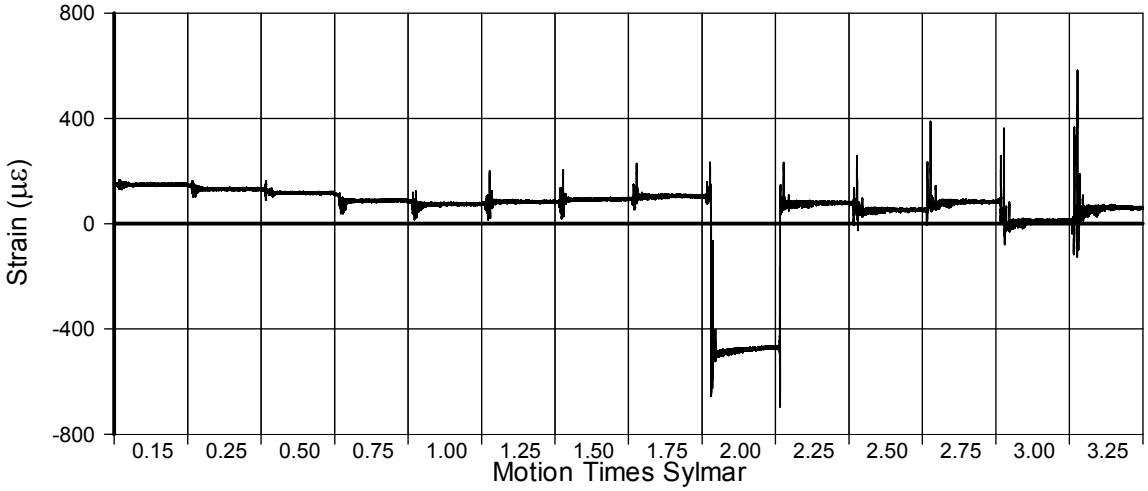

Fig. A-390 - Measured Strain in Gauge No. 141 for SFCD2

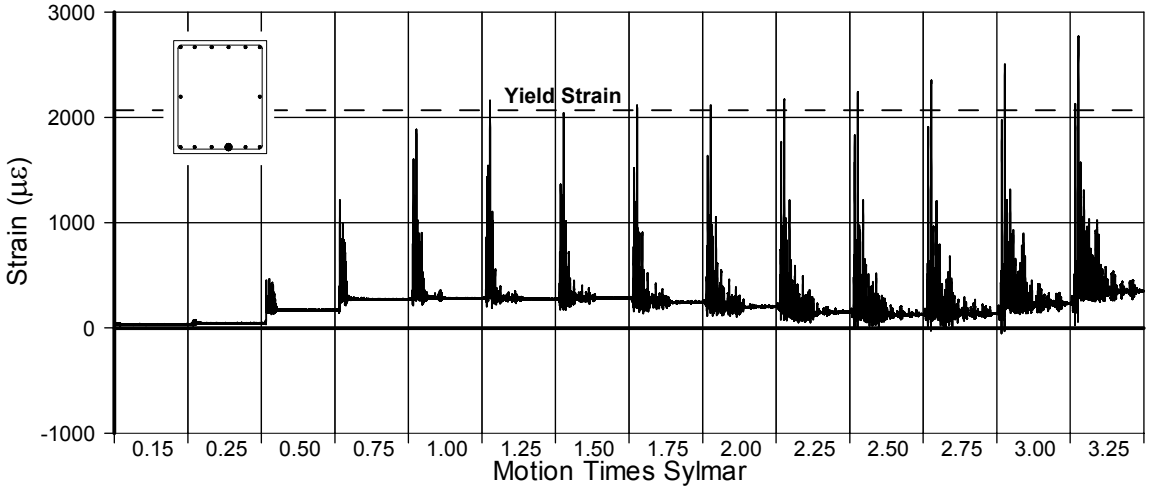

Fig. A-391 - Measured Strain in Gauge No. 144 for SFCD2

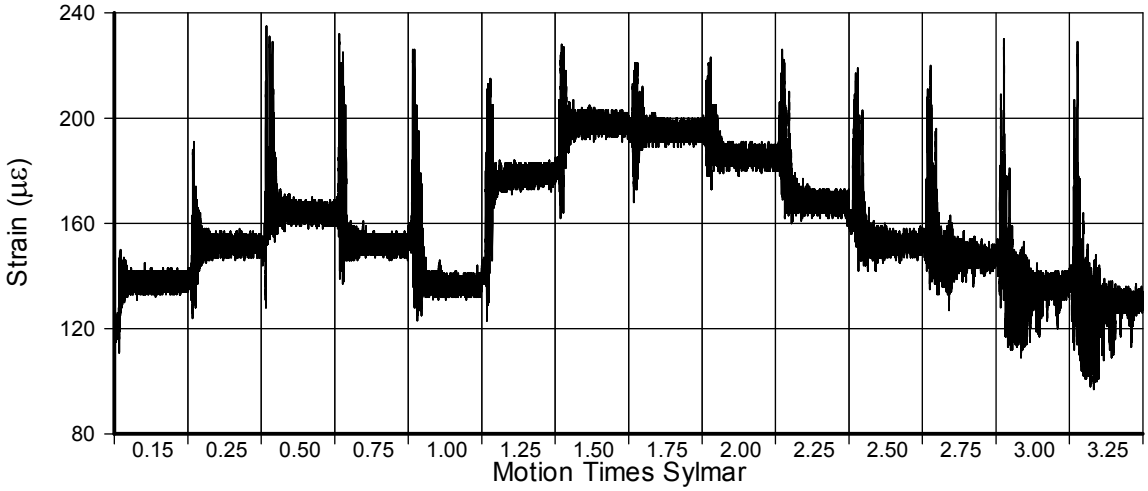

Fig. A-392 - Measured Strain in Gauge No. 145 for SFCD2

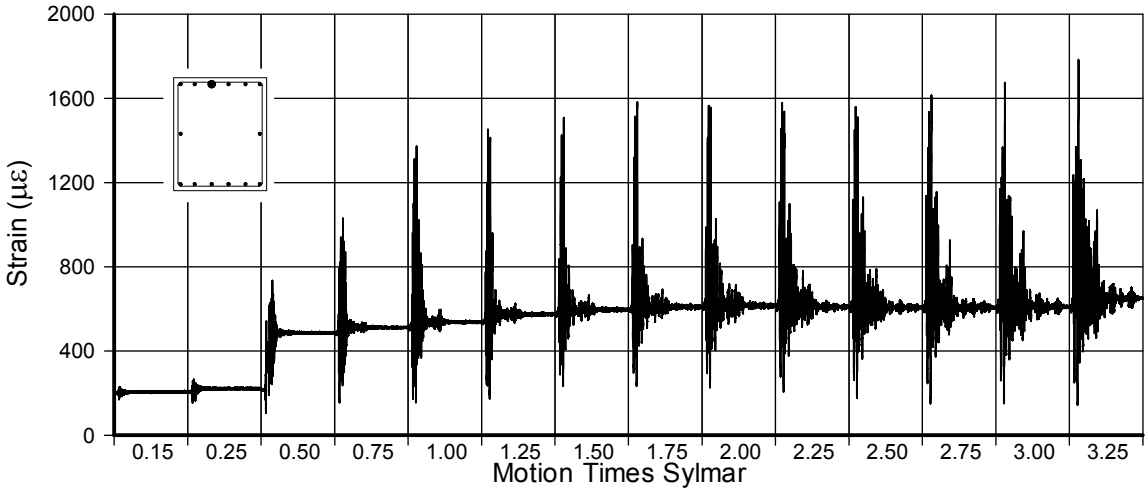

Fig. A-393 - Measured Strain in Gauge No. 146 for SFCD2

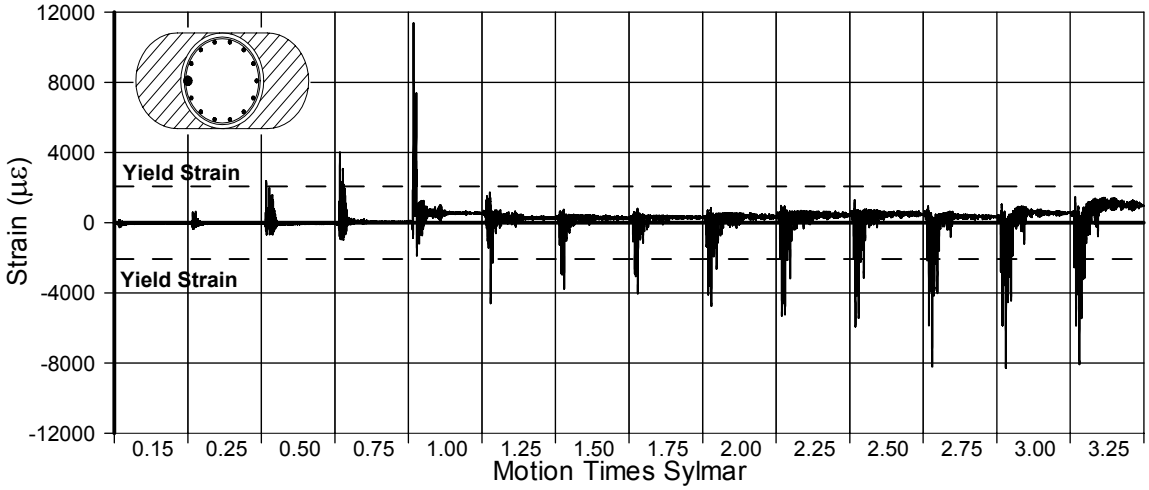

Fig. A-394 - Measured Strain in Gauge No. 148 for SFCD2

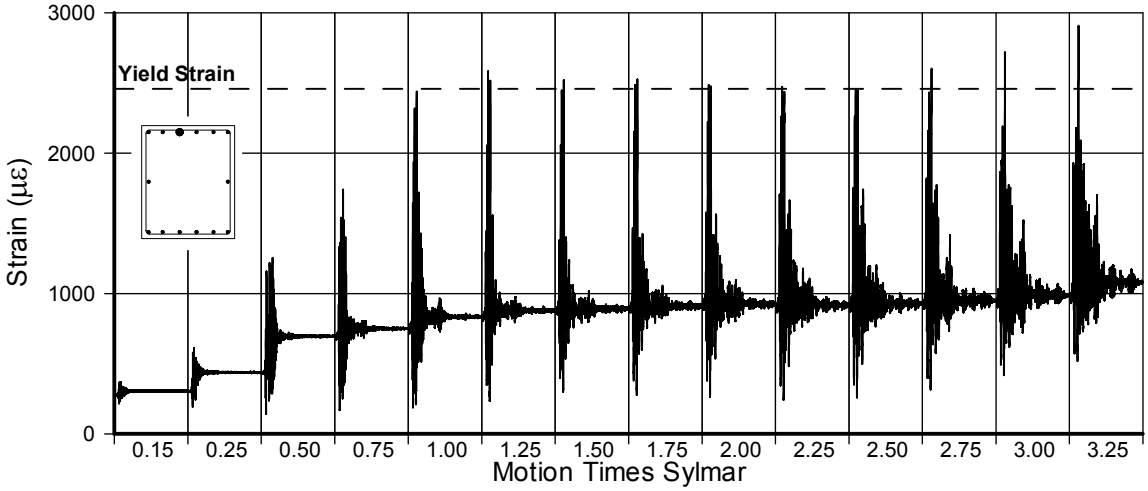

Fig. A-395 - Measured Strain in Gauge No. 149 for SFCD2

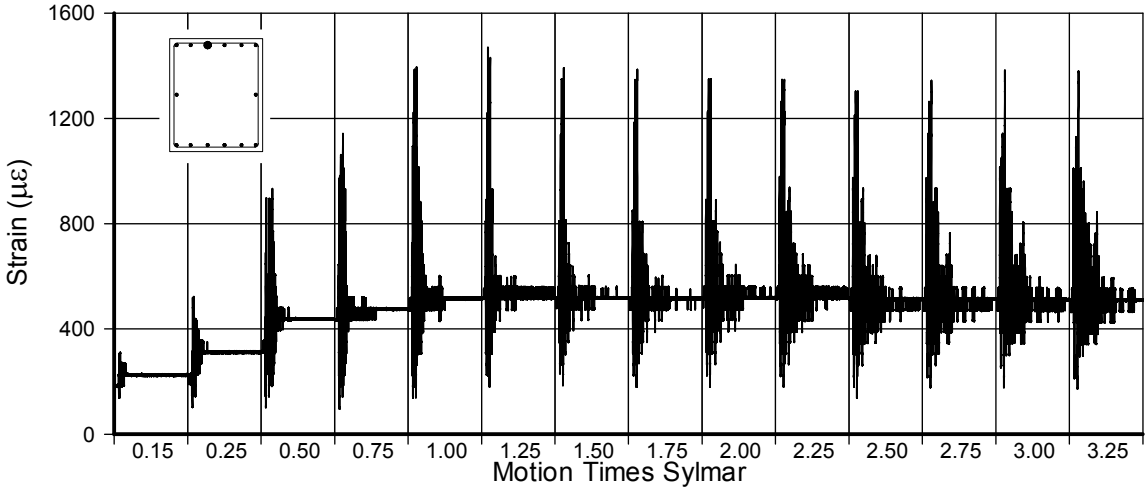

Fig. A-396 - Measured Strain in Gauge No. 150 for SFCD2

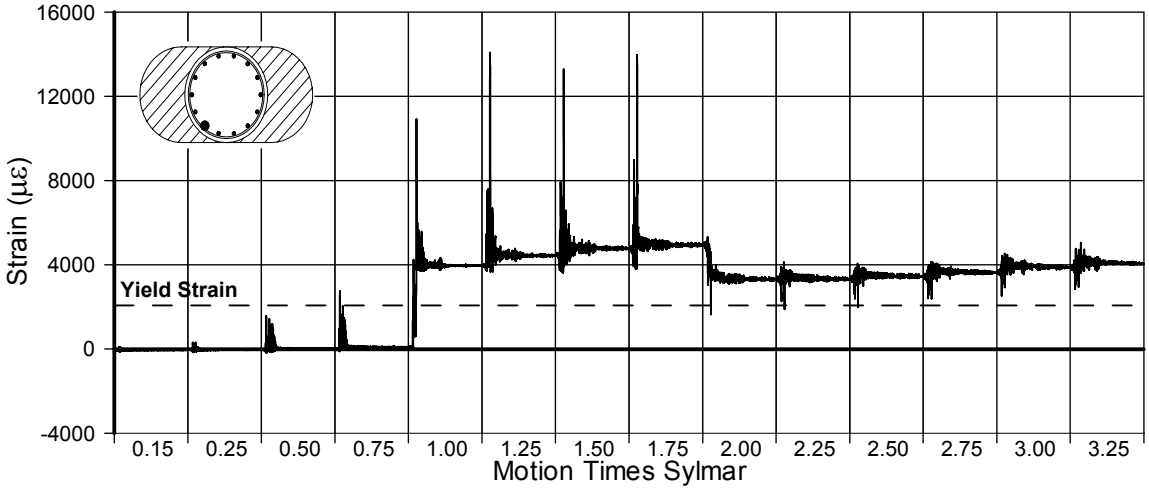

Fig. A-397 - Measured Strain in Gauge No. 151 for SFCD2

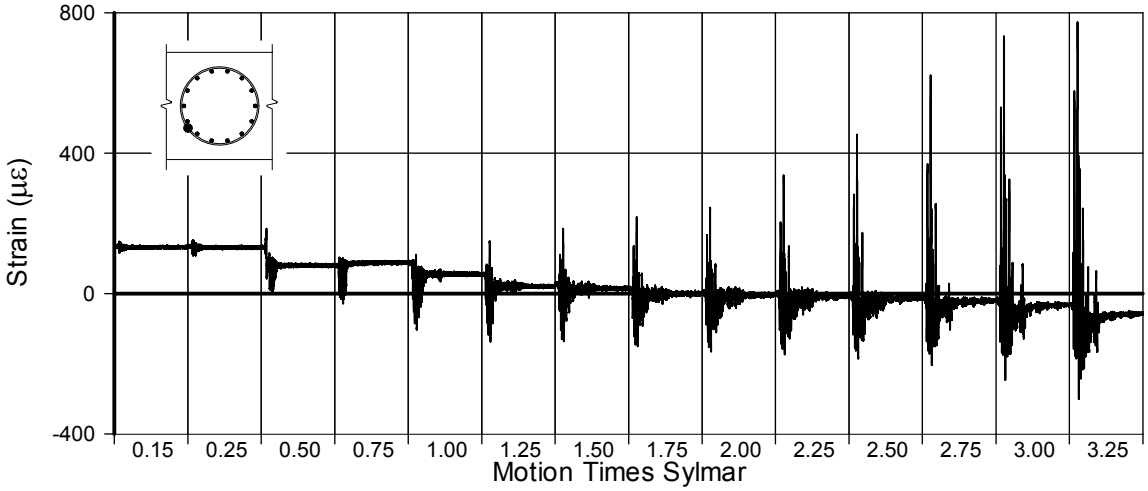

Fig. A-398 - Measured Strain in Gauge No. 152 for SFCD2

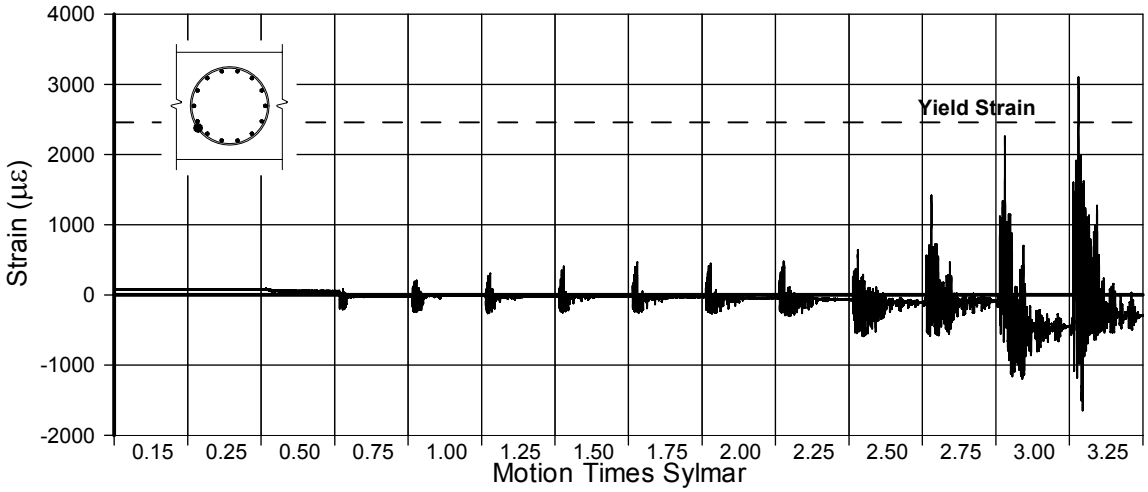

Fig. A-399 - Measured Strain in Gauge No. 153 for SFCD2